DESIGNING AND BUILDING THE EVRYSCOPES, FAST TRANSIT SEARCH RESULTS

Jeffrey K. Ratzloff

A dissertation submitted to the faculty at the University of North Carolina at Chapel Hill in partial fulfillment of the requirements for the degree of Doctor of Philosophy in the Department of Physics and Astronomy.

Chapel Hill
2020

Approved by:

Nicholas Law

Brad Barlow

Fabian Heitsch

Christian Iliadis

Dan Reichart

ABSTRACT

Jeffrey K. Ratzloff: Designing and Building the Evryscopes, Fast Transit Search Results.
(Under the direction of Nicholas Law)

Fast astronomical events offer a window into exciting stellar, binary, and planetary astrophysics that enhance our understanding of stellar formation and evolution, binary interaction, planet characteristics, and lead to new discoveries of object types not seen before. Typically the events are very rare, from a combination of factors - the astrophysical causes are infrequent *and* the sources with these types of events are rare *and* the objects are observationally challenging. Leading-edge research areas include hot subdwarf (HSD – small, dense stars, under-luminous for their high temperatures) transits or eclipses (from a gas planet or compact star), white dwarf (WD – final stage stellar remnants) transits, late dwarf star transits, and a host of sought after fast transient events including high-amplitude flares and supernovae.

Our solution to the challenges of detecting fast transits, eclipses, and transients is the Evryscope - a new type of telescope that monitors the entire sky, continuously, and at high cadence, with good resolution. The first part of this work describes the Evryscope concept and how the wide field-of-view, observation strategy, and 2-minute images provide sensitivity to the sought after fast events while seeing enough rare targets necessary for detection. We describe the design process, the 3-D models created to test and finalize the design, the construction and deployment. We also describe the innovative camera and optics automated alignment system (the Robotilters), critical in reaching the level of image quality necessary to support our science goals.

The second part of this dissertation work presents three fast transit surveys (Polar, WD and HSD) conducted with Evryscope light curves. We discovered numerous HSD reflection

effect and eclipsing binaries, and peculiar variability. Two of the discoveries (both compact binaries with remnant stellar cores) are new-class objects. EVR-CB-001 is a progenitor system that will likely merge into a *single* HSD (single HSDs are observed and predicted but progenitor systems have been elusive). The primary of EVR-CB-004 is likely a HSD that has exhausted its core fuel and is in the short-lived final shell burning stage predicted by stellar evolution models but not seen before in a compact WD + HSD system.

To my parents, the older I get the more I appreciate you.

ACKNOWLEDGMENTS

First let me acknowledge and thank my adviser, Dr. Nicholas Law for his guidance, wisdom, and patience throughout the Evryscope project. It has been rewarding to work with you to complete the many goals we set for ourselves, and to see the instrument we made begin to contribute to the astronomy community in a variety of different fields.

To Dr. Brad Barlow: Your guidance on the hot subdwarf survey and followup work was invaluable. Thank you for the continued advice and help, and I look forward to continued collaborations on more hot subdwarf discoveries.

Christian Illiadis and Fabian Heitsch were extremely helpful in their advice throughout the PhD process, and I appreciate the thoughtful feedback on my research.

Thank you to Dan Reichart for your advice especially on the followup of our discovery targets, and the generous support of the PROMPT telescopes.

I would like to acknowledge our collaborators for their expertise in hot subdwarfs, model fitting, spectra and RV analysis, and stellar evolution. Brad Barlow: for all things hot subdwarf and for being an excellent collaborator. Thomas Kupfer: thank you for all the help on the EVR-CB-001 and EVR-CB-004 projects. Veronika Schaffenroth: for all of your help on the HW Vir discoveries. Thank you to Kyle Corcoran, Evan Bauer, Stephen Walser, and Péter Németh for your contributions to the hot subdwarf papers. To David Schneider, Stephan Geier, Tom Marsh, and Uli Heber: I appreciate the thoughtful advice and contributions in helping to understand our compact binary discoveries.

To the Clemens group (and in particular Erik Dennihy) for your help with the SOAR telescope and Goodman spectrograph.

To Robert Quimby for the opportunity to build the MLO Evryscope.

Special thanks to David Norris, Cliff Tysor, and Philip Thomson from the UNC machine shop for their careful work and advice.

To the UNC physics and astronomy professors and staff for their support.

To my labmates: for all of the teamwork throughout my time here.

I am thankful to my friends and family for their help during this time.

Let me thank God - it has been a privilege to study your creation and to help discover a small part of it.

Foremost, I would like to thank my parents. This has been quite a trying journey - it would not have been possible without you.

TABLE OF CONTENTS

LIST OF TABLES

LIST OF FIGURES

LIST OF ABBREVIATIONS

AGB	Asymptotic Giant Branch
APASS	AAVSO Photometric All-Sky Survey
ASAS-SN	All Sky Automated Survey for SuperNovae
ATLAS	Asteroid Terrestrial-impact Last Alert System
AU	Astronomical Unit
BHB	Blue Horizontal Branch
BLS	Box Least Squares
CAD	Computer-aided design
CCD	Charge-coupled device
CE	Common Envelope
CRTS	Catalina Real Time Transient Survey
CSTAR	Chinese Small Telescope Array
CTIO	Cerro Tololo Inter-American Observatory
CV	Cataclysmic Variable
EHB	Extreme Horizontal Branch
FoV	Field of view
FWHM	Full Width at Half Maximum
GMM	Gaussian Mixture Model
HAT	Hungarian Automated Telescope
HSD	Hot Subdwarf
KELT	Kilodegree Extremely Little Telescope
LMC	Large Magellanic Cloud
LS	Lomb-Scargle
LSST	Large Synoptic Survey Telescope
MASCARA	Multi-site All-Sky CAmeRA
MESA	Modules for Experiments in Stellar Astrophysics

MJD	Modified Julian Date
MLO	Mount Laguna Observatory
NLL	Negative Log Likelihood
Pan-STARRS	Panoramic Survey Telescope and Rapid Response System
PN	Planetary Nebula
PROMPT	Panchromatic Robotic Optical Monitoring and Polarimetry Telescopes
PSF	Point Spread Function
PTF	Palomar Transient Factory
RLOF	Roche Lobe Overflow
RGB	Red Giant Branch
SA	Spherical Aberrations
sdB	B-type Hot Subdwarf
SDE	Signal Detection Efficiency
sdO	O-type Hot Subdwarf
SDSS	Sloan Digital Sky Survey
SIMBAD	Set of Identifications, Measurements and Bibliography for Astronomical Data
SNR	Signal to noise ratio
SMARTS	Small and Modern Aperture Research Telescope System
SOAR	The Southern Astrophysical Research
SuperWASP	Wide Angle Search for Planets
SVM	Support Vector Machine
TESS	Transiting Exoplanet Survey Satellite
TPI	Threads per Inch
WD	White Dwarf
VSX	Variable Star Index
ZTF	Zwicky Transient Facility

CHAPTER 1: INTRODUCTION

The research in this work is divided primarily into two categories - instrumentation and astronomical surveys. My first task was to design and build a new type of telescope, starting from the concept (shown in Figure 1.1) and completing all of the necessary stages in the process to turn the idea into a working, finished instrument. The new telescope (the Evryscope) is unique in that it simultaneously observes the entire visible sky with fast 2-minute images, continuously each night. This combination of extremely wide field of view (FoV), high cadence, and continuous monitoring is sensitive to astrophysical signals lasting only a short time. Some of the highest value discoveries are rare, short-timescale signals and the Evryscope is well placed to find these rare events with the combination of all sky, continuous, fast cadence observing. The second phase of my work was to conduct several fast-transit surveys searching for rare events using Evryscope data from the first three years of operation. The Evryscope images are used to produce photometric light curves, which we search for periodic changes in brightness indicative of rare companions or unexpected systems. This includes transiting exoplanets with exotic host stars, select eclipsing binaries, and compact systems.

This research led to seven first author publications, in select astronomical journals driven by the content. As of the time of this writing, five are published, one is submitted and under review, and the last is in the final editing stage and will be submitted in March 2020. An additional paper is in preparation, pending further simulations. These full works are presented in Chapters 2-9 of this dissertation, with a brief description of each survey here in the following paragraphs.

In the first survey, I used Evryscope observations from the 2016 season (the first data available from the instrument) to explore the Southern Polar region (declinations $-75°$

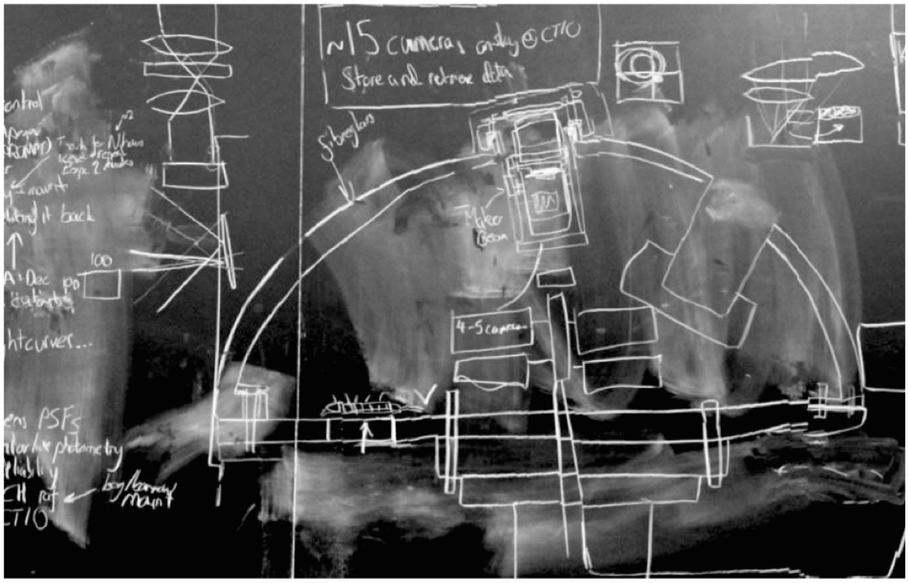

Figure 1.1: The Evryscope conceptual design. My instrumentation work was to take this concept and turn it into a working, finished telescope.

to $-90°$). The survey goal was to detect gas-giant planet candidates or low-mass stellar companions orbiting smaller, cooler stars (late K-dwarfs and M-dwarfs). The Polar region is comparatively less explored than other sky areas, and is observed with a single Evryscope camera with a consistent airmass (telescope elevation) which minimizes systematics in the light curves. Planets orbiting smaller, cooler stars are an active research area, with relatively few known compared to main-sequence solar-like stars. Less common low-mass star properties are not well understood or characterized, and eclipsing binary discoveries aid in the understating of these objects.

The second survey was a search for planets transiting white dwarfs (WD). WDs are understood to be the final evolutionary stage of most stars (including lower to medium mass stars), resulting in an extremely compact and dense remnant object. The rather violent formation sequence, including an extensive expansion in the Red Giant phase (RGB), and ejection of the outer layers in the Planetary Nebula phase (PN), suggests that planets of the stellar progenitors would not survive. Conversely, evidence for orbiting debris and even disintegrating objects suggests that WDs might host planets. Discovery would help in our understanding of the WD formation cycle, planet formation or survive-ability, and exoplanet science.

The third survey was a search for short-period companions (including planets, low-mass stars, and stellar remnants) to hot subdwarf (HSD) stars. HSDs are peculiar small, dense, under-luminous stars given their high temperatures. They are thought to form via a mechanism that strips the hydrogen layer of a post-main sequence star, leaving a compact and hot Helium core burning star. HSD binaries provide a wealth of information on stellar evolution, close binary formation, and companion properties.

The Evryscope all-sky coverage, continuous observing, and fast-cadence are well suited to support the surveys I conducted. Transits and eclipses of smaller host stars are expected to be fast for late K-dwarfs or M-dwarfs (1-2 hours or less), and extremely fast for the remnants (20 minutes for HSDs and a few minutes for WDs). The signals are expected to be deep (several percent for the dwarf stars, and from 10% to fully eclipsing for HSDs and WDs depending on the companion and inclination), which lessens the light curve precision requirement. Observing enough targets is problematic in all three surveys, as the desired targets are observationally challenging. The difficulty for the late dwarf stars is obtaining enough *bright* targets (for signal detection and precision followup), the WDs is reaching enough total targets (WDs are abundant but so dim that comparatively few are observable), and the HSDs is reaching enough targets without too many contaminants (HSDs are rare and problematic to separate from other blue stars). The fast-cadence and continuous observations of the Evryscope are sensitive to the fast signals, and the wide FoV and reasonable resolution (13" per pixel) provide enough targets to conduct the surveys.

My work is a combination of instrumentation and astronomical surveys. The survey work is designed to exploit the Evryscope advantages in order to explore scientific areas that are not well understood, and to facilitate new discoveries. In this introduction chapter, I begin with the design process and the Evryscope instrument, followed by the fast transit surveys. I briefly discuss the significant discoveries and refer the reader to corresponding chapters for further details.

1.1 Motivation for the Evryscope and Comparison to other Instruments

The Evryscope is intended to discover variability lasting only a short time in astronomical objects. The variability or the astronomical object (or both) are typically rare, combined with the fast variability signal make these detections challenging. The fast signals can be periodic, with a variety of sources including binary stars, substellar objects, or stellar variability. They can also be non-periodic including outbursts, stellar activity, and galactic events. In this section, I describe other surveys and instruments before the Evryscope and show the parameter space challenging to current systems that we are well placed to cover.

There are two primary approaches taken in wide-field surveys - the larger aperture deep sensitivity versus the smaller aperture wider field design. I begin here with the larger instruments (for example PTF, ZTF, Pan-STARSS, SkyMapper, and LSST), describing the design, their science goals and parameter spaces, and notable discoveries.

PTF was a transient survey capable of high (minute level) cadence and good depth (M_g ≈21) with the scientific focus on extragalactic signals. The survey strategy used a 48 inch primary telescope paired to a high resolution mosaic CCD resulting in an 8 square degree FoV. A 60 inch telescope was used for real-time followup to generate light curves on interesting targets. Both instruments were fully automated and located at the Palomar observatory in southern California. The PTF instruments observed from 2009 to 2017, with various observing and cadence strategies that tiled across fields for wide coverage or focused on specific regions for deep coverage. The project yielded many discoveries including the youngest supernova discovered, superluminous supernovae, compact binaries, and a host of other transients. The PTF instrument is described in detail in [1], and a summary of significant discoveries can be found in [2]. ZTF is the PTF replacement, with first light in late 2017 and using the same primary telescope but with an upgraded camera and software system. This results in an increased FoV (now 47 square degree) and a faster, more robust alert system. More information on the system can be found on the project webpage (https://www.ztf.caltech.edu) and in [2].

Pan-STARRS is an optical imaging survey with faint capability (M_g ≈24) and a similar FoV (7 square degree) to PTF. It uses a larger 1.8m primary mirror with a gigapixel segmented CCD. The primary survey aim is detection of asteroids and comets potentially dangerous to Earth, and to monitor solar system objects. Secondary goals are to study supernovae and other indicators useful in cosmology. The instrument has been operating on Haleakala on Maui since 2010. The instrument is the primary detector of asteroids and comets approaching Earth, scanning the entire sky each month and has identified over 10,000 near earth objects (NEOs). A description of the instrument and science cases can be found in [3] and additional information (including highlighted publications and discoveries) is available on the project webpage (https://panstarrs.ifa.hawaii.edu/pswww/).

The SkyMapper telescope is another medium size (1.3m) instrument used for a wide field survey, in its case with a 5.7 square degree FoV. The survey is focused on the Southern Sky, with numerous science goals including solar system objects, nearby young stars, and the Milky Way dark matter halo. The instrument has been operational since 2008, located at the Siding Spring Observatory in Australia. It has made a number of interesting stellar related discoveries including hypervelocity stars and very old stars. A description of the instrument can be found in [4] with discoveries and publications noted on the project webpage (http://skymapper.anu.edu.au).

The upcoming LSST project will be a larger 8.4m, 10 square degree FoV telescope designed to image the sky in multiple bands with the ability to reach very faint objects (M_g ≈25). The survey will primarily explore dark matter and energy, search for supernovae, gamma ray bursts, and other energetic transients, as well as small solar system objects. As with the large aperture surveys described here (and others), LSST will take several weeks to survey the entire sky before repeating. A description of the instrument and science cases can be found in [5].

I now turn to the smaller aperture and comparatively wider field instruments, beginning with the HATNet telescopes. The primary science mission of the project has been to detect exoplanets. As of this writing they have discovered nearly 140 planets (with most all being 14 mag or brighter host stars), and are one of the most successful ground based exoplanet surveys. The majority of the discoveries are gas giants, with a variety of host star types. Several smaller planets have been discovered including Neptune size and some rocky planets. A variety of interesting features have been seen in the discoveries - retrograde orbits, very high mass hot Jupiters, and inflated radii to name a few. The HATNet project has been observing since 2001 with several iterations bringing it to the current state of a network of 6 telescopes, located in Arizona, Chile, and Australia. The northern cites use Canon 11 cm lenses with commercial CCDs resulting in an approximately 110 square degree FoV. The southern cites rely on 18cm lenses with upgraded CCDs which cover 67 square degrees in each field. They use 3-5 minute images and stare at a field for 3+ months before moving to the next sky area. This results in several thousand data points on average per target, with millimag level photometry on the brighter stars. A description of the instrument, pipeline, and survey update can be found in [6, 7].

Another prominent exoplanet survey is the SuperWASP project. It has discovered nearly 200 planets, with many being short period gas giants orbiting bright (with most all being 12 mag or brighter) stars. The combined HATNet and SuperWASP surveys have found many interesting (and surprising) planets and provided valuable information on the parameters of giant planets, including the mass vs. radius relation. SuperWASP was deployed in 2006 and has instruments in the Canary Islands and in South Africa. They use larger 20cm Canon lenses, mounted together in a cluster to achieve 480 square degree FoV. They have a faster 30 second cadence with an observation strategy that images one sky area for a short time and moves to the next to cover approximately the complete sky each night. Please see [8] for a detailed description of the SuperWASP instrument.

Several other surveys use camera lenses or small telescope optics to search for variability, typically with a more specific science goal. KELT [9], XO [10], MASCARA [11] for instance are primarily aimed at discoveries of hot Jupiter planets orbiting very bright stars (which greatly aids in the followup work). MEarth [12] is focused on the discovery of earth like planets orbiting nearby M-dwarf stars, with the larger aperture system designed to detect the more challenging signals from the dimmer stars. Each has found a handful of the highly sought after systems they were intended to. A few other instruments using consumer optics and CCDs with a focused science goal are Flys Eye (asteroid detection) [13], Pi of the Ski (GRBs) [14], and ASAS-SN (supernova) [15].

The space-based TESS exoplanet-survey mission, covers the entire sky in 2,000 square-degree chunks, covering the majority of the sky for ≈27 days. The very high precision light curves allow for the detection of rocky planets with periods up to approximately two weeks. The primary science goal of TESS is to discover Earth size planets in the habitable zones of the brightest M-type stars. TESS achieved first light in late 2018, with the observational sectors still underway as of the time of this writing. Instrument and mission details can be found in [16].

The surveys discussed here (along with other wide field instruments) are not sensitive to the diverse and very interesting class of shorter-timescale objects. This includes transiting exoplanets, young stellar variability, eclipsing binaries, microlensing planet events, gamma ray bursts, young supernovae, and other exotic transients, which are currently only studied with individual telescopes continuously staring at relatively small fields of view. Rare, rapid events simply cannot be seen without monitoring the entire sky simultaneously. With its unique design and monitoring strategy, the Evryscope is the only telescope which can observe these short-timescale events over the entire sky simultaneously.

This technique has been prohibitively expensive up to now because of the cost of the extremely large number of pixels required to cover the sky with reasonable sampling, and the consequent data-storage and analysis facility requirements. The rise of consumer digital imaging and low-cost hard disks offer solutions to both these problems. The Evryscope uses mass-produced compact CCD cameras and lenses with a novel mounting scheme to make a low-cost robotic telescope that points a 7cm telescope at every part of the accessible visible sky simultaneously.

The Evryscope builds on several ideas from the surveys presented here, but with an all sky FoV (8150 square degree), with high cadence and continuous monitoring. The optics and high performance CCDs give sub percent level light curve performance on bright stars, with a competitive pixel scale (13" per pixel) compared to many of the systems mentioned above (9" HATNet north and 4" for HATNet South, 13" SuperWASP). The Evryscope FoV and pixel scale is demonstrated in Figure 1.2.

The Evryscope is also well placed to complement several of the other surveys. For instance, by the TESS launch time the Evryscope had collected three years of data on each of TESSs ≈100,000 Southern targets, at half the pixel size and with similar apertures to the TESS cameras. The Evryscope dataset will enable a high-cadence search of every TESS potential target for eclipsing binaries (of all periods), flare stars, exotic binaries, rotational modulation, sunspots, and all other intrinsic photometric variability, on timescales similar to the TESS cadence. The TESS light images are collected in a much redder filter than the Evryscope, a difference useful in the analysis of many of these discoveries. Examples of this can be found in our HSD search (chapter 6), especially useful in HSD reflection effect and compact binaries.

The Evryscope is designed to open a new parameter space for optical astronomy, trading instantaneous depth and sky sampling for continuous coverage of much larger sky areas. The Evryscope has the largest étendue (collecting area × FoV) or light-collecting power of

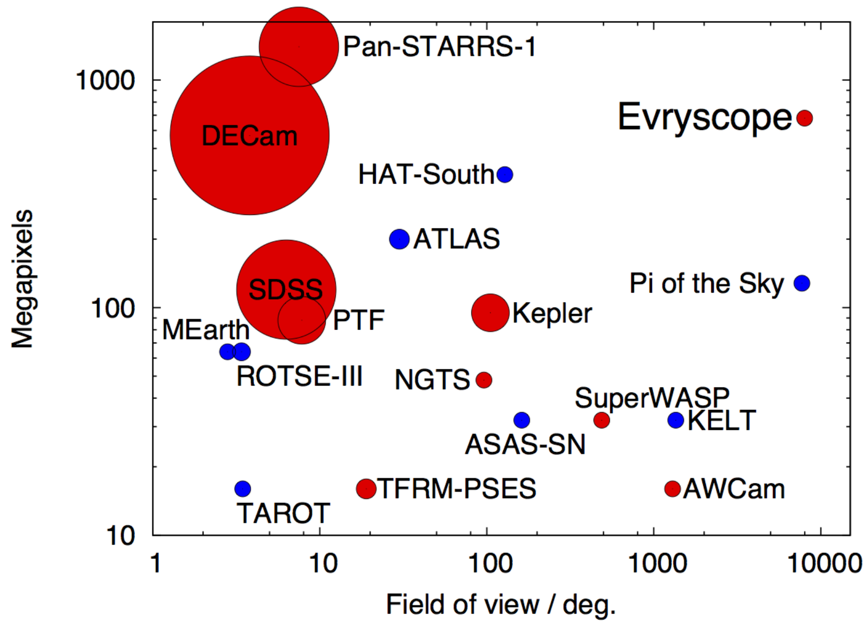

Figure 1.2: The unique parameter space of the Evryscope compared to operating sky surveys. Points are sized by telescope aperture, with a minimum size for small apertures (for visibility). Red and blue points indicate single vs multiple sites, respectively.

any current ground-based survey (Figure 1.3), and has 10% of the enormous planned LSST étendue.

This parameter space includes many exciting and cutting edge research areas, and is the motivation for building the Evryscope. The fast transit and eclipse HSD and WD surveys are the focus of this work. Other areas being explored by members of our team include habitability affecting superflares, eclipse timing exoplanets, supernovae, lensing, and other transient detections. For a complete discussion of the Evryscope science cases, please see [17]. Exciting news, discoveries, and publications can be found on our project webpage (http://evryscope.astro.unc.edu). Find out about the latest in group activities on twitter.com/evryscopectio.

1.2 The Evryscope

The Evryscope instrumentation process included creating multiple potential designs using 3D CAD software, simulating performance using estimated loads similar to expected observing

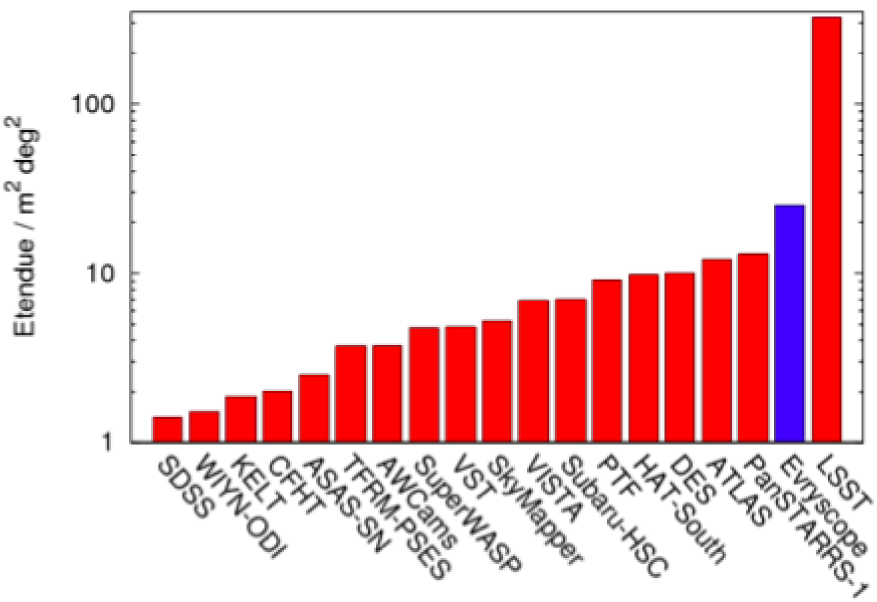

Figure 1.3: The Evryscopes étendue (collecting area × FoV) compared to current ground based surveys.

conditions, and choosing the best design. I produced design models and engineering drawings so that our CNC machine shop could manufacture the instrument components. This included mounts and adapters for the optics and CCD cameras, which were designed to be modular forming identical telescope units that observe smaller patches of the sky with a combined all-sky FoV. The telescope assemblies are shown in Figure 1.4. The design also required protective optical windows with sealed mounts, adjustable focus mechanisms controllable remotely, and a method to align the optics and camera of each telescope unit reliably to a level more precise than typical machining tolerances in order to reach the image quality necessary for the project. Working with my adviser, we were able to solve these challenges and deliver a final design within budget and on-time. As part of the instrument design, I also created a design for the support structures, array placement, and main-telescope mount interface. This included providing final designs to specialty vendors for manufacturing, and assisting in problem resolution. Other accessory components such as power supplies, cooling, and servo controls (as a few examples) were designed and tested in house.

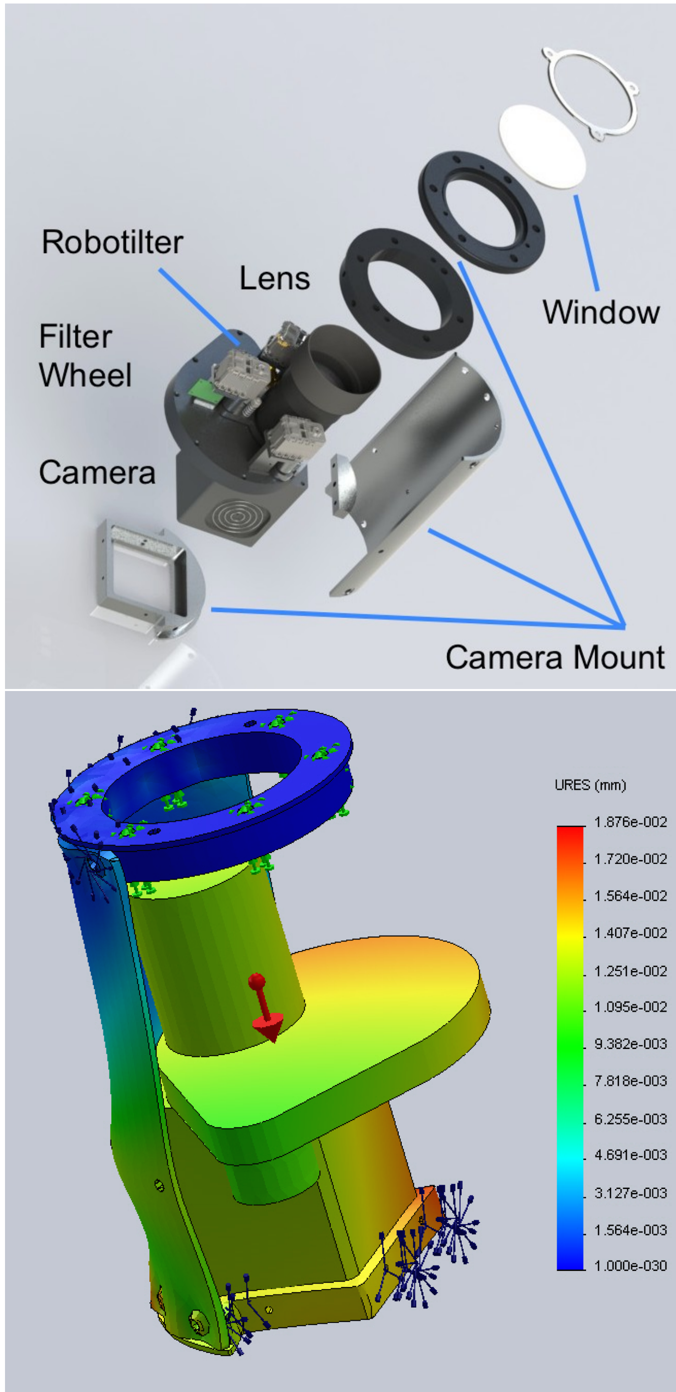

Figure 1.4: The Evryscope unit camera assembly. *Top:* The 3D model of the camera assembly and mount together forming the modular telescope units. *Bottom:* The stress and flexure simulation testing to help retire telescope failure and tracking concerns.

I led the instrument construction, and fabrication of other minor parts needed to complete the telescope. Final testing was done in Chapel Hill in mid 2015. I was part of the deployment team (to CTIO Chile) shortly thereafter, with my primary duty to re-assemble the telescope on mountain, fix unseen problems that arose, and test and complete all mechanical design related aspects of the instrument deployment. I also assisted with the deployment of the data storage and processing computers as well as the wiring and cable routing. The telescope has been running reliably and collecting data since the original deployment with only minor down-time for service. As of October 2019, we have taken over 4.0M images resulting in 700TB of raw data. The resulting database has light curves for 9.3M targets brighter than $M_g = 15$, averaging 32,600 data points per target through 2018.

To illustrate the Evryscope approach, it is useful to consider how conventional surveys searching for periodic variables are typically performed. A popular approach taken by conventional astronomical surveys is to observe a small patch of the sky (a few-degree-wide field) with a large aperture telescope constantly for a predetermined observing time. The instrument is then moved to a subsequent part of the sky and the process is repeated until the observations cover the complete target sky area. Examples of very successful surveys using this method include the Palomar Transient Factory [1], Pan-STARRS [3, 18], SkyMapper [4], and many others. These surveys are optimized for events that occur on day-or longer timescales (the time it takes to complete the observation fields), and are not sensitive to shorter-timescale objects. A different strategy is to observe specific sky areas with smaller apertures and wider FoVs. This allows the survey to reach very fast cadence and good sensitivity, but at the expense of all sky coverage. HAT [6], SuperWASP [8], KELT [9], are some of the most successful ground based exoplanet detection telescopes using this dedicated short-timescale, smaller sky area survey method.

The unique Evryscope design allows it to reach fast, rare events through a combination of continuous 2-minute imaging, all sky coverage, and many years of observations. To accomplish this the Evryscope uses an array of 22 telescopes (27 at full capacity) to cover the visible

Southern sky down to approximately 30 degrees above the horizon in each exposure. The Evryscope features mass-produced compact CCD cameras and lenses, and a novel camera mounting scheme to make a reliable, low-cost gigapixel scale robotic telescope. A single mount rotates the mushroom to track the sky with every camera simultaneously for 2 hours, before "ratcheting" back and starting tracking again (shown in Figure 1.5). A full description of the telescope can be found in our Evryscope instrument paper [19].

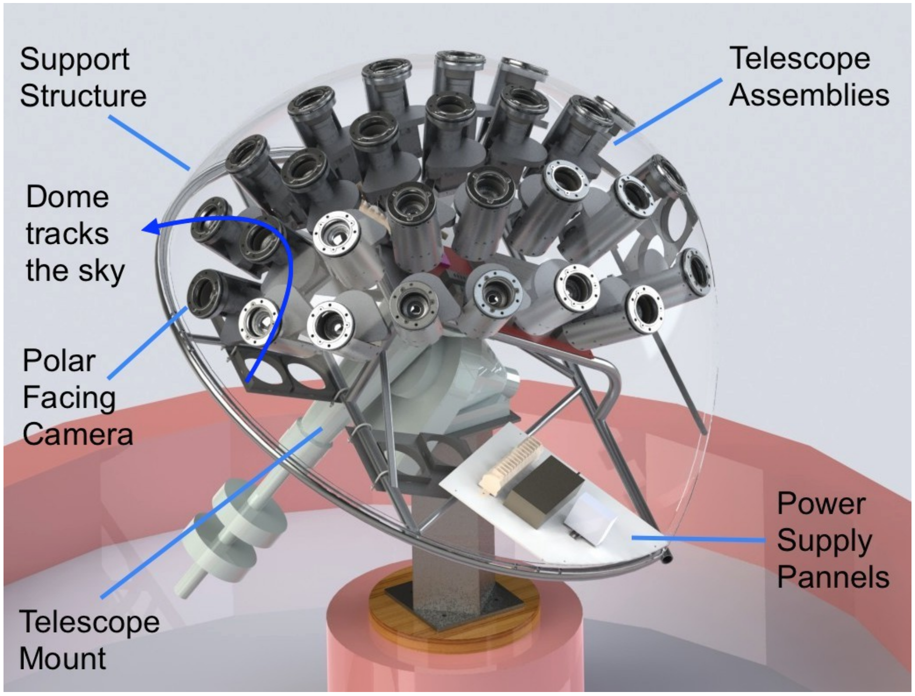

Figure 1.5: Cutaway rendering of the Evryscope showing the telescope mount, camera locations, and primary instrument components.

To see how the Evryscope can detect fast-transit rare systems, it is helpful to consider a recent discovery (EVR-CB-001 [20]) from my hot subdwarf (HSD) survey. EVR-CB-001 is a compact binary with fast varying features and rare primary and secondary stars. I discuss the astrophysical significance of the discovery later in this work, but for this discussion concerning the Evryscope potential, I focus on the light curve variability. Figure 1.6 shows the photometric light curve of EVR-CB-001 with the brightness on the y-axis. The brightness of the object varies in a quasi-sinusoidal way with different minima and maxima that alternate in even and odd cycles. The time is shown on the x-axis, but with a modification typical in astronomy known as phased time. Phased time simply recasts the time of each image as a fraction of the period, with the zero point set to the primary transit point.

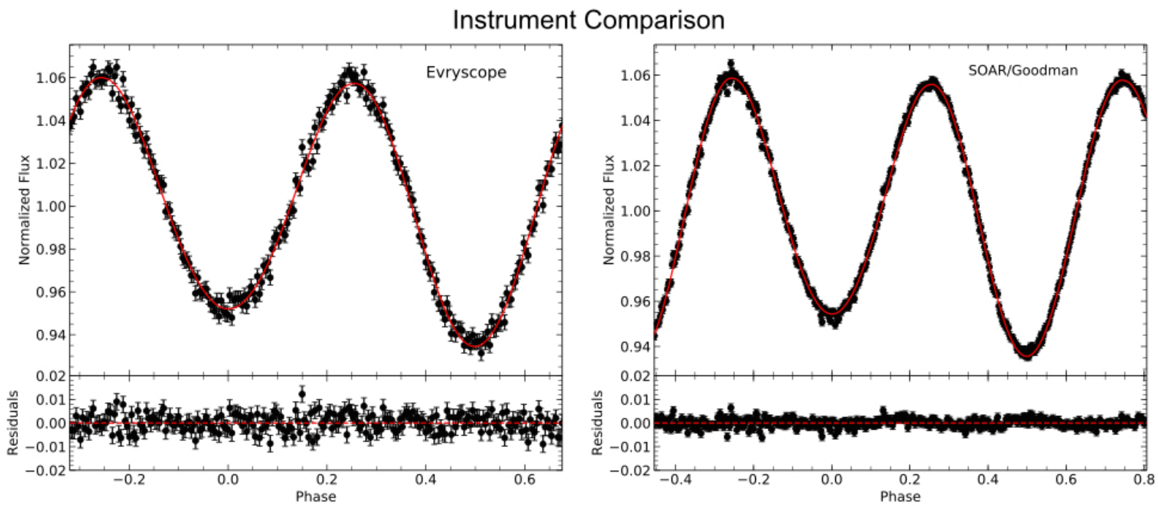

Figure 1.6: Instrument comparison of the Evryscope and SOAR telescopes. Left Panel: The Evryscope binned-in-phase light curve and the residuals after removing the best fit from the astrophysical signal. Right Panel: The SOAR light curve and the residuals after removing the best fit from the astrophysical signal. The flux and residual scales are the same for both instruments to aid in the comparison. The Evryscope aperture is ≈ 4500 times smaller than SOAR, but produces a competitive light curve when binned-in-phase. This result is made possible by the improvement from combining the many period observations over the multi-year Evryscope survey time.

We can understand this concept by looking at the right panel of Figure 1.6, which shows the light curve for EVR-CB-001 generated from observations taken with the 4.3 meter SOAR telescope in Chile covering just over one 2.5 hour period. In this case the phased time light curve shown would be no different than a light curve with actual timestamps – the x-axis would shown dates and times instead of fractions. The Evryscope light curve (the left panel of Figure 1.6) is generated from a completely different situation. Data to construct the Evryscope light curve took over 2.5 years, with nearly 54,000 measurements taken. The 2.5 year light curve is condensed by stacking according to phase, referred to as phase folding. The 54,000 point phase folded Evryscope light curve is then binned-in-phase to reduce the number of points, but increase the light curve precision while preserving the time resolution.

Consider the following instrument comparisons: The Evryscope cameras are 6.1 cm diameter while the SOAR telescope is 4.1 meter diameter. The Evryscope instrument cost approximately $300K, while the SOAR telescope cost approximately $28M. The competitive Evryscope light curve is made possible because the SOAR light curve took 2.5 hours of observing time, while the Evryscope light curve took 2.5 years. SOAR observed 1 period, while the Evryscope observed over 1000. An individual Evryscope period observation has only a modest precision, but with the proper photometric pipeline, the final combined and binned-in-phase light curve improves as $\sqrt{N_{periods}}$ in this case $\sqrt{1000}$.

It is important to emphasize that SOAR (or any other large telescope) and Evryscope are very different instruments. SOAR has many capabilities that Evryscope does not - spectroscopy, radial velocity measurements, and multi-band photometry just to name a few. However, the Evryscope has a 8150 sq. deg. field of view with continuous 2-minute cadence that provides light curves just like the one for EVR-CB-001, but for 9.3M targets. While some are better quality and some are worse depending on target brightness and location, EVR-CB-001 is a representative example.

The Evryscope is a robotic system that requires minimal human intervention, with low construction and operating costs, and provides a dataset that facilitates the discovery of rare, difficult to detect, fast event systems like EVR-CB-001. EVR-CB-001 was the definitive Evryscope discovery demonstrating the Evryscope instrument works and the advantage the system can leverage. With the proper processing of the discovery light curve, very high levels of binned-in-phase precision can be reached. Importantly for the fast transit HSD survey, the minutes level time precision is preserved in the binned-in-phase approach and was critical in the discovery of the HSD transits, eclipsing binaries, and compact binaries detailed in the following sections.

The Evryscope has already contributed to a wide variety of science cases, ranging from precision studies of single targets [21, 22], to statistical studies of stellar activity (Howard et al., in prep), transient discovery and followup [23, 24], and discoveries from the Polar and

HSD surveys (from Ratzloff et al., discussed later in the manuscript). In our instrument paper [19] we describe some of the first Evryscope discoveries from general stellar searches. We also summarize the hardware and performance of the Evryscope, including the lessons learned during telescope design, electronics design, a procedure for the precision polar alignment of mounts for Evryscope-like systems, robotic control and operations, and safety and performance-optimization systems. We measure the on-sky performance of the Evryscope and discuss its data-analysis pipelines. A previous paper [17] describes the detailed Evryscope science cases. Subsequent papers will describe the data analysis pipelines in detail.

Figure 1.7: The Evryscope, a two-dozen-camera array mounted into a 6 ft-diameter hemisphere, deployed at the CTIO observatory.

1.3 The Robotilters

The Evryscope uses Rokinon camera lenses (61mm effective diameter F1.4) and Finger Lakes Instrumentation (FLI) ML29050 camera units. This combination of commercially available optics and CCDs provides the wide FoV, reasonable resolution (13” per pixel), and high performance necessary and at a modest cost. Commercial camera lenses are used on successful wide field surveys such as SuperWASP [8], HAT [6], KELT [9], and several others. They have discovered a variety of photometrically variable objects including exoplanets, binaries, stellar phenomenon, and galactic events. Although the camera lens with a compact CCD camera design offers many advantages for wide FoV surveys, image quality is a significant challenge. Here the extremely wide FoV, fast optics, and under-sampled sources work against the image quality. Variance in quality across the image field, especially the corners and edges compared to the center, is a significant challenge in wide-field astronomical surveys like the Evryscope. The individual star Point Spread Functions (PSFs) typically extend only a few pixels and are highly susceptible to slight increases in optical aberrations in this situation.

The lens and CCD must be connected by an adapter, and the multiple mating surfaces combined with typical machining and assembly tolerances for commercially available optical systems cause a slight misalignment (tilt) between the lens and CCD. The tilt results in inconsistent quality across the image and degraded PSFs. This in turn places extra burdens on the light curve generation pipeline by decreasing the accuracy of the astrometry solution (star positions), requiring larger photometric apertures (the aperture necessary to enclose the star flux), as well as decreasing the signal-to-noise (SNR) of most sources with the dimmer stars being especially susceptible.

As part of my dissertation work, I worked with the Evryscope PI to design and build an automated alignment system (the Robotilters) to solve the misalignment challenge. The Robotilters optimize 4 degrees of freedom - 2 tilt axes, a separation axis (the distance between the CCD and lens), and the lens focus (the built-in focus of the lens by turning the lens barrel which moves the optical elements relative to one another) in a compact and low-cost package. The design uses precise servos to move the lens relative to the CCD (as the lens is the smaller and lighter component in our case), the concept is shown in Figure 1.8.

A common struggle among wide-field surveys is the negative impact of PSF distortions and poor image quality on the photometric precision and dim star performance. This adds to the difficulty in reaching the sub-percent level required for typical exoplanet searches.

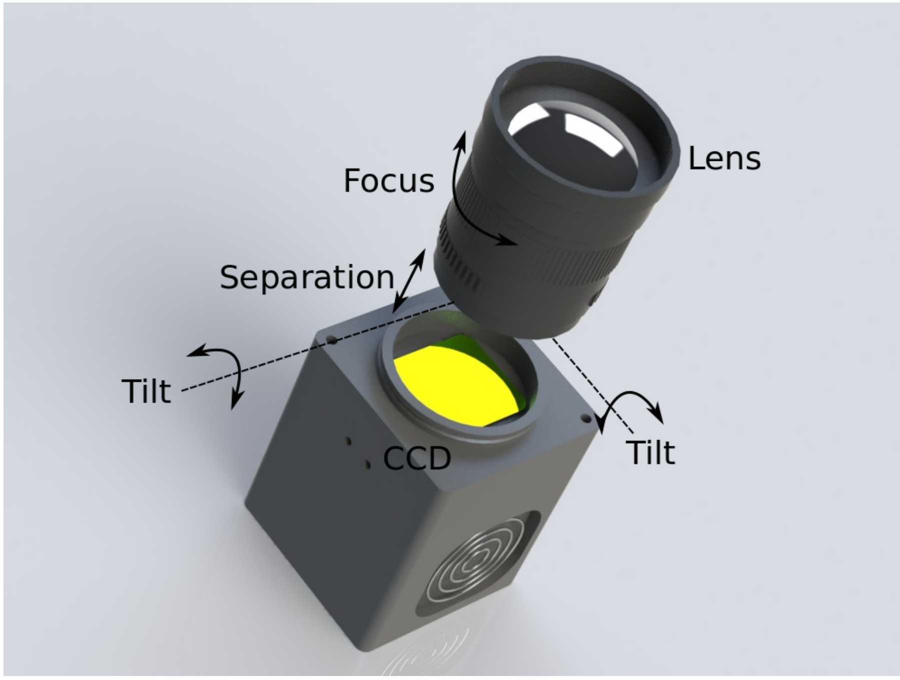

Figure 1.8: The Robotilter concept. The lens is moved relative to the CCD in two tilt axis, a separation axis, with an adjustable lens focus.

Extensive software development is put into the calibrations, pipeline, aperture photometry, and systematics removal to try and maximize light curve quality given the challenges of a very wide field. Additionally, considerable resources are dedicated by lens manufacturers in the optical design (using multiple elements) to reduce aberrations and increase throughput. Great care is also taken in the assembly process to ensure the multiple optical elements (inside the lens barrel) are aligned relative to each other for the same reasons.

Given the effort in light curve software, and in optical design and manufacturing, we were surprised to find very little discussion regarding the alignment of the lens and CCD in wide field astronomical surveys. The Robotilters were designed for the Evryscope telescope units, and constrained to fit into the filter wheel and camera mount footprint. However, the Robotilter design certainly could be modified to work on other instruments, with different apertures and CCD choices. The Robotilters remove tilt and optimize focus in the Evryscope telescopes at the sub 10 micron level, are completely automated, take 2 hours to run, and remain stable for multiple years once aligned. In our Robotilter paper, we show the Robotilter

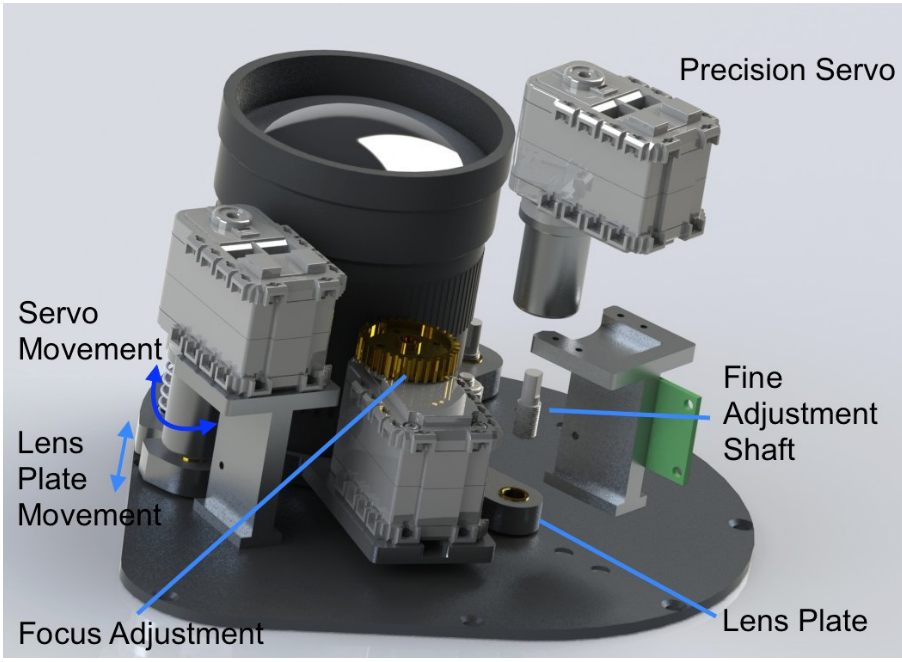

Figure 1.9: The Robotilter automated tilt/alignment/focus system

alignment solution improves PSFs with less distortion, smaller extent, and better consistency across the image. The Robotilter solution also resulted in a limiting magnitude improvement of .5 mag in the center of the image and 1.0 mag in the corners for typical Evryscope cameras. We installed the Robotilters in November 2015 and began testing hardware and camera alignment software on select cameras in early 2016. All cameras were aligned by mid 2016 and have been stable for three years with only minor focus adjustments. The Robotilter design is shown in Figure 1.9.

1.4 Polar Survey

1.4.1 Polar Survey Background

Eclipsing binary discoveries provide critical information on stellar properties and formation channels. Eclipsing binaries with low mass components (and very low-mass secondaries) are especially useful. A late K-dwarf or M-dwarf host star is less likely to dominate the luminosity compared to a small stellar companion, so spectroscopic features can be seen from both the primary and secondary stars (double line binaries). Detailed followup of eclipsing binary discoveries of this type can precisely measure the of masses, radii, and temperatures. The brighter discoveries are the most useful, due to the increased SNR of the spectra and light curves used in modeling the systems. Lower mass eclipsing binaries are observationally challenging due to the low intrinsic brightness of the star, and more systems are needed to properly characterize the mass/radius relationship in stellar models [25–27]. In addition to eclipsing binaries, gas-giant planets transiting late K-dwarf and M-dwarf stars are also useful in stellar formation theory and more systems are needed. Gas giant planets are rare in late K-dwarf and M-dwarf systems and difficult to explain from formation theory, as insufficient material is thought to be available to form comparatively high mass planets in low mass central star systems. The Polar Survey was concentrated on the Southern Polar sky area region to primarily search for eclipsing binaries with low-mass companions and gas-giant planets transiting late K-dwarfs or M-dwarfs.

The questions we wanted to explore in the Polar Survey are to the nature of eclipsing binaries in bright stars in the polar region. What is the extent of variability, how are they distributed among stellar types, and can the Evryscope discover and identify additional low-mass companions in binaries with late dwarf primaries necessary for stellar models. The secondary question we investigated is in regards to gas-giant planets orbiting late dwarf stars. Can the fast cadence Evryscope detect these objects, can we confirm their rarity, and in the event of discoveries what properties do they reveal about the host and planet.

1.4.2 Polar Survey

The Southern Polar region is observed with a single camera and with a consistent airmass (telescope elevation), which minimizes systematics in the Evryscope light curves. Our survey strategy filters the bright stars $M_v < 15$, then uses detection power to narrow the targets, followed by a spectral classification to identify high priority candidates (those with potential low-mass secondaries). More precise light curves, identification spectra, and higher resolution spectra for radial velocity measurements were obtained for select candidates.

Detection of variables relies on the Box Least Squares (BLS) [28], [29] and Lomb-Scargle (LS) [30], [31] algorithms. These tools fold the target light curve over a range of test periods (in this survey 3-720 hours) to identify the period with the highest power. The power is determined by the best fit to a predetermined model, representative of the expected signal. BLS uses a model preferring a shallow decrease in flux, which effectively identifies transit and eclipse signals. LS uses a sinusoidal model that recovers stellar variability and is useful in finding eclipsing binaries with strong reflection or ellipsoidal deformation effects.

Identification of the stellar and variability type, along with an accurate measurement of the variability pattern and amplitude for each of the discoveries is especially important in a wide field search such as the Polar survey. These properties reveal the variability source, and critically they flag potential high value targets – a difficult step given the many candidates and similar light curve features. For instance, the light curve of an eclipsing binary with a low mass secondary would likely show a reasonably deep primary eclipse lasting 2-3 hours, with a mild ellipsoidal deformation, and a shallow secondary eclipse. An example is shown in the top panel of Figure 1.11 in the following section. The light curve of a gas giant planet candidate with a late dwarf host star shows a much shallower and narrower transit, and a flat out of transit shape (an example transit is shown in Figure 1.10). Knowing the host star type, estimations of the stellar properties (radius and mass) can be made, followed by the companion size. This is critical in separating similar looking light curves eclipsing binaries with more massive, but unexceptional components. In the case of planet candidates, only the light from the host star is visible, so the transit depth and duration are only useful if we know the star size.

The most accurate determination of the stellar type is to compare the the target spectra to models or spectra from known stars. This is impractical and unnecessary given the few expected high value candidates compared to the many search targets. As part of the Polar survey, I instead developed a spectral classifier based upon color / magnitude spaces common in the field, but tailored for the Evryscope data. The Evryscope classifier uses publicly available data, and a multiple-step machine learning algorithm to classify our targets. The Evryscope classifier was used to classify all discoveries in the Polar survey, and to identify likely K-dwarf and M-dwarf systems for further followup.

We also developed a fast, accurate, and reliable fitting algorithm that uses Gaussians to measure transits and primary eclipses. Sinusoids are used to measure general variables. With these scripts, the variation was measured for multiple hundreds of targets in an automated way, and when combined with the Evryscope classifier helped filter the high-value candidates. The Evryscope classifier and fitting scripts were originally designed for the Polar survey, and were later enhanced and used in the HSD and WD surveys.

1.4.3 Polar Survey Results

We identified 4 planet candidates from variability in the light curves based on the transit depth, shape, and duration and the suspected host star type. These were later shown to be stellar in nature, as the followup radial velocity measurements revealed companions that must be more massive than planets. We also found several eclipsing binaries with uncommon low-mass stellar companions.

The most exciting planet candidate was a 9.3 hour period, 1.7 R_J gas giant with a late-k-dwarf primary. The Evryscope light curve is shown in Figure 1.10. The transit depth, seemingly flat bottom, ≈1.5 hour transit duration, and lack of secondary features or other variation on a late K-dwarf spectral type made this a high priority candidate. Further followup revealed system to instead be a 18.6 hour grazing eclipsing binary with apparently nearly identical primary and secondary stars.

We performed spectroscopic followup on select eclipsing binaries to confirm the stellar type and secondary size. Radial velocity measurements reveal that seven of the eclipsing binary discoveries are low-mass (.06 - .34 $M_\odot$) secondaries with K-dwarf primaries. An

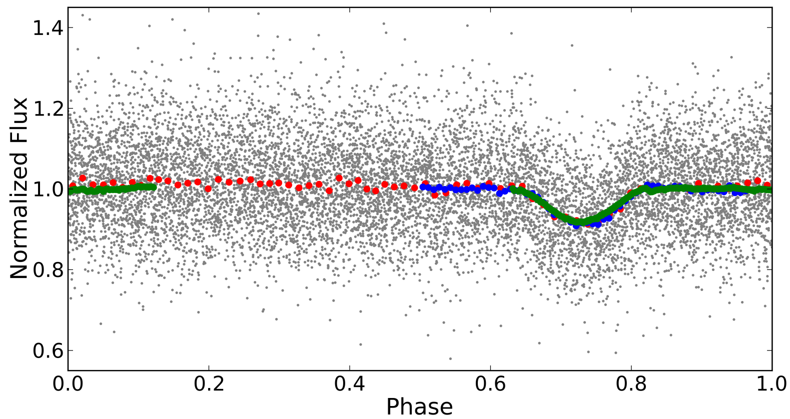

Figure 1.10: A gas giant planet transit candidate from the Polar search.

example of a late k-dwarf with a low mass stellar companion is shown in Figure 1.11. These candidates were flagged to the community as potentially useful for more precise followups.

In the Polar Survey paper, we reported the discovery of 303 total new variables (approximately half eclipsing binaries and the other half sinusoidal like variables) including the seven eclipsing binaries with low-mass secondary stars. Most are noted as general variables; the estimated spectral classification is reported for all, as is the period, amplitude, and variability type. We note the ASAS-SN group also conducted a search for general variability [32] in a similar part of the southern sky (submitted and under review at a similar time) and independently found many of the same general variables presented in our Polar survey. Of the common discoveries, we classified all discovery stellar types, identified potential high priority targets, and did followup work on select discoveries. Our Evryscope survey found 96 variables that the ASAS-SN group did not, while the ASAS-SN survey pushed to deeper magnitudes and found dimmer variables that were outside of our survey goal.

1.5 Exoplanet candidates followup

We took followup observations and performed more detailed analysis for the planet candidates to test for false positives, and on the low mass eclipsing binaries to measure system properties. In the first step, we obtained wide-coverage spectra used to identify the

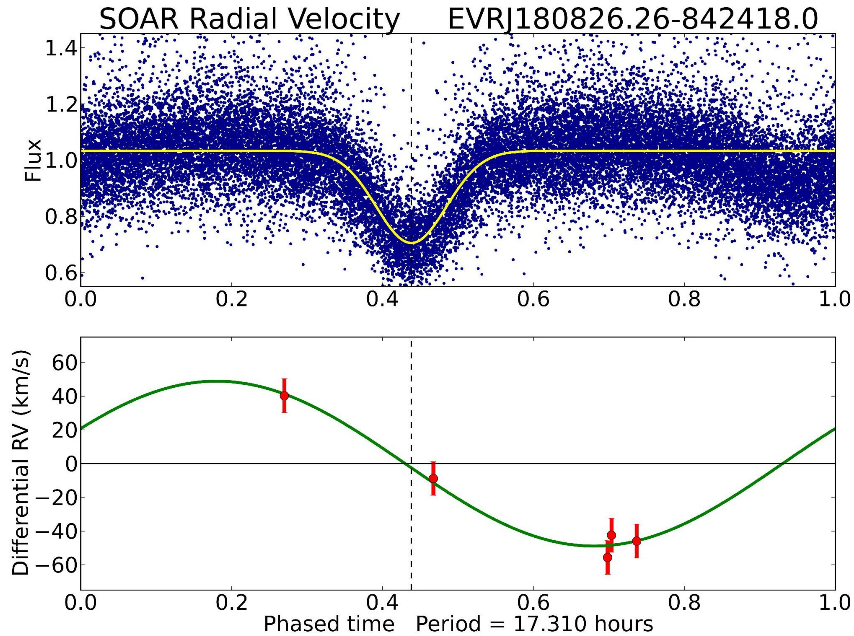

Figure 1.11: A late K-dwarf with a low mass stellar companion.

stellar type of the host star. The ID spectra were taken with the Goodman spectrograph [33] on the SOAR 4.1 m telescope at Cerro Pachon, Chile. We used the 600 mm-1 grating blue preset mode, 2x2 binning, and the 1" slit. This configuration provided a wavelength coverage of 3500-6000 A with a spectral resolution of 4.3 A (R=1150 at 5000 A). We processed the spectra with a custom pipeline written in Python; designed to extract, wavelength calibrate, and flux calibrate the spectra (optimized for this wavelength coverage and instrument setup). For additional details, we refer the reader to [20], where the pipeline is explained fully. Each spectra was visually inspected and fit to the best stellar atmospheric model. Candidates from the Polar search (suspected K-dwarfs) were fit using PyHammer [34]. Candidates from the HSD survey were fit using the stellar atmosphere model service for early type stars from AstroServer [1] [35] to confirm the spectral type and precisely measure temperature and surface gravity. An example ID spectra of a transit candidate from the HSD search is shown in Figure 1.12.

[1]http://www.astroserver.org

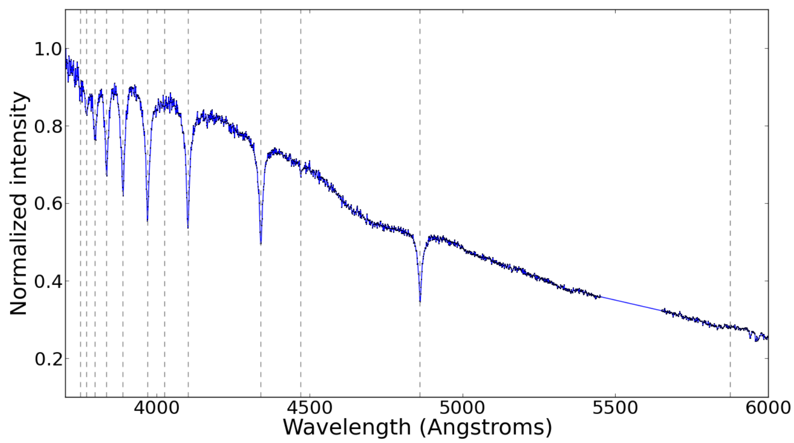

Figure 1.12: ID spectra of a HSD planet transit candidate from the HSD search. The continuum, deep and wide Balmer absorption features, and otherwise clean spectra are indicative of a HSD. The temperature, surface gravity, and metal abundances are measured using best spectral fits and confirm this candidate is an sdB HSD star.

Candidate Evryscope light curves are verified as necessary from followup photometric observations taken with the PROMPT telescopes [36] or with SOAR. The transit signals are compared to the Evryscope light curve and if warranted measured to determine the precise light curve features (using the modeling code *lcurve* [37] for select HSD discoveries for instance).

Select candidates were tested by taking radial-velocity measurements from SOAR or CHIRON [38]. Radial velocities were determined with the following procedure. We visually inspected each spectral order and chose high signal-to-noise absorption features for fitting (Balmer lines and select He lines depending on the target). Within each of their respective orders, we crop out a small section of the spectrum encompassing the absorption feature, fit a polynomial to the surrounding continuum, divide by the best-fitting polynomial to normalize the spectrum, and fit a Gaussian to the absorption feature. We use the centroid of the best-fitting Gaussian as the observed wavelength in order to derive a velocity. Each spectrum is assigned a final radial velocity/uncertainty using a weighted average/uncertainty from all individual line results. Finally, we convert these measurements to heliocentric velocities using PyAstronomy's *baryCorr* function. A sine wave fit to the data reveals a velocity semi-amplitude.

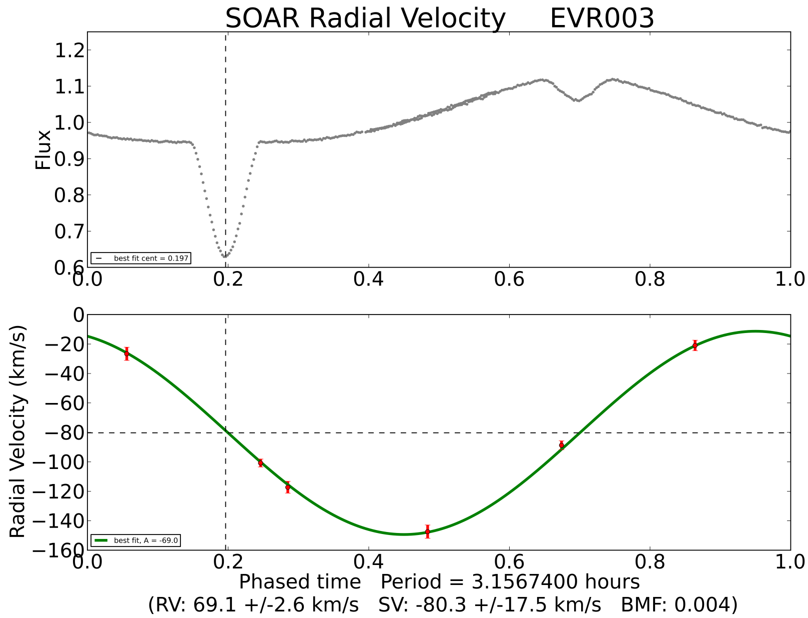

Figure 1.13: *Top:* The SOAR light curve of a HSD planet transit candidate from the HSD search, revealed to be an HW Vir system. *Bottom:* The Radial Velocity curve of the same system, used to measure the mass of the secondary.

The same example HSD candidate is shown in Figure 1.13. In this case, the strong reflection effect and secondary eclipse are clearly visible in the SOAR light curve but were not prevalent in the Evryscope light curve as the field was crowded and at a challenging air mass. The radial-velocity results revealed a stellar companion (an M6 assuming a canonical HSD mass). Although a planet false positive, this discovery is an HW Vir - a rare and sought after HSD eclipsing binary.

1.6 WD Survey

1.6.1 WD Background

A few dozen WDs are known to show infrared excess indicating dusty debris discs [39], and 1/4 to 1/3 reveal atmospheric metal pollution [40] thought to originate from deposited material. The source of the dust and metal is still an area of active research, but the preferred explanation is that planets or asteroids have migrated to the Roche limit and disintegrated leaving behind material that forms a disc or deposits onto the WD [41]. The donor planets or asteroids are thought to have survived the WD evolution cycle, meaning their orbits would have started at greater than 1 AU (the asymptotic-giant-branch phase radius). Given a canonical WD mass of $\approx .6M_{\odot}$, a rocky planet orbiting a WD at 1 AU will have a period of over 6 months. Planets are expected to disintegrated at periods close to 4 hours, and debris discs are thought to exist at distances equivalent of ≈10 hour planets.

Due to the small size of the white dwarf host (similar in radius to the Earth), transit signals are expected to be very deep (up to completely eclipsing for larger planets) but also quite short at only a few minutes in length. The more advantageous transit depths can result in high recovery rates, with less sensitivity to light curve precision, if the short-timescale signals can be preserved by the instrument. In contrast to the transit signal, the transit fraction (typically given by R_{star}/a, where a is the separation distance) of planets orbiting WDs is not favorable.

Here the small size of the WD reduces the transit fraction, on all but the shortest periods. In spite of the challenges, ground based surveys are still considered as a prime means to detect WD transits given the deep transit depths along with the fast cadence and high FOV requirements. Agol argued the merits of such a survey and proposed a preferred survey design in [42]. Faedi conducted the first survey in [43] with several other groups conducting searches for transiting exoplanets around WDs thereafter including Fulton [44], Hermes [45], and van Sluijs [46]. Each survey reports similar null-detection results. They estimate maximum occurrence rates typically to a few percent for gas-giant planets (within a limited short period range) and less well constrained for rocky planets (although still shown to be rare).

There are no known planets orbiting WDs and no candidates have been detected in the transit surveys published to date. The 1 known WD disintegrating planetesimal, WD 1145+017 [47], is a dimmer object and beyond the magnitude range of many surveys (it is also a very short period and different signal than an expected transiting intact planet). The only other objects in a WD transit survey that would produce light curve variability similar to transiting WD planets are double WD eclipsing binaries. Double WD eclipsing binaries are rare and challenging objects to detect in their own right, for a recent discovery and list of the 6 known systems see [48]. In many cases, the known double WD eclipsing binaries are also outside of the instrument window (either in FoV or magnitude or both). The survey must then rely completely on transit simulations in evaluating detection efficiency. In the case of null-detections, the survey typically would like to say something about maximum occurrence rates – here again the survey is completely reliant on transit simulations (for the detection efficiency) now combined with estimates from the transit fraction and number of survey targets. It is also difficult to cover a significant range of the period space (given the transit fraction challenges) where planets are expected to be found.

1.6.2 WD Survey

We have conducted an all southern sky (all RA, Dec $< +10°$), bright ($m_V < 15$) WD survey aimed at finding transiting planets. As with the HSD survey described following, we use the fast, 2-minute cadence photometric observations from the Evryscope to look for periodic signals in the light curves. While we cannot push to 1 AU, our period range searches separation distances from the Roche limit up to 25 solar radii. This corresponds to a test period range from beyond the shortest periods ($>$ 4 hours) up to 480 hours a favorable parameter space to search for WD planets.

We explored several questions in conducting the WD survey - can we discover a WD planet or candidate with the fast cadence Evryscope, and are our results consistent with the handful of other surveys concluding WD planets are quite rare. In the event of a null-detection, do we have sufficient means to declare upper limits? Do different assumptions about the survey parameters (especially in determining the number of sources and the recovery of simulated transits) alter the results in a significant way? We would also like to understand what is the relation between how rare WD planets might be versus how hard they are to detect, and if the latter is dominating the survey.

WD transit signals are expected to be challenging detections given the very short durations (a few minutes), and small transit fractions (less than a percent for even the shortest periods). This situation is quite different than the traditional shallow (less than 1%) and longer (at least a few hours) transits. We developed a custom code, called the outlier detector, to find the narrow and deep signals characteristic of WD transits. An example detection from the outlier detector of a simulated rocky planet transiting a WD host (produced from injecting the signal into an actual Evryscope light curve) is shown in Figure 1.14. The narrower and deeper the transit signal, the better the outlier detector performs and the more likely we are to recover a candidate.

1.6.3 WD Survey Results

We did not detect any planet candidates from the Evryscope WD transit survey. We performed extensive detection recovery simulations, which show a high expected recovery rate for Earth and larger size planets throughout the range of periods searched. We certainly could combine this analysis with the theoretical transit fractions to estimate maximum population occurrence rates. Initial estimates using this approach are not in disagreement with results from prior surveys.

Concerned with the reliance on simulated transits and estimated transit fractions, we analyzed the survey sensitivity using methods with less assumptions and with additional parameters to determine if the more simplified analysis method was biased in some way. This included independent testing of the WD target search list (by spectroscopically testing a random sample of the targets) to confirm the number of targets in the survey, and the identification of blended sources (by comparing the magnitude and coordinates of the light curve returned from the query to the input target) as minimal contributors since the signal is likely suppressed below the detection threshold. We also account for grazing transits

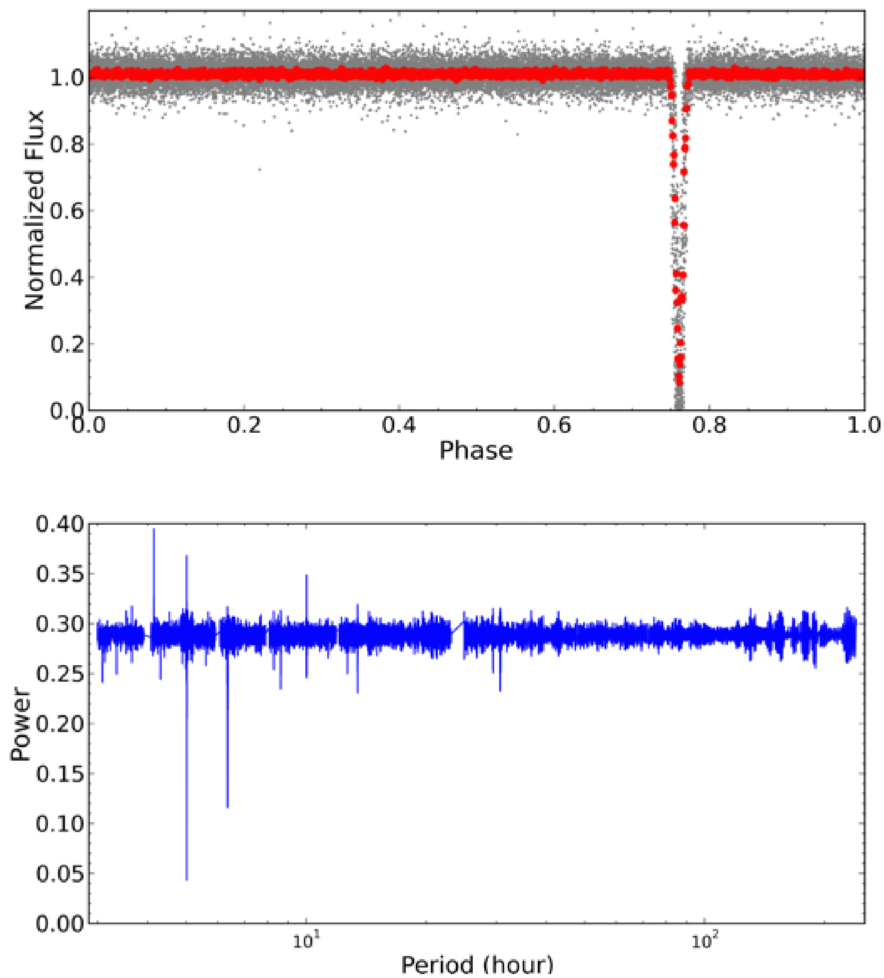

Figure 1.14: *Top:* The Evryscope light curve of a simulated rocky planet transiting a WD host (produced from injecting the signal into an actual Evryscope light curve) folded on its period of 5.02 hours. Grey points = 2 minute cadence, blue points = binned in phase. *Bottom:* The outlier detector (the fast-transit algorithm designed for the WD survey in this work) power spectrum with the minimum spike at the 5.02 hour detection.

in the light curve recovery simulations as they are expected to completely dominate given the similar sizes of the WD host and transiting planets. This is done by incorporating the inclination angle into the Monte Carlo transit simulation (a task that is still in process). Instead of assuming an edge on orientation and multiplying by a theoretical transit fraction, we combine this step to eliminate the assumption of an edge on transit. We also use actual Evryscope light curves as the base to inject the transit signals for recovery testing (as opposed to synthetic light curves), preserving the actual systematics of the instrument in addition to the observing window.

I am still in the process of reanalyzing the survey sensitivity and it has required considerably more resources, especially in regards to the light curve simulations. However the initial results have proved enlightening. Every additional method used to reanalyze showed the original approach overstated survey sensitivity. Taken together, the combined effects overstated the Evryscope WD survey substantially, and I estimate the final difference will be approximately a factor of 10.

The main result of the Evryscope WD survey is identifying and quantifying the effects different analysis approaches and assumptions have on survey results. This is especially critical in determining the simulated transits and transit fraction. In our survey, this change was so severe that it became no longer justifiable to report population occurrence rates, but instead showed the need to increase survey sensitivity (most obviously by increasing the number of targets). A manuscript in the draft stage with these results is awaiting the modifications to the simulations. I expect to complete and publish this work later in 2020. The WD search identified the survey limitation and helped us design a followup survey, to be conducted by a fellow graduate student in the Evryscope group, Nathan Galliher.

The Evryscope pipeline is currently processing data from 2019 and dim targets. Once these processes are complete, we will conduct this second WD survey in an effort to address the main challenges faced in the current survey. We briefly discuss the effects of these changes following. WDs are biased in distribution toward the faint magnitudes, not surprising given the compact nature of these stars. The WD suspects in our survey from the GAIA based source list of [49] show 6 times more candidates with $m_g < 17.0$ versus those with $m_g < 15.0$ (the cutoff in our WD survey). The increased FoV by adding the Evryscope North (would again double the WD sources. The net gain of these changes is an ≈12 times increase in the number of WD targets. This increased scope survey is in the planning stages and although still a formidable task, should be sensitive to a more reasonable number of potential transiting WD planets and be less speculative in nature.

1.7 HSD Survey

1.7.1 HSD Background

Hot subdwarfs (HSD) are small, dense, under-luminous stars for their high temperatures. They are thought to be Helium cores with a thin Hydrogen layer, formed from stripping of the main hydrogen shell during the red-giant phase by a binary companion. The hydrogen stripping is believed to prevent the asymptotic giant branch (AGB) phase, outer layer ejection, and planetary nebula phase associated with the typical post red giant cycle. Instead the HSD will be a stable, helium core burning star that is underluminous for its temperature. A thorough analysis of the formation of HSDs via binary interaction can be found in [50, 51]. The peculiar high temperature (typically 25,000 K to 40,000 K) with a small radius and mass (R≈0.2 $R_\odot$ and M≈ $0.5 M_\odot$) is attributed to the interruption in stellar evolution at this critical juncture. A comprehensive review of HSDs can be found in [52].

Given this evolutionary theory most HSDs are thought to have companions, with observations generally supporting this idea [53–55], although there is a non-trivial fraction (≈1/3) of observed single HSDs that is challenging to explain. HSD are observed with companions ranging from white dwarfs up to F stars, and periods from a few hours to several years. HSD binaries include compact degenerate systems, with a few massive systems thought to be potential supernovae progenitors [56–59], and a handful of peculiar systems thought to be very rare merger candidates [20, 60]. Compact HSD systems can also be found with late stellar or Brown Dwarf companions (designated as HW Virs, for a complete list of known solved systems see [61]), and wider systems (with some demonstrated double line spectra).

HSD binaries are generally placed into two groups based on the nature of the companion interaction during the formation process. Progenitor systems with comparatively smaller and closer companions are thought to be unable to accrete matter (from the hydrogen shell of the red-giant, HSD progenitor) at a fast enough rate to be stable. Referred to as a common envelope (CE), the CE phase will result in matter being ejected during the mass transfer with a resulting loss in angular momentum of the system and a tightening of the binary period. A description of the HSD formation CE channel can be found in [62]. Post CE HSD binaries typically have periods from 2 hours up to 30 days, with a few known exceptionally short period systems. Common companions are M-dwarfs, K-dwarfs, and white dwarfs; although more exotic remnant companions are possible. Progenitor systems with larger and farther companions form the second group of HSD binaries as they are thought to be able to accrete matter at a sufficient rate to avoid substantial mass ejection. This Roche Lobe Overflow (RLOF) formation is credited with producing wider HSD systems [63], containing earlier (G and earlier) main sequence companions with typical periods greater than 30 days.

1.7.2 HSD Survey

We have conducted an all southern sky (all RA, Dec $< +10°$), bright ($m_V < 15$) HSD survey aimed at finding post CE phase binaries and variables along with transiting planets. We use the fast, 2-minute cadence photometric observations from the Evryscope to look for periodic signals in the light curves. Most importantly for the HSD search, the Evryscope is highly sensitive to the observationally challenging, approximately twenty-minute duration transits expected from HSDs. The continuous, 2-minute Evryscope images ensure the transits are well sampled even at the shortest expected periods. The wide FoV and continuous observing provides light curves for enough bright sources (9.3M with $m_V < 15$), that we have a substantial number of HSD targets for our survey (several thousand), despite their rarity. The multi-year observing strategy provides tens of thousands of epochs per target, increasing the chance of capturing enough fast transits to enable detections. Our survey covers periods from 2-720 hours, with sensitivity to few-percent level variation.

The questions we strove to answer in the HSD Survey are primarily two-fold. First, what can we learn about the post CE phase binary population? Can we make significant new discoveries that will meaningfully add (with the fundamental HSD properties that the solutions bring) to the limited number of known compact, eclipsing, and reflection effect systems? Second is to the unknown, can the fast-cadence, all-sky Evryscope make discoveries of systems that are unexpected and surprising? Can we discover HSD planets or identify candidates? Can we constrain any of the post CE binary population occurrence rates?

As a complement to the Evryscope light curves, I developed the machine-learning based spectral classifier (see the Polar survey section) further to help identify potential HSD targets in the Evryscope database, and to provide a confidence level to prioritize discovery followup. A subset of targets is spectroscopically confirmed as a test of the HSD target list performance, and to more accurately estimate the total HSD targets in the survey. The homogeneous, single instrument light curve dataset helps greatly in our estimation of the survey sensitivity, which we combine with the classifier results to estimate occurrence rates for several of the HSD binary types.

1.7.3 HSD Survey Results

The HSD survey in this work identified 117 variables with 79 known and 38 new discoveries. 14 of the new discoveries are HSD binaries. Four of the new discoveries were published in separate discovery papers. EVR-CB-001 [20] is a 2.34 hour compact binary with a low-mass white dwarf unseen companion and white dwarf progenitor (a very rare pre-He WD formed after the RGB phase and contracting toward a fully degenerate He WD, and at a stage that places it nearest to HSDs on color-magnitude and temperature-surface gravity diagrams). The

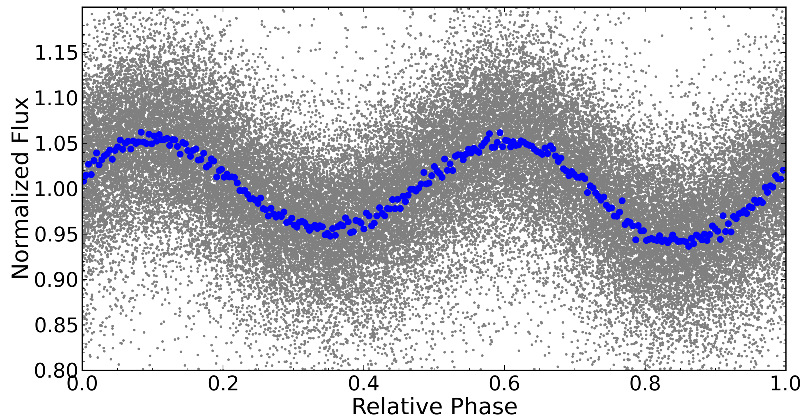

Figure 1.15: The Evryscope discovery light curve of EVR-CB-001 folded on its period of 2.34249 hours. Grey points = 2 minute cadence, blue points = binned in phase.

low masses of each component, the favorable mass ratio, and the expected clean interaction between the components also makes EVR-CB-001 a strong merger candidate to from a single HSD. Single HSDs are observed and predicted by double WD merger simulations, but progenitor systems have remained elusive. EVR-CB-004 (Ratzloff et al., submitted) is a 6.08 hour compact binary with an unseen WD companion and an odd sdO – most likely a more evolved stellar remnant. Both systems show strong light curve variation due to ellipsoidal deformation effects, and both systems are quite rare from the nature of the primaries and the combination of primary and secondary components. The Evryscope discovery light curve for EVR-CB-001 is shown below in Figure 1.15. EVR-CB-002 and EVR-CB-003 (see chapter 9) are bright, new HW Vir discoveries. The peculiar variability of the systems discussed here was a key factor in their discovery, and demonstrates an advantage of the light curve driven HSD survey approach.

We also detected 3 planet transit candidates. These candidates were later shown to be false positives, appearing as potential planets because of a nearby source blended in the Evryscope pixel or due to a challenging, high airmass observational field. The recovery of these candidates demonstrated the ability of the survey to detect HSD planet like signals (as opposed to simulations) in actual Evryscope light curves. An example Evryscope discovery light curve is shown below in Figure 1.16. A subsequent survey with additional targets and

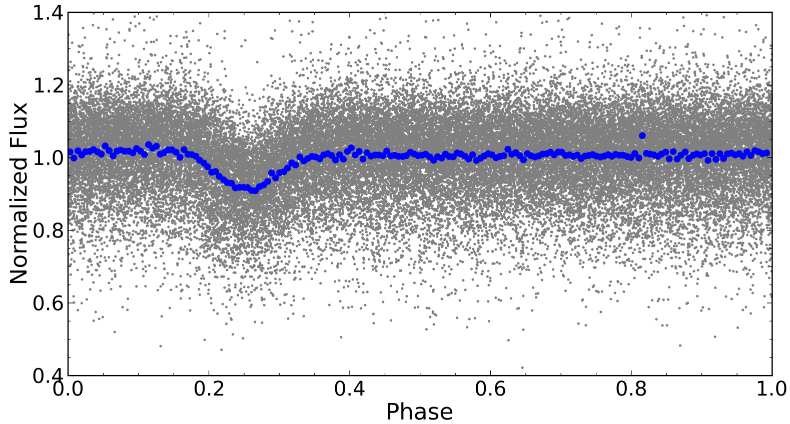

Figure 1.16: The Evryscope light curve of a 2.68 hour transit, originally flagged as a HSD planet candidate. Grey points = 2 minute cadence, blue points = binned in phase.

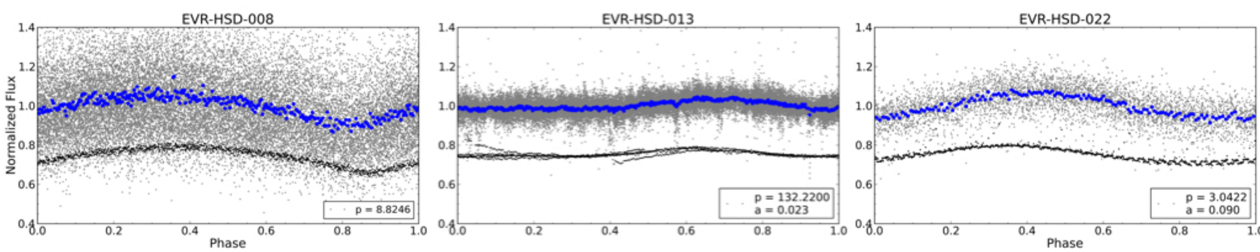

Figure 1.17: The Evryscope light curves of a potential high mass system, double-line binary, and close binary with an sdO primary. Grey points = 2 minute cadence, blue points = binned in phase.

observations would increase our sensitivity and cover longer periods, potentially recovering a transiting planet.

We found several reflection effect HSD binaries, one is solved in detail (EC 01578-1743) using followup light curve and radial velocity analysis to determine the masses and radii. Other reflection effect HSD binaries include a rare sdO primary, a 9-hour peculiar shaped light curve that could be indicative of a very high mass system, and a potential double-line binary (offering a rare opportunity to measure the HSD mass directly). Each of these systems deserve more detailed analysis, we report the discoveries along with our initial analysis and interpretation here. We partner with several collaborators (who are experts in the sub-fields) to guide and complete the followup analysis.

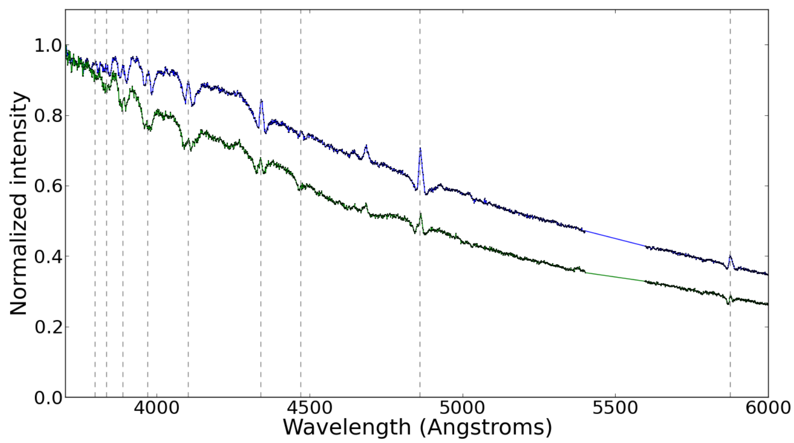

Figure 1.18: The SOAR ID spectra of a suspected debris disc discovered from the Evryscope light curve from the HSD survey, showing broadened absorption features and a high temperature consistent with a WD but with emissions indicative of debris or evolving accretion. The emission features change in amplitude as seen by comparing spectra taken in March 2019 (Blue) and September 2019 (Green). H-α to H-10(dashed lines) are shown for reference.

The survey revealed other potentially high-priority targets for followup. The most promising are an odd quasi-sinusoidal variable that also shows a shallow (4%) transit signal at a secondary period and a likely debris disc or low amplitude accretor. Again, we report the discoveries along with our initial analysis and interpretation in this work, and suggest followup analysis.

1.8 MLO Evryscope

In 2018, our group built and deployed an updated version of the Evryscope to Mount Laguna observatory (MLO) California, to complement the CTIO Evryscope by adding *Northern* all-sky coverage. I again led the design, construction, and deployment of all mechanical and structural components. The MLO Evryscope has been collecting images since early 2019, and the data is currently being processed by our photometric pipeline.

1.9 Future Work

Future planet searches will build on the three surveys described here. The Evryscope group will focus on HSD, WD, and late-K-dwarf transits as these are not well studied, are potential high-value discoveries, and they match the Evryscope instrument strengths. The WD and K-dwarf second surveys can benefit from specific changes, highlighted by the constraints identified from the first surveys. The WD survey needs more targets, as discussed previously and our second WD survey specifically focuses on this issue. The original K-dwarf planet survey (which was part of the Polar search) could have benefited from two primary changes. First, to identify the brightest potential K-dwarf targets and search this target group regardless of signal power. Second (and probably even more important) is having a more effective pipeline to process the light curves so that there are less residual systematics. This would allow for smaller transit signals (approaching 1% transits) to be detected, which are more likely to be gas-giants instead of false positives. The next generation Evryscope pipeline is re-processing all data from mid 2016 to current, we expect improvements in the systematics that will help detect gas-giants planets. The HSD survey was well matched to the Evryscope and did not require any major changes as illustrated by the favorable results and many discoveries. The next HSD survey will expand in scope and depth to build on the first survey, but with the added benefits that come with additional observations and an upgraded pipeline.

We also have a conceptual design for the next generation Evryscope, along with a prototype single telescope and camera unit. The new system will feature the same FoV and fast cadence as the current system, but with greatly increased resolution, sensitivity, and targets. I plan to focus my efforts on the HSD and next generation prototype work, and help other group members that want to explore the other areas. This is of course dependent on many still fluid factors, but is my goal.

1.10 Other

Throughout the course of my research it was necessary to develop a considerable amount of code (written almost exclusively in Python) in order to analyze data or control telescope components. The most significant codes are the spectral classifier (developed to identify the likely targets in the Evryscope dataset for our surveys), the Robotilter control software (designed to find the best alignment solution between the optics and camera given the four degrees of freedom and severe degeneracy), the discovery panel plot (used to efficiently inspect the potential targets for periodic transits), and the outlier code (designed to find difficult fast transit signals). Code details are provided throughout this work, in the chapters most relevant to the particular use.

1.11 Other Published Works

The Evryscope data has led to publications in research areas distinct from the focus of this thesis. The discovery of a superflare from the nearby M-dwarf Proxima Centauri is reported in [23] and a pre-discovery nova is discussed in [24]. Soon to be published are the results of long-term monitoring of flares from cool stars in the southern sky (Howard et al., submitted) and flare monitoring of Trappist (Glazier et al., submitted). I am a contributing author on each of these works.

1.12 Document Structure

The work in this thesis is organized by paper, beginning with the two instrument related papers. The Evryscope design and construction manuscript is presented in Chapter 2, and the Robotilter solution is described in Chapter 3. The surveys are presented next with the Polar in Chapter 4, the WD survey (draft) in Chapter 5, and the HSD survey in chapter 6. Select individual discoveries from the HSD survey that warranted their own publication comprise chapters 7-9. I briefly discuss future work and conclude in chapter 10.

CHAPTER 2: BUILDING THE EVRYSCOPE: HARDWARE DESIGN AND PERFORMANCE

This section presents results published in the *Publications of the Astronomical Society of the Pacific*.[1,2]

2.1 Introduction

The Evryscope is a telescope array designed to open a new parameter space in optical astronomy, detecting short timescale events across extremely large sky areas simultaneously. The system consists of a 780 MPix 22-camera array with an 8150 sq. deg. field of view, 13” per pixel sampling, and the ability to detect objects down to $m_{g'} \simeq 16$ in each 2 minute dark-sky exposure. The Evryscope, covering 18,400 sq.deg. with hours of high-cadence exposure time each night, is designed to find the rare events that require all-sky monitoring, including transiting exoplanets around exotic stars like white dwarfs and hot subdwarfs, stellar activity of all types within our galaxy, nearby supernovae, and other transient events such as gamma ray bursts and gravitational-wave electromagnetic counterparts. The system averages 5000 images per night with ~300,000 sources per image, and to date has taken over 3.0M images, totalling 250TB of raw data. The resulting light curve database has light curves for 9.3M targets, averaging 32,600 epochs per target through 2018. This paper summarizes the hardware and performance of the Evryscope, including the lessons learned during telescope design,

[1]Ratzloff JK, Law NM, Fors O, Corbett H, Howard W, Del Ser D, and Haislip J. Building the Evryscope: Hardware Design and Performance. *Publications of the Astronomical Society of the Pacific* 2019; 131:075001. DOI: 10.1088/1538-3878/ab19d0.

[2]The writing in this paper was split 60/40 between Ratzloff and Law. I focused on the overall paper, mechanical design, expected surveys, and preliminary results sections, while Law focused on the scientific cases, software control and pipeline sections. In the actual system design, integration and testing, I created all of the 3D design models, did all the simulation based testing, and led the assembly and mechanical components of the entire system.

electronics design, a procedure for the precision polar alignment of mounts for Evryscope-like systems, robotic control and operations, and safety and performance-optimization systems. We measure the on-sky performance of the Evryscope, discuss its data-analysis pipelines, and present some example variable star and eclipsing binary discoveries from the telescope. We also discuss new discoveries of very rare objects including 2 hot subdwarf eclipsing binaries with late M-dwarf secondaries (HW Vir systems), 2 white dwarf / hot subdwarf short-period binaries, and 4 hot subdwarf reflection binaries. We conclude with the status of our transit surveys, M-dwarf flare survey, and transient detection.

Astronomical surveys searching for time-variable objects and events typically observe few-degree-wide fields repeatedly, use large apertures to achieve deep imaging, and tile their observations across the sky. The resulting survey, such as the Palomar Transient Factory [1], Pan-STARRS [3, 18], SkyMapper [4], ATLAS [64], CRTS [65], ZTF [2], and many others, is necessarily optimized for events such as supernovae that occur on day-or longer timescales. These surveys are not sensitive to the very diverse class of shorter-timescale objects, including transiting exoplanets, young stellar variability, eclipsing binaries, microlensing planet events, gamma ray bursts, young supernovae, and other exotic transients, which are currently only studied with individual telescopes continuously monitoring relatively small fields of view, or groups thereof. Short-timescale surveys including HAT [6], SuperWASP [8], KELT [9], and many others observe dedicated sky areas to reach very fast cadence and good sensitivity, but at the expense of all sky coverage. The Evryscope is designed to reach bright but rare events by optimizing for shorter-timescale observations with continuous all sky coverage continued for many years.

The Evryscope (Figure 2.1) uses an array of 22 telescopes to cover the Southern sky down to an airmass of $\approx$2.0 in each exposure. The system averages 5000 images per night with $\sim$300,000 sources per image. The Evryscope features mass-produced compact CCD cameras and lenses, and a novel camera mounting scheme to make a reliable, low-cost 0.8 gigapixel robotic telescope. We built the Evryscope at UNC Chapel Hill in early 2015 and deployed it

Figure 2.1: The Evryscope, a two-dozen-camera array mounted into a 6 ft-diameter hemisphere, deployed at the CTIO observatory.

to CTIO in Chile in May 2015. The system has collected data continuously since first light in May 2015. As of March 2019, we have taken over 3.0M images resulting in 250TB of raw data. The resulting light curve database has light curves for 9.3M targets down to m_g=15 (and fainter for selected targets), averaging 32,600 epochs per target through 2018.

The Evryscope mounts an array of individual telescopes into a single hemispherical enclosure (the "mushroom"). The array of cameras defines an overlapping grid in the sky providing continuous coverage of 8,150 square degrees. The camera array is mounted onto an equatorial mount which rotates the mushroom to track the sky with every camera simultaneously for 2 hours, before "ratcheting" back and starting tracking again on the next sky area (Figure 2.2). Each of the telescopes has three-hundred-square-degree fields of view, 28.8 megapixels, and a 6.1cm aperture. The Evryscope allows the detection and monitoring of objects and events as faint as $m_{g'}$=16.5 in few-minute exposures ($m_{g'}$=15-16 under typical sky conditions) and as faint as $m_{g'}$=19 after co-adding. The telescope specifications are given in Table 2.1.

The Evryscope has already contributed to a wide variety of science cases, ranging from precision studies of single targets [20–22] and (Ratzloff et al., submitted), to statistical studies of stellar activity (Howard et al., in prep), variable star discoveries [66], hot subdwarf / white dwarf short-period binary discoveries (Ratzloff et al. submitted), and transient discovery and followup [23, 24]. In this paper we, in addition to describing the Evryscope hardware, describe some of the first Evryscope discoveries from general stellar searches. A previous paper [17] describes the detailed Evryscope science cases. Subsequent papers will describe the data analysis pipelines in detail.

This paper is organized as follows: in § 2.2 we explain the Evryscope system, design, and primary components. In § 2.3 we describe the on sky performance. § 2.4 describes the transit detection methods, and shows example light curves and select first discoveries. In § 2.5 we conclude.

2.2 System design

2.2.1 Science requirements

The Evryscope's science requirements were based on a study of the science possibilities for an all-sky telescope with an Evryscope-like design, detailed in [17] and summarized in Table 2.2. With eighteen major science cases for the system, each of which having somewhat different needs, the setting of exact requirements was challenging. To constrain the design space and allow choices to be made, we settled on three simple requirements: a field of view around 8,000 square degrees, a 3-sigma limiting magnitude of $m_{g'} \simeq$16, a pixel scale sufficient to avoid crowding for 90% of sources above a galactic latitude of 15°, photometric precision better than 1% for bright stars, and the ability to co-add images to increase the target depth.

Table 2.1: The specifications of the Evryscope

Hardware	Description
Telescope mounts	27 (22 populated); shared equatorial mount
Telescope glass	61mm Rokinon F1.4 lenses
Mechanical mounting	Fiberglass dome with aluminium supports
Detectors	28.8MPix KAI29050 interline-transfer CCDs
	7e- readout noise at 4s readout time
	≈50% QE @500nm; 20,000 e- full-well capacity
Field of view (Measured on sky)	8150 sq. deg. total (excluding ≈10% overlaps)
Sky coverage per night	18,400 sq. deg. (2-10 hours per night coverage)
Total detector size	780 MPix
Sampling	13" /pixel
Observing strategy	Track for 2 hours; reset and repeat
Data storage	All data recorded for long-term analysis
	∼50TB / year after all overheads
Performance	**Description**
PSF 50% enclosed-energy diameter	2 pixels in central 2/3 of FoV; 2-4 pixels other
Exposure time	120s
Limiting magnitude	$m_{g'}$=16.0 (3-sigma; 120s exposure)
Photometric performance	1% photometry on $m_{g'}$ <12 stars every 2 minutes
	6 % photometry on $m_{g'}$=13.5 every 2 minutes
	10 % photometry on $m_{g'}$=15.0 every 2 minutes

2.2.2 Overall design

Starting with the general plan of an array of telescopes mounted together, we evaluated several concepts for the overall system design, including a flat tracking platform with each camera bolted to it, adjustable trusswork supporting each camera, and a spherical-shape rotated around its polar axis [67]. We settled on a hemispherical dome mounted on an equatorial mount (the "mushroom"). This offered two advantages: the camera support structure could be a single piece with no per-camera adjustment or alignment required, and the tracking mount, the single moving main structure and therefore critical to reliability, could be a single off-the-shelf system. We summarize our overall design in Figure 2.2.

Table 2.2: The Evryscope science cases

Field	Description
Exoplanets	White-dwarf transits & debris disks
	Hot-subdwarf transits & debris disks
	Habitability-affecting superflares
	Eclipse timing exoplanet detections
	Confirmation of TESS single-giant-planet-transit events
	Long-period rocky exoplanets transiting M-dwarf stars
Stellar astrophysics	Low-mass-star rotation and activity
	Long-period eclipsing binaries for mass-radius relations
	Young-star activity and multiplicity
	Star-planet activity interactions
	Interacting binary outbursts
	Long-period dust dips
Transients	Gravitational-wave electromagnetic counterparts
	Microlensing exoplanet detection
	Galactic nova events
	Nearby, young supernovae
	Gamma-ray burst counterparts
	Fast-radio-burst counterparts

2.2.3 Camera array design

An Evryscope-type array telescope design has an enormous range of possible design choices. The choice of CCD array size must be traded-off against the choice of lens, the point-spread-function (PSF) quality available over the chosen array size, the pixel scale resulting from a particular lens/CCD combination, and more subtle factors like vignetting and angular quantum efficiency. With the CCD detectors being the driving cost, the science requirement flowdown to the technical requirements was informed by a hardware-budget target of ≈$300k.

2.2.3.1 Lens and CCD choice

With dozens of lenses and CCD-arrays available from a multitude of manufacturers, we performed a comprehensive trade study of the possible lens/CCD combinations. The pixel scale was set by the anti-crowding science requirement to be smaller than 20 arcsec, and we set the field of view to 8,000 square degrees. With those parameters fixed, we evaluated

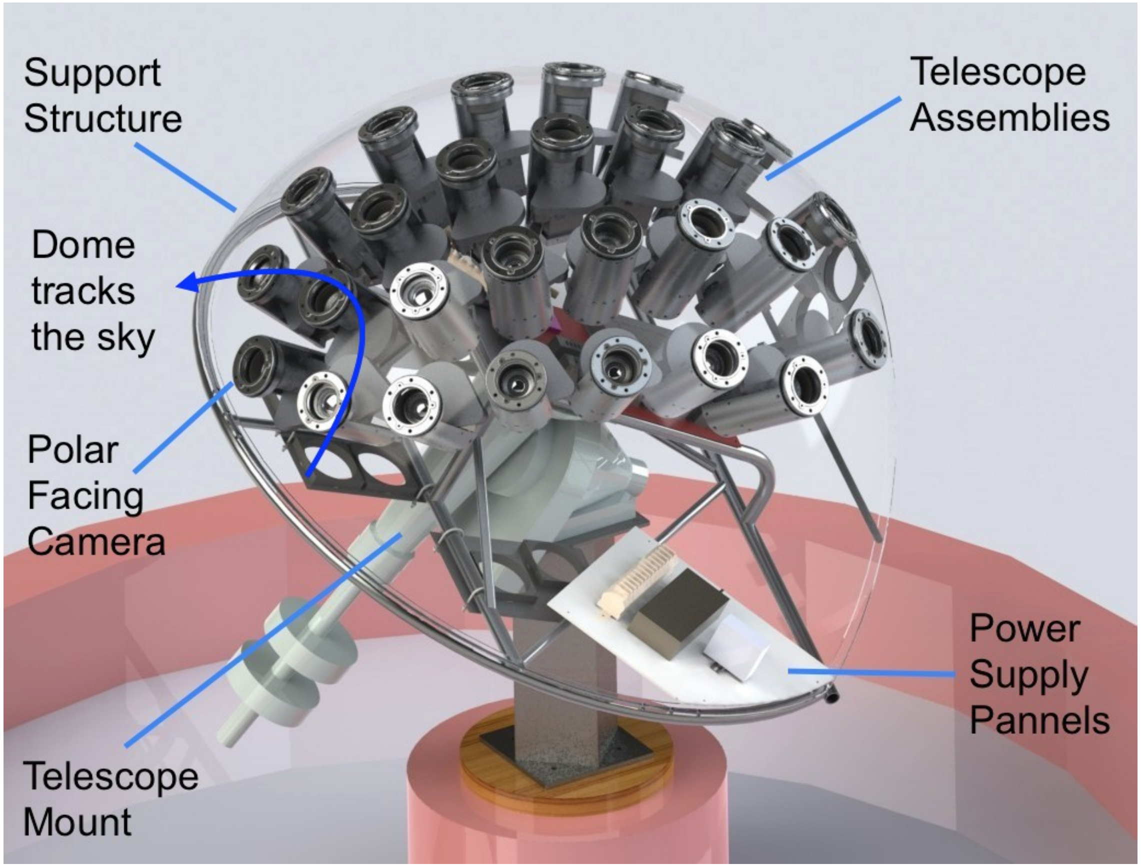

Figure 2.2: Cutaway rendering of the Evryscope showing the telescope mount, camera locations, and primary instrument components.

each lens/CCD combination based on the SNR that could be achieved all-sky on a $m_{g'}$=16 source. The SNR calculations included the likely PSFs and vignetting generated by each lens/CCD combination, the expected sky background and source photon noise contributions, the detector characteristics, and many other factors, and most lens/CCD combinations were not able to achieve the required SNR because of one of those factors.

We elected to limit our CCD selections to interline-transfer chips which have electronic shutters. Our prototype systems [68] both suffered mechanical shutter failures during their arctic deployments, with the achieved number of error-free exposures being just over one-tenth the specification. Although the failures were correctable by individually adjusting the tension of internal springs every few months, this is untenable in a robotic system with dozens of cameras. The use of electronic shutters effectively eliminates this failure mode.

The trade study resulted in a single workable choice for lens/CCD combination: a Rokinon 85mm F/1.4 lens combined with a KAI29050 CCD array. All other combinations resulted in unacceptably-low SNR or budgets factors-of-several times larger than our target amount. The KAI29050 array had a particular advantage in its rectangular format: most photographic lenses have rapid fall-offs in PSF quality towards the edges of the frame, and square arrays can therefore have poor image quality in the corners [68]. Compared to a square format, a rectangular array trades off highly-off-axis image area at the corners for less-off-axis area at the left and right edges of the array, and thus has more uniform PSFs across the image than a square CCD with equivalent area. Based on our positive experience with previous similar cameras, we elected to use thermoelectrically-cooled Finger Lakes Instrumentation ML29050 units.

2.2.3.2 Camera position optimization and system field of view

We next built a metric to optimize the camera positions in the array. Each camera produces a rectangular field on the sky, with a large enough field of view that spherical geometry must be taken into account for even simple sky-area calculations. We designed the camera array positions to 1) optimally tile over the above-airmass-two field of view; and 2) avoid large areas of overlap between cameras; 3) retain a few-degree overlap between each camera to constrain systematics.

We designed a code to project the field of view of each camera onto the sky, taking spherical geometry into account. The code then divides the sky into patches approximately 0.3° across, counts the number of cameras pointed at each patch, and measures the total sky area and overlap areas covered between different combinations of cameras. Starting with a simple arrangement of cameras divided into rows of declination, we then varied the position of each camera in the array using an annealed downhill-simplex algorithm, optimizing for overlap and covered sky area [69]. The optimization converged on an arrangement very similar to the input declination-separated grid of cameras; other camera arrangements we explored did not produce significantly better performance metrics. For ease of fabrication we used the simple declination-separated grid to place the cameras, with spacing parameters inherited from the fully-optimized solution (Figure 2.3).

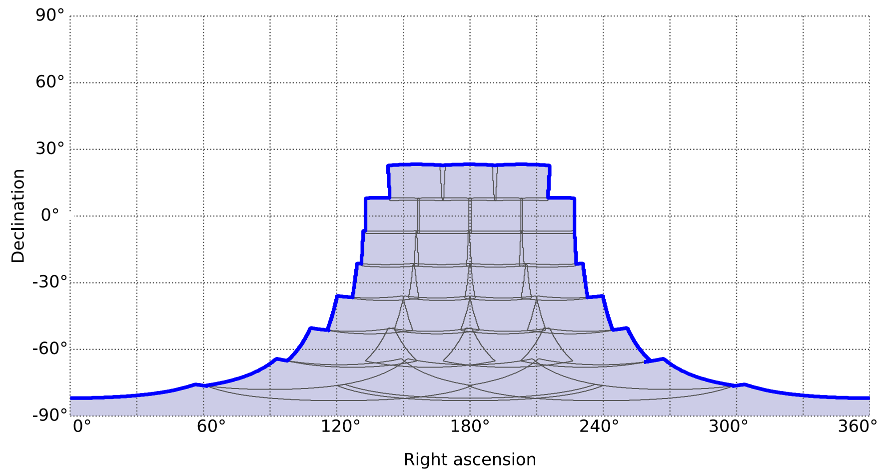

Figure 2.3: The Evryscope camera placement when deployed at the CTIO observatory (some of the Northern camera spots are currently unpopulated).

Each camera assembly rotates in a circular arc around the pole facing camera as the mushroom tracks the sky. Over the course of a typical night the system covers $\approx 18,000$ sq. deg. (Figure 2.4), with each part of the sky being observed at two-minute cadence for 4-10 hours per night.

Each CCD is orientated so that its long axis (designated as the x-axis) is tangential to this arc; this ensures the objects in each image remain in a constant orientation throughout the night. There are seven rows, with the cameras in each row sharing the same pointing declination, equidistant from the pole camera. The camera mounting flanges (and therefore the CCDs) are normal to the surface of the mushroom dome, which ensures that the cameras are pointed in the proper direction without manual alignment being necessary. We designed the mushroom to be capable of supporting 27 telescopes; at CTIO 24 are Southern hemisphere

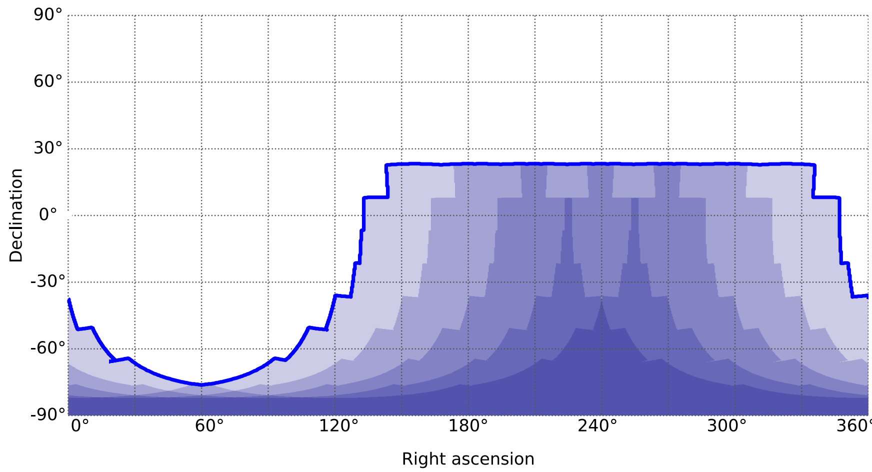

Figure 2.4: The 18,000 square degree coverage of the system over a single night. The depth of coloration corresponds to the number of two-hour ratchets covering each part of the sky; each ratchet includes sixty two-minute epochs.

facing and three cover positive declinations. The number of operational cameras has varied slightly during the course of the project: 22 or 23 cameras have been operational in 2015-2017, with another camera reserved for testing. We plan to fill in all available slots in the near future.

2.2.4 Telescope structure, tracking and image quality optimization

Mechanically, the Evryscope consists of an array of cameras mounted into a hemisphere (the mushroom), which in turn is mounted onto a German-equatorial mount which keeps all the cameras tracking.

2.2.4.1 Camera hardware units

The camera hardware units fix the cameras to the mushroom, provide mechanical support of the components, and a mount for a protective window. The camera mounts have three primary constraints on their design: flexure limits, size and weight. Although atmospheric refraction precludes keeping each star on the same pixel while tracking [17], we designed the camera mounts to not contribute any extra drift throughout the Evryscope's range of motion, requiring the relative camera mount flexure to be less than 13 arcsec. The size of the mushroom was set to a 6-foot diameter by our target dome, and this set the packing requirements for the cameras. Since there are two dozen camera mounts with relatively heavy CCD units, they and the systems they contain are the primary drivers of the weight of the system. A trade study of available mounts suggested that significant cost savings were possible if the total mushroom weight could be kept below 400 lbs.

We used 3D modeling to test several hardware unit designs, with the goal to minimize weight, flexure, and complexity. The final version (Figure 2.5) features interlocking sections for added rigidity, weighs less than 4 lbs (supporting imaging hardware which weighs 8.0 lbs), and provides a maximum differential flexure of less than 10 arcsec. The maximum flexure in the vertical orientation is $\approx$.02 mm and over the course of a telescope ratchet the differential movement due to the changing camera orientation is well within our 1 pixel goal. The camera mounts are interchangeable, have locator pins to easily place the cameras into the proper orientation in the mushroom, and perform equally well in flexure for all cameras regardless of the declination row (which have considerably different gravitational vectors).

Each mount has an outer window to protect the lenses and electronics from dust, water, and other possible contaminants, enabling easy cleaning as well a providing a backup to the observatory dome. The high transmission (over 96% in the visible range) optical window is mounted on a soft o-ring with a stainless steel retaining ring, and allows for easy cleaning of dust during maintenance.

Interline transfer CCDs cannot take darks without extra mechanical shutters, so we elected to use a filter wheel with a blocked position to allow calibrations to be taken. The Finger Lakes Instrumentation CFW-5-1 filter wheels also provide a sunshield (§ 2.2.7.4) and science filter changing capability.

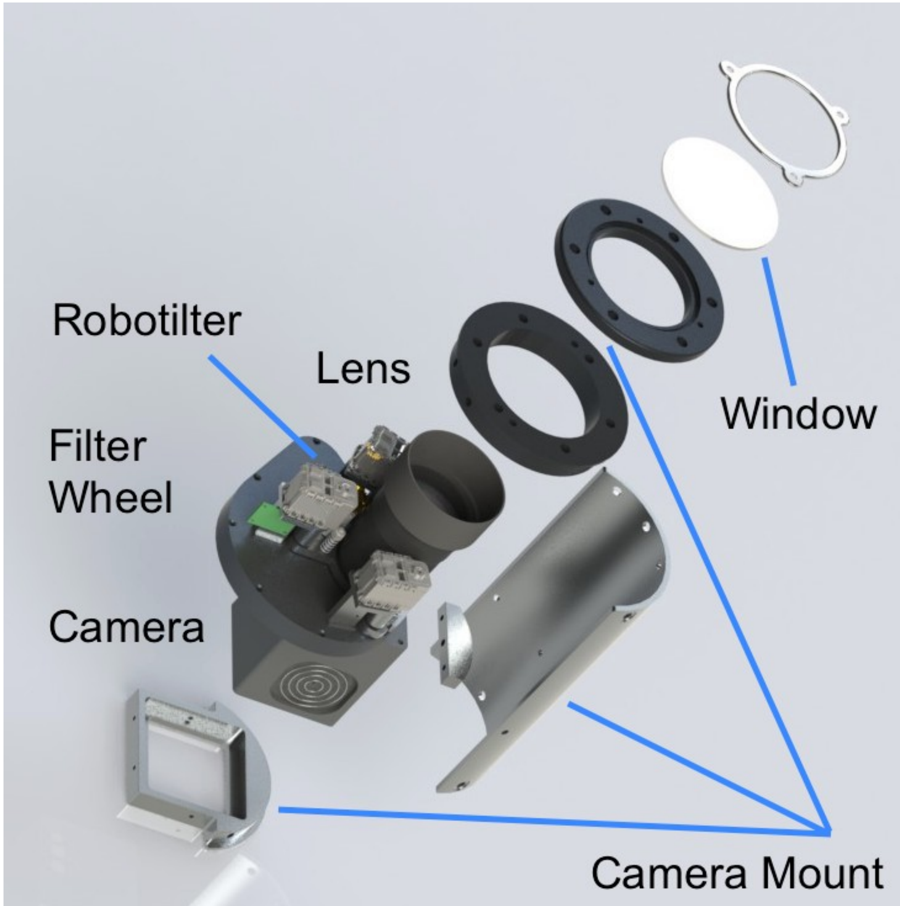

Figure 2.5: The Evryscope unit camera assembly

2.2.4.2 Precision lens/CCD alignment systems ("Robotilters")

Camera lenses are used on SuperWASP [8], HAT [6], KELT [9], XO [10], and other transiting exoplanet surveys to reach as much as 1000 square degree fields of view. Other surveys types such as the ASAS-SN (supernova) [15], Pi of the Ski (gamma ray bursts) [14], Fly's Eye (asteroid detection) [13], and HATPI [3] also use camera lenses to reach wide sky coverage. These types of wide field surveys and many others including the Evryscope are susceptible to image quality tilt and focus challenges. Even a slight misalignment between the optics and the CCD causes a tilt which results in an unacceptable increase in size of the PSF FWHM towards the edges and corners of the image. For the Evryscope, the very wide field of view (380 sq. deg.), fast F# of each lens and the small 5.5μm pixels exaggerate this effect.

[3] `https://hatpi.org`

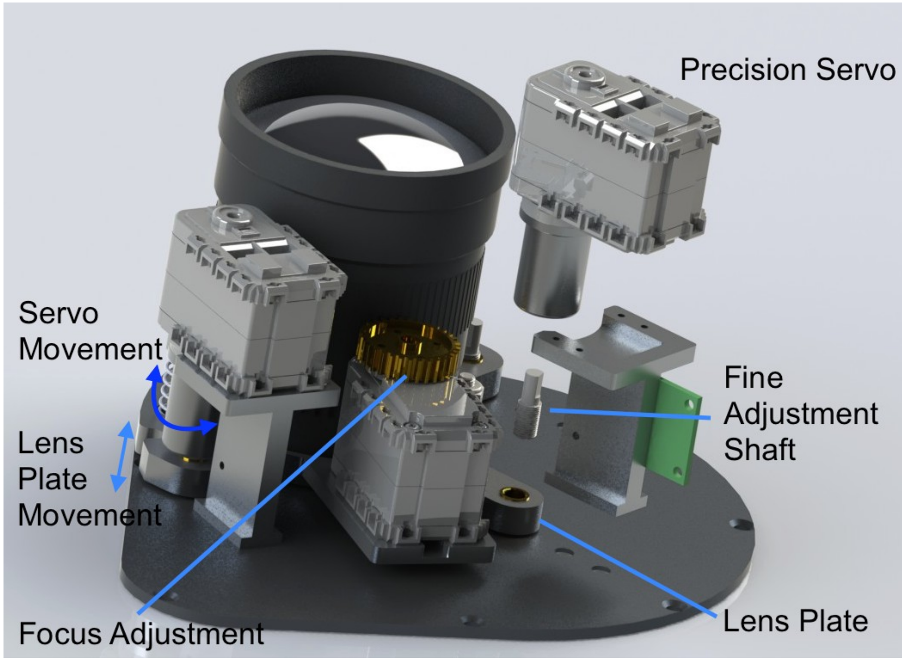

Figure 2.6: The Robotilter automated tilt/alignment/focus system

While the machining tolerances (+/-.005 inch in most cases) and the assembly tolerances of the mass produced lenses, adapters, filter wheels, and CCD assemblies is reasonable for their standard usages, it is not precise enough to achieve the absence of tilt required for the needed Evryscope image quality.

We designed a robotic tilt adjustment mechanism (Figure 2.6) to address those challenges, with the ability to remotely and precisely re-align the camera assemblies. The Robotilter (Figure 2.6) uses three precision servos controllable to within 4 degree steps coupled to an 80 thread per inch adjuster to move the lens position relative to the CCD. This allows adjustment of the tilt as well as the lens/CCD separation in increments as fine as .003 inch. The design uses specialized flexible shaft couplings to prevent binding and tension springs to hold the lens accurately in place. The assembly mounts to the top plate of the filter wheel to avoid costly re-configuring of the existing filter wheel, CCD, or camera mount. A separate servo independently adjusts the lens focus position to compensate for tolerance differences due to temperature changes throughout the year. The Robotilters were installed in November 2015 and the cameras were aligned remotely in early 2016; the installation of the Robotilters was the final step in commissioning the system. The Robotilters and resulting image improvements are described in detail in our technical paper [70].

2.2.4.3 Mushroom structure and wind shake

The camera support structure (the mushroom, Figure 2.1) needs to provide the same limited flexure as the camera mounts, while also bearing the 400lbs load of up to 27 camera assemblies and related components. We chose a molded fiberglass hemisphere with support ribs along the bottom and back for extra strength and rigidity, and a sturdy mounting point. The material is hand-laid cloth weave fiberglass, providing light weight and minimal flexure with excellent durability. The mushroom also features reinforced and precison-located inner and outer camera-mount flanges to provide accurate and secure mounting points. The camera flanges are normal to the surface, and the holes are CNC cut into the mushroom to ensure the precise location necessary to achieve the desired field coverage without holes or excessive overlap. The manufacturing tolerances are .020 inch on the hole locations, and based upon this the camera alignment is fixed normal to the mushroom surface and the long side CCD is perpendicular to the rotation axis. Our 3D model simulation predicts that despite the close packing of the cameras and considerable weight, the stress is mostly compression and results in absolute movements on the scale of .02 mm. Differential camera movements over the tracking cycle are on the order of microns ensuring accurate camera pointing. On-sky pointing accuracy is well within the simulated performance.

The hemispherical shape of the mushroom, along with the placement of the instrument so that the dome leafs in the open position are slightly higher than the mushroom base, help make the Evryscope resilient to wind shake. The system is able to operate in 30 mph winds without a measurable change in image quality.

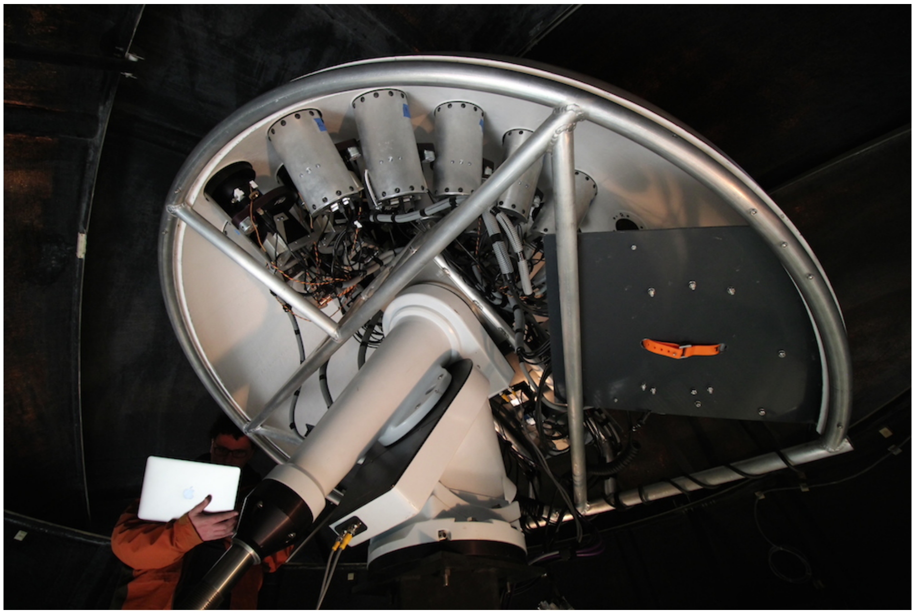

Figure 2.7: The Mathis German Equatorial mount, the tubular base structure, and the mounted mushroom - showing the instrument inset, mass alignment, and camera accessibility.

2.2.4.4 Tracking mount

The base structure (Figure 2.7) attaches the mushroom to the Mathis 750 mount, via a mount plate attached to the tracking mount and a structure which transfers the mechanical load from the mushroom fiberglass. We tested several design ideas via finite element analysis and found a reinforced round tubing design to be most effective. Using aluminum tubing, we reduced the weight in half from a similar design made of steel and kept the total flexure within requirements. The differential camera displacement of the mounting base throughout the telescope tracking is on the order of microns, and combined with the mushroom and camera mount flexure is simulated to be within our total goal of 1 pixel, with comparable performance measured on-sky.

The proper location of the center of mass is critical to reliable telescope mount operation. We inset the mount plate significantly into the mushroom so that the effective lever arm of the Evryscope cameras is minimized (Figure 2.7). The center of mass is only 10 inches from the mount plate, which greatly reduces the load on the telescope mount compared to simpler designs. The base structure positions the Evryscope so that the center of mass in the mounted position is directly over the telescope mount axis center, further reducing stress on the telescope mount and easing the balancing of the instrument.

The polar alignment of the mount is critical to the tracking performance of the system. Because the system's field of view is such a large fraction of the sky, conventional pointing models cannot be used, because they optimize the performance on one part of the sky by reducing performance on other parts of the sky. For this reason we developed a precision polar alignment procedure specifically for Evryscope-like instruments (§A.1).

On sky performance confirms the predictions of the flexure and center of mass simulations. The camera pointing is accurate within a tenth of a degree, providing the proper field of view overlaps without gaps (except for one initial, now corrected, misalignment caused by a contaminated bolt thread). The camera orientations remain constant throughout sky tracking. The telescope mount tracks the sky consistently without stalling or shifting, and we conclude that the total flexure is very close to the 1 pixel goal.

2.2.4.5 Dome

The Evryscope is located in an AstroHaven clamshell dome originally built for the PROMPT network of telescopes [36]. The dome had already been used for routine long-term operation, and no mechanical changes beyond a custom pier structure were necessary for the Evryscope deployment. Careful electrical design was necessary, however; the large dome opening/closing motors can induce strong transients onto power and potentially signal lines from the dome. To avoid possible interference or even damage, we separated the dome electrical systems on a separate UPS system. A Raspberry-Pi single-board computer runs the dome-control daemon and communicates with the rest of the system via an electrically-isolated ethernet connection; there are no other direct electrical links between the Evryscope and the dome.

Figure 2.8: The Evryscope in PROMPT dome 4.

2.2.4.6 Observatory site & weather-related design

The Evryscope is deployed at CTIO in Chile in PROMPT [36] dome 4 (Figure 2.8). The site was chosen for the large number of usable nights ($>$ 320 per year), dark sky conditions ($m_v = 21.8$ moonless night background average), and Southern sky visibility. UNC affiliated hardware and support synergies, especially the PROMPT Program, were also advantageous.

The dome and observatory site introduced several design constraints: 1) a maximum power consumption of 15A/120V; 2) operation with a relatively small internet bandwidth that precludes the realtime off-site transport of data; 3) the potential for lightning strikes and earthquakes (§ 2.2.7); 4) potential external temperature ranges of $-15°$C to $+25°$C; and 5) extremely dry conditions.

The low end of the temperature range is outside that which most off-the-shelf electronics are rated for. Wherever possible we purchased industrial components rated for low-temperature operation (typically $-20°$C). In some cases we tested and used off-the-shelf consumer electronics (for example, Raspberry-Pi single-board computers); testing was performed in fridge-freezer units under a range of relative humidity (see [68, 69] for testing details).

The potential for extremely dry weather spells required careful electronic and mechanical design. For example, Nylon becomes brittle under extremely dry conditions [71]; this can cause failures in cable insulation and zip-tie-type harnesses in a matter of months, leading to possible short circuits or mechanical interference between cables and moving parts. The static electricity discharges prevalent in dry conditions can cause electronic failures, especially while personnel are maintaining the system. Many power supplies and similar units are rated only to 20% relative humidity, while the CTIO site can regularly reach low-single-digit humidity. We mitigated these concerns by using only plastics, connectors, and electronics rated for long-term extremely dry conditions. All metal components are grounded, with isolators used to avoid ground loop conditions, and we take operational steps to ground personnel before working on the system.

2.2.5 Electrical and electronic design

The Evryscope mushroom contains over 600ft of cabling, with further ancillary systems located outside the main telescope body. Figure 2.9 shows an overview of the power and data paths within the dome.

2.2.5.1 Power distribution

The Evryscope cameras together require a maximum of $\approx 170A$ of 12V power; the ancillary systems with the mushroom (Robotilters, filter wheels, fans, USB hubs, etc.) together require a further ≈20A of 12V power. The AWG-1 (quarter-inch-diameter) cables required to safely carry the required 200A into the mushroom would be bulky and inflexible, and risky if frayed or overheated. Powering each camera from its own 12V supply would lead to a very bulky and heavy power distribution system, beyond the load capacity of the mushroom mount. For those reasons we elected to send 120V AC power into the mushroom

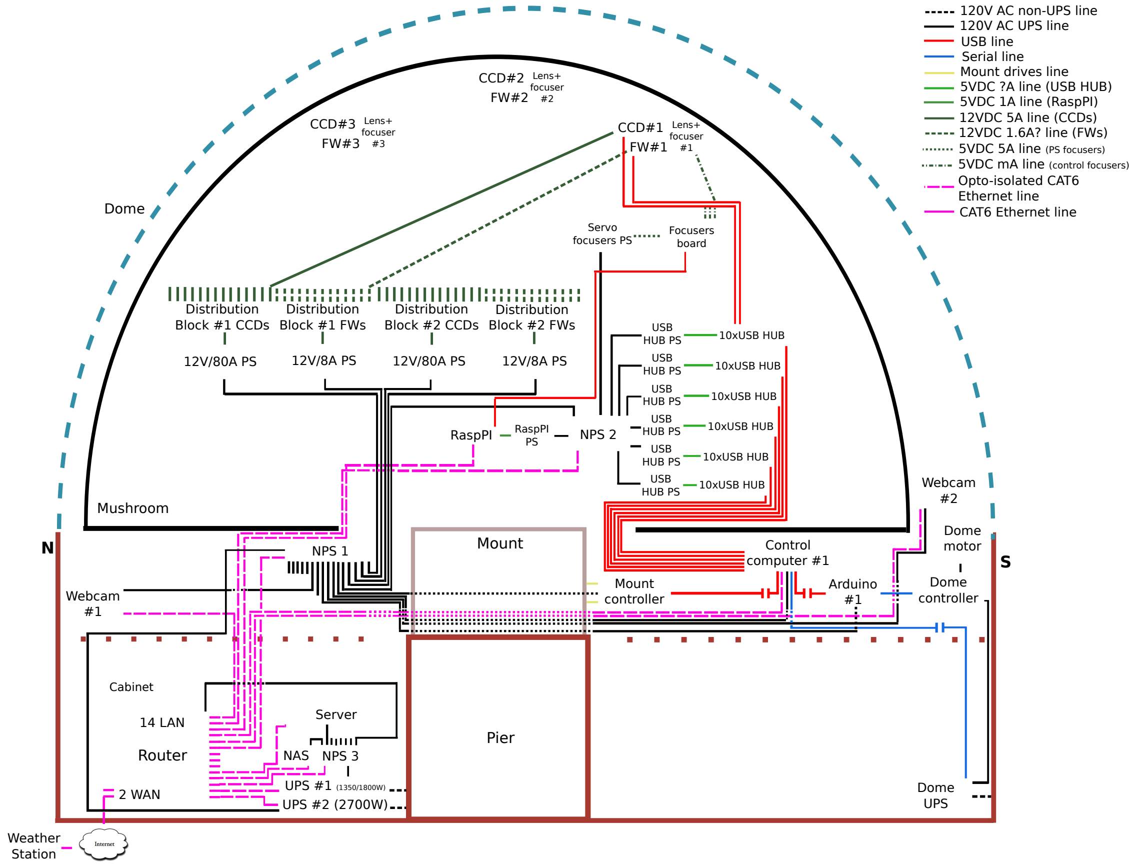

Figure 2.9: The Evryscope Wiring Diagram.

over a single flexible small-diameter cable, and use two 120A-capable 12V power supplies to power the main camera systems. We deliberately overspecified the power supplies to reduce the need for active cooling and the associated vibrations. Ancillary systems are powered from their own smaller 12V power supplies, with Digital Loggers Network Power Switches allowing computer-controlled switching of each component. Although it has proven reliable, this setup resulted in over 600ft of cabling inside the main mushroom, because each camera has six separate cables going into it (3 power, 3 data). These cables are heavy and impede airflow; the Northern Evryscope, currently under commissioning, has relay and control systems built into each camera to reduce the number of required cables to two per camera.

The two 120V input / 12V 80A output power supplies are mounted on panels attached to the wings of the base inside the mushroom (Figure 2.10) . Fused distribution blocks with custom cabling connects the power to the cameras. The filter wheels use a similar, but

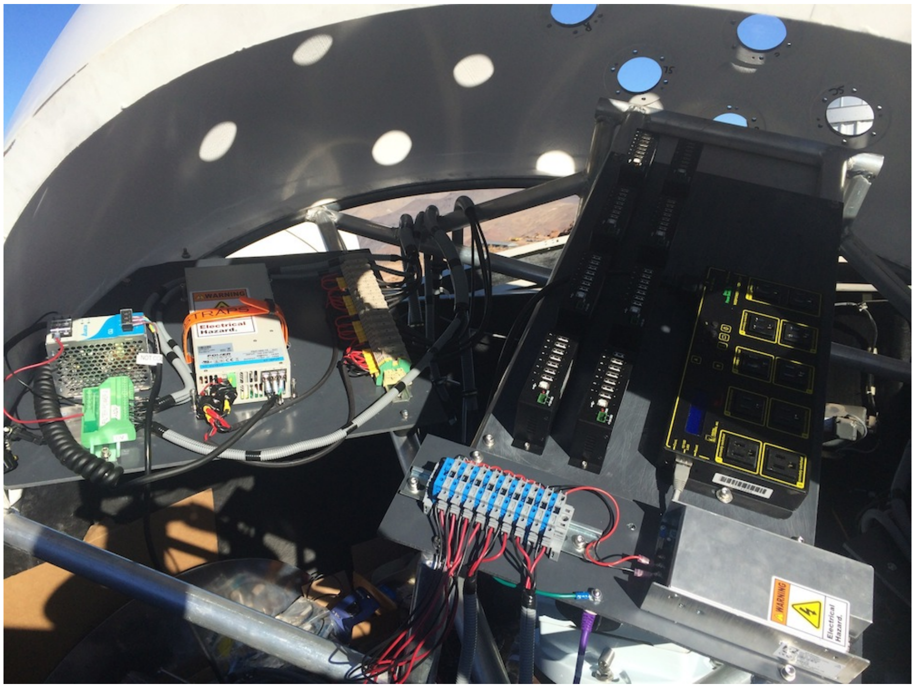

Figure 2.10: The power supply panels; left is the camera and filter wheel power/distribution and the right are the USB hubs and NPS.

smaller 120V input / 12V 8A output power and distribution located on the same panels. An additional 120V input / 12V 8A output power supply is also available on each panel to supply the focus servos, cooling fans, and other accessories. A panel attached to the center of the base over the mount (Figure 2.10) holds a Network Power Supply (NPS) and a power supply for the USB hubs used to control the cameras assemblies. The selection and placement of the power systems allows for proper balancing of the mushroom assembly, cooling of the electronics, access to all of the components, and provides a safe supply of power to many different systems confined in a small area.

2.2.5.2 Cooling

The Evryscope uses up to 1.2kW when all cameras are cooling at maximum power, producing a significant amount of heat within a 6-ft semi-enclosed space. In-lab tests showed that parasitic heating between cameras could lead to a thermal runaway under some environmental conditions: cameras pulling in warm air exhausted by the thermoelectric coolers of neighbouring cameras must work harder to cool their sensors, increasing the amount of waste heat exhausted, and causing other cameras to further increase their cooling power. This process headed for runaway when the air temperature inside the mushroom exceeded $\approx 32°C$. Although several layers of protection prevent hardware damage from overheating (§ 2.2.6) this could have impacted system uptime during summers.

We implemented three systems to eliminate the parasitic heating. First, we built aluminum deflectors to move the camera exhaust air towards the center of the mushroom. Second, we added a bank of 8 120mm low-vibration 12V fans to direct cool air to the top of the mushroom. Third, we added external Vornado high-volume industrial fans to direct large amounts of external cool air to the mushroom (when rarely necessary). Together, these systems produce a coherent flow of cool air from the front-bottom of the mushroom to the top of the dome and down again out of the back of the systems. Testing showed no measurable effect on image quality when all systems are activated. The thermal protection systems have not triggered a shutdown since this system was commissioned.

2.2.5.3 Environmental Monitoring

We monitor the hardware status with sensors distributed around the mushroom and dome, all linked to the main control system via ethernet or USB connections. The main control computer runs automated analysis and control scripts, and alters the state of fans as necessary to maintain stable temperatures around the cameras. Logs of all sensor values are recorded each minute.

Inside the mushroom, each camera has an external temperature sensor, measuring the air temperatures at 22 points around the dome. An environment-monitoring Raspberry-Pi is located at the center of the mushroom. Its custom-built sensor board monitors the overall mushroom temperature with a wide-angle infrared thermometer, the center-mushroom temperature with a built-in sensor, and the tilt of the mushroom using a precision three-axis accelerometer. A timing GPS system is also connected at that location. A summary of all sensors is shown in Table 2.3.

Table 2.3: The Evryscope Environmental Monitoring Sensors

Description	Location
Mushroom interior temperature	22 sensors in cameras
Overall mushroom temperature	Watchdog RasPi
Mushroom electronics temperature	Watchdog RasPi
Three-axis-accelerometer tilt	Watchdog RasPi
GPS timing sensor	Watchdog RasPi
Webcam dome light level sensor	Dome control RasPi
Rain sensor	Dome control RasPi
Smoke detector	Dome floor
Pier-base temperature sensor	Mount controller
Weather station	PROMPT array

Outside the mushroom, two webcams continuously monitor the system from the North and the South. The Northern webcam is a pan/tilt unit; the Southern webcam is a Raspberry-Pi camera which, in addition to providing a view of the mushroom internals, automatically monitors the light level in the dome. If the light level is consistent with the dome being unexpectedly open in daytime, a loud alarm bell is sounded and the Evryscope team is alerted via email.

We use the PROMPT weather monitoring system [36] for dome open/close decisions; this system has been in reliable operation for almost a decade. The PROMPT weather station monitors cloud levels, wind, and dewpoint. We use the RASICAM [72] system to log cloud measurements for data-quality testing.

2.2.5.4 Data & control signal distribution

The main control computer, watchdog and environment-monitoring computers and data-storage and analysis servers are located within the telescope dome, with optical fiber connections to a backup storage site in an adjacent PROMPT dome. The Evryscope data and control bus is a gigabit ethernet system operating as a separate subnet behind a router connected to the main CTIO network.

A single sealed and fanless Logic Supply ML600G-30 rugged computer runs the robotic control software (§ 2.2.6) and the USB-controlled devices, including the cameras, filter wheels, Robotilters, and the mount.

Over 50 individual USB devices are connected to the control computer, which produces challenges to reliable system operations (ethernet control was not available for our chosen cameras at the time of system design). We initially connected groups of 4-8 USB devices together using powered USB hubs. However, lab testing showed occasional USB-bus-voltage brownouts, where the 5V power supply in a typical computer could be pulled out of voltage specification just by connecting dozens of USB devices, even when the devices were powered off and connected via powered hubs. This could prevent the control computer starting up or cause unreliable operation, and occurred for all tested brands of USB hubs. We eliminated this problem by finding and removing an undocumented jumper inside Starlink ST7200USBM rugged USB hubs which completely disconnects the upstream USB power rails from the downstream devices; this produces reliable operation with at least 60 USB devices connected.

2.2.6 Robotic control software

The Evryscope is controlled by custom Python framework running on several computers within and outside the mushroom. We use a daemon-based software model, where each subsystem is controlled by an individual script operating as a separate process; this ensures that crashes related to individual hardware components do not stop the control of the other components. Critical systems such as emergency watchdogs are located on separate computers, allowing the entire system to enter a safe mode in an emergency even if the main control computer is disabled. The 18 daemons comprise 18,000 lines of Python code and communicate via a JSON-based protocol on TCP/IP sockets.

A supervisory daemon is responsible for overall control, working as a finite-state machine to decide on the current best system operation mode from a range of options (science operations, taking calibrations, waiting for good weather, waiting for sunset, resetting mount for the next ratchet, and emergency shutdown mode). Transitions between modes are handled automatically by issuing commands to the relevant daemons and waiting for confirmation of hardware states as necessary. Commands to the hardware daemons range from simple (changing a filter position for example), to complex operations that can take many hours and involve large amounts of computing resources (executing a 3D-surface focus map for a camera, for example). A manual mode allows humans to issue commands directly to each daemon as necessary using the Evryscope status webpage (Figure 2.11), although the supervisory daemon must be informed, or the unexpected hardware states will be detected as error conditions.

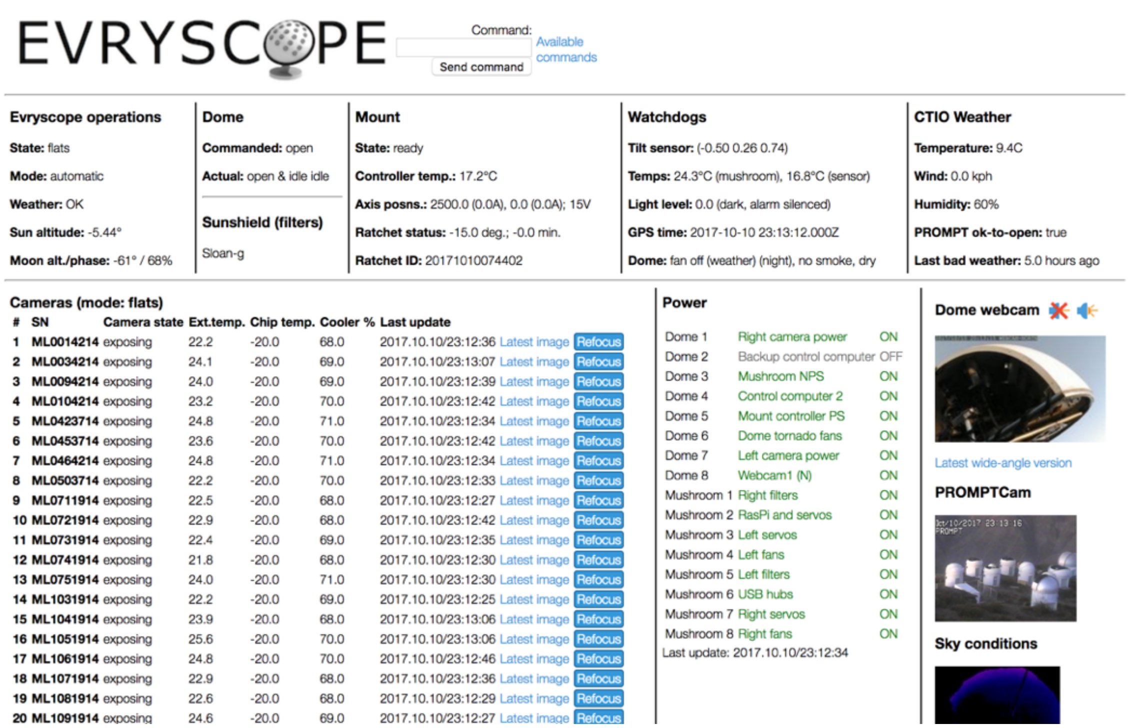

Figure 2.11: The Evryscope status webpage, used for system monitoring and control. Commands can be issued to each hardware and software system using buttons or a simple text interface.

The system is designed to fail-safe, entering a safe mode on all important errors. Each subsystem daemon is responsible for the safety of its individual hardware components. This is relatively trivial in the case of filter wheels and similar low-impact systems, but is safety-critical for some components like the dome, the camera power supplies and the tracking mount. To produce a fail-safe mode, where the hardware is protected in the case of a system error or unexpected condition, the supervisory daemon issues a "heartbeat" ping to each daemon every 15 seconds. If the ping is not received on schedule, each individual daemon enters a safe mode – closing the dome, powering off the cameras, placing the filter wheels into sunshield position (§ 2.2.7.4), and so on. Conversely, if a daemon does not respond to the heartbeat ping, suggesting it has crashed, the supervisory daemon triggers an error condition and stops issuing heartbeats to the other daemons. On any unhandled error condition the entire system enters semi-safe mode within $\approx$ 15s (dome closed, mount stopped), and fully-safe (sunblocks enabled, cameras powered off) within a minute. When this occurs, an email is sent to the Evryscope team for manual checks. This typically occurs once every few months, usually because of a communications glitch with an external component.

2.2.7 System robustness & failure mode mitigation

The Evryscope is designed for fully-robotic operation with minimal on-site support. A rigorous analysis and mitigation of potential failure modes is vital to ensure robust operation. We categorized possible failure modes into a) problems that would allow the system to keep running with degraded performance and b) catastrophic failures that could cause permanent hardware damage. For the first type, we designed the system control software to monitor all hardware systems continuously and fail-safe into a known-good state on detection of errors (see § 2.2.6). For the potentially catastrophic problems, we designed multiply-redundant backup systems:

2.2.7.1 Fire

The Evryscope uses up to 1.2kW of power when all systems are simultaneously operating, within a fairly-small enclosure. Two 120A/12V power supplies supply power to the camera systems, and a short-circuit on a 120A-capable line could easily produce enough heat to ignite surrounding material. We mitigated these concerns by a) breaking apart the high-current lines very close to the power supplies for individual camera power; b) individually fusing each power supply line; c) powering the system via GFCI breakers to produce a rapid shutdown in the event of a ground fault; d) specifying all plastics to be flame retardant; e) wrapping all exposed cables in flame-retardant material; f) placing an omni-directional infrared temperature sensor in the dome which shuts the power down on detection of an overheat condition; g) placing a Raspberry-Pi connected smoke detector in the dome to rapidly shut off power and sound an alarm if smoke is detected.

2.2.7.2 Lightning

Electrical storms are rare at CTIO, but the Evryscope has so far experienced one extremely-nearby lightning strike that damaged equipment in nearby domes. To mitigate the possible lightning impact, we applied surge protectors to every power line and isolators to every USB and ethernet cable longer than three feet; this also mitigates the effects of possible ground loops. No lightning damage has been experienced by the system.

2.2.7.3 Earthquakes

Chile regularly experiences large earthquakes, and telescope systems must be designed to survive large ground accelerations. As with the other main instrument components (§ 2.2.4) we evaluated the Evryscope pier mount design using 3D modeling finite element analysis. We simulated the telescope weight on the pier design over several angles to mimic positions during the ratchet cycle. The final pier design is 1/2" wall structural grade steel box tubing, with a strength failure several orders of magnitude above any level the Evryscope is likely to see. An accelerometer inside the mushroom measures the tilt of the mushroom and any other accelerations, and places the system in safe mode if limits are exceeded. On September 16, 2015 CTIO was hit by a magnitude-8.3 earthquake at a distance of 115 miles. The Evryscope automatically went into safe mode; no structural damage occurred and after quick manual checks the system was able to restart with no maintenance required.

2.2.7.4 Sun exposure

With a telescope pointing at almost the entire sky, if the dome is opened during the day at least one camera would be pointing directly at the sun. The resulting heat buildup in the sun-pointing region of the CCD chip would be likely sufficient to cause significant CCD damage. If the dome was left open for an entire day, during maintenance or as a result of equipment failure, it is possible that an entire row of cameras could be damaged or destroyed. We addressed this with 1) a daylight alarm which sounds a loud bell and contacts the Evryscope team; 2) sunshields built into each camera.

The sunshields are contained within the cameras' filter wheels and consist of a 3mm-thick steel washer backed by a mirror; sunlight entering the lens will be very out of focus at the filter position, preventing the formation of hotspots. Experiment at Chapel Hill showed no dangerous heating of the lens over hours of sun exposure. The sunshields are a primary safety system and as such are engaged immediately upon error conditions; each morning the system engages the sunshields as part of the shutdown procedure (apart from fans, the sunshields are the only moving parts inside the mushroom that are used nightly).

2.2.8 Data analysis

Here we describe briefly the Evryscope data analysis pipeline, forced-aperture photometry, and light curve generation; a full description will be published in upcoming work (Corbett et al. in prep.). As with many wide-field surveys, the Evryscope data analysis platform adapts established methods into a custom solution. The extremely wide field, concomitant optical distortions and flat-fielding challenges, and the very large quantity of data are the primary challenges. Each night, the Evryscope opens up and takes calibrations and science images automatically. 15-20 darks and twilight flats are taken each night for each camera and on a typical observing night, with good weather, each of the 22 cameras will take 250-300 science images.

2.2.8.1 On-site data analysis infrastructure

The Evryscope generates approximately 6500 55MB science images each night. This data volume precludes transmitting the data for off-site processing with the current CTIO internet link. All data is therefore stored and processed on-site. Images are stored in an FPACK-compressed format across multiple Synology DS-2415+ network storage appliances, each of which is equipped with twelve 8 or 12 TB drives. In addition to image storage, we have provisioned a separate data store exclusively for our photometry database, consisting of 12 helium-filled 8 TB drives directly attached via a SAS backplane to our database server.

Data processing is split between two servers, both housed in the PROMPT domes at CTIO. The original server, a 12-core Intel Xeon based machine, was installed with the system. Post deployment, the mainboard of this server suffered some mechanical damage, limiting its RAM capacity to 112 GiB. In January of 2016, a second server was installed and the original was reprovisioned to support a calibrations and image indexing database, while all other analysis tasks were migrated. The second server is also based on the Intel Xeon platform, with 36 physical cores and 256 GiB of RAM.

2.2.8.2 Pipeline design

The Evryscope currently runs a forced-aperture-photometry pipeline. The pipeline takes incoming images, calibrates them with darks and flats, generates a precision astrometric solution from the bright stars, estimates local background light and noise across each image, and measures aperture photometry for all sources from a reference catalog. The Evryscope pipeline consists of $\sim$ 50,000 lines of custom Python and C++ code, with custom code performing flat-fielding, astrometric distortion correction, local background and noise estimation, precision aperture photometry, transient detection, and large-volume data storage. We expect to upgrade the pipeline to full image subtraction in the future.

We extensively tested standard data analysis software with Evryscope images (for example, the SExtractor [73] and astrometry.net [74] software suite used in PTF [1] and the AWCams [68]). However, we found that the standard software struggles with our crowded images with large lens distortions: astrometry.net had a $> 20\%$ probability of failing to find a good astrometric solution at the edges of the frames, often producing distortion solutions several pixels off. SExtractor often could not attain a good background noise estimate for our crowded images, and therefore set the source-detection requirements extremely high; often several-degree-wide regions of the Evryscope images did not show any detections despite tens of thousands of stars being clearly visible by eye. A few percent of the Evryscope images also showed SExtractor photometry very divergent from adjacent images, with stars' brightness measurements changing by tens of percent with no discernible by-eye difference in the input images; these problems persisted regardless of the input settings. For these reasons we developed a completely-custom pipeline, although we do use astrometry.net for initial rough astrometric solution and SExtractor for quick source-detection for camera focusing; both codes work very well for those applications.

Each processed night consists of $\approx$360GB of raw imaging data, resulting in several hundred new data points for each of $\approx$10M stars. On our current computing hardware, the pipeline is capable of processing $\sim$7 nights (2.5TB of imaging data) every 24 hours. This speed is necessary to allow us to re-reduce our current three-year dataset in a reasonable time.

2.2.8.3 Image quality checks & calibrations

Each Evryscope science image is subjected to an initial quality control script which evaluates the image quality based on the presence of stars in the image, PSF shape (avoiding rare tracking errors), and background levels. Images that pass (>90%) are masked for known bad pixels and columns.

Darks are taken daily with the filterwheel in the closed position, and monthly midnight darks are taken for comparison to check for light leaks. Masterdarks are generated by combining and median averaging several hundred darks. Our CCD characteristics are sufficiently stable to use the masterdarks for a season.

Twilight and sunrise flats are taken daily and evaluated with a quality control check for stars and clouds. Residual point sources are removed. Lens vignetting and small scale interpixel variation in CCD sensitivity are removable to the one percent level with standard flattening procedures, however the large scale sky gradient due to the extremely wide field of view necessitates a more complex procedure. We constrain the large-scale variations on using on-sky photometric measurements of starfields, and measure the small-scale variations from the high-frequency structure in twilight flats.

2.2.8.4 Photometry and light curves

Our current dataset includes 9.3M stars with an average of 32,600 photometric measurement points. The photometric points are stored in a flat-file based custom backend storage system written in Python. The system is partitioned by sky position using HEALPix pixels [75]. HEALPix pixels divide the sky into equal area regions; we selected a 3.5 sq. deg. HEALPix pixel size for convenience to limit the number of stars in a particular region. This aids in processing of the light curves (done per HEALPix pixel) and allows for multi-threading and tiling the database writing steps. We evaluated database management systems (DBMS), but found that for our extremely-consistent-format numerical data our custom system could reduce storage requirements by a factor of five compared to PostgreSQL while increasing access speed by a factor of ten. We also evaluated similar commercial and open-source flat-file numerical data storage systems and found that the performance was generally comparable to our flat-file-based system, but with significantly higher implementation complexity and programming overhead. The flat-field storage system stores approximately 15TB/yr of light-curve data.

Each star's photometry is measured in five different photometric apertures, allowing an optimization of the SNR for each star (for example, selecting larger apertures for brighter stars; this technique is used by several surveys, e.g. [8]). Each measured data point also includes the star's measured RA & Declination, CCD position, estimated SNR, limiting magnitude at that point, background light level, peak flux level, and a GPS-based precision timing signal with tested 1 s accuracy [76].

We periodically generate precision light curves for each star based on the typically tens of thousands of photometric points recorded for each star. The light-curve generation code processes each HEALPix pixel separately, performing differential photometry on the contained group of several thousand stars. Atmospheric extinction variations from clouds and airmass are corrected for using differential photometry among the thousands of stars in each HEALPix pixel. First, images pass through an image quality check which rejects images with high background, low numbers of detectable sources, or suspect PSF shapes. Next, the least-variable stars are automatically selected to form a consistent set of reference stars (this procedure is iterated with the differential photometry to find the stars most indicative of the overall photometric variations). For each single-camera image accepted by the pipeline for processing, which typically have a few 100,000 stars, each source is checked for possible blending, local background issues, non-detection and saturation. Flags are issued for suspect data points. Flux errors are estimated based on the local background noise for all epochs, for all sources. Airmass and differential chromaticity errors are removed by SysREM [77] in the default pipeline operation; we tested removing explicit correlations with star color and measured airmass, but did not find a significant improvement in photometric precision. These procedures work for the large majority of the dataset, but a small fraction ($< 20\%$) of the epochs are subject to largely un-removable variability due to thin clouds with spatial scales smaller than a HEALPix pixel. We detect and remove these epochs by searching for periods of higher-than-average photometric variability among all sources in the healpix, as well as higher-than-average extinction. We are currently developing methods to instead flag and recover these epochs for usable data.

We have implemented several layers of systematics removal, which can be applied depending on the science goals. All light curves are automatically decorrelated by two iterations of SysREM [77]. Further iterations of SysREM further remove systematic errors, but there is also a risk of removing astrophysical variability. If only short-term variability is to be measured, such as in a transit or eclipse search, we add decorrellations of photometric variability with CCD chip position and airmass. We found that some long-term variables such as low-amplitude long-period rotation curves correlate with those telescope variables, and so we offer users the option of using uncleaned light curves.

Processed light data is inserted to a PostgreSQL database, also partitioned into HEALPix pixels to increase performance. This database does not include much of the per-epoch metadata, and only contains results from the optimal photometric aperture. Each of the 6000 populated HEALPix pixels contains 0.2-2GB of light curve data, for a total light curve database size of ∼10TB. We query the database for target groups, and download the results to Chapel Hill for astrophysical analysis.

2.3 Performance

2.3.1 Operations statistics

The Evryscope saw first light on May 20, 2015 and has been operating continually since then with only brief maintenance shutdowns. From first light to August 1, 2018, 15.9% of the nights were missed due to weather and equipment issues and 2.3% of the nights were skipped due to planned maintenance. The maintenance trips occurred during November 11-20, 2015 (Robotilter installation and camera alignment); January 4-15, 2017 (lens cleaning, data storage increase, second analysis server installation, and general maintenance); and

July 18-25, 2018 (lens cleaning and general maintenance). The fail-safe shutdowns occurred for the following reasons: excessive heat warning (20%), dome control warnings (33%), and smoke/dust/other warning (47%). Almost all of the fail-safe shutdowns were false alarms, but we designed the system to be conservative with the goal of detecting real danger situations at the expense of some false positives.

2.3.2 Hardware reliability

The Evryscope has operated reliably for over three years, with only minor hardware issues. The mount has tracked over 5700 2-hour ratchet cycles with no major problems; during the 2017 maintenance trip we greased and tightened the worm gear adjustment which helped smooth the mount operation at peak stress positions. The support structures, including the fiberglass mushroom, have been durable and shown no signs of excessive wear or stress. The power supply units (cameras, filter-wheels, servos, USB hubs and accessories) have all performed without issue. The cameras have also run reliably and without failure. Three filter-wheels have failed over the course of three years. One broke a drive chain, while the other two stuck during routine cycling. One was stuck in the Sloan-g position so it did not affect imaging, the others were stuck closed so we lost the ability to image with two cameras until the next maintenance trip. One power cable to a camera USB hub failed in mid 2018 which disrupted operation of four cameras and filter-wheels; it was easily replaced during the June 2018 maintenance trip. The system is well sealed and minimal dirt and dust accumulates inside the mushroom. The optical windows need to be manually cleaned each trip, but the lenses can be cleaned simply with compressed air and/or off-the-shelf DSLR camera lens-cleaning pens.

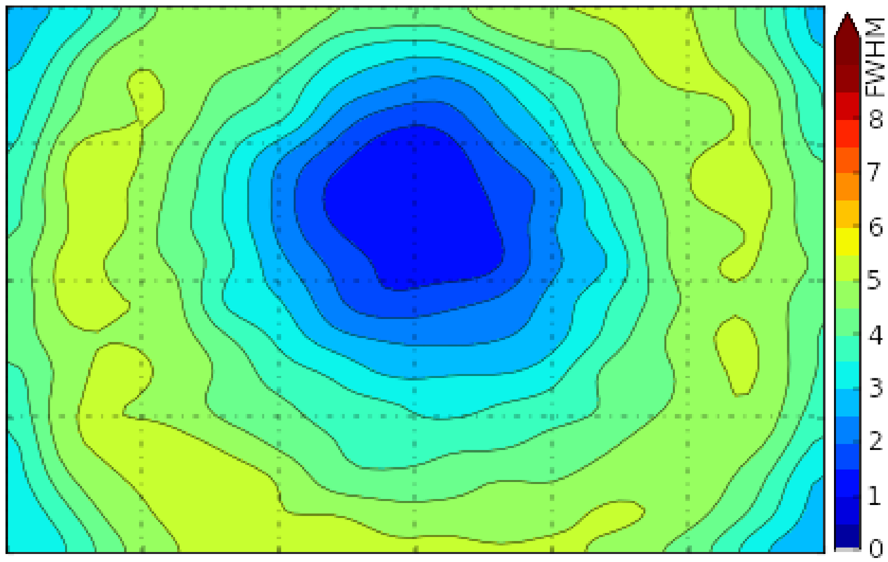

Figure 2.12: The FWHM map of the camera pointing toward the South Celestial Pole. The image quality shows little tilt and a symmetric pattern.

2.3.3 Imaging Performance

The Evryscope imaging performance sets the limiting magnitude, photometric performance, and ease of source separation and image subtraction. In this subsection we explore the system's performance over the first three years of operation.

2.3.3.1 Point Spread Functions

The Robotilter camera/CCD automated alignment system is designed to remove tilt, minimize PSF distortions, optimize the focal plane, and defocus the image center. The FWHM (PSF full-width-at-half-maximum) map of a well aligned, representative camera is shown Figure 2.12). Very little tilt across the image is evident, and PSF widening toward the corners due to lens coma, focus, and vignetting is within the expected range for our lenses. The PSFs range from 1-5 pixel FWHM across much of the image – 60 percent are less than 4 pixels and 90 percent are less than 6 pixels. Figure 2.13 shows point spread functions for the central region and edges of a representative camera.

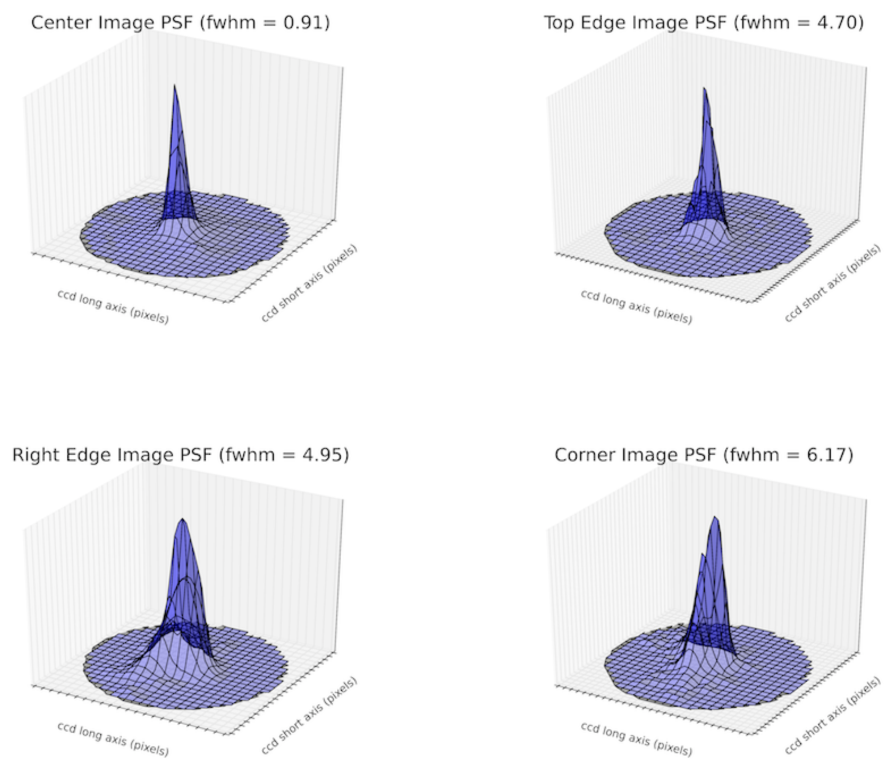

Figure 2.13: Example medium brightness stars' PSFs from the center, edges, and corner of a representative camera.

2.3.3.2 Limiting magnitudes and coaddition

We calculate the limiting magnitude achieved by the system in each epoch by taking the faintest stars in each healpix and fitting the SNR decrease as a function of the g-band magnitude as measured by APASS. The dark-sky limiting magnitude (Figure 2.14) reaches our expectation of $m_{g'} \approx 16$, with crowding from the galaxy reducing the limiting magnitude by approximately a magnitude in low-galactic-latitude areas. A horizontal stripe pattern is visible in the limiting-magnitude map; this is caused by the falloff in PSF quality towards the edge of camera fields of view.

The camera gains, data compression and calibration fidelities are selected so that coadding the data achieves greatly improved signal to noise, with depth increasing with approximately

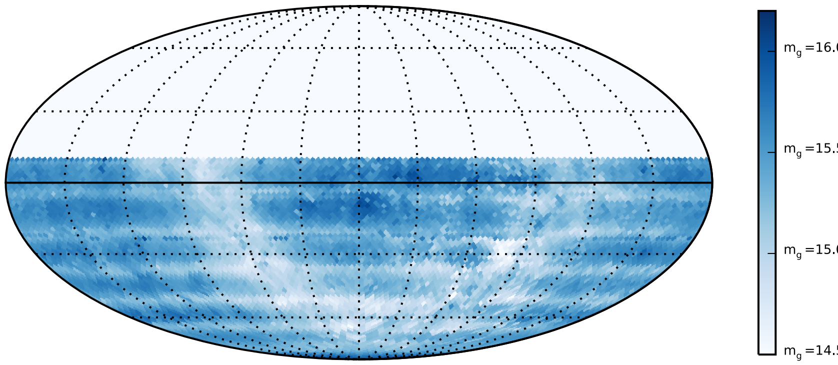

Figure 2.14: The median dark-sky limiting magnitude for Evryscope data, measured in ≈32,000 epochs over three years of operations. The crowding effects of the galactic plane are visible, along with the striping from falloff in PSF quality towards the edges of the cameras' fields.

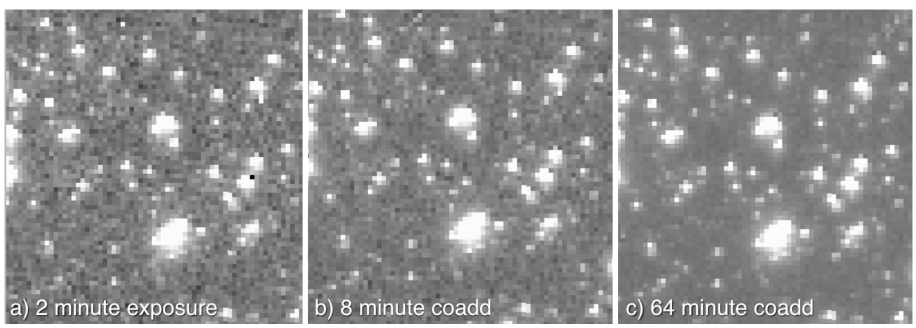

Figure 2.15: Progressive coaddition of a selected sky region, with image scaling applied to show the noise structure in the images. As well as increasing depth, coaddition with the slow star position changes over a ratchet allows the removal of bad and hot pixels.

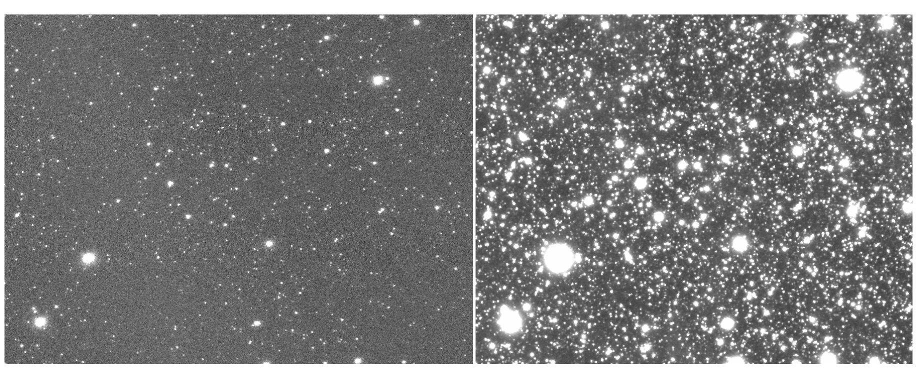

Figure 2.16: *Left:* a selected region of a single two-minute Evryscope exposure. *Right:* co-addition of a full night of data from the same region, with scaling to show the increased number of stars and the bright-star PSFs.

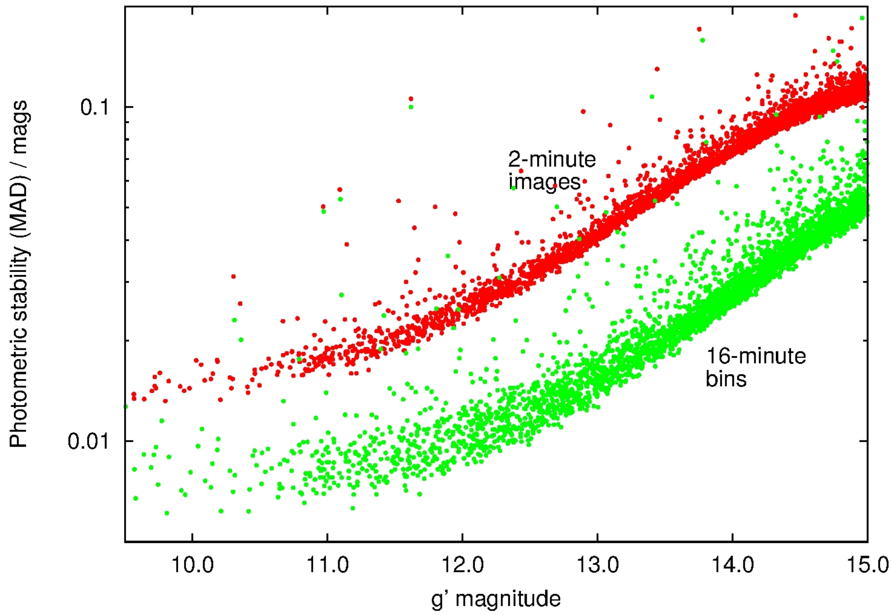

Figure 2.17: Evryscope light curve photometric performance per magnitude for three years of data under all moon and cloud conditions. Stars in a representative HEALPix pixel of the Evryscope database targets is shown for visual clarity. The high RMS outlier points are astrophysical variable stars.

the square root of the number of exposures (Figure 2.15). In uncrowded regions of the sky during dark nights, the system typically achieves $m_{g'} = 17$ in 8 minutes coadding (4 exposures), $m_{g'} = 17.5$ in 32 minutes, $m_{g'} = 17.8$ in 64 minutes, and $m_{g'} = 18.5$ in 360 minutes (the latter crowding-limited over much of the sky; Figure 2.16).

2.3.3.3 Photometric precision

Light curve performance reaches our expected performance levels of near 1% rms on bright stars and $\sim$ 10% on dim stars, over three years of data under all moon and cloud conditions (Figure 2.17). With binning and/or aggressive removal of poor conditions data and systematics, the performance is improved to the 6-millimag level. These levels are greatly improved when coadding epochs for the detection of periodic objects, where we have published clear signals at the few-millimag level [21].

2.4 Example light curves, discoveries, and on-going surveys

The Evryscope has a wide variety of on-going surveys (§ 2.1). In this section we detail results from some of the current surveys, provide example Evryscope light curves and discoveries from a selected region of the sky; many more comprehensive surveys are currently ongoing.

2.4.1 Candidate Detection

The Evryscope team uses a wide range of detection tools, given the variety in the science survey goals (see § 2.1). Box Least Squares (BLS) [28], [29] is the primary search tool used for conventional (wide, shallow, many points) transit like detections. The box size, sampling, and period range are selected depending on the host star and expected companion type. To find potential transiting planets with compact host stars such as white dwarfs or hot subdwarfs, where the transit times are orders of magnitude shorter, we developed a custom code written in Python which we call the outlier detector. It excels in finding very short time (on the order of a few minutes to tens of minutes) transits with deep (ten percent or more) depths, even for faint objects. We use several iterative processes to select low outlying points and find the period with lowest in phase deviation. Flares are discovered and characterized with an automated flare-analysis pipeline which uses a custom flare-search algorithm, including injection tests to measure the flare recovery rate. The algorithm searches for flares by first dividing each lightcurve into segments of continuous observations and subsequently fitting an exponential-decay matched-filter to each contiguous segment of the light curve. Matches with a significance greater than 4.5σ are verified by eye. Microlensing events are detected with a differential image / matched filter Python code that triggers an alert if required parameters are met. Lomb Scargle (LS) [30], [31] is the primary algorithm used to find stellar variability and binaries.

Visual inspection and systematic assessment is a key to detection and false positive elimination. We have developed several visual tools including the display panel plot (Figure

2.18) that allows for simple and effective visual confirmation of candidates. In the same panel plot, we test the candidates for signs of systematics by comparisons to nearby reference stars, examining binned data, and checking for alias and data gaps. Fit power, ordering, and selection of top targets is available to narrow the candidates depending on the search and number of targets. This display is available for all Evryscope light curves, on request.

2.4.2 First discoveries

The Evryscope team (and collaborators from 17 institutions) are engaged in a wide variety of astrophysical projects with the light-curve dataset. The first major Evryscope result, the first detection of a superflare from Proxima Centauri, was recently published in ApJL [23]. Several other papers are currently under review, and many more results in prep. Here we show some examples of variability discoveries from the Evryscope database, and results from a test search in a selected region of the sky. We follow with updates on the various surveys that are underway.

2.4.2.1 New Eclipsing Binary / Variable Star Discoveries

A test search limited to the northern region (declinations from +5 to +10), filtering the targets by magnitude (bright stars) and color (likely K-dwarfs or M-dwarfs) yielded 59 new eclipsing binaries and variables. Representative examples of an eclipsing binary and a low amplitude variable are shown in Figure 2.19. The search was run by selecting all of the sources in the Evryscope database with light curves with greater than 5000 epochs, with magnitudes brighter than 14.5, and with sources that matched to PPMXL [78] and APASS-DR9 [79] catalogs which could be classified as potential K-dwarf or M-dwarfs based on reduced proper motion (RPM) and B-V colors. After removing known variables, BLS and LS were run on the filtered list; the example eclipsing binary and low amplitude variable BLS and LS detections are shown in Figure 2.20. The BLS and LS results were ordered by significance and the top 10% were inspected using the detection panel plots. Those passing

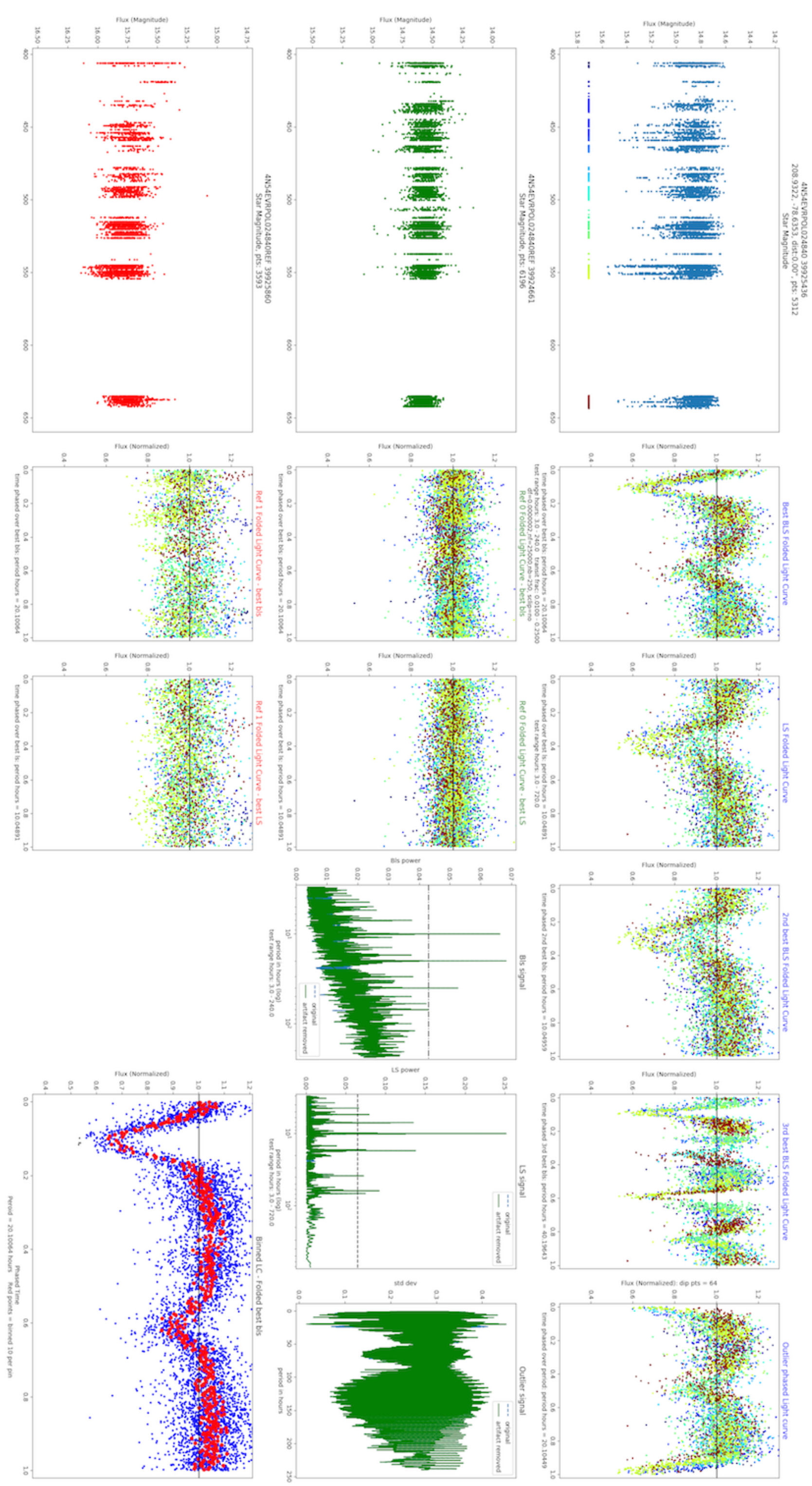

Figure 2.18: Evryscope transit detection display panel, with a newly discovered eclipsing binary. The left panels show the target and two reference star light curves, as well as the BLS and LS phase folded on the best period. The coloring of points shows the mixing of the best period find and comparison to nearby references for identification of systematics. The right panels show the outlier results and the binned light curve folded on the best period.

the visual inspection and systematics test were sent to the next stage. Eclipsing Binaries were fit with a Gaussian to measure the eclipse depth using the detected period and phase as the prior. Variables were fit using Lomb-Scargle to determine the amplitude. Example eclipsing binary and low amplitude variable fits are shown in Figure 2.21. The full discovery list and light curves for each discovery are shown in the appendix.

2.4.2.2 Transit Surveys

One major Evryscope transit survey has been completed and two are underway, with several others in the planning stages. A transit search for variable stars in the southern polar region led to 300 variable and eclipsing binary discoveries, with six of the eclipsing binaries having low-mass secondaries (Ratzloff et al., submitted). An exoplanet survey of $\approx$ 2500 southern sky white dwarf (WD) targets $m_v < 15.0$ is underway. A transit survey of $\approx$ 3500 hot subdwarf (HSD) targets is in progress and has already discovered several rare systems: 2 HSD / low-mass-secondary eclipsing binaries (HW Vir systems), 4 HSD reflection binaries, and 2 HSD / WD short-period binaries (all Ratzloff et al., in prep). From these surveys, there have been 5 planet candidate detections; subsequent followup showed these candidates to be grazing eclipsing binaries with almost identical stars or low-mass stellar companions. These detections demonstrate the Evryscope is capable of detecting planets orbiting post main-sequence stars as well as M and K-dwarfs with our current light curves and search algorithms. We have used the initial results of these first surveys to refine our transit searches; we briefly describe the status of the key Evryscope transit surveys below.

White Dwarfs (WD): Recent discoveries of WD debris discs and disintegrating planetesimals have fueled the speculation that planets could be present in WD systems [80], [81]. WD exoplanets would have very short (few minutes to tens of minutes) transit duration and very deep ($\sim$ 100 percent for earth size planets) transit depths. WDs are extremely numerous in the sky as $>$ 90 percent of main sequence stars will eventually become WDs, however the low luminosity and small size make these stars observationally challenging. We leverage the Evryscope fast cadence and all-sky coverage to search for WD planets. Our first results from ≈ 2500 southern sky WD targets $m_v < 15.0$ did not return any candidates. We have improved our systematics removal, increased our coverage to 3.5 years, and added targets down to $m_v < 16.0$ and will search again once the database processing is complete (Ratzloff et al., in prep). In the event of a null detection, we can provide upper limit constraints on WD planetary populations.

Hot Subdwarfs (HSD): HSD planet or low-mass-secondary transit durations are on the order of tens of minutes, and reasonably deep transit depths (~ 10 percent for Neptune size planets). A transit survey of HSD planets and other variability from a target list [82] of ≈ 3500 known HSD is in progress (Ratzloff et al., in prep). Although the survey is currently underway, several candidates, including the 8 mentioned above, have been identified and are pending further followup.

M and K-dwarfs: The Evryscope is capable of detecting ~ 2 Earth radii M-dwarf planets and gas giant K-dwarf planets. A transit search for variable stars in the southern polar region detected a 1.7 R_J planet candidate with a late K-dwarf primary. This system was later shown to be a grazing eclipsing binary, but demonstrated the Evryscope detection capability. An exoplanet survey of M and K-dwarf stars based on identifying candidates in our fields from spectral classification is planned for the entire sky when the HSD and WD surveys are completed.

2.4.3 Other Variability Searches

2.4.3.1 Solar Flares and CME

Flares and coronal mass ejections (CMEs) are capable of severely affecting the survivability of potentially habitable worlds. A comprehensive flare survey of M-dwarf stars (including known exoplanet hosts) of the southern sky is underway (Howard et al., in prep). These results, when combined with CME observations will be used to estimate the effects on long-term habitability of rocky planets orbiting M-dwarf stars.

2.4.3.2 Transient Detection

We have developed tools for rapidly generating small cutouts from full-frame Evryscope images and performing high-precision photometry on uncataloged sources not included in our primary forced-photometry reduction, including difference image analysis for objects in crowded regions of the sky. This tool chain is designed to provide early pre-discovery photometry to help constrain the evolution of novae and supernovae.

An example of Evryscope transient capability is a recent classical nova (Nova Carinae 2018) with pre-discovery Evryscope coverage [24], which is currently under analysis and a detailed light curve will be presented in an upcoming paper (Corbett, et. al., in prep). The Evryscope data complements the later discovery by the All Sky Automated Survey for SuperNovae (ASASSN [83]) and the serendipitous space-based photometry of the Bright Target Explorer (BRITE [84]). High-cadence and high-coverage observations of classical novae can provide insight into the shock physics that drive light curve evolution [85]. Also shown in Figure 2.22 is transient discovery from the variable star test search (§ 2.4.2.1).

2.5 SUMMARY

The Evryscope was deployed to CTIO in May 2015 and has recently been joined by a Northern-hemisphere telescope at MLO. The Evryscope is designed to detect short timescale events across extremely large sky areas simultaneously. The 780 MPix 22-camera array has an 8150 sq. deg. field of view, 2 minute cadence, and the ability to detect objects down to $m_{g'} \simeq 16$ in each dark-sky exposure. We have collected over 250TB of images and produced 25TB of light curves. In this paper we described the Evryscope hardware and explained why we designed the telescope as we did. The time from conceptual design to deployment was one year and the total hardware cost was ≈$300K, meeting our time and budgetary goals. We demonstrated the on sky performance met our goals for telescope operation and reliability, sky tracking, threat mitigation, and reliability. Image quality reached our predictions for signal, noise, background, and PSF quality. The photometric pipeline produces light curves with the precision necessary to support the planned Evryscope science. We demonstrated the photometric performance by presenting select variable star discoveries and discussing rare hot subdwarf and white dwarf eclipsing binary discoveries. Updates on the status of our transit surveys, M-dwarf flare survey, and transient detection were also given.

This research was supported by the NSF CAREER grant AST-1555175, NSF/ATI grant AST-1407589, and the Research Corporation Scialog grants 23782 and 23822. HC is supported by the NSF GRF grant DGE-1144081. OF and DdS acknowledge support by the Spanish Ministerio de Economía y Competitividad (MINECO/FEDER, UE) under grants AYA2013-47447-C3-1-P, AYA2016-76012-C3-1-P, MDM-2014-0369 of ICCUB (Unidad de Excelencia 'María de Maeztu').

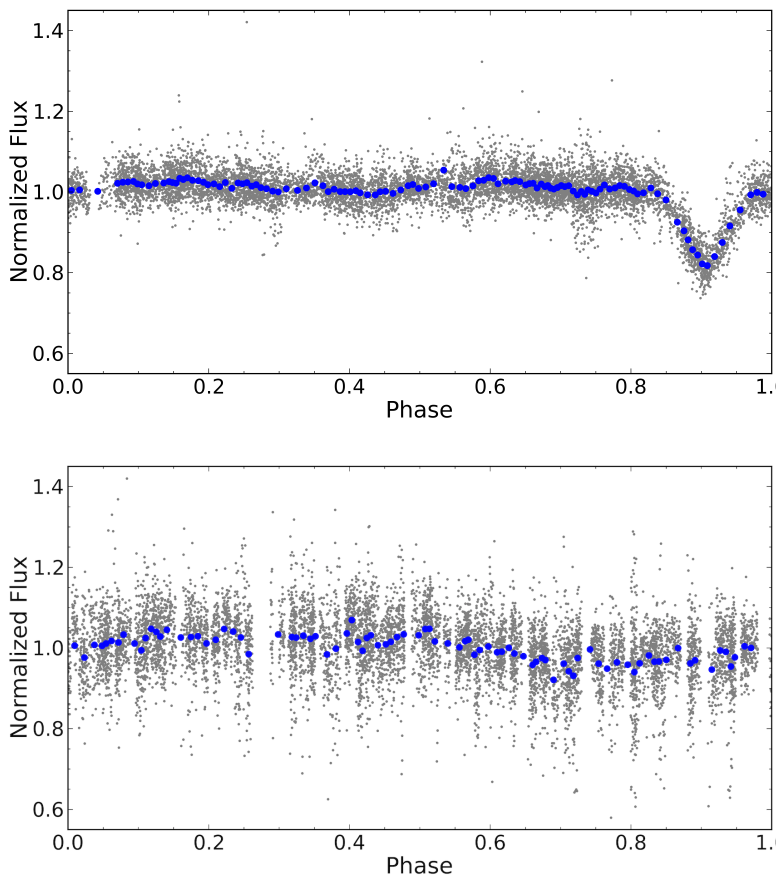

Figure 2.19: Top: An eclipsing binary discovery folded on its 61.4905 hour period representative of Evryscope variable discoveries. Bottom: A variable star discovery folded on its 219.8386 hour period representative of Evryscope variable discoveries.

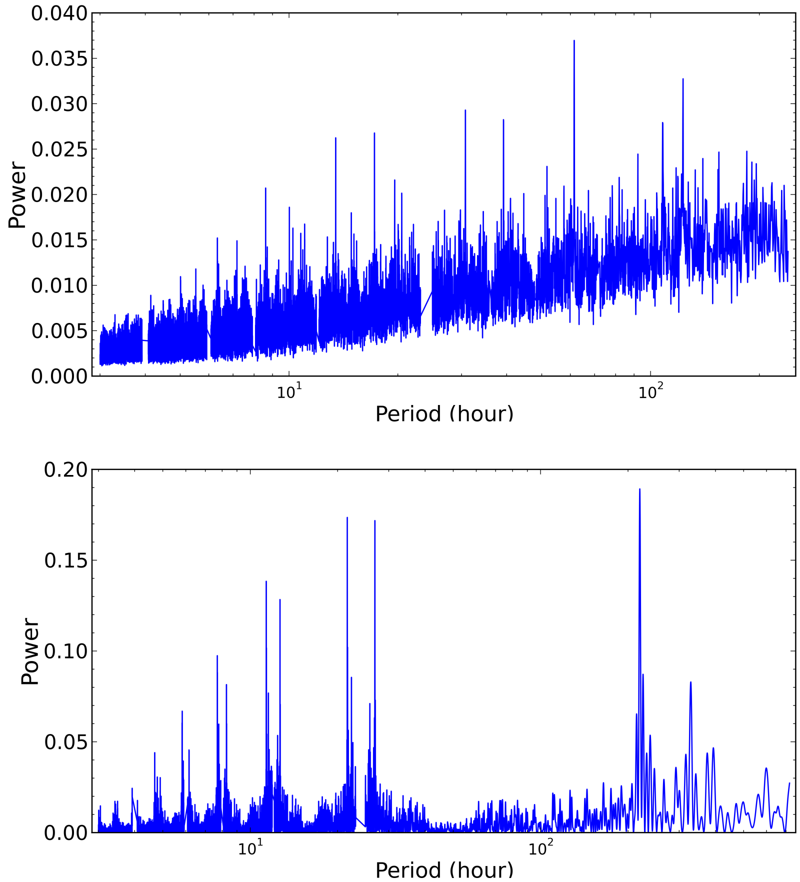

Figure 2.20: Top: The BLS power spectrum (to the 61.4905 hour eclipse in Figure 2.19) with the highest peak at the 61.4905 hour detection. Bottom: The LS power spectrum (to the 219.8386 hour variable star in Figure 2.19) with the highest peak at the 219.5521 hour detection.

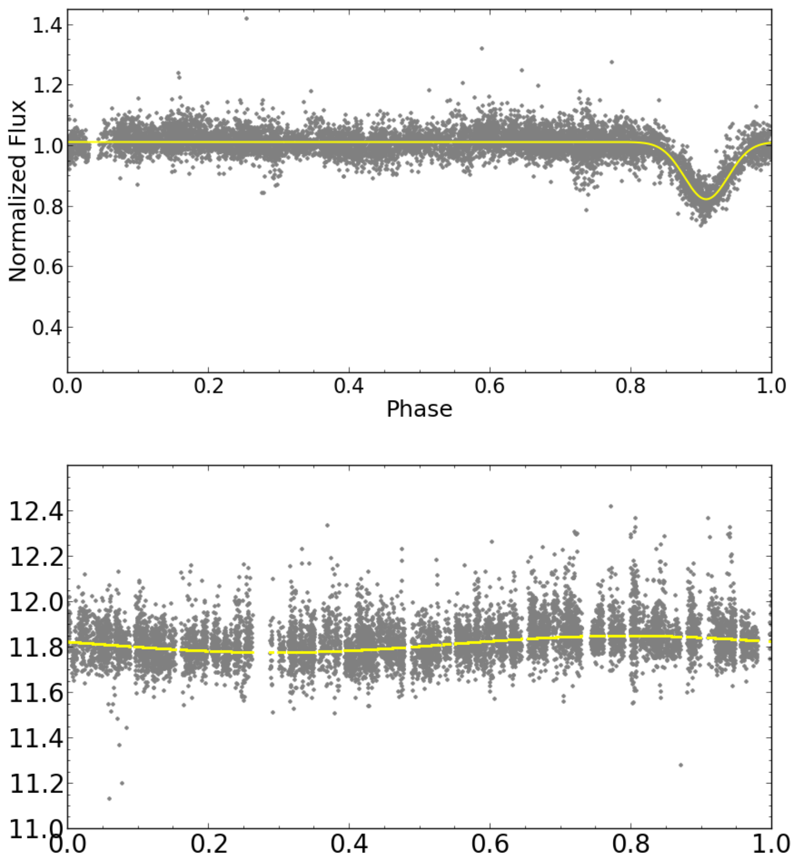

Figure 2.21: Top: The best fit (to the 61.4905 hour eclipse in Figure 2.19) to measure the depth. Gray points are two minute cadence, red points are binned in phase, yellow is the best Gaussian fit. Bottom: The best fit (to the 219.8386 hour variable star in Figure 2.19) to measure the amplitude. Gray points are two minute cadence, red points are binned in phase, yellow is the best LS fit.

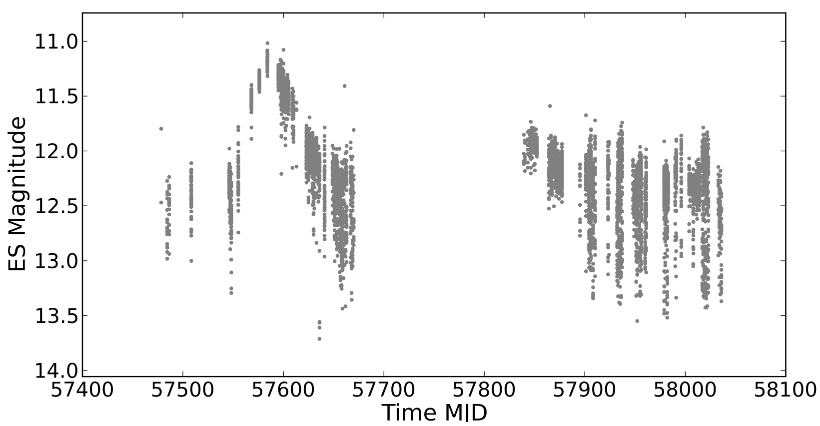

Figure 2.22: A transient discovery with ~ 100 day duration and 1.5 magnitude increase. Other long-period variables and transients including supernovae, novae, and microlensing events are detectable with the Evryscope.

CHAPTER 3: THE ROBOTILTER: AN AUTOMATED LENS / CCD ALIGNMENT SYSTEM FOR THE EVRYSCOPE

This section presents results published in the *Journal of Astronomical Telescopes, Instruments, and Systems.*[1,2]

3.1 Introduction

Camera lenses are increasingly used in wide-field astronomical surveys due to their high performance, wide field-of-view (FOV) unreachable from traditional telescope optics, and modest cost. The machining and assembly tolerances for commercially available optical systems cause a slight misalignment (tilt) between the lens and CCD, resulting in PSF degradation. We have built an automated alignment system (Robotilters) to solve this challenge, optimizing 4 degrees of freedom - 2 tilt axes, a separation axis (the distance between the CCD and lens), and the lens focus (the built-in focus of the lens by turning the lens focusing ring which moves the optical elements relative to one another) in a compact and low-cost package. The Robotilters remove tilt and optimize focus at the sub 10 μm level, are completely automated, take $\approx$ 2 hours to run, and remain stable for multiple years once aligned. The Robotilters were built for the Evryscope telescope (a 780 MPix 22-camera array with an 8150 sq. deg. field of view and continuous 2-minute cadence) designed to detect short timescale events across extremely large sky areas simultaneously. Variance in

[1]Ratzloff JK, Law NM, Corbett H, Fors O, and Del Ser D. The Robotilter: An Automated Lens / CCD alignment System for the Evryscope. *Journal of Astronomical Telescopes, Instruments, and Systems* 2020; 6(1), 018002, DOI: 10.1117/1.JATIS.6.1.018002.

[2]I wrote this entire paper, with multiple rounds of comments from Law and a few figures from Corbett. I did the design work, 3D modeling, testing, problem resolution, and final design details. The software solution was a joint effort between Ratzloff and Law (approximately 70/30) with the most substantial parts being the image sweep, quality metric, and grid approach.

quality across the image field, especially the corners and edges compared to the center, is a significant challenge in wide-field astronomical surveys like the Evryscope. The individual star PSFs (which typically extend only a few pixels) are highly susceptible to slight increases in optical aberrations in this situation. The Robotilter solution resulted in a limiting magnitude improvement of .5 mag in the center of the image and 1.0 mag in the corners for typical Evryscope cameras, with less distorted and smaller PSFs (half the extent in the corners and edges in many cases). In this paper we describe the Robotilter mechanical and software design, camera alignment results, long term stability, and image improvement. The potential for general use in wide-field astronomical surveys is also explored.

Commercial camera lenses are used on SuperWASP [8], HAT [6], HatNet and HATSouth [7], KELT [9], XO [10], MASCARA [11], and other transiting exoplanet surveys to reach as much as 1000 square degree fields of view. Other surveys types such as the ASAS-SN (supernova) [15], Pi of the Ski (gamma ray bursts) [14], and Fly's Eye (asteroid detection) [13] also use camera lenses to reach wide sky coverage. The Evryscope (described in detail in [19]) also uses camera lenses to provide continuous all-sky coverage with fast cadence, aimed at finding rare short-time events. Each of these surveys pair the camera lenses with compact CCD cameras to achieve the FOV and pixel sampling necessary at a modest cost. They have discovered a variety of photometrically variable objects including exoplanets, binaries, stellar phenomenon, and galactic events.

These types of wide field surveys and many others including the Evryscope are susceptible to image quality challenges from CCD / lens misalignment (tilt) and sub-optimal focus. The tilt and focus challenges are driven by two primary factors - mechanical and software. The mechanical challenge is to align the optics with respect to the camera to the level necessary to minimize PSF differences across the image; for very wide fields and fast optics, this requires precision beyond typical machining and assembly tolerances. The software challenge involves optimizing 4 degrees of freedom (2 in tilt, 1 in lens / CCD separation, and 1 in focus position - see Figure 3.4 later in the manuscript) with severe degeneracies and local extremes. The software solution also requires a method to measure image quality, across all regions, in the presence of tilt – a non trivial task. The image quality measurement must be capable of handling PSF differences due to focus, off-axis aberrations, and SNR variations.

There are very few discussions concerning removing image tilt or optimising the focal plane in wide-field astronomical surveys, and we found none that use an integrated tilt removal system as part of their main instrument design. Conversely, the majority of the surveys [6, 8, 9, 11] discuss the challenges of PSF distortions and focal plane issues from the wide fields. A common struggle is the negative impact on the photometric precision, poor performance on dim stars, and the difficulty in reaching the sub-percent level required for typical exoplanet searches. Extensive software development is put into the calibrations, pipeline, aperture photometry, and systematics removal of each of these instruments to try and maximize light curve quality given the challenges of a very wide field. Several new solutions resulted from these struggles including multi-aperture forced photometry, wide-field astrometry solutions, and methods for maximizing under-sampled PSFs. A reliable method to remove image tilt and optimize the focal plane would complement and reduce the burden on the software solution, and potentially improve limiting magnitude and light curve precision. With the Evryscope F1.4 optics and 384 sq.deg. individual camera FOV (among the most aggressive of the current wide field surveys), image tilt removal is more necessity than option.

Photometric surveys that use small consumer telescopes or custom optics instead of camera lenses, for example MEarth [12] and PROMPT [36] and many others, typically have FOVs on the order of a few sq. deg. or less. The smaller FOVs tend to have much slower optics than the camera lens based surveys, combined with finer pixels, lessens the PSF challenges due to optics misalignment. These surveys function well without the need of an advanced tilt removal solution.

Turning to larger aperture instruments with wide fields, the process typically starts by fixing the primary mirror and aligning the secondary, then progressing to any other elements, and finishing with the CCD. Pan-STARRS [86] used an auto-reflecting telescope, developed a custom alignment software, combined with ≈ 1 month of observing time to realign the optics to a level of tens of microns. LSST [87] will align the optics and CCD using laser targets fixed to the primary and the off-axis aberration characteristics of the wide field to characterize and remove tilt. They plan to also align sequentially proceeding from the secondary to the CCD, and simplify the procedure by designing the primary and tertiary from the same blank (so that they are fixed in alignment). ZTF [2, 88] uses on sky images to match each of the 16 CCD portions to the focal plane within $\approx 10\mu m$, in order to meet their photometric precision requirements. Although these are considerably different instruments on entirely different cost and complexity scales, some of the alignment principles used helped confirm our solution ideas for the camera lens / CCD based Evryscope. Moving only one element and holding all others fixed simplifies the process, and in many cases is the only practical way to avoid alignment degeneracies. Using on-sky images offers the advantage of the same focus position and conditions as science images. Reliably measuring image quality across wide fields with significant PSF distortion is challenging, even more so in the condition of under-sampled PSFs. The instrument differences are also evident, the Robotilters must be simple, economical, and avoid complex components such as laser targets and resource intensive steps such as camera disassembly / shimming / reassembly for alignment. We also note that moving individual lens elements relative to each other is not an option as the lenses are sealed, and there are no external adjustments for the lens components. The Robotilter solution must be modular to work on all cameras and fields, and ideally could be scaled to work on other instruments.

The primary source of the misalignment stems from the way wide field instruments using camera lens attach the lens to the CCD through a series of elements. Typically, the CCD is mounted to a camera housing, the housing is mated to a filter wheel, which is in turn mated to a lens mount (bayonet ring), and the lens turns and locks onto the bayonet ring. The manufacturing tolerances, and the multiple mating points and assembly steps causes a misalignment in the lens and CCD. Even a slight tilt will result in an unacceptable increase in size of the PSF FWHM towards the edges and corners of the image.

To estimate the increase in PSF size due a tilted image, we estimate the blur diameter $B_d \propto \frac{\Delta}{F}$, where Δ is the defocus and F is the F number of the lens. The defocus is dependent on the tilt (θ) between the lens and CCD and on the distance (d) of the source from the center of the CCD. The estimated PSF increase (in pixels) is then $PSF_{inc} \propto \frac{\theta \times d}{F \times pixelsize}$. For sources near the edges and corners of the field, the effect is strong given the aggressive F1.4 optics of the Evryscope. We originally estimated that for the Evryscope cameras, even a very small tilt at the level of a 5 μm difference in *opposite edges* of the CCD (a .02 degree tilt) would result in excessive ($\approx$ one pixel) PSF increases toward the edges of the CCD.

The lens mounting surface (the region where the lens contacts the filter wheel and subsequently where the filter wheel contacts the CCD housing) is 3 times larger than the CCD. This relaxes the 5 μm tilt difference at the CCD edges to $\approx$15 μm difference in *opposite edges* of the lens mounting surface. This is still challenging given the Evryscope fast optics. For example, a .100 mm thickness difference (from normal machining tolerances) in opposing edges of the lens mounting ring results in a .4 degree tilt between the CCD plane and the lens focal plane. The PSF FWHM could increase by as much as double or triple in this situation. In images taken with misaligned optics (hereafter misaligned images), the PSF shape is often compromised leading to elongation - in severe cases the width of one axis might grow to double or triple the width of the long axis of the elongated PSF. In most cases the center of the image is well focused, and a severely tilted image will have an edge-of-CCD region that is out of focus below the focal plane and a region opposite that is out of focus above the focal plane. The elongation and distortion of these two regions are different. We interpret these observed effects as out of focus regions in the presence of field aberrations (likely dominated by coma and astigmatism.)

Consumer lenses are designed to operate over a wide focus range, however finding the lens focus position that focuses each region in the image similarly well is a challenge. The steep light cone associated with fast lenses increases the demands on optical design, manufacturing precision, and material quality to achieve required performance levels. If severe enough, the tilt and focus problems will compromise the desired science goals by causing errors in astrometry, aperture photometry, inconsistent star observations, and increased noise in the light curves.

In this work we describe several new mechanical design and software solution approaches, develop a novel mounting design, and combine them into a compact and effective tilt removal and focus optimization system. The Robotilters are an inexpensive (they cost only a few percent of the total Evryscope instrument cost), completely robotic, on-sky tilt removal system for the very wide field Evryscope cameras. We demonstrated the concept and showed initial results in [89], here we describe the full solution and results. The Robotilters take 2 hours to run, remove tilt to the sub 10 μm level (as measured from opposite sides of the lens mounting surface or equivalently the Robotilter servo shafts) on a typical camera, optimize the focus across the image, and remain stable for multiple years once the final solution is found. We show the Evryscope image quality challenges introduced by tilt and focus, and their detrimental effect on limiting magnitude, astrometry, PSFs, and SNR. We demonstrate our solution to remove tilt and optimize focus across the image. We also briefly discuss the potential of the Robotilter design for use on other wide field surveys. We installed the Robotilters in November 2015 and began testing hardware and camera alignment software on select cameras in early 2016. All cameras were aligned by mid 2016 and have been stable for three years with only minor focus adjustments. The Evryscope hardware and optics, combined with the moderate night-to-night temperature changes at the CTIO observing site do not require constant refocusing; instead only periodic refocusing is done in response to seasonal temperature swings.

We discuss the system requirements in § 3.2, and show the Robotilter system in § 3.3. The optimization software is explained in § 3.4, and the alignment results and image improvement presented in § 3.5. We discuss the results in § 3.6, and conclude in § 3.7.

3.2 System Requirements

3.2.1 Science Requirements

3.2.1.1 Image Quality Requirements

The planned Evryscope surveys [17] requires sub percent level photometric precision on stars $m_g = 12$ and brighter and few percent level on stars $12 < m_g < 15$, continuously in each 2 minute exposure. In order to achieve this level of photometric precision, our models show the PSF FWHM needs to be between two and four pixels to avoid over or under-sampling, the loss of significant signal to background, or the necessity for large photometric apertures (the circle used to define the pixels included in the PSF, hereafter photometric aperture). The limiting magnitude and photometric precision benefits from the PSFs being round without distortion, and they need to be consistent across the image.

The Evryscope pixel scale was driven by several requirements, mostly by the very wide field-of-view ($\sim$ 10,000 sq. deg.), the signal-to-noise (SNR) required to detect transits, the limiting magnitude required to achieve enough sources, and the target of less than 30 cameras (to limit overall instrument complexity), along with using commercial components (reliability and cost). Given the final selection of components, the pixel scale is 13 arcsec per pixel. This is acceptable, with the main concern being that too coarse of a pixel scale results in a higher fraction of blended sources (nearby stars being blended in the pixel).

3.2.2 Functional Requirements

3.2.2.1 Mechanical Constraints - The Evryscope Telescope Modules

The Evryscope [19] is an array of 27 identical individual telescopes mounted into a hemispherical shell, called the mushroom, with a single common telescope mount. It uses Rokinon 61mm effective diameter F1.4 lenses paired to 28.8 MPix KAI29050 CCDs. The Evryscope uses FLI CFW-5-1 filter wheels, which have the capacity to accommodate 5 different filters. We use a single science filter (a modified SDSS G) with the other positions populated with sunshields used to protect the system in the event of a dome failure during the day. The science filter is designed with the parallelism and surface quality necessary to avoid measurable aberrations given the Evryscope lens and CCD specifications. All images shown and referred to in this manuscript were taken in the single science filter mode.

Camera mounts support and point the telescopes to form modules as shown in Figure 3.1. The telescope modules have to be as compact as possible to keep the size of the mushroom to less than 6 feet in diameter to meet the size and weight constraints of the Evryscope and the CTIO observing dome. The Robotilters need to fit into a small 8"x6"x4" space of the telescope module mounting on top of the filter wheel, between the lens and CCD. The Evryscope budget and resource limitations require the Robotilters to be simple with minimal components and few moving parts, without exotic materials, and using only readily available hardware. The unit cost target is $1000 or less, assembly time must be modest, and they need to perform reliably without human intervention.

3.2.2.2 Operations Constraints - Automation

The Evryscope currently has 22 cameras with the capacity for 5 more and is located at the remote observing site in CTIO, Chile. The system operates robotically, averaging 5000 images per night with ≈300,000 sources per image. Using the conventional method to fix the slight misalignment between the optics and CCD (by inserting shims or small thumb screws between the CCD and the lens and manually adjusting the thickness in an iterative way) is unfeasible for a system like the Evryscope. The time and resource requirements to adjust the very small physical distances necessary to correct PSFs are excessive. We demonstrate in § 3.5.3 that leaving the lens / CCD misalignment uncorrected has a negative effect on light curve precision and reduces detection efficiency. This requires our tilt correction solution be automated, efficient, and repeatable, and remain consistent for multiple years once aligned.

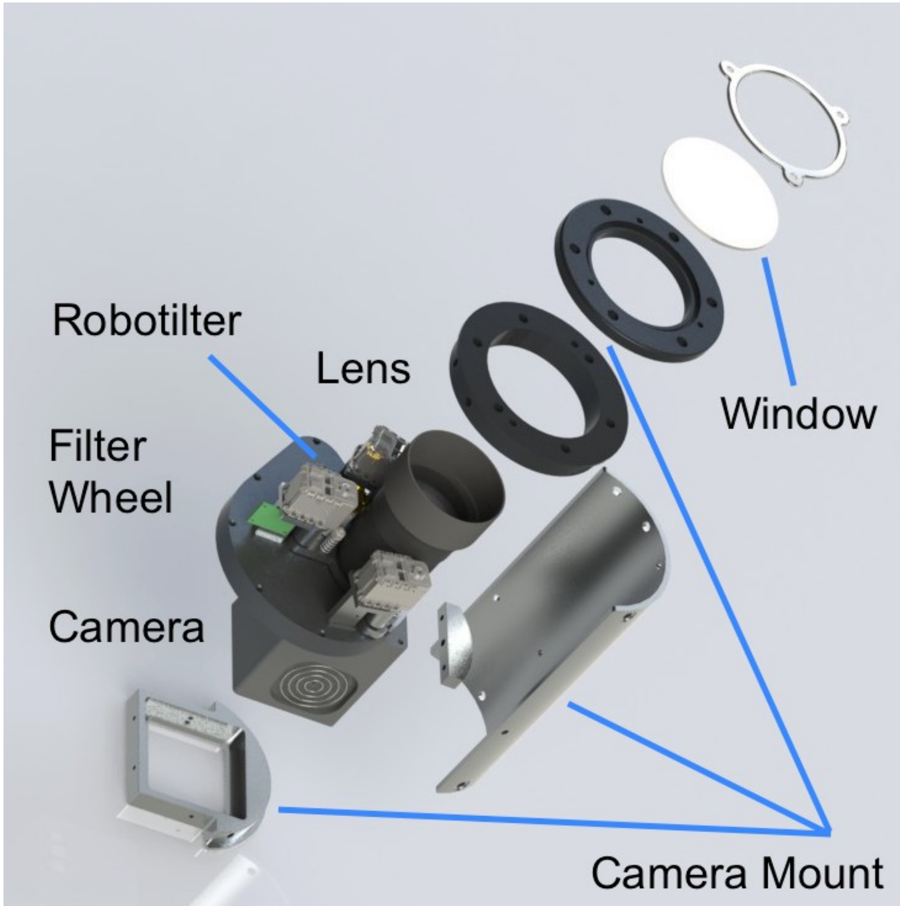

Figure 3.1: The Evryscope telescope modules, showing the mount, CCD camera, filter wheel, lens, optical window, and the Robotilter automated alignment system. The Robotilter uses three precision servos to adjust the separation and rotation between the lens and CCD to remove tilt and align the optical system. A separate servo is used to adjust the lens focus.

In addition to tilt removal, a focus step must optimize quality across the image with the ability to automatically compensate for temperature changes.

3.2.2.3 Image Quality Measurement

A small physical difference within normal machining tolerances of only ≈75 microns (a few thousandths of an inch as it is commonly expressed in CNC machining precision) can significantly degrade PSF quality in a wide-field image, especially with fast optics. Figure 3.2 shows a pre-Robotilter image with tilt from the upper left corner to the lower right corner. The image center is well focused, while the upper left and lower right corners are out of focus and on opposite sides of the focal plane. The opposing corner regions show distinct differences in PSF shape, distortion, and extent. A PSF FWHM contour plot is also shown for the same image, demonstrating the challenge in quantifying PSF quality in severely tilted images. The low quality of the lower right corner is well captured by the high FWHM values, and the high quality of the center is well captured by the low FWHM values. However, the low quality of the upper left corner is not well captured by the low FWHM values nor is there a distinction for regions out of focus on opposite sides of the focal plane. This turned out to be the most difficult challenge of the Robotilter project. We developed our own image quality metric and image comparison method as explained in § 3.4 in order to remove image tilt.

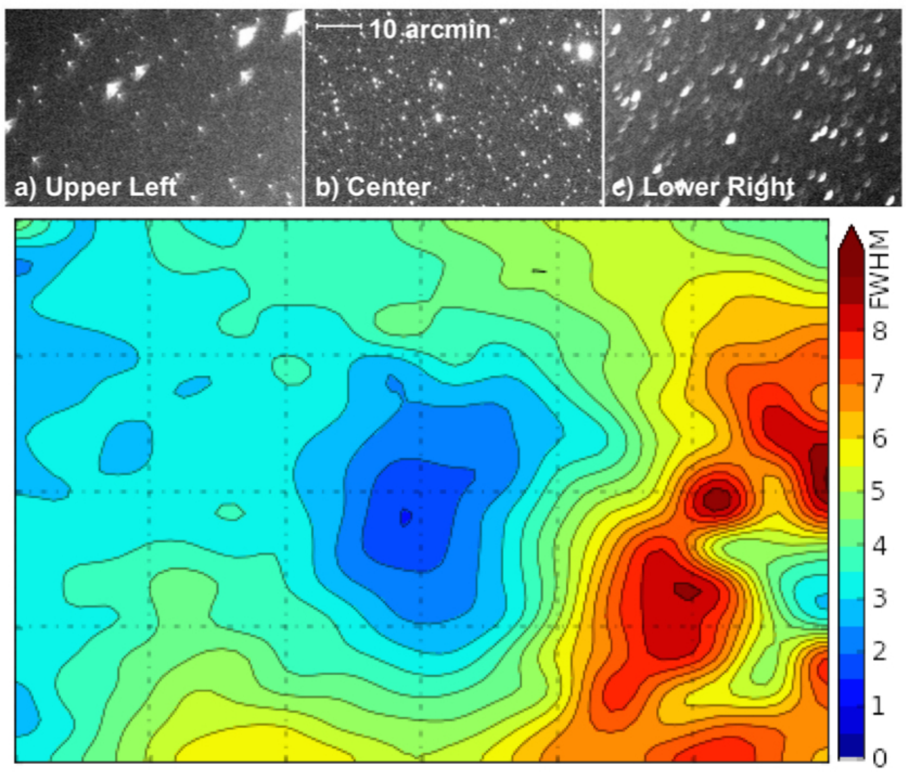

Figure 3.2: *Top: a)* An initial deployment (pre-Robotilter) image from the polar facing camera showing a 300 x 200 pixel closeup of problematic upper left corner. *b)* Closeup of the center of the same image. *c)* Closeup of the problematic lower right corner of the same image. *Bottom:* A PSF FWHM contour plot for the full image, demonstrating the challenge in quantifying PSF quality in severely tilted images and the lack of distinction for regions out of focus on opposite sides of the focal plane.

We use Source Extractor [73] for all measurements taken to determine image quality, regardless of the quality metric used (FWHM, Strehl, number of sources, or custom quality metrics described later in the manuscript). Each image used in the Robotilter algorithm is first processed with the standard Evryscope pipeline calibrations and image quality checks. Master-flats and darks are applied depending on the camera the image was taken with, bad pixels are masked, and images with very high overall background levels or obvious quality issues (clouds, streaks, or jitters) are discarded. For further details of the Evryscope pipeline and data processing we refer the reader to our Evryscope instrument paper [19]. Source Extractor uses a threshold above a local average of flux values (measured at each pixel) to detect sources above this level. Sources with adjacent pixels above this local average are counted as detections. A centroiding step provides the source location and a photometric aperture (a circle encompassing a radius of pixels) is used to sum the flux from the source.

Source Extractor offers a variety of input settings, including background significance level, minimum number of pixels in the aperture, and aperture size (expressed as a pixel radius). As a starting point, we relied on the settings from our photometric pipeline. Given the FOV and pixel scale of the Evryscope (13 arcsec / pixel) we expect and find that most use-able sources are 3σ above the background, the source PSFs have pixel counts ranging from a few for dim sources and $\approx$100 for the very brightest non-saturated sources, and the average best photometric aperture is modest in size at $\approx$3 pixel radius. Again, we refer the reader to [19] for further Evryscope instrument details. For the Robotilter algorithm we require a 4σ above background threshold and a minimum pixel count of 15 per PSF; the more stringent requirements filter very poorly sampled and dim sources unlikely to be use-able in calculating PSF quality.

For the sources with only a few pixels in the PSF, we include these in a number of sources count. The count is used as a separate quality metric, found to be independent of others such as the FWHM and Strehl. The sources count is very susceptible to observing conditions and to the observation field. However as we describe later in the manuscript, for the observations taken to align an individual camera we hold the field constant and take the observations over a short range of time with similar sky conditions to minimize the bias. Although we do not directly use the dimmer sources in the standard quality metrics, they make a valuable separate contribution in determining detected sources.

We tested a small range of input settings near the values described in the previous paragraphs (expected to be reasonable for given the Evryscope instrument characteristics) and found they did not help the FWHM or Strehl performance. As we show throughout this work, the the FWHM especially struggles to perform over the likely range of image misalignment. This is a result of the metric, the coarse pixel sampling, the wide-field and amount of tilt, and not due to software settings. The Source Extractor FWHM value is determined by fitting a two-dimensional Gaussian to the extracted PSF and calculating the weighted average of the width at half the maximum value. As a second check we used our own photometric aperture to extract pixel counts and values (thus only relying on Source Extractor for the source locations) and recalculated the FWHM directly and found no noticeable difference.

The testing and analysis of the more traditional quality metrics like the FWHM and Strehl ultimately influenced the approach we took to finding a solution the image quality challenge. While these traditional quality metrics struggle in many image regions and tilted images, they can work in limited ranges and if the PSF pixel sampling is good enough. If the metrics are somewhat independent (they succeed or fail in different situations), they might still be leveraged together to form an effective quality metric. Later in this work we show that we combined several traditional metrics and some custom ones as components to form our final composite type quality metric. This approach produced a reliable, simple, and fast solution for the Evryscope images.

3.2.2.4 Optimal Image Focus

An image taken from a camera with well aligned optics (hereafter a well aligned image) can be brought into focus by measuring the average PSF FWHM or Strehl for a small region in the center of an image. This on-axis focusing prescription works well in almost all situations, however in a very wide-field image like the Evryscope a focus optimization can provide an improvement in average PSF quality across the image. Figure 3.3 shows a flat image with no tilt and a very well focused image center, but with a compromise in PSF quality as the radial distance increases resulting in a ring feature. In § 3.4 we discuss our solution to defocus the image center in the direction and amount that optimises the overall image focus. We were able to incorporate this step with the tilt removal procedure so that our final solution concurrently removes image tilt and optimizes image focus.

3.2.2.5 Wide Field Survey Issues

Wide field surveys suffer from additional challenges that degrade image quality including field aberrations (predominantly coma, astigmatism, and curvature) and spherical aberrations (SA). The field aberrations and SA challenges are due to the difficulty of achieving a very wide field of view with a large aperture lens. The effects can be mitigated (but not completely removed) by the lens and CCD choice, FOV requirements, proper image calibration, photometric aperture selection, and removal of systematics.

An additional significant challenge for the Evryscope survey is lens vignetting. Although this issue is present in most lenses, it is normally more impact-full in wide field surveys. The vignetting is assumed to be radially symmetric and centered in the image, however the properties and magnitude must be characterized with photometric calibrations and are unique to each camera assembly.

Pixel drift (drift) is a challenge all telescopes face, even more so for a wide field like the Evryscope. The drift primarily arises from the telescope misalignment or camera flexure. The Evryscope is aligned based on the polar facing camera as all tracking is from this pointing.

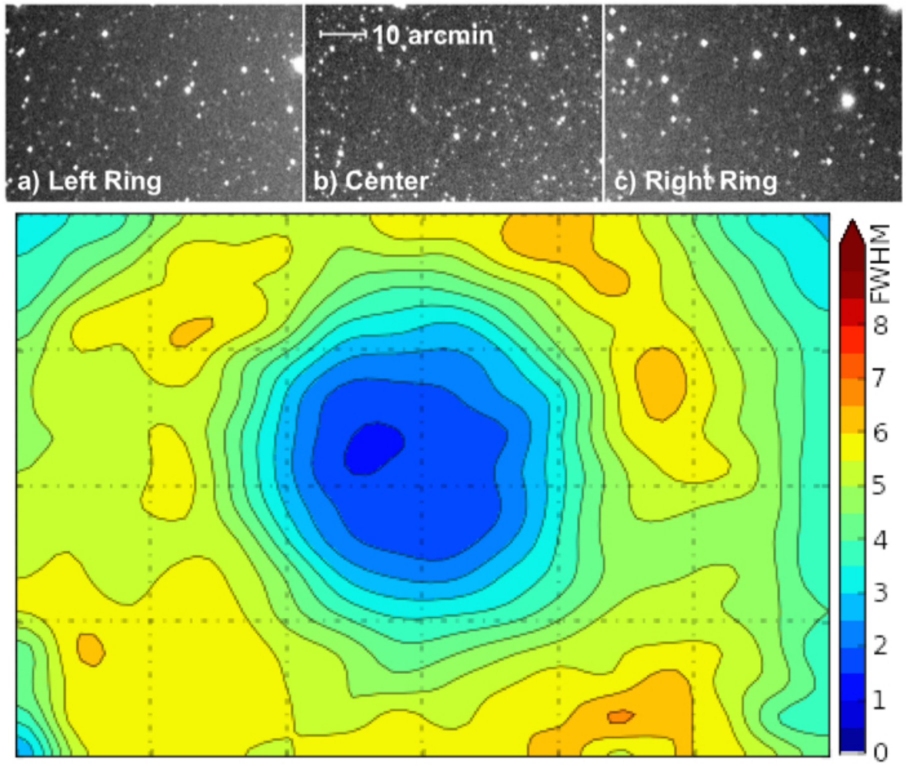

Figure 3.3: *Top:* An image from a tilt corrected zenith facing camera but without the Robotilter focus optimization. This image solution is found by maximizing the center image focus at the expense of the outer regions. *a)* Shown is a 300 x 200 pixel closeup of the left side of the image showing the problematic defocused ring. *b)* Closeup of the well focused center of the same image. *c)* Closeup of the right side of the image showing the same problematic ring. *Bottom:* A PSF FWHM contour plot for the full image, demonstrating the challenge in optimizing the focus of the entire image - here resulting in unnecessarily large PSFs toward the outer field and a ring-like feature.

The higher elevation cameras are over 90° in declination from the polar camera, so even a small misalignment can be challenging for the Evryscope.

In this work, we do not address lens choices or how they might affect field aberrations, lens vignetting, and SA; nor do we explore telescope mount designs to prevent pixel drift. The Coma, lens vignetting, SA, and drift challenges as they relate to the Evryscope are described in [19] and [89], in this work we concentrate on the image quality challenges introduced by tilt and focus and our solution to remove tilt and optimize focus across the image.

To summarize the ideas in this section, a corrected Evryscope image will be flat enough that the PSFs in opposing corners or sides will be similar in shape and size (within a pixel difference in extent from the center of the PSF). This maximizes the dim source detection (limiting magnitude) and avoids large photometric apertures which can degrade light curve precision. The corrected images will still have differences in PSFs in the image center versus the corners and the corners especially will still have elongations due to the effect of aberrations inherent to the optical system.

3.3 THE ROBOTILTER DESIGN

The Robotilter approach is to move the lens relative to the CCD, and adjust the focus via the lens focus and separation distance. Figure 3.4 shows the arrangement, resulting in 4 degrees of freedom - 2 tilt axes (also known as tip/tilt, referred to as tilt throughout this manuscript), a separation axis (the distance between the CCD and lens), and the lens focus (the built-in focus of the lens by moving the lens barrel which moves the optical elements relative to each other). We elected to fix the CCD camera and move the lens because the lens is the smaller and lighter of the two components.

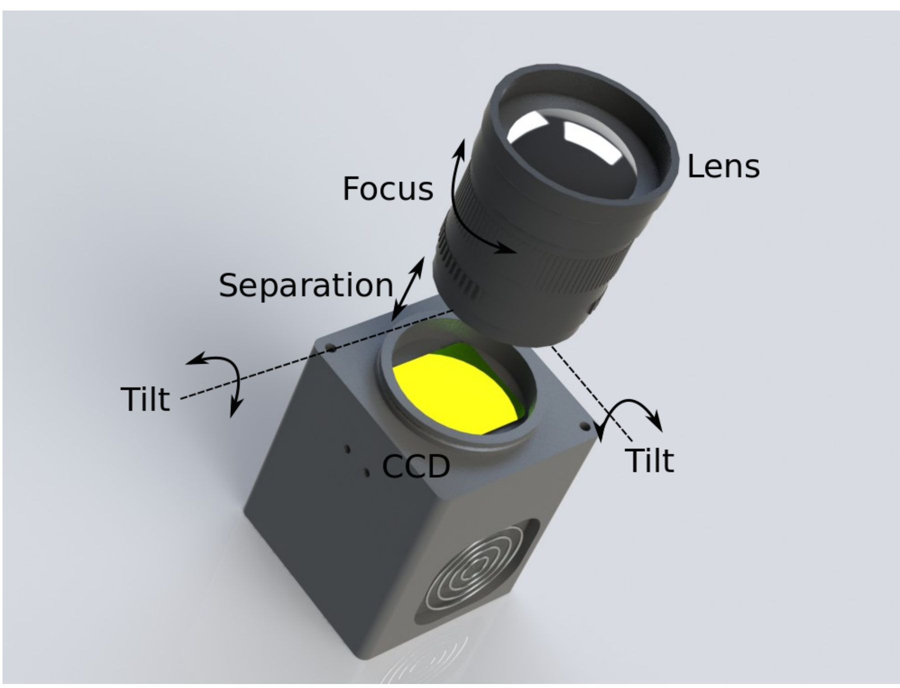

Figure 3.4: The Robotilter concept: the lens is moved relative to the CCD to remove tilt and optimize image quality.

A conventional mounting system fixes the lens to the CCD by mounting the lens bayonet ring to the filter wheel top (which is in turn fixed to the CCD housing)[6–9, 11, 15]. The lens turns onto the bayonet ring and locks into place via a spring and set screw[3]. The Robotilter instead replaces the fixed mounting system with a movable lens base-plate as shown in Figures 3.5 and 3.6. The lens bayonet ring now fixes to the lens base-plate and the base-plate is suspended above the filter wheel top by 3 threaded shafts. As each shaft turns, the base-plate moves up or down at the shaft axis relative to the filter wheel top. The three shafts are positioned in a triangular pattern and are held firmly against the filter wheel top by tension springs regardless of telescope orientation. The stainless steel shafts use a very fine 80 threads per inch (TPI) for precise movement capability and the lens base-plate has pressed-in brass inserts for smooth operation. Each of the threaded shafts are connected to a flexible coupler which fixes the input and output in rotation, but allows for a small angular difference and for changes in length. This prevents binding as the base-plate is moved. Servo piers are attached to the filter wheel top providing a secure mounting point for the servos.

Dynamixel MX-12 servos turn the couplers and shafts. Combined movements of the servos adjust the tilt of the base-plate and lens relative to the CCD. The lens can also move toward or away from the CCD without changing the tilt if the three servos are moved in the same direction and in equal steps. To adjust the lens focus a fourth servo is attached to a brass gear which contacts a plastic gear track fixed to the lens; as the brass gear turns, the lens focus adjusts. In this way, the four degrees of freedom (the two tilt axis, the separation axis, and the lens focus) can be optimized.

3.3.1 Mechanical Design Features

The Robotilter is designed for precise movements of the lens relative to the CCD. The tilt adjustment servos are controllable to within 2 degree accuracy in rotation and when coupled to the 80 TPI adjuster, the tilt and lens / CCD separation can be adjusted in increments

[3]https://www.canon.ie/lenses/tech-guide/

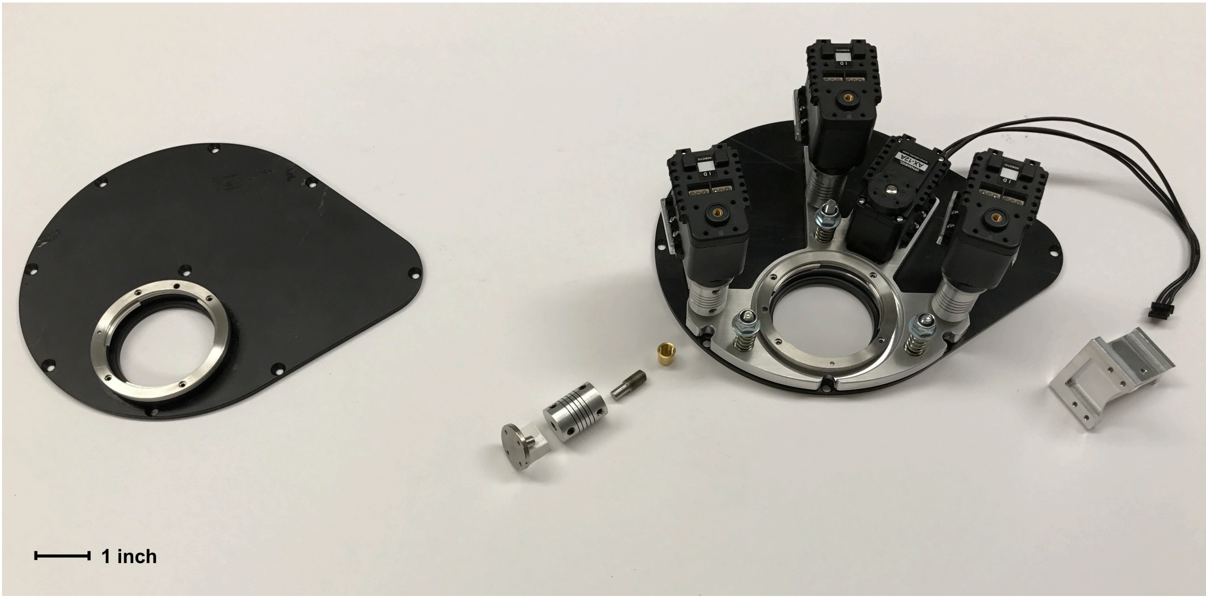

Figure 3.5: *Left:* The conventional mounting system with the lens bayonet ring fixed to the top of the filter wheel. *Right:* The Robotilter design. The lens bayonet ring is instead fixed to the lens base-plate. Three threaded shafts suspend the base-plate above the filter wheel top and are turned by precision servos. As each shaft turns, the base-plate moves up or down at the shaft axis relative to the filter wheel top and adjust the tilt and separation of the base-plate and lens relative to the CCD. A fourth servo is attached to a brass gear which contacts a plastic gear track fixed to the lens; as the brass gear turns, the lens focus adjusts. The four degrees of freedom - the two tilt axis, the separation axis, and the lens focus can be optimized.

(theoretically) as fine as .0001 inch (3 μm). The fine movements are consistent and repeatable, and at the sub 10 μm precision necessary to remove tilt and optimize focus. The servos can be turned multiple rotations, and the lens base-plate has enough travel ($\pm$ 15,000 steps) to cover the range necessary ($\pm$ 6000 steps) to find the optimal position. Once the final solution is found, the servos can be locked and remain in place reliably.

The optical path is sealed using several approaches to prevent light loss or dust contamination. Critical mating surfaces are recessed, the lens bayonet ring and the lens base-plate for example, to produce an overlap. At the movement interface, a light-trapping ring extends below the lens base-plate to prevent stray light from entering the optical system without impeding lens movement. Light and dust trapping foam is used between the base-plate and the filter wheel top as an additional seal.

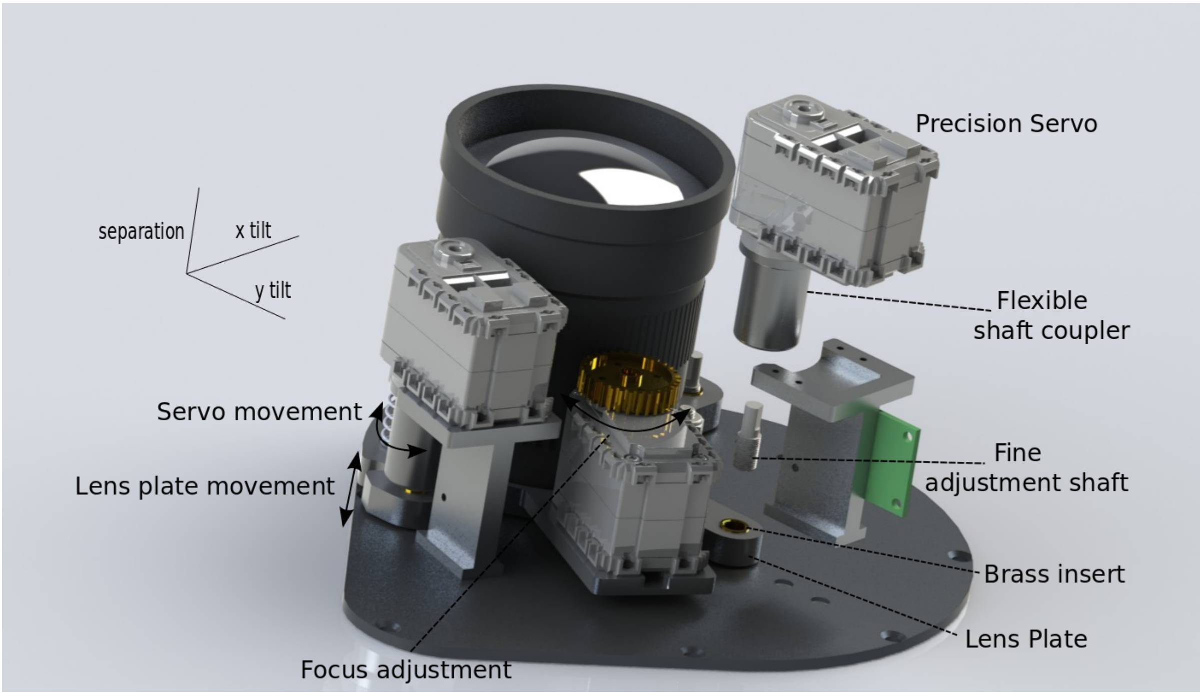

Figure 3.6: The Robotilter automated tilt removal and focus optimization mechanism. Servo movement adjusts the lens plate relative to the CCD. Exploded views of the servo, flexible shaft coupler (to prevent binding), fine adjustment shaft, and brass insert are shown along with the focus adjustment servo and gear.

The servo piers are slotted to match the bottom surface of the servos, and the filter wheel top is slotted to match the bottom of the servo piers. The shaft couplers use dual setscrews to securely fasten to the shafts, and each shaft is machined with a flat slot for the setscrews to contact. Thread-locker is used on all high stress parts. When assembled, the components are locked and resist twisting from the high torque servos, and the servo axes are precisely located. The lens base-plate is also slotted to support the focus servo to ensure the focus adjustment works consistently. The focus servo travels with the lens base-plate and operates regardless of tilt.

An ideal design places the servo axes equal distances from the image center and at equal separation angles so that the servo torques are equal, and the servo movements required to adjust a given tilt are the same. The filter wheel used in the Evryscope is a rotating carousel style, with its center axis necessarily offset from the image center. This complicated the Robotilter design by requiring the servo locations to be offset from the image center in order to fit on the filter wheel top and within the camera mounts. We mitigated this constraint somewhat by orientating the servo bodies toward the filter wheel space allowing the servo rotation axes to be moved closer to the image center. The arrangement features two opposing servos and a central one with a different lever arm and torque demand. These differences are managed in our software (described in § 3.4).

The Robotilter assembly mounts to the top plate of the filter wheel to avoid costly re-configuring of the existing filter wheel, CCD, or camera mounts. The footprint of the mechanism is contained within the camera mounts (Figure 3.7) so that the tight packing of the cameras in the mushroom is unchanged. The Robotilter upgrade was completed entirely on mountain and with minimal down time.

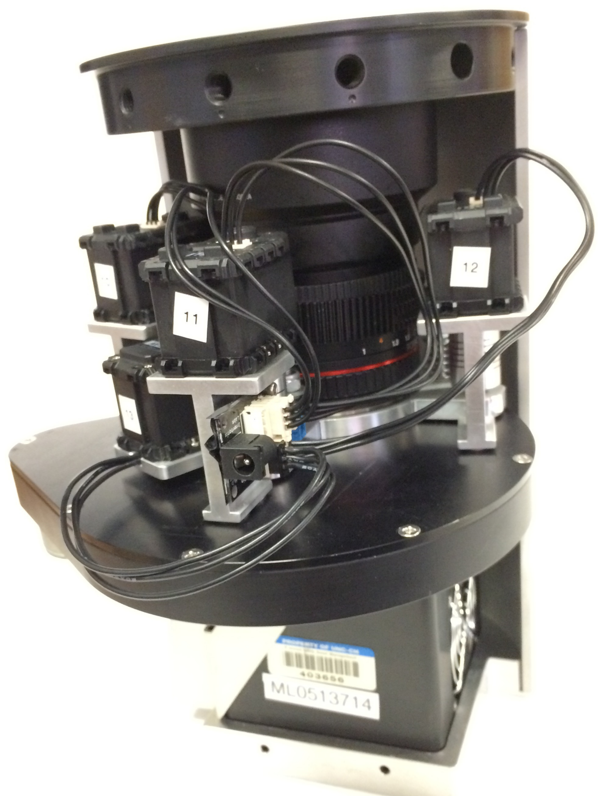

Figure 3.7: The Robotilter mounted in the camera mounts, fitting within the footprint of the filter wheel.

3.3.2 Electrical Design

Each Robotilter is powered by a 12V input line which is supplied by the accessory power supply units on the panels located in the sides of the mushroom. Each of the servos is connected to the input power line and are operated sequentially to limit total current drawn. A separate signal line connects all the servos to USB control boards which in turn are routed to the control computer. Multiple Robotilters form a serial-addressed network containing up to 14 cameras (56 servos) to reduce the number of wires, boards, and USB cables routed to the control computer. Communications over the serial line follow the Dynamixel half-duplex protocol; the large number of devices and line branches required a reduction in baud rate to 9.6kbps to enable error-free transmission (this speed is not a limiting factor for the system operation).

3.4 The Robotilter Software Solution

In order to find the optimal image quality, the Robotilters need to position the lens to the theoretical starting point and explore in 4 dimensions (x and y tilt, separation, lens focus) to find the optimal combination. Image quality must be expressed in mathematical terms while consistently capturing the tilt, focus, focal plane, and PSF aberrations in order for a software tilt and focus solution to work properly.

3.4.1 Potential Approaches

Several approaches could seemingly remove image tilt and optimize focus. We discuss the most obvious ones (to us) here, our first attempts to solve the problem, and how the pixel scale and PSF distortions from the very wide field influenced our final solution. It is reasonable to begin with a conventional approach, but the Robotilters are a unique instrument and it is difficult to define a ”conventional” approach to guide the software solution. However, we can combine conventional elements of image quality measurement and optics alignment as a beginning point. We first discuss this method, variations tried, and the insights learned that helped develop the final solution.

3.4.1.1 Conventional Approach

The most conventional approach we can imagine would use standard PSF quality measurements (FWHM and Strehl) to characterize image quality per region to test the parameter space and converge on a solution that maximizes total image quality. Although the Strehl is typically used for diffraction-limited images, very far from the Evryscope image quality, we use the definition here in an analogous way. Strehl in the Evryscope images measures the amount of light contained the peak of the PSF, and is thus a measure of encircled energy in the region of the PSF most important for determining the systems limiting magnitude.

There are two primary challenges with this conventional method. First, how to test the parameter space, and second how to measure *total* image quality. Using a simple grid-parameter search is ideal, however, it was not obvious how to define a grid that would test all the parameters (two tilt axes, lens / CCD separation, and lens focus position) without being overly complicated or vulnerable to degeneracies. Using a random parameter search, such as an exploratory simplex algorithm, could in principle deal with these issues but with the challenge of avoiding local minimums. Measuring total image quality is also challenging - as shown in § 3.2.2.3, out of focus sources show different distortions if they are above or below the image plane, adding to the difficulty in comparing quality.

3.4.1.2 Original Approach

The original strategy we tried was a variation of the approach described in the preceding paragraph. We used the FWHM and Strehl to measure image quality in several regions and compute a total image quality, combined with a simplex algorithm to explore different tilt, lens / CCD separation, and lens focus position to maximize total image quality. This approach failed for several reasons - the difficulty in capturing PSF quality, defining total image quality, and avoiding local minimums. We found the FWHM and Strehl ineffective at reliably displaying image quality in the presence of tilt and with coarsely sampled PSFs. In many cases a particular region can be optimized at the expense of another and return a higher total image quality measurement, adding to the difficulty in identifying images with significant tilt. The exploratory approach frequently converged on a local minimum with less than desired results, and the solutions were rarely repeatable.

3.4.1.3 Modified Approaches

We tried modifying the test space and quality metric of the alignment algorithm, however, the poor solution results and inconsistency persisted. We developed an auto-correlation quality metric that showed initial promise, but it still struggled with similar issues as the FWHM and Strehl. A grid with different tilt axes replaced the simplex algorithm to test the parameter space in a non-random way, again with similar poor solutions. Further testing revealed the challenges were independent of the camera or observing field. We then reduced the parameter space by holding the lens focus and lens / CCD separation constant, and only tested the two tilt axes. When this change did not significantly improve results, we tried visually locating the tilt axis and only exploring tilt about this axis, reducing the number of parameters to one. This modification still did not produce the desired results, and it became apparent that changing the tilt (in order to adequately test the parameter space for the best tilt) was causing a deeper dependence to emerge and prevent a converging solution. This dependence is best understood by analyzing the quality metric.

3.4.2 The PSF Problem

In order to measure PSF quality, the FWHM and Strehl measurements require a finely sampled PSF and the FWHM assumes a symmetric profile. Wide-field images with potentially severe field aberrations (including coma and astigmatism) and coarse pixel sampling do not have these characteristics. Images with tilt worsen the asymmetry and significantly reduce the effectiveness of the FWHM and Strehl to reliably displaying image quality in this situation. The main challenge is the structure of the PSF core and halo, and the coupled effect that the focus, tilt, signal, and CCD position have on each of them.

Consider an average PSF in the center region of a well focused wide-field, coarse pixel image, with little tilt as shown in Figure 3.8. The PSFs (row a, middle column) are narrow with almost all of the flux contained within the central pixel, and with a symmetric halo that is insignificant for most sources. Changing the focus (for this discussion by adjusting the lens / CCD separation) results in a widening of the PSF to form a blob that is again symmetric and still limited in extent, shown by the right columns in row a. Changing the focus in the opposite direction gives a similarly widened PSF blob, mostly indistinguishable from the first focus movement. The separation change between columns is a constant 20 μm, considerably larger than the level the Robotilters are intended to remove, chosen for better visualization. The FWHM measured for the center region (row b) generally captures the quality change due to the focus change, but not at the level necessary as demonstrated by the very similar measurements in columns 5-7. The focus sweep, also known as a through focus sequence, demonstrates a further challenge of the FWHM measurement - the FWHM does not change significantly around the focused position. This is to be expected in situations with minimal aberrations (as exist in the image center) and coarse sampling. The FWHM response curve from the focus sweep is parabolic, and is in the shallow region of the parabola when the image is in focus, with little discrimination between changes in this narrow parameter space. Testing a wide focus range is necessary to estimate the best position. The fit is also asymmetric as shown by the difference in response below and above the focal plane (shown in the plot as steep on the left and gradual on the right columns).

The situation is more challenging for sources located in regions other than the center of the image. Consider an average PSF on the lower right corner of the same camera displayed in row c of Figure 3.8. The center columns show elongated and distorted PSFs, even thought the region is in focus. A significant amount of the flux is in the halo. The PSFs in the right

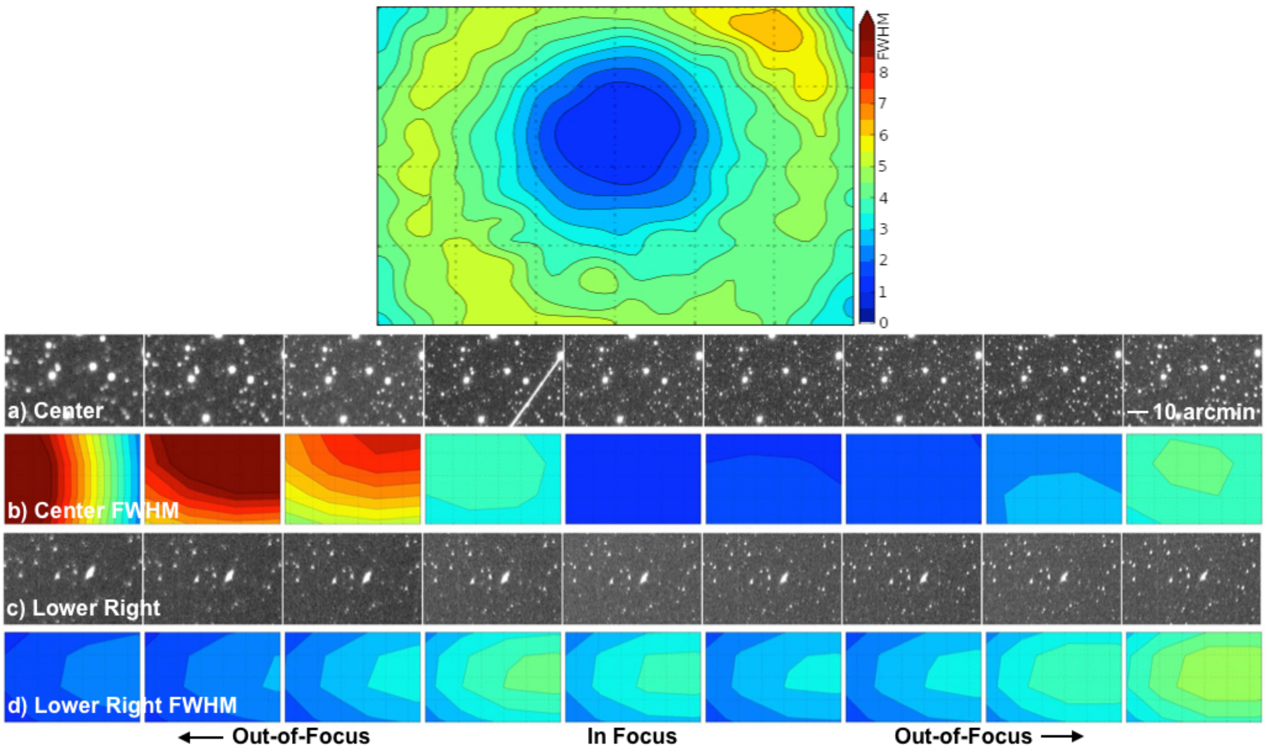

Figure 3.8: *Top:* The FWHM plot from an Evryscope wide-field image with little tilt. *Bottom:* A sweep of images with different focus positions, the center columns are in focus while the left columns are out-of-focus below the focal plane and the right columns are out-of-focus above the focal plane. The steps between images is constant at several times larger than the sub 10 μm level necessary to remove tilt (chosen to aid in visualization). *a)* 300 x 200 pixel closeups of the center region of the images. *b)* The FWHM of the same center region. Three focus positions show similarly good quality, and the response is different below and above the focal plane. *c)* 300 x 200 pixel closeups of the lower right corner region of the images. *d)* The FWHM of the same lower right corner region. The quality metric struggles to discriminate between the focus positions, finds more than one minimum, and the best quality is located at the very out-of-focus position shown on the far left. These issues are exaggerated in images with tilt. The challenge in capturing quality in wide-field, large pixel images with tilt led us to develop a custom tilt driven quality metric that analyzes the images as a grid and uses a predetermined movement sequence to capture images for analysis.

columns are out of focus but also elongated and distorted in a more severe way. Most of the flux is contained in the halo, which is not symmetric. The images on the opposite side of the focal plane are affected differently, as shown in the left columns. Here a significant fraction of the flux is in the core with a dispersed halo in addition to being distorted. As the lens is moved further, the signal decreases so severely that the halo disappears and only a faint core is detectable. The number of sources also decreases significantly.

Unfortunately, from a quality standpoint the PSF appears narrow and with almost all of the signal in the center pixel. There is very little discernment in image quality across the focus positions (which spans ≈20 times the level of tilt the Robotilters are designed to remove). More troublesome, the position of best measured quality is the far left column corresponding to a very out-of-focus position, driven by the disappearing halos and dim sources. This position of a severely unfocused region scores high from a traditional quality metric. The FWHM measurements are shown, but we found the Strehl suffers from similar issues with different best positions.

It is also important to point out that the best and worst quality of each region (the center versus the lower right corner as shown in Figure 3.8) are in no way comparable. The best quality in the center region is much better than the best in the lower right corner, with a similar disparity in worst qualities. This behavior is expected in a system with field aberrations (including coma and astigmatism), and are worsened with the fast Evryscope optics. Here we have shown the center and lower right corner regions, other regions suffer from similar challenges and manifest in different ways.

If we adjust the image tilt (while holding the image center fixed) the lower right corner PSFs will distort differently than before due to the changed tilt, but the focus will also change. This can be seen in the lower right corner shown in Figure 3.2 of the same camera but with significant tilt. Now the perceived PSF quality will depend on the coupled tilt and focus effects, the loss of signal, and the compromised halo. Adding to the difficulty, the tilt and focus challenges vary by region. In this example camera, the PSF shape in the upper left corner is approximately opposite of that in the lower right corner, and the PSFs in the edges are completely different than those in the corners or center.

Moving image tilt to explore the parameter space changes the PSF characteristics, is coupled to the focus, and the PSF effect is region dependent. This places a severe burden on a quality metric. Even without changing image tilt for comparison, measuring quality in a tilted image is challenging as is comparing quality across regions.

To summarize the ideas in this section, standard techniques (described above as well as additional commonly used metrics that were tested but not discussed) failed to capture PSF quality. With the Evryscope lens and CCD package the PSF halo tends to degrade so rapidly when out of focus, that it becomes undetectable. This leaves only the small core that appears as good image quality but actually only encloses a small amount of the signal. Only limited sources in the Evryscope images are bright enough to counter this challenge and the common methods optimize the size of the small cores, which drives the image further out of focus.

3.4.3 The Robotilter Approach

From the challenges described in § 3.4.1 and § 3.4.2 we developed the Robotilter software solution that uses a custom tilt driven quality metric, analyzes the image as a grid, and uses a predetermined movement sequence to capture images for analysis. The solution reliably removes tilt (from normal manufacturing and installation tolerances) and optimizes image focus in the same step, is repeatable, and takes approximately 2 hours to run. Cameras with excessive initial tilt (starting values far from optimal) benefited from additional optimization runs. We found that in this situation, the algorithm iteratively converges to the the optimal solution after repeated runs. We describe the process below.

3.4.3.1 Tilt Driven Quality Metric

We developed a new image quality metric designed to measure quality in the presence of image tilt and to differentiate sources above and below the focal plane. The quality metric is combination of standard PSF measurements, custom PSF measurements, and regional measurements to give a combination score which we call the *combo*. The *combo* is calculated for a small (≈1 sq. deg.) region of an image by calculating different quality measurements and multiplying the normalized values for an overall region score. The algorithm uses Source Extractor [73] to extract data from sources in the region. To filter out the dim and poorly sampled sources, we require the detections to be greater than 4 σ above the background, not have blending flags, and the PSFs to comprise at least 15 pixels. Here the pixels are defined to be part of the PSF if they are above the background limit, and increasing the photometric aperture (the circle used to define the pixels included in the PSF, hereafter photometric aperture) size by one pixel does not increase the number of pixels in the PSF.

For each of the filtered sources, we calculate the PSF FWHM and Modified Strehl (M_S), which is the standard Strehl scaled by a multiplication factor appropriate for the Evryscope (this is not a real Strehl but still forms a useful metric component). Although the M_S still struggles with the coarse Evryscope pixel scale, the multiplication factor effectively normalizes it near a value of 1 in conditions of peak quality. As discussed below, the FWMH is also modified (inverted) and combined with other elements similarly scaled so that each component contributes similarly. We also calculate custom PSF measurements for each source. 1) The Radius Ratio (R_R): defined as the photometric aperture radius required to enclose all pixels in the PSF divided by the ideal radius necessary to enclose the same number of pixels in the PSF, if the PSF was perfectly round. 2) The Distortion Factor (D_F): defined as the average distance of the pixels in the PSF from the PSF center divided by the the ideal average distance the same number of pixels in the PSF would be from the center, if the PSF was perfectly round. We then calculate the average FWHM, M_S, R_R, and D_F for each region. We also count the number of filtered sources for each region and normalize across the image sweep (N_S). The FWHM, R_R, and D_F average quality elements are inverted so that all factors treat a higher number as a higher quality. They are combined to give the *combo* quality for the region:

$$combo = \left(\frac{1}{FWHM}\right) M_S \left(\frac{1}{R_R}\frac{1}{D_F}\right) N_S \tag{3.1}$$

The *combo* metric benefits from the pooled effectiveness of the different elements to offset a particular ineffectiveness of an individual element. The FWHM measurement tends to capture out-of-focus PSF quality on one side the focal plane but fails on the opposite side. The Strehl tends to perform similarly but in the opposite way as the FWHM. The radius ratio, distortion factor, and number of sources tend to capture the variation in quality regardless which side of the focal plane the PSF is unfocused, but they are not discriminatory enough by themselves to capture the quality of the region. When combined as in the *combo* equation, the metric effectively captures the region quality especially on tilted images. We demonstrate in § 3.4.3.4 the *combo* solution converges on all regions of the Evryscope images when used in our full solution algorithm.

3.4.3.2 Analysing the Image as a Grid

Images are split into a 16 x 24 grid resulting in 384 regions with ≈1 sq. deg. FOV each. This grid size is chosen to obtain a fine enough sampling of the image field and to have enough bright stars in each region. For each region, the quality is calculated using the *combo* (§ 3.4.3.1) metric. The *combo* scores are not compared across regions, they are instead captured for each of the 384 regions of a particular image. The servos are moved and the *combo* scores captured for each region of the new image. Regions can be compared across images to determine if a servo movement helped or hurt the quality of each part of the image independently.

3.4.3.3 Predetermined Movement Sequence

We use a predetermined sequence (which we call the focus sweep) to move the servos and acquire a series of images for the Robotilter solution. The critical idea of this approach is to hold the tilt constant and only change the lens separation distance. Admittedly, this is counter-intuitive. A conventional approach (§ 3.4.1) adjusts the tilt and separation to explore those parameters and search for an optimal solution to the tilt and separation. While it seems reasonable to adjust the parameters that are to be optimized; in this case the image quality, focal plane, and local minimum challenges described in the previous sections are prohibitively difficult to overcome. The focus sweep approach avoids these problems altogether by instead finding the best focus for each region. It is similar to focusing a standard telescope - sweep in distance over the potential focus range and move to the position of best quality. In the Robotilter focus sweep we capture the best position of each region independent of the tilt since it is constant over the image.

3.4.3.4 The Combined Solution

The Robotilter solution holds the tilt constant and gathers a series of images in a focus sweep, splits the images into a grid, and measures the quality per region as described in the previous sections. Figure 3.9 shows the process on a representative camera. A focus sweep (holding the tilt constant § 3.4.3.3) of 200, 30-second images is acquired with a separation distance of 60 servo steps (4.5 μm) between each exposure. Each image in the stack is split into a grid of 384 regions (§ 3.4.3.2) and the quality of each region is calculated using the *combo* metric (§ 3.4.3.1). The servo positions are determined for each region corresponding to the optimal quality; the position in servo steps is then converted to a distance. As the lens / CCD separation distance sweeps from a maximum to a minimum, the image quality is low and reaches a maximum value before falling off, and we fit a Lorentzian to measure the best position. The Lorenzian profile was an empirical fit to the data, providing a much-improved match over a standard Gaussian or parabolic fit. The choice of a Lorenzian was motivated by the need for a more-peaked function, without physical motivation. An example from the center region of a camera with significant tilt is shown in Figure 3.9. The pixel position of the chip is expressed in a distance from the chip center, and is combined with the quality information to create a 3-D contour of the focal plane.

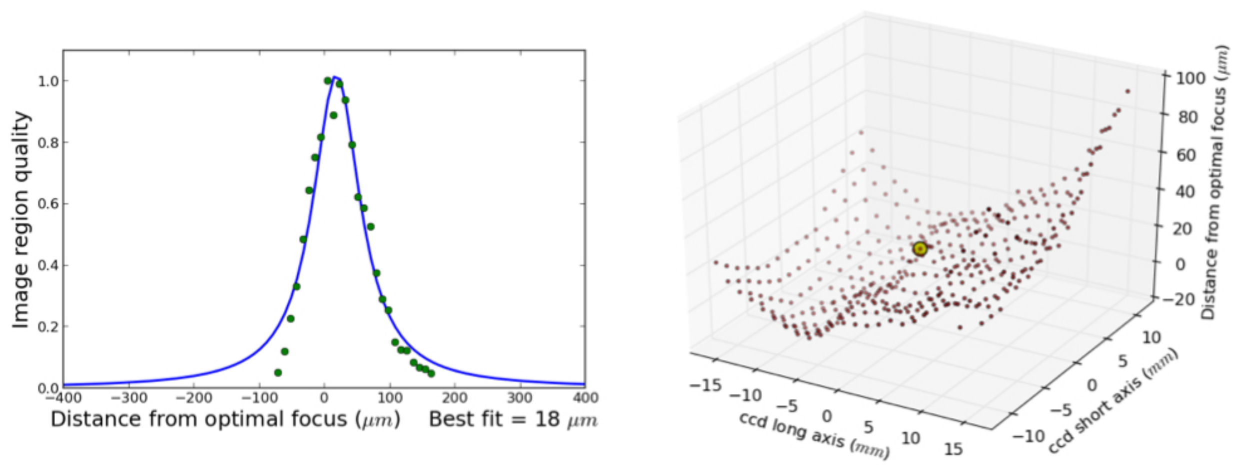

Figure 3.9: The Robotilter solution holds the tilt constant and gathers a series of images in a focus sweep by adjusting the lens / CCD separation, splits the images into a grid, and measures the quality per region as described in § 3.4.3.4. *Left:* The quality for a small region in the center of the image as a function of the distance from optimal focus as determined by the servo positions. As the lens / CCD separation distance sweeps from a maximum to a minimum, the image quality is low and reaches a maximum value before falling off as demonstrated by the green points. We fit a Lorentzian (the solid blue line) to measure the position of the best quality (18 μm) for this region of the image. *Right:* The same small region in the center of the image is shown as the yellow circle with the 18 μm distance from optimal focus. The image is divided into 384 regions and the image quality is calculated for each region in the same way as the example in the left panel. The pixel location of the center of each region is converted to a physical position from the image center, and the information is combined to construct the focal plane (the red points) capturing the tilt and 3 dimensional nuances.

Additional examples of the *combo* quality metric are shown in Figure 3.10 for the top, bottom, edge, and corner of the image. The quality measurements converge regardless of region, despite the challenges from the tilted images, regional differences, and inconsistent PSFs. The image sweep provides 200 data points with fine separation, which aids in the accuracy of the quality fits. Additionally, points at far distances from optimal focus provide such low quality that they help constrain the base of the Lorentzian fit. These very low quality points (not shown in the plots) are flagged using a low source and high FWHM threshold, and are assigned a low value near zero. We found this to be an effective way to aid in the automated Lorentzian fit and to focus the peak width. We experimented with Gaussian and parabolic fits, but found them less reliable, and more prone to wider peaks with less accurate results.

To remove the tilt a plane is fit (shown in blue) to the measured 3-D contour focal plane using the *Scipy* module, shown in Figure 3.11. Using the locations of the Robotilter servo axes relative to the center of the CCD (from the Robotilter mechanical design), we calculate the distance of the fit plane at each servo axes from zero (z=0). We move the servos by the calculated amounts but in the opposite direction. This moves the fit plane so that it is co-planar to the xy-plane. In this way, the tilt between the lens (fit plane) and CCD (xy-plane) is removed. An image sweep taken after the Robotilter solution producing the untilted 3-D contour for the same camera and field is shown in Figure 3.11. In most cameras and fields, we are able to measure focal plane features and remove tilt at the sub 10 μm level (as measured from opposite edges of the Robotilter servo shafts). We show in § 3.5 that this level of correction removes PSF differences in opposing corners and edges to the level necessary to avoid large photometric apertures (with similar size apertures needed for opposing corners and edges), and to increase the limiting magnitude by .5-1 magnitude depending on the region and amount of tilt.

We experimented with fitting more complicated shapes (paraboloids for instance), but found they did not capture the tilt in a more robust way than the simple plane fit, and they

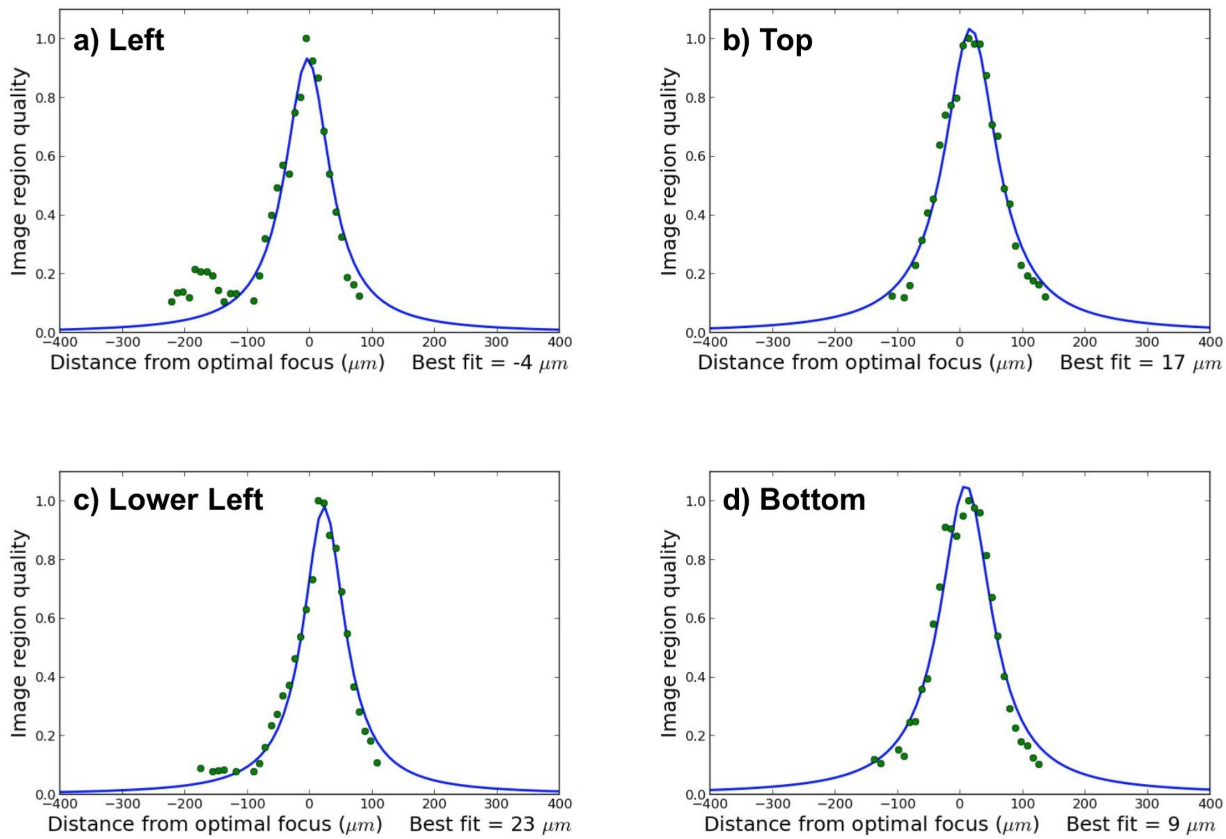

Figure 3.10: *Top: a)* The quality for a small region near the left edge of the image. The region is challenging with distorted PSFs, as illustrated by the scatter in the points and the secondary maximum near -200 μm. The feature is caused by the FWHM component struggling to accurately measure quality in this circumstance (out of focus below the focal plane). The robustness of the *combo* quality metric is demonstrated by the ability to overcome the shortcomings of a single element by pooling all of the elements, and by scaling the elements so that one does not dominate. The best fit is accurate for the region and is consistent with the best fit in nearby regions and with the overall focal plane. *b)* The quality of the top of the image. *c)* The quality of the lower left corner of the image. *d)* The quality of the bottom of the image.

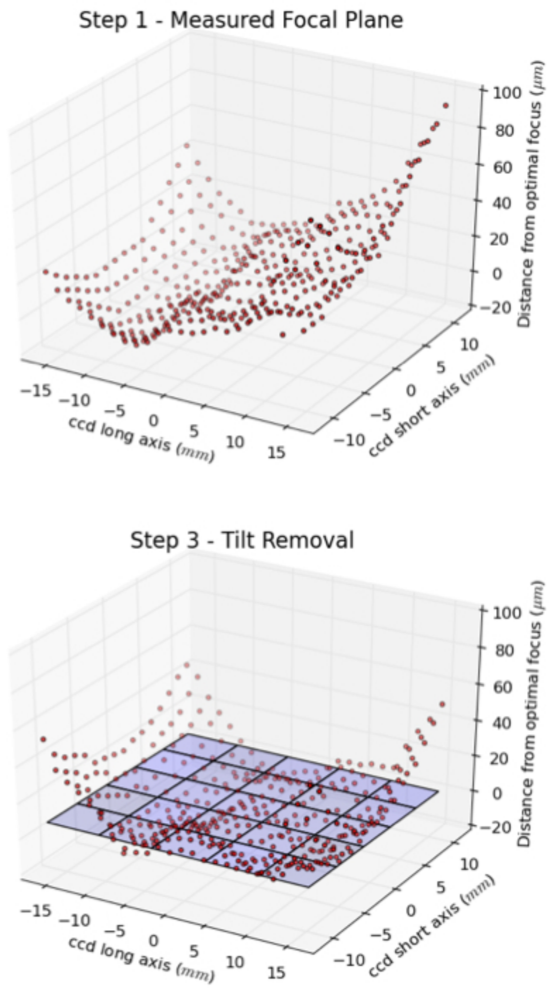

Figure 3.11: *Step 1:* The measured 3-D contour focal plane as described in § 3.4.3.4 and Figure 3.9. *Step 2:* The plane fit to the measured 3-D contour focal plane. *Step 3:* We move the servos so the fit plane is co-planar to the xy-plane. In this way, the tilt between the lens (fit plane) and CCD (xy-plane) is removed. *Bottom Right:* The detailed mesh plot of the measured 3-D contour focal plane taken after the Robotilter solution for the same camera.

were more prone to fail in a catastrophic way. Using the plane fit offers another significant advantage - it averages the best focus across the image. Because the fit plane slices the measured 3-D contour by minimizing residuals, it finds the best overall image focus instead of maximizing one region at the expense of the rest of the image. Thus with the plane fit approach, we remove image tilt and simultaneously optimize the focus of the image field.

3.4.3.5 Focal Plane

Camera lenses offer a wide range of focus settings, the Rokinon lenses used on the Evryscope can focus from 1 meter to infinity. The lens focus mechanism (turning the lens body relative to the lens base) can actually go slightly past the infinity mark, common in photographic lenses as a margin to cover the infinity focus in the event of temperature changes. The focus servo used on the Robotilters has a fine enough control that this small range in lens adjustment corresponds to ≈100 servo steps. We tested this range on several cameras by removing the tilt and optimizing the focus with the lens focus at slightly different positions. In this way, we test the flatness of the field (unrelated to tilt and only dependant on lens focus position and lens / CCD separation).

The lens focus mechanism moves a group of the lens optical elements relative to other elements. This motion is different than simply moving the entire lens relative to the CCD, as we can do by moving the three Robotilter servos. With the lens focus mechanism, we actually change the optical properties - very slightly. The focal plane position is changed, as is the focal length. The optical aberrations (chromatic, spherical, field coma, and field astigmatism) are also changed. Most relevant to the Evryscope images, the focal plane position and off-axis aberrations (coma and astigmatism) are changed. The difference in focal plane position can be compensated for by the Robotilter adjusters. Different combinations of the lens focus position and the CCD / lens separation distance (within a small in-focus range) return different image quality across the field. A focus and separation combination

Figure 3.12: *Left:* The potential focus range of the lenses. *Right:* The field flatness as a function of lens focus position (530-590 in servo position for this lens), by computing the residuals of the plane fit to the measured 3-D focal plane contour. The flattest field is at ≈15 servo steps from the maximum lens focus, on average for the Evryscope camera assemblies.

that results in a high quality image with a flat field is advantageous for wide-field surveys like the Evryscope since the PSFs will be closer to in-focus regardless of position on the CCD.

We find that for the Evryscope optics, the flattest field is located not at the max lens focus but slightly "off infinity" as shown in Figure 3.12. The test cameras all returned similar results, and we used 15 steps off maximum lens focus as our best solution for all Evryscope cameras.

3.4.3.6 On-Sky Images

The Robotilter solution uses on-sky images for all alignment and focusing. We did experiment with in-lab alignment, but found this approach challenging with undesirable results. For the in-lab alignment approach, we used a dark room with a printout of objects (lines or synthetic PSFs) for the camera to image. Having enough different regions on the printout and sufficient objects per region was cumbersome, and the tilt removal software suffered from the same quality, focus, and convergence challenges described in § 3.2.2.3 and § 3.4.1. The focus position of the in-lab setup is necessarily much shorter than the on-sky focus position. A tilt removal solution from a lab setup based on such a large focus difference does not necessarily apply to on-sky conditions. The potential benefit from in-lab alignment is to avoid alignment during telescope time, or to avoid on-mountain troubleshooting. By testing the Robotilters in lab to verify the assembly and moving the servos to the home

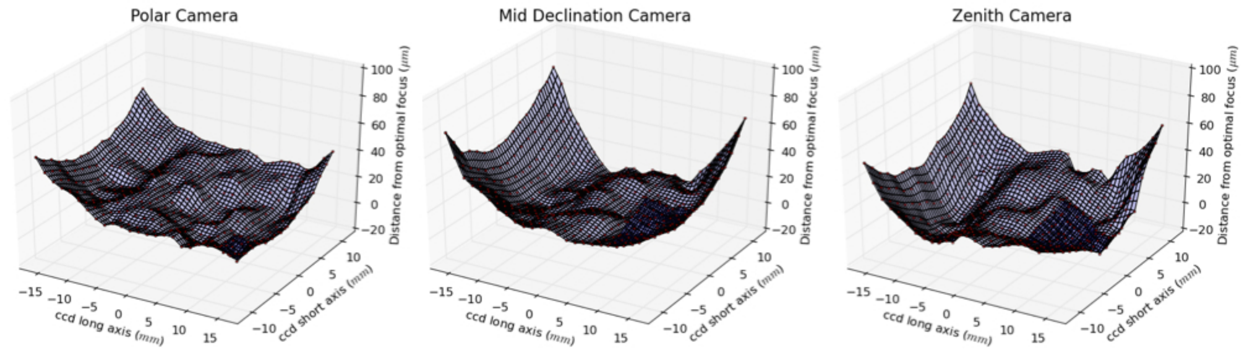

Figure 3.13: The post-Robotilter camera alignment results for three additional cameras, distributed in declination. Shown is the polar facing camera, a mid-declination camera, and a zenith facing camera. The tilt removal is to the sub 10 μm level. Differences in the quality and flatness of field of the optics (unrelated to lens / CCD tilt) are clearly visible.

position, we were able to realize most of the in-lab potential benefit, and use the robust on-sky Robotilter tilt removal solution to efficiently align the cameras.

3.5 RESULTS

3.5.1 ALIGNMENT RESULTS FOR ALL CAMERAS

Using our software solution described in § 3.4, all Evryscope cameras were aligned in mid 2016 during dark sky conditions. A few cameras that were initially very far out of alignment benefited from a second run (with a smaller range and finer steps) using the initial solution as the starting point. We show 3-D contour plots for several Robotilter corrected cameras (in addition to the one shown in § 3.4.3.4) in Figure 3.13.

The Evryscope control computer uses a scripting daemon to run the alignment algorithm. Before a nightly observation, cameras must be manually selected for alignment and placed in a queue. In order to limit power draw over 88 separate actuators, we restrict the number of camera alignments to two at a time. The post-Robotilter alignment quality for each camera was verified with the 3-D contour plot and inspection of test images taken from its Robotilter solution. Camera alignment stability is verified with a daily e-mail of a FWHM display of all

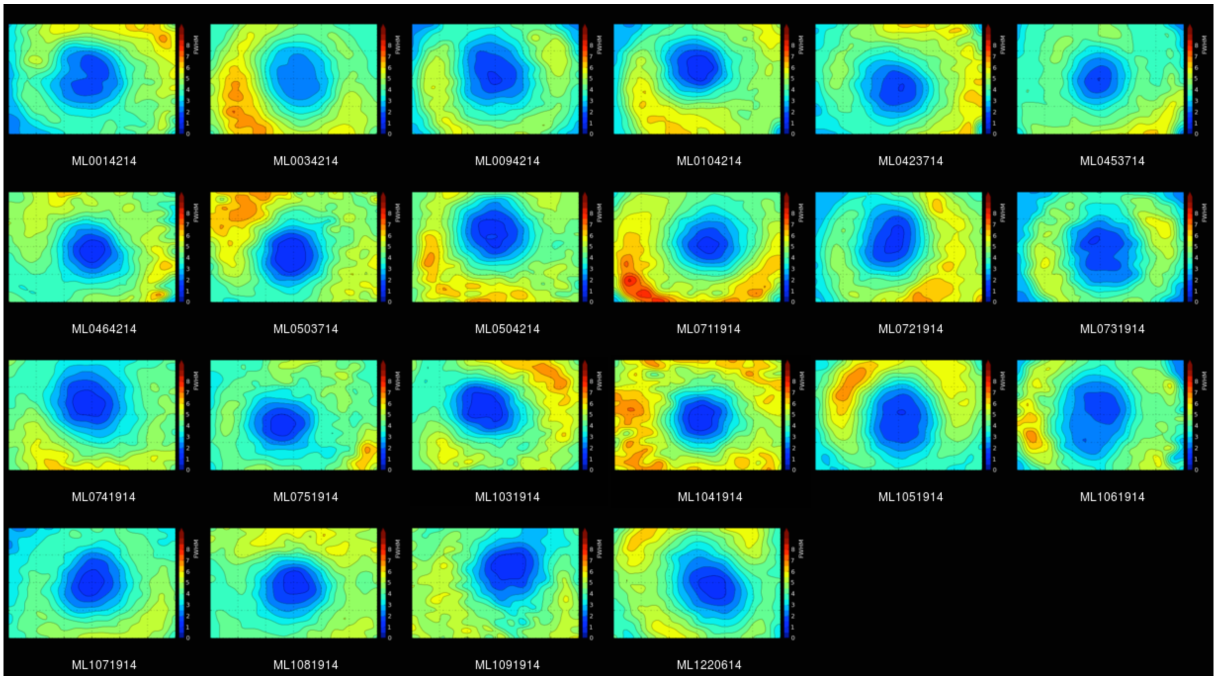

Figure 3.14: The Robotilter camera alignment results, as shown with a daily e-mail of the FWHM display of all cameras. Although not robust enough for the full tilt removal solution, the FWHM display can be calculated on a single science image taken for each camera during the night and does not require the servos to me moved, or an image sweep to be taken. If a camera shows signs of movement, or the appearance of a very troublesome area, we can re-run the Robotilter software.

cameras, a recent example is shown in Figure 3.14. Although limited, the FWHM display can be calculated on a single science image taken for each camera during the night and does not require the servos to be moved, or an image sweep to be taken. If a camera shows signs of movement, or the appearance of a very troublesome area, we can re-run the Robotilter software. Other than a few cameras requiring disassembly for maintenance (replacing faulty filter wheels, lenses, or cables), the aligned cameras have remained fixed since the 2016 alignment with no requirement to move even during seasonal temperature changes.

3.5.2 IMAGE QUALITY IMPROVEMENT

Upon initial deployment of the Evryscope, the on-sky performance of many cameras showed a compromised image quality due to tilt and focus issues, despite careful shim-based on-sky alignment. The edges and corners of the images suffered the most, with noticeable differences in PSF shapes depending on the region and position above or below the focal plane. Here we demonstrate the improvements from the Robotilters by showing select cameras before and after the Robotilter solution.

Figure 3.15 top left shows the FWHM plot of the camera facing the South Celestial Pole (the polar camera) upon deployment, a tilt from the lower right to the upper left corner is visible. This is the same camera described in § 3.2.2.3 and shown in Figure 3.2. The top right shows the same camera after installation of the Robotilter, but before running any software tilt correction. The bottom left shows the results after the Robotilter optimization. The Robotilter upgrade improved the Evryscope image PSF FWHM and removed the wide-scale tilt. Figure 3.15 bottom right shows the focus optimization results. The image quality now meets the PSF FWHM pixel target across the image with very little tilt and acceptable widening toward the edges.

Figure 3.16 shows 300 x 200 pixel closeups of the problematic corner regions of the polar camera, before and after the Robotilter solution. The upper left and lower right corners are especially troublesome, with severe corner to corner tilt and with opposing corners on opposite sides of the focal plane. The unfocused and poorly sampled PSFs are improved by the Robotilter solution in shape and brightness. The flux is more concentrated in the PSFs, dimmer stars are visible, and more sources are detected in the images. The image improvements are realized without negatively affecting the central region.

Figure 3.17 shows 300 x 200 pixel closeups of the problematic edge regions of a zenith camera, before and after the Robotilter solution. This is the same camera discussed in § 3.4 and shown in Figure 3.11, now showing improved results and consistent quality across the regions.

Figures 3.18 and 3.19 show 300 x 200 pixel closeups of the edge regions of an additional zenith and mid-declination camera, before and after the Robotilter solution. These are the same cameras shown in Figure 3.13. The Robotilter correction again shows improvement in quality consistency across regions.

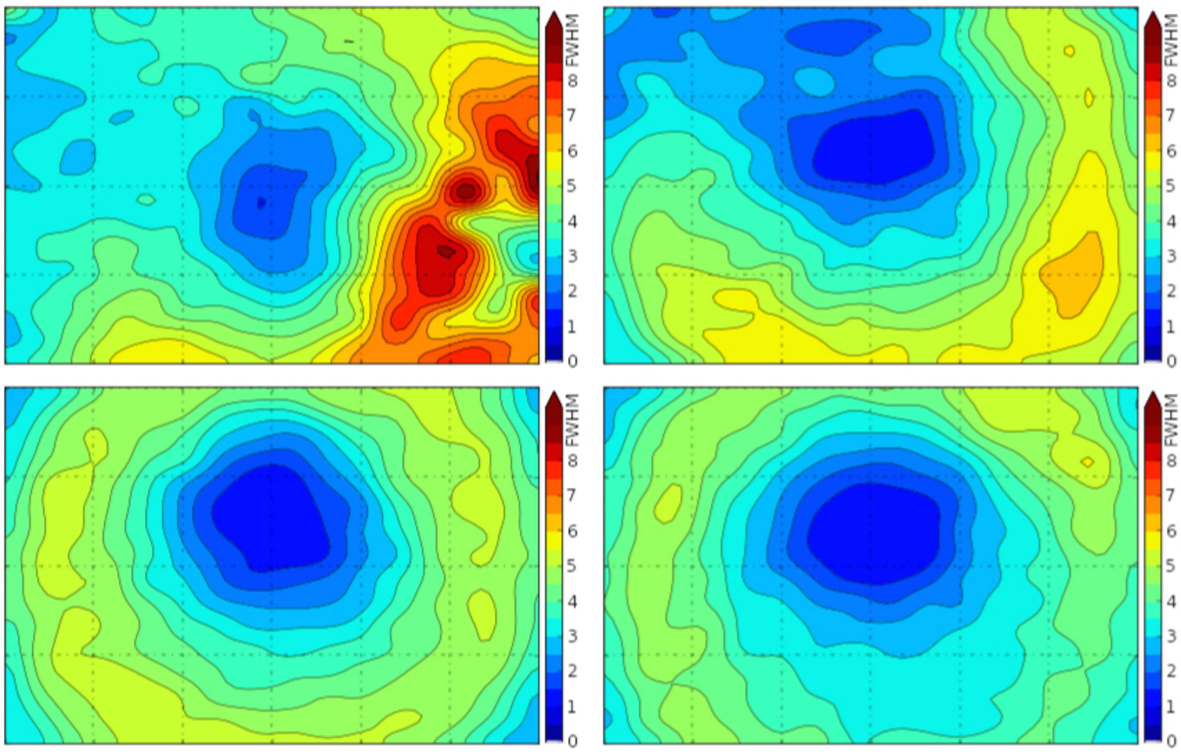

Figure 3.15: *Top Left:* Initial Deployment (pre-Robotilter) South Celestial Pole facing camera (polar camera) FWHM PSF plot. *Top Right:* Same camera post Robotilter deployment, but before running software correction sequence. *Lower Left:* Same camera post Robotilter correction showing the wide-scale tilt removal. *Lower Right:* Same camera after the focus optimization showing the flatter field.

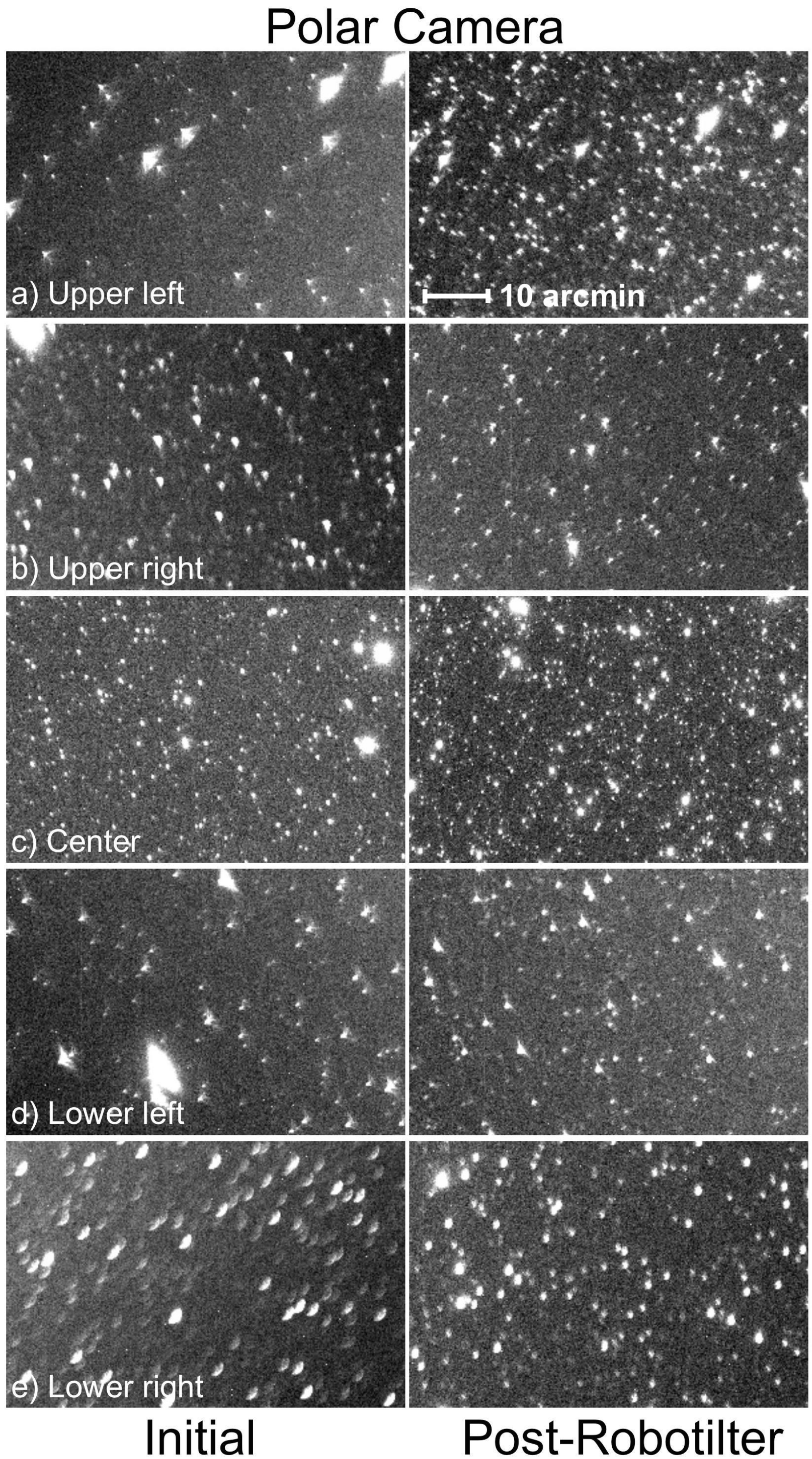

Figure 3.16: *Left:* Initial Deployment (pre-Robotilter) polar camera PSF closeup of the problematic corners. *Right:* Same camera post Robotilter correction showing improvement in size, shape, and focus.

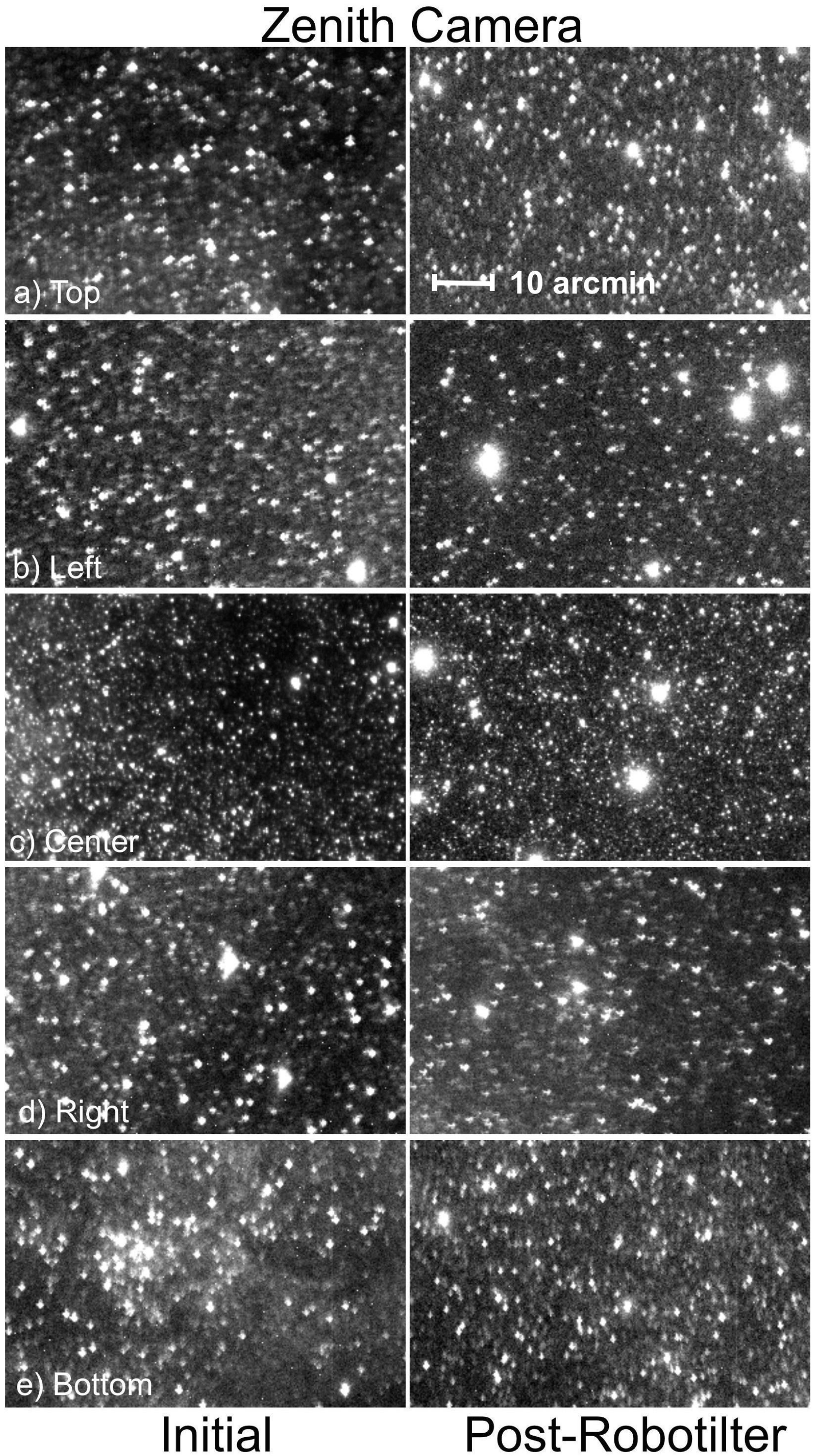

Figure 3.17: *Left:* Initial Deployment (pre-Robotilter) zenith camera PSF closeup of the problematic edges. *Right:* Same camera post Robotilter correction showing improvement in quality consistency across regions.

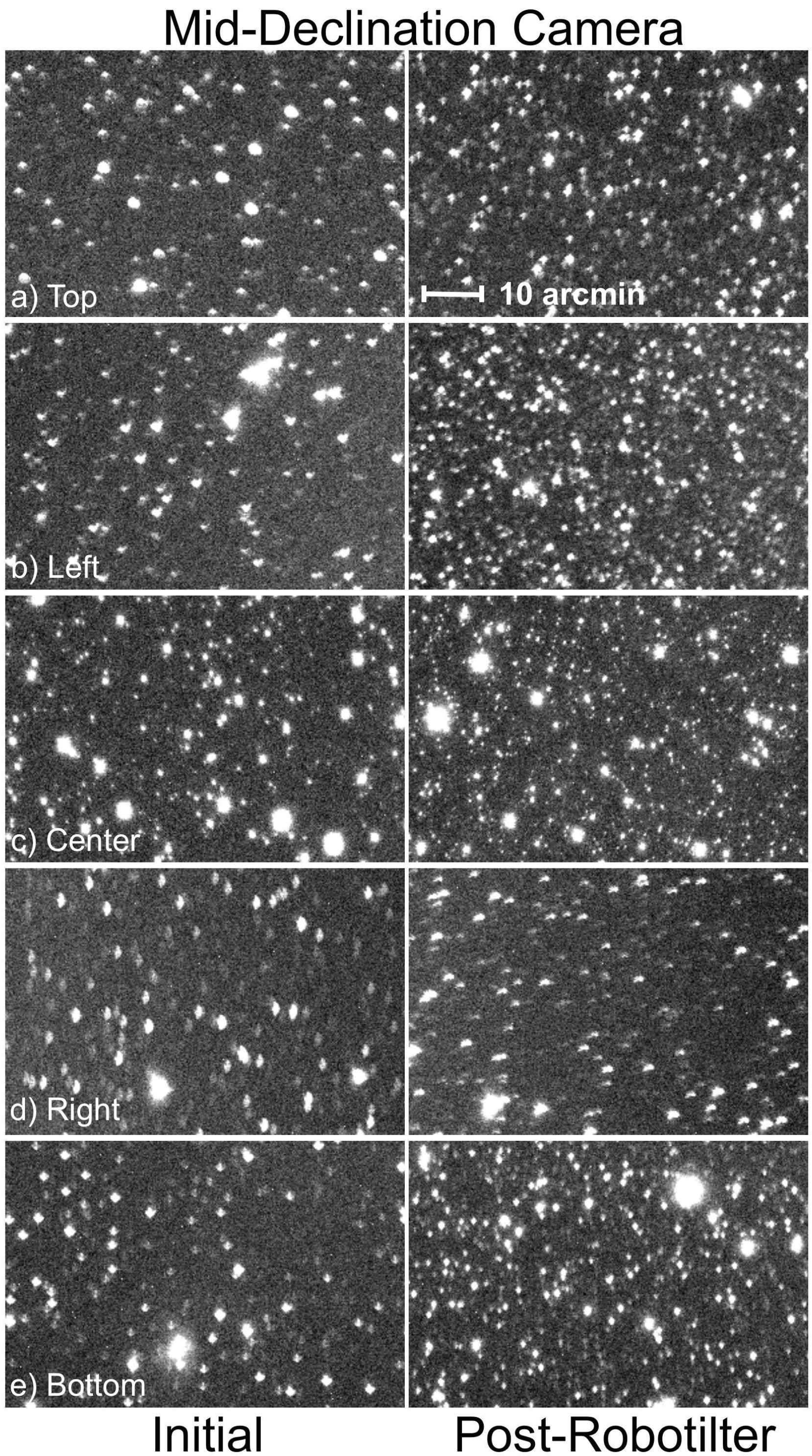

Figure 3.18: *Left:* Initial Deployment (pre-Robotilter) mid-declination camera PSF closeup of the edges. *Right:* Same camera post Robotilter correction showing improvement in quality consistency across regions.

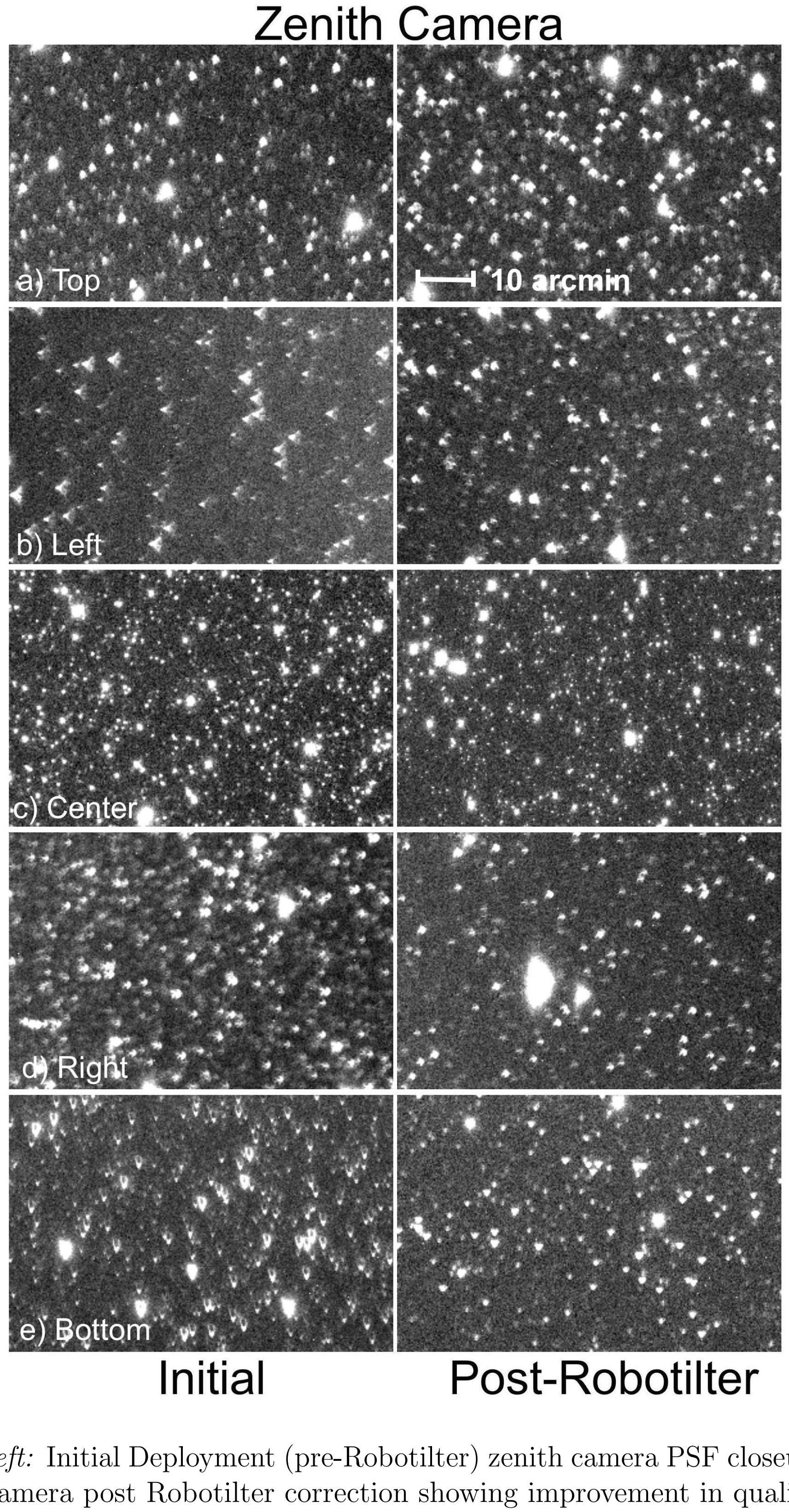

Figure 3.19: *Left:* Initial Deployment (pre-Robotilter) zenith camera PSF closeup of the edges. *Right:* Same camera post Robotilter correction showing improvement in quality consistency across regions.

3.5.3 EFFECTS OF CAMERA ALIGNMENT ON EVRYSCOPE DATA

We compared the limiting magnitude and average PSFs of images before and after the Robotilter corrections to determine the effects of the improved image quality due to the tilt removal and focus optimization. We selected cameras spread in declination (the same cameras used in § 3.5.2) and analyzed images from nights with similar dark sky, moonless, cloudless conditions. The pre-Robotilter images were collected on nights in July and September of 2015. The post-Robotilter images were taken from nights in April and July 2017. Cutouts of small regions from select images are shown in § 3.5.1.

We first solve the astrometry of the images using our reduction pipeline, with APASS-DR9 [79] as our source catalog. We measure the zero point of each region in the image, and perform aperture photometry on each image to measure SNR of each source. We calculate the limiting magnitude reached by the system in dark sky conditions based on the g-band magnitude measured by APASS. The average PSF shape per region is determined using an image subtraction approach.

PSF performance of a representative pre and post-Robotilter camera is shown in Figure 3.20. The PSFs from images in the corrected cameras are less distorted, especially in the corners and edges, and are smaller and more consistent across each image. The limiting magnitude improves by $\approx .5$ magnitude in the center of the field and ≈ 1 magnitude in the corners. This is camera and condition dependent; we show a representative camera in dark sky conditions in Figure 3.21. The SNR for most sources is higher (using the same photometric aperture captures a higher signal or capturing the same signal is possible with a smaller photometric aperture), and the burden on the astrometry solution is lessened by the more round PSFs (facilitating the centroiding step).

The improved PSFs from the post Robotilter images also improves the photometric performance of the light curve pipeline; however, we did not collect sufficient pre-robotilter data to make a quantitative comparison. Additionally, other non-constant factors such as

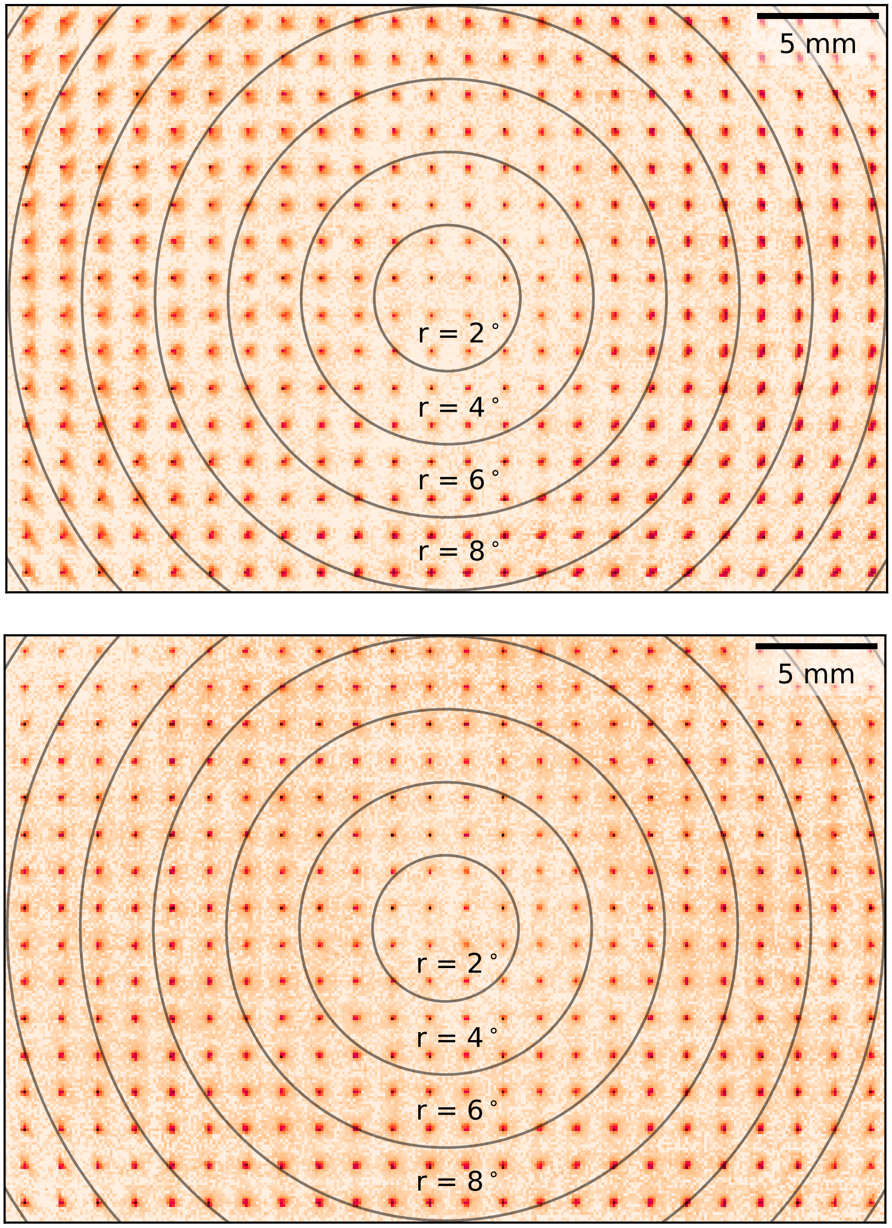

Figure 3.20: A grid of the average PSF shape shown by region for the full field of a representative Evryscope camera. *Top:* The pre-Robotilter PSF performance. *Bottom:* The same camera post-Robotilter demonstrating the improved PSF consistency across the field due to the tilt removal and focus optimization. The PSF distortions are reduced, are consistent, and are symmetric about the center of the image. Compared to the pre-Robotilter image, the post-Robotilter image has an improved limiting magnitude especially on regions away from the image center. The SNR for most sources is higher (using the same photometric aperture captures a higher signal or capturing the same signal is possible with a smaller photometric aperture), and the burden on the astrometry solution is lessened by the more round PSFs (facilitating the centroiding step).

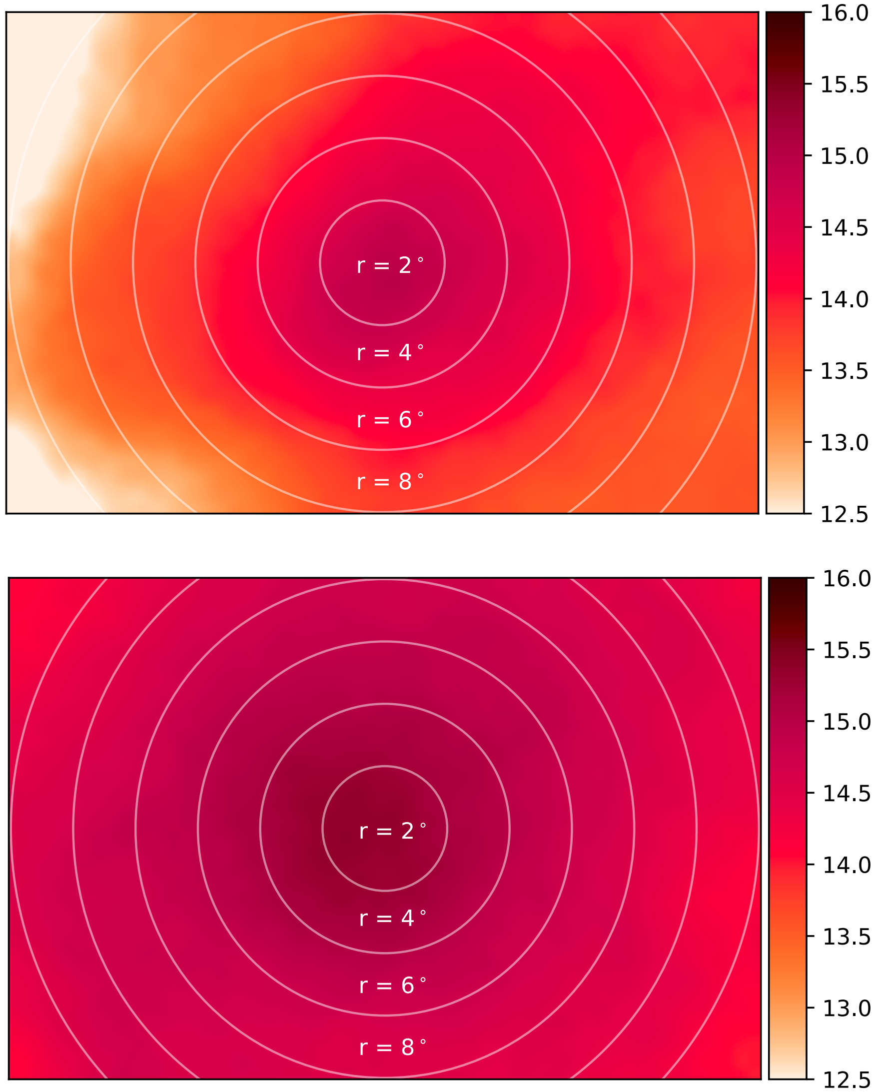

Figure 3.21: Limiting magnitude (based on APASS-DR9 g-band) of a representative Evryscope camera. *Top:* Pre-Robotilter. *Bottom:* Post-Robotilter showing an improvement across the image of .5 - 1 magnitude depending on the region and the amount of initial tilt.

improved telescope tracking and periodic cleaning of the optics effect light curve precision and are difficult to separate.

3.6 DISCUSSION

3.6.1 Robotilter Design Improvements

We deployed the Evryscope North (an updated version of the CTIO Evryscope) to Mount Laguna Observatory, California in November of 2018. The Robotilters installed on the Evryscope North feature several improvements. Limit switches are mounted on the lens base-plate to locate the home position in case the servos are moved out of range. A separate Raspberry-Pi single board computer controls the camera and Robotilter for each unit, allowing more than two Robotilters to be run simultaneously and reducing the number of cables and hubs. The servo piers are locked to the filterwheel top in a more robust way that locates the servo axes more precisely. The Rokinon lenses and FLI CCD cameras used on the Evryscope North are 4 years newer than those used on the CTIO system and feature mild improvements in optics and chip sensitivity. Initial image quality results from the Evryscope North point to mild improvements in image flatness and PSF quality.

3.6.2 Lessons Learned

Several lingering challenges slowed our progress over the course of the Robotilter project. The primary issues were related to assembly, servo control, and software.

The Robotilters must precisely locate and hold the 4 servos and all of the components into a small space on top of the filter wheel. This results in a considerable amount of hardware and small pieces, and the assembly is not trivial. The spring tension, shaft couplers, and the threaded shafts were the most challenging to assemble. Cycling each Robotilter assembly in the lab, for several hours over a range of servo positions, helped prevent on-sky issues. This procedure also helped identify misaligned shaft couplers or over-torqued springs. The threaded shafts needed liberal amounts of Goop lubricant to work smoothly with the brass inserts in the base-plate. Multiple cycling helped to mate the interacting surfaces, and to identify any defects that might have caused issues later. Tightening the fasteners at critical mounting points could twist the assembly resulting in the lens center not being concentric with the CCD. We made the locking slots on the servo piers more robust on the northern system which helped resist twisting. Some cameras in the CTIO system suffered from the various challenges described here, requiring on site troubleshooting. We were able to mitigate these issues in the Northern system with the minor assembly and testing corrections learned from the CTIO Evryscope.

The servos are controllable to within $\approx$200 steps when commanded to move. The accuracy also depends on how far the servo is commanded to move and on the individual servo. This was less than ideal for the Robotilter tilt correction step, and we added a software correction to compensate for the mechanical backlash causing this servo accuracy challenge. We rely on multiple servo movements to solve this issue. In the first movement, we command the servos to move past the intended target and in a second movement to go past the target in the other direction but by a smaller amount. We then repeat this process but for a much narrower overshoot before commanding to the final position. In this way, we are able to move the servos to within 15-20 servo steps on average.

The Robotilter servos move 4096 steps per turn, and use an offset to count multiple turns. For example, one-half turn is counted as a position of 2048, and one and one-half turns is a position of 2048 plus an offset of 1. An issue that arises (and is common with servos) is in the event of a power loss the position is retained but not the offset. We addressed this issue by resetting the servo offsets to zero once the alignment was completed, so that the servo values are always within one turn, and by recording the servo positions each night.

It is possible for servos to become stuck if they are moved very far away from the home position by mistake, or if one servo is moved relative to the others that puts an extreme angle on the lens base-plate. We set the maximum servo torque low so that in the event one becomes stuck, we can manually increase the torque and move it the opposite direction to release. For the Northern system, we added independent locator switches to identify the home position and help avoid errant movements.

We underestimated the software challenge of the Robotilters, which resulted in telescope time being used for Robotilter software development. This turned out not to be a significant problem, and it was not completely avoidable. In retrospect, we might have used the pre-deployment Evryscope test camera more in the Robotilter software development. Most likely, this would have required a dedicated robotic telescope using the single Evryscope test camera. This approach would have required extra resources, and if it would have provided a benefit greater than the cost is debatable. We elected instead to deploy the Robotilters once ready, use a few select cameras to test and refine the Robotilter software, and observe with all the other cameras during that time. Once the software was completed, we aligned all the cameras and have observed continuously since then.

3.6.3 As an Optics Quality Measurement

A by-product of the Robotilter solution is the precise and finely sampled 3-D focal plane, as demonstrated in Figures 3.11 and 3.13. The quality of the optics is clearly captured, including the flatness of the field, the image profile, regional structure, and differences between cameras. The Robotilters can be used to identify optics that will likely perform well, as well as those that could be troublesome. As an extreme example, Figure 3.22 shows a problematic lens with an odd sheer feature visible in the measured 3-D focal plane. We replaced this lens on a maintenance trip and the camera showed an improvement in image quality. We suspect one of the lens elements was damaged, possibly with a hairline crack, in transport.

3.6.4 Applications for Other Instruments

The Robotilters were designed for the Evryscope; we did not test them or simulate their potential on any other instrument. However, the Robotilter solution described in this work

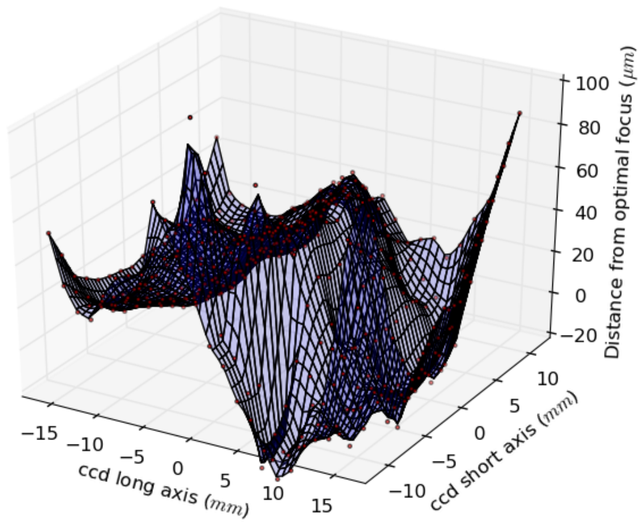

Figure 3.22: Using the Robotilters to measure optics quality; shown is a problematic lens with an odd sheer feature visible in the measured 3-D focal plane. We replaced this lens on a maintenance trip and the camera showed an improvement in image quality. We suspect one of the lens elements was damaged (hairline crack) in transport.

certainly could be adapted for use on wide field surveys using lenses or small telescopes. The basic mechanical design should scale to a variety of lens sizes and types; most likely with only simple modifications to the servo spacing, placement, and component sizes. The software solution approach using a focus sweep, image grid, and tilt driven quality metric with on-sky images should also be effective for instruments with different FOVs and pixel scales; with appropriate adjustments to the number of images, step and grid sizes, and quality metric components. It is also reasonable to consider using the Robotilter solution on larger instruments, but move the CCD instead of the optics.

3.7 SUMMARY

The Robotilter lens / CCD automated alignment upgrade was installed on the Evryscope at the end of 2015. The Robotilter hardware has performed reliably and consistently, and has demonstrated the ability to hold tilt position over several years. We developed the software necessary to align the cameras, which is specialized to remove tilt, minimize PSF distortions, optimize the focal plane, and balance focusing within the full image field. The Robotilters are completely automated, use on-sky images, remove image tilt to the sub 10 μm level, in less than 2 hours. The tilt removal and focus optimization solutions work independent of camera or field. The Robotilter solution resulted in measurable improvements in image quality, SNR, limiting magnitude, and astrometric solutions. The average PSF extent was reduced by a factor of 2 on the edges and corners for the images, and the limiting magnitude was improved by .5 to 1 magnitude for most cameras. In this work we described in detail the challenges, development and design, software strategy, and lessons learned.

This research was supported by the NSF CAREER grant AST-1555175, NSF/ATI grant AST-1407589, and the Research Corporation Scialog grants 23782 and 23822. HC is supported by the NSF GRF grant DGE-1144081. OF and DdS acknowledge support by the Spanish Ministerio de Economía y Competitividad (MINECO/FEDER, UE) under grants AYA2013-47447-C3-1-P, AYA2016-76012-C3-1-P, MDM-2014-0369 of ICCUB (Unidad de Excelencia 'María de Maeztu').

Special thanks to David Norris, Cliff Tysor, and Philip Thomson from the UNC machine shop for their careful work and advice.

CHAPTER 4: VARIABLES IN THE SOUTHERN POLAR REGION EVRYSCOPE 2016 DATASET

This section presents results published in the *Publications of the Astronomical Society of the Pacific.*[1,2]

4.1 INTRODUCTION

The regions around the celestial poles offer the ability to find and characterize long-term variables from ground-based observatories. We used multi-year Evryscope data to search for high-amplitude ($\approx 5\%$ or greater) variable objects among 160,000 bright stars (mv < 14.5) near the South Celestial Pole. We developed a machine learning based spectral classifier to identify eclipse and transit candidates with M-dwarf or K-dwarf host stars - and potential low-mass secondary stars or gas giant planets. The large amplitude transit signals from low-mass companions of smaller dwarf host stars lessens the photometric precision and systematics removal requirements necessary for detection, and increases the discoveries from long-term observations with modest light curve precision among the faintest stars in the survey. The Evryscope is a robotic telescope array that observes the Southern sky continuously at 2-minute cadence, searching for stellar variability, transients, transits around exotic stars and other

[1]Ratzloff JK, Corbett HT, Law NM, Barlow BN, Glaizer A, Howard W, Fors O, Del Ser D, and Trifonov T. Variables in the Southern Polar region Evryscope 2016 dataset. *Publications of the Astronomical Society of the Pacific* 2019; 131:084201. DOI: 10.1088/1538-3873/ab1d77.

[2]I wrote almost all of this paper, with detailed suggestions from Law and Barlow to improve the final version. I did all of the preparation for the survey including the target list, survey scope, light curve query, and detection tools. I generated and reviewed the inspection panels, and identified candidates, and I also fitted the signals to measure the variations precisely. Corbett and Barlow reviewed and confirmed the candidates and verified with the results. I took the PROMPT and SOAR followup measurements and wrote the code to analyze the light curves, spectra, and final results of the survey. The CHIRON data was taken by Barlow, and he was a great help in advising the development of our RV code. I created the Evryscope classifier, wrote the code, gathered the data for the training set (with help from Howard and Glaizer), refined the design and applied it to our discoveries.

observationally challenging astrophysical variables. The multi-year photometric stability is better than 1% for bright stars in uncrowded regions, with a 3-sigma limiting magnitude of g=16 in dark time. In this study, covering all stars 9 < mv < 14.5, in declinations -75 to -90, and searching for high-amplitude variability, we recover 346 known variables and discover 303 new variables, including 168 eclipsing binaries. We characterize the discoveries and provide the amplitudes, periods, and variability type. A 1.7 RJ planet candidate with a late K-dwarf primary was found and the transit signal was verified with the PROMPT telescope network. Further followup revealed this object to be a likely grazing eclipsing binary system with nearly identical primary and secondary K5 stars. Radial velocity measurements from the Goodman Spectrograph on the 4.1 meter SOAR telescope of the likely-lowest-mass targets reveal that six of the eclipsing binary discoveries are low-mass (.06 - .37 $M_{\odot}$) secondaries with K-dwarf primaries, strong candidates for precision mass-radius measurements.

Variable star discoveries provide information on stellar properties, formation, and evolution, and are critical for determining distances and ages of astronomical objects. Eclipsing binaries allow the measurement of masses, radii, and temperatures, and can be used to test stellar formation theory predictions. Lower mass eclipsing binaries are observationally challenging due to the low intrinsic brightness of the star, and more systems are needed to properly characterize the mass/radius relationship in stellar models [25–27]. Ground-based surveys such as the Palomar Transient Factory [1], ATLAS [64], HAT [6], HAT-South [90], SuperWASP [8], KELT [9], CSTAR [91], and many others are very successful in detecting variables (including transiting exoplanets) and adding to known variable star catalogs such as the Variable Star Index[3] (VSX). These surveys either observe at day or longer time-scale cadences, or observe dedicated sky areas to reach fast cadence at the expense of all sky coverage. In contrast, the Evryscope is optimized for shorter-timescale observations with continuous all sky coverage and a multi-year period observation strategy. The continuous, fast-cadence, all-sky Evryscope light curves are sensitive to variations (including transits and

[3]http://www.aavso.org/vsx/

eclipses) lasting only a few minutes, and provide fine sampling for ten minute level variations or longer.

The Evryscope is a robotic camera array mounted into a 6 ft-diameter hemisphere which tracks the sky [17]. The telescope is located at CTIO in Chile and observes continuously, covering 8150 sq. deg. in each 120s exposure. The Evryscope was deployed with 22 cameras and can accommodate 27 total cameras (with a corresponding increased field of view of 10,000 sq. deg). Each camera features a 29MPix CCD providing a plate scale of 13"/pixel. The Evryscope monitors the entire accessible Southern sky at 2-minute cadence, and the Evryscope database includes tens of thousands of epochs on 16 million sources. In this paper, we limited the search field to the region around the South Celestial Pole, and chose the brighter stars in order to maximize the number of epochs per source and minimize systematics.

The Southern Polar sky area is less explored than other parts of the sky, primarily due to the difficulty in reaching it. This is evidenced by the comparatively low number of planet, eclipsing binary, and variable star discoveries in this region. For example, the sky area in the declination region of -75 to -90 comprises 3.4% of the southern sky's total area; however the VSX catalog of known variables in the same region accounts for only 1.2% of the southern sky total. Surveys of the Southern Polar sky region typically either use a telescope located at a low latitude South American site or an instrument in the Antarctic. The former choice can be challenging depending on the airmass of the target region, while the second poses engineering difficulties due to the harsh environment [91, 92].

We use the Evryscope to explore the Southern Polar region (declinations -75 to -90). While the airmass is non-optimal (~ 1.7 average), the Evryscope monitors the Southern Polar region continuously every night for the entire night at 2 minute cadence, with the same camera for multiple years. This long-term, same-camera coverage at short cadence results in many continuous data points with consistent airmass, and minimizes systematics. Targets in this region average over 60,000 epochs per year. Our observing strategy results in several hundred thousand light curves with targets ranging in brightness from $9 < mv < 15$. The light curves have the precision necessary to potentially detect eclipsing binaries, variable stars, transiting gas-giant planets around small-cool host stars, and short-transit-time planets around small compact stellar remnants including white dwarfs and hot subdwarfs. With additional filtering, the light curves are precise enough to potentially detect gas-giant planets around bright solar type stars; we will address this in future work. These Evryscope light curves also facilitate searches with wide period ranges (for the Polar Search we searched from 3-720 hours), longer periods, and wide amplitude ranges. Long-period discoveries are typically non-interacting stars and are challenging to detect due to the low number of transits.

The primary target of this paper's search is eclipsing binaries, particularly low-mass and long-period systems. The secondary target of this paper's search is gas-giant planets around M-dwarf or late K-dwarf primaries. This survey relies on detection power to narrow the candidates and uses observations from mid 2016 to early 2017. The more challenging transiting exoplanet detections will be conducted with additional systematics removal steps, additional candidate filtering to push to lower power detections, and will use the full three plus year data set (Ratzloff et al., in prep).

Eclipsing binaries are the best calibrators for determining relations between mass, radius, luminosity, and temperature. Relatively few low-mass (M-dwarf or late-K-dwarf secondary) eclipsing binaries have been discovered [93–95], and many are too faint for easy radial-velocity followup measurements. This has limited our ability to measure the mass/radius relation at low masses, where many low-mass systems suggest larger radii than stellar models predict [25–27]. This is particularly important for the determination of transiting planet radii around low-mass single stars, where some of the most exciting nearby planets are likely to be discovered [16, 96, 97].

In this paper, we report the discovery of 303 new variables including seven eclipsing binaries with low-mass secondary stars. We perform spectroscopic followup on select eclipsing binaries to confirm the stellar type and secondary size. Radial velocity measurements reveal that seven of the eclipsing binary discoveries are low-mass (.06 - .34 $M_\odot$) secondaries with K-dwarf primaries.

In § 4.2 we describe the Evryscope photometric observations that led to the discoveries as well as our analysis of the light curves and detection algorithms for identifying variables. In § 4.3 we describe the followup observations performed for the low-mass eclipsing binaries including PROMPT [36] followup photometry, identification spectra and radial velocity followup using the Goodman [33] spectrograph on the 4.1 meter SOAR telescope and the CHIRON [38] echelle spectrometer on the CTIO/SMARTS 1.5 meter telescope. In § 4.4 we present and characterize our discoveries. We also detail our analysis of the radial velocity followup work including the Monte-Carlo simulation to fit the masses, radii, and other parameters. We conclude in § 4.5.

4.2 OBSERVATIONS AND VARIABILITY SEARCH

4.2.1 Evryscope Photometry

All eclipsing binary and variable discoveries were detected in a transit search of the polar region (declinations -75 to -90). The observations were taken from August 9, 2016 to April 4, 2017. The exposure time was 120s through a Sloan-g filter and each source typically had 16,000 epochs. We briefly describe the calibration and reduction of images and the construction of light curves; further details will be presented in an upcoming Evryscope instrumentation paper. Raw images are filtered with a quality check, calibrated with masterflats and masterdarks, and have large-scale backgrounds removed using the custom Evryscope pipeline. Forced photometry is performed using APASS-DR9 [79] as our master reference catalog. Aperture photometry is performed on all sources using multiple aperture sizes; the final aperture for each source is chosen to minimize light curve scatter. The primary systematics challenges are: background and airmass changes and the subsequent effects on stars of different magnitude and color, the ratchet observing cycle causing the targets to switch cameras and appear in different positions on the CCD chips over the observing season, daily aliases, source blending, PSF distortions, and vignetting. We use the quality filter, calibrations, aperture photometry, along with a custom implementation of the SysRem [77] algorithm to remove the systematics challenges described above.

4.2.2 Detection of Variables

Filtering by declination and magnitude returns 239,991 initial targets from the Evryscope light curve database. 76,407 are eliminated by an additional quality filter based on non-blended sources. The remaining 163,584 are analyzed using Box Least Squares (BLS) [28, 29] with the pre-filtering, daily-alias masking, and settings described in § 4.2.4. The light curves are then sorted by BLS detection power, in terms of Signal Detection Efficiency (SDE) [28]. Figure 4.1 shows the BLS SDE distribution for the targets along with the distribution of detected periods. Targets with an SDE > 10 and with nearby reference stars gives 9104 suspects for further inspection. The 10-SED cutoff is chosen to: 1) limit the number of targets to an amount that is reasonable for human followup (in this case $\sim$ 10,000), 2) ensure a reasonable chance of detecting high-amplitude candidates without accumulating excessive false-positives, and 3) reach three percent level signal depths on bright stars to potentially detect low-mass secondaries and gas-giant planets around M-dwarfs or late K-dwarfs.

We compare the target light curve (both unfolded and folded to the best BLS period) to two nearby reference stars of similar magnitude looking for any signs that the detected variation is present in the references indicating systematics (see § 4.2.5). The folded plots are colored by time to check how well-mixed the detection is, since a transit or eclipse with only a single or few occurrences is more likely to be an artifact of the detection algorithm. The light curves are also folded on the second and third best BLS periods to check for aliases, as well as the best Lomb-Scargle (LS) [30, 31] period to check for sinusoidal variability. From visual inspection, we identify 649 variables from the machine filtered 9104 suspects. 346 are known variables and 303 are new discoveries.

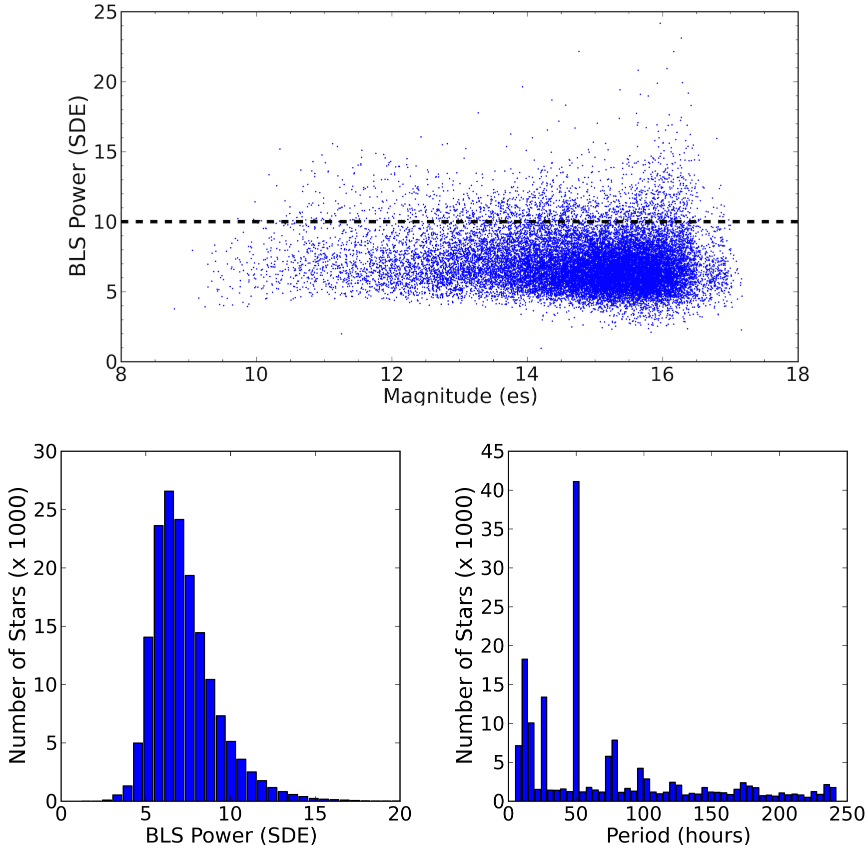

Figure 4.1: Detection characteristics from the BLS results of the polar search. The top panel shows the BLS power in SDE vs. magnitude (15% of the points are shown for better visualization), the lower left panel is the histogram of BLS power in SDE, the lower right is the histogram of periods found. Targets with an SDE > 10 are selected for further inspection.

4.2.3 Machine-Learning Stellar Classification

We developed a machine-learning based classifier that uses publicly available catalog data to estimate stellar size from a B-V color/magnitude space, and to estimate spectral type from multiple color-differences. The discovery candidates were matched to APASS-DR9 [79] and PPMXL [78] catalogs to obtain reduced proper motion (RPM) and color differences (B-V, V-K, J-H, H-K) for each target. Modifying the method in [98] with a two step machine learning process described below, we classify stars based on B-V and RPM to identify stellar size - main sequence, giants, white dwarfs, or sub dwarfs. The RPM and B-V combination provides a high return on our target catalog (99% of our targets are classified as demonstrated below) and captures spectral information using available data. After the stellar size estimation is completed, the four color differences are used to approximate the spectral type.

In the first step of the machine learning process, we use a support vector machine (SVM) from the SKYLEARN python module [99] to identify likely hot subdwarfs (HSD) from all other stars. The HSD are challenging to separate since they can be close to main sequence O/A stars in this parameter space. We find the SVM to be an effective way to segregate the HSD, shown in the top panel of Figure 4.2 as the small confined area enclosed in the black border. This is done by using a training set of HSD from [82] and other types of stars from SIMBAD [100], filtering the outliers, then computing the contour boundaries. The SVM method is a non-probabilistic two-class classifier that computes a hard boundary (decision boundary) by minimizing the distance (or margin) between the points closest to the boundary. As with any classifier there are missed targets and contaminants, and there are physical reasons the results can be skewed (reddening for example). Our goal in this step is to separate the most challenging class (the HSD) from all the other classes while providing a boundary with a reasonable contingency space to the nearby white dwarf and main sequence regions.

Once the HSD are identified, all remaining objects are classified using a Gaussian Mixture Model (GMM) [99] with three classes to identify white dwarfs, main sequence, and giants. We again use an outlier filtered training set of stars of each type from SIMBAD (20,972 main sequence, 1515 white dwarfs (WD), and 10,000 giants). The GMM classifier results are shown in the bottom panel of Figure 4.2. The GMM method is a best fit to 2-D Gaussian function (probability density function), using the training points to adjust the Gaussian centers, orientations, and elongations. Our application of this method uses three dimensions (WD, main sequence, and giants). Although more dimensions are possible, overlapping or poorly separated classes tend to give poor results (part of the motivation of using the SVM for the HSD step). The GMM produces contour lines with Negative-log-likelihood (NLL) values that can be converted ($LH = 10^{-NLL}$) to give an estimate of the confidence level the data point belongs in the class.

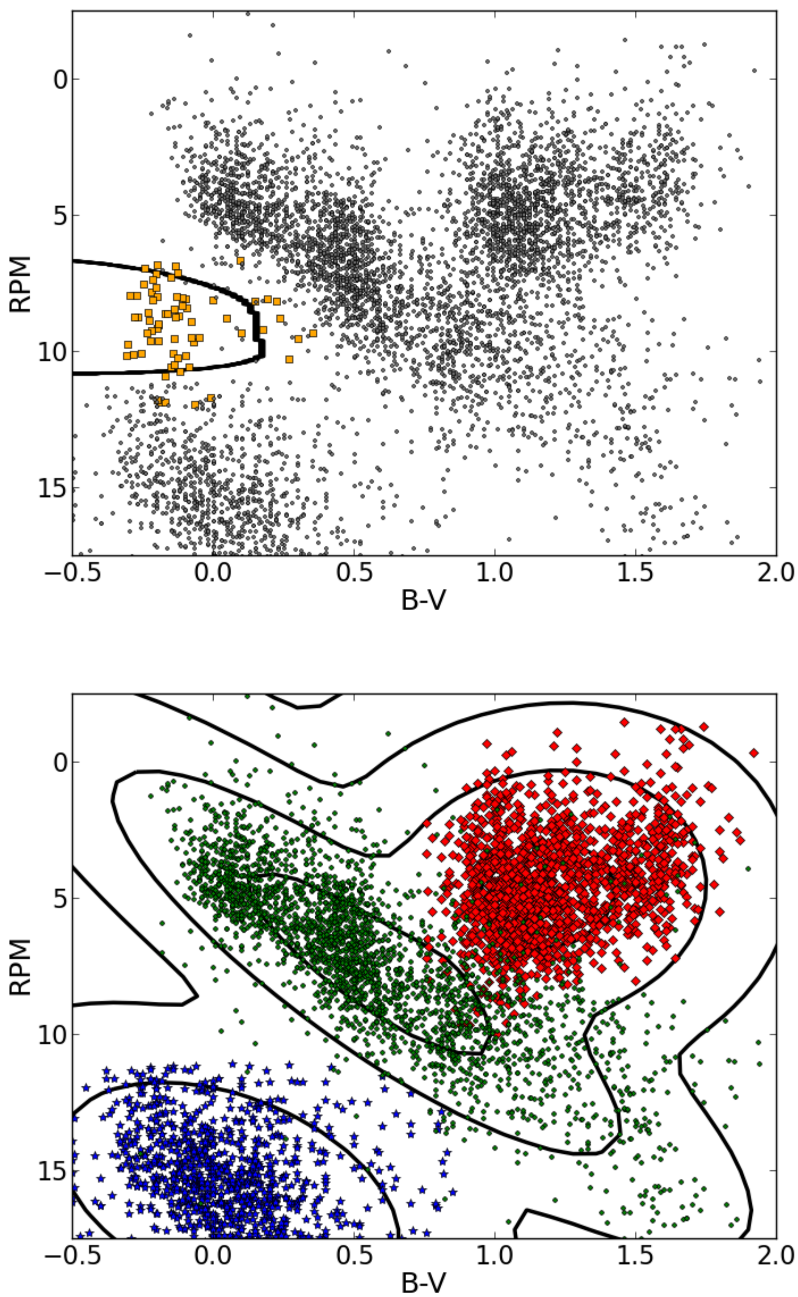

Figure 4.2: The Evryscope Target Classification - We use B-V color differences and reduced proper motion (RPM) data with a two step machine learning algorithm to classify star size. Top: the training data (gold squares=hot subdwarfs, grey=all others) for the support vector machine (SVM) which returns the resulting hot subdwarf classification region (the area inside the black border). Bottom: the training data (blue stars=white dwarfs, green=main sequence, red diamonds=giants) for the Gaussian Mixture Model (GMM) which returns the resulting classification contours. Negative log likelihood plot-lines 1, 1.7, 2.8 are shown.

We use the spectral type and temperature profiles in [101] to derive a function (using 1-D interpolation) that uses available color differences to derive an estimate for spectral type (Figure 4.3). If only B-V is available, we classify simply by the letter (O,B,A,F,G,K,M); if multiple colors are available we average the fits and choose the closest spectral type (G9, K4, M3 for example). For main sequence stars we add the luminosity class V. The code produces a function with RPM and color differences inputs and outputs the star size, star type, and NLL score for the GMM step. We used this to classify all of our discoveries, with the added requirement that the HSD also be apparent spectral type O or B and that the WD have a NLL score of less than 4.0. The added requirements help filter contaminants from main sequence A stars for the HSD, and borderline WD stars. Candidates identified as likely K or M-dwarfs with shallow (typically less than 10%) eclipses or transits are identified as potentially high value targets and analyzed in more detail.

The Evryscope classifier is designed to: 1) facilitate identification of as many of the target light curves as practical, 2) identify targets to be included in Evryscope transit searches (white dwarfs, hot subdwarfs, K and M-dwarfs), and 3) classify variability discoveries helping to identify those as potentially interesting for further followup. For the Polar Search, 98.5% of our targets have B-V and RPM data available, and 91.0% have all four color differences and RPM data. Tests using 485,000 targets spread across the entire southern sky (all RA and declinations +10 to -90) have demonstrated very high returns - 99% of Evryscope targets have all four color differences and RPM data available for classification. Once the catalogs were compiled and matched, the classifier took only a few minutes to classify the 485,000 test targets, making it practical for use on the full Evryscope database. All discoveries in this work are classified using the APASS-DR9 [79] and PPMXL [78] catalogs as described above. A similar approach using the GAIA-DR2 [102] catalog will be used as an additional target filter for the transiting exoplanet searches (Ratzloff et al., in prep).

We tested the Evryscope classifier in several ways. We chose known WD from APASS [103] and high confidence (>.80) WD suspects from ATLAS [104] and SDSS [105] with mv

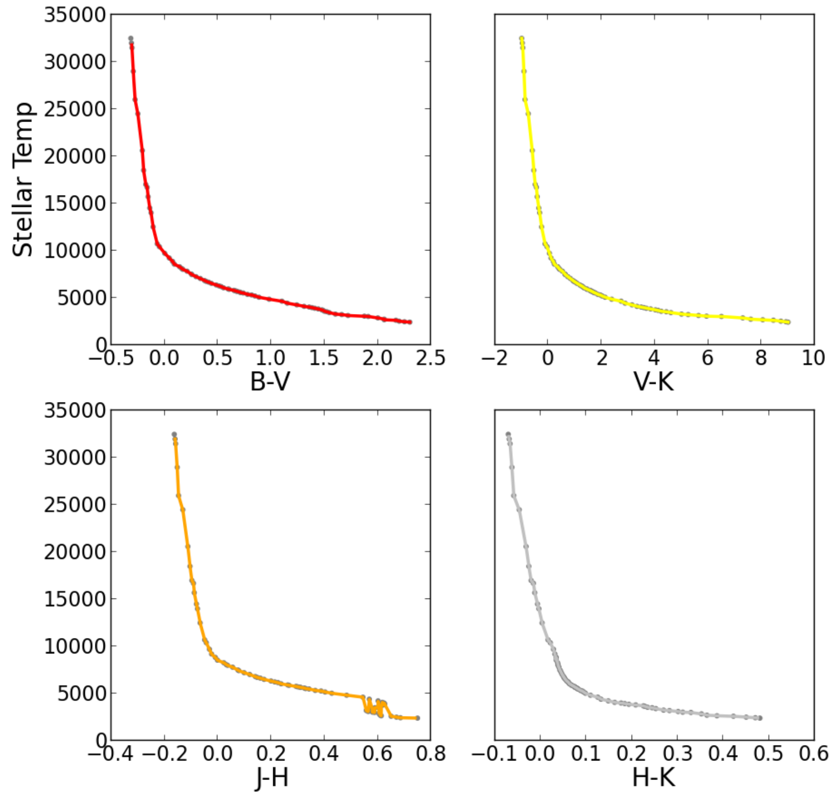

Figure 4.3: The Evryscope Target Classification - We use (B-V, V-K, J-H, H-K) color differences to estimate temperature and spectral type using the data in [101] to interpolate profiles for each color difference. The data are the grey points and the interpolations are the colored lines in the figures. We average the four results and pick the closest spectral type.

< 16.5, for a total of 211 classifier test targets. Using [82] with mv < 15.0, we obtain 1560 HSD classifier test subjects (which may include WD due to the difficulty in separating the two groups). We use [106] to obtain 3764 high-confidence M-dwarfs. Using [107] and filtering out the bright stars we have 999 main sequence, 452 giants, and 895 K-dwarfs for classifier testing.

Table 4.1 shows the performance of the classifier to correctly determine star size (ms/-giant/WD/HSD). Table 4.2 shows the performance of the classifier to correctly determine letter spectral type (O,B,A,F,G,K,M). Table 4.3 shows the performance of the classifier to correctly determine full spectral type (O0 - M9). Shown is the mean difference and variance

Table 4.1: Evryscope Classifier star size (ms/giant/WD/HSD) performance.

Test group	Star size	ES Classifier % correct
M-dwarfs	ms	95.3%
K-dwarfs	ms	86.2%
M-giants	giant	98.7%
Main Sequence	ms	94.1%
HSD	HSD	54.5 (77.7 w/WD)%
WD	WD	87.0%

Table 4.2: Evryscope Classifier letter spectral type (O,B,A,F,G,K,M) performance.

Test group	letter spectral type	ES Classifier % correct
M-dwarfs	M	95.2%
K-dwarfs	K	81.1%
M-giants	M	97.9%
Main Sequence	O-M	69.5%
HSD	O,B	76.5%

in classifier performance numerical class versus the known class. The last column shows the percent of the test group that is classified correctly to within 3 of the known numerical class.

We also compared the classifier results to SOAR ID spectra taken for the low-mass eclipsing binaries (§ 4.4.7). 7 of the 8 were classified as the correct spectral type (K for example), and within +/- 1 numeric class (K5 or K6 for example) (Table 4.4).

4.2.4 Variability search algorithms

We selected sources in the polar region with mv < 14.5 and with light curves that passed quality tests to eliminate sources with blending, narrow time coverage, or low number of epochs (§ 4.2.2). Light curves (with MJD timestamps) were pre-filtered with a Gaussian

Table 4.3: Evryscope Classifier full spectral type (O0 - M9) performance.

		ES Classifier		
Test group	spectral type	mean	variance	% +/-3
M-dwarfs	M0-M9	-.50	1.9	95.3%
K-dwarfs	K0-K9	-.98	2.7	81.6%
M-giants	M0-M9	-2.0	1.7	78.0%
Main Sequence	O0-M9	-.87	3.7	63.1%

Table 4.4: Comparison of the Evryscope Classifier to SOAR ID spectra.

ID (EVR+)	SOAR ID Sptp	ES Classifier Sptp
J053513.22-774248.2	G7V	K1V
J06456.10-823501.0	G8V	G9V
J103938.18-872853.8	K7V	K6V
J110815.96-870153.8	K4V	K3V
J165050.23-843634.6	K5V	K4V
J180826.26-842418.0	G5V	G6V
J184114.02-843436.8	K2V	K3V
J211905.47-865829.3	K5V	K6V

smoother to remove variations on periods greater than 30 days, and a 3rd order polynomial fit was subtracted to remove long-term variations. Light curves were then searched for transit-like, eclipse-like, and stellar variability signals using the Box Least Squares (BLS) [28, 29] and Lomb-Scargle (LS) [30, 31] algorithms.

We tested the recovery rates on Evryscope light curves with different BLS settings - with periods ranging from 2-720 hours, 10,000-100,000 periods tested, and transit fractions from .001 to 0.5. Recovery rate tests were run on known eclipsing binaries in our magnitude range with different transit depths ranging from .01 to .25, and on simulated few-percent level transit signals injected onto Evryscope light curves representative of low-mass secondaries. The tests showed that a very wide BLS test period range (2-720 hours) led to decreased detections as the periodogram becomes biased to long periods or spikes in longer periods arise from data gaps. This challenge combined with the survey 6-month time coverage (§ 4.1), shows too aggressive of a period range can detect fewer eclipsing binary candidates. Based on these tests, the final BLS settings used on the Evryscope Polar Search were a period range 3-250 hours with 25,000 periods tested and a transit fraction of .01 to .25.

Period detections of 24-hours and corresponding aliases (4, 6, 8, 16, 36, 48, and 72 hours) were masked in +/- .1 hour widths. The results were sorted by BLS signal detection strength - BLS periodogram peak power in terms of sigmas above the mean power. Targets with peak power greater than 10-sigma were verified visually with a panel detection plot. We use the Lomb-Scargle (LS) algorithm to identify sinusoidal variables. For LS, we used a period range 3-720 hours to include sensitivity to longer period variables. We recover slightly lower amplitude variables (minimum discovery amplitude in this work = .008) than eclipsing binaries (minimum discovery depth in this work = .029) as shown in the Appendix.

Figure 4.4 shows the phase-folded Evryscope light curve for EVRJ110815.96-870153.8 a K4V primary and .21 $M_{\odot}$ secondary with a BLS detected period of 12.28 hours. Figure 4.5 shows the light curve for EVRJ032442.50-780853.9 a variable star with a LS detected period of 4.67 hours.

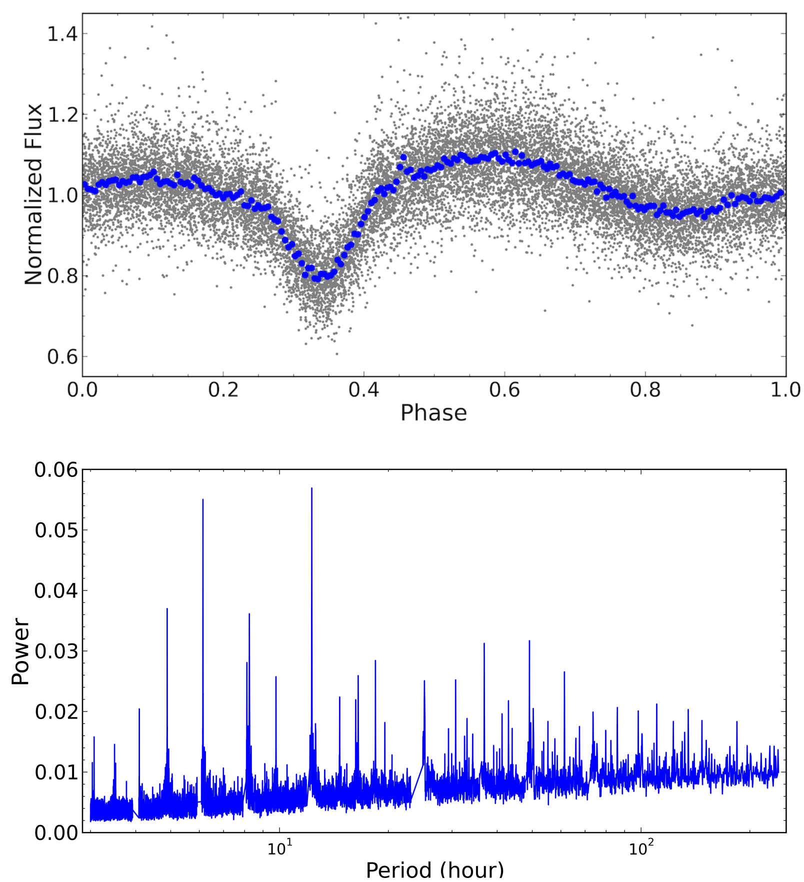

Figure 4.4: An example low mass eclipsing binary discovery (EVRJ110815.96-870153.8) from this survey. The Evryscope light curve phased on its period of 12.277 hours is shown on the top panel. Grey points = 2 minute cadence, blue points = binned in phase. The bottom panel shows the BLS power spectrum with the highest peak at the 12.277 hour detection.

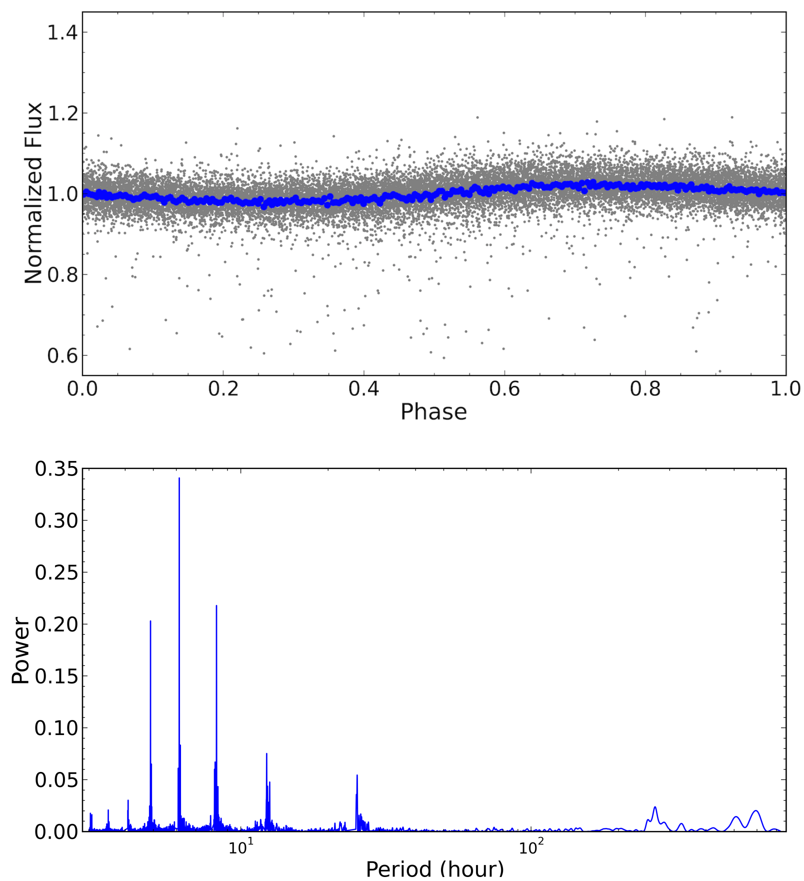

Figure 4.5: An example variable discovery (EVRJ032442.50-780853.9) from this survey. The Evryscope light curve phased on its period of 4.676 hours is shown on the top panel. Grey points = 2 minute cadence, blue points = binned in phase. The bottom panel shows the LS power spectrum with the highest peak at the 4.676 hour detection.

4.2.5 False Positive Tests

We performed several tests to verify the variability signals were not false positives. First, we compared the candidate light curve with several nearby reference star light curves looking for similar variation to test for systematics or PSF blending. The nearest reference stars within 0.2 degrees of the reference star were filtered by magnitude and light curve coverage. The nearest three with magnitudes within 0.5 mag of the target star and with a light curve coverage and number of data points within 20% of the target light curve are chosen for comparison. The references are folded at the same period as the detected period of the candidate, and are inspected visually for signs of similar signals, offsets, or outliers.

Candidates with references showing similar variability are assumed to be systematics and thrown out.

Next we tested how well-mixed in phase the observations were, with poor mixing potentially indicating matched-filter fits to systematics or data gaps instead of astrophysical signals. This is performed by folding the candidate on the detected period and color coding the points by time (ranging from a blue-to-red scheme mapped to early-to-late times) and visually inspecting the resulting plot. For each discovery, we also compared the phased light curve of the first and the second half of the data looking for inconsistency. Candidates with marginal results from these tests were reviewed by an additional person and thrown out if both agreed the target is suspect.

Eclipsing binary light curves that did not reveal a secondary eclipse or out-of-transit ellipsoidal variation were tested further. For these candidates, we folded the light curves at twice the detected period, looking for differences in odd/even transit depths to rule out finding half of the actual period. Candidates passing these tests were then flagged as probable variable discoveries and analyzed further as detailed in § 4.4.

4.3 FOLLOWUP OBSERVATIONS

Followup observations for select eclipsing targets were made with the PROMPT telescopes [36] in order to confirm the Evryscope detection. We used the SOAR Goodman spectrograph [33] for stellar classification and intermediate-resolution radial velocity measurements. We used the CHIRON [38] spectrograph for high-resolution radial velocity measurements to measure the companion masses of select suspected low-mass secondaries.

4.3.1 SOAR Goodman ID Spectroscopy

We observed the low mass candidates on April 29, 2018 on the SOAR 4.1 m telescope at Cerro Pachon, Chile with the Goodman spectrograph. We used the red camera with the 400 1/mm grating with a GG-455 filter in M1 and M2 preset mode with 2x2 binning and the

1” slit (R $\sim$ 825). The red camera [4] is optimized for the optical red part of the spectrum and when used with the M1 and M2 presets provides a wavelength coverage of 3500-9000 Angstroms. The Goodman spectra are 2-D, single order. We took eight consecutive 60s spectra for each of the targets and for the standard LTT3864. For calibrations, we took 3 x 60s FeAr lamps, 10 internal quartz flats using 50% quartz power and 10s integrations, and 10 bias spectra.

We processed the spectra with a custom pipeline written in Python by the Evryscope team; this pipeline is described in detail here. The eight spectra for each target are median-combined, bias-subtracted, and flat-corrected. A 3rd-order polynomial is fit to the brightest pixels in each row; the spectra are then extracted in a 10-pixel range and background subtracted. We identify 8 prominent lamp emission lines for each preset (including 3749, 4806, 6965 Angstroms and many others spread across the entire wavelength range) and compare with the known lines of the Iron-Argon arc lamp using a Gaussian fit of each feature. We use a 4th-order polynomial to fit the Gaussian peaks and wavelength-calibrate each spectrum. We used the standard star LTT3864 to flux-calibrate by first removing prominent absorption features then fitting a 7th-order polynomial to the continuum. The resulting SOAR standard star spectra was visually matched to the template from the ESO library and verified to fit within the template precision. The spectra were normalized and the results from the M1 and M2 presets were combined for each target with a wavelength coverage of 3500-9000 Angstroms.

Errors in the SOAR spectra arise from instrumentation systematics, observational conditions, and the extraction pipeline. Instrumentation error sources are dominated by flexure, component alignment, and limitations in optical quality due to manufacturing constraints; see [33] for an elaborate discussion of these contributions. Observational sources of errors are primarily due to background noise, airmass, and atmospheric effects. Errors in the spectra from the extraction process are discussed in detail in [108]; the chosen standard, normal-

[4] http://www.ctio.noao.edu/soar/content/goodman-red-camera

Table 4.5: PROMPT observations of select targets.

ID (EVR+)	Date	Images	B/R(s)
J06456.10-823501.0	Dec 10, 2017	412	40/20
J114225.51-793121.0	Oct 30, 2017	190	90/60
J114225.51-793121.0	Feb 16, 2018	288	90/60
J184114.02-843436.8	Dec 19, 2017	202	100/45
J211905.47-865829.3	Nov 21, 2017	120	130/90

ization process, and resolution are the error sources relevant to this work. The Goodman spectrograph has been operating consistently for over 15 years, and we use the accumulated knowledge to minimize errors from instrumentation, observation, and processing sources. In § 4.4.2 we compare the SOAR ID spectra to the spectra of stars with known stellar types. The known spectra are from different instruments, observational strategies, and pipelines; additionally the available known spectra are limited to an accuracy of ≈1-2 in the luminosity class. The combined errors in the high SNR SOAR ID spectra are less than this limitation. We demonstrate this in § 4.4.2 by comparing the results from different stellar classification methods, which are consistent to ≈1-2 in the luminosity class.

4.3.2 PROMPT Photometry

EVRJ114225.51-793121.0, EVRJ06456.10-823501.0, EVRJ184114.02-843436.8, and EVRJ211905.47-865829.3 were observed with the PROMPT P8 60cm telescope located at CTIO Chile. All observations were taken with Johnson B and Johnson R filters, interleaved. Table 4.5 summarizes the PROMPT followup work.

The PROMPT followup observations confirm the candidate variability is astrophysical and not an Evryscope systematic by observing the Evryscope detection signal with a separate instrument and different eclipse time. The PROMPT telescopes have a 100 times larger aperture than the Evryscope cameras, giving the PROMPT light curves a lower root-mean-square (RMS) scatter and improved signal-to-noise-ratio (SNR) compared to the Evryscope discovery light curves. The amount of improvement depends on many factors including target brightness and sky background; here we show a representative example, EVRJ211905.47-

865829.3 in Figure 4.6. The light curve RMS (after removing the eclipse) for this target is .006 in PROMPT and .108 in Evryscope (unbinned 2-minute cadence). This corresponds to a SNR of ≈ 167 for the PROMPT single transit light curve and ≈ 9.5 for the Evryscope one year light curve. These results compare nicely to estimated theoretical SNR of 175 and 12 for PROMPT and Evryscope respectively, using reasonable values for sky background, throughput, and airmass for these telescopes observing an $mv = 14.0$ magnitude target. We point out that the Evryscope binned light curve can reach the SNR of the PROMPT light curve, in this example with reduced sampling. In an upcoming white dwarf / hot subdwarf fast binary discovery paper (Ratzloff et al., in prep) we demonstrate the ability to reach higher than PROMPT SNR with multiple year binned Evryscope data. In this work, we use PROMPT to verify the Evryscope candidates and better characterize the eclipse depth and shape to reduce the error in the companion radii calculation. For this target, we also observed the secondary eclipse for comparison with the primary eclipse shown in Figure 4.6. The PROMPT data also provides an additional eclipse time (several months past the latest Evryscope eclipse), and by phase-folding both light curves, the period accuracy is increased.

The PROMPT images were processed with a custom aperture photometry pipeline written in Python. The images were dark and bias-subtracted and flat-field-corrected using the master calibration frames. Five reference stars of similar magnitude are selected and aperture photometry is performed using a range of aperture sizes. The background is estimated using a sigma clipped annulus for each star scaled by the aperture size. A centroid step Gaussian fits the PSF to calculate the best center and ensures each aperture center is consistent regardless of pixel drift. The light curve rms variation is computed for the range of apertures, and the lowest-variation aperture size is chosen. A final detrending step using a 3rd order polynomial is applied to remove remaining systematics. Photometric errors are calculated per epoch using the estimated CCD aperture photometry noise in [109] and the atmospheric scintillation noise approach in [110]. A detailed summary of the photometric error calculation is given in [111]. We combined the PROMPT and Evryscope light curves for final inspection. An

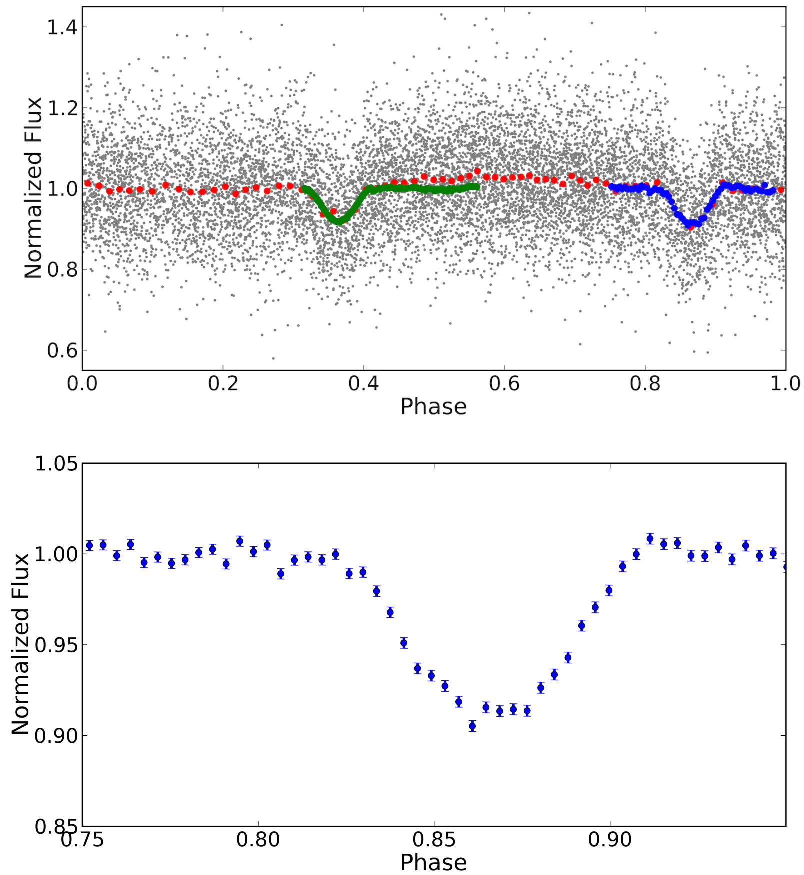

Figure 4.6: *Top:* Combined light curves of EVRJ211905.47-865829.3. This object was flagged as a potential 9.3 hour transiting gas giant planet as the transit depths are unchanged by color and in odd/even phase. There is a slight out of phase ellipsoidal variation when folded at the 18.6 hour period indicating it is most likely a grazing eclipsing binary with nearly identical primary and secondaries. *Bottom:* A detailed view of the transit in the PROMPT light curve with 1σ errors shown.

example of a grazing eclipsing binary originally flagged as a 1.7 RJ planet candidate is shown in Figure 4.6. Radial velocity follow-up with the HARPS [112] spectrograph on the ESO La Silla 3.6m telescope combined with the detailed light curve analysis confirms the candidate is a grazing eclipsing binary.

4.3.3 Intermediate-resolution Spectroscopy and Radial Velocity

EVRJ114225.51-793121.0, EVRJ06456.10-823501.0, EVRJ053513.22-774248.2, EVRJ184114.02-843436.8, and EVRJ211905.47-865829.3 were observed on November 15 and

19, 2017 and December 15 and 16, 2017 on the SOAR 4.1 m telescope at Cerro Pachon, Chile with the Goodman spectrograph. EVRJ110815.96-870153.8, EVRJ180826.26-842418.0, EVRJ165050.23-843634.6, and EVRJ103938.18-872853.8 were observed on February 12, 2018 and March 3, 2018. We used the blue camera with the 2100 1/mm grating in custom mode with 1x2 binning and the 1" slit (R $\sim$ 5500). We took four 300-360s spectra depending on the target and conditions. For all targets, we took 3 x 60s FeAr lamps after each group of science images. We took 10 internal quartz flats with 80% quartz lamp power and 60s integration, and 10 bias spectra.

The spectra are processed using a modified version of the Python code described in § 4.3.1 and radial velocity measurements are calculated (§ 4.4.3). The SOAR spectra return radial velocity precision of $\approx$ 10 km/s for our targets, which allows us to characterize the secondary mass for small late M-dwarf stars. This also allowed us to rule out potential planetary-mass secondaries - the case in several of the grazing eclipses.

4.3.4 High-resolution Radial Velocity

EVRJ06456.10-823501.0 and EVRJ053513.22-774248.2 were observed between January 28, 2018 and March 25, 2018 on seven nights (one data point per night) with the SMARTS 1.5 m telescope at CTIO, Chile with the CHIRON spectrograph. EVRJ184114.02-843436.8 was observed on March 23, 2018. Spectra were taken in image slicer mode (R $\sim$ 80000). One 1500 to 1800 second spectrum was taken depending on the target and conditions. Spectra of RV standard HD131977 were taken to verify processing results.

Spectra were wavelength calibrated by the CHIRON pipeline, which we processed using a custom python code to measure radial velocity. We visually inspected the spectral orders and chose the top seven by SNR and with prominent atmospheric absorption features. The orders are spread throughout the wavelength range, and we select the most prominent atmospheric feature per order. Within each of the selected orders, for each observation, we clip a small section (typically 20 Angstroms) encompassing the best absorption feature. For example order nine uses the 4957 Angstrom feature, order fourteen uses the 5328 Angstrom feature, and order thirty-seven uses the 6563 Angstrom feature. We fit a Lorentzian to the absorption features and measure the wavelength shift of each observation in each order. For each observation, we sigma clip any outlier orders and use the average shift to calculate the velocity. Using the standard deviation of the measured shifts between the orders, we place error limits. The error in the RV standard is measured to $\approx$ 200 m/s, while the errors in the fainter targets are $\approx$ 1km/s. An example is shown in Figure 4.7; the best fit RV amplitude from the CHIRON data is 69.0 km/s and for the SOAR data is 64.7 km/s.

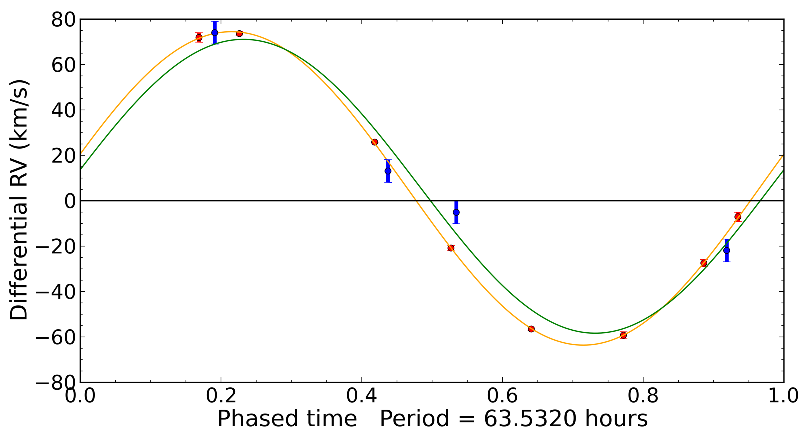

Figure 4.7: Combined Radial Velocity curves for target EVRJ06456.10-823501.0. The red data points are from CHIRON RV data, and the blue points are SOAR data with the yellow and green curves of best fit.

4.4 DISCOVERIES

In this section we present the discoveries beginning with the eclipsing binaries and variables. We measure the amplitudes of the variation, and for select targets we use the radial velocity measurement to estimate the companion mass. We show distributions of the periods, amplitudes, and magnitudes of the discoveries and summarize the important statistics of the search. All results are summarized in the appendix.

4.4.1 Discovery candidates parameter estimations

Candidates passing the false positive checks (§ 4.2.5) are separated by variation type (eclipse-like or sinusoidal variable-like) and measured. The eclipsing binary light curves are folded on the best period and fit with a Gaussian using the approximate phase and depth from the visual inspection plot as the prior. For the variable candidates, we use the best sinusoidal fit from the LS detection. Given the large number of candidates, fitting the light curve amplitude consistently and automatically is key. An additional challenge is the degeneracy due to orbital angle, limb darkening, and orbital eccentricity. We find the Gaussian (for eclipsing binaries) and best sinusoidal fit from the LS detection (for variables) methods to be effective and efficient to measure the variability of the discoveries, while select targets with followup data can be fit with more complicated tools (see § 4.4.3). Figure 4.8 shows an example eclipsing binary and variable star fit.

4.4.2 Identification Spectra

For the discoveries with potential low-mass secondaries, we compare the SOAR ID spectra to ESO template spectra (available at www.eso.org), see Figure 4.9. After finding the closest matching spectra, we compare the results from the color differences classifier described in the previous section. Finally, we use the PyHammer [113] spectra fitting tool to confirm our fits. PyHammer uses empirical templates of known spectral types and performs a weighted least squares best fit to the input spectra and returns the estimated spectral type. For the the low-mass secondary eclipsing binaries, the results from the three methods are in agreement to within 1-2 in the luminosity class. The spectral types are shown in Table B.1.

4.4.3 Radial Velocity - SOAR Data

We cross-correlate the SOAR spectra and measure the velocity shift throughout the period found in the Evryscope photometry. Using the color differences in § 4.2.3, and the stellar type,

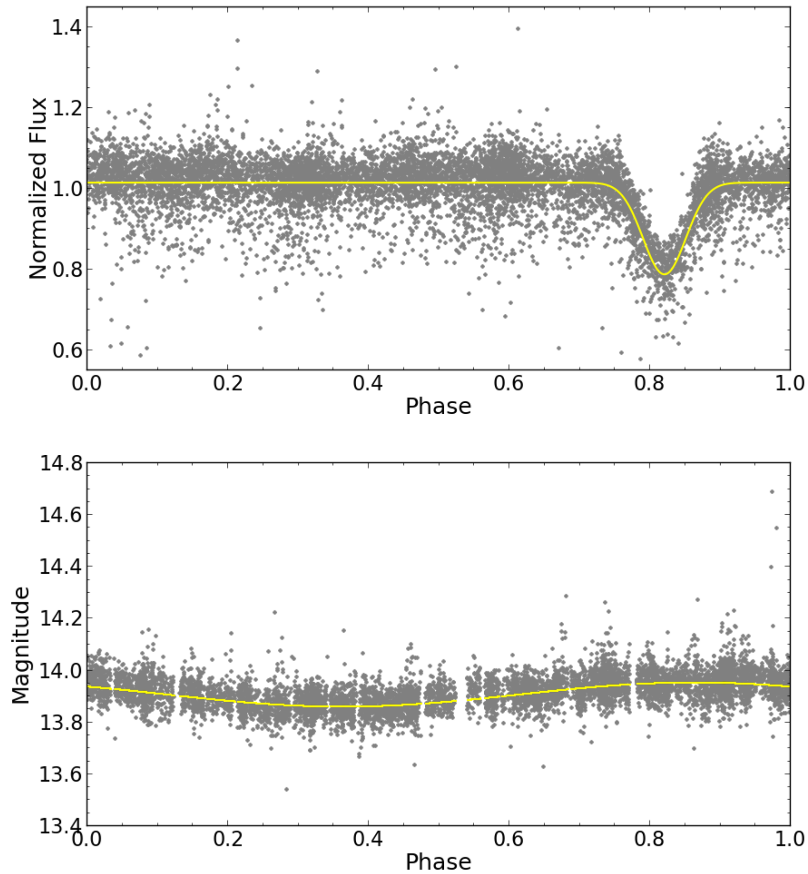

Figure 4.8: Top: Eclipsing binary discovery EVRJ131324.31-792126.3 folded on its 33.7 hour period representative of 100's of Evryscope variable discoveries. Gray points are two minute cadence and yellow is the best Gaussian fit to measure depth. Bottom: variable star discovery EVRJ131228.85-782429.2 folded on its 136.665 hour period representative of 100's of Evryscope variable discoveries. Gray points are two minute cadence and yellow is the best LS fit to measure amplitude.

radii, and mass profiles from [101], we derive functions (using 1-d interpolation) to estimate the primary radius and mass. The secondary radius and mass are then determined using Keplarian/Newtonian calculations described in the following section. For this step, we assume a circular orbit, zero inclination angle, and no limb-darkening. We run a Monte Carlo (MC) simulation to estimate the radius and mass ranges. Due to the simplifying zero-inclination angle assumption and the uncertainty in the SOAR RV measurements, our mass calculations for the secondaries are lower limits. More detailed modeling will be addressed in future work.

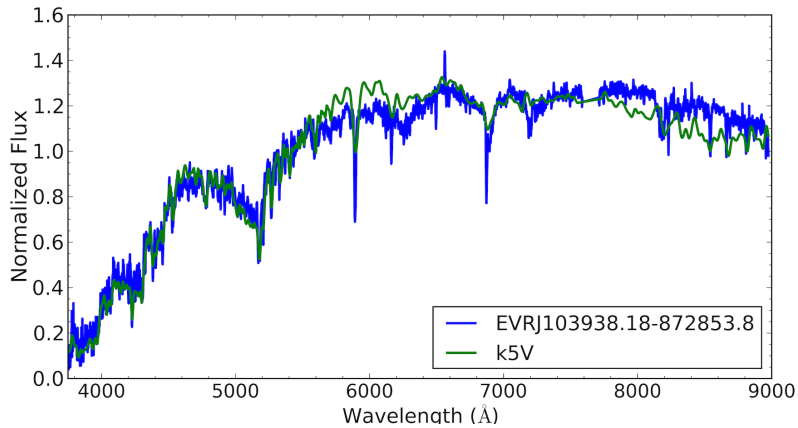

Figure 4.9: An example low mass eclipsing binary discovery (EVRJ103938.18-872853.8) ID spectra taken with the Goodman Spectrograph on the 4.1m SOAR telescope at CTIO, Chile. The green line is a K5V template from the ESO library.

We discuss our final solutions in § 4.4.7. The results are listed in Table B.1 and plots of the photometric and radial velocity light curves are shown in the appendix.

4.4.3.1 Secondary mass and radius determination

Photometry: From visual inspection of the candidate light curves, an initial guess is made for the transit phase and depth and fit with a Gaussian (Figure 4.10). The data is fit with a least squares minimization using scipy to measure the amplitude and phase.

Radial Velocity: An initial sine curve fit is made using a guess for the amplitude and zero point, while the phase and period are controlled by the transit time and the period found in the photometric light curve (Figure 4.10). The amplitude and zero point are used as inputs to a sine fitting function that uses a sine curve with a fixed phase and period. The function fits the data with a least squares fit; this is the gold line and it returns an RV of 56 km/s for target EVRJ110815.96-870153.8. This assumes a circular orbit and edge on geometry. We leave more detailed analysis with additional variables to future work.

4.4.3.2 MC best fit of mass and radius

Using the methods described in the previous section, we perform a Monte Carlo simulation (as described in [114]) to determine the best fit and distribution of the primary and secondary mass and radius.

From the Evryscope photometry, we use a bootstrap technique to leverage the very large number of epochs. We randomly choose half of the data points for each iteration with 5000 trials, and fit the data with a least squares minimization for each iteration. We also vary the radius of the primary for each trial by the range in [101] (spanning +/- 1 in numeric class). From the radial velocity data, we choose a random number in the error bar range of each of the data points (red) and fit the best sine curve (the silver curves) shown in Figure 4.10. We vary the mass of the primary for each trial by the error range in the estimated mass. The propagated results are shown in Figure 4.11.

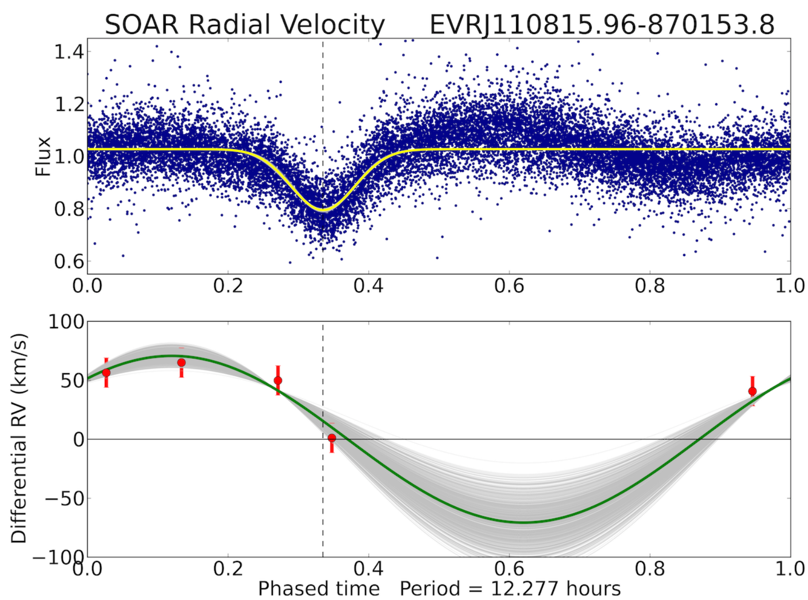

Figure 4.10: EVRJ110815.96-870153.8 K-dwarf eclipsing binary eclipse and radial velocity fit. Top: The best fit (yellow) to the Evryscope photometry using a Gaussian with an initial guess to measure the depth and determine secondary radius. Bottom: The best fit (green) to the SOAR RV data (red points) using a sine curve with an initial guess to measure the velocity and determine the secondary mass. The silver lines are the MC simulation to determine the best fit and error range.

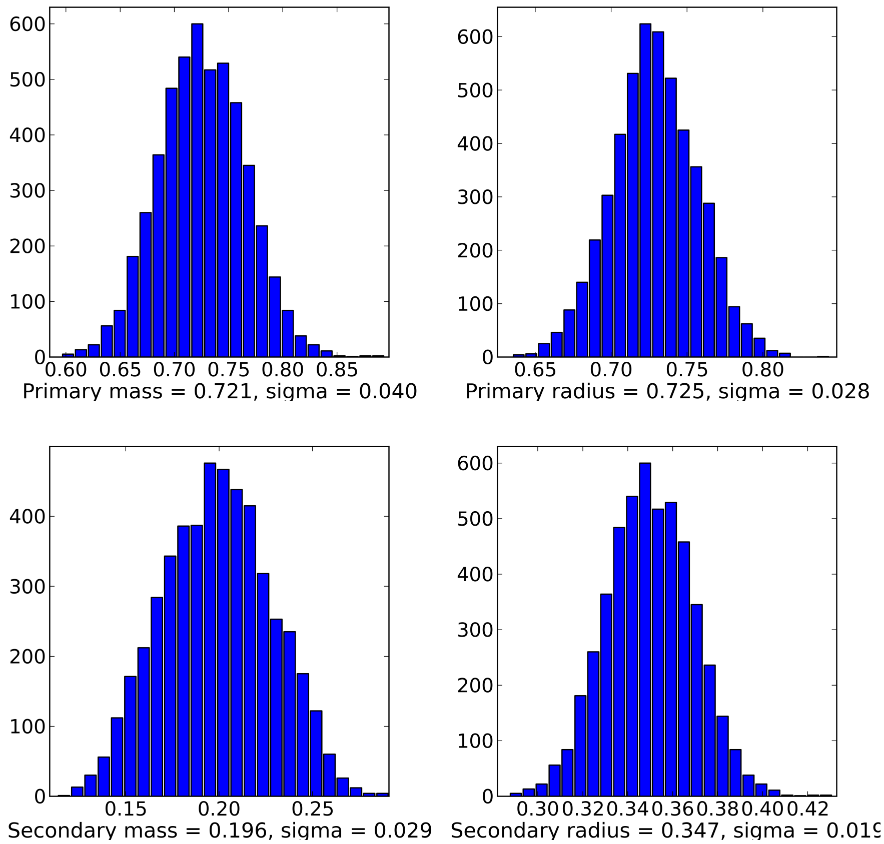

Figure 4.11: Primary and secondary mass and radius determined from our MC simulation. The top panels are the mass and radius of the primary in solar units, the bottom panels are the mass and radius of the secondary. The y-axis is the counts from the MC simulation totaling 5000 trials.

4.4.4 Search Statistics

Sorting by BLS sigma power and choosing only the top candidates greater than 10 sigma narrows the candidates to 5.6% (9104/163,584) of the filtered list. Visual inspection yields 7.3% (649/9104) actual variables from the BLS 10 sigma power list. The fraction of all discoveries to all searched is .40% (649/163,584). The false positive BLS rate is 5.2% (8455/163,584). Of 649 total variables detected, 346 are known in VSX. The total known periodic variables listed in VSX for the same sky area as the Evryscope Polar Search is 1928, giving a return of 17.9% (346/1928). There are 1050 known variables in the widest period ranges (3-720 hours) we searched, giving 33.0% return. There are 858 known variables in the period ranges (3-240 hours) we searched with BLS, giving 40.3% return.

4.4.5 Eclipsing Binaries and Variables - Distribution of results

Histograms of the eclipsing binary discoveries are shown in Figure 4.12. We discovered a total of 168 eclipsing binaries; most periods found are 75 hours or less, and most amplitudes found are 5-25%. The results of the variables are shown in Figure 4.13, we found 135 total and most are smaller amplitudes and shorter periods.

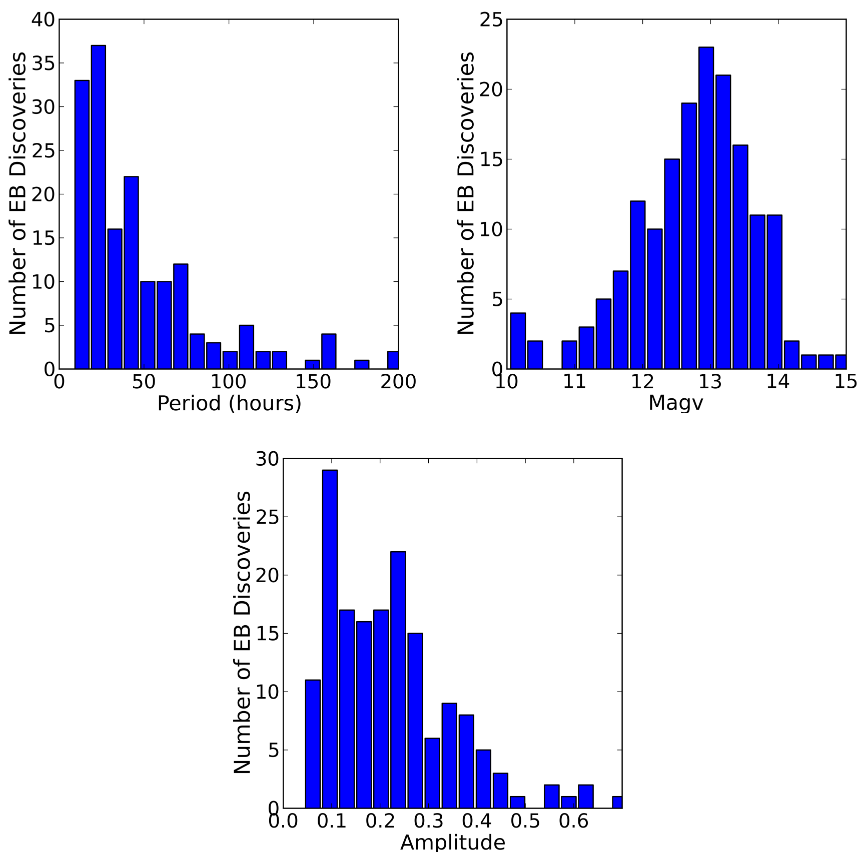

Figure 4.12: Histogram plots summarizing the eclipsing binary discovery results. We are sensitive to periods of several hundred hours and a large fraction of our discoveries are greater than 10% amplitude.

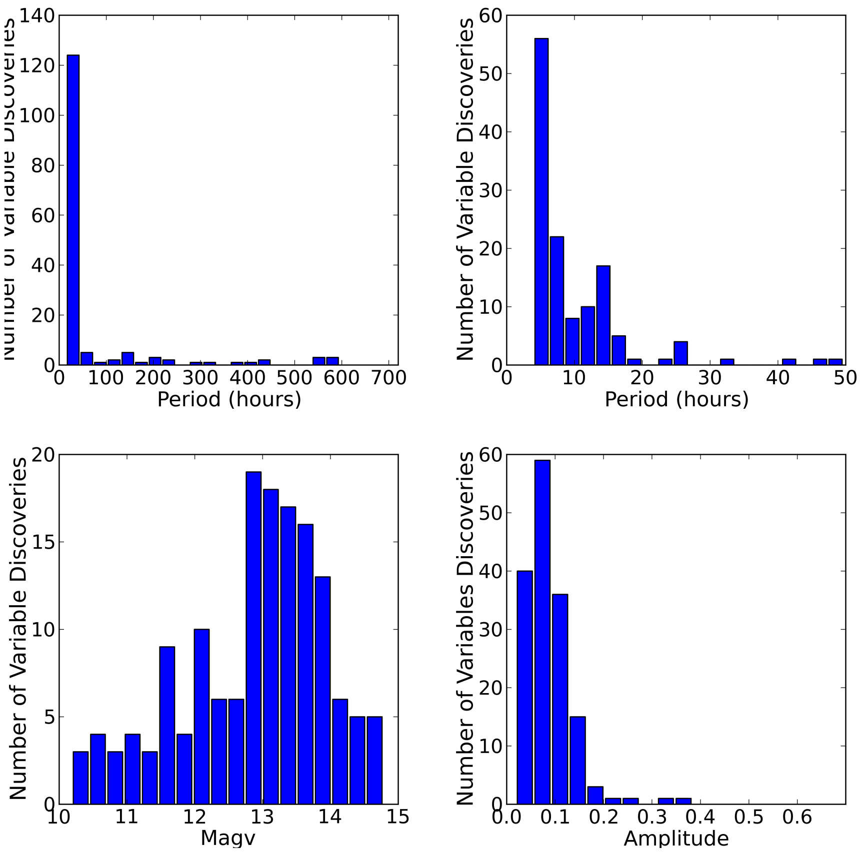

Figure 4.13: Histogram plots summarizing the variable discovery results. A larger fraction of the variable star discoveries are small amplitude and short period.

4.4.6 Classification

The discovery classification results are shown in Figure 4.14. We find 267 are main sequence, 34 are giants, and two are not classified. Spectral type G is the most common, with the spectral types shown in Table 4.6. We find more giant variables (24) than giant eclipsers (10) as shown in Figure 4.14. Also shown are the discoveries by star size and spectral type compared to total targets searched (Table 4.7).

4.4.7 Eclipsing Binaries with low-mass secondaries

We identified seven of the eclipsing binary discoveries as hosting potential low-mass secondaries and found that four are less than .25 solar mass. Three of the systems are fully eclipsing binaries (p = 12.3 to 25.9 hours) with dwarf primaries (SpTp = G5V, K4V,

Table 4.6: Classification discovery results - spectral type

Classifier Spectral Type	Number of Discoveries	Percent
B	2	0.7
A	14	4.6
F	89	29.4
G	109	36.0
K	76	25.1
M	11	3.6
none	2	0.7
Total	303	100

Table 4.7: Classification discovery results - compared to total searched

Classification	Total Searched	Number of Discoveries	Percent
ms	114585	267	0.23
giant	40775	34	0.08
HSD	335	0	0.00
WD	21	0	0.00
O	20	0	0.00
B	331	2	0.60
A	4110	14	0.34
F	26102	89	0.34
G	49560	109	0.22
K	60964	76	0.12
M	14629	11	0.08

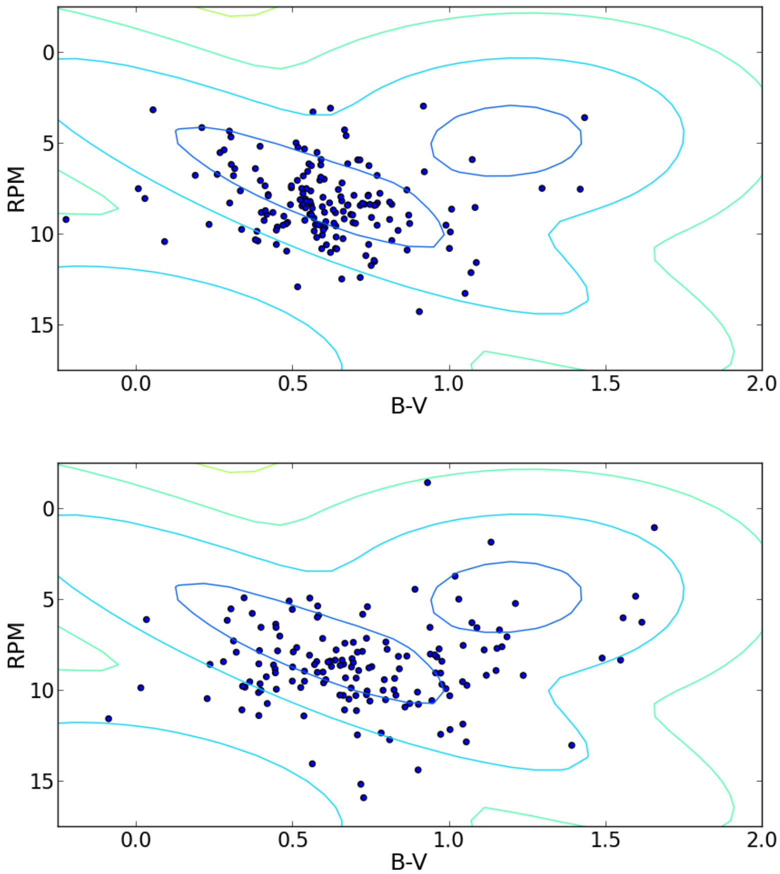

Figure 4.14: Classification results of the eclipsing binary and variable discoveries - Negative log likelihood plot-lines 1, 1.7, 2.8 shown. Top: Eclipsing Binaries. Bottom: Variables.

K5V) and M-dwarf secondaries (mass = .06 - .20 $M_{\odot}$). The other three systems are grazing eclipses with (p = 20.8 to 137.1 hours) with dwarf primaries (SpTp = G8V, K2V, K7V), M-dwarf secondaries (mass = .24 - .37 $M_{\odot}$) and minimum radii (r = .20 to .26 $r_{\odot}$). Table B.1 presents a list of all low-mass secondary targets. Also included is a likely visual binary EVRJ114225.51-793121.0 (separated in SOAR observations) and EVRJ211905.47-865829.3 a grazing EB with nearly identical primary and secondaries.

4.5 SUMMARY

The Evryscope was deployed to CTIO in May 2015 and has been operational since that time. We conducted a variability search of the southern polar area using the first 6-months of available data and by selecting the brighter stars (mv < 14.5) and limiting the declination range (-75 to -90). We sorted by detection power and visually searched the top 5 % for variability. We recovered 346 known variables and discovered 303 new variables, including 168 eclipsing binaries. Six of which we identify as low-mass (.06 - .37 $M_{\odot}$) secondaries with K-dwarf primaries. We encourage the community to followup further on these targets. We measured amplitudes, periods, and variability type and provide a catalog of all discoveries in the Appendix.

This research was supported by the NSF CAREER grant AST-1555175 and the Research Corporation Scialog grants 23782 and 23822. HC is supported by the NSFGRF grant DGE-1144081. BB is supported by the NSF grant AST-1812874. OF and DdS acknowledge support by the Spanish Ministerio de Economía y Competitividad (MINECO/FEDER, UE) under grants AYA2013-47447-C3-1-P, AYA2016-76012-C3-1-P, MDM-2014-0369 of ICCUB (Unidad de Excelencia 'María de Maeztu'). The Evryscope was constructed under NSF/ATI grant AST-1407589.

CHAPTER 5: WD ALL-SOUTHERN-SKY FAST TRANSIT SURVEY WITH THE EVRYSCOPE

This section presents a draft version of preliminary results to be submitted to the *The Astrophysical Journal* in mid 2020.

5.1 INTRODUCTION

Chapter one of this work describes in detail the background of white dwarf (WD) transit searches and the motivation for our survey. Here I only briefly recap and refer the reader to the thesis introduction for more details. Since observations suggest debris and dust orbit at least some non-trivial fraction of WDs, and some WDs show evidence of metals being actively deposited into the atmosphere, it a reasonable assumption that orbiting rocky bodies are the source of the material. Seemingly, some of the planets orbiting the main-sequence stars that were the WD-precursors survived the RBG / planetary nebula phase or migrated inward at some point after. These suspected planets should be visible in transit surveys, but non have been found so far. We have conducted a transit survey with Evryscope data, searching for planets orbiting WD hosts, and also found none.

We estimate our survey sensitivity using the conventional approaches used in other surveys, as well as explore the effects of more stringent assumptions and less simplified simulations that seem more reasonable to us. The effects on the results are significant, and demonstrate that WDs planets are quite difficult to detect. On our survey the effects show that it is beyond our reach to place population occurrence rate limits, but instead shows that many more targets are needed to effectively explore the parameter space. WD planets may or may not be rare, but they are certainly difficult to find. We encourage the community to consider assumption and simulation modifications we explore in this work. I note again here that this chapter is a work in progress, and with the completion of further recovery simulations, we will be able to complete and submit this work for publication in mid 2020.

5.2 OBSERVATIONS AND VARIABILITY SEARCH

5.2.1 Evryscope Photometry

The white dwarf (WD) survey in this work is based on Evryscope photometric observations taken from January, 2016 to June, 2018. The exposure time was 120 s through a Sloan g filter providing an average of 32,600 epochs per target. Here the wide-seeing Evryscope with continuous 2-minute cadence is well placed to look for the expected very short-timescale WD transits. The calibration, reduction, and extraction of light curves from the Evryscope is the same as in the Polar and HSD surveys. For a detailed description we refer the reader to our Evryscope instrumentation paper [19].

5.2.2 Evryscope Target Search Lists

The Evryscope white dwarf target search list is a combination of four sources, two published lists and two internally generated lists to match our light curve database.

5.2.2.1 Published Search Lists

The two external lists are:

1) A composite source based white dwarf candidate list, built from multiple sources: APASS [103], ATLAS [104], MWDD (Dugour et al. 2017), RH11 [115], SDSSNGF15 [105], Kepler16 [116], ELMSurvey [117], and SIMBAD.

2) A GAIA-DR2 [102] based white dwarf candidate list [49].

Filtering the lists to match our field-of-view and magnitude range, provides 2418 and 1436 targets respectively.

5.2.2.2 Machine-Learning Generated Search Lists

The two internally generated lists are:

1) A machine-learning based stellar classifier (Evryscope Classifier) we developed based on publicly available data from APASS [79] and PPMXL [78], which we use to select white dwarf candidates. The Evryscope Classifier is described in detail in [66]; it is a multi-step classifier that determines stellar size and spectral type. It uses reduced proper motion and B-V color differences to segregate targets by stellar size with a combination of a support vector machine (SVM) and a Gaussian mixture model (GMM). The contour boundaries are calculated using training data of known stars in each category. Multiple color differences (B-V, V-K, J-H, H-K) are then used to estimate spectral type. The classifier results are shown in Figure 5.1 with the white dwarf candidates in blue.

2) A modified version of the Evryscope Classifier that uses GAIADR2 data (Evryscope GAIA Classifier, see § 5.2.2.3).

Filtering the lists again to match our field-of-view and magnitude range, provides 8,810 and 1,222 targets respectively.

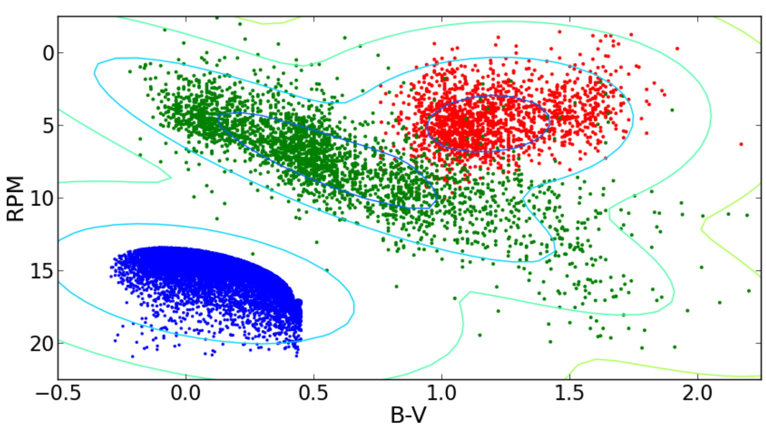

Figure 5.1: The Evryscope APASS/PPMXL based Classifier (see § 5.2.2.2), a two step Machine Learning based classifier. The black contours are the results of the GMM using training data from known giants (red diamonds), main sequence stars (green circles), white dwarfs (blue squares). The WD candidates, identified with the blue points. We combine these results with external lists (§ 5.2.2) to identify objects as likely WDs and check for photometric variability in the Evryscope light curves.

5.2.2.3 Machine-Learning Stellar Classification

The Evryscope GAIA Classifier uses the GAIA G-band absolute magnitude (corrected using only the GAIA parallax) and the GAIA B-R color. The same support vector machine and Gaussian mixture model machine-learning approach from the Evryscope Classifier (see § 5.2.2.2) is used to define the classification contours. The training set from [66] is again used, but with the GAIA data to construct the G magnitude / B-R color space. The classifier results are shown in Figure 5.2 with the WD candidates in blue.

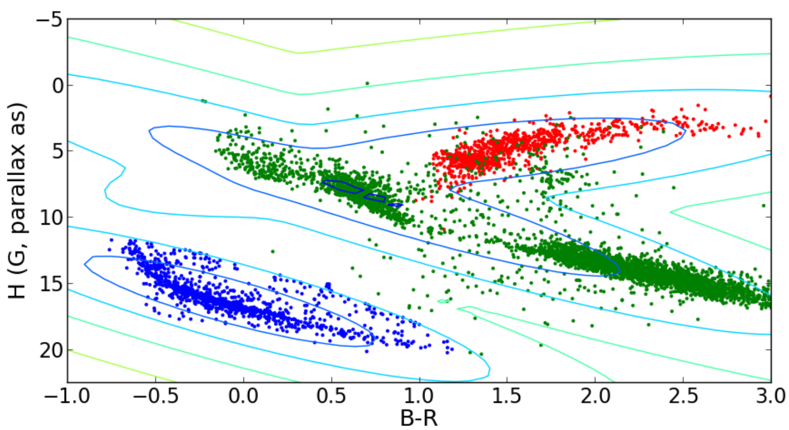

Figure 5.2: The Evryscope GAIA based Classifier (see § 5.2.2.3), a two step Machine Learning based classifier. The black contours are the results of the GMM using training data from known giants (red diamonds), main sequence stars (green circles), white dwarfs (blue squares). The WD candidates, identified with the blue points.

5.2.2.4 Testing List Performance

We tested the performance of the source lists in several ways (and summarized in Table 5.1):

(1) We compare the WD targets from each list to the spectral type from the SIMBAD database [100]. We require the coordinate crossmatch to be within 25 arcsec, and the magnitude comparison (GAIA m_g or APASS m_V vs SIMBAD m_V where available) to be within 2 magnitudes. For crossmatched targets that have an available SIMBAD SpT (none or N/A are discarded), those with DA-DZ matched to the lists are counted as recovered and

the other spectral types are false positives. The recovery rates increase as the classification requirement is relaxed, however the false positive rate also increases (as expected and shown in Table 5.1).

(2) We compare the WD targets from each list to the spectroscopically verified known WD's from [118, 119]. After filtering to our magnitude and declination range, the same crossmatch and magnitude comparison requirements from step (1) are used to identify which sources lists recover the known targets. The recovery rates are shown in Table 5.1.

(3) We use the P_{WD} and completeness estimate of 85% from [49] applied to sources in our FOV and magnitude range. Given the smaller number of targets and recoveries, we rely on this GAIA based list and the spectroscopic tests from step (1) to estimate our WD targets.

The target selection performance is summarized in Table 5.1.

Table 5.1: Target Selection Performance

WD

Method / Confidence	Recovery	Rate	False Positive	Rate
(1) SIMBAD SpT (WD/DA-DZ)				
Very High[a]	460/565	81.4%	15/475	3.2%
High[b]	511/565	90.4%	20/531	3.8%
Fusillo GAIA List	520/565	92.0%	90/610	14.8%
Evryscope GAIA List	528/565	93.5%	22/550	4.0%
All	565	–	539/1104	48.8%
(2) Spectroscopically Known WD's				
Very High[a]	201/236	91.8%	–	–
High[b]	207/236	94.5%	–	–
Geier GAIA List	210/236	95.9%	–	–
Evryscope GAIA List	207/236	94.5%	–	–
All	236	–	–	–
(3) P_{WD} Estimate.				
Fusillo GAIA List	–	–	–	10%

[a]Requires targets selected from 3 or 4 source lists (see § 5.2.2.4).
[b]Requires targets selected from both GAIA based source lists.

5.2.2.5 Summary of Targets

Potential targets for the WD survey is shown in Figure 5.3; their distribution in RA, Dec, and magnitude are as expected. The Evryscope database contains light curves for 9.3M targets with $m_g < 15$, with epochs through 2018. Dimmer sources and latter epochs are currently being processed. We added the additional filter requiring a minimum number of epochs (1000), and discarded sources with likely photometry issues (indicated by excessive flags).

The database query returned 5200 potential WD light curves. We estimate the fraction of incorrect light curves by comparing the magnitude error (m_g or m_V from the input lists less the mean Evryscope magnitude from the light curve) to the error in distance (the input list coordinates versus the centroid coordinates of the Evryscope pipeline). We also compare the list magnitude to the distance error. The average accuracy of correct targets is $\approx$ 1-2 arcsec and clearly sub-pixel (13.3"). There is a significant bias toward a brighter star recovered, indicating the likelihood of missed targets substituted with a nearby bright star. Our analysis revealed that light curves returned from the target search that were more than 3 magnitudes in error or greater than 20 arcsec in distance were more than 90% likely to be the wrong target. Applying this criteria to the survey query, the WD light curves are 68% likely to be the wrong targets, with the dimmer sources suffering the greatest contamination.

The majority of these wrong targets (67% of the *wrong targets*) are sources in the galactic plane or LMC, expected to be problematic given the Evryscope pixel scale. They are also heavily skewed as being identified from the least stringent of the filters (the Evryscope APASS/PPMXL classifier) and are likely not WDs. The average wrong targets rate for sources not in the galactic plane or LMC is $\approx 22\%$ $(.68 \times (1 - .67))$, in reasonable agreement with the predictions in [17] for blended sources in the Evryscope images.

To estimate the likely number of targets from the survey, we begin with the number of light curves returned from the database query for each classifier confidence level. The totals are adjusted by the likely wrong targets fraction (which depends on the confidence level, and as expected improves in the higher confidence level classifiers). From the rates in Table 5.1, we calculate the average recovery and false positive values per confidence level. We divide the adjusted number of targets by the recovery rate and subtract the false positives to estimate the total sources. A summary of the WD targets are shown in Table 5.2.

All of the 5200 light curves were inspected, however the classification confidence level and distance flags (indicating likely wrong light curves from being in the galactic plane, LMC, or other issues) were included for each source. This helped prioritize the followup of variable candidates. We also use this source information in the calculation of the estimated occurrence rates in § 5.4.1. The WD search especially suffered from a low target return due to the dim nature of these stars and high fraction of targets in the LMC or galactic plane, we discuss potential improvements in the next survey in § 5.4.

Table 5.2: Survey Targets

WD

Total Targets	Confidence	Likely Blended	Recovery	False Positive	Likely WDs
312	Very High[a]	.35	.87	.03	225
457	High[b]	.46	.92	.04	255
611	GAIA	.46	.94	.12	307
509	ES GAIA	.49	.94	.04	266
5200	All	.68	1.0	.80	332
Survey					277 $\pm$42

[a]Requires targets selected from 3 or 4 source lists (see § 5.2.2.4).
[b]Requires targets selected from both GAIA based source lists.
See § 5.2.2.5 for calculation of Likely WD's

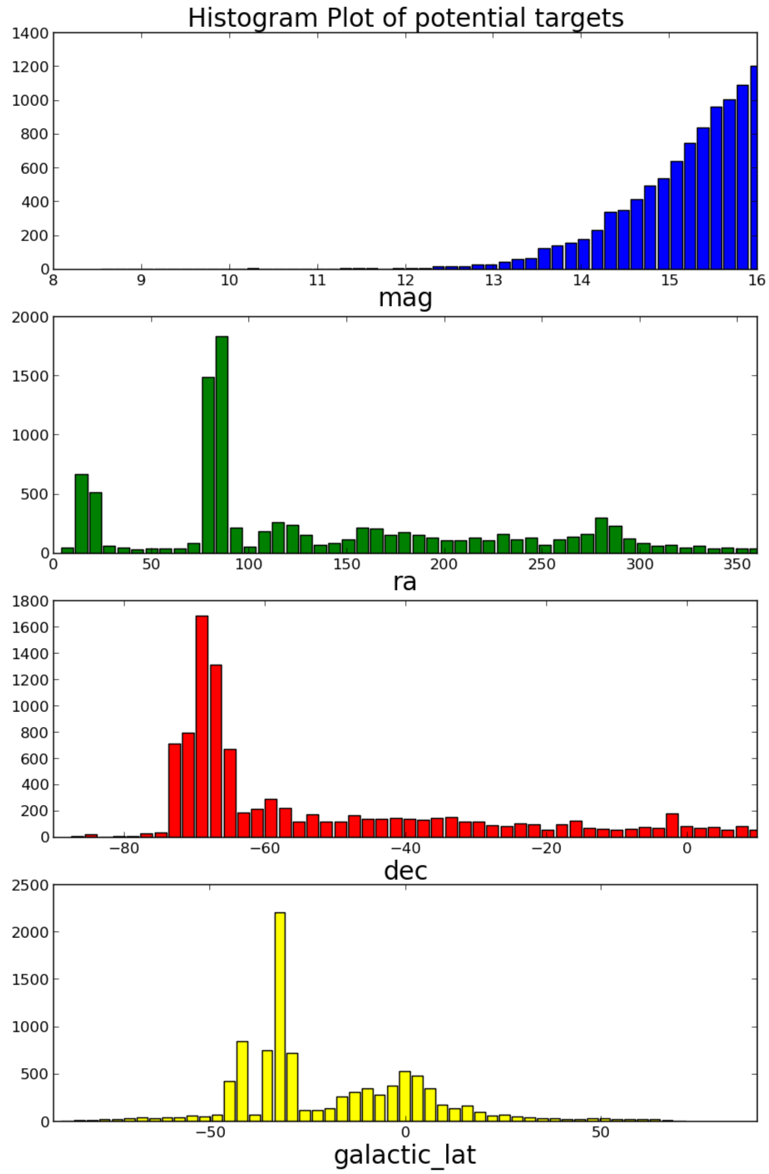

Figure 5.3: The potential WD targets, selected from 4 different methods explained in § 5.2.2. The noticeable imbalance in targets in the LMC and galactic plane is mostly due to missclassified targets from the Evryscope APASs/PPMXL based classifier. Although this selection method is more prone to false positives, it also identifies potential targets the more stringent filters miss. We reviews all targets for variability. In estimating the total targets in the survey, we considered the likely false positive rate, over-densities in the LMC and galactic plane, and blended sources.

5.2.2.6 Blended Sources

Given the correlation between the likely wrong targets identified in § 5.2.2.5 and the galactic plane or the LMC, we conclude blended sources accounts for substantially all of the errant light curves. The likely sources that are WDs blended with brighter source light curves is 588 ($277/.32 \times .68$) WD blended sources (with the note that since the sources are dominated by the classifier with the highest false positive rate, a good number of these will not be WDs even if they are blended). Although any WD transit signal would be greatly reduced from the blended brighter source, a fraction of the systems may detectable depending on how much brighter the contaminant is and how deep the variability signal. Although we are still investigating this point, initial analysis shows the fraction of usable blended systems will be negligible. We also remind the reader that since the blended fraction is considerably less for the higher confidence levels, the total blended sources in the survey (and that are actually WDs) is probably even less.

5.2.3 Detection of Variables

5.2.3.1 Detection Process

The timestamps in the Evryscope light curves were converted from Modified Julian dates to Heliocentric Julian dates using PyAstronomy's *helCorr* function. We pre-filtered the light curves with a Gaussian smoother to remove variations on periods greater than 30 days, and a 3rd order polynomial fit was subtracted to remove long-term variations. Light curves were then searched for transit-like, eclipse-like, and stellar variability signals using the Box Least Squares (BLS) [28, 29] and Lomb-Scargle (LS) [30, 31] algorithms, along with a custom search tool (the outlier detector) designed to find fast transits characteristic of HSDs and WDs. Details of the search methods, algorithms, and settings are described in detail in our HSD survey [120].

WD transits are expected to be fast (on the order of a few minutes), and deep (up to completely eclipsing if the orientation is optimal). Even with periods as short as a few hours, the transit fraction is still small, and the most significant points in the light curve are very dim outliers. This situation is quite different than the traditional shallow (less than 1%) and longer (at least a few hours) transits BLS was designed to find, and completely different than the sinusoidal signals LS excels at. Here, the custom code we developed (the outlier detector - see the introduction of this thesis), excels at finding the narrow and deep signals characteristic of WD transits.

5.2.4 Search Algorithm Performance

We use 150 Evryscope light curves, distributed in magnitude, RA, and Dec as the basis for testing our search algorithm performance. WD transit signals are injected onto the light curves for a variety of planet sizes and periods. The simulations assume a star size of .01 $R_{\odot}$. For each planet size, the period search range is split into 100 test periods. We perform 10 iterations at each test period (each iteration adjusted with a random variation of $\pm$ 1 %), for each light curve, and test if the transit is detected. A detection is counted if either BLS or the outlier detector finds the period or an alias (half or double the period) within 1% of the correct period.

To test the WD recovery rates, we simulated transits using planet sizes ranging from sub-Earth to Jupiter. We performed the computations with a 16 core / 32 thread machine with an Intel(R) Xeon(R) Gold 6130 CPU @2.10GHz and 128 GB of DDR4-2666 RAM. Recovery rates are favorable for Earth size planets and larger out to multiple day periods. Here the very deep transits (up to completely eclipsing) aid in the detections. The detection efficiency tests are shown later in this chapter.

5.3 RESULTS

5.3.1 Null-Detections

5.3.1.1 White Dwarf Transits

There are no known planets orbiting WDs and we did not detect any candidates in our survey. The 1 known WD planetesimal, WD 1145+017 [47], is not in our magnitude range. The only other objects in our survey that would produce light curve variability similar to transiting WD planets are double WD eclipsing binaries, and as we did not detect any of these systems (see § 5.3.1.2), we must rely completely on our transit simulations in evaluating our detection efficiency. We discuss the WD planet transit results in more detail in § 5.4.

5.3.1.2 White Dwarf Eclipsing Binaries

Double WD eclipsing binaries are rare and challenging objects to detect, for a recent discovery and list of the 6 known systems see [48]. We did not detect any candidate double WD eclipsing binaries, and the known systems are outside of our instrument window (either in FOV or magnitude or both). However, we did recover two known WD eclipsing binaries with main-sequence companions (CD-56 7708 a 55.26 hour binary with a G-dwarf and FS Cet a 101.56 hour binary with an M-dwarf).

5.4 DISCUSSION

5.4.1 Survey Sensitivity

To test the survey sensitivity, we combine the estimated detection efficiency, the transit fraction, and total survey targets. This offers visibility to the number of likely targets for a range of periods, and for a particular transit type. In all cases the survey is target limited.

5.4.1.1 WD Transits

We estimate the sensitivity of the WD transit survey. Panel (a) of Figure 5.4 shows the recovery of various solar system size planet transit simulations with WD host stars. The small size of the WD leads to deep transit depths (up to completely eclipsing for the larger planets) with short transit durations of less than ten minutes. The fast cadence, multi-year Evryscope data and detection algorithms (especially the outlier detector) effectively recovery signals from even rocky planets over a wide range of test periods out to several weeks. In panel (c) the survey limitation is clearly visible in transit fraction. The WD transit fraction is more than an order of magnitude worse than of the already challenging HSD transiting planets. Assuming a WD primary with .6 $M_{\odot}$ and .013 $R_{\odot}$ the transit fraction for Earth size planets is $\approx 1/750$ - $1/5000$ for all but the shortest periods (> 10 hours). Only the gas giant Jupiter size planets are above 1 in 100 for any appreciable period range. From the estimated number of WD targets in the survey (see § 5.2.2.5) the potential targets with transits is shown in panel (e) of Figure 5.4.

The unfavorable transit fraction and shortage of bright targets place a severe burden on the WD survey recovery. Obviously, more targets are needed to improve the chances of recovering transiting WD planets, especially at periods beyond 10 hours. In the following section, we discuss our efforts to increase the number of sources.

The test period range from beyond the shortest periods (> 10 hours) up to 480 hours in the WD survey might be the most favorable parameter space to search for WD planets. A few dozen WDs are known to show IR excess indicating dusty debris discs [39], and 1/4 to 1/3 reveal atmospheric metal pollution [40] thought to originate from deposited material. The source of the dust and metal is still an area of active research, but the preferred explanation is that planets or asteroids have migrated to the Roche limit and disintegrated leaving behind material that forms a disc or deposits onto the WD [41]. The donor planets or asteroids are thought to have survived the WD evolution cycle, meaning their orbits would have started at greater than 1 AU (the asymptotic-giant-branch phase radius). While we cannot push to 1

AU, our period range searches separation distances from the Roche limit up to 25 solar radii as seen in panel (b) of Figure 5.4. We could explore this potentially rich region if we had significantly more targets.

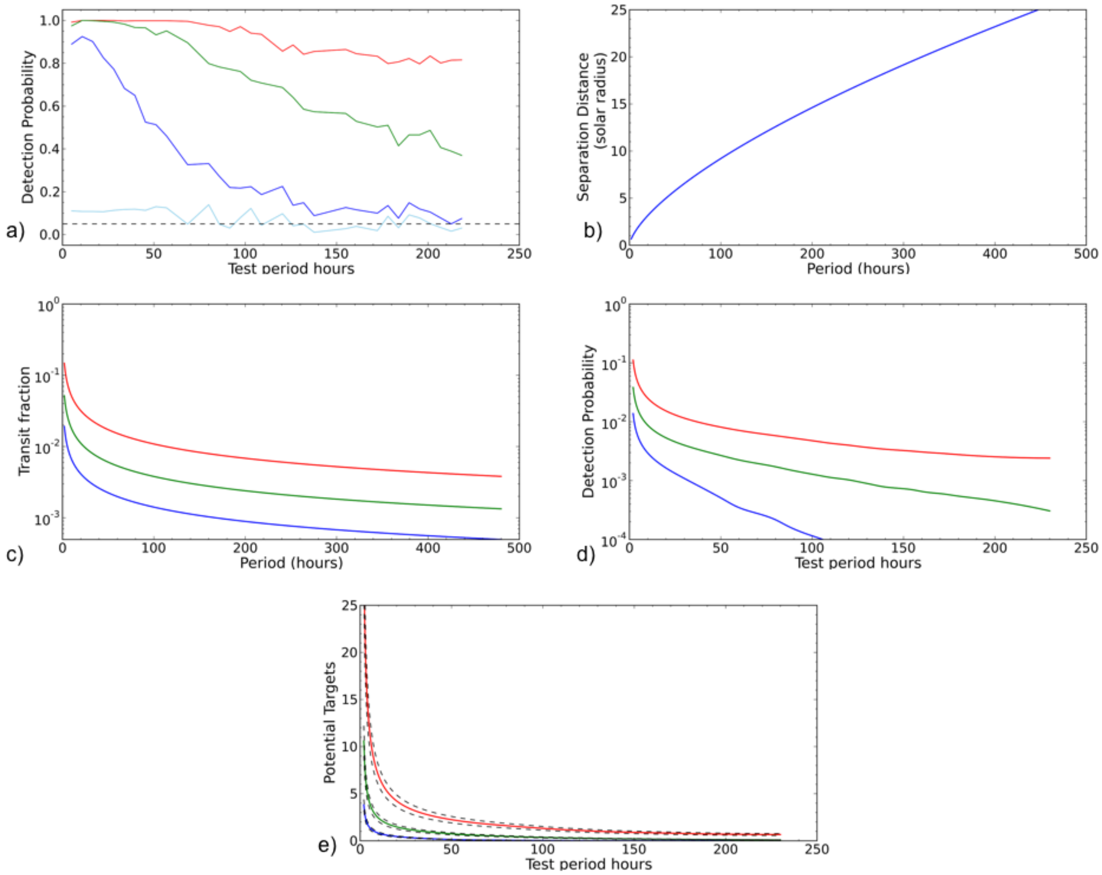

Figure 5.4: WD planet survey sensitivity. *(a)* The detection efficiency for Jupiter (red line), Neptune (green line), Earth (blue line), and Moon (sky blue line) size planets transiting WDs. *(b and c)* The theoretical separation distance and transit fraction. *(d)* The final detection probability (note the logarithmic scale) is driven down significantly ($\approx$ 1/1000 to 1/10,000) for all but the shortest periods due to the transit fraction. *(e)* The potential targets that transiting planets could be detected in, found by multiplying (d) by the estimated total number of WDs in the survey. The dashed lines are the estimated 1σ errors. The unfavorable transit fraction and challenging target pool place a severe burden on the survey recovery.

5.4.1.2 WD Survey 2

The suspected WDs are biased in distribution toward the faint magnitudes, not surprising given the compact nature of these stars. The WD suspects in the GAIA based source list of [49] show 6 times more candidates with $m_g < 17.0$ versus those with $m_g < 15.0$ (the cutoff in our WD survey). The increased FOV by adding the Evryscope North would again double the WD sources. The net gain of these changes is an ≈ 12 times increase in the number of WD targets. The results of these improvements is shown in Figure 5.5.

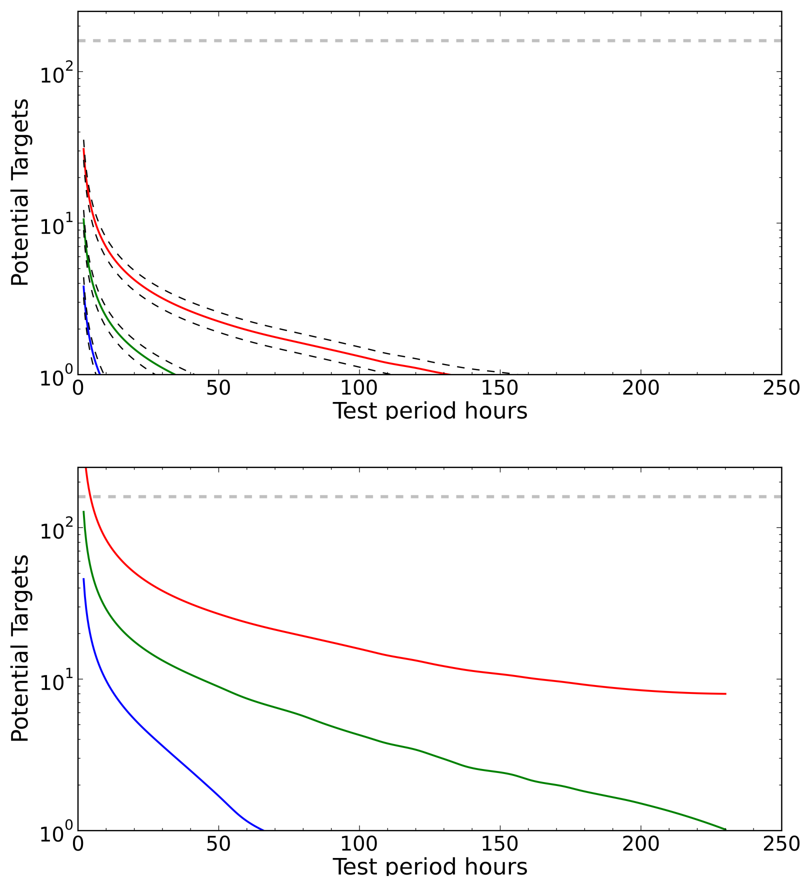

Figure 5.5: The potential targets that transiting planets could be detected in, Jupiter size planets (red line) and Earth size (blue line) are shown. *Top:* The WD survey in this work. *Bottom:* The Survey 2 with increased magnitude and FOV coverage.

5.4.2 Comparison to WD surveys

Agol suggested a WD survey strategy in [42], with Faedi [43] conducted the first survey. Fulton [44], Hermes [45], and others [46] have searched for transiting exoplanets around WDs with similar null-detections and reporting of maximum occurrence rates. Our survey has several distinctions in design and execution (aside from the instrument FoV and cadence), when taken together result in non trivial differences compared to prior surveys. The generation of the target search list, independent testing of these targets as WDs to estimate the number of targets in the survey, identification of blended sources as minimal contributors, accounting for grazing transits in the light curve recovery simulations, using actual light curves to inject the transit signals for recovery testing, and using a robust number (150) of these distributed representatively in RA and declination are key features of our survey. We discuss the distinctions and their ramifications below, followed with brief comments.

5.4.2.1 Distinct Evryscope WD Survey Features

(1) The Evryscope Target Search List: Our target search list was generated using 4 different sources and tested to independently confirmed WDs to estimate the recovery and false positive rates (see § 5.2.2). This approach also allows us to compare the performance of color / color, composite, and GAIA based generated lists. The [104] GAIA based list (see § 5.2.2.1), as well as the high-confidence level classifier and spectroscopically confirmed WD testing (see § 5.2.2.4) show that the color / color and pre-GAIA based lists are likely to have significant false positives of nearly 50%. Even GAIA based lists are prone to significant false positives, especially if the parameter space is difficult to separate as in the case of the HSDs. The [104] GAIA based WD list is exceptional in limiting false positives (by leveraging multiple color / magnitude spaces), but there are still 10-15% likely non-WD targets. By performing the classifier analysis (Table 5.2), we likely prevented overestimated our targets by at least 25%.

(2) Identifying Blended Sources: As shown in § 5.2.2.5, the blended sources outnumber the uncrowded sources by approximately 3 to 1. The blended sources are not expected to contribute to the detection of WD transit signals since the contaminant star is much brighter in most cases and significantly dilutes even the deep transits. Including these blended sources in the WD survey would have considerably overstated the usable targets.

(3) Simulating Grazing Transits: For typical transit simulations (planets transiting a main-sequence star), the star is much larger than the transiting planet and grazing transits are assumed to be negligible. The light curve used in the simulation is injected with a transit with an edge-on ($i = 90$) orientation, and the detection probability is determined for a range of periods and planet sizes. The transit fraction is computed from the theoretical relation R_{star}/a and multiplied by the detection probability to give the final detection efficiency (as discussed in § 5.4.1) and shown in Figure 5.4.

With the small size of a typical WD, transiting planets are expected to be of similar size (or larger) than the WD host. Grazing transits are common in this scenario, and present a challenge for recovery simulations. The approach taken in the WD community has been to increase the transit fraction to $(R_{star} + R_{planet})/a$ and ignore the effect of the decreased signal from the grazing effect.

A separate group of WD simulations will be included in this work (currently in development) conducted instead by including the inclination term ($\sin i$) and adding a variable for the inclination into the MC parameter space. This has the disadvantages of lost visibility to the transit fraction (now integrated in the simulation) and increased computing times. The computing times are helped by optimizing and running the code on a multi-processed, high memory machine. The simulations are still resource consuming, and are expected to take several weeks to run the final WD detection efficiency scenario. A prelimary comparison of the generous transit fraction approach versus the integrated inclination term approach for a rocky planet transiting a WD shows a greatly reduced detection efficiency. Our recovery rates decrease by several factors for most periods, and the non-detectable level begins at a shorter period.

(4) Simulations Using Actual Light Curves: We generated a synthetic light curve using the window function, number of epochs, and noise (based on the light curve RMS) for a sample of light curves in the survey. Shown in Figure 5.6 is the recovery performance based on injecting transits to the synthetic light curve versus the actual light curve. The detection efficiency and period coverage is improved in most cases by a factor of 4 when using the synthetic light curve.

(5) A Diverse Pool of Base Light Curves for Simulations: We calculated the recovery rates for a rocky planet orbiting a WD using three different input light curves with polar, mid-declination, and zenith locations for similar brightness ($M_v = 12.5$) sources. The recovery (as shown in Figure 5.6) is target dependent, not surprising given the variance in window functions, systematics, and epochs. Averaging the results from many input light curves lessens the possibility of errant recovery rates due to unrepresentative base light curves. This approach again has the disadvantage of significant computing time, we optimized the code and streamlined this process to the point that it was acceptably slow.

5.4.2.2 Ramifications of the Survey Features

The survey features described in the previous section all resulted in a reduced reported survey sensitivity than if we had not implemented them. The combined effect is at least a factor of 10 difference and potentially larger depending on the assumptions made. While the approaches taken in our survey are more conservative than in previous surveys, they are not overly so and we feel are accurate for our instrument and data. Perhaps surprising is the very challenging potential targets that the survey is sensitive to finding planets given the wide sky coverage, multi-year observations, fast cadence and other advantageous attributes of the data and detection tools.

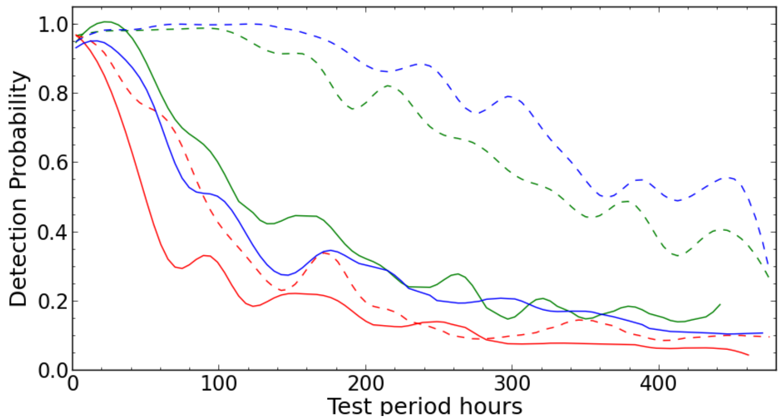

Figure 5.6: The WD survey sensitivity for a super Earth ($R = 2R_{\odot}$) size planet. The solid lines are 3 similar magnitude ($M_v \approx 12.5$) test light curves at different declinations (polar shown in blue, mid shown in green, and zenith shown in red) and with different observational coverage (75, 31,and 11K epochs). The more sparse coverage in the zenith light curve shows a reduced recovery (.5 at 50 hours versus .9 at 50 hours) and a reduced period sensitivity(.5 at 50 hours versus .5 at 100 hours). We use 150 light curves spread in declination (and RA and magnitude) as base light curves for the transit simulation tests to mitigate the light curve selection effect and not overstate our recovery rate. The dashed lines are the same recovery tests using synthetic light curves (the same epochs from the light curves but with Gaussian distributed noise at the overall rms instead of the measured magnitude values. Using synthetic light curves as the base light curves for the recovery of simulated transits results in overstating the recovery rate and period coverage by nearly a factor of 4. We do not use synthetic light curves in any of our simulations to avoid overstating our detection efficiency.

5.4.3 Comparison of HSD and WD survey results

The HSD survey (see Chapter 6) and WD survey in this chapter offer an enlightening comparison between the two types of systems. The surveys were conducted with the same instrument, pipeline, cadence, observation date range, FoV, and using similar target selection and detection algorithms.

Planets or small stars transiting HSDs are considerably deeper than conventional transits (the same size object transiting a main sequence star), however the transit time and transit fraction are more challenging. The number of HSDs is arguably the most challenging aspect of the survey as there are just a few thousand HSDs brighter than $m_g = 15.0$. These characteristics are quite well matched to the Evryscope instrument capabilities. The expected

$\approx$ few percent to 30% level variability signals are reliably detected in Evryscope light curves. The expected 20-30 minute duration signals are recovered consistently with the Evryscope 2 minute cadence. Although the targets are scarce, the entire southern sky FOV coverage provides several thousand bright sources that reasonably offsets the transit fraction. Overall the survey is well balanced, and the results reflect this with the discoveries of several rare and hard to find compact binaries, HW Virs, reflection binaries, transit candidates, and other variables, as well as the recovery of the expected known systems.

The WD survey is in a completely different regime. While the compact nature of the WD aids in the recovery of the transit signal, as demonstrated by the very high detection efficiency, it is extremely burdensome in every other significant aspect. The transit times are more challenging and the transit fraction is absolutely devastating. Here the Evryscope cadence is matched to the expected few minute transits, but with much less contingency than the HSD transits. The limited number of bright WDs, even with all sky coverage, still cannot overcome the transit fraction for all but the shortest periods. In the WD survey in this work we expected to potentially find a few short period transits, but not more than this given the challenges described above. The actual results were very different than the HSD survey with no WD discoveries and only a few variables from misclassified stars.

5.5 SUMMARY

We proposed modifications to the WD survey approach in an effort to make the search less speculative. The increased targets and other adjustments certainly will help improve the sensitivity and extend the periods to a range more likely to have planets, but the situation is still very challenging and much less complete than the HSD survey. Several WD transiting planet surveys have been completed in the last decade, also with null-detections. We suggest to the reader that the WD exoplanet community may have overstated the deep transit signals and underscored the challenging transit times, available targets, and especially the transit fraction. The meaningful result of the WD survey in this work is not the null-detections or calculation of maximum occurrence rates from low number statistics. Instead it is the identification of the limiting factor - covering a period range extensive enough where likely transits occur without missing the very short transits, and having enough targets to offset the extremely difficult transit fraction. We described in the previous section our planned next survey (Evryscope WD Survey 2, Galliher, et al., planning stage) in an attempt to address these challenges. Even with full sky coverage, nearly 10,000 targets, 2 minute integration time, 2 minute cadence, multi-year continuous data, and custom search algorithms optimised to find WD transit signals, the search is still formidable - but also intriguing.

CHAPTER 6: HOT SUBDWARF ALL SOUTHERN SKY FAST TRANSIT SURVEY WITH THE EVRYSCOPE

This section presents results published in the *The Astrophysical Journal*.[1][2]

6.1 INTRODUCTION

We have conducted a survey of candidate hot subdwarf stars in the southern sky searching for fast transits, eclipses, and sinusoidal like variability in the Evryscope light curves. The survey aims to detect transit signals from Neptune size planets to gas-giants, and eclipses from M-dwarfs and brown dwarfs. The other variability signals are primarily expected to be from compact binaries and reflection effect binaries. Due to the small size of hot subdwarfs ($R \approx 0.2R_{\odot}$), transit and eclipse signals are expected to last only ≈twenty minutes, but with large signal depths (up to completely eclipsing if the orientation is edge on). With its 2-minute cadence and continuous observing Evryscope is well placed to recover these fast transits and eclipses. The very large field of view (8150 sq. deg.) is critical to obtain enough hot subdwarf targets, despite their rarity. We identified ≈11,000 potential hot subdwarfs from the 9.3M Evryscope light curves for sources brighter than $m_g = 15$. With our machine learning spectral classifier, we flagged high-confidence targets and estimate the total hot subdwarfs in the survey to be ≈1400. The light curve search detected three planet transit

[1]Ratzloff JK, Barlow BN, Németh P, Corbett HT, Walser S, Galliher NW, Glazier A, Howard W, and Law NM. Hot Subdwarf All Southern Sky Fast Transit Survey with the Evryscope. *The Astrophysical Journal* 2020; 890:126 DOI: 10.3847/1538-4357/ab64f3.

[2]I wrote the larger majority of the HSD Survey paper, with Barlow and Németh contributing the remainder. I prepared the target list including the modified classifier, analyzed the search list performance, performed the detection simulations, took all the data for and processed the followup spectra, obtained the TESS confirmation light curves, and identified the candidates. Németh found the best fits to the ID spectra, while Barlow guided the structure and goals of the survey, reviewed the candidates, and helped prioritize the discoveries.

candidates, shown to have stellar companions from follow–up analysis. We discovered several new compact binaries (including two with unseen degenerate companions), two eclipsing binaries with M-dwarf companions, as well as new reflection effect binaries and others with sinusoidal like variability. Four of the discoveries are being published in separate followup papers, and we discuss the followup potential of the other discoveries.

Hot subdwarfs (HSD) are small, dense, under-luminous, high temperature stars. Most are thought to be helium cores with a thin hydrogen layer, formed from stripping of the main hydrogen shell during the red-giant phase by a binary companion. The hydrogen stripping is believed to prevent the core collapse, outer layer ejection, and degenerate remnant associated with the typical post red giant cycle. Instead the HSD will be a stable, helium core burning star that is underluminous for its temperature. A thorough analysis of the formation of HSDs via binary interaction can be found in [50, 51]. HSDs are observed with temperatures typically in the 25,000 K to 40,000 K range and with a small radius and mass ($R \approx 0.2R_{\odot}$ and $M \approx 0.5M_{\odot}$). A comprehensive review of HSDs can be found in [52].

Given this evolutionary theory, most HSDs are thought to have companions, with observations generally supporting this idea [53–55], although there is a non-trivial fraction ($\approx 1/3$) of observed single HSDs that are challenging to explain. HSD are observed with companions ranging from white dwarfs up to F stars, and periods from a few hours to several years. HSD binaries include compact degenerate systems, with a few massive systems thought to be potential supernovae progenitors [56–59], and a handful of peculiar systems thought to be very rare merger candidates [20, 60]. Compact HSD systems can also be found with late stellar or brown dwarf companions. The eclipsing type are designated as HW Virs (for a complete list of known solved systems see [61]), and two examples of non-eclipsing, reflection effect systems can be found in [121]. Wider systems with K-type, G-type, and earlier main sequence companions have also been discovered; a proven approach uses photometric color data [122, 123] to identify likely composite sources. Spectroscopic work by [124] revealed some long-period systems with demonstrated double line spectra. Planet companions are thought possible, with a few circumbinary candidates, although none have been demonstrated conclusively. An interesting chronicle of HSD circumbinary planet hunting can be found in [52]. The rich extent of HSD variability allows for testing of formation and evolution theory, and for careful measurement of HSD properties.

HSD binaries are generally placed into two groups based on the nature of the companion interaction during the formation process. Progenitor systems with comparatively smaller and closer companions are thought to be unable to accrete matter (from the hydrogen shell of the red-giant, HSD progenitor) at a fast enough rate to be stable. Referred to as a common envelope (CE), the CE phase will result in matter being ejected during the mass transfer with a resulting loss in angular momentum of the system and a tightening of the binary period. A description of the HSD formation CE channel can be found in [62]. Post CE HSD binaries typically have periods from 2 hours up to 30 days, with a few known exceptionally short period systems. Common companions are M-dwarfs, K-dwarfs, and white dwarfs; although more exotic remnant companions are possible. Progenitor systems with larger and farther companions form the second group of HSD binaries as they are thought to be able to accrete matter at a sufficient rate to avoid substantial mass ejection. This Roche Lobe Overflow (RLOF) formation is credited with producing wider HSD systems [63, 125], containing earlier (G and earlier) main sequence companions with typical periods between 400 and 1600 days. There is a period "gap" between 30 and 300 days with few observed systems in this period range, likely due to differences in the two formation channels.

We have conducted an all-southern-sky (all RA, Dec $< +10°$), bright ($m_V < 15$) HSD survey aimed at finding post CE phase binaries and variables, as well as transiting planets. We use the fast, 2-minute cadence photometric observations from the Evryscope to look for periodic signals in the light curves. The wide-seeing (8150 sq. deg. instantaneous field-of-view (FoV)) Evryscope is a gigapixel-scale telescope that is optimized to find rare, fast transit objects (including compact binaries, short period eclipsing binaries, and planet transits lasting only tens of minutes or less). It is designed for short-cadence observations with continuous all sky coverage and a multi-year-period observation strategy [17, 126]. Most importantly for the HSD search, the Evryscope is highly sensitive to the observationally challenging, approximately twenty-minute duration transits and eclipses expected from HSDs. The continuous, 2-minute Evryscope images ensure the transits are well sampled even at the shortest expected periods. The wide FoV and continuous observing provides light curves for enough bright sources (9.3M with $m_g < 15$M), that we have a substantial number of HSD targets for our survey (several thousand), despite their rarity. The multi-year observing strategy provides tens of thousands of epochs per target, increasing the chance of capturing enough fast transits to enable detections. Our survey covers periods from 2-720 hours, with typical sensitivity to few-percent level variation.

As a complement to the Evryscope light curves, we developed a machine-learning based spectral classifier to help identify potential HSD targets in the Evryscope database, and to provide a confidence level to prioritize discovery followup. A subset of targets is spectroscopically confirmed as a test of the HSD target list performance, and to more accurately estimate the total HSD targets in the survey. The homogeneous, single instrument light curve dataset helps greatly in our estimation of the survey sensitivity, which we combine with the classifier results to estimate occurrence rates for several of the HSD binary types.

The HSD survey in this work identified 117 variables with 79 known and 38 new discoveries (including 14 HSDs). Two of the new discoveries are compact binaries showing strong light curve variation due to ellipsoidal deformation effects from an unseen degenerate companion. Two others are bright, new HW Vir discoveries. The peculiar variability of these systems was a key factor in their discovery, and demonstrates an advantage of the light curve driven HSD survey approach. We also detected 3 planet transit candidates, later shown to be stellar companions. We found several reflection effect HSD binaries, and others with sinusoidal like variability. The survey revealed several other potentially high-priority targets for followup, which we discuss in § 6.5. See Table 6.1 for a summary of the discoveries in this work.

Table 6.1: Survey Detections

Detection	HSD[a]	Other[b]	Total
New Discoveries	14	24	38
Known Recoveries	14	65	79
Total	28	89	117

[a]Spectroscopically confirmed HSDs.
[b]Other stellar type than HSD.

This paper is organized as follows. In § 6.2 we describe the observations leading to the discoveries as well as the variability search including the generation of the target list, survey coverage and estimated number of HSDs. In § 6.3 we detail the detection process and expected recovery based on transit simulations. We show the followup observations in § 6.4 including identification spectra, radial velocity for a select target, and confirmation light curves. The discoveries from the survey are shown in § 6.5, along with the best fit to the photometric variability and ID spectra. We also discuss unique features and characteristics of the discoveries, and suggest additional followup. We discuss the survey sensitivity and the potential for a followup survey in § 6.6, and conclude in § 6.7.

6.2 OBSERVATIONS AND VARIABILITY SEARCH

6.2.1 Evryscope Photometry

The hot subdwarf survey in this work is based on Evryscope photometric observations taken from January, 2016 to June, 2018. The exposure time was 120 s through a Sloan g filter providing an average of 32,600 epochs per target. The wide-seeing Evryscope is optimized to find rare, fast transit objects. It is a robotic 22 camera (each with 29MPix) array mounted into a 6 ft-diameter hemisphere which tracks the sky [17, 126]. The instrument is located at CTIO in Chile and observes continuously, covering 8150 sq. deg. in each 120s exposure. The Evryscope monitors the entire accessible Southern sky at 2-minute cadence, providing tens of thousands of epochs on 16 million sources (with 9.3M sources brighter than 15M in m_g).

Here we only briefly describe the calibration, reduction, and extraction of light curves from the Evryscope; a detailed description can be found in the Evryscope instrumentation paper [126]. Raw images are filtered with a quality check, calibrated with master flats and master darks, and have large-scale backgrounds removed using the custom Evryscope pipeline. Forced photometry is performed using APASS-DR9 [79] as our master reference catalog. Aperture photometry is performed on all sources using multiple aperture sizes; the final aperture for each source is chosen to minimize light curve scatter. Systematics removal is performed with a custom implementation of the SysRem [77] algorithm.

6.2.2 Evryscope Target Search Lists

6.2.2.1 Hot Subdwarfs as a Spectral Type

The HSDs in this work are defined as a spectral type, with the initial selection chosen by color / magnitude space and the final determination decided by surface gravity and temperature obtained from followup spectra. This approach includes the traditional sdB, sdO, and other variants (sdOB, He-sdB, He-sdO), all understood to be evolutionary track driven HSDs. Also included are some extreme horizontal branch (EHB), blue horizontal branch (BHB), post asymptotic giant branch (AGB), and transitioning objects passing through the color magnitude space occupied by sdB and sdO HSDs. The surface gravity and temperature requirements for our sdB and sdO discoveries are $\log g > 4.8$ and $T_{\text{eff}} > 20,000K$, with other exotic HSD discoveries (pre-He WD, BHB, or post-AGB) designated as distinct objects.

6.2.2.2 The Evryscope Hot Subdwarf Search List

The Evryscope hot subdwarf target search list is a combination of four sources: two published lists and two internally generated lists to match our light curve database. All lists are generated using a form of color / color or color / magnitude parameter space selection. Each approach has differences in the data or selection method used, that provide a confidence level (recovery and false positive estimates) unique to the particular approach. Here we define the confidence levels, which we demonstrate in the following sections and use to estimate the number of HSD targets in our survey, as well as to prioritize HSD variable candidates for further followup.

Very High Confidence Level: Target is a member of 3 or 4 of the search lists.

High Confidence Level: Target is a member of both of the GAIA-DR2 [102] based search lists.

Medium Confidence Level: Target is a member of one of the GAIA-DR2 based search lists.

Global Confidence Level: All Targets in the survey regardless of origin.

See the following sections for further search list generation details.

6.2.2.3 Machine-Learning Generated Search Lists

The two internally generated lists for the hot subdwarfs are:

1) A machine-learning based stellar classifier (hearafter the Evryscope Classifier) we developed based on publicly available data from APASS [79] and PPMXL [78], which we use to select hot subdwarf candidates. The Evryscope Classifier is a multi-step machine-learning algorithm that uses reduced proper motion and B-V color differences to determine stellar size and spectral type. When available, we use additional color differences (V-K, J-H, H-K) to determine the luminosity class.

2) A modified version of the Evryscope Classifier that uses GAIA-DR2 [102] data (Evryscope GAIA Classifier), with a similar machine-learning approach but with absolute G magnitude (parallax corrected) and B-R color differences.

Filtering the lists to match our field-of-view (Dec $< +10$) and magnitude range ($m_V < 16$), provides 10,892 and 5957 targets respectively.

6.2.2.4 Published Search Lists

The two external lists for the Hot Subdwarfs are:

1) [82], a composite source based Hot Subdwarf candidate list.

2) A GAIA-DR2 [102] based Hot Subdwarf candidate list [127].

We filter the lists to match our field-of-view (Dec $< +10$) and magnitude range ($m_V < 16$), yielding 1900 and 5963 targets respectively.

6.2.2.5 Evryscope Classifier

We developed a machine-learning based classifier that uses publicly available catalog data to estimate stellar size from a B-V color/magnitude space, and to estimate spectral type from multiple color-differences. All sources in Evryscope database were matched to APASS-DR9 [79] and PPMXL [78] catalogs to obtain reduced proper motion (RPM) and color differences (B-V, V-K, J-H, H-K) for each target. With:

$$RPM = M_V + 5\log(\sqrt{(pm_{ra}^2 + pm_{dec}^2)/1000}) + 5 \tag{6.1}$$

Modifying the method in [98] with a two step machine learning process described below, we classify stars based on B-V and RPM to identify stellar size - main sequence, giants, white dwarfs, or subdwarfs.The RPM and B-V combination provides a high return on our target catalog ($\approx 99\%$ of our targets are classified) and captures spectral information using available data. After the stellar size estimation is completed, the four color differences are used to approximate the spectral type.

In the first step of the machine learning process, we use a support vector machine (SVM) from the SKYLEARN python module [99] to identify likely hot subdwarfs (HSD) from all other stars. The HSD are challenging to separate since they can be close to main sequence B or A stars in this parameter space. We find the SVM to be an effective way to segregate the HSD, shown in the top panel of Figure 6.1 as the small confined area enclosed in the black border. This is done by using a training set of HSD from [82] and other types of stars from SIMBAD [100], filtering the outliers, then computing the contour boundaries. The SVM method is a non-probabilistic two-class classifier that computes a hard boundary (decision boundary) by minimizing the distance (or margin) between the points closest to the boundary. As with any classifier there are missed targets and contaminants, and there are physical reasons the results can be skewed (reddening for example). Our goal in this step is to separate the most challenging class (the HSD) from all the other classes while providing a boundary with a reasonable contingency space to the nearby white dwarf and main sequence regions.

Once the HSD are identified, all remaining objects are classified using a Gaussian Mixture Model (GMM) [99] with three classes to identify white dwarfs, main sequence, and giants. Although not the focus of this work, the solutions to main sequence stars and white dwarfs provide boundaries that are necessary as a comparison check to the HSD boundary from the first machine learning step described in the previous paragraph. We briefly describe the process here and refer the reader to [66] for further details. The GMM method is a best fit to 2-D Gaussian function (probability density function), using the training points (20,972 main sequence, 1515 white dwarfs (WD), and 10,000 giants selected from SIMBAD) to adjust the Gaussian centers, orientations, and elongations. The GMM classifier results are shown in the bottom panel of Figure 6.1. The GMM produces contour lines with Negative-log-likelihood (NLL) values that can be converted ($LH = 10^{-NLL}$) to give an estimate of the confidence level the data point belongs in the class.

We use the spectral type and temperature profiles in [101] to derive a function (using 1-D interpolation) that uses available color differences to derive an estimate for spectral type. The multiple color differences are averaged to choose the closest spectral type and luminosity class. The code produces a function with RPM and color differences inputs and outputs the star size, star type, and NLL score for the GMM step. We used this to select potential HSDs from our input catalog, with the added requirement that the HSD also be apparent spectral type O or B. The added requirements help filter contaminants from main sequence A stars.

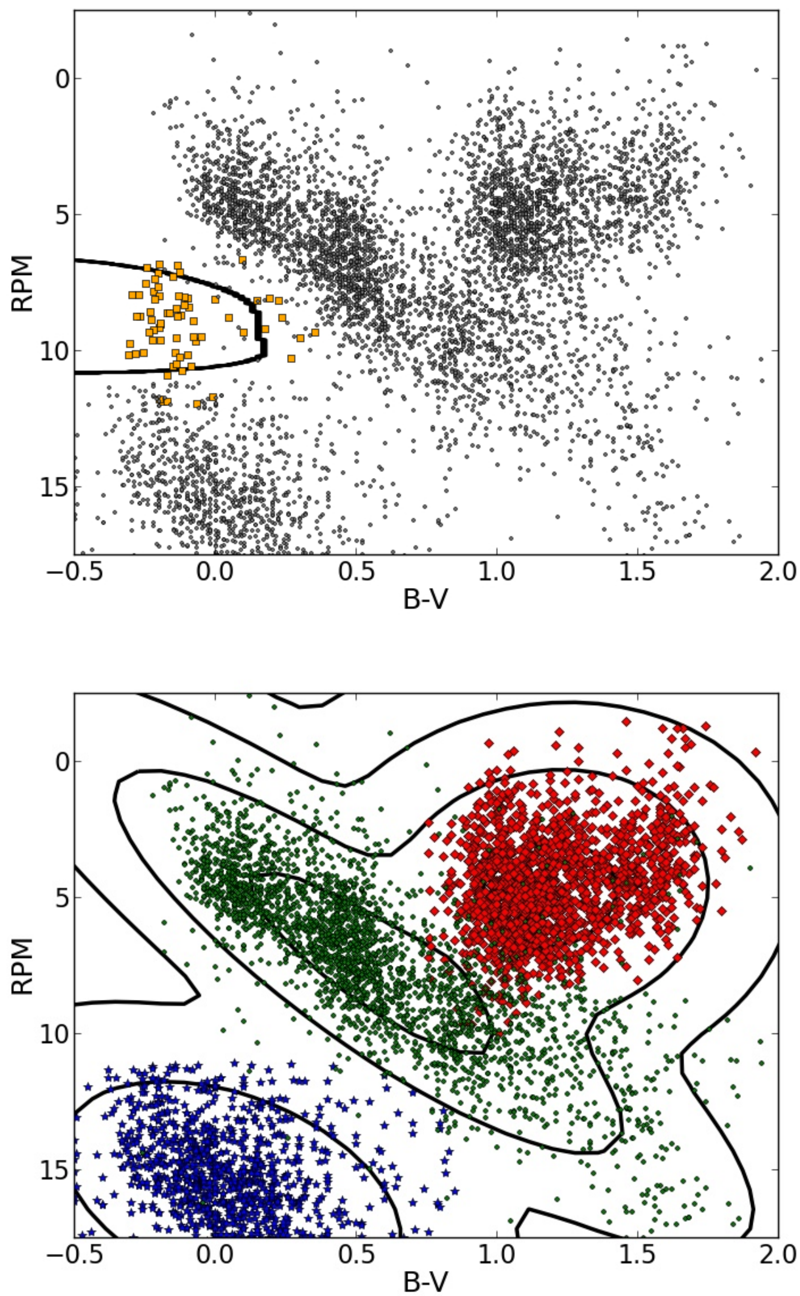

Figure 6.1: The Evryscope Target Classification - We use B-V color differences and reduced proper motion (RPM) data with a two step machine learning algorithm to classify star size. *Top:* the training data (gold squares=hot subdwarfs, grey=all others) for first step, the support vector machine (SVM) which returns the resulting hot subdwarf classification region (the area inside the black border). *Bottom:* the training data (blue stars=white dwarfs, green=main sequence, red diamonds=giants) for second step, the Gaussian Mixture Model (GMM) which returns the resulting classification contours. Negative log likelihood plot-lines 1, 1.7, 2.8 are shown. This figure is originally presented in [66] and reproduced here.

Further details on the design, testing, and performance of the Evryscope Classifier can be found in [66].

6.2.2.6 Evryscope GAIA Classifier

The Evryscope GAIA Classifier uses the GAIA-DR2 G-band absolute magnitude (corrected using only the GAIA-DR2 parallax) and the GAIA-DR2 B-R color. The same support vector machine and Gaussian mixture model machine-learning approach from the Evryscope Classifier (see § 6.2.2.5) is used to define the classification contours. The same training set from [66] is again used, but with the GAIA-DR2 data to generate the G-band absolute magnitude and B-R color space. Here:

$$G_{abs} = G + 5\log(Parallax/1000) + 10 \tag{6.2}$$

6.2.2.7 Classifier Results and Potential Targets

The classifier results are shown in Figure 6.2 with the HSD candidates in gold. We combine these results with external lists (§ 6.2.2.4) to identify objects as likely HSDs. Potential targets for the HSD survey is shown in Figure 6.3; their distribution in RA, Dec, and magnitude are as expected. There are noticeable over-densities in the galactic plane and Large Magellanic Cloud (LMC). HSDs are not expected to be in the galactic plane or LMC at the bright magnitudes in our survey, however a significant number of viable targets should be visible in these fields as foreground stars. We use the results of the Evryscope database query to assist in identifying the HSDs in these challenging regions that are potentially useful to the survey.

6.2.2.8 Light Curve Query

The Evryscope database contains light curves for 9.3M targets with $m_g < 15$, with epochs through 2018. Dimmer sources and latter epochs are currently being processed. We added the additional filter requiring a minimum number of epochs (1000), and discarded sources

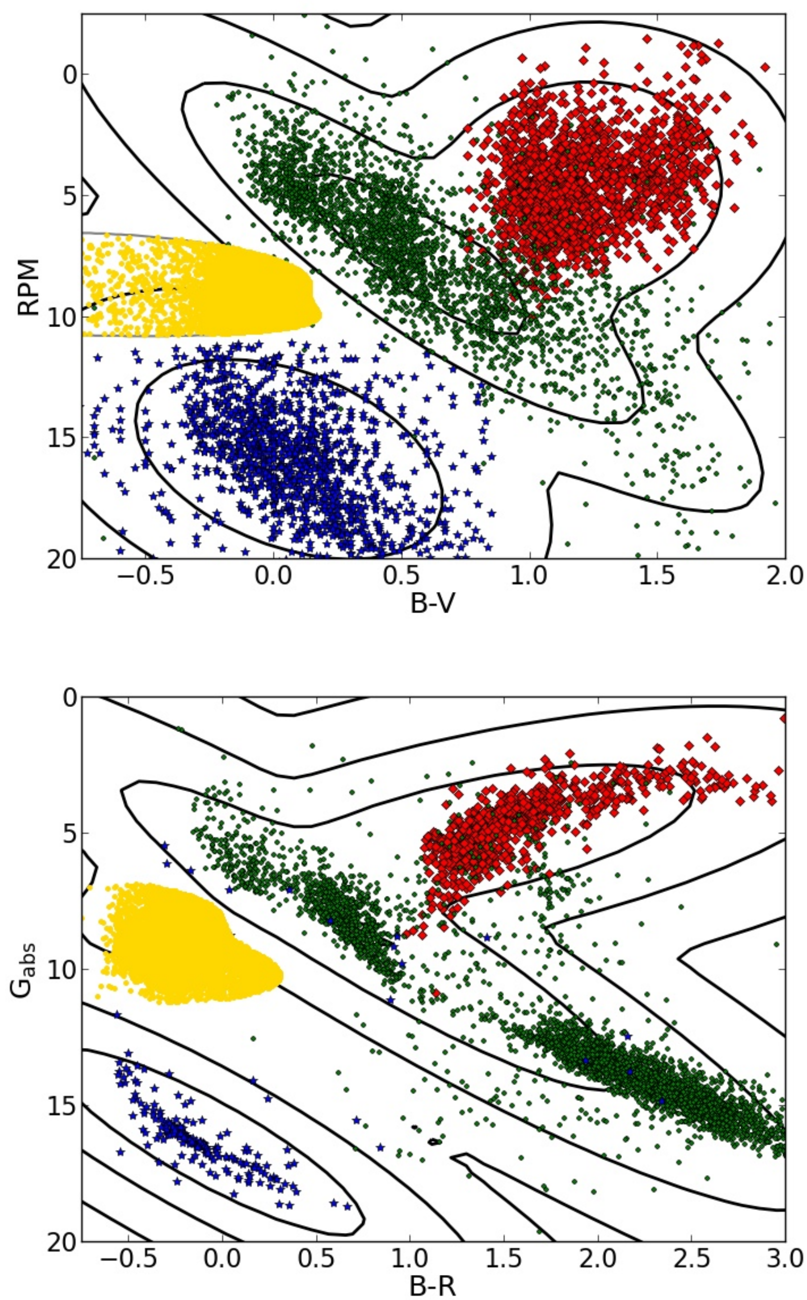

Figure 6.2: The Evryscope Classifiers (see § 6.2.2.5), two step Machine Learning based spectral classifiers used to select HSD candidates. The black contours are the results of the GMM using training data from known giants (red diamonds), main sequence stars (green circles), white dwarfs (blue stars). The potential hot subdwarf (HSD) candidates are identified with a SVM step and are shown as the yellow grouping above the white dwarfs (WD) and to the left of the main sequence stars. *Top:* The APASS / PPMXL based classifier. *Bottom:* The GAIA-DR2 based classifier. We combine these results with external lists (§ 6.2.2.4) to identify objects as likely HSDs and check for photometric variability in the Evryscope light curves.

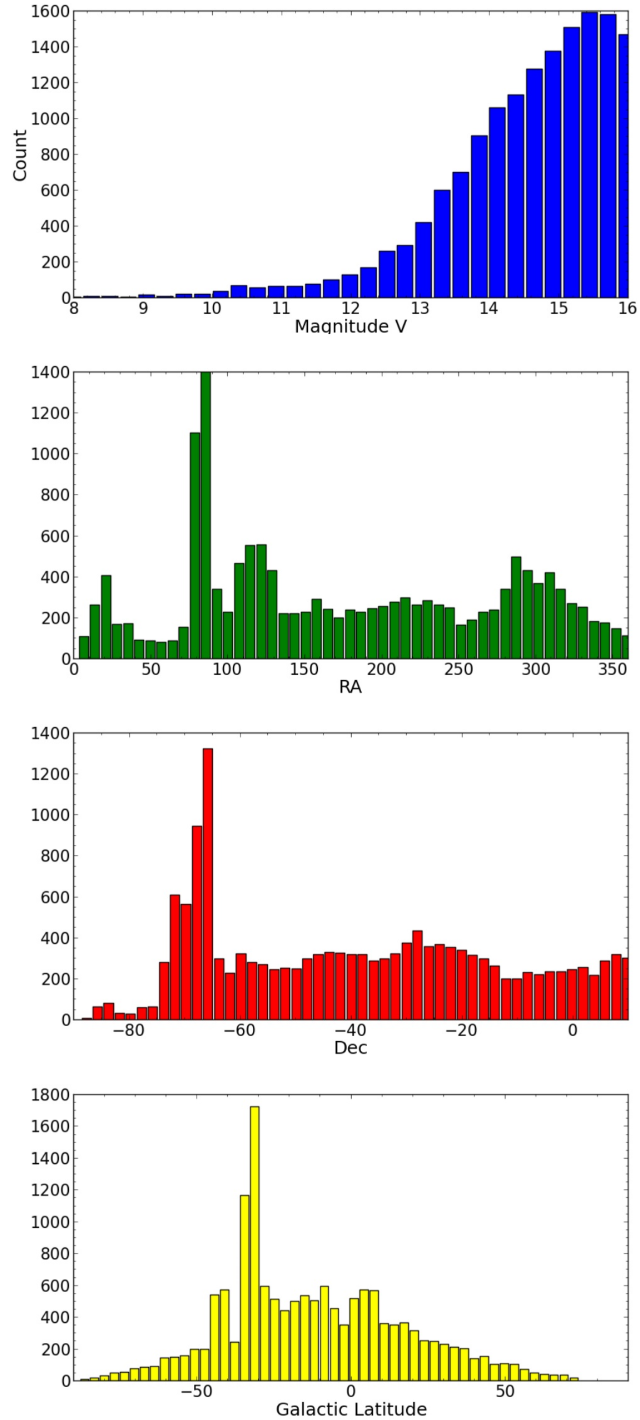

Figure 6.3: The potential hot subdwarf (HSD) targets for the Evryscope survey. The distribution of targets in RA, Declination, and magnitude are as expected but with noticeable over-densities in the galactic plane and Large Magellanic Cloud (RA=80.89 Dec=-69.76). We apply an additional filtering step to flag likely impostor targets, biased toward not eliminating actual foreground HSDs that lie in these regions.

with likely photometry issues, or likely crowding (indicated by excessive flags). The database query returned 11,220 potential HSD light curves from the 18,388 unique potential targets (which extend to $m_v = 16$) identified from the input lists described in the previous sections.

6.2.2.9 Crowded Fields - Galactic Plane and LMC

The crowded fields of the galactic plane and LMC are problematic due to blended sources, high background and increased noise, and the decreased accuracy of color difference measurements. Even with the GAIA-DR2 [102] based data, [127] found an excess density of targets in these fields and a higher rate of false positive HSDs. To address this issue they applied an additional filter in these regions based on excessive variance in the photometric measurements and background noise. [127] also reported the distribution of distances for HSDs for a representative sample in their survey and show that ≈90% of HSDs are within 2 kpc at a limiting magnitude of G=19. Given the galactic plane and LMC distances and the Evryscope HSD survey limit in this work of $m_g < 15$, we do not anticipate detecting any HSDs in these actual regions. However, we do expect some to be in the fields as foreground HSDs, such as AA Dor [128] and in densities similar to the rest of the survey. In general, sources in the galactic plane or LMC fields are expected to be problematic given the Evryscope pixel scale [17]. Evryscope targets in these regions are typically blended sources and the limiting magnitude increases by ≈ 1 mag due to the increased background and other challenges.

To identify HSD impostors in crowded fields we compare the magnitude and coordinates from the input target lists to the values returned by the light curve query. This results in a magnitude error (m_g or m_V from the input lists less the mean Evryscope magnitude from the light curve) and an error in distance (the input list coordinates versus the centroid coordinates of the Evryscope pipeline). We also compare the list magnitude to the distance error. The average accuracy of correct targets is ≈ 1-2 arcsec and is clearly sub-pixel (13.3”). There is a significant bias toward recovering a brighter star indicating the likelihood of missed targets substituted with a nearby bright star (or blended with the nearby bright star so that the light curve is completely dominated by the bright source).

An analysis of the variable candidates from this work revealed that light curves returned from the target search that were more than 3 magnitudes in error or greater than 20 arcsec in distance were more than 90% likely to be a wrong or blended target (referred to hereafter as blended). Applying these criteria to the survey query, 38% of the HSD light curves showed signs of strong blending, with the dimmer sources suffering the greatest contamination. The majority of these blended targets (58% of *blended targets*) are sources in the galactic plane or LMC, expected to be problematic given the Evryscope pixel scale. Said another way, over 90% of returned Evryscope light curves in the HSD survey in galactic plane or LMC regions are blended sources, consistent with the expectations in [17] and with the approximate factor of 10 in overdensity in potential HSDs of these regions in the target lists.

We also note here that the average blended targets rate for sources *not* in the galactic plane or LMC is $\approx 16\%$, in good agreement with predictions [17] for blended sources in the Evryscope images, given the Evryscope pixel scale.

6.2.2.10 Blended Sources

Given the correlation between the likely blended targets identified in § 6.2.2.9 and the galactic plane or the LMC, the all sky blended source agreement with the predictions in [17], and the agreement of overdensity in crowded regions to the blended sources in those regions, we conclude blended sources account for substantially all of the errant light curves and HSD impostors. To complete the survey in this work, two determinations must be made regarding the blended sources. First in regards to the inspection of the light curves and second in regards to estimating the number of HSD targets in the survey.

The light curve query returned 11,220 potential HSD light curves (see § 6.2.2.8), and later in the manuscript (§ 6.6) we show the survey is target limited. Given the manageable number of light curves (each is visually inspected), and the need for targets, we inspect all light curves regardless of likely blended sources. A flag identifies if the source is in a problematic region or with large errors in distance or magnitude. In the event of a discovery, followup work reveals if the system is a HSD. Several discoveries later shown to be rare HSD systems (see § 6.5), were made in crowded fields that would have been missed had these targets instead been eliminated from the light curve query.

In estimating the number of HSD targets in the survey, we use the non-blended sources along with the recovery and false positive rates found in § 6.2.2.11, to determine the likely number of HSDs. We then use the global blended sources rate (16%) and analyze this much smaller group of likely HSDs (but blended with a nearby source) depending on the search type. Although any HSD transit signal would be greatly reduced from the blended brighter source, a fraction of the systems may detectable depending on how much brighter the contaminant is and how deep the variability signal. We discuss the contribution of these blended sources in § 6.6.

6.2.2.11 Testing Spectral-ID Performance

We tested the performance of the source lists in several ways, with the goals of quantifying the recovery rate and the false positive rate in order to estimate the likely HSD targets in our survey. We tested the targets to spectroscopically known HSDs from other works, and to confirmed HSDs from this work. The results are summarized in Table 6.2.

(1) We compare the HSD targets from each list to the spectral type from the SIMBAD database [100]. We require the coordinate crossmatch to be within 25 arcsec, and the magnitude comparison (GAIA m_g or APASS m_V vs SIMBAD m_V where available) to be within 2 magnitudes. For crossmatched targets that have an available SIMBAD SpT (none or N/A are discarded), those with sdB or sdO matched to the lists are counted as recovered and the other spectral types are false positives. The recovery rates increase as the classification requirement is relaxed, however the false positive rate also increases (as expected and shown in Table 6.2). The SIMBAD results show lower false positive rates for HSD's than the other

testing methods (steps 3-4 following), however the comparative pattern between confidence levels is very consistent with the other testing methods. We attribute this difference to the less stringent SIMBAD classification of hot subdwarfs than that of the known HSD systems and spectroscopically confirmed HSD's.

(2) We compare the HSD targets from each list to the spectroscopically verified known HSD's from [129–131]. After filtering to our magnitude and declination range, the same crossmatch and magnitude comparison requirements from step (1) are used to identify which source lists recover the known targets. The recovery rates are shown in Table 6.2.

(3) The HSD survey recovered 79 known variables, described later in the manuscript in § 6.5. Fourteen of these are HSDs and the balance are variables of some other spectral class, the result of misclassification from one of the search lists. The most common contaminates were various variable types (RRlyrae, Cephied, Mira Cet, LPV, CV, and Novae), and the most common stellar contaminates were A and B stars. Of the 14 correctly classified known HSD variables, 9 were from 3 or 4 of the source lists (including both GAIA based lists), 1 originated from two source lists, and 4 appeared on a single list. The recovery rate for the 3 or 4 source based targets and the targets with both GAIA lists is 64.3% (9/14).

Of the 65 misclassified known recoveries, none are classified on 3 or 4 of the lists. Five are classified with both GAIA based lists, and the remaining 59 are only classified from a single list (15 from the Geier GAIA list, 17 from the ES GAIA list, and the rest from the APASS/PPMXL based list). The false positive rate for the 3 or 4 source based targets is 0%, 35.7% (5/14) for targets appearing in both GAIA based lists, while individual lists show a false positive rate of greater than 60%.

(4) Select HSD variability discoveries from this work (see § 6.3) are spectroscopically confirmed by ID spectra taken with the SOAR 4.1 m telescope at Cerro Pachon, Chile with the Goodman spectrograph [33]. The results of the classification from the spectra are compared to each of the source lists. The spectra provide a wavelength coverage of 3700-6000 Å with a resolution of 4.3 Å. The prominent hydrogen and helium features are easily identified and

measured, along with the temperature from the continuum. Full details of our instrument setup and processing pipeline are provided in [66].

We obtained ID spectra for 36 of the discoveries, 12 are confirmed HSDs, and 24 are not HSDs (mostly main sequence B stars). Of the 12 correctly classified known HSD variables, 9 are from 3 or 4 of the source lists, and 10 are from both GAIA based lists; 11 are from the [127] GAIA based list, and 10 are from the Evryscope GAIA classifier. The recovery rates for the 3 or 4 source based targets and the targets with both GAIA lists are 75.0% (9/12) and 83.3% (10/12). Targets from a single GAIA list return 91.7% (11/12) and 83.3% (10/12). The other lists show less return that the GAIA based lists; similar to the test of spectroscopically confirmed targets and known recoveries described in the previous paragraphs.

Of the 24 misclassified targets, one is classified on 3 or 4 of the lists and 4 with both GAIA based lists. The individual GAIA based lists have 13 and 14 misclassifications. The false positive rate for the 3 or 4 source based targets and for targets from both GAIA based lists is 10% and 28.6%. The false positive rate for the GAIA based list and the Evryscope GAIA classifier are 54.2% (13/24) and 58.3% (14/24).

The target selection performance is summarized in Table 6.2.

6.2.2.12 Other Considerations

The primary challenge of selecting the targets (common to all of the methods), is balancing the missed targets with the false positives. The [127] GAIA based list very effectively selects HSD candidates with a fraction of contaminants; they estimate the primary contamination is from cool stars, blue horizontal branch, and post-AGB stars. We measure the false positive rate to be 47% (see Table 6.2) in our FoV and magnitude range, reasonable given the difficulty in separating HSDs from impostors. The Evryscope GAIA classifier uses an alternate color space and different selection approach to include some extra candidates and exclude others. The Evryscope APASS / PPMXL based classifier has a higher contamination rate, but includes more potential targets and it is the same source catalog we use for our forced

Table 6.2: Testing Target List Performance in Identifying HSDs

Comparison Test	Confidence Level	List Requirement	Recovery	Rate	False Positive	Rate
(1) SIMBAD SpT (sdB/sdO)	Very High	3 or 4 source lists	845/1199	70.5%	39/884	4.4%
	High	Both GAIA based lists	988/1199	82.4%	100/1088	9.2%
	Medium	Geier GAIA List	1155/1199	96.3%	381/1536	24.8%
	Medium	Evryscope GAIA List	1012/1199	84.4%	352/1364	25.8%
	Global	All targets	1199	–	1639/2838	57.8%
(2) Spectroscopically Known HSD's	Very High	3 or 4 source lists	97/140	69.3%	–	–
	High	Both GAIA based lists	123/140	87.9%	–	–
	Medium	Geier GAIA List	136/140	97.1%	–	–
	Medium	Evryscope GAIA List	126/140	90.0%	–	–
	Global	All targets	140	–	–	–
(3) Recoveries of known variables						
(this work)	Very High	3 or 4 source lists	9/14	64.3%	0/9	0%
	High	Both GAIA based lists	9/14	64.3%	5/14	35.7%
	Medium	Geier GAIA List	9/14	64.3%	15/24	62.5%
	Medium	Evryscope GAIA List	9/14	64.3%	17/26	65.4%
	Global	All targets	14	–	65/79	82.3%
(4) Spectroscopically Confirmed						
(this work)	Very High	3 or 4 source lists	9/12	75.0%	1/10	10.0%
	High	Both GAIA based lists	10/12	83.3%	4/14	28.6%
	Medium	Geier GAIA List	11/12	91.7%	13/23	54.2%
	Medium	Evryscope GAIA List	10/12	83.3%	14/24	58.3%
	Global	All targets	12	–	24/36	66.7%
Test Summary (Averaged Values)	Very High	3 or 4 source lists	–	70%	–	5%
	High	Both GAIA based lists	–	79%	–	24%
	Medium	Geier GAIA List	–	87%	–	47%
	Medium	Evryscope GAIA List	–	81%	–	50%
	Global	All targets	–	all	–	69%

See § 6.2.2.11 for further details.

photometry pipeline. The HSD survey in this work is target limited, and benefit from the extra potential targets. Additionally, we developed a few ways to segregate the likely targets from the impostors.

A powerful feature of our target selection method is the duplication of sources. Based on the list performance false positive results discussed above and shown in Table 6.2, candidates identified in 3 or 4 of the lists are greater than 90% likely to be HSDs. Candidates with both GAIA based sources are greater than 70% likely to be HSDs. Using this along with the recovery rates, we identify the high-likelihood targets and estimate the total number of HSDs in our search.

The compact nature of HSDs drives the transit and eclipse times. They are expected to be fast ($\approx$ 20 minutes) with deep depths. A light curve from an eclipsing binary with a main sequence A star would have a much longer (3-4 hour) eclipse time indicating the target is likely to be a HSD imposter, even more so if the classifier results are marginal. Eclipsing binary candidates in this work with marginal classifier results and long eclipse durations were identified as low-priority followup (given the HSD focus of our search), and presented in the appendix.

6.2.2.13 Summary of Targets

To estimate the likely number of targets from each survey, we begin with the number of light curves returned from the database query for each classifier confidence level. The totals are adjusted by the likely blended targets fraction. From the rates in Table 6.2, we calculate the average recovery and false positive values per confidence level. We divide the adjusted number of targets by the recovery rate and subtract the false positives to estimate the total sources. A summary of the HSD targets is shown in Table 6.3.

Table 6.3: Survey Targets

HSD				
Total Targets	Confidence	Recovery	False Positive	Likely HSDs
1071	Very High[a]	70%	5%	1203
1843	High[b]	79%	24%	1087
3497	Medium[c]	87%	47%	1314
3465	Medium[d]	81%	50%	1341
11,220	Global	all	69%	2167
Survey				1422 ±428

[a]Requires targets selected from 3 or 4 source lists (see § 6.2.2.11).
Note: The very high confidence level likely HSD number is extrapolated, since the false positive rate is much lower than the missed targets (1-recovery) rate.
[b]Requires targets selected from both GAIA based source lists.
[c]Requires targets selected from the Geier GAIA based source list.
[d]Requires targets selected from the ES GAIA based source list.
See § 6.2.2.13 for calculation of Likely HSD's

6.2.3 HSD frequency

The Evryscope database contains 9.3 million light curves for stars brighter than 15.0M in m_g, and we estimated that 1422 of these are hot subdwarf stars. The HSD frequency is $1422/9.3M$ or $\approx$ 1 in 10,000 stars in the Evryscope field are HSDs. A space-density conversion is beyond the scope of this paper as the primary goal here is searching for photometric variation. In § 6.6.3.1 we discuss the followup HSD survey (Evryscope HSD survey 2) to this work, which will be expanded in FoV (North and South all-sky coverage), limiting magnitude, and observational coverage. We will estimate the space-density in the Evryscope HSD survey 2.

6.2.3.1 Survey Completeness

From the classifier testing described in § 6.2.2.11 (methods (1) and (2)) we compare the total HSD recovered to the total available in our magnitude and declination range. This leads to SIMBAD completeness rate of 80% (1199 / 1499) for the HSD survey. The confirmed spectra completeness rate is 86% (140 / 162). We average these rates and decrease the results by the likely wrong target fractions from the previous section to estimate the completeness of 51% for southern sky targets brighter than 15.0M in m_g for the HSD survey.

6.3 Detection of Variables

6.3.1 Detection Process

All of the 11,220 potential HSD light curves were visually inspected for variability. The classification confidence level and distance flags are included for each source to help evaluate the likelihood the target is a HSD and to prioritize followup. Prior to inspection, the light curves were first processed to remove systematics and identify nearby reference stars for comparison as described below.

The timestamps in the Evryscope light curves were converted from Modified Julian dates to Heliocentric Julian dates using PyAstronomy's *helCorr* function. We pre-filtered the light curves with a Gaussian smoother to remove variations on periods greater than 30 days, and a 3rd order polynomial fit was subtracted to remove long-term variations. Light curves were then searched for transit-like, eclipse-like, sinusoidal and quasi-sinusoidal variability signals using the Box Least Squares (BLS) [28, 29] and Lomb-Scargle (LS) [30, 31] algorithms, along with a custom search tool (the outlier detector, see § 6.3.2.2) designed to find fast transits characteristic of HSDs. Details of the algorithm settings are described in the following sections.

The target light curve (both folded and unfolded) is compared to nearby reference stars for any indications that the detected signals may be systematics. The plots are colored by time to check how well-mixed the detection is, since a transit or eclipse with only a few occurrences is more likely to be an artifact of the detection algorithm. All detections are filtered to mask likely daily-alias periods indicative of systematics as described in [66]. The power spectrum of each detection algorithm is displayed for each target, however we do not filter by power. All targets are visually inspected, as we wish to search potential candidates since lower detection signals may be indicative of shallow transits or fast transits with only a few periods captured. Variability candidates were then vetted with a separate reviewer confirming the candidate light curves.

6.3.2 Variability Search Algorithms

6.3.2.1 Conventional Search Algorithms

We tested different BLS settings to maximize the recovery rates on Evryscope light curves in [66], a variability survey of the southern polar region (Evryscope polar search). The HSD survey features longer light curve coverage (2.5 years compared to 6 months in the polar search), and the variability signals are expected to be faster. Consequently, we extended the period coverage and retested the settings on known variables in our magnitude range, with amplitudes we expected to find in the HSD surveys (0.01 to 0.50 in fractional normalized intensity). We verified the setting adjustments did not hinder detection performance at the shorter periods, as demonstrated in Figure 6.4. The final BLS settings used on the HSD search were a period range 2-480 hours with 50,000 periods tested and a transit fraction of 0.01 to 0.25. We used an LS range of 2-720 hours.

The lower period cutoff in the BLS and LS period range does not preclude us from finding one hour signals or less as aliases of the true period, demonstrated by our recovery of the known 1.17 hour system CD-30 11223 shown later in the manuscript (see § 6.5). Very short period binaries (with tens-of-minutes periods) would benefit from additional systematics processing and modified detection algorithms. We discuss these modifications and the potential very short period search in § 6.6.3.

6.3.2.2 The Outlier Custom Search Algorithm

HSD transits are expected to be fast (on the order of tens-of-minutes), and deep (up to completely eclipsing if the orientation is optimal, e.g.: Konkoly J064029.1+385652.2 [132]). Even with periods as short as a few hours, the transit fraction is still small, and the most

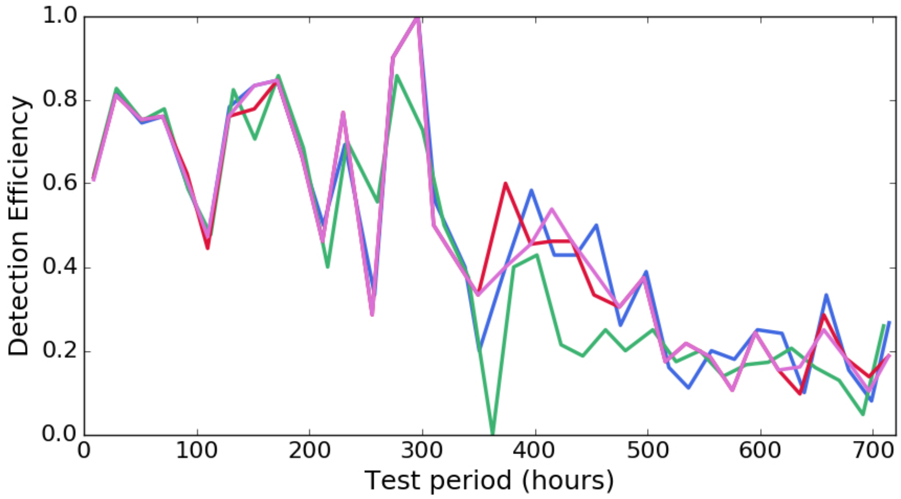

Figure 6.4: Detection efficiency of known variables in the FOV, magnitude, and amplitude ranges of the HSD survey with different BLS and LS settings. Green line: BLS maximum period 240 hours, number of periods 25,000, and LS maximum period of 720 hours. Blue line: BLS maximum period 480 hours, number of periods 50,000, and LS maximum period of 1440 hours. The red and magenta lines hold the same long period BLS and LS settings, but with coarse period sampling shown in the red (25,000) and finer period sampling shown in the magenta (100,000). These tests on known variables helped establish the transit fraction and number of periods in order to effectively cover the period search range of 2-720 hours. We used simulated transits in § 6.3.3 to confirm the final settings.

significant points in the light curve are very dim outliers. This situation is quite different than the traditional shallow (less than 1%) and longer (at least a few hours) transits BLS was designed to find, and completely different than the sinusoidal signals LS excels at. We developed a custom code, called the outlier detector, to find the narrow and deep signals characteristic of HSD transits. Although not the focus of this survey, transits of white dwarfs are expected to be even faster (on the order of a few minutes) than HSD transits and also very deep. The outlier detector was developed to find both HSD and WD transit signals, given the similarities. The results of our WD transit survey will be discussed in an upcoming work (Ratzloff et al., in prep).

The outlier detector uses several iterative approaches to search for fast transits. The light curve is normalized (in flux), then the 1-σ error is computed. Data points with a normalized flux value of 3-σ below the mean are flagged. The number of flagged points is compared to a minimum value (set by the survey type, periods searched, and expected variability). For the

HSD search, the minimum value is 50 (determined by requiring at least 5 transits with each 20 minute transit consisting of 10 data points given the Evryscope's 2-minute cadence). If the number of flagged points is less than the minimum value, the processed is restarted using 2.9-σ and continues with .1 reductions in the σ requirement until the minimum number of flagged points is met. In almost all cases where there is an actual fast, deep transit (from astrophysical or simulated signals) the original 3-σ cutoff selects many more points than the minimum value given the tens of thousands of epochs in the typical Evryscope light curve. This initial iterative process helps the limiting case of a long period, fast transit that may only have a few transits even in a multi-year light curve.

The flagged points (i.e. the outlier points) are then kept and all other points discarded for the next steps. The outlier points are then phase folded at 250,000 different periods (spread evenly in period space) in the test period range. For both the HSD and WD searches, we tested periods from 2-480 hours. For each period, we calculate the standard deviation in *phased-time*, without regard to the normalized flux of the outlier points. The first step (described in the previous paragraph) set the outlier points, here we are only interested in how well the points align in phased-time. We then sigma-clip the outlier points (using 3 iterations and 2-σ from the mean in phased-time). This sigma-clip step helps remove errant low flux points not associated with the periodic signal. We recalculate the standard deviation in *phased-time* of the sigma-clipped outlier points. The period with the lowest standard deviation, calculated in this way, is selected as the best period.

The same process is repeated for a smaller range ($\pm$ 3 minutes centered on the best period), testing 5000 periods, but in finer increments than in the previous step. This fine period step narrows the detection period, and increases the accuracy to levels necessary in very short period HSD and WD systems.

An example detection from outlier detector for the known short period HSD system HW Vir is shown in Figure 6.5. The best detection is the minimum spike (the period phase-folded with lowest standard deviation of the outlier points) at the 2.80126 hour period. Here, the deep transit (≈ 0.50) of the primary drives the detection, the variation from the secondary or the reflection effect is inconsequential.

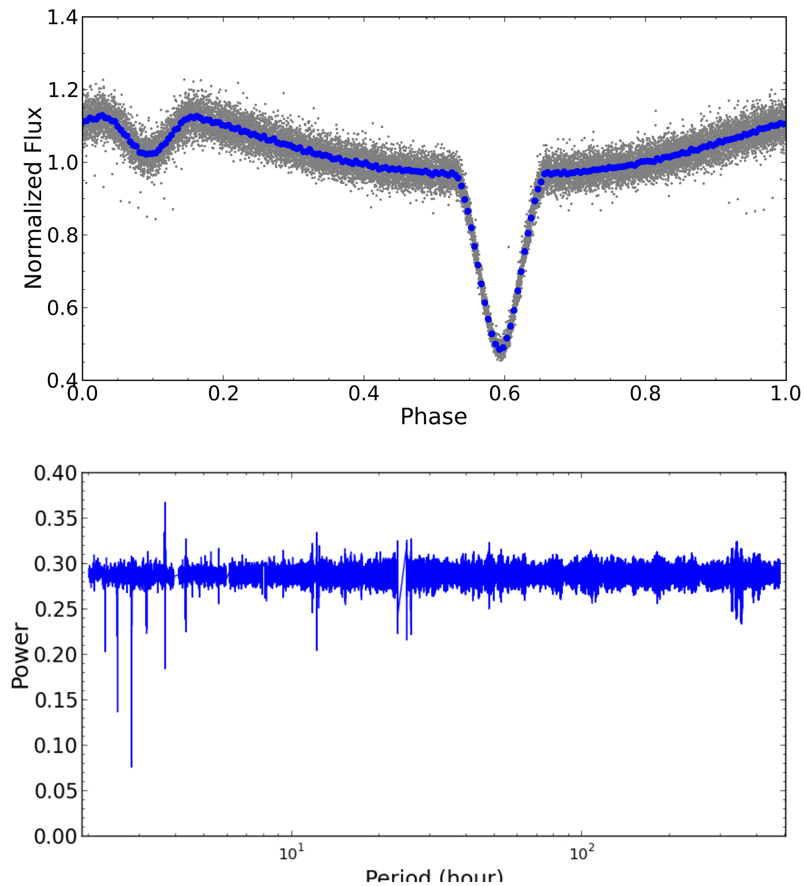

Figure 6.5: *Top:* The Evryscope light curve of the known HSD system HW Vir folded on its period of 2.80126 hours. Grey points = 2 minute cadence, blue points = binned in phase. *Bottom:* The outlier detector (the fast-transit algorithm § 6.3.2.2 designed for the HSD and WD surveys) power spectrum with the minimum spike at the 2.80126 hour detection.

The outlier detector uses only a subset of points significantly below the mean flux value as it tests the best fit over the period range. This lessens the processing burden since the many fold periods are tested with a much smaller number of data points. The outlier detector code is optimized for speed and takes ≈ 5 seconds to run on an average Evryscope light curve (similar to BLS and LS). Expressing the power in terms of the standard deviation in phased-time has the added benefit of stabilizing the test space - periods with no particular signal cluster around .3 since the range is between 0 and 1 and in this situation the mean is

.5. Alias periods tend to be suppressed or score poorly since the standard deviation of the outlier points in this situation is increased. In light curves with deep, fast transits the outlier detection signal tends to be sharp and separated from the noise floor.

6.3.3 Search Algorithm Performance

We use 150 Evryscope light curves, distributed in magnitude, RA, and Dec, as the basis for testing our search algorithm performance. Since the planet transit signals are the most difficult to recover, we developed the custom search algorithm to find the fast and deep planet transits. The HW Vir type eclipsing binaries are recovered more easily due to the larger companion. HSD transit signals are injected onto the Evryscope light curves for a variety of planet sizes and periods. To create the transit signals, we assume a uniform source and use the analytical solution from [133] to generate a transit curve for each planet size and period. We use 250 points per transit (which translates to $\approx$ 5 seconds in time between points and varies slightly depending on the period) to ensure a fine sampling that captures the ingress, transit, and egress features. We then repeat the generated transit curve to cover the complete time coverage of the Evryscope light curves. The generated transit curve points are then averaged in groups to match the Evryscope integration time 2 minutes, typically with $\approx$ 25 points averaged to simulate a 2 minute epoch. We choose a random point in the first period of the generated transit curve and assign it to the Evryscope timestamp; all other times are propagated from this initial epoch. Matching times in the generated transit curves and the Evryscope light curves are then multiplied (in normalized flux) so that any transit values are injected into the Evryscope light curves, while preserving variation from the actual light curves.

The HSD simulations assume a star size of 0.2 $R_{\odot}$. For each planet size, the period search range is split into 100 test periods. We perform 15 iterations at each test period (each iteration adjusted with a random variation of $\pm$ 1 %), for each light curve, and test if the transit is detected. A detection is counted if either BLS, LS, or the outlier detector finds the period or an alias (half, 1/3, 1/4 or double, triple, or quadruple the period) within 1% of the correct period.

We used 5 planet sizes to test the HSD recovery rates, ranging from Earth to Super-Jupiter size, with 1.1M simulations performed. Each simulation takes approximately 25 seconds, requiring 7500 hours of computing time, which we performed with a 16 core / 32 thread machine with an Intel(R) Xeon(R) Gold 6130 CPU @2.10GHz and 128 GB of DDR4-2666 RAM. From these tests, we expect high sensitivity to gas giant planets with periods up to at least 250 hours, with decreasing recovery at longer periods and smaller planets. The detection efficiency tests are shown in Figure 6.6. We note the detection floor is near a Neptune size planet for all but the shortest periods. The simulation results here assume an inclination angle of $i = 90°$, and are the maximum expected recovery values. Further in the manuscript in § 6.6, we calculate the transit fraction and propagate the final detection probabilities and survey sensitivities per planet size.

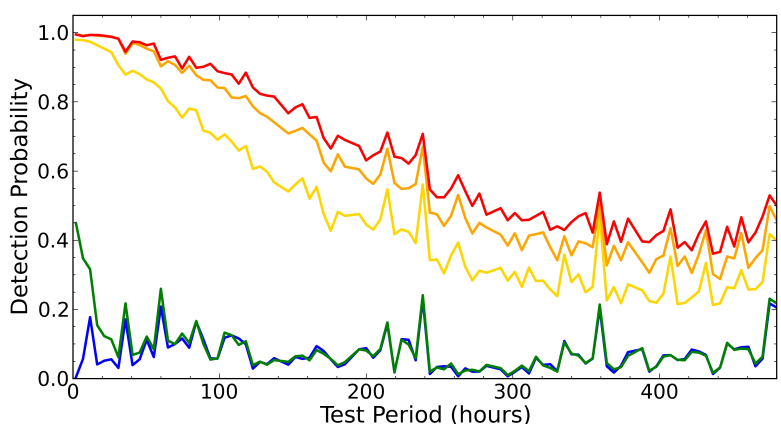

Figure 6.6: The simulated recovery of HSD transiting planets with the Evryscope light curves and detection algorithms. The simulated transits are shown in decreasing size from red to blue. Red = late M-dwarf or brown-dwarf (.15 $R_\odot$), orange = Super-Jupiter (.125 $R_\odot$), yellow = Jupiter (.1 $R_\odot$), green = Neptune (.035 $R_\odot$), blue = Earth (.01 $R_\odot$). The simulation results here assume an inclination angle of $i = 90°$. In § 6.6, we calculate the transit fraction and survey sensitivity per planet size.

6.3.4 False Positive Tests

To test the discovery candidates, we compare the target light curve to the light curves from nearby reference stars looking for signs of similar variation indicative of systematics. We also check how well mixed in phase the detected period is, looking for data gaps or poor mixing that might be a result of the matched-filter fitting to systematics instead of an astrophysical signal. A separate researcher reviewed all the discovery candidates, and those with suspect quality or detection were thrown out. Additional details of the false positive tests performed by the Evryscope lab are available in [66]. All discoveries in this work were folded on alias periods (half and double of the detected period) looking for additional signs of systematics, and to verify the correct period.

6.4 FOLLOWUP OBSERVATIONS AND ANALYSIS

6.4.1 SOAR / Goodman ID Spectroscopy

We obtained spectra for select HSD variability candidates on February 9, 2019, March 5, 2019, August 2, 2019, and September 9, 2019 with the Goodman spectrograph [33] on the SOAR 4.1 m telescope at Cerro Pachon, Chile. We use the 600 mm^{-1} grating blue preset mode, 2x2 binning, and the 1" slit. This configuration provided a wavelength coverage of 3500-6000 Å with a spectral resolution of 4.3 Å (R$\sim$1150 at 5000 Å). We took four 360 s spectra of all targets and the spectrophotometric standard star BPM 16274. For calibrations, we obtained 3 x 60 s FeAr lamps, 10 internal quartz flats using 50% quartz power and 30 s integrations, and 10 bias frames.

We processed the spectra with a custom pipeline written in Python; designed to extract, wavelength calibrate, and flux calibrate the spectra (optimized for this wavelength coverage and instrument setup). For additional details, we refer the reader to [20], where the pipeline is explained fully. We detect strong H Balmer lines in all variability candidates and He lines in many. Each spectrum was visually inspected and fitted using the stellar atmosphere model service for early type stars from *Astroserver*[3] [35]. From the best fits, we measure the effective temperature, surface gravity, projected rotational velocity, helium abundance and approximate the metallicity. For the metallicity, we use the C, N, and O abundances as a proxy. From these parameters we determine the spectral type. Discoveries determined to be HSDs are presented later in the manuscript in the top panel of Table 6.10, and the false positives (main-sequence B stars in almost all cases) are shown in the the bottom panel of the same table. The spectra and best fits for the subluminous stars are shown in Figure 6.7 and HSD imposters (mostly main sequence B stars) are shown in Figure 6.8. The spectrum for a potential debris disc is shown in Figure 6.9.

6.4.1.1 ID Spectra Analysis with Astroserver

The *Astroserver* service uses XTgrid [131] which has been developed to automate the spectral analysis of early type stars with Tlusty/Synspec [134–136] non-Local Thermodynamic Equilibrium (non-LTE) stellar atmosphere models. The procedure applies an iterative steepest-descent chi-square minimization method to fit observed data. It starts with a initial model and by successive approximations along the chi-square gradient it converges on the best fit. The models are shifted and compared to the observations by a piecewise normalization, which also reduces systematic effects, such as blaze function correction, or absolute flux inconsistencies due to vignetting or slit-loss. XTgrid calculates the necessary Tlusty atmosphere models and synthetic spectra on the fly and includes a recovery method to tolerate convergence failures, as well as to accelerate the converge on a solution with a small number of models.

During parameter determination of hot stars the completeness of the opacity sources included, and departures from LTE are both important for accuracy. We concluded that Tlusty models with H, He, C, N and O composition deliver reliable results given the spectral resolution, coverage and signal-to-noise of the survey data. Although Mg and Si lines are

[3] http://www.astroserver.org

visible in many spectra, these elements have relatively small effects on the atmospheric structure compared to C, N and O.

Parameter errors are evaluated by mapping the chi-square statistics around the solution. The parameters are changed in one dimension until the 60% confidence limit is reached. Correlations near the best-fit values are also included in the final results as demonstrated for surface temperature and gravity for a representative example and shown in Figure 6.10.

6.4.2 TESS Photometry

HSD variable discoveries were confirmed with TESS light curves (where available) using the ELEANOR pipeline [137]. We used the PSF photometric setting for bright stars ($m_g < 12.0$) and the standard aperture setting for all other targets. We also verified there was not a significant light curve variation between the different settings. The ELEANOR pipeline data are from TESS full frame images (FFI) with a 30 minute cadence. For one of the discoveries (EC 01578-1743 see § 6.5.4) we instead used the available TESS TOI light curve, which has a 2 minute cadence. The TESS followup and Evryscope discovery light curves are shown later in the manuscript.

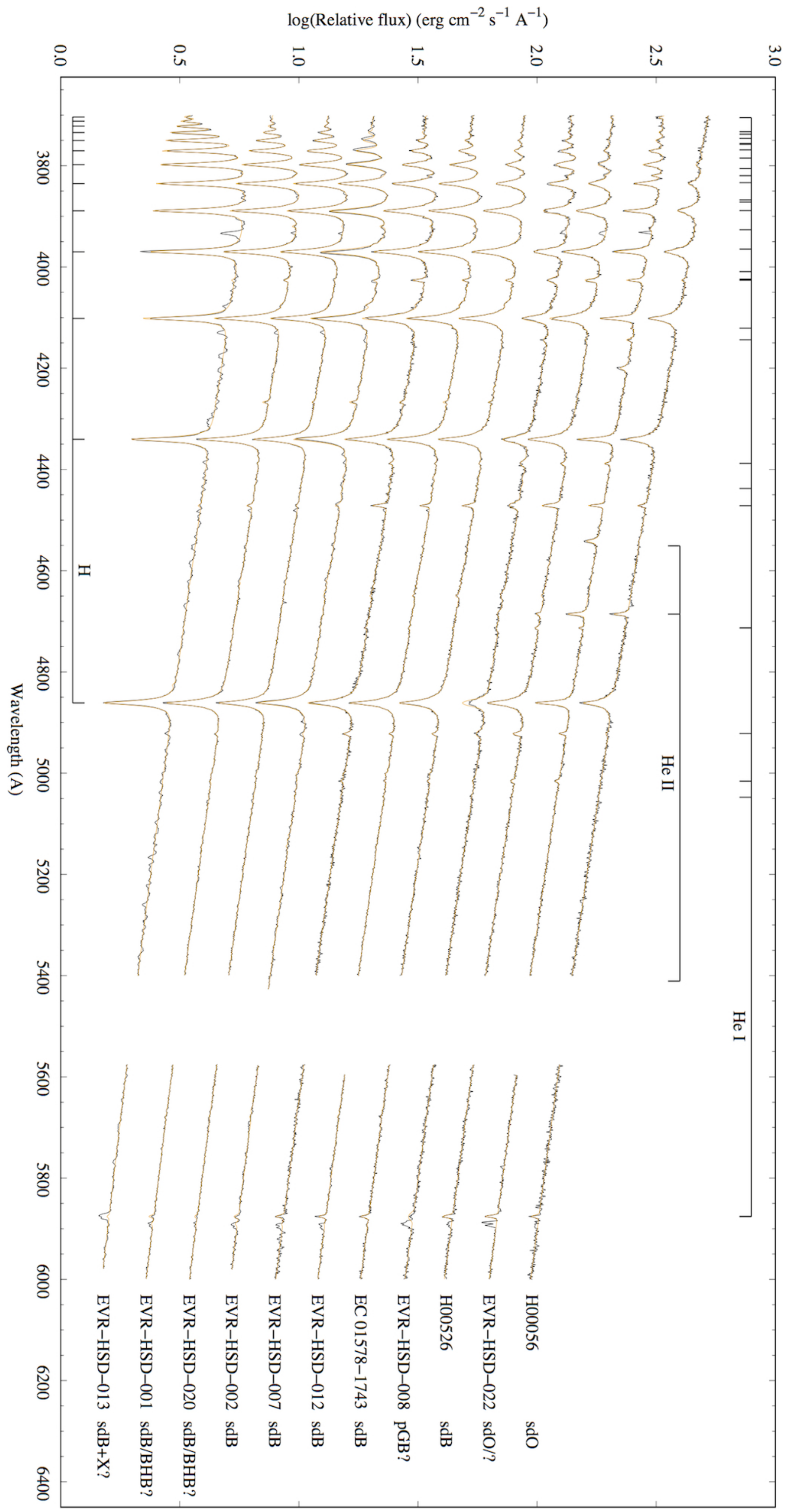

Figure 6.7: Subluminous stars (black) in the EVERYSCOPE sample together with their best-fit TLUSTY/XTGRID models (orange). The sample covers a wide range of objects along the blue horizontal branch from 20,000 K to 45,000 K surface temperature and gravity $\log g > 4.6\,\mathrm{cm\,s^{-2}}$. The observed continua have been adjusted to the models to improve the figure.

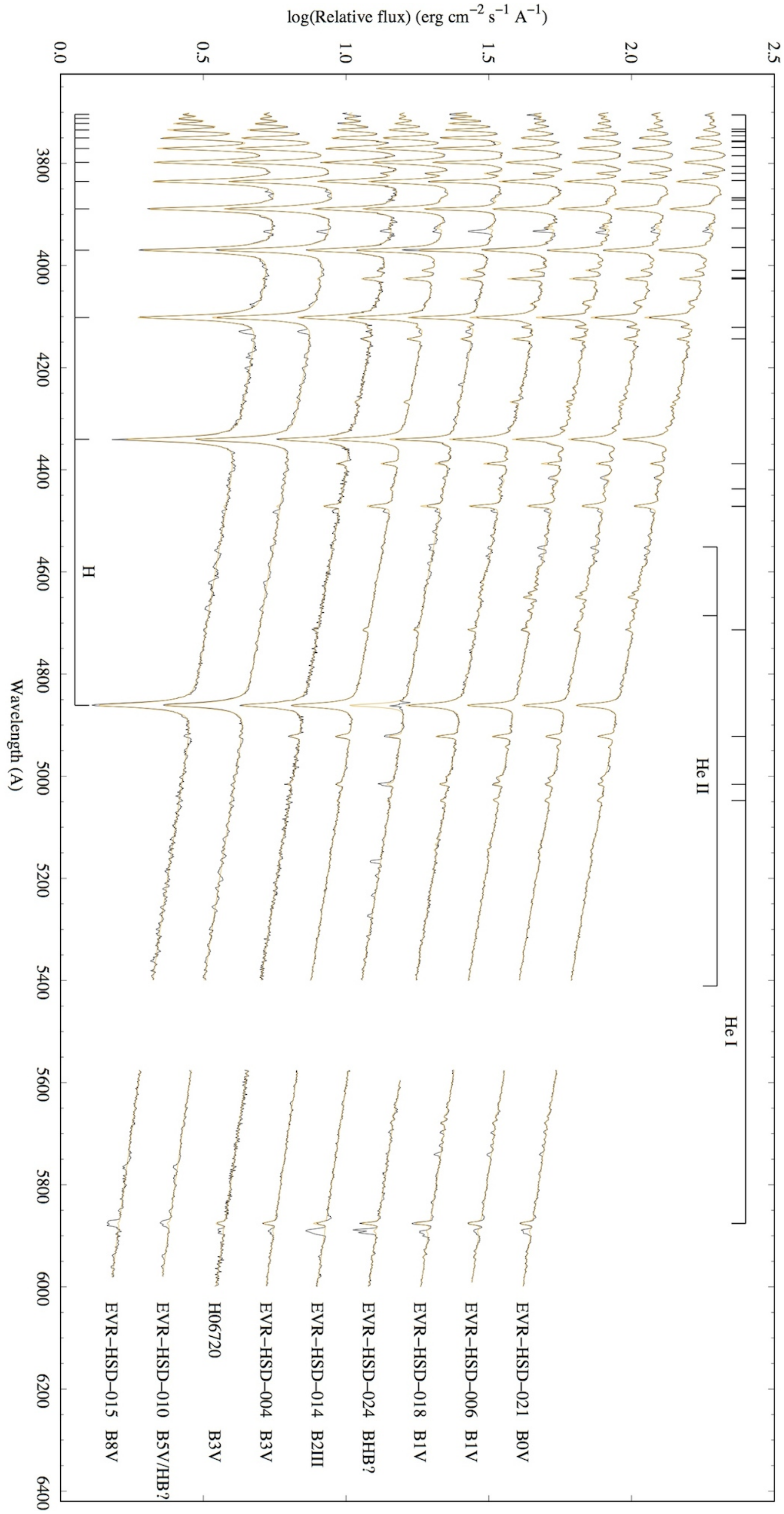

Figure 6.8: Main sequence O and B type stars (black) in the Everyscope sample together with their best-fit Tlusty/XTgrid models (orange). The sample covers a wide range of objects from 12,000 K to 55,000 K surface temperature and gravity $\log g < 4.5\,\mathrm{cm\,s^{-2}}$. The observed continua have been adjusted to the models to improve the figure.

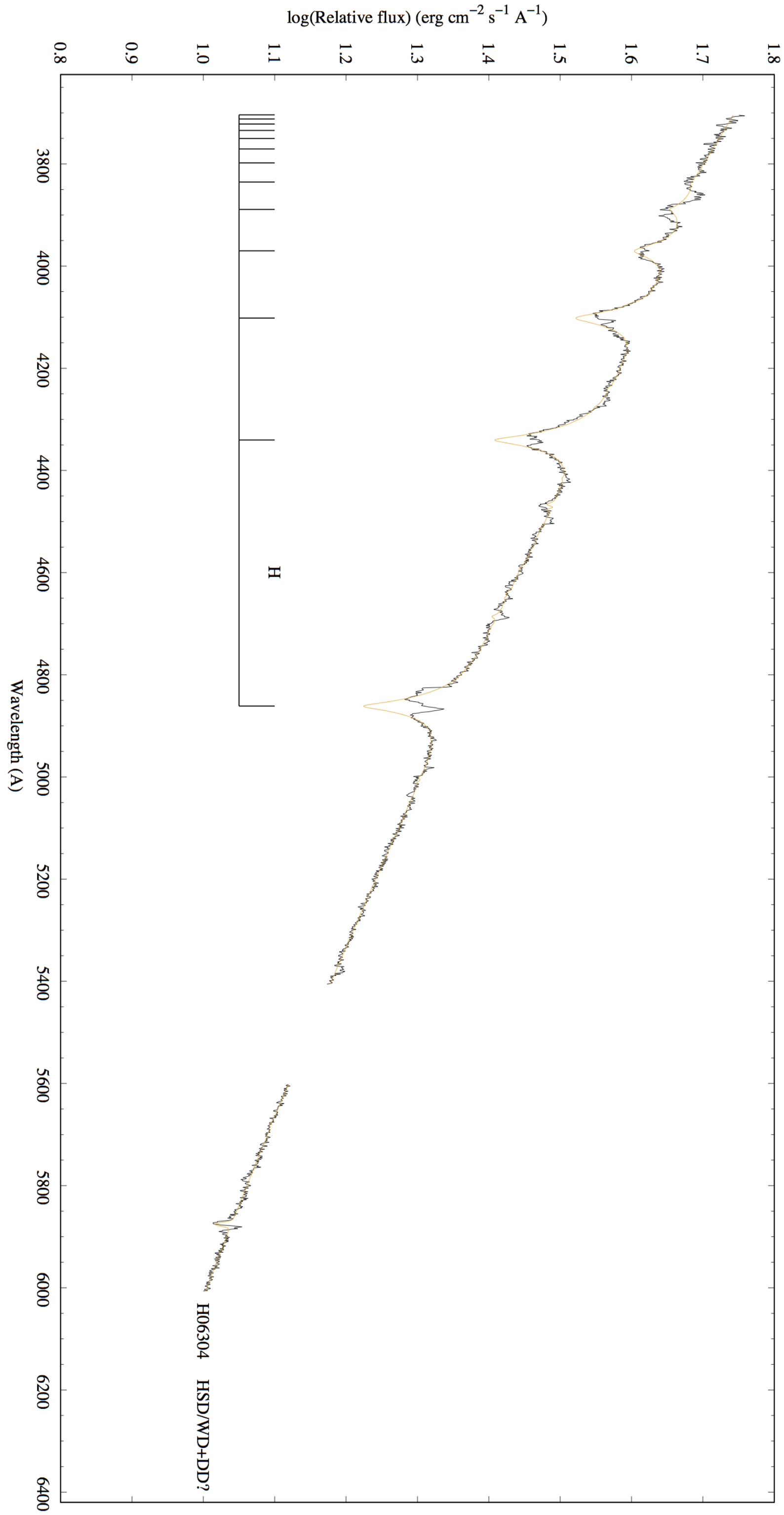

Figure 6.9: A cataclysmic variable like spectrum together with a 40,000 K DAO type white dwarf model (orange). The observed continuum have been adjusted to the model to improve the figure.

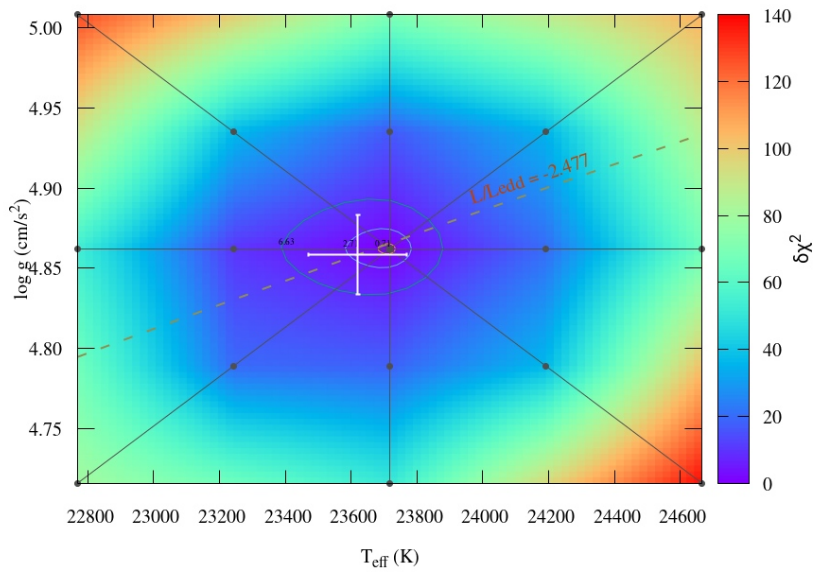

Figure 6.10: Surface temperature and gravity correlations for EVR-HSD-020. The 40, 60 and 99% confidence interval contours are marked. The white error bars show the final results. The dashed line is the iso-Eddington-luminosity curve corresponding to the best-fit.

6.5 DISCOVERIES

The HSD survey in this work identified 38 new variable discoveries. Fourteen of the new discoveries are HSD binaries, including the compact binaries EVR-CB-001 and EVR-CB-004 both showing strong light curve variation due to ellipsoidal deformation effects from an unseen companion, and HW Virs EVR-CB-002 and EVR-CB-003 discussed below. We also detected 3 planet transit candidates, later shown to be false positives, appearing as potential planets because of a nearby source blended in the Evryscope pixel or due to a challenging, low airmass observational field. We found several reflection effect HSD binaries, and other spectroscopically confirmed HSD discoveries that exhibit sinusoidal like variability. The survey also revealed several other potentially high-priority targets for followup, which we discuss in § 6.5.5

6.5.1 Compact Binaries

EVR-CB-001 [20] and EVR-CB-004 (Ratzloff et al., in prep), shown in Figure 6.11, are compact binary discoveries from the HSD survey, published in separate discovery papers with detailed followup and solutions. Both of these systems have a HSD spectral type primary and an unseen, degenerate companion. The variability in their light curves is dominated by the ellipsoidal deformation of the primary from the unseen companion, but also shows smaller amplitude effects due to Doppler boosting and gravitational limb darkening. We also recovered the only known system (CD-30 11223 [138]) in our magnitude range and FoV. A summary of the compact binary discoveries is shown in Table 6.4; we discuss the rarity of the systems in § 6.6.1.

Table 6.4: Compact Binaries

ID	RA	Dec	mag [G]	Period [h]
New Discoveries				
EVR-CB-001[a]	132.0648	-74.3152	12.58	2.3425
EVR-CB-004[b]	133.3023	-28.7684	13.13	6.0842
Known Recoveries				
CD-30 11223[c]	212.8173	-30.8844	12.32	1.1755

[a][20], [b]Ratzloff et al., in prep,
[c][138]

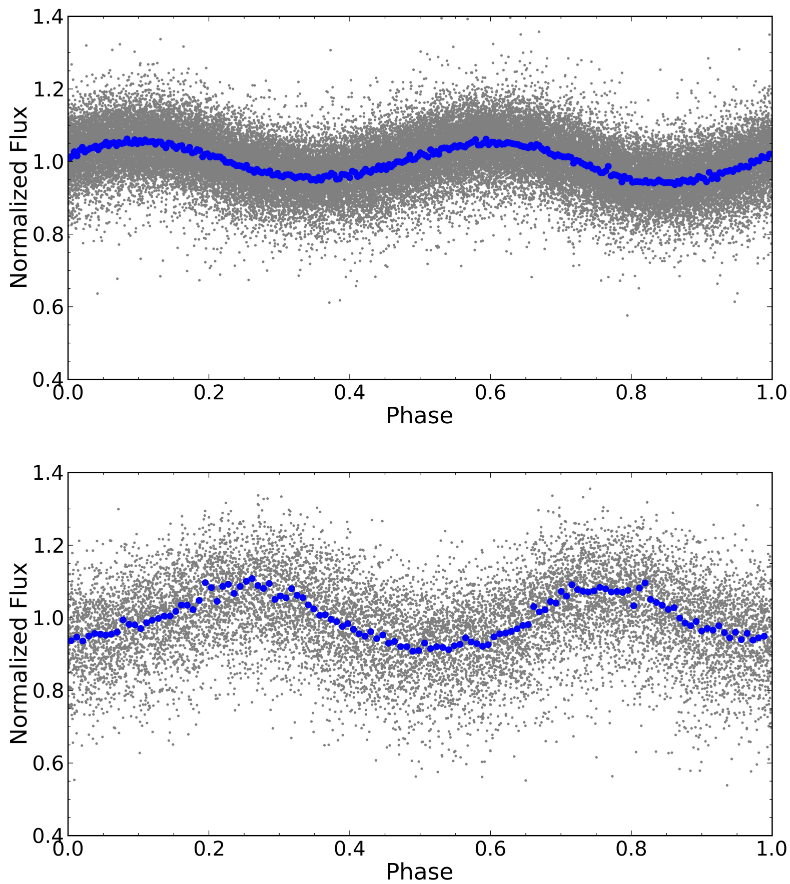

Figure 6.11: *Top:* The Evryscope light curve of EVR-CB-001 a 2.34 hour compact binary, with a very low mass unseen WD companion and a pre-He WD primary. *Bottom:* The Evryscope light curve of EVR-CB-004 a 6.08 hour compact binary. Grey points = 2 minute cadence, blue points = binned in phase. The systems show ellipsoidal deformation of the primaries due to the unseen companions, as well as Doppler boosting and gravitational limb darkening.

6.5.2 HW Vir systems

EVR-CB-002 and EVR-CB-003 (Ratzloff et al., in prep) are HW Vir discoveries from the HSD survey, with detailed followup and solutions published in a separate discovery paper. The discoveries are bright, southern sky systems facilitating followup and precise solutions. EVR-CB-002 features a high mass secondary (for HW Vir systems) of $M_2 >\approx 0.2M_\odot$ and EVR-CB-003 shows a very high reflectivity for HW Vir systems. We also recover all 5 of the known systems in our magnitude range and FoV (see [61] for a list of the 20 known, solved HW Vir systems). The Evryscope discovery light curves are shown in Figure 6.12 and the recovery of HW Vir (the namesake system) is shown in Figure 6.5. A summary of the HW Vir discoveries is shown in Table 6.5; we estimate the occurrence rate of the systems in § 6.6.1.

Table 6.5: HW Vir Systems

ID	RA	Dec	mag [G]	Period [h]
New Discoveries				
EVR-CB-002[a]	79.9486	-19.2816	13.61	6.5901
EVR-CB-003[a,b]	210.4810	-75.2260	13.53	3.1567
Known Recoveries				
HW Vir[c]	191.0843	-8.6713	10.61	2.8013
AADor[d]	82.9182	-69.8839	11.16	6.2769
NSVS 14256825[e]	305.0019	4.6324	13.25	2.6490
NYVir[f]	204.7006	-2.0303	13.39	2.4244
EC10246-2707[g]	156.7353	-27.3825	14.44	2.8443

[a]Ratzloff et al., in prep,
[b]also identified in Jayasinghe et al. (in prep) as a general variable (ASASSN-V J140155.45-751333.7), [c][139],
[d][128], [e][140], [f][141],
[g][142]

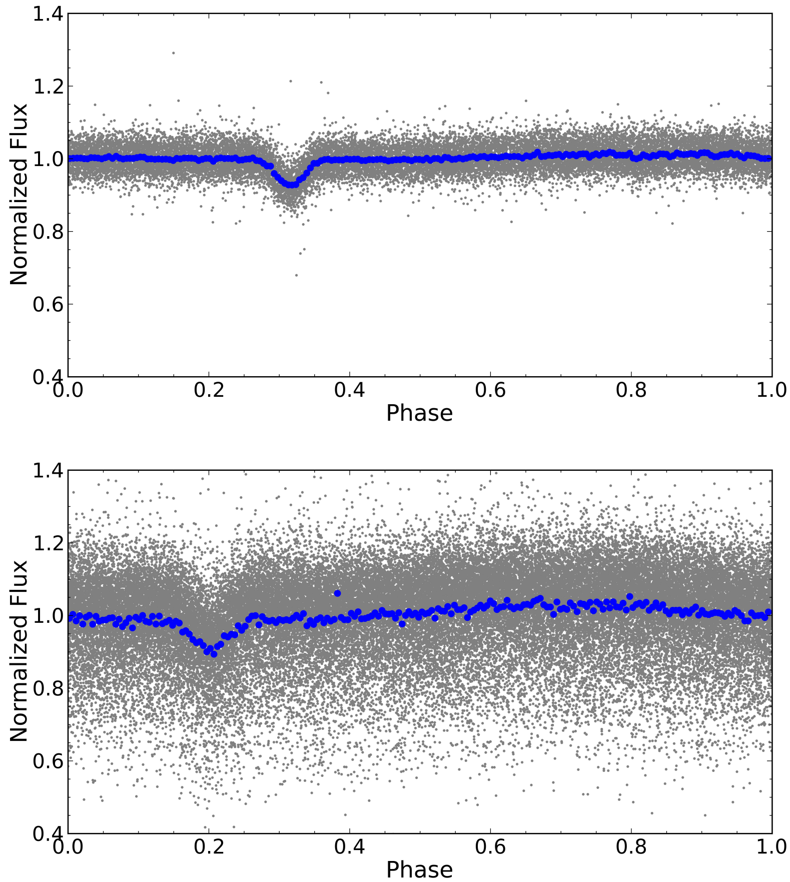

Figure 6.12: *Top:* The Evryscope light curve of EVR-CB-002 a 6.59 hour HW Vir. *Bottom:* The Evryscope light curve of EVR-CB-003 a 3.16 hour HW Vir. Grey points = 2 minute cadence, blue points = binned in phase. The systems were challenging discoveries due to blended sources or crowded fields with high-airmass observations. Followup with higher resolution instruments separated the sources and revealed the HW Vir signals (Ratzloff et al., in prep).

6.5.3 Planet Transit Candidates

Three planet candidates were identified from the HSD search, all showing transit times of ≈ 20 minutes and depths of less than 10%. The discovery light curves do not show signs of secondary eclipses or grazing transits. Assuming the host star for each system is a HSD with a 0.2 $R_\odot$ radius, the transiting object would be sub-Jupiter in size. Photometric followup revealed two of the candidates to be the HW Vir systems (EVR-CB-002 and EVR-CB-003) presented in § 6.5.2. The actual transit depths are much deeper than in the Evryscope discovery light curves because of a nearby star that was blended in the Evryscope pixels (EVR-CB-002) and a high-airmass observing field (EVR-CB-003). Spectroscopic followup revealed the final candidate to be a suspected Cataclysmic Variable, but with odd HSD like features in the spectrum. Neither the discovery or the followup light curves show signs of outbursts. The Evryscope light curve is shown in Figure 6.13. We are still exploring the nature of this candidate.

As there are no known exoplanets transiting HSDs, we are forced to rely completely on simulations to test our recovery algorithms and to estimate our detection efficiency. The transit signals of these three candidates are very similar to expected HSD transiting gas giant planets (slightly smaller than Jupiter size), and demonstrate the ability of our HSD survey to recover fast transit planet signals in actual Evryscope light curves.

6.5.4 Reflection Effect or Partially Eclipsing Binaries

We discovered the HSD reflection binary EC 01578-1743, first presented in [143], and reported in detail here. We discovered 9 additional HSD variables with periods ranging from 3 to 386 hours. The photometric variation is likely due to binary effects. A summary of the results is shown in Table 6.6. The Evryscope light curves are shown in Figure 6.14. The discovery amplitudes and periods are from the best LS detection and fit to the Evryscope light curves. The LS detection powers are significantly above the survey average (32.2 compared to 15). The TESS light curves are shown for comparison wherever available. Additional

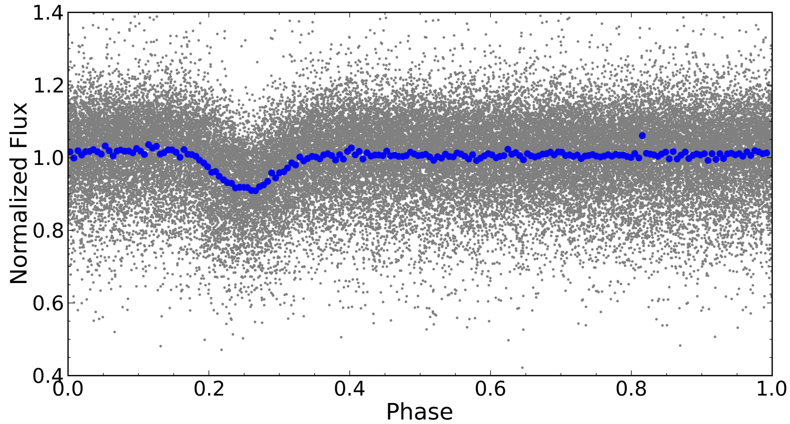

Figure 6.13: The Evryscope light curve of a 2.68 hour transiting system, originally flagged as a HSD planet candidate. Grey points = 2 minute cadence, blue points = binned in phase. Followup revealed the target to instead be a suspected Cataclysmic Variable. We discovered two other planet candidates in the HSD search, which were later shown to be stellar in nature. These recoveries demonstrate the ability of our HSD survey to reach transit signals of sub-Jupiter size planets, from light curves with similar astrophysical signals.

discovery details including spectral types from the best fits to the spectra are shown in Table 6.10, along with a listing of all discoveries from this work.

The HSD survey recovered 4 of the 6 known short period HSD reflection binaries in our magnitude range and FoV. The two known systems that were not recovered, CPD-64481 and PHL 457 [121], were missed due to low amplitude (sub-1%) variability and a close source that was blended in the Evryscope pixels. A list of known, solved HSD binaries showing reflection effects can be found in [144]. The HSD search also recovered four known eclipsing binaries: V1379Aql [145] a HSD/K-giant, EC21049-5649 [146], EC23257-5443 [147] and GALEX J175340.5-500741 [148] HSD/Fs. A list of known HSD eclipsing binaries can be found in [148].

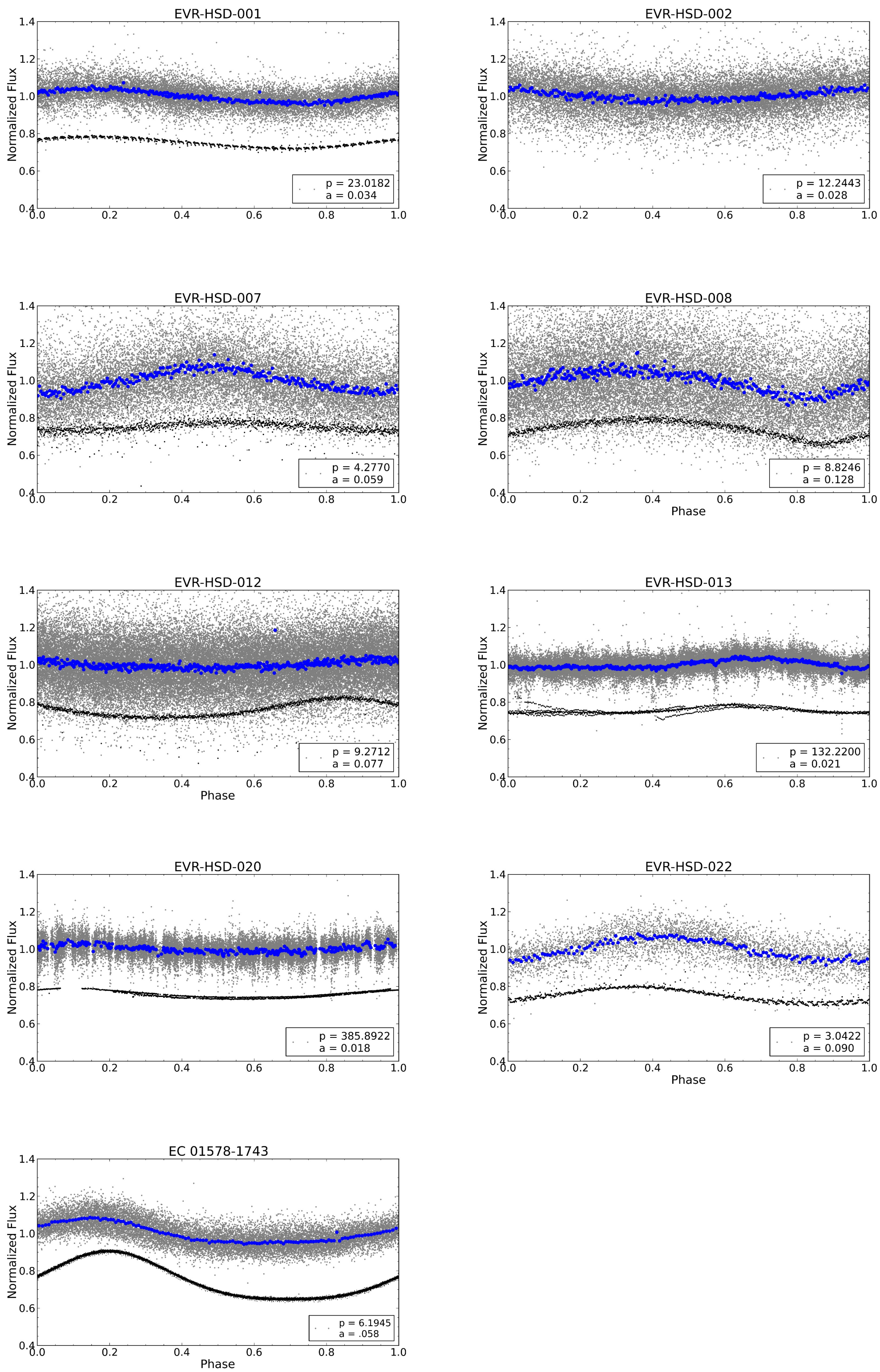

Figure 6.14: The Evryscope light curves of HSD variable discoveries showing reflection or sinusoidal signals with periods ranging from 3 to 386 hours.

Table 6.6: HSD Reflection Effect or Eclipsing Binaries

ID	RA	Dec	mag [G]	Period [h]
New Discoveries				
EC 01578-1743[a,b]	30.0553	-17.4788	12.05	6.1945
EVR-HSD-001	40.2665	-19.0032	12.55	23.0182
EVR-HSD-002	97.1064	-18.7484	13.19	12.2443
EVR-HSD-007	271.7181	-43.5589	13.47	4.2769
EVR-HSD-008	73.7044	-65.8895	14.87	8.8246
EVR-HSD-012	151.4384	-63.5280	13.09	9.2712
EVR-HSD-013	158.7382	-53.8975	11.58	132.223
EVR-HSD-020	295.0117	-49.4531	12.03	385.89
EVR-HSD-022	133.3023	-28.7684	13.13	3.0422
Known Recoveries				
TYC 7709-376-1[c]	155.8412	-37.6166	11.71	3.3425
TW Crv[d]	180.0235	-19.0344	15.03	7.8629
KV Vel[e]	163.6690	-48.7841	12.18	8.5709
BPS CS22169-0001[f]	59.0972	-15.1554	12.86	5.2057
J175340.5-500741[g]	268.4189	-50.1284	12.88	2.1778
V1379Aql[h]	294.9117	-6.0637	7.81	624.77
EC21049-5649[i]	317.1796	-56.6181	14.37	6.3976
EC23257-5443[j]	352.1339	-54.4532	14.53	6.6334

[a][143], [b](also noted as an unidentifiable variable
ASAS J020013-1728.7) [149],
[c](also known as ASAS 102322-3737.0) [150],
[d](also known as EC11575-1845) [151],
[e][152], [f][153],
[g][148], [h](also known as HD 185510) [145],
[i](also known as DDE 98) [146], [j][147]

6.5.5 Highlighted Discoveries

6.5.5.1 EC 01578-1743

From the best fit to the SOAR ID spectra using *Astroserver* [35], we measure $T_{\text{eff}} = 31,980K$, $\log g = 5.78$ cm s^{-2}. We classify EC 01578-1743 as an sdB, and identify it as a reflection effect HSD binary. Initial light curve and radial velocity solutions indicate a late M-dwarf companion. A full, detailed solution of EC 01578-1743 including precise fitting of the TESS and Evryscope light curves will be presented in an upcoming work (Schaffenroth, et al., in prep).

6.5.5.2 EVR-HSD-001, EVR-HSD-002, EVR-HSD-007, EVR-HSD-022

The variables identified here are short period, moderate amplitudes, and with binary reflection effect signals. Each has been spectroscopically confirmed as an sdB. The bright magnitudes will also aid in photometric or radial velocity followup.

6.5.5.3 EVR-HSD-008

From the best spectral fit, EVR-HSD-008 is a hot sdB or post GB star but with a very high projected rotational velocity (which could also be indicative of other broadening mechanisms such as magnetic, instrumentational, or orbital smearing that might be seen in a higher resolution spectrum). The short period and very distinct features are confirmed in the TESS light curve. EVR-HSD-008 is also identified as a potential post AGB candidate in [154]. There is also a slight phase offset between the Evryscope and TESS light curves that we are unable to explain, and requires further followup. This target is a strong candidate for RV measurements and additional analysis (Galliher et al., in prep).

6.5.5.4 EVR-HSD-012

A very strong sdB reflection candidate, with the 9.2712 hour period confirmed with the TESS light curve. The TESS amplitude is higher than that seen in the Evryscope light curve, potentially a consequence of the reflection effect observed in different filters.

6.5.5.5 EVR-HSD-013

An sdB reflection binary candidate with a long 5.5 day period. From the spectral fit, this is *potentially* a double line system which would offer a rare opportunity to measure the mass of the HSD directly. Followup with a higher resolution spectrum is needed to confirm or reject this hypothesis.

6.5.5.6 EVR-HSD-020

A difficult to find long period (385.8922 hour) variable with a reflection like shape. We note here that since EVR-HSD-020 is quite a long period variable, the TESS light curve is from a single sector (13 the only one available at the time of our survey). The reflection shape and longer period could be indicative of an earlier main sequence companion. The spectral fit classifies this star as an sdB or BHB.

6.5.6 Spectroscopically Confirmed HB and B Variables

The remaining spectroscopically confirmed variable discoveries are horizontal branch (HB) and B stars. The light curves show sinusoidal or reflection features in periods ranging from a few hours to nearly 5 days. The results are shown in Table 6.7 and the light curves in Figure 6.15. Additional discovery details including spectral types from the best fits to the spectra are shown in Table 6.10, along with a listing of all discoveries from this work.

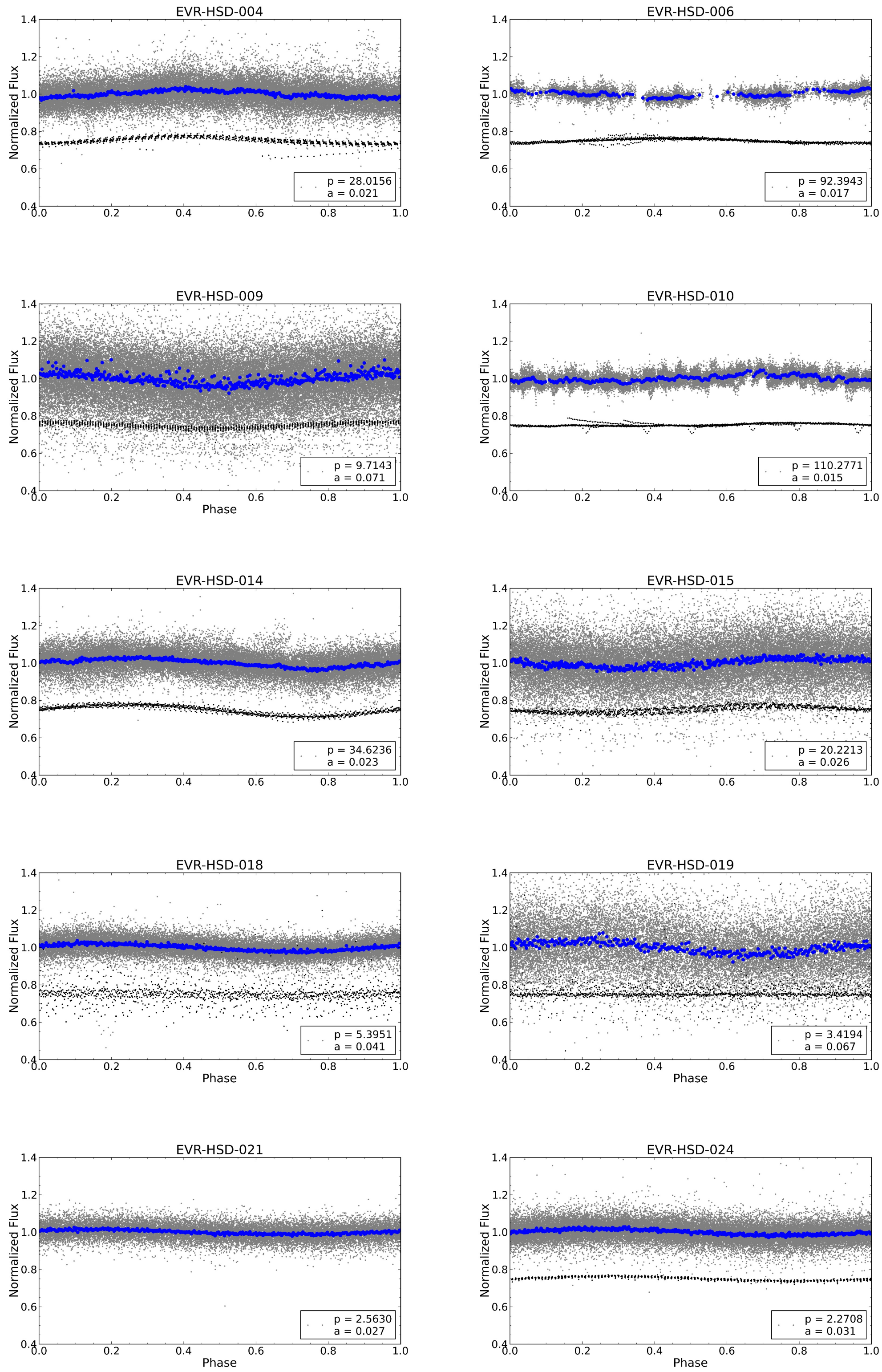

Figure 6.15: The Evryscope light curves of variable discoveries showing reflection or sinusoidal signals with periods ranging from 2.5 hours to 110 hours.

Table 6.7: HB and B Variables

ID	RA	Dec	mag [G]	Period [h]
New Discoveries				
EVR-HSD-004	194.6749	-35.3798	12.22	28.0156
EVR-HSD-006[a]	263.4460	-70.9357	10.60	92.39
EVR-HSD-009	75.0706	-65.8073	15.09	9.7143
EVR-HSD-010	107.7860	-7.1754	10.22	110.277
EVR-HSD-014	162.6241	-39.7614	12.00	34.6236
EVR-HSD-015	170.0517	-57.3402	12.98	20.2213
EVR-HSD-018	267.0839	-49.6796	11.81	5.3951
EVR-HSD-019	285.2468	-35.4992	13.14	3.4194
EVR-HSD-021	301.6089	-6.5474	11.41	2.5630
EVR-HSD-024	211.1865	-49.2117	11.90	2.2708

[a](also CPD-702387, noted as a potential OB star) [155]

6.5.7 Cataclysmic and other Outbursting Variables

Although not a focus of the surveys, we recovered several known Cataclysmic Variables and Novae. The nature of these systems (WD host and compact binaries) leads in some cases to light curve features similar to those expected from a HSD planet transit. The short periods, depths, and shapes (but with somewhat longer transits) are comparable to the HSD planet simulations; and demonstrates in a separate target group the ability of our detection algorithms to recover transit signals in actual Evryscope light curves.

Table 6.8: Cataclysmic Variables and Novae

ID	RA	Dec	mag [G]	Period [h]
Known Recoveries				
AO Psc[a]	343.8249	-3.1778	13.23	3.5910
UU Aqr[b]	332.2740	-3.7716	13.58	3.9259
TX Col[c]	85.8340	-41.0318	15.62	5.7192
EC21178-5417[d]	320.3606	-54.0763	13.74	3.7087
RR Pic[e]	98.9003	-62.6401	12.41	3.4806
SV CMi[f]	112.7851	5.9802	16.03	3.7440

[a][156], [b][157], [c][158], [d][157], [e][159], [f][157]

6.5.8 Peculiar Discoveries

6.5.8.1 EVR-HSD-010

EVR-HSD-010 is a HB star with the spectral fit indicating a lower temperature and surface gravity than a typical HSD. The 110.277 hour sinusoidal (or possible reflection) variability is confirmed in the TESS light curve but at a lower amplitude. Also visible in the TESS light curve are shallow (4%) eclipses at a different period (77.9885 hours). The ≈ 4 hour duration shallow eclipse, HB star type, and period suggest a reasonably large (solar radius or larger) primary and small, dim secondary (most likely a late M-dwarf). The bright magnitude would aid in further followup of this system (Galliher et al., in prep). We show the light curve folded to the eclipse period in Figure 6.16.

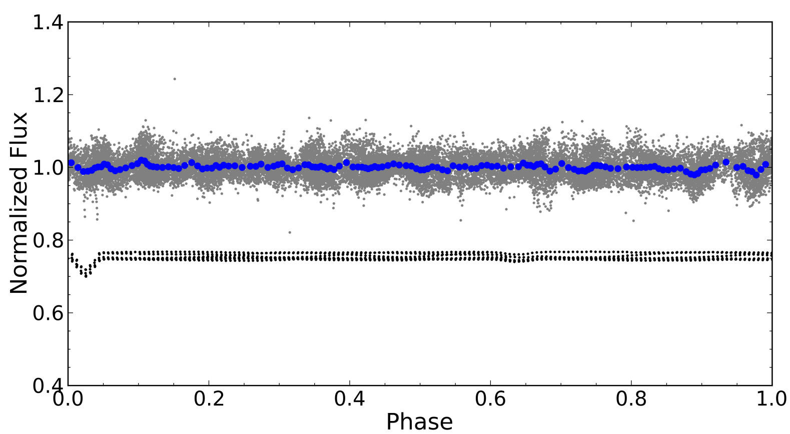

Figure 6.16: The Evryscope and TESS light curves of the multi-variable system EVR-HSD-010, folded here on the 77.9885 hour eclipsing period. Grey points = 2 minute cadence, blue points = binned in phase. The TESS light curve is shown with a .25 offset in normalized flux for better visualization.

6.5.8.2 EVR-HSD-019

The EVR-HSD-019 Evryscope light curve indicates short period reflection effect or sinusoidal like variability, however the effect is not present in the TESS light curve. This could be due to a color effect, or it could be a systematic in the Evryscope light curve instead of an astrophysical signal.

6.5.9 CPD-634369

CPD-634369 is a short period variable that shows peculiar spectral features, which warrant further investigation. Our initial followup SOAR spectra (with measurements taken over the photometric period), show broad absorption features and superimposed emissions that change over the period cycle. The photometric and spectral features are shown in Table 6.9 and in Figure 6.17. We identify CPD-634369 as a potential cataclysmic variable (CV) in a low-mass transfer state, perhaps similar to V379 Vir or comparable systems [160–163]. The low amplitude emission lines suggest mass loss perhaps with an accretion disc, while it is also possible the object has a debris disc. A very hot, blue star CPD-634369 was noted as a OB candidate in [155]. We identify the object as a probable WD primary, cataclysmic-variable-like oscillations, and possibly with a debris disc. Additional spectroscopic and RV followup is necessary for confirmation (Galliher and Barlow et al., in prep).

Table 6.9: CV candidate / WD Debris Disc

ID	RA	Dec	mag [G]	Period [h]
New Discoveries				
CPD-634369	274.7516	-63.3006	12.30	3.2177

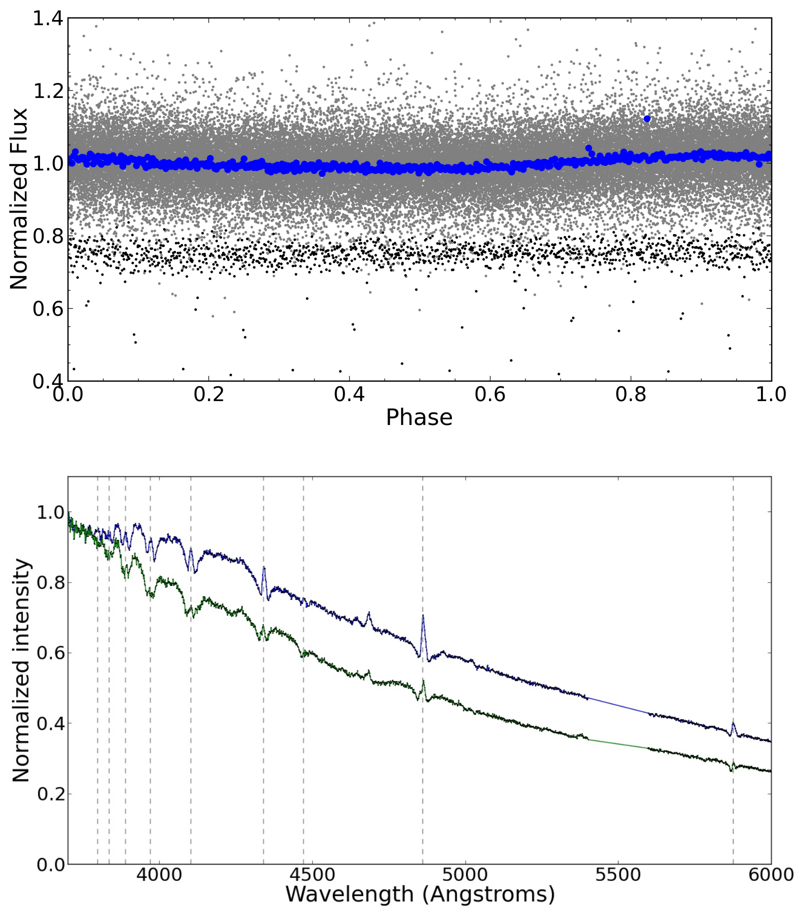

Figure 6.17: *Top:* The Evryscope light curve of the potential CV or debris disc CPD-634369, folded here on the 3.2177 hour period. Grey points = 2 minute cadence, blue points = binned in phase. The TESS light curve (black points) is shown with a .25 offset in normalized flux for better visualization. *Bottom:* The SOAR ID spectra, showing broadened absorption features and a high temperature consistent with a WD but with emissions indicative of mass transfer. The emission features change in amplitude as seen by comparing spectra taken in March 2019 (Blue) and September 2019 (Green). H-α to H-10(dashed lines) are shown for reference.

6.5.10 Other Discoveries

Other discoveries from the HSD survey are shown in the appendix. They are suspected misclassified stars (from only 1 source, see § 6.2.2.11) - most likely A or B stars. While not the focus of the surveys, there is a variety of variability including reflection binaries, eclipsing binaries, sinusoidal variables, and peculiar variables. The best period and amplitude fits are also provided.

6.5.11 Discoveries Summary

Discoveries from this section are summarized in Tables 6.10 and 6.11. GAIADR2 data is listed for the ID cross-reference, RA, Dec, and mag[G]. The effective temperature, surface gravity, and projected rotational velocity are determined from the best fit to the SOAR ID spectra (see § 6.4). We use the values determined from the spectral fits to determine a spectral type and consider the light curve variation as a reasonableness check. Periods listed are from the best BLS or LS fit from the light curve discovery.

Table 6.10: Summary of Discoveries from this work (Spectroscopically Confirmed Spectral Type)

ID	RA	Dec	mag [G]	$T_{\rm eff}$ [K]	$\log g$	$\log n\mathrm{He}/n\mathrm{H}$	SpT	Period [h]
HSD Spectral Type								
Compact Binaries								
EVR-CB-001 (H06771)	132.0645	-74.3151	12.581	18,500 ±500	4.96 ±.04	-1.43 ±.03	pre-He WD	2.3425217(5)
EVR-CB-004 (H03930)	133.3023	-28.7683	13.127	41,800 ±1400	4.63 ±.11	–	sdO?	6.0842 ±.0001
HW Virs								
EVR-CB-002 (H03281)	79.9486	-19.2816	13.608	27,963 ±224	5.39 ±.033	–	sdB	6.590132(8)
EVR-CB-003 (H00250)	210.4805	-75.2258	13.534	32,552 ±152	5.78 ±.032	–	sdB	3.1567 ±.0001
Reflection Effect and Other Variables								
EC 01578-1743 (H00061)	30.0553	-17.4788	12.052	31,980 ±100	5.78 ±.02	-2.09 ±.04	sdB	6.19449 ±.00001
EVR-HSD-001 (H00098)	40.2665	-19.0032	12.547	20,950 ±150	4.83 ±.04	-2.87 ±.07	sdB	23.0182 ±.0002
EVR-HSD-002 (H00182)	97.1064	-18.7484	13.193	24,920 ±200	5.30 ±.03	-2.98 ±.06	sdB	12.24434 ±.00005
EVR-HSD-007 (H05026)	271.7181	-43.5589	13.468	27,390 ±230	5.40 ±.04	-2.04 ±.04	sdB	4.27691 ±.00001
EVR-HSD-008 (H17205)	73.7044	-65.8895	14.866	33,130 ±800	4.41 ±.11	-1.10 ±.08	pGB/sdB?	8.82458 ±.00001
EVR-HSD-012 (H06317)	151.4384	-63.5280	13.087	29,060 ±260	5.49 ±.05	-2.42 ±.03	sdB	9.27121 ±.00002
EVR-HSD-013 (H05722)	158.7382	-53.8975	11.578	14,660 ±100	4.05 ±.08	-2.35 ±.23	sdB+X?	132.223 ±.006
EVR-HSD-020 (H05487)	295.0117	-49.4531	12.033	23,620 ±150	4.86 ±.03	-3.85 ±.34	sdB/BHB?	385.89 ±.06
EVR-HSD-022 (H08435)	133.3023	-28.7684	13.127	40,160 ±330	4.63 ±.06	-1.08 ±.04	sdO/?	3.04223 ±.00002
CV or Debris Disc								
(H06304)	274.7516	-63.3006	12.296	≈40,000	≈8.0	≈-2.3	WD+DD?	3.21766 ±.00003

Table 6.11: Summary of Discoveries from this work (Spectroscopically Confirmed Spectral Type)

ID (ES Internal ID)	RA	Dec	mag [G]	T_{eff} [K]	$\log g$	$\log n\text{He}/n\text{H}$	SpT	Period [h]
HB or B stars								
Variables								
EVR-HSD-004 (H04413)	194.6749	-35.3798	12.217	18,250 ±130	3.95 ±.03	-1.00 ±.03	B3V	28.0156 ±.0002
EVR-HSD-006 (H06662)	263.4460	-70.9357	10.596	27,190 ±890	3.89 ±.08	-0.83 ±.04	B1V	92.39 ±.02
EVR-HSD-009 9.7143 ±.0003 (H17223)	75.0706	-65.8073	15.090	–	–	–	–	B?
EVR-HSD-010 (H16764)	107.7860	-7.1754	10.222	14,900 ±100	4.32 ±.05	-2.47 ±.14	B5V/HB?	110.277 ±.004
EVR-HSD-014 (H04749)	162.6241	-39.7614	12.000	18,460 ±640	3.21 ±.07	-1.17 ±.03	B3III	34.6236 ±.0004
EVR-HSD-015 (H10605)	170.0517	-57.3402	12.978	12,760 ±270	4.25 ±.07	-2.12 ±.25	B8V	20.2213 ±.0001
EVR-HSD-018 (H05499)	267.0839	-49.6796	11.810	26,790 ±200	3.80 ±.02	-0.78 ±.04	B1V	5.39506 ±.00001
EVR-HSD-019 (H16409)	285.2468	-35.4992	13.142	–	–	–	B?	3.41941 ±.00001
EVR-HSD-021 (H02701)	301.6089	-6.5474	11.409	28,860 ±100	4.09 ±.02	-0.82 ±.08	B0V	2.56304 ±.00001
EVR-HSD-024 (H10104)	211.1865	-49.2117	11.897	24,270 ±240	4.23 ±.03	-0.88 ±.02	BHB?	2.27081 ±.00001
Non-variables in the ES LCs								
(H06720)	236.5023	-72.8776	13.97	18,170 ±100	4.04 ±.02	-1.40 ±.05	B3V	–

6.6 DISCUSSION

6.6.1 Survey Sensitivity

To test the survey sensitivity, we combine the estimated detection efficiency shown in Figure 6.6, the transit fraction, and total survey targets. This offers visibility to the number of likely targets for a range of periods, and for a particular transit type (HW Vir systems, HSD / gas giant planets, and WD / planets). In all cases the survey is target limited. As demonstrated below, the survey is most sensitive to HW Vir systems (given the favorable transit likelihood and short periods) and least sensitive to long period planets.

6.6.1.1 HW Vir systems

From the estimated detection efficiency (determined from transits simulated on to actual Evryscope light curves, see § 6.3.3 and Figure 6.6), we limit the period range to 2 - 10 hours, and assume a HSD primary with 0.5 $M_\odot$ and 0.2 $R_\odot$, with a companion of 0.10 $M_\odot$ and 0.15 $R_\odot$, given the parameters of the known, solved systems [61]. The detection efficiency of the HSD survey for HW Vir systems is shown in panel (a) of Figure 6.18 along with the noise floor. This assumes the inclination angle $i = 90°$. The theoretical separation distance (a) and the transit fraction (using R_{HSD}/a) are shown in panels (b) and (c). From the detection efficiency, we subtract the noise floor and assume a 20% reduction due to reduced signals from blended sources in the Evryscope pixels, difficult observing fields that affect the pipeline, or other systematics that reduce light curve quality or algorithm effectiveness. The final detection probability is shown in panel (d); and using the estimated number of total HSDs in the survey (1422 ± 428 see § 6.2.2.13) we show in panel (e) the potential targets that we could detect HW Vir systems. We take the average over this narrow period range to be the potential targets $= 165 \pm 50$.

6.6.1.2 HW Vir Occurrence Rate Estimation

We detected seven HW Virs in our HSD survey (2 new and 5 known see Table 6.5), including all 5 of the known systems in the declination (Dec $< +10$) and magnitude ($m_g < 15$) range of the survey. Using the findings from the previous section, the frequency (7/165) is $4.3\% \pm 0.6\%$ HW Vir systems in HSDs.

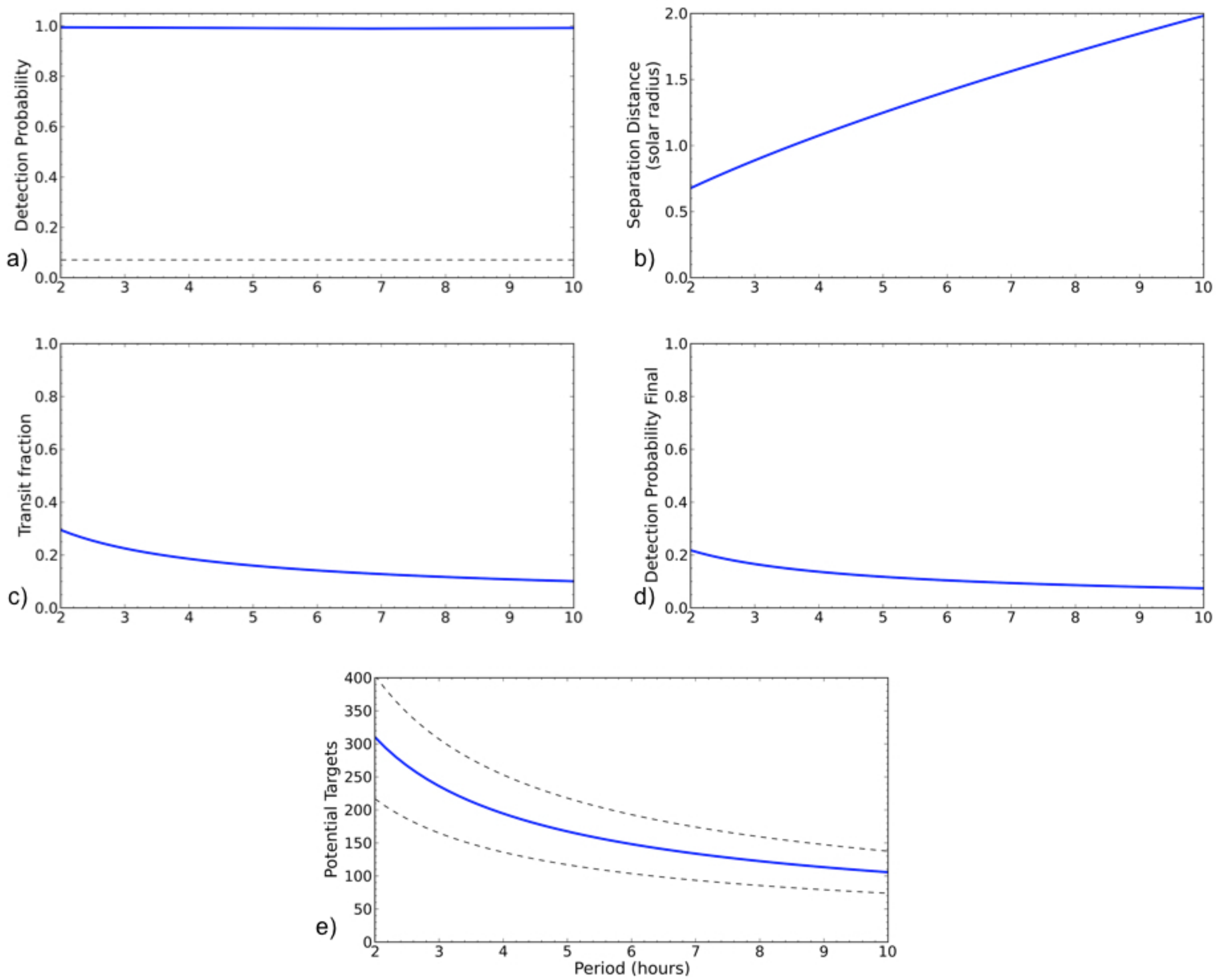

Figure 6.18: HW Vir survey sensitivity. *(a)* The detection efficiency estimated from the recovery of HW Vir like transit signals injected into Evryscope light curves (inclination angle $i = 90°$). The high return is the result of the fast period, many epochs, multi-year data, and high cadence light curves. The noise floor is indicated by the dashed line. *(b and c)* The theoretical separation distance and transit fraction (see § 6.6.1.1). *(d)* The final detection probability, calculated by multiplying (a) and (c) with a few adjustments for systematics (again see § 6.6.1.1). *(e)* The potential targets that HW Vir systems could be detected in, found by multiplying (d) by the estimated total number of HSDs in the survey. The dashed lines are the estimated 1σ errors.

6.6.1.3 HSD Planet Transits

Using the estimated detection efficiency over the full period range of the survey (2-480 hours), we calculate the recovery rates for Super-Jupiter (5 M_J and 0.125 $R_\odot$), Jupiter, and Neptune size planets transiting a canonical HSD. The gas-giant planets are recovered over the full range of the survey, while the recovery of the smaller planets decreases with increasing periods (as shown in Figure 6.19). Using the same prescription as the HW Vir systems, see § 6.6.1.1, we calculate the separation distance, transit fraction, and final detection probability as shown in panels (b-d). The final detection probability is completely dominated by the transit fraction, and falls off significantly for periods longer than $\sim$ 20 hours. Here we keep the scaling for comparison to the different systems (HW Vir) and between different components (recovery versus transit fraction). Further in the manuscript we discuss the limiting factors for the survey. Again using the estimated number of total HSDs in the survey (1422 ± 428 see § 6.2.2.13) we show in panel (e) the potential targets that we could detect HSD transiting planets.

6.6.1.4 HSD Planet Transits Survey Sensitivity

We detected 3 potential transiting planets, later confirmed to be other objects (see § 6.5.3). It is well known that exoplanet transit surveys suffer from high false positive rates, for example the very successful HATNet and HATSouth surveys have discovered $\sim$140 substellar objects with $\sim$ 2300 false positives as of early 2018 [90]. Although no transiting HSD planets have been discovered yet, and consequently the false positive rate is not known, there is no indication the HSD planet false positive should be particularly different than false positives for planets orbiting main sequence stars. The culprits are still likely to be eclipsing binaries or misidentified star types (HW Virs, Cataclysmic Variables, or A or B-stars in the case of HSDs). Perhaps more importantly, the instrumentation and light curve challenges that drive false positives (blended sources due to coarse pixels, crowded fields, background contamination, bad pixels, grazing eclipses, and other factors) for the Evryscope are similar to other transit surveys including the HAT instruments.

Assuming a similar false positive rate ($\sim$ 1 in 20 planet candidates will be confirmed), we would ideally want at least a few hundred potential targets that we could detect HSD transiting planets to have a decent chance of discovery. The estimated potential targets that we could detect HSD transiting gas giant planets (from § 6.6.1.3) are shown in Figure 6.20. The potential targets are above 100 only for the very short periods for the large planets. We also show the number of targets estimated in the HW Vir analysis (the silver dashed line), providing a comparison point since we detected 7 HW Vir systems (2 new and 5 known) in the survey. Since the fall-off in potential targets is dominated by the transit fraction (see the previous section), the survey is constrained by the number of total HSD targets. In § 6.6.3.1 we show that by increasing the total survey targets by a factor of $\sim$5 would improve the potential targets that we could detect HSD transiting planets nearer to desired levels over a wider range of periods.

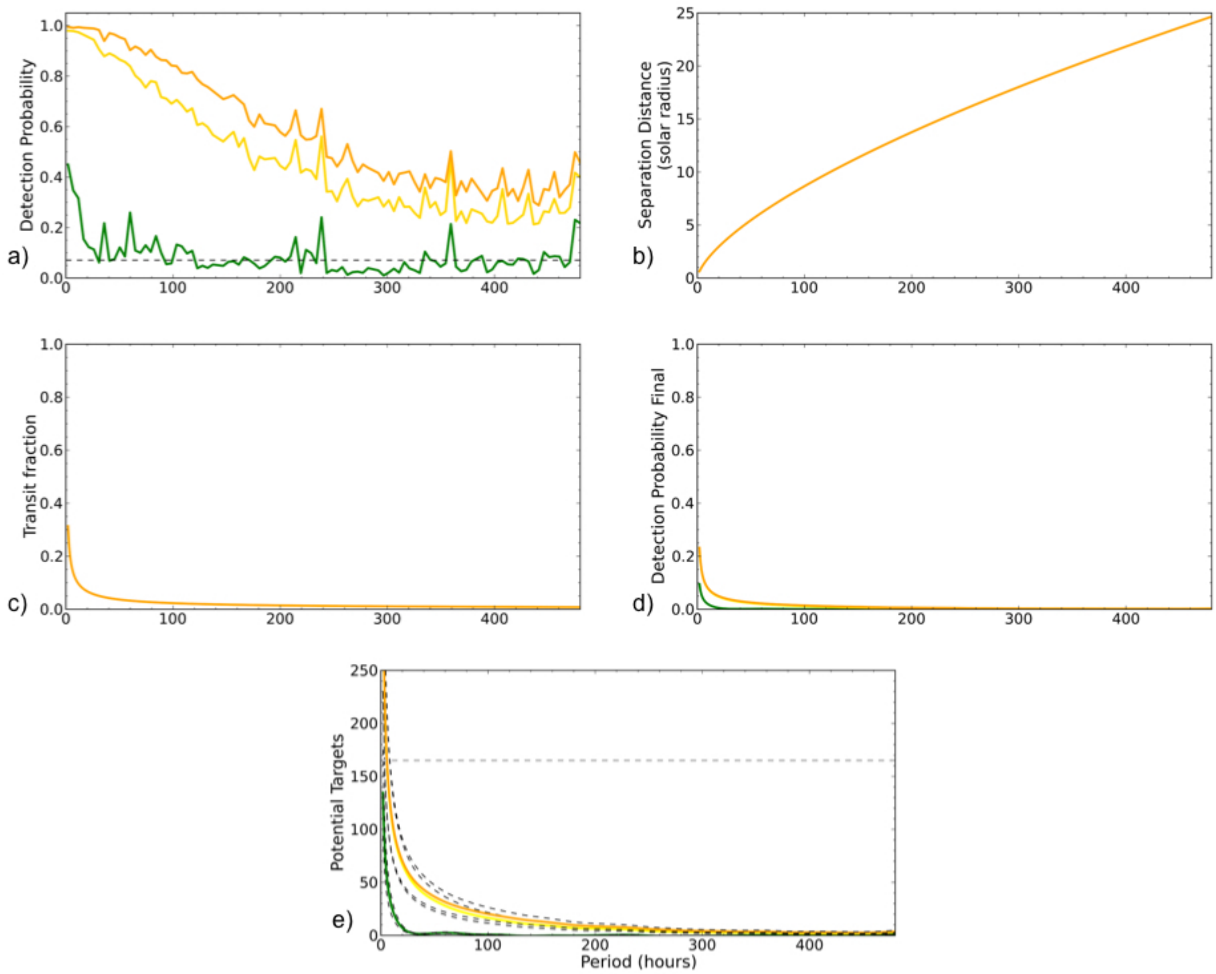

Figure 6.19: HSD planet survey sensitivity. *(a)* The detection efficiency for Super-Jupiter (orange line), Jupiter (yellow line) and Neptune (green line) planets transiting HSDs (inclination angle $i = 90°$). *(b and c)* The theoretical separation distance and transit fraction. *(d)* The final detection probability is driven down significantly for higher periods by the larger separation distance and resulting transit fraction. *(e)* The potential targets that transiting planets could be detected in, found by multiplying (d) by the estimated total number of HSDs in the survey. The dashed lines are the estimated 1σ errors. Here we keep the scaling for comparison to the different systems (HW Vir) and between different components (recovery versus transit fraction). Further in the manuscript we discuss the limiting factors for the survey and show increased detail over the period range.

6.6.2 Contribution of Blended Sources

Additional likely HSDs targets are expected to be included in the survey as blended sources. In § 6.2.2.10 we estimated an additional 265 blended HSD sources that can potentially contribute to the search. EVR-CB-002 offers insight as to the usefulness of these types of sources, as it is an HW Vir discovery with a nearby bright star in the field. The transit signal was reduced from 50% to 8% due to the blended sources (a combination of the 11.5 magnitude nearby bright star and the 13.5 magnitude target star). The transit signal from the HW Vir system and favorable inclination angle is near the deepest we would expect, and the reduced signal is near our detection limit. Given the average magnitude difference of 3 for blended Evryscope sources, EVR-CB-001 is a representative example. Thus although we did discover this system, it seems likely that we would not recover signals with a more grazing eclipse or from smaller transiting objects. For HW Vir systems if we assume an ≈25% recovery, this still only gives an additional 65 targets - minor compared to the total targets and well below the estimated error range.

6.6.3 Compact Binaries

In this section, we consider compact binaries showing a light curve variation due to ellipsoidal deformation, with an asymmetric shape due to gravitational limb darkening and Doppler beaming. The unseen companion is assumed to be a WD, but could potentially be a more compact object, while the primary is a HSD or HSD like in color-magnitude space and spectral features. In the HSD survey, we found 3 of these systems (1 known and 2 discoveries) out of 1422 likely HSD targets. The recoveries were found with BLS, with relatively low power near the survey average, and one of the detections was at a half-period alias. LS missed two and found one at half the period, the Outlier detector is not designed for these signals and did not recover any of the systems. The systems we recovered all showed amplitudes above 5%, and at least a 1% difference in even versus odd depths.

The detection of this type of system faces the difficulties of the HSD search (fast timescale variability and a limited number of targets), but with the added challenge of discriminating the asymmetric shape from the common sinusoidal like variable. The typical failures are for the matched filter to either miss the variability or find the half-period alias, or for the reviewer to not recognize the multi-component variability and mistake the object for an unexceptional variable.

The HSD survey in this work was designed to search for a variety of variable signals over a wide period range. A subsequent search concentrating on very short periods only (10 minutes to 10 hours), with more aggressive systematics removal for all variability longer than 10 hours, and with a custom detection algorithm designed specifically for the unique asymmetric even / odd cycle light curve could potentially recover additional systems. We leave that search for future work.

We can only make a rough estimate of the occurrence rate given the subjectivity in the recovery ability, and low number of discoveries. As the limiting factor for detection in this work is the size of the difference in even versus odd depths, we require this to be 1% or more which means the main amplitude in the light curve variation to be $\approx 5\%$ or more. Even with an inclination of 63 degrees, EVR-CB-001 (see § 6.5) has an amplitude well above this. We assume these systems are detectable in Evryscope light curves up to a 45 degree inclination, and that our detection efficiency is less than the HW Vir systems but still reasonably high at ≈ 0.8 (given the very short periods and many periods captured in the light curves). The estimated frequency is: $3/(45/90 \times 0.8 \times 1422) = 0.005$. Less than a half percent of HSDs are likely to be compact binary systems with a HSD like primary and unseen companion.

6.6.3.1 HSD Survey 2

The survey in this work is comprised of southern sky targets with magnitudes brighter than 15.0M in m_g. Based on the Geier based GAIA HSD list, including stars to $m_g < 16$ approximately doubles the number of targets. The Evryscope North (a copy of the CTIO system) was deployed to Mount Laguna Observatory (MLO) in late 2018. In two years time it will have collected a similar number of epochs for a similar number of sources as the CTIO data the survey in this work was based off. This would approximately double again the number of HSD targets. In Figure 6.20, we show the effect of the increased survey scope. The potential targets with detectable planets is at or above 100 out to periods of $\approx$ 100 hours for super-Jupiter and Jupiter size planets, and is favorable for Neptune size planets to at least several days. We would also expect on order tens of targets over the full test period range.

The increased scope survey (Evryscope HSD Survey 2, Ratzloff, et al., in prep), is expected to find a similar fraction of rare, fast transit HSD systems including compact binaries, HW Virs, and reflection binaries, but at an increased total yield of $\approx$ 4 times driven by the increased number of targets. From Figure 6.19, we demonstrate the combination of Evryscope 2 minute cadence, photometry, and detection algorithms are effective at recovering potential HSD transiting planet signals. The recovery of actual planet candidates in this work, even though they are false positives, further validates the survey performance. Relative to the planet search, with the increased targets we should be well placed to explore the more untapped regions past the very short periods with sensitivity to potentially make discoveries.

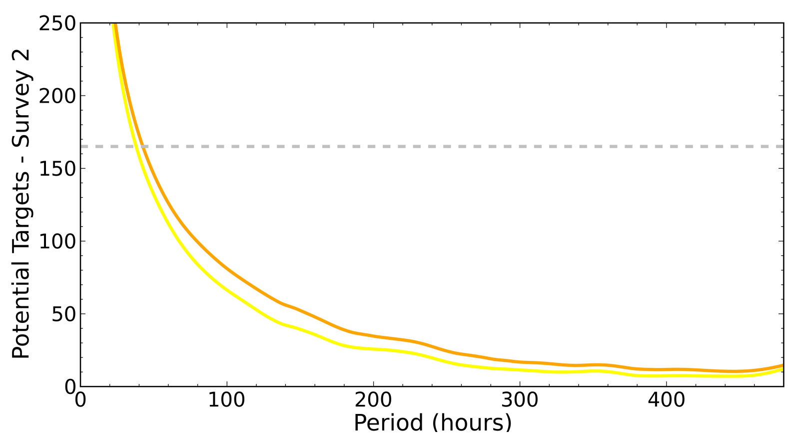

Figure 6.20: The potential targets that transiting planets could be detected in, Super-Jupiter size (orange line) and Jupiter size planets (yellow line) are shown. The Survey 2 with increased magnitude and FOV coverage increases the potential detectable transit targets to nearly 100 for periods up to 100 hours.

6.7 SUMMARY

We conducted an all southern sky survey of bright HSDs searching for fast transit signals in the Evryscope light curves. The Evryscope data is 2 minute cadence, with continuous all southern sky observing for multiple years. We estimate the number of HSD targets in this work to be approximately 1400. Based on our recovery rates from transit simulations and the fraction of transiting objects, we expected to be sensitive to HSD variability of different types including compact binaries, HW Vir systems, transiting planets, reflection binaries, and other variables. We discovered 14 new HSD variables including 2 very rare compact binaries with unseen WD companions, 2 bright HW Virs, several reflection effect binaries and sinusoidal variables. Four of the systems are published in separate discovery papers solving the system parameters in detail. We also discovered 24 other variables in the survey including several post GB, HB, and BHB variable systems. We obtained spectra for the discoveries and determined the spectral types, and we identified the discoveries that are good candidates for future followup. A planned followup survey expanding the targets in this work by at least a factor of 4 is discussed.

Acknowledgements

This research was supported by the NSF CAREER grant AST-1555175 and the Research Corporation Scialog grants 23782 and 23822. HC is supported by the NSFGRF grant DGE-1144081. BB is supported by the NSF grant AST-1812874. The Evryscope was constructed under NSF/ATI grant AST-1407589. This work was supported by the National Science Foundation through grant PHY 17-148958.

This work includes observations obtained at the Southern Astrophysical Research (SOAR) telescope, which is a joint project of the Ministério da Ciência, Tecnologia, Inovações e Comunicações (MCTIC) do Brasil, the U.S. National Optical Astronomy Observatory

(NOAO), the University of North Carolina at Chapel Hill (UNC), and Michigan State University (MSU).

This research has used the services of `www.Astroserver.org` under reference EVRY01. P.N. acknowledges support from the Grant Agency of the Czech Republic (GAČR 18-20083S).

This paper includes data collected by the TESS mission. Funding for the TESS mission is provided by the NASA Explorer Program.

This research has made use of the SIMBAD database, operated at CDS, Strasbourg, France.

This research has made use of the VizieR catalogue access tool, CDS, Strasbourg, France (DOI : 10.26093/cds/vizier). The original description of the VizieR service was published in AAS 143, 23.

This research has made use of the International Variable Star Index (VSX) database, operated at AAVSO, Cambridge, Massachusetts, USA.

CHAPTER 7: EVR-CB-001: AN EVOLVING, PROGENITOR, WHITE DWARF COMPACT BINARY - DISCOVERED WITH THE EVRYSCOPE

This section presents results published in the *The Astrophysical Journal*.[1][2]

7.1 INTRODUCTION

We present EVR-CB-001, the discovery of a compact binary with an extremely low mass ($.21 \pm 0.05 M_{\odot}$) helium core white dwarf progenitor (pre-He WD) and an unseen low mass ($.32 \pm 0.06 M_{\odot}$) helium white dwarf (He WD) companion. He WDs are thought to evolve from the remnant helium-rich core of a main-sequence star stripped during the giant phase by a close companion. Low mass He WDs are exotic objects (only about .2% of WDs are thought to be less than .3 $M_{\odot}$), and are expected to be found in compact binaries. Pre-He WDs are even rarer, and occupy the intermediate phase after the core is stripped, but before the star becomes a fully degenerate WD and with a larger radius ($\approx .2 R_{\odot}$) than a typical WD. The primary component of EVR-CB-001 (the pre-He WD) was originally thought to be a hot subdwarf (sdB) star from its blue color and under-luminous magnitude, characteristic of sdBs. The mass, temperature ($T_{\rm eff} = 18,500 \pm 500 K$), and surface gravity ($\log(g) = 4.96 \pm 0.04$) solutions from this work are lower than values for typical hot subdwarfs. The primary is likely to be a post-RGB, pre-He WD contracting into a He WD, and at a stage that places it

[1]Ratzloff JK, Barlow BN, Kupfer T, Corcoran KA, Geier S, Bauer E, Corbett HT, Howard W, Glazier A, and Law NM. EVR-CB-001: An Evolving, Progenitor, White Dwarf Compact Binary Discovered with the Evryscope. *The Astrophysical Journal* 2019; 883:51. DOI: 10.3847/1538-4357/ab3727.

[2]The writing on this paper was approximately 50% Ratzloff, 30% Barlow, and 20% Kupfer. I discovered the system, took the followup SOAR spectra and light curve, processed the data, and researched close binaries, HSDs, and ELMs to gather background necessary in understanding this system. Barlow performed the period analysis, took and processed the RV spectra, and examined the evolution history of the system. Kupfer performed the detailed atmospheric and light curve modeling, and worked with Bauer to compare EVR-CB-001 to stellar evolutionary tracks.

nearest to sdBs on color-magnitude and T_{eff}-log(g) diagrams. EVR-CB-001 is expected to evolve into a fully double degenerate, compact system that should spin down and potentially evolve into a single hot subdwarf star. Single hot subdwarfs are observed, but progenitor systems have been elusive.

Compact binaries are highly sought after and studied objects because of their potential to test stellar formation and evolution theory, and measure primary and secondary parameters to high precision. Compact binaries are the suspected progenitors to astrophysical phenomena that are not well understood, including many classes of supernovae, single hot subdwarf B (sdB) stars, and low-mass white dwarfs (see [168] and references therein). The primary and secondary components of compact binaries influence the usefulness of the system to explain key formation or evolution phases [169]. Photometric variability from eclipses, ellipsoidal deformation, gravitational limb darkening, Doppler beaming, or from combinations of these effects enables system parameters to be solved more fully and with higher precision than from radial velocity alone [48, 59, 170]. Systems that are evolving into highly-sought-after and poorly understood objects are useful for testing theory and allowing for detailed observations of rare progenitors [138, 171–173]. We discuss these points in the context of white dwarf (WD) binaries and show EVR-CB-001 to be a rare combination of almost all of these desired traits.

Many compact binaries are thought to form as stars evolve from the main sequence to the giant phase, with an increasing radius that engulfs the companion and facilitates mass transfer. If the companion is unable to accrete at a high enough rate, a common envelope (CE) is formed and angular momentum is transferred to the envelope, thereby decreasing the orbital period. Eventual ejection of the CE leaves behind a compact binary with short orbital period [144]. Double WD or WD / sdB binaries with orbital periods below a few hours lose angular momentum predominantly from gravitational wave radiation, meaning that once the CE phase is completed this type of compact binary system will remain relatively unchanged.

These systems are good candidates to study the CE phase, especially the later stage [169]. EVR-CB-001 is a WD binary of this type with a potentially clean post CE phase.

The CE phase is also important for understanding the formation processes that lead to sdBs and low-mass He WDs. Low mass WDs must be formed through binary interactions (e.g. [169]) and most hot subdwarfs are thought to form from a red giant progenitor that is stripped of its outer hydrogen envelope during CE interactions with a nearby companion [174, 175]. This process leaves behind a $\approx 0.5 M_\odot$ helium-burning core (the hot subdwarf) in a close orbit with the companion that led to its formation. A comprehensive summary of hot subdwarfs can be found in [176–178]. If the mass of the He core in the progenitor is not high enough to start He burning when the star gets stripped the object will bypass the horizontal branch and contract onto the white dwarf cooling sequence as a He WD [179, 180]. If the He core is relatively young (not long past the CE phase), then it will be a pre-He WD with similar spectroscopic characteristics to an sdB (temperature, color and absolute magnitude) but with lower mass. Discovery of a pre-He WD at this juncture offers an opportunity to study a key intermediate stage of the He WD. The EVR-CB-001 primary is a pre-He WD apparently caught at a very early stage, with sdB–like characteristics; we actually discovered EVR-CB-001 in an sdB variability search due to its similar color/magnitudes.

The combined mass and the mass ratio of the primary and the companion is a key driver for studying compact binaries. Compact binary searches originally targeted high mass WD/WD or WD/sdB mergers as they are thought to be the most promising type Ia supernovae (SN Ia) progenitors [181]. Compact binaries with the necessary mass and short period have proven elusive, with just a handful of promising candidates despite decades of searching [56, 59, 138, 182] and [172, 173].

More recently, searches have aimed to find low-mass systems with the goal of explaining the formation of He WDs and other exotic objects. He WDs with masses less than $.3 M_\odot$ do not have a known mechanism to fuse helium, and would have to evolve from the giant phase and cool to form final He WD. This is expected to take longer than the age of the galaxy

[169]. A CE stage from a close companion would interrupt this lengthy stellar evolution process, and extremely low mass He WDs are expected to be members of compact binaries. The ELM project, using color-color cuts from the SDSS and spectra from the Hypervelocity Star Survey (HVS), has found a few dozen extremely low mass He WDs as well as pre-He WDs [117, 180, 183, 184].

Compared to these known extremely low mass He WD systems, the primary of EVR-CB-001 has the lowest surface gravity of all known systems and a higher temperature than all but a few, and is quite rare in that the primary and secondary are both extremely low mass for WDs. The system is compact with a fast period, and will evolve into a fully double degenerate binary. It is then expected to shrink via gravitational wave radiation, and merge into a single helium-rich object or if the merge can be prevented into a stably accreting AM CVn binary. In § 7.6 we discuss EVR-CB-001 as viable progenitor candidate for a single hot subdwarf with a mass (estimated from the pre-merger mass of $.47 M_{\odot}$), very close to the canonical hot subdwarf mass.

Only a small fraction of compact detached binaries show photometric ellipsoidal and radial velocity variations necessary for detailed solutions. Only five such fast-period hot subdwarf + WD binaries have been published in the literature [56, 138, 185–187], and fewer than ten WD/WD compact systems with either eclipses or ellipsoidal modulations [48]. EVR-CB-001 shows high amplitude photometric variability with multiple components, large radial velocity variations, and it is bright ($m_G = 12.581 \pm .003$), characteristics which allow for a precise solution of the system.

Here we report the discovery of the pre-He WD+He WD binary Gaia DR2 5216785445160303744 (hereafter, "EVR-CB-001"), which shows strong ellipsoidal modulations and gravitational darkening. We note that ASAS-SN listed the source as a unidentifiable variable (ASASSN-V J084815.55-741854.3) in [32]. EVR-CB-001 was found from a southern all-sky hot subdwarf survey searching for low-mass companions (Ratzloff et al., in prep) using the Evryscope.

This paper is organized as follows: in § 7.2 we describe the observations and reduction. In § 7.3 we describe our spectroscopic analysis to determine the orbital and atmospheric parameters of the pre-He WD. In § 7.4 we model the photometric light curve to determine ellipsoidal modulations and test for eclipses. In § 7.5 we solve the system and show our results. In § 7.6 we discuss our findings and conclude in § 7.7.

7.2 Observations & Reduction

7.2.1 Evryscope Photometry

We discovered photometric oscillations in EVR-CB-001 from analyzing 2.5 years of data from the Evryscope, obtained from January, 2016 to June, 2018. Data were taken through a Sloan g filter with 120 s integration times, providing a total of 53,698 measurements. The wide-seeing Evryscope is a gigapixel-scale, all-sky observing telescope that provides new opportunities for uncovering rare compact binaries through photometric variations. It is optimized for short-timescale observations with continuous all sky coverage and a multi-year period observation strategy. The Evryscope is a robotic camera array mounted into a 6 ft-diameter hemisphere which tracks the sky [17, 19]. The instrument is located at CTIO in Chile and observes continuously, covering 8150 sq. deg. in each 120s exposure. Each camera features a 29MPix CCD providing a plate scale of 13"/pixel. The Evryscope monitors the entire accessible Southern sky at 2-minute cadence, and the Evryscope database includes tens of thousands of epochs on 16 million sources.

Here we only briefly describe the calibration, reduction, and extraction of light curves from the Evryscope; for further details we point the reader to our Evryscope instrumentation paper [19]. Raw images are filtered with a quality check, calibrated with master flats and master darks, and have large-scale backgrounds removed using the custom Evryscope pipeline. Forced photometry is performed using APASS-DR9 [79] as our master reference catalog. Aperture photometry is performed on all sources using multiple aperture sizes; the final aperture for each source is chosen to minimize light curve scatter. Systematics removal is performed with a custom implementation of the SysRem [77] algorithm.

We use a panel-detection plot that filters the light curves, identifies prominent systematics, searches a range of periods, and phase folds the best detections from several algorithms for visual inspection. It includes several matched filters to identify candidate hot subdwarfs for variability and is described in detail in [66]. EVR-CB-001 was discovered using Box Least Squares (BLS; [28, 29]) with the same settings, pre-filtering, and daily-alias masking described in [66]. The discovery tools and settings were tested extensively to maximize recovery of the fast transits and eclipses characteristic of hot subdwarfs and white dwarfs. As part of our testing, we also recovered CD-30 [138], the only known fast-period hot subdwarf + WD binary in our field of view and magnitude range. The BLS power spectrum revealed EVR-CB-001 to be a 2.34 hr binary exhibiting strong (12%) modulations due to the ellipsoidal deformation of the primary from the unseen, more massive companion. The detection power in terms of Signal Detection Efficiency (SDE) [28] is 33.5, compared to an average SDE of 8 for targets in the hot subdwarf survey [120] that EVR-CB-001 was discovered in. Figure 7.1 presents both the BLS power spectrum and phase-folded light curve.

Our detection tools also include Lomb-Scargle (LS) [30, 31] and interestingly, the LS detection of the short periods in both EVR-CB-001 and CD-30 are relatively weak and are overpowered by longer periods (the search range in our survey is 2-720 hours for LS in an effort to recover a wide range of variables). Narrowing the period search range and further filtering of low frequency signals recovers the same period from LS as the BLS discovery. The high amplitude photometric variability in EVR-CB-001 results in an asymmetric signal, with a difference in even versus odd phase that is significant enough to affect the LS (optimized for sinusoidal signals) recovery. In this work, we show the BLS signal as it is the algorithm that led to the discovery, and is confirmed to be the correct period in § 7.3. In the Evryscope hot subdwarf survey [120], we compare the effectiveness of BLS and LS in detecting compact

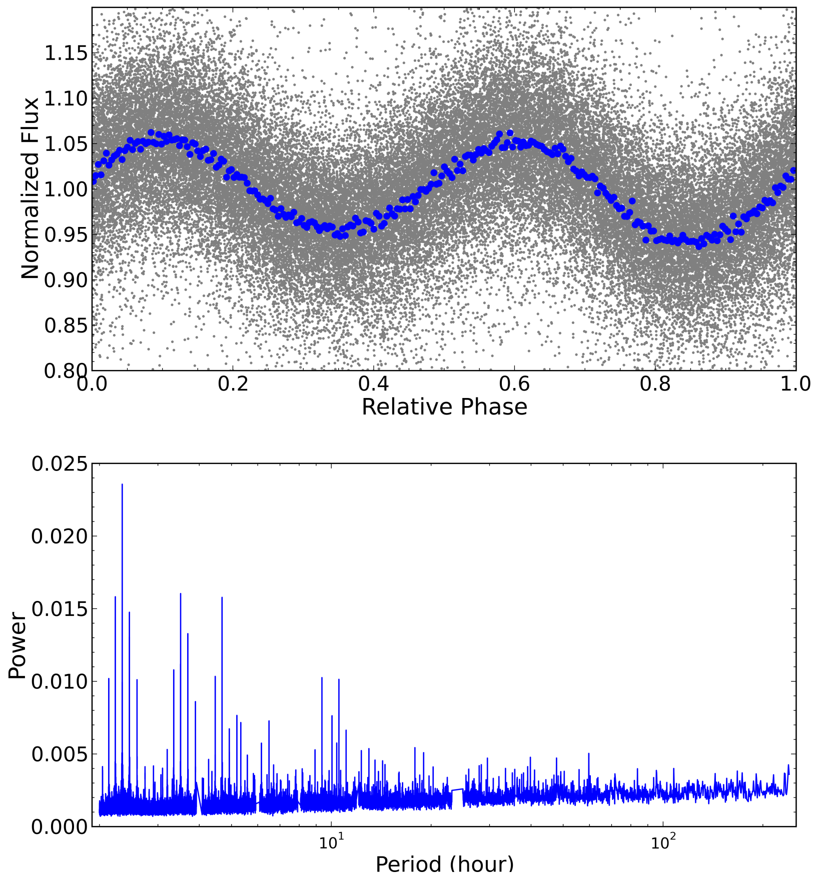

Figure 7.1: The Evryscope discovery light curve of EVR-CB-001 folded on its period of 2.34249 hours is shown on the top panel. Grey points = 2 minute cadence, blue points = binned in phase. The bottom panel shows the BLS power spectrum with the highest peak at the 2.34249 hour detection.

ellipsoidal systems with multiple light curve features and discuss the modifications to our original search in an effort to maximize the recovery of these compact binary systems.

A subtle asymmetry in the light curve (a sub 1% difference in the height of alternating peaks) is observed, indicative of Doppler boosting with the higher peak corresponding to the orbital position where the pre-He WD is moving toward us most quickly. The difference in minima is due to gravitational darkening of the deformed primary, with the lower minimum corresponding to the orbital position where the pre-He WD is farthest from us.

7.2.2 SOAR/Goodman Photometry

In order to obtain a higher S/N light curve for modeling, we observed EVR-CB-001 on January 5, 2019 using the SOAR 4.1 m telescope at Cerro Pachon, Chile, with the Goodman spectrograph [33] in imaging mode. We used the blue camera with Bessel-V blocking filter and took 409 images with 15 s integration times. The image Region of Interest (ROI) was reduced to 1700 x 1000 pixels with 1x1 binning, which resulted in a 60% duty cycle. The surrounding field is sparse, and so a larger-than-ideal ROI was needed to capture a sufficient number of comparison stars. For calibrations, we took 10 dome flats using 25% lamp power and 10 s integrations, 10 darks also with 10 s integrations, and 10 bias frames.

The SOAR frames were processed with a custom aperture photometry pipeline written in Python. The object images were bias-subtracted, dark-subtracted, and flat-field-corrected using master calibration frames. Five reference stars of similar magnitude were selected, and aperture photometry was performed on all frames using a centroid algorithm and range of aperture sizes. The reference stars were confirmed to be non-variable. We also use the photometric aperture on dark areas of the image near the reference stars to capture background counts. The reference star counts are combined for the image and the background is subtracted (using the average per-pixel background times the pixels in the aperture). The background subtracted reference star counts are recorded for each image, and normalized by the mean. The target star counts are background subtracted in the same way and recorded for each image. The background subtracted target star counts are divided by the normalized background subtracted reference star counts to remove sky variations. The result is normalized by the mean to produce the final light curve.

In order to choose the best aperture, we removed variability from each light curve and chose the aperture with the lowest residual rms values. At this juncture, we did not have an exact model of the astrophysical variability of the system, but needed a reliable estimate of the variability so that it could be removed to measure the residual rms and choose the best photometric aperture. We used a Savitzk-Golay filter from the scipy.signal module

Table 7.1: Overview of Observations for EVR-CB-001

Telescope	Date	Filter/Resolution	Epochs	Exposure
Photometry				
Evryscope	Jan 2016 - Jun 2018	Sloan g	53,698	2 min
SOAR/Goodman	Jan 5, 2019	Bessel-V	409	15 s
Spectroscopy				
SMARTS 1.5-m/CHIRON	Dec 2018 - Jan 2019	28,000	29	600 s
SOAR/Goodman	Dec 2, 2018	1150	4	360 s

[188], holding the the filter settings constant for all apertures. We also explored different settings to confirm the filter was not biasing the results. The filter was only used in this step to determine the best aperture, and is in no way applied to the photometry. The solution converged nicely with the minimum rms corresponding to a photometric aperture of 36 pixels, as shown in Figure D.2 in the appendix. The resulting differential light curve from SOAR, which we use to model EVR-CB-001, is shown later in the manuscript, in Figure 7.7.

7.2.3 SMARTS 1.5-m/CHIRON Spectroscopy

We observed EVR-CB-001 on 29 nights between December 19, 2018 and January 28, 2019 with the SMARTS 1.5 m telescope and CHIRON, a fiber-fed cross-dispersed echelle spectrometer [38]. Spectra were taken in image fiber mode (R $\sim$ 28000) and covered the wavelength range 4400-8800 Å. We used integration times of 600 s to obtain just enough S/N for radial velocity measurements; longer integrations would have resulted in too much phase-smearing. Spectra were obtained every few days at specified epochs until full phase coverage was achieved. All raw spectra were reduced and wavelength-calibrated by the official CHIRON pipeline, housed at Georgia State University and managed by the SMARTS Consortium[3]. In addition to Hα and Hβ, which span multiple orders, the spectra show four He I lines, including 6678 Å, 5876 Å, 5016 Å, and 4922 Å. All of these lines are synced in phase, with no signs of absorption due to a companion, and we conclude they emanate from a single star.

[3]http://www.astro.yale.edu/smarts/

7.2.4 SOAR/Goodman Spectroscopy

The CHIRON spectra have too high a resolution to easily model atmospheric parameters using the H Balmer lines, which span multiple orders. As such, we also obtained low-resolution spectra on December 2, 2018 with the Goodman spectrograph using the 600 mm^{-1} grating blue preset mode, 2x2 binning, and the 1" slit. This configuration provided a wavelength coverage of 3500-6000 Å with spectral resolution of 4.3 Å (R∼1150 at 5000 Å). We took four 360 s spectra of both the target and the spectrophotometric standard star BPM 16274. For calibrations, we obtained 3 x 60 s FeAr lamps, 10 internal quartz flats using 50% quartz power and 30 s integrations, and 10 bias frames.

We processed the spectra with a custom pipeline written in Python. The spectra were individually bias-subtracted and flat-corrected. A 3rd-order polynomial was fitted to the brightest pixels in each row; the spectra are then extracted in a 10-pixel range and background subtracted. We identify 16 prominent lamp emission lines and compare with the known lines of the FeAr lamp using a Gaussian fit to each feature. We used a 4th-order polynomial to fit the wavelength solution and calibrate each spectrum. We used our observations of BPM 16274 to flux-calibrate the EVR-CB-001 spectra by removing prominent absorption features and fitting a 7th-order polynomial to the continuum. Each spectrum was then rest-wavelength calibrated using a Gaussian fit to the Hβ through H11 absorption features, as well as several prominent He absorption features. The resulting spectra were median-combined to form a final spectrum for atmospheric modeling. As shown in Figure 7.4, we detect strong H Balmer lines, from Hβ through H13, and one He I line at 4472 Å. As was the case for the CHIRON spectra, we find no evidence of absorption features due to the companion star; EVR-CB-001 appears to be a single-lined binary. Table 7.1 presents a brief overview of all of the photometric and spectroscopic data used in our analysis of EVR-CB-001.

7.3 Orbital and Atmospheric Parameters

The long baseline and dense coverage of the Evryscope photometry means we can determine the orbital period with high precision through O–C analysis. First, we converted all Evryscope time stamps from Modified Julian dates to Barycentric Julian dates, BJD_{TDB}, using the web tool provided by [189]. As an initial guess for the ephemeris, we used a Lomb Scargle periodogram to approximate the orbital period (P) and used a sine wave fit to the entire data set to estimate a reference time of minimum (T_0). From these, we generated several predicted times of minima (C values). Observed times of minima (O values) were determined by breaking up the entire Evryscope light curve into several segments, each containing approximately 10 orbits of data, and performing least-squares fits of sine waves to the segments. We then plotted O–C against O and adjusted T_0 and P iteratively until there was no residual slope and the mean O–C value was zero. From this process we report the following orbital ephemeris for times of light minima, with E representing the cycle number:

$$\begin{aligned} t_{min} &= \mathrm{BJD\,UTC}\ (2457812.75378 \pm 0.00005) \\ &+ (0.09760507 \pm 0.00000002\,\mathrm{d}) \times E \end{aligned}$$

The O-C diagram is fitted well with a linear trend, and we currently find no statistically significant evidence of a parabolic trend due to secular evolution or oscillations from reflex motion. We limit changes in the orbital period to $|\dot{P}| < 8 \times 10^{-9}$ s s^{-1}.

Radial velocities were determined using data from CHIRON. We visually inspected each spectral order and chose the following high signal-to-noise absorption features for fitting: He I 4922 Å, He I 5016 Å, He I 5876 Å, Hα 6563 Å, and He I 6678 Å. Within each of their respective orders, we crop out a small section of the spectrum encompassing the absorption feature, fit a polynomial to the surrounding continuum, divide by the best-fitting polynomial to normalize the spectrum, and fit a Gaussian to the absorption feature. We use the centroid

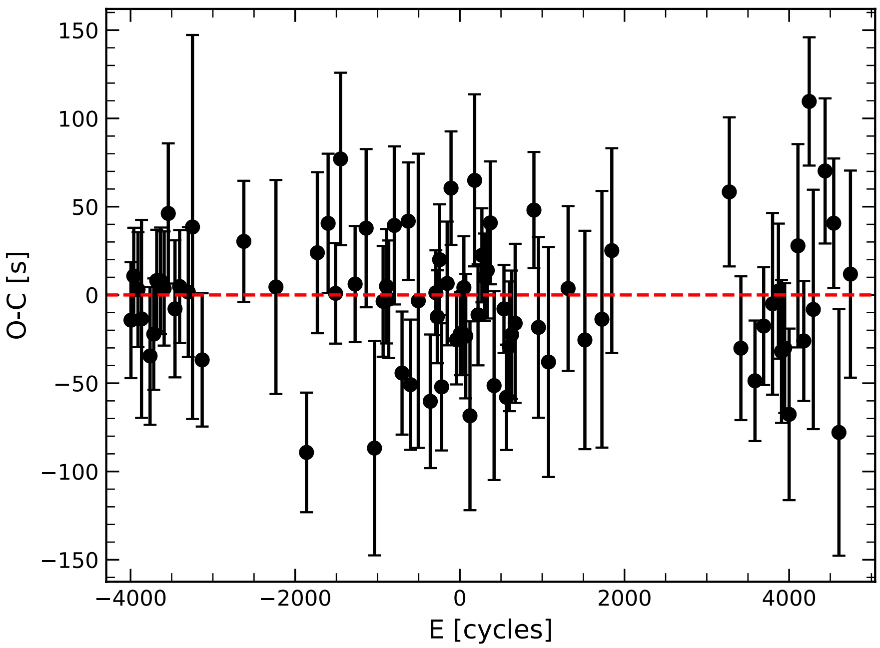

Figure 7.2: O–C diagram constructed from the Evryscope light curve. The 2.5–year light curve was broken into 77 segments, each with 10 orbits worth of data (∼700 measurements), and sine waves were fitted to the segments to determine phases. We limit any changes in the orbital period to $|\dot{P}| < 8 \times 10^{-9}$ s s^{-1}.

of the best-fitting Gaussian as the observed wavelength in order to derive a velocity. Each spectrum is assigned a final radial velocity/uncertainty using a weighted average/uncertainty from all five individual line results. Finally, we convert these measurements to heliocentric velocities using PyAstronomy's *baryCorr* function. A sine wave fit to the data reveals a velocity semi-amplitude of $K = 200.6 \pm 2.3\,\mathrm{km\ s^{-1}}$, as shown in Figure 7.3, with all radial velocity data provided in Table D.1 in the appendix. However, our individual exposure times were non-negligible fractions of the orbital period (∼7.1%). Orbital phase smearing leads to our measuring only 0.9917 of the full semi-amplitude (derivation shown in [190]); thus, we should inflate our measurement by a factor of 1.0084 to recover the true value. We report as our final semi-amplitude for the hot subdwarf primary $K = 202.3 \pm 2.3$ km s^{-1}. Additionally, we report a systemic velocity of $\gamma = 18.4 \pm 1.5\,\mathrm{km\ s^{-1}}$ for the binary.

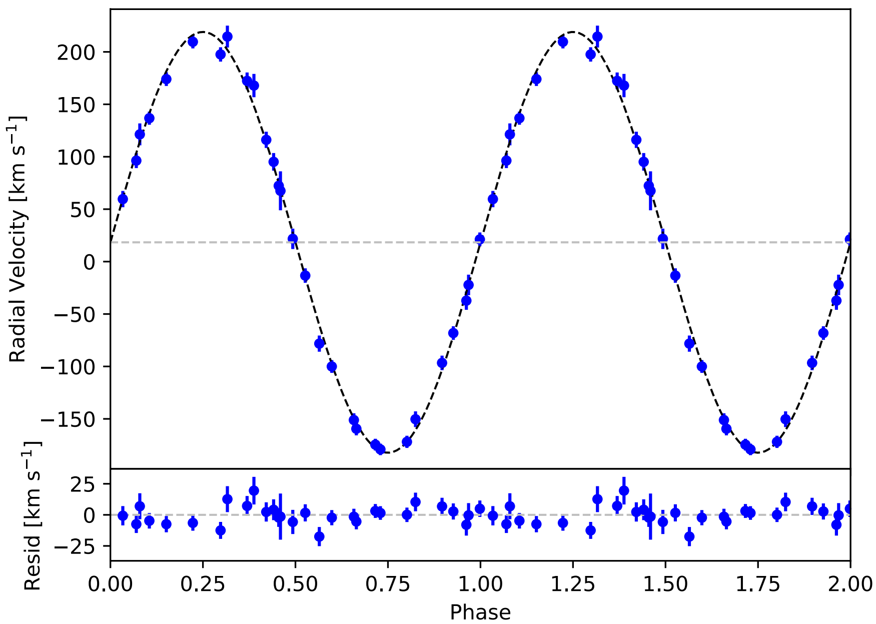

Figure 7.3: *Top panel:* Phase-folded, heliocentric radial velocity measurements from SMARTS 1.5-m/CHIRON, plotted twice for better visualization. The solid line denotes the best-fitting sine wave to the data. After correcting for slight phase smearing, we find a velocity semi-amplitude of $K = 202.3 \pm 2.3$ km s^{-1} and systemic velocity of $\gamma = 18.4 \pm 1.5$ km s^{-1}. *Bottom panel:* Residuals after subtracting the best-fitting sine wave from the data.

We use the rest-wavelength-corrected average SOAR spectrum to determine the primary star's atmospheric parameters by a simultaneous fitting of H and He line profiles with metal-line-blanketed LTE synthetic spectra, as described in [191]. The primary star's surface gravity ($\log(g)$), effective temperature ($T_{\rm eff}$), and helium abundance ($\log(y) = \log[n_{\rm He}/n_{\rm H}]$) are determined by fitting H Balmer profiles H13 through Hβ, along with He I 4472 Å. We note that the Balmer lines closest to the Balmer jump are the most sensitive to $\log(g)$ and $T_{\rm eff}$. We find $T_{\rm eff} = 18500 \pm 500$ K, $\log(g) = 4.96 \pm 0.04$, and $\log(y) = -1.34 \pm 0.11$. Errors were derived using a χ-squared minimization. While the high-resolution CHIRON spectra are not suitable for determining $T_{\rm eff}$ and $\log(g)$, due to the H Balmer lines spanning multiple orders, they are sufficient for measuring the projected rotational velocity $v_{\rm rot} \sin i$ and more precisely determining the He abundance. After Doppler-correcting all CHIRON spectra to the same rest frame and stacking them to create a master high-resolution spectrum, we fitted the same synthetic models to the data, this time fixing $T_{\rm eff}$ and $\log(g)$ to the values determined from the SOAR spectrum. We find a helium abundance of $\log(y) = -1.43 \pm 0.03$, in agreement with the SOAR/Goodman result, along with a rotational velocity of $v_{\rm rot} \sin i = 112 \pm 4$ km s^{-1}.

All final results from the atmospheric modeling are shown in Table 7.2. The derived parameters place the primary star in EVR-CB-001 at the extreme cool edge of known hot subdwarf B stars.

7.4 Light Curve Analysis

Since only spectral features from the primary star are detected, we must rely on light curve modeling to compute the mass ratio q and constrain the system's parameters. We use the modeling code LCURVE [37] to analyze both the SOAR and Evryscope light curves. LCURVE models the surface of each star using Roche lobe geometry and grids of points, and it takes into account gravity darkening, limb darkening, Doppler boosting, and mutual illumination effects. In order to constrain the parameter space searched by the models, we use several assumptions, boundary conditions, and results from spectroscopy. We assume the orbit is circular, and that the primary star's rotation is synchronized with the orbit. For the invisible companion we assume a lower limit to the radius (mass), using the zero-temperature mass-radius relation by Eggleton (quoted from [192]). The limb darkening prescription and the passband specific gravity darkening prescription was used following [193, 194] and as tabulated in [195]. For the gravity darkening we used $b = 0.41 \pm 0.03$ for V and $b = 0.40 \pm 0.03$ for g'. For limb darkening we used $a_1 = 0.76, a_2 = -0.18, a_3 = 0.10, a_4 = -0.03$ for V band and $a_1 = 0.71, a_2 = -0.27, a_3 = 0.17, a_4 = -0.05$ for g'. Using the results for surface gravity ($\log g$), effective temperature ($T_{\rm eff}$), and rotational velocity ($v_{\rm rot} \sin(i)$) from § 7.3 as a prior, combined with the orbital period (P) and radial velocity (K), we determine the inclination angle (i), the mass ratio (q), as well as the scaled radii and velocity scale ($(K_1 + K_2)/\sin i$). Additionally we used a third order polynomial to account for residual airmass effects in

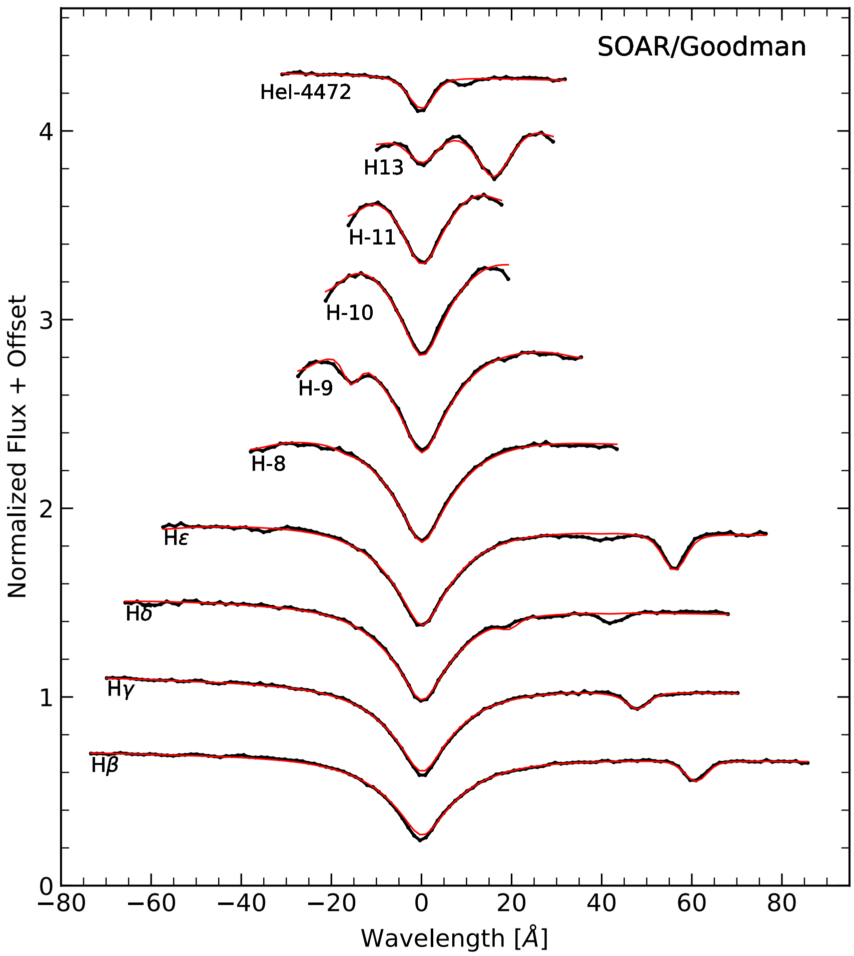

Figure 7.4: Normalized SOAR/Goodman spectrum of EVR-CB-001 (black line) with best–fitting atmospheric model (red line). Parameters associated with the best-fitting LTE model spectrum are shown in the figure.

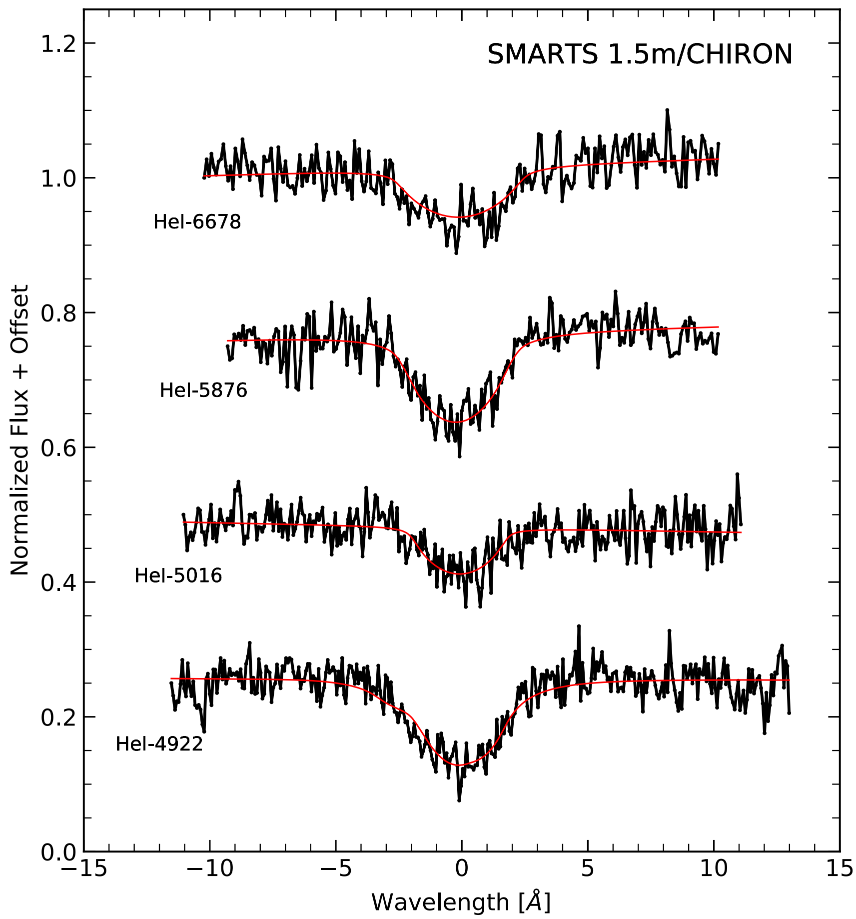

Figure 7.5: Normalized SMARTS 1.5-m/CHIRON spectrum of EVR-CB-001 (black line) with best–fitting atmospheric model (red line). Parameters associated with the best-fitting LTE model spectrum are shown in the figure. $T_{\rm eff}$ and log g were held as fixed parameters during the model fitting, set to the values determined from the SOAR/Goodman spectrum.

the SOAR lightcurve. The subscript 1 is used for the object which dominates the light (K_1, M_1, R_1), and the subscript 2 is used for the invisible companion (K_2, M_2, R_2).

This solution requires the additional assumptions of a lower limit He WD radius and fixed limb darkening coefficients explained in detail in [186]. The assumptions regarding the unseen companion suggest that it does not contribute substantially to the light curve. We test our assumptions by comparing the luminosity contributions of the primary and secondary for a range of likely radii and temperatures for the He WD companion. Using conservative estimates of 0.03 $R_\odot$ and T_{eff} of 10,000 K for the He WD companion, the luminosity contribution is 0.5%. This increases to 2.5% if the He WD companion has an effective temperature of 20,000 K. In a test run of our solution, we included the He WD effective temperature and radius as free parameters and found that both were unconstrained in the model fits. Because the luminosity contribution is very small and the He WD fit is unconstrained, we have assumed a fixed T_{eff} of 6000 K and a fixed radius of 0.02 $R_\odot$ for the He WD companion which implies a negligible luminosity contribution of 0.1%. The overall result of our solution (§ 7.5) did not change with this assumption.

We combine LCURVE with the MCMC implementation EMCEE [196] to explore the parameter space, converge on a solution, and to determine the uncertainties. We used 512 chains and let them run for 2500 trials well beyond a stable solution was reached. The corner plot of the final solution is shown in the appendix.

We use the binary mass function

$$f_m = \frac{M_2^3 \sin(i)^3}{(M_1 + M_2)^2} = \frac{PK^3}{2\pi G} \tag{7.1}$$

and assuming a tidally locked, circular orbit can be combined with

$$\sin(i) = \frac{(v_{rot} \sin(i))P}{2\pi R_1} \tag{7.2}$$

along with the standard mass-radius relation

$$R_1 = \sqrt{\frac{M_1 G}{g}} \tag{7.3}$$

to solve the system for the masses and radii of the visible (M_1, R_1) and invisible component (M_2, R_2). Full details of the approach are found in [182, 186]. The final fits using the Evryscope binned in phase light curve is shown in Figure 7.6 and the SOAR light curve is shown in Figure 7.7. The ellipsoidal deformation dominates the photometric variation in the light curve, but Doppler boosting and gravity darkening effects are also present. We compare the Evryscope binned in phase light curve to the SOAR light curve in § 7.6.4.

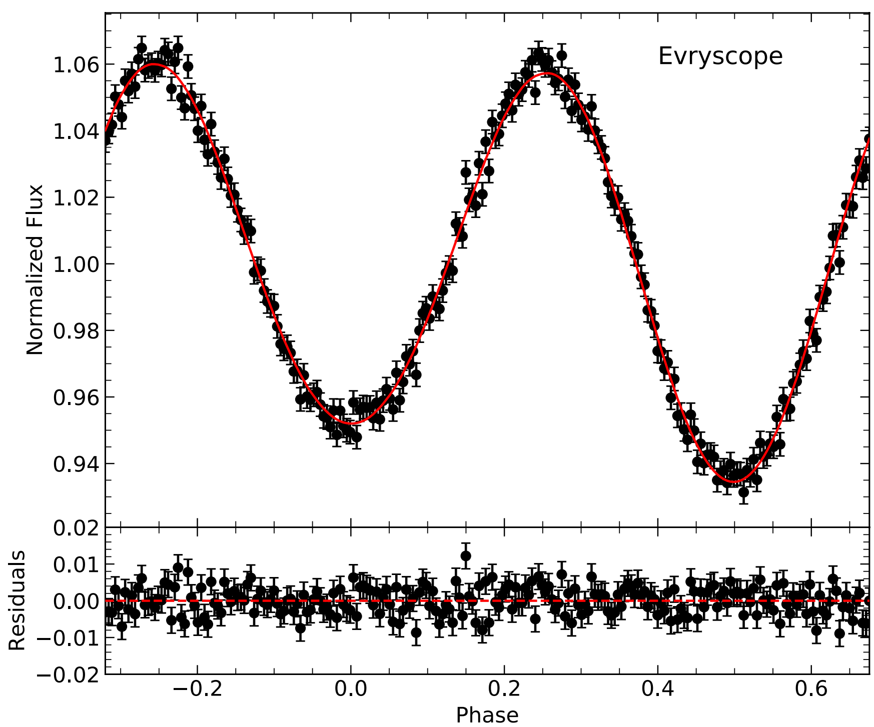

Figure 7.6: *Top panel:* The binned in phase Evryscope g light curve phase-folded on the 2.34252168 hour period with the best-fitting model determined by LCURVE. The original light curve has 53,698 epochs, and is binned using the unbiased $\sqrt{\#Epochs} = 232$ points. *Bottom panel:* Residuals after subtracting the best-fitting model.

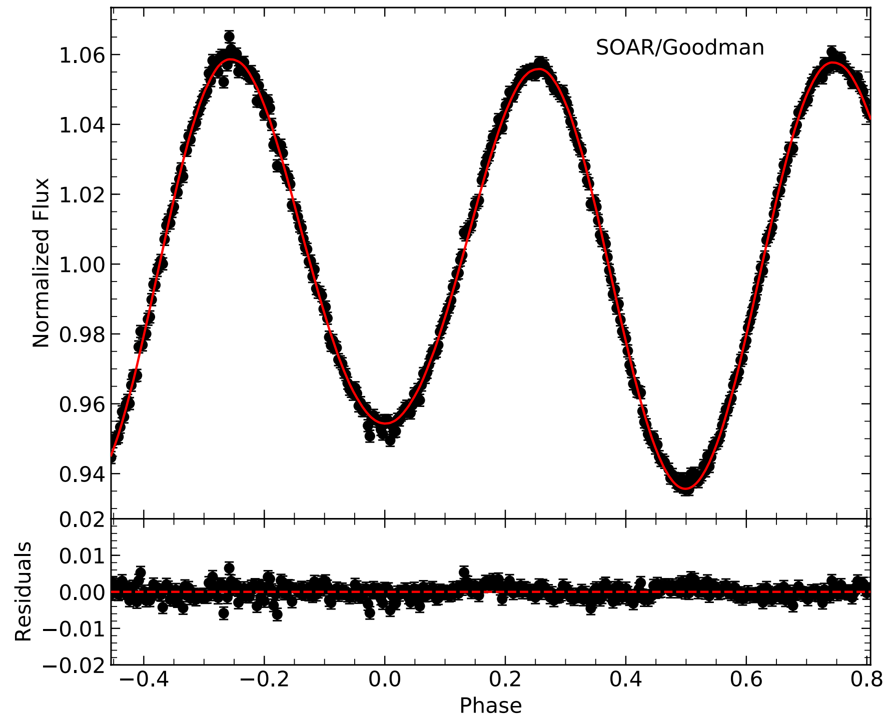

Figure 7.7: *Top panel:* SOAR/Goodman V light curve with the best-fitting model determined by LCURVE. *Bottom panel:* Residuals after subtracting the best-fitting model.

7.5 System Parameters

EVR-CB-001 is a single-lined binary that does not show eclipses; consequently, we cannot determine a unique solution for the system from the light curve analysis alone. However, we can still constrain the masses and radii of the two stars by combining the results of the light curve modeling with results from the spectroscopic fitting and the assumption that the primary component is tidally synchronized with the orbit. Parameters derived in this way are summarized in Table 7.2.

Our solution converges on a mass ratio of $q = M_1/M_2 = 0.66 \pm 0.07$, with individual masses of $M_1 = 0.21 \pm 0.05$ $M_\odot$ and $M_2 = 0.32 \pm 0.06$ $M_\odot$. We reiterate that the lower-mass star of the two is the dominant source of light in the system, and the one showing ellipsoidal modulation. This object has a radius of $R_1 = 0.24 \pm 0.03$ $R_\odot$ showing that the low-mass primary star is a low-mass pre-WD. The radius (R_2) of the unseen companion cannot be determined, due to the lack of eclipses. However, since it does not produce any detectable light in the system despite its higher mass, the companion is consistent with a low-mass Helium white dwarf (He WD).

Table 7.2: Overview of Derived Parameters for EVR-CB-001

Description	Identifier	Units	Value
	Basic Information		
Evryscope ID	EVR-CB-001		
GAIA DR2 ID	5216785445160303744		
Right ascension[a]	RA	[deg]	132.06452462505
Declination[a]	Dec	[deg]	-74.31507593399
Magnitude[a]	G	[mag]	12.581±0.003
Parallax[a]	ϖ	[mas]	2.239±0.042
Distance	d	[pc]	447±9
Absolute Magnitude	M_G	[mag]	4.33±0.05
	Atmospheric Parameters of the Pre-He WD		
Effective temperature	T_{eff}	[K]	18500±500
Surface gravity	$\log(g)$		4.96±0.04
Helium abundance	$\log(y)$		-1.43±0.03
Projected rotational velocity[c]	$v_{\mathrm{rot}} \sin i$	[km s^{-1}]	112±4
	Orbital Properties		
Period	P	[hr]	2.3425217(5)
Reference phase[b]	T_0	[BJD UTC]	2457812.75378(5)
RV semi-amplitude	K	[km s^{-1}]	202.3±2.3
Systemic velocity	γ	[km s^{-1}]	18.4±1.5
	Derived Parameters		
Mass Ratio	q		0.66±0.07
Pre-He WD mass	M_1	[$M_\odot$]	0.21±0.05
Pre-He WD radius	R_1	[$R_\odot$]	0.24±0.03
He WD mass	M_2	[$M_\odot$]	0.32±0.06
Orbital inclination	i	[°]	63±7
Separation	a	[$R_\odot$]	0.72±0.05

[a] *Gaia* G magnitude taken from the Gaia DR2 catalog [197]
[b] Time of light minimum, which corresponds to phase = 0.5 throughout the paper.
[c] Slight phase smearing

7.6 DISCUSSION

The primary component in EVR-CB-001 was originally thought to be a hot subdwarf B star, but the mass and surface gravity we have derived fall below the values of typical hot subdwarfs. Consequently, it is likely to be a post-RGB, pre-He WD, currently evolving through the cool end of the $T_{\rm eff}$-log(g) diagram occupied by hot subdwarfs. We independently estimate the mass of the pre-He WD and discuss its probable formation and evolution below.

7.6.1 Independent mass estimate of the pre-He WD

7.6.1.1 Magnitude / Distance

We tested our interpretation of the primary as a pre-He WD by estimating the pre-He WD radius and mass independently from the light curve modeling. Using the parallax from GAIA-DR2 [197] we determine the distance, and with the Johnson V-band magnitude from APASS [79] we use the distance modulus to determine the absolute magnitude (with the bolometric and extinction corrections described below). With the mass-radius relation (equation 3), we express the luminosity ($L = 4\sigma\pi R^2 T^4$ from the Stephan-Boltzman equation applied to a black body) as a function of mass and surface gravity instead of radius. Using the zero-point luminosity, we solve for the mass, combine constants, and simplify to the following formula:

$$
\begin{aligned}
M_1[M_{\rm odot}] \quad &= 4.06609 \times 10^{10} \times 10^{\log g} \times T_{\rm eff}[K]^{-4} \\
&\times 10^{-0.4 \times (BC_{\rm V} + m_{\rm V} - A_{\rm V} + 5 \times \log \varpi[arcsec])}
\end{aligned}
$$

In addition to the previously derived values for $T_{\rm eff}$ and $\log g$ from § 7.3, and the Gaia parallax ϖ, we adopted the apparent magnitude in the Johnson V-band $m_{\rm V} = 12.619 \pm 0.051$ mag from the APASS catalog. To account for the significant variability of the star, we adopted a higher uncertainty of 0.12 mag. The bolometric correction $BC_{\rm V} = -1.76 \pm 0.075$ was interpolated from Vizier table J/A+A/333/231/table3 [198] for the appropriate spectroscopic parameters. The extinction $A_{\rm V} = 0.3007 \pm 0.027$ mag was taken from the Stilism 3D maps of the local interstellar medium[4] [199] adopting the parallax distance from GAIA. To derive the mass uncertainty we used the Python Monte Carlo error propagation *mcerp* package assuming that all input parameters are normally distributed. From the resulting distribution we adopted the maximum value and the mass values at FWHM to derive the uncertainties.

In this way we derive $M_1 = 0.30^{+0.17}_{-0.10}\,M_\odot$ consistent with the mass determination from the binary analysis and indicating a low-mass pre-He WD. Using the mass-radius relation the radius of the pre-He WD $R_1 = 0.30^{+0.09}_{-0.07}$ is derived to be slightly larger than from the light curve analysis, but still consistent within the uncertainties.

7.6.1.2 MESA Stellar Evolution Code

To understand the nature of the primary, we have constructed pre-helium WD models for different masses using the MESA stellar evolution code [200–203], release version 10398. The models were constructed using an initially $1.0\,M_\odot$ star (thought to be the most likely progenitor when starting at the main-sequence stage) that ascends the red-giant branch (RGB), building a helium core before it starts He-core burning. Once the helium core reaches a specified mass, all but $0.01\,M_\odot$ of the hydrogen envelope is stripped. Residual hydrogen shell burning then governs the timescale for evolution as the star contracts and evolves toward hotter $T_{\rm eff}$ as seen in the resulting tracks (solid lines) in Fig. 7.8.

Additionally, we also computed MESA models of $0.461\,M_\odot$ (understood to be the beginning of the helium burning stage post RGB) He-burning stars with two different hydrogen envelope masses: 1.0 and $3.0 \times 10^{-3}\,M_\odot$. Our models use the MESA predictive mixing scheme for core convection to allow for proper growth of the convective He core and yield the correct core burning lifetime and luminosity [203]. The tracks for these models extend from the beginning of core He burning through exhaustion of He in the core 150 Myr later. After this phase, the stars will begin He shell burning and evolve toward a hotter effective temperature. Our measured $T_{\rm eff}$ and $\log(g)$ intercepts tracks with masses in the

[4]https://stilism.obspm.fr/

range $0.22 - 0.23$ $M_\odot$, which is in agreement with the mass determined from our light curve modeling (see § 7.5) as well as the determination using Gaia DR2 (see the previous paragraph). Known hot subdwarfs from [144] are shown for comparison, clearly hotter and with higher surface gravity than EVR-CB-001. Overall, the compact binary EVR-CB-001 appears to contain a pre-He WD that is ellipsoidally deformed due the gravitational presence of an unseen He WD companion.

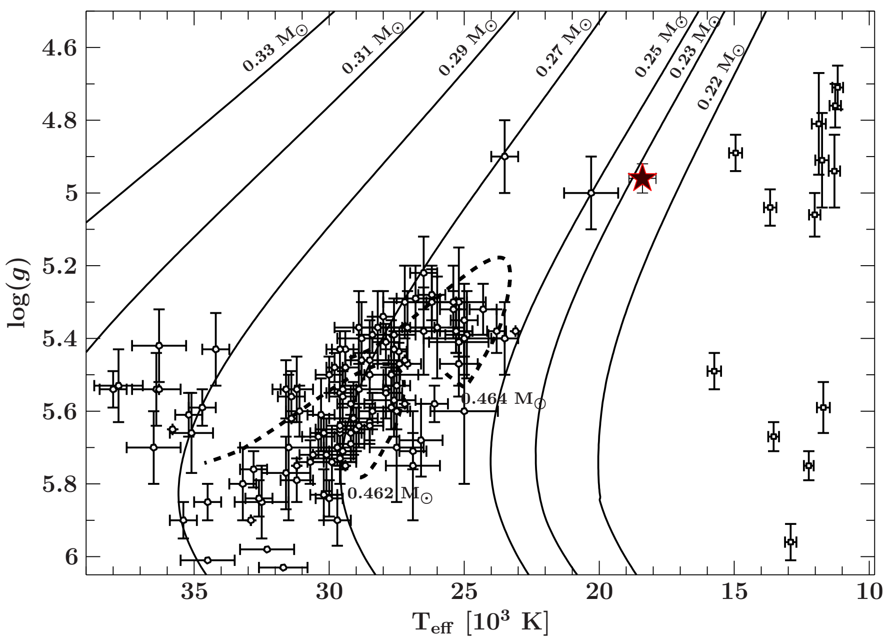

Figure 7.8: MESA evolutionary tracks for a variety of pre-He WDs and low-mass He-burning star models. EVR-CB-001's atmospheric parameters are overplotted and show the primary star is likely a pre-He WD with mass near 0.2 $M_\odot$, in agreement with our light curve modeling solution. Known hot subdwarfs (open circles; [144]) and some binaries from the ELM sample (open squares; [117]) are shown for comparison. EVR-CB-001 lies clearly in between the hot subdwarfs and the ELM sample.

7.6.2 Comparison to other Ellipsoidal Systems

There does not appear to be an exact known analog for EVR-CB-001. In the following discussion, we compare the prominent features and components to known systems.

The photometric variability of EVR-CB-001 most resembles one of the exceptional massive WD / hot subdwarf compact binaries such as KPD 1930+2752, KPD 0422+5421, or CD-30

11223 [56, 138, 185] but with a higher amplitude in light curve variability. This is reasonable given the lower mass and surface gravity as well as the bloated nature of the pre-He WD of EVR-CB-001 compared to hot subdwarfs. CSS 41177 is a rare eclipsing WD / WD compact binary with deep eclipses and relatively low mass WDs [204]. However, both of the WDs are mature and there is no ellipsoidal deformation given the high surface gravity of each WD.

Short period WD / WD binaries with extremely low mass secondaries have been recently discovered showing tidal distortions [205, 206] and eclipses in the case of the exceptional system J0651+2844 [207]. The ELM survey [208] has discovered compact binaries and potential merger systems with extremely low mass secondary components. The higher temperature, lower surface gravity, early evolutionary stage, and extreme light curve variation of EVR-CB-001 are quite different compared to the ELM binaries, as is the mass ratio of the primary and secondary.

The companion of HD 188112 [209] is perhaps most similar to the pre-He WD of EVR-CB-001, however it is higher mass, surface gravity, and temperature. The system is quite different than EVR-CB-001 with a high mass WD primary, a longer period, and without photometric variation. WD 1242-105 [172] is an example double degenerate binary with similarly favorable conditions to EVR-CB-001 that will potentially merge into a single hot subdwarf B star. The higher total mass and similar primary and secondary WDs highlight some of the differences to the EVR-CB-001 system. OWJ074106.0-294811.0 [187] is an ultra compact system with large photometric variability, but with quite different components (more massive, hotter, and higher surface gravity). EVR-CB-001 is best understood as combining interesting parts of each of these rare binaries to form a peculiar system.

7.6.3 Formation History & Future Evolution

EVR-CB-001 likely formed via two separate stages of mass transfer. The original binary consisted of two main sequence stars. As the more massive of these evolved off the main sequence first and ascended the red giant branch, it filled its Roche lobe and started transferring mass onto its less massive companion. Whether this stage of mass transfer was dynamically stable (stable RLOF) or unstable (CE formation) depends on many unknown parameters, most notably the mass ratio at the time of transfer. Either way, enough mass was stripped from the red giant that its remnant was unable to fuse helium thereafter and formed a He WD.

The second phase of mass transfer, which commenced once the lower-mass main sequence star reached the giant phase, was undoubtedly unstable and led to the formation of a common envelope. Its He WD companion was unable to accrete at a sufficiently high rate, and significant mass was ejected, further tightening the orbit. Once again, the stripped object was left with insufficient mass for fusing He, causing it also to bypass the horizontal branch and collapse onto the white dwarf cooling sequence as another He WD. We appear to have caught EVR-CB-001 fairly shortly after this second mass transfer stage: the object that was most recently stripped of its outer layers appears as a hot and bloated pre-He WD, on its way to becoming a fully-degenerate WD. Assuming that the progenitor of the pre-He WD was a $\sim$1 $M_{\odot}$ star, we can calculate the orbital period of EVR-CB-001 at the moment when the progenitor filled its Roche lobe. Using the same MESA model as used in § 7.6.1.2 we find that a $1\,M_{\odot}$ progenitor has a radius of 4 - $9\,R_{\odot}$ when the helium core has built up a mass of 0.17 - $0.23\,M_{\odot}$. Assuming a $0.3\,M_{\odot}$ companion we find that the progenitor system consisting of a He-WD with a red giant had a period of $\approx$1 - 3 days when the red giant filled its Roche Lobe and started unstable mass transfer. This shows that the orbit must have shrunken substantially during the common envelope phase when the pre-He WD was formed.

EVR-CB-001 represents a viable candidate progenitor system for the He WD merger channel leading to single hot subdwarf B stars (e.g. [174, 210]). Eventually, the pre-He WD we now observe will evolve onto the white dwarf cooling sequence, and EVR-CB-001 will become a full-fledged double-degenerate system. At such a short orbital period, gravitational wave radiation will cause the system to shrink until the less massive He WD (currently a pre-He WD) fills its Roche lobe in about $\approx 1\,$Gyr, at an orbital period of a few minutes. If the initiated mass transfer is dynamically unstable, the less massive He WD will be dynamically disrupted and form an accretion disk around its companion [211, 212]. Depending on the details of the evolution of the accretion disk and accretion rates, it is possible for the more massive He WD to increase its mass to the point where it ignites He shell burning and becomes a core He-burning hot subdwarf B star with $\sim$0.5 $M_\odot$. Unlike the other formation channels presented by [174, 175], which all leave behind a *binary* hot subdwarf system, this He WD merger channel produces a *single* hot subdwarf B star.

Although EVR-CB-001 is a candidate to form a single hot subdwarf B star, the system has a mass ratio (.66 $\pm$ .07) which might prevent the merger and instead evolve into a stable accreting AM CVn type binary. We briefly discuss this possibility here. For double white dwarf systems, commonly in the literature a system with a mass ratio $q = M_2/M_1 < 2/3$, M_1 being the mass of the accretor, is assumed to prevent the merger. However, [213] and [214] studied the effect of coupling of the accretor's and donor's spin to the orbit when the larger objects starts to fill its Roche Lobe. They found that a strong coupling and therefore a strong feedback of angular momentum to the orbit can destabilize systems with mass ratios lower than $q = M_2/M_1 < 2/3$,M_1 being the mass of the pre-He WD. Most recently, [215] proposed that even accreting double WD binaries with extreme mass ratios will merge due to classical nova-like outbursts on the accretor. Dynamical friction within the expanding nova shell causes the binary separation to shrink and the donor to dramatically overfill its Roche lobe, resulting in highly super-Eddington mass transfer rates that lead to a merger. This result was supported by [216] who found that the merger rate of extremely low mass (ELM) white dwarfs exceeds the formation rate of AM CVn binaries by a factor of 40 concluding that most ELM white dwarf binaries merge. Thus, although we cannot definitively conclude either way, EVR-CB-001 is a viable candidate to merge and form a hot subdwarf B star.

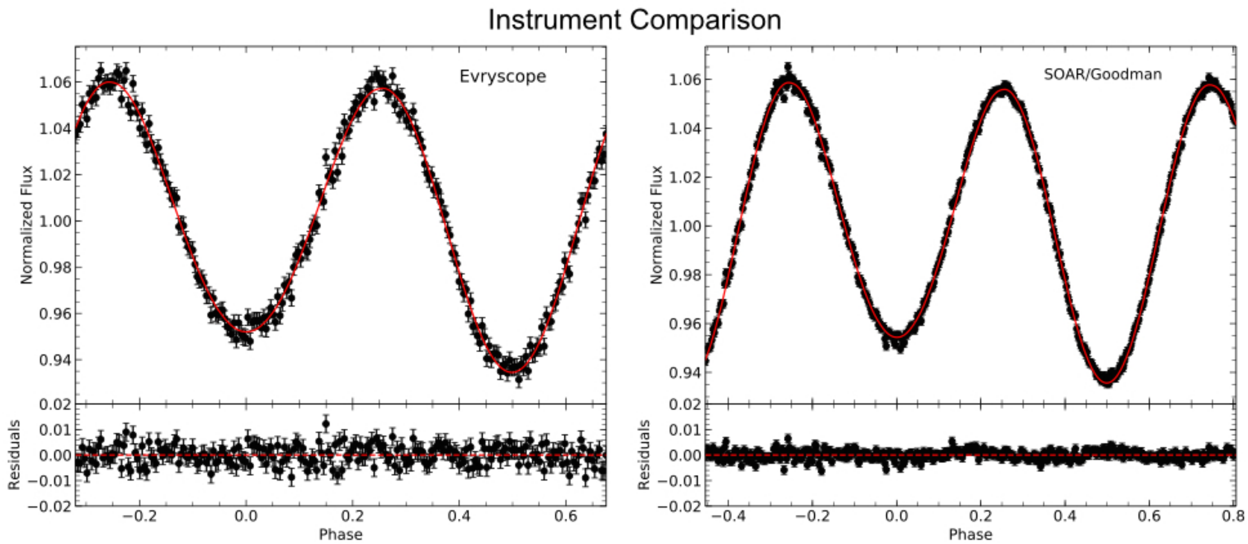

Figure 7.9: Instrument comparison of the Evryscope and SOAR telescopes. *Left Panel:* The Evryscope binned-in-phase light curve and the residuals after removing the best fit from § 7.4. *Right Panel:* The SOAR light curve and the residuals after removing the best fit from § 7.4. The flux and residual scales are the same for both instruments to aid in the comparison. The Evryscope aperture is ≈ 4500 times smaller than SOAR, but produces a competitive light curve when binned-in-phase. This result is made possible by the improvement from combining the many period observations over the multi-year Evryscope survey time.

7.6.4 The Potential of the Evryscope

The Evryscope is a new instrument, different than a conventional telescope, and potentially misunderstood. Comparison of the Evryscope EVR-CB-001 discovery light curve to the SOAR followup light curve gives a powerful example of the Evryscope potential. Figure 7.9 shows the binned-in-phase Evryscope light curve and SOAR light curve. The flux and residual scaling is the same in both plots. The astrophysical signal is fit with the best solution in § 7.4 and removed from both curves leaving the residuals. The residual RMS of the SOAR and Evryscope light curves is 0.00155 and 0.00354 respectively. Consider the following instrument comparisons: The Evryscope cameras are 6.1 cm diameter while the SOAR telescope is 4.1 meter diameter. The Evryscope instrument cost $\approx \$300K$, while the SOAR telescope cost $\approx \$28M$. The competitive Evryscope light curve is made possible because the SOAR light curve took 2.5 hours of observing time, while the Evryscope light curve took 2.5 years. SOAR observed 1 period, while the Evryscope observed over 1000. An individual Evryscope period observation has only a very modest precision (in this case $\approx .05$ RMS), but with the proper photometric pipeline and systematics removal, the final combined and binned-in-phase light curve improves as $\approx \sqrt{\#periods}$ (in this case $\approx \sqrt{1000}$).

It is important to emphasize that SOAR (or any other large telescope) and Evryscope are very different instruments. SOAR has many capabilities that Evryscope does not - spectroscopy, radial velocity measurements, and multi-band photometry just to name a few. It offers rapid precision followup on high value targets that the Evryscope cannot match. However, the Evryscope has a 8150 sq. deg. field of view with continuous 2-minute cadence that provides light curves just like the one for EVR-CB-001, but for 9.3M targets brighter than $m_v = 15$. While some are better quality and some are worse depending on target brightness and location, EVR-CB-001 is a representative example. The Evryscope is a robotic system that requires minimal human intervention, with low construction and operating costs, and provides a dataset that facilitates the discovery of rare, difficult to detect, fast event systems like EVR-CB-001. With the proper processing of the discovery light curve, very high levels of binned-in-phase precision can be reached.

7.7 SUMMARY

We present the discovery of EVR-CB-001 - a close binary with an unseen low mass ($0.32M_\odot$) helium white dwarf (He WD) and an extremely low mass progenitor helium white dwarf ($0.21M_\odot$) (pre-He WD) companion. This object was discovered using Evryscope photometric data in a southern-all-sky hot subdwarf variability survey. EVR-CB-001 is a unique system: a short period (2.34 hours), large amplitude ellipsoidal modulation (12.0% change in brightness from maximum to minimum) He WD / pre-He WD compact binary. Gravitational wave radiation will cause the system to shrink, and the helium rich WDs will potentially merge into a single hot subdwarf B star.

Acknowledgements

This research was supported by the NSF CAREER grant AST-1555175 and the Research Corporation Scialog grants 23782 and 23822. HC is supported by the NSFGRF grant DGE-1144081. BB is supported by the NSF grant AST-1812874. The Evryscope was constructed under NSF/ATI grant AST-1407589. This work was supported by the National Science Foundation through grant PHY 17-148958. We acknowledge the use of the Center for Scientific Computing supported by the California NanoSystems Institute and the Materials Research Science and Engineering Center (MRSEC) at UC Santa Barbara through NSF DMR 1720256 and NSF CNS 1725797.

CHAPTER 8: EVR-CB-004: AN INFLATED HOT SUBDWARF O STAR + UNSEEN WD COMPANION IN A COMPACT BINARY - DISCOVERED WITH THE EVRYSCOPE

This section presents results to be published in the *The Astrophysical Journal*.[1,2]

8.1 INTRODUCTION

We present the discovery of EVR-CB-004, a close binary with a remnant stellar core and an unseen white dwarf companion. The analysis in this work reveals the primary is potentially an inflated hot subdwarf (sdO) and more likely is a rarer post-blue horizontal branch (post-BHB) star (post-BHBs are the short-lived shell-burning final stage of a blue horizontal star or hot subdwarf before transitioning to a WD). It is also possible the sdO in EVR-CB-004 is a post-asymptotic giant branch (post-AGB) remnant (post-AGBs are the final transitioning stage of the red-giant core before forming a WD), however this interpretation is less likely given the challenges of forming a post-AGB in such a compact binary. We discuss our spectroscopic analysis and comparisons to stellar evolution models which prefer the more evolved remnant interpretation, as well as suggestions for future work that could more definitively identify the nature of the primary. This object was discovered using Evryscope photometric data in a southern-all-sky hot subdwarf variability survey. The photometric light

[1]Ratzloff JK, Kupfer T, Barlow BN, Schneider D, Marsh TR, Heber U, Corcoran KA, Hämmerich S, Bauer E, Corbett, HT, Glaizer A, Howard W, Law NM. EVR-CB-004: An Inflated Hot Subdwarf O Star + Unseen WD Companion in a Compact Binary - Discovered with the Evryscope. *The Astrophysical Journal* 2020; Submitted February 2020, currently under review.

[2]The writing in this paper was approximately 60% Ratzloff, 20% Kupfer, and the balance from Barlow and Schneider. I found the system, took and processed the followup SOAR data including the ID spectra, RV spectra, and light curve. Barlow and I worked together on the RV analysis, secondary variability, and overall paper. I researched close binaries and remnant objects and wrote the majority of the introduction and discussion sections. Kupfer performed the detailed light curve fits with help from Marsh. Kupfer and Bauer compared the system to stellar evolutionary models. Schneider was responsible for the atmospheric modeling, and along with Heber provided insights to the nature of the primary.

curve for EVR-CB-004 shows multi-component variability from ellipsoidal deformation of the primary and from Doppler boosting as well as gravitational limb darkening. EVR-CB-004 is one of just a handful of known systems, and has a long period (6.08426 hours) and large amplitude ellipsoidal modulation (16.0 % change in brightness from maximum to minimum) for these extremely close binary systems, while the properties of the primary make it a truly unique system. EVR-CB-004 also shows a peculiar (and not seen before in these close binaries) low-amplitude (less than 1%) sinusoidal light curve variation with a period that is a 1/3 resonance of the binary period. We tentatively identify this additional variation source as a tidally-induced resonant pulsation (other explanations such as asynchronous rotation or eccentricity are also discussed but do not fit the data well), and we suggest followup observations that could verify the source of the low-amplitude signal. From the evolutionary state of the system, its components, and its mass fraction, EVR-CB-004 is a strong merger candidate to form a single high-mass ($\approx 1.1 M_{\odot}$) WD. Post-BHBs, post-AGBs, tidally induced pulsations, and single high-mass WDs are all observationally challenging to discover and are active areas of research. EVR-CB-004 offers a glimpse into a brief phase of a remnant core evolution and into a strange secondary variation (likely a tidally induced resonant pulsation), not seen before or expected in a compact binary.

Hot subdwarfs are small, dense stars, under-luminous for their high temperatures. Most are compact helium core burning stars with a thin hydrogen shell, a canonical size of $R = 0.2 R_{\odot}$ and $M = 0.5 M_{\odot}$, and temperatures greater than $\approx$ 20,000K. There are two primary categories based upon spectral features, B-types (sdB) are observed with typical temperature ranges of 20,000-40,000K and O-types (sdO) ranging from 40,000-100,000K (see [217] for a description of hot subdwarf properties and types). SdOs tend to exhibit a wider range in their physical attributes; for a few recent examples see [218], and for a large sample of sdO atmospheric parameters see [130]. SdOs are also rarer than their sdB counterparts, seen at an $\approx 1/3$ sdO/sdB ratio.

Hot subdwarfs are thought to form through one of two main mechanisms: (i) the merging of two helium–core white dwarfs (WDs), or (ii) binary interactions involving Roche lobe overflow (RLOF) or common envelope (CE) evolution that result in significant hydrogen stripping from a red giant progenitor. We demonstrate further in the manuscript that the latter mechanism is relevant to this work and thought to occur when the hot subdwarf progenitor is near the tip of the red giant branch. The process leaves behind a binary system with a hot subdwarf and a companion including white dwarfs, red dwarfs, Solar–type stars, and, in some cases, substellar objects. Without a thick outer hydrogen layer, hot subdwarfs generally will neither ascend the asymptotic giant branch (AGB) nor experience the traditional planetary nebula phase, as expected for low–mass stars, but instead will evolve directly onto the white dwarf cooling sequence. Depending on their hydrogen envelope hot subdwarfs are considered to be extreme horizontal branch (EHB) stars (for hydrogen envelopes $\lesssim 0.01\,\mathrm{M}_{\odot}$) or blue horizontal branch (BHB) stars (for hydrogen envelopes of a few hundreds $\mathrm{M}_{\odot}$). A recent review of hot subdwarfs can be found in [178], including a description of all formation channels. A analysis on the evolution of EHB stars, along with a helpful discussion on the potentially confusing terminology of EHB/HB/hot subdwarfs can be found in [219].

Hot subdwarf progenitor systems with comparatively smaller and closer companions are thought to be unable to accrete matter (from the hydrogen shell of the red-giant, hot subdwarf progenitor) at a fast enough rate to be stable. A CE forms and some matter is ejected from the system, resulting in a loss of angular momentum and tightening of the binary. A full description of the CE formation channel can be found in [62]. Post–CE hot subdwarf binaries typically have periods from 2 hours up to 30 days, with a few known exceptionally short period systems. Common companions are M-dwarfs, K-dwarfs, and white dwarfs; more exotic remnant companions are also possible.

The CE formation channel for sdB and sdO stars is modelled extensively by [50, 51], with simulations resulting in short period binaries between 2 hours and 10 days, and a hot subdwarf mass near $0.46M_{\odot}$. Different initial conditions, including the hydrogen shell mass, helium core mass, and mass loss, lead to a range of temperature and surface gravity values that are in general agreement with observed sdB and sdO binaries.

A rare and interesting subset of post–CE hot subdwarf binaries are the compact, very short period binaries with unseen white dwarf (WD) companions. Only a handful of these systems are known after decades of searching. To highlight these systems: KDP 1930+2752 [220] is a high mass system found as part of the Kitt Peak - Downes survey of UV excess objects, later determined by [221] to be a 2.28 hour period binary sdB + WD. Work by [56] identified this system to be a strong SN Ia progenitor candidate. The slightly lower mass but shorter period sdB + WD binary systems KPD 0422+5421 [185, 222] and CD-30 11223 (first reported in [138], with subsequent followup in [59]) are the only systems that show evidence of eclipses, helping to separately verify the sdB radius, and to constrain the inclination angle as well as the sdB and WD sizes more tightly. PTF1J082340.04+081936.5 [186], is the second shortest period system at 1.41 hours and has a low mass WD companion, a surprising find in such a tight orbit. The recent discovery of EVR-CB-001 [20] reveals a 2.34 hour period compact binary system with exceptionally low mass components. The primary is a rare transitioning object (pre-He-WD) appearing as an sdB in color magnitude space, and the system is a strong merger candidate to form a single hot subdwarf (single hot subdwarfs are observed but their formation is difficult to explain). Lastly, OWJ074106.0-294811.0 [187] is an ultra-compact (44.7 minute) sdO + WD system with a non-canonical mass sdO.

The photometric light curves in the above systems show sinusoidal-like variations due to ellipsoidal deformation of the hot subdwarf from the WD companion, with differences between even and odd phases due to Doppler boosting and gravity darkening. These unique light curve features, combined with spectral and radial velocity analysis, allow for precise solutions to the system. The multi-component photometric variations can aid in the discovery of these rare systems, however the detections are challenging as the half-period alias folded light curves look nearly indistinguishable from an unexceptional variable with a simple sinusoidal signal.

In this work we present the discovery of EVR-CB-004, an sdO hot subdwarf (or post-BHB or post-AGB refered to as sdO hereafter, understood to encompass these evolved states as well) + WD compact binary (Gaia DR2 5642627428172190000) with a 6.084 hour period. EVR-CB-004 shows strong multi component photometric variability, high radial velocity amplitudes, and is bright ($m_G = 13.1$), characteristics that aid in the system solution. EVR-CB-004 was found in a southern all-sky hot subdwarf survey searching for low mass companions [223] using the Evryscope [17, 19], a new type of telescope with fast-cadence and all-sky capability.

The binary modeling solution for EVR-CB-004 reveals several surprising characteristics. The sdO is shown to have a considerably lower surface gravity ($\log g = 4.57$) than expected for a standard core-fusing sdO hot subdwarf (typically $\log g = 5.5 - 6.0$ see [219]), with a corresponding large radius of $0.6 R_{\odot}$. These properties also drive the exceptionally large amplitude (16.0% change in brightness from maximum to minimum) ellipsoidal modulations. While these values are non-canonical for an sdO, the larger spread in sdO properties indicates this could be a peculiar (inflated) sdO especially considering the mass, temperature, and compact binary system characteristics are consistent with an sdO primary. We were suspect of this interpretation given the very large difference from expected values, however, and we rule it out completely because additional spectral analysis revealed the system to be ≈10-100 times more luminous than expected for a core-fusing sdO. Despite its small size and mass, EVR-CB-004 is ≈1000 times the solar luminosity.

Our analysis (see § 8.6.3) shows the primary in EVR-CB-004 is likely a more evolved hot subdwarf, found during the final stage (known as a post-BHB) of its evolution before forming a WD. The post-BHB cycle of HSD evolution is not well understood, with a limited number of examples to test and verify theoretical models. Finding a post-BHB in a compact binary with a WD is very suggestive that this evolutionary theory is correct, however none have been found. Although additional followup is needed to definitively confirm the primary in EVR-CB-004 as a post-BHB, the evidence from our discovery and followup is strong (the bright luminosity is consistent with a shell-fusing post-BHB, the mass is consistent with a post-BHB that evolved from a core-fusing hot subdwarf, the radius and surface gravity are consistent as is the high temperature with a post-BHB, and the formation track is plausible and matches stellar models well - see § 8.6). The EVR-CB-004 system is the first viable candidate for a post-BHB + WD compact binary, and with the advantageous characteristics of a compact binary (high amplitude and multiple component variability in the light curve, large radial velocity, a robust spectra with many well resolved features, and is bright) that allow for a complete and precise solution. It offers an excellent opportunity to study late-stage HSD evolution theory and compact binary models.

Besides the post-BHB and rare compact binary, EVR-CB-004 revealed other surprising features. With the inflated radius and high temperature (post-BHBs are larger and hotter than core-fusing sdOs) as well as the close separation (a 6.08 hour period), the primary is very close to filling its Roche Lobe and is potentially an active accretor. We suggest X-ray followup could confirm and measure the likely accretion. The final state of the system is also intriguing. EVR-CB-004 is expected to first form a WD + WD binary once the post-BHB and final WD contraction phases complete; it will then likely merge into a very-high mass single WD or a double-detonation under-luminous supernova. Not surprisingly, progenitors to these final stages are sought after and needed to advance our understanding.

In addition to the ellipsoidal modulation, Doppler boosting, and gravitational limb darkening components, the light curve of EVR-CB-004 also shows a completely unexpected sinusoidal variation at the 0.4% level with a period that is a 1/3rd resonance (2.028 hours) of the orbital period. This low-amplitude variation has not been seen before in sdO/sdB + WD compact binaries, and is a surprising feature. In section § 8.6 we discuss our followup analysis to verify this signal is astrophysical, possible explanations, and our preferred interpretation.

This paper is organized as follows: in § 8.2 we describe the discovery and observations. In § 8.3 we describe our spectroscopic analysis to determine the orbital and atmospheric parameters of the sdO. In § 8.4 we model the photometric light curve to determine ellipsoidal modulations and test for eclipses. In § 8.5 we solve the system and show our results. In § 8.6 we discuss our findings and conclude in § 8.7.

8.2 OBSERVATIONS AND REDUCTION

8.2.1 Evryscope Photometry

Evryscope photometric observations taken from February 2017 to June 2017 led to the discovery of EVR-CB-004. Data were taken through a Sloan g filter with 120 s integration times, providing a total of 4,812 measurements. The wide-seeing Evryscope is a gigapixel-scale, all-sky observing telescope that provides new opportunities for uncovering rare compact binaries through photometric variations. It is optimized for short-timescale observations with continuous all sky coverage and a multi-year period observation strategy. The Evryscope is a robotic camera array mounted into a 6 ft-diameter hemisphere which tracks the sky [17, 19]. The instrument is located at CTIO in Chile and observes continuously, covering 8150 sq. deg. in each 120s exposure. Each camera features a 29MPix CCD providing a plate scale of 13"/pixel. The Evryscope monitors the entire accessible Southern sky at 2-minute cadence, and the Evryscope database includes tens of thousands of epochs on 16 million sources.

The Evryscope EVR-CB-004 light curve has a less than average number of data points because observations for additional seasons (the Evryscope has been observing since mid 2015) were removed as problematic points due to the difficult observing field (source crowding and unfavorable airmass). The additional epochs were not necessary for the discovery of EVR-CB-004, but are expected to be recovered with the upgraded photometric pipeline (currently processing light curves for all Evryscope sources including 2019 observations).

Here we only briefly describe the calibration, reduction, and extraction of light curves from the Evryscope; for further details we point the reader to our Evryscope instrumentation paper [19]. Raw images are filtered with a quality check, calibrated with master flats and master darks, and have large-scale backgrounds removed using the custom Evryscope pipeline. Forced photometry is performed using APASS-DR9 [79] as our master reference catalog. Aperture photometry is performed on all sources using multiple aperture sizes; the final aperture for each source is chosen to minimize light curve scatter. Systematics removal is performed with a custom implementation of the SysRem [77] algorithm.

We use a panel-detection plot that filters the light curves, identifies prominent systematics, searches a range of periods, and phase folds the best detections from several algorithms for visual inspection. It includes several matched filters to identify candidate hot subdwarfs for variability and is described in detail in [66]. EVR-CB-004 was discovered using Box Least Squares (BLS; [28, 29]) and Lomb-Scargle (LS) [31] with the same settings, pre-filtering, and daily-alias masking described in [66]. The discovery tools and settings were tested extensively to maximize recovery of the fast transits and eclipses characteristic of hot subdwarfs and white dwarfs. As part of our testing, we also recovered CD-30 11223 [138], the only known fast-period hot subdwarf + WD binary in our field of view and magnitude range, and discovered the compact evolving WD binary EVR-CB-001 [20]. The BLS and LS power spectrum peaks correspond to 3.0423 hour and 3.04219 hour periods, respectively. Both detections found a period alias of half the actual period, and the candidate was originally thought to be a hot subdwarf reflection effect binary. Further analysis showed the candidate to be a 6.08 hr binary exhibiting strong (16%) modulations due to the ellipsoidal deformation of the primary from the unseen, more massive companion. Figure 8.1 presents both the BLS power spectrum and phase-folded light curve. A subtle asymmetry (a sub 1% difference in the height of alternating peaks) is observed, indicative of Doppler boosting with the higher peak corresponding to the orbital position where the sdO is moving toward us most quickly.

The difference in minima is due to gravitational darkening of the deformed sdO, with the lower minimum corresponding to the orbital position where the sdO is farthest from us.

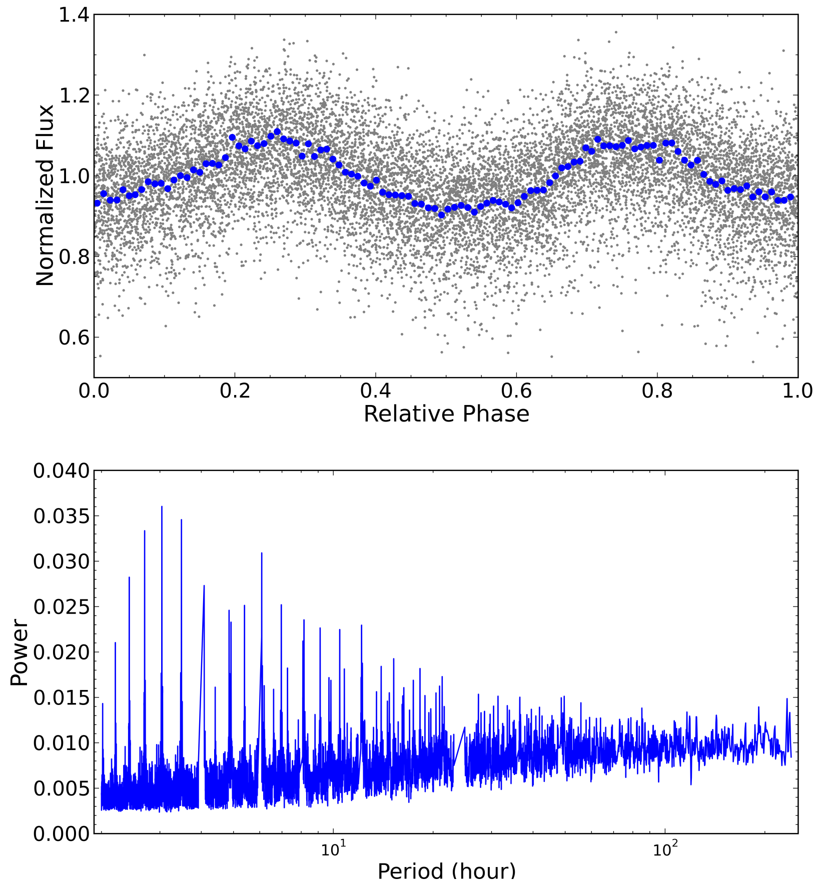

Figure 8.1: The Evryscope discovery light curve of EVR-CB-004 folded on its period of 6.0846 hours is shown on the top panel. Grey points = 2 minute cadence, blue points = binned in phase. The bottom panel shows the BLS power spectrum with the highest peak at the 3.0423 hour detection (an alias of half of the actual period).

8.2.2 SOAR/Goodman Photometry

In order to obtain a higher signal-to-noise (S/N) light curve for modeling, we observed EVR-CB-004 on April 9, 2019 on the 4.1-m SOAR 4.1 m telescope at Cerro Pachon, Chile, with the Goodman spectrograph [33] in imaging mode. We used the blue camera with Bessel-V blocking filter, and took 515 images with 20 second exposure times. The image ROI was reduced to 1200 x 1200 pixels with 1x1 binning, which gave a 69% duty cycle. For calibrations, we took 10 dome flats using 25% lamp power and 10s integrations, 10 darks also with 10s integrations, and 10 bias images.

The SOAR images were processed with a custom aperture photometry pipeline written in Python. The images were dark and bias-subtracted and flat-field-corrected using the master calibration frames. Six reference stars of similar magnitude are selected and aperture photometry is performed using a range of aperture sizes. The background is estimated using the same size aperture for dark regions near each reference star. For full details of our SOAR photometry code, we refer the reader to [20]. The resulting SOAR light curve is used to model EVR-CB-004 and check for eclipses and is shown later in the manuscript, in Figure 8.7.

Since the TESS light curve is available for EVR-CB-004 (see the following section), the SOAR light curve provides an independent measurement in a much bluer band and is used as one of our two primary modeling solutions. The final solutions are consistent regardless of filter or instrument (see § 8.4). The SOAR light curve was also used to rule out the shorter time scale eclipses (the TESS cadence is 2 min, while the SOAR cadence is 20 seconds, and expected eclipses would last $\approx$ 10 minutes).

We demonstrate later in the manuscript that EVR-CB-004 shows a small amplitude ($\approx$ .3% in SOAR and $\approx$ .4% in TESS) sinusoidal variation in the light curve, distinct from the main binary variability. This small amplitude variability is quite unexpected, and we needed to make sure it was not instrumental. The SOAR light curve is used to confirm this signal and measure it in a different band-pass to check for a wavelength dependent amplitude (see § 8.6.5).

8.2.3 TESS Photometry

EVR-CB-004 (TIC 1973623) was observed by TESS in Sector 8, from February 2-27, 2019, using Camera #2. Photometry was obtained in the 120-second cadence mode and consists of 13,206 individual measurements spanning 24.5 days, including a short interruption near the middle of the sequence to allow for the data to be downlinked. We use for our analysis the PDC light curve extraction [224, 225] provided by the TESS Science Processing Operations Center [226]. These data are made publicly available through the Mikulski Archive for Space Telescopes. A LS periodogram analysis shows a clear detection of the 6.08 d binary signal and its harmonics. We find no other statistically significant peaks out to the Nyquist frequency (360 d^{-1}) and limit additional variability to amplitudes <550 ppm. We used the TESS light curve for our light curve analysis solution with a red band-pass, independent from the SOAR light curve.

The coarse TESS pixel scale is prone to blending from nearby stars, potentially contaminating the signal from the target. The very fine SOAR pixels (.15" per pixel) easily resolve nearby stars in the field, and the SOAR image revealed three nearby stars that were potential contaminants in the TESS pixel. Simple tests (see § 8.6) showed these to be constant, much lower in flux than the target, and to not affect the light curve or solution to EVR-CB-004.

8.2.4 PROMPT Photometry

We observed EVR-CB-004 with the PROMPT MO1 46cm telescope [36] located at Meckering Australia, in Johnson R band. The PROMPT photometric observations provided an intermediate filter to the SOAR and TESS data, and verified the light curve solution in § 8.4. The observations were taken on March 30, 2019, continuously over the period with 120 s exposure times. We also obtained bias, flat, and dark calibration images. The images were processed with a custom pipeline that uses standard calibration and aperture photometry, using 5 nearby reference stars of similar magnitude to correct for airmass and observing conditions. For a detailed description of the pipeline, we refer the reader to [66].

8.2.5 SMARTS 1.5-m/CHIRON Spectroscopy

We observed EVR-CB-004 with the SMARTS 1.5 m telescope and CHIRON, a fiber-fed cross-dispersed echelle spectrometer [38]. Six spectra were obtained in image fiber mode

(R $\sim$ 28,000) between March and July 2019 and covered the wavelength range 4400-8800 Å. We used integration times of 1200 s to obtain just enough S/N for radial velocity (RV) measurements; longer integrations would have resulted in too much phase-smearing. All raw spectra were reduced and wavelength-calibrated by the official CHIRON pipeline, housed at Georgia State University and managed by the SMARTS Consortium[3]. In addition to Hα and Hβ, which span multiple orders, the spectra show four He I lines, including 6678 Å, 5876 Å, 5016 Å, and 4922 Å, and two He II lines 4686 Å and 5412 Å. All of these features are synced in phase, with no signs of absorption due to a companion, and we conclude they emanate from a single star.

8.2.6 SOAR/Goodman Spectroscopy

8.2.6.1 Low-Resolution (for Atmospheric Modeling)

We obtained low-resolution spectra for atmospheric modeling on February 9, 2019 with the Goodman spectrograph using the 600 mm^{-1} grating blue preset mode, 2x2 binning, and the 1" slit. This configuration provided a wavelength coverage of 3500-6000 Å with spectral resolution of 4.3 Å (R$\sim$1150 at 5000 Å). We took four 360 s spectra of both the target and the spectrophotometric standard star BPM 16274. For calibrations, we obtained 3 x 60 s FeAr lamps, 10 internal quartz flats using 50% quartz power and 30 s integrations, and 10 bias frames.

We processed the spectra with a custom pipeline written in Python, described in [20]. Each of the processed spectra was then rest-wavelength calibrated using a Gaussian fit to the Hβ through H11 absorption features, as well as several prominent He absorption features. The resulting spectra were median-combined to form a final spectrum for atmospheric modeling. As shown in Figure 8.3, we detect strong H Balmer lines, from Hβ through H13, and several He lines. In this resolution mode, we find no evidence of absorption features due the companion star; EVR-CB-004 appears to be a single-lined binary.

[3]http://www.astro.yale.edu/smarts/

Table 8.1: Overview of Observations for EVR-CB-004

Telescope	Date	Filter/Resolution	Epochs	Exposure
Photometry				
Evryscope	Jan 2017 - Jun 2017	Sloan g	4,812	2 min
SOAR/Goodman	April 9, 2019	Bessel-V	515	20 s
TESS	Feb 2-27, 2019	600-1000nm	13,206	2 min
PROMPT	March 30, 2019	Johnson-R	180	2 min
Spectroscopy				
SMARTS 1.5-m/CHIRON	Mar 2019 Jul 2019	28,000	6	1200 s
SOAR/Goodman	Feb 9, 2019	1150	4	360 s
SOAR/Goodman	March 5, 2019	11930	32	360 s

8.2.6.2 Medium-Resolution (for Radial Velocity)

To measure the RV of EVR-CB-004, we also obtained medium-resolution spectra on March 5, 2019 with the Goodman spectrograph using the 2100 mm^{-1} grating in custom mode, 1x2 binning, and the 0.46” slit. This configuration provided a wavelength coverage of 3700-4400 Å with spectral resolution of 0.34 Å (R$\sim$11930 at 4000 Å). We took 32, 360 s spectra of the target and 3 x 60 s FeAr lamps after every fourth spectrum. We observed uninterrupted to cover the half of the period from minimum to maximum. For calibrations, we obtained 10 internal quartz flats using 80% quartz power and 60 s integrations, and 10 bias frames.

We processed the spectra with a custom pipeline written in Python, described in [20]. The groups of 4 processed spectra were median-combined to form a final spectrum used to determine the RV. As shown in Figure 8.6, We detect strong H Balmer lines, from Hγ through H10, and several He lines. In this resolution mode we also find CaH and CaK lines that originate from a different source than all other features. We discuss the origin of the Ca lines in § 8.6.

Table 8.1 presents a brief overview of all of the photometric and spectroscopic data used in our analysis of EVR-CB-004.

8.3 ORBITAL AND ATMOSPHERIC PARAMETERS

To measure radial velocities (RVs), we first inspected the SOAR spectra (see § 8.2.6.2) and selected prominent absorption features with the highest signal to noise, found to be Hγ-H10. These features (3750Å, 3835Å, 3889Å, 3970Å, 4102Å, 4340Å) are then used for fitting, by clipping small regions encompassing each absorption line and measuring the central value using a Gaussian fit. We measure the shift, calculate the velocity, and use the standard deviation in the velocities of the 6 absorption features to determine the uncertainty. The resulting velocities were converted to heliocentric velocities using PyAstronomy's *baryCorr* function.

The CHIRON spectra are processed in a similar way but using the absorption features falling in the CHIRON wavelength coverage. The CHIRON and Goodman measurements were combined together and phase-folded using the period determined from the light curve. With the period and phase fixed to values determined from the photometry, we fitted a sine wave to the radial velocity curve and find a semi–amplitude of K = 190.5 ± 2.8 km/s. Figure 8.2 presents the radial velocity curve and best–fitting sine wave.

The H Balmer lines span multiple orders in the high-resolution CHIRON spectra, making them insufficient to determine reliable atmospheric parameters (effective temperature $T_{\rm eff}$, surface gravity $\log(g)$, and helium abundance $\log n(\mathrm{He})$), and they were not suitable to determine the projected rotational velocity $v_{\rm rot}\sin i$ due to phase smearing caused by the necessarily long exposure times. Therefore, we Doppler-corrected all SOAR RV spectra to the same rest frame and stacked them to create a master medium-resolution spectrum as done for the low-resolution SOAR data. We then used both SOAR resolutions for our spectroscopic analysis.

To determine the atmospheric parameters, we simultaneously fitted the observed H and He line profiles (see Fig. 8.3 to 8.6). The rotational velocity $v_{\rm rot}\sin i$ was determined from the average medium-resolution spectrum only. The H Balmer lines closest to the Balmer jump were of special interest to us since they are most sensitive to $\log(g)$ and $T_{\rm eff}$. We calculated

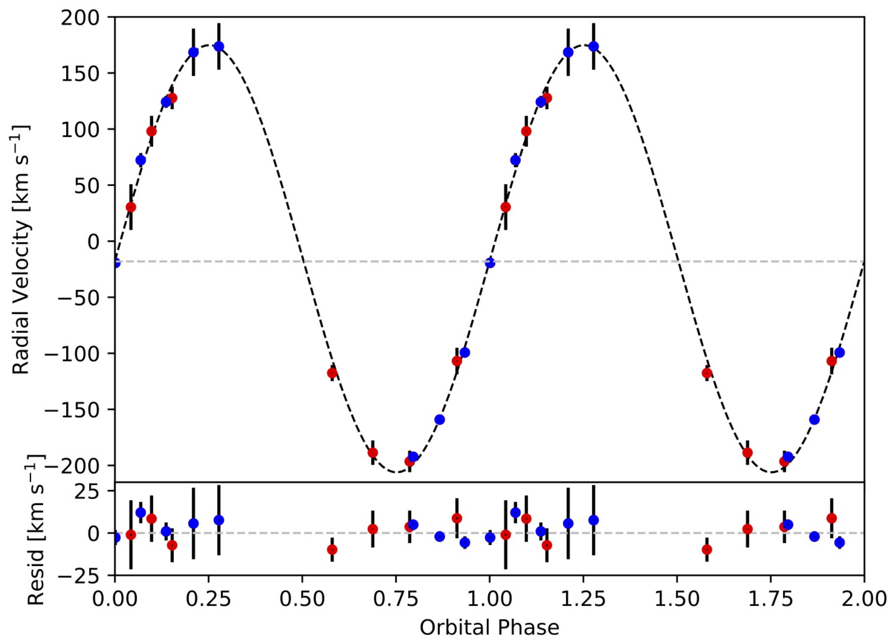

Figure 8.2: *Top panel:* Phase-folded, heliocentric radial velocity measurements from SMARTS 1.5-m/CHIRON (red) and SOAR/Goodman (blue), plotted twice for better visualization. The black dashed line denotes the best-fitting sine wave to the data. After correcting for slight phase smearing, we find a velocity semi-amplitude of K = 190.5 ± 2.8 km s^1 and a systemic velocity of γ = -18 ± 4 km s^1. *Bottom panel:* Residuals after subtracting the best-fitting sine wave from the data.

a grid of non-local thermodynamic equilibrium (NLTE) model atmospheres with TLUSTY 205 and the spectral synthesis was realized with SYNSPEC 51 [134–136, 227–229]. Radiative and hydrostatic equilibrium, plane-parallel geometry as well as chemical homogeneity were assumed. The temperature and density stratification in the hydrogen and helium line-forming regions were well constrained, once carbon, nitrogen, and oxygen were included as absorbers (see also [230] for details). These non-fully opacity sampled metal line-blanketed models also saved us a lot of time since models including iron and nickel are very computational-intensive. Making use of the detailed model atoms listed in Table 8.2, the following ionization stages with mean metallicities for hot subdwarf B stars from [231] were synthesized: H I, He I/II, C II/III/IV, N II/III/IV/V, and O II/III/IV. For each element, the ground state of the next higher ionization stage was also included. Stark broadening tables for H I according to [232], for He I according to [233] and [234], and for He II according to [235] were used.

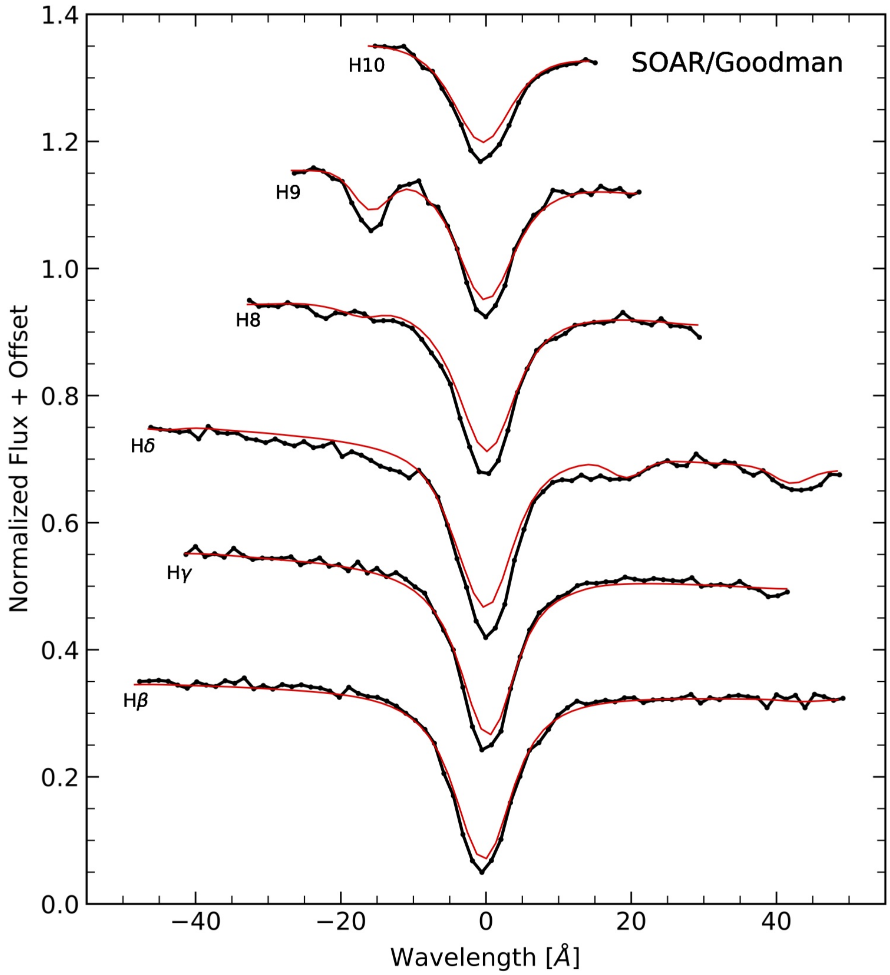

Figure 8.3: Normalized and stacked low-resolution SOAR/Goodman spectrum of EVR-CB-004 (black line) with best–fitting atmospheric model (red line). The H Balmer lines are shown.

The selective fitting routine used is based on the FITSB2 spectral analysis program [236], the "Spectrum Plotting and Analysis Suite" SPAS [237], and the χ^2-based fitting procedure described by [238]. Cubic spline interpolation was used to interpolate between different synthetic spectra and the actual fit to the preselected hydrogen and helium lines in the observed spectrum was performed via the downhill *simplex* algorithm from [239]. The continuum was set at the edges of the preselected lines and the synthetic spectrum was folded with the instrumental profile.

From our NLTE quantitative spectral analysis, we were able to consistently fit the He I and He II lines, indicating that $T_{\rm eff}$ is well constrained. The Balmer line wings could be

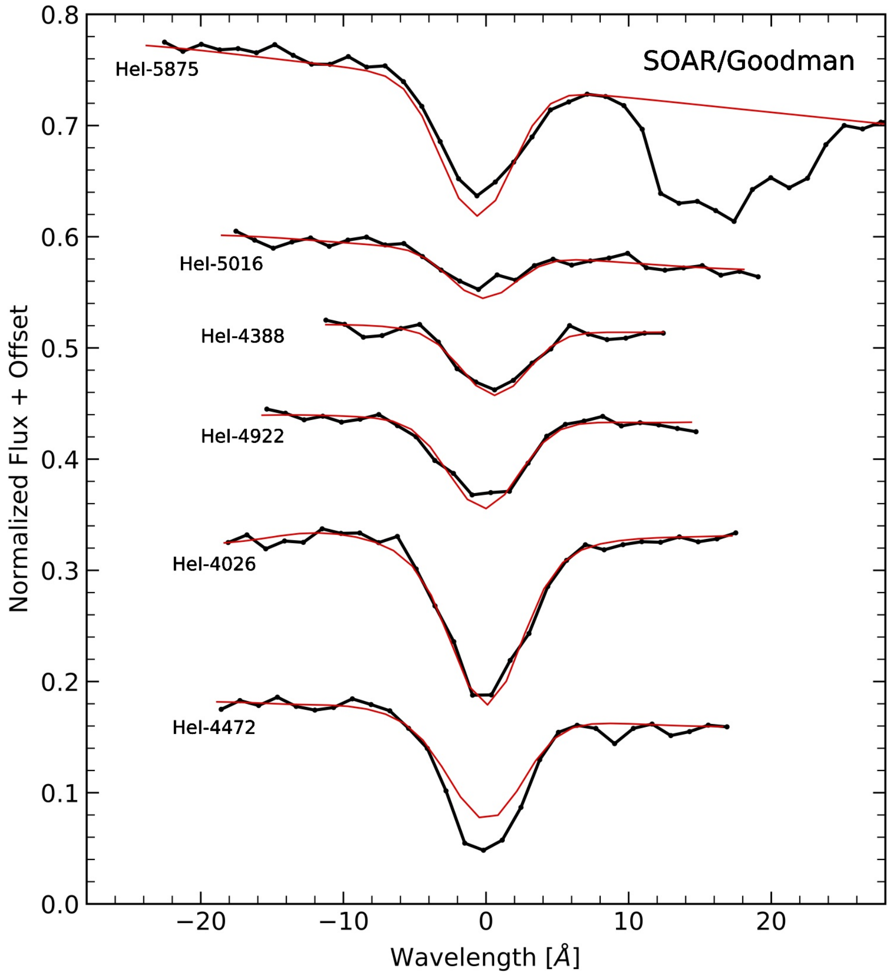

Figure 8.4: Normalized and stacked low-resolution SOAR/Goodman spectrum of EVR-CB-004 (black line) with best–fitting atmospheric model (red line). The the He I lines are shown.

matched, but there is no way to fit the cores simultaneously (see Fig. 8.3 & 8.6). This is most likely due to shortcomings of the model atmospheres which do not include metal line blanketing beyond carbon, nitrogen, and oxygen. However, the derived surface gravity is reliable, since the Balmer line wings are matched reasonably well.

We found $v_{\rm rot}\sin i = 116.5 \pm 8.1\,{\rm km\,s^{-1}}$, $T_{\rm eff} = 41000 \pm 200\,{\rm K}$, $\log(g) = 4.55 \pm 0.03$, and $\log n({\rm He}) = -0.84 \pm 0.02$ from the medium-resolution and $T_{\rm eff} = 41500 \pm 1100\,{\rm K}$, $\log(g) = 4.60 \pm 0.12$, and $\log n({\rm He}) = -0.90 \pm 0.09$ from the low-resolution SOAR data. In the latter case, we fixed $v_{\rm rot}\sin i$ to the value derived from the medium-resolution spectrum. Given 1σ statistical errors were derived using a simple bootstrapping method, whereby the

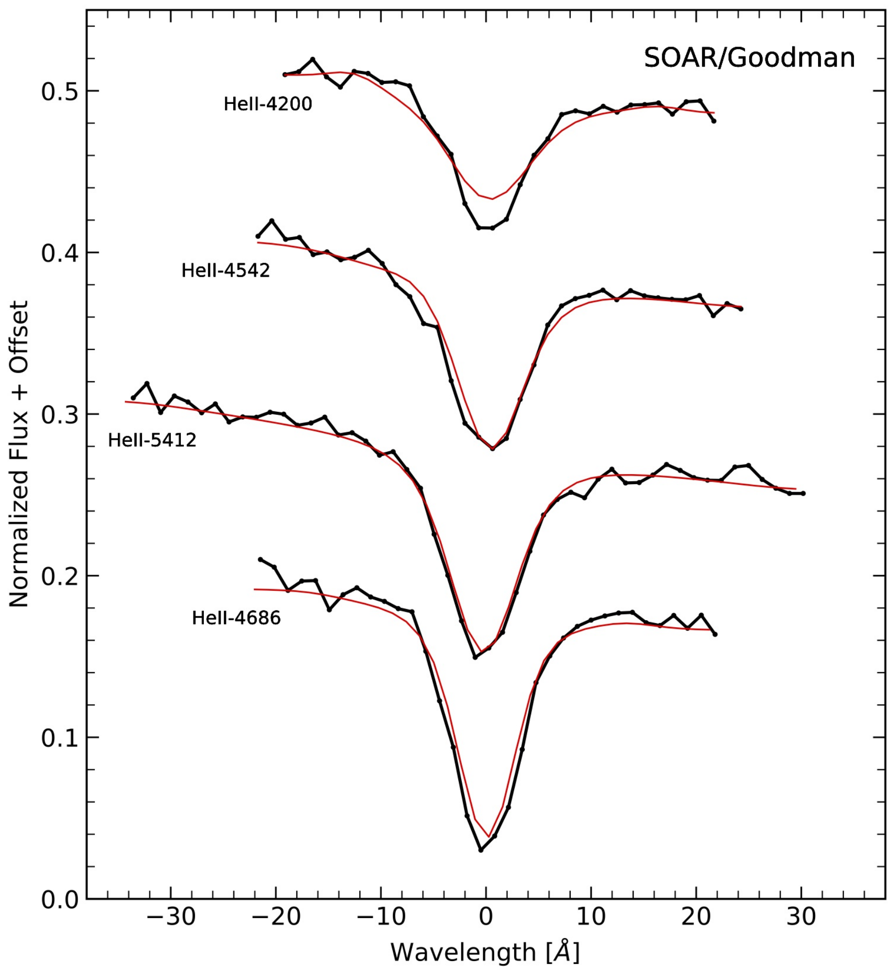

Figure 8.5: Normalized and stacked low-resolution SOAR/Goodman spectrum of EVR-CB-004 (black line) with best–fitting atmospheric model (red line). The He II absorption features are shown.

data themselves were randomly resampled with replacement a large number of times and a parameter fit for each of the iterations was performed. Finally, the 1σ standard error for each parameter was derived from the standard deviation of the respective parameter bootstrap distribution.

Due to the near perfect agreement between the low and medium-resolution results, we took the averages of each of the atmospheric parameters derived and consider them as the final results of the atmospheric modeling. Table 8.4 lists them: $T_{\rm eff} = 41250 \pm 560\,{\rm K}$, $\log{(g)} = 4.575 \pm 0.062$, and $\log n({\rm He}) = -0.87 \pm 0.05$ (1σ statistical errors only). The error budget on the atmospheric parameters is not dominated by statistical, but rather by

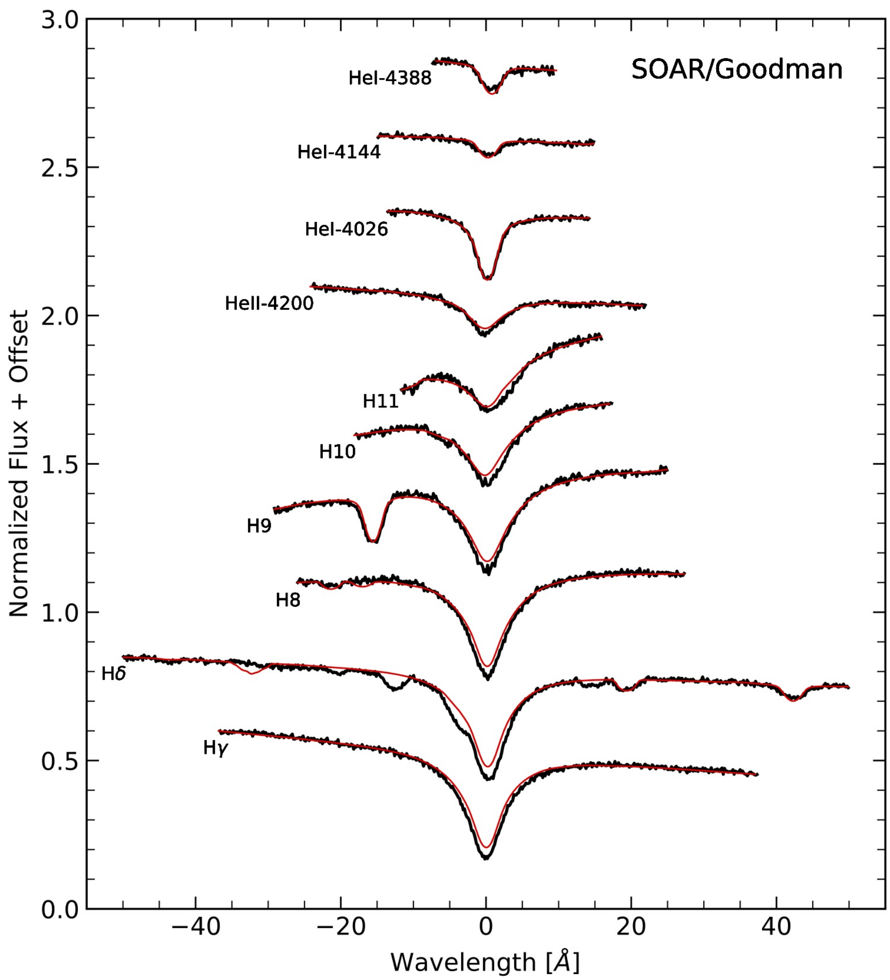

Figure 8.6: Normalized and stacked medium-resolution SOAR/Goodman spectrum of EVR-CB-004 (black line) with best–fitting atmospheric model (red line).

systematic uncertainties, which are always difficult to estimate in spectroscopy. We decided to use $\Delta T_{\rm eff}/T_{\rm eff} = 3\,\%$, $\Delta \log(g) = 0.10$, and $\Delta \log n(\mathrm{He}) = 0.13$, which is rather conservative.

8.4 LIGHT CURVE ANALYSIS

Since only spectral features from the primary star are detected, we must rely on light curve modeling to compute the mass ratio q and constrain the system's parameters. We use the modeling code LCURVE [37] to analyze the TESS I-band, SOAR V-band and PROMPT R-band light curves. We assume that the orbit is circular. The flux that each point on the grid emits is calculated by assuming a blackbody of a certain temperature at the bandpass

Table 8.2: Ionization stages for which detailed model atoms were used in the model atmosphere calculations for TLUSTY/SYNSPEC. The number of levels (L) and super-levels (SL) is listed. For each element the ground state of the next higher ionization stage was also included, but is not listed here.

Ion	L	SL	Ion	L	SL
H I	16	1	N III	25	7
He I	24	0	N IV	34	14
He II	20	0	N V	10	6
C II	17	5	O II	36	12
C III	34	12	O III	28	13
C IV	21	4	O IV	31	8
N II	32	10			

Table 8.3: Overview of the fixed parameters for the LCURVE fit

Parameter	TESS I-band	PROMPT R-band	SOAR V-band
Beaming Factor (F)	1.24	1.30	1.35
gravity darkening β	0.26	0.26	0.27
limb darkening a_1	1.34	1.39	1.38
limb darkening a_2	-2.25	-2.23	-2.06
limb darkening a_3	2.03	1.97	1.79
limb darkening a_4	-0.69	-0.66	-0.595

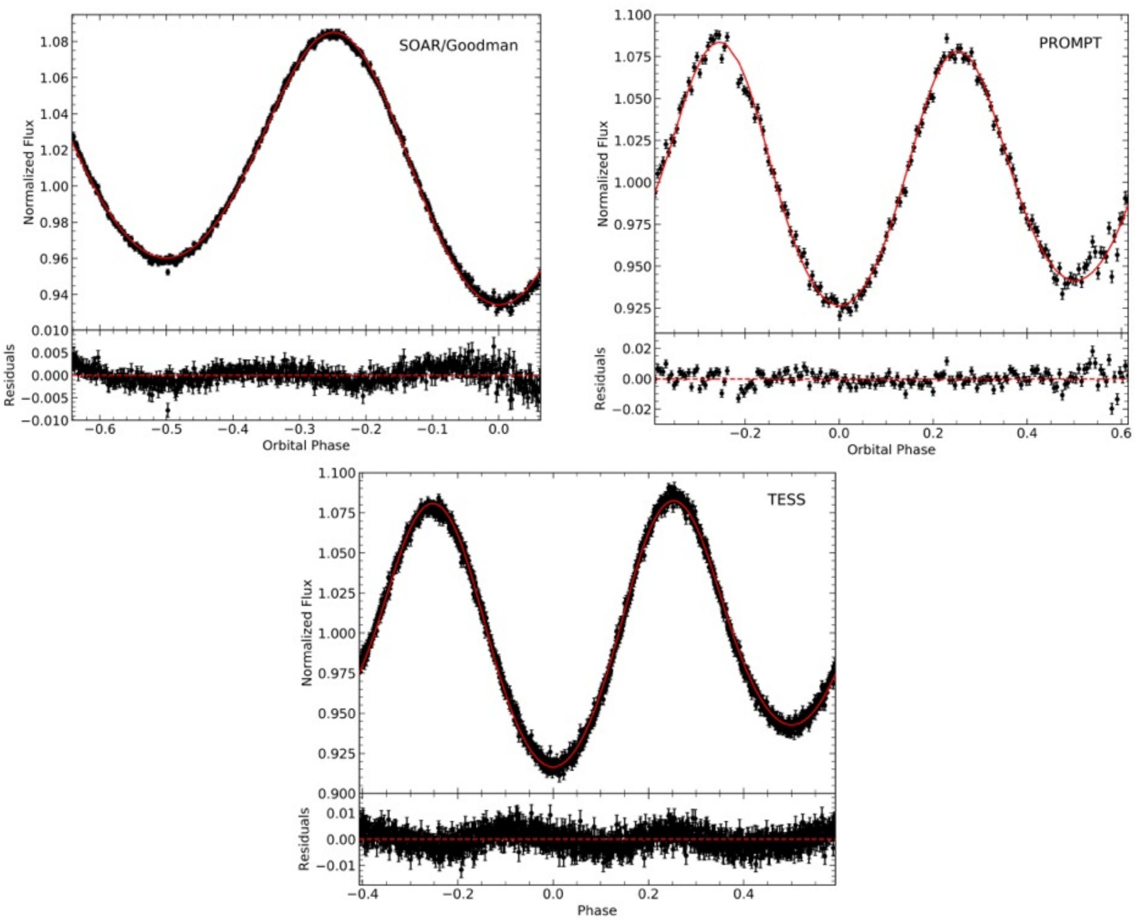

Figure 8.7: The SOAR/Goodman (top left; V filter), PROMPT (top right; R filter), and TESS (bottom; ∼I filter) light curves with the best-fitting model determined from LCURVE. The best–fitting model was determined from simultaneous fits to all three light curves. The PROMPT and SOAR data were taken continuously, while the TESS light curve shown was produced by phase–folding and binning the full 27-d light curve. The residuals show a coherent signal at 1/3 the orbital period, which is discussed in Section 8.6.5.

wavelength, corrected for limb darkening, gravity darkening, Doppler beaming and the reflection effect.

The light curve of EVR-CB-004 is dominated by ellipsoidal modulations due to tidal distortion of the sdO star. Ellipsoidal modulations are sensitive to the mass ratio, the size of the distorted star relative to the orbital separation and the limb and gravity darkening [240]. For the invisible companion we assume a lower limit to the radius (mass), using the zero-temperature mass-radius relation by Eggleton (quoted from [192]). The limb darkening prescription and the passband specific gravity darkening prescription were used following

[193, 194] and as tabulated in [195]. The values used for the beaming, limb darkening and gravity darkening are shown in Table. 8.3. Additionally, we added a constant third light component to the TESS light curve to account for the contributions from the close-by stars (see § 8.2.3) and a first order polynomial to the SOAR and PROMPT lightcurve to account for an airmass effect.

Using the results for surface gravity ($\log g$), effective temperature ($T_{\rm eff}$), combined with the orbital period (P) and radial velocity (K_1), we determine the inclination angle (i), the mass ratio (q), the secondary temperature $T_{\rm WD}$, as well as the scaled radii and velocity scale ($(K_1 + K_2)/\sin i$). The subscript 1 is used for the sdO star which dominates the light (K_1, M_1, R_1), and the subscript 2 is used for the invisible companion (K_2, M_2, R_2).

Using this model we were not able to find a consistent solution with flat residual. In each light curve we find a coherent signal at 1/3 the orbital period with a low amplitude of $\approx$0.5 %. We obtained a reduced $\chi^2 \approx 1.5$. Even allowing the limb, gravity darkening coefficients or the beaming factor to float free (and to iterate towards implausible values), the residuals remain in the light curve fit. We discuss possible explanations for the residuals in § 8.6.5.

We combine LCURVE with the MCMC implementation EMCEE [196] to explore the parameter space, converge on a solution, and to determine the uncertainties. We used 256 chains and let them run for 2000 trials well beyond a stable solution was reached. The corner plot of the final solution is shown in the appendix. The final fits using the TESS, SOAR and PROMPT light curve are shown in Figure 8.7. The ellipsoidal deformation dominates the photometric variation in the light curve, but Doppler boosting and gravity darkening effects are also present.

8.5 RESULTS

Although EVR-CB-004 is a single-lined binary, we can still constrain the masses and radii of the two stars by combining the results of the light curve modeling with results from the spectroscopic fitting. Parameters derived in this way by a simultaneous fit to the SOAR, PROMPT and TESS light curves and are summarized in Table 8.4.

Our solution converges on a mass ratio of $q = M_1/M_2 = 0.72 \pm 0.03$, with individual masses of $M_1 = 0.66 \pm 0.03$ M$_\odot$ and $M_2 = 0.47 \pm 0.04$ M$_\odot$. We reiterate that the sdO star is the dominant source of light in the system, and the one showing ellipsoidal modulation. This object has a radius of $R_1 = 0.62 \pm 0.02\,R_\odot$ showing that the primary star is inflated for an sdO. We find a Roche Lobe filling factor ($f = R_1/R_L = 0.98 \pm 0.02$), where R_L is the Roche Radius, close to 1 and consistent with 1 which shows that the sdO is close to filling its Roche Lobe and even consistent with filling its Roche Lobe entirely. The radius (R_2) of the unseen companion cannot be determined, due to the lack of eclipses. However, since it does not produce any detectable light in the system despite its higher mass, the companion is consistent with a white dwarf (WD).

From the system parameters we find that the sdO should have a projected rotational velocity $v_{\rm rot}\sin i = 115 \pm 5\,{\rm km\,s^{-1}}$ to be synchronized to the orbit. The measured $v_{\rm rot}\sin i = 116.5 \pm 8.1\,{\rm km\,s^{-1}}$ is very close to the predicted value and therefore we conclude that the sdO exhibits synchronous rotation as expected in a compact post-CE binary.

8.6 DISCUSSION

8.6.1 Independent mass estimate of the hot subdwarf - The Spectrophotometric Approach

We measured the mass and radius of the sdO independently from the light curve modeling to test the solution and verify the larger than expected sdO radius, using the atmospheric solution from § 8.3 and publicly available distance and photometric data. *Gaia* data release 2 (DR2; [102]) allows access to accurate parallax ($\varpi_{\rm Gaia}$), and thus distance ($d_{\rm Gaia}$) measurements for >1.3 billion stars, including EVR-CB-004 ($\varpi_{\rm Gaia} = 0.4529 \pm 0.0474\,{\rm mas}$, $\Delta\varpi_{\rm Gaia}/\varpi_{\rm Gaia} \lesssim 0.105$). The combination of $\varpi_{\rm Gaia}$, surface gravity g, effective temperature $T_{\rm eff}$, and stellar angular diameter θ allowed us to independently determine the fundamental stellar parameters

Table 8.4: EVR-CB-004 Parameters. †: 1σ statistical errors only.

Description	Identifier	Units	Value
Evryscope ID	EVR-CB-004		
GAIADR2 ID	5642627428172190000		
Right ascension	RA	[degrees]	133.30233
Declination	Dec	[degrees]	-28.76838
Magnitude	m_g	[mag]	13.127 ±.002
HSD Atmospheric Parameters			
Effective temperature	T_{eff}	[K]	$41\,250 \pm 560^{\dagger}$
Surface gravity	$\log{(g)}$		$4.575 \pm 0.062^{\dagger}$
Helium abundance	$\log n(\mathrm{He})$		$-0.87 \pm 0.05^{\dagger}$
Projected rotational velocity	$v_{\mathrm{rot}} \sin i$	[$\mathrm{km\,s^{-1}}$]	$116.5 \pm 8.1^{\dagger}$
Orbital Parameters			
Orbital Period	P	[hours]	6.0842 ±.0001
RV semi-amplitude	H	[km $\mathrm{s^{-1}}$]	190.5 ± 2.8
System velocity	γ	[km $\mathrm{s^{-1}}$]	18 ± 4
Solved Parameters			
mass ratio	$q = \frac{M_{\mathrm{sdO}}}{M_{\mathrm{WD}}}$		0.72±0.03
Hot subdwarf mass	M_{sdO}	[$M_{\odot}$]	0.47±0.04
Hot subdwarf radius	R_{sdO}	[$R_{\odot}$]	0.62±0.02
White dwarf mass	M_{wd}	[$M_{\odot}$]	0.66±0.03
Orbital Inclination	i	[°]	69.5±1.0
Separation	a	[$R_{\odot}$]	1.76±0.03

(radius R, mass M, and luminosity $\log L/L_{\odot}$) of the primary. This is referred to as the Spectrophotometric Approach:

$$R \overset{\theta \ll 1}{\approx} d \cdot \frac{\theta}{2} = \frac{\theta}{2\varpi} \cdot 1\,\mathrm{AU} \tag{8.1}$$

$$\log(L/L_{\odot}) = \log\left(4\pi R^2 \sigma T_{\mathrm{eff}}^4 / L_{\odot}\right) \tag{8.2}$$

$$M = \frac{g\theta^2}{4G\varpi^2} \cdot (1\,\mathrm{pc})^2\,, \tag{8.3}$$

where 1 AU is the astronomical unit, σ is the Stefan-Boltzmann constant, G is the Gravitational constant, and $1\,\mathrm{pc} = 2.06265 \cdot 10^5\,\mathrm{AU}$. The respective uncertainties are derived from

Gaussian error propagation:

$$\Delta R = \frac{1\,\mathrm{AU}}{2\varpi}\sqrt{(\Delta\theta)^2 + \theta^2 \cdot \left(\frac{\Delta\varpi}{\varpi}\right)^2} \tag{8.4}$$

$$\Delta \log(L/L) = \frac{2}{\ln 10}\sqrt{\left(\frac{\Delta R}{R}\right)^2 + 4 \cdot \left(\frac{\Delta T_{\mathrm{eff}}}{T_{\mathrm{eff}}}\right)^2} \tag{8.5}$$

$$\Delta M = M\sqrt{(\ln 10 \Delta \log g)^2 + 4\left(\frac{\Delta\theta}{\theta}\right)^2 + \left(\frac{\Delta\varpi}{\varpi}\right)^2} \tag{8.6}$$

We decided not to take the *Gaia* DR2 parallax zero point offset into account as also recommended by [241] and [242], since it depends on the types of astrophysical objects investigated and is still under debate (see, for instance, the different results of [241], [243], [244], or [245]). Furthermore, the zero point offset is a function of the coordinates since it depends on *Gaia's* scanning pattern [242], which makes it even more difficult to correct for it. Last but not least, we decided not to correct for possible small-scale variations for the parallax measurements, since it is almost impossible to determine them for a single object like EVR-CB-004 [241].

The necessary atmospheric parameters (T_{eff}, $\log g$) have already been determined in § 8.3. Based on T_{eff}, $\log(g)$, and $\log n(\mathrm{He})$, the stellar angular diameter θ can be derived from a spectral energy distribution (SED) fit to appropriate photometric data according to the analysis methodology presented in [246].

We made use of the following photometric data available on VizieR[4]: SkyMapper DR1 [247], *Gaia* DR2 [102], SDSS DR9 [248], PanSTARRS DR1 [249], 2MASS [250], and AllWISE [251, 252]. All magnitudes used are listed in the Appendix.

The objective χ^2-based SED fit was carried out within the "Interactive Spectral Interpretation System" ISIS, which was designed at the Massachusetts Institute of Technology (MIT) by [253]. We used two free fit parameters. The stellar angular diameter θ has the effect of shifting the SED up and down according to $f(\lambda) = [\theta^2 F(\lambda)]/4$, where $F(\lambda)$ is the

[4]https://vizier.u-strasbg.fr/viz-bin/VizieR

synthetic model flux at the stellar surface and $f(\lambda)$ is the observed flux at the detector position, whereas the interstellar reddening $E(B-V)$ reddens the spectrum. We treated the interstellar extinction according to [254] via $A(\lambda)$, describing the interstellar extinction in magnitude at wavelength λ. $A(\lambda)$ is a function of the color excess $E(B-V)$ and the extinction parameter $R_V := A(V)/[E(B-V)]$, whereby we fixed R_V to 3.1, the value for the diffuse interstellar medium.

We added a generic uncertainty of 0.015 mag in quadrature to each of the magnitudes used to account for systematic uncertainties like shortcomings in the system response curves or in the calibration of the data. Furthermore, we rescaled all uncertainties to guarantee a best fit of $\chi^2_{\rm red} \sim 1$. 1σ single confidence intervals for θ and $E(B-V)$ were calculated in the following way: Starting from the best fit with $\chi^2_{\rm red} \sim 1$, we increased/decreased the parameter under consideration, while fitting the other one, until a certain increment $\Delta\chi^2$ from the minimum χ^2 was reached. Chosen values for $\Delta\chi^2$ determined the confidence level of the resulting interval, for instance, $\Delta\chi^2 = 1$ yielded 1σ single confidence intervals.

Figure 8.8 shows the resulting SED. Thanks to the very precise photometric data, the uncertainty on the angular diameter ($\Delta\theta/\theta$) is of the order of 1.6 % only. Therefore, the mass uncertainty is dominated by the surface gravity uncertainty and the parallax measurement (see Eq. 8.6).

Table 8.5 summarizes the spectrophotometric results based on *Gaia*. The given uncertainties on the fundamental stellar parameters result from Eqs. (8.4), (8.5), and (8.6), whereby we used the 1σ statistical and systematic errors for $T_{\rm eff}$ and $\log(g)$ from § 8.3, and $\Delta\theta/\theta \sim 1.6\,\%$. While M and $\log(L/L)$ match the theoretical predictions of [50, 51] for hot subdwarf stars, R is well above the canonical regime between ~ 0.10 and $\sim 0.30\,R_\odot$. An inflated radius for the primary of EVR-CB-004, however, is expected due to the strong ellipsoidal deformation.

We also determined the fundamental stellar parameters from distances derived from Bayesian methods. We used the distance from [255], converted it to the parallax space via the usual relationship $d = 1/\varpi$ and again determined R, M, and $\log(L/L)$ via the

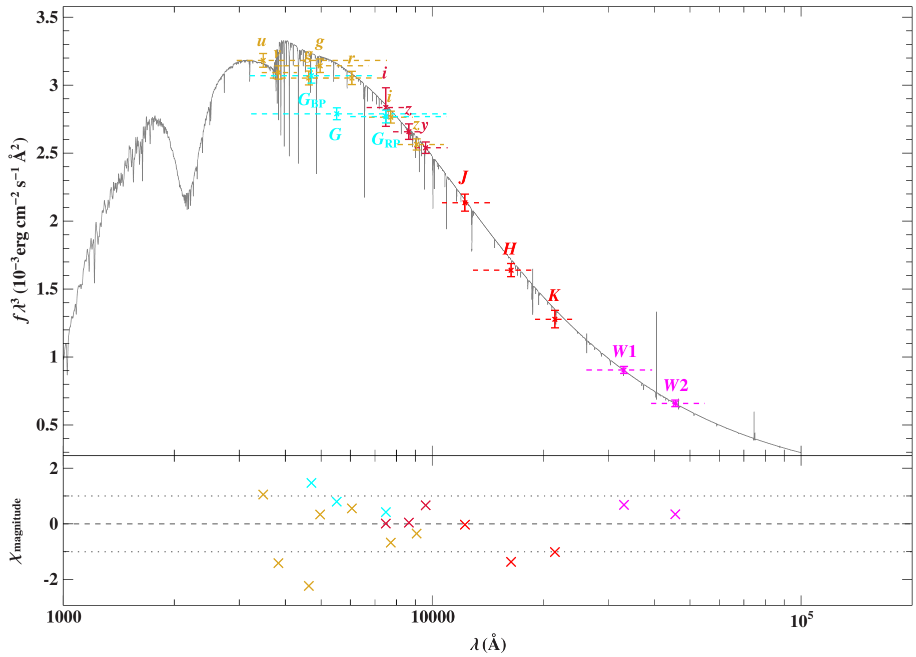

Figure 8.8: Comparison of a synthetic spectrum with photometric data for EVR-CB-004. Filter-averaged fluxes are shown as colored data points that were converted from observed magnitudes (the dashed horizontal lines indicate the respective filter widths). The gray solid line represents a synthetic spectrum based on the final atmospheric parameters derived from the low and medium-resolution SOAR spectra (see Table 8.4). The residual panel at the bottom side shows the differences between synthetic and observed magnitudes. The following color codes are used to identify the photometric filter systems: SkyMapper and SDSS (yellow), Gaia (cyan), PanSTARRS and 2MASS (red), and WISE (magenta). The flux density times the wavelength to the power of three ($f_\lambda \lambda^3$) as a function of wavelength is plotted in order to eliminate the steep slope of the constructed SED over the displayed broad wavelength range.

Spectrophotometric Approach. The results based on Bailer-Jones and the ones derived from *Gaia* are in good agreement (see Table 8.5). Both results are also consistent with the light curve modelling.

8.6.2 Surprising properties of the sdO in EVR-CB-004

The primary star in EVR-CB-004 is consistent with known hot subdwarf O-type stars based on temperature and mass, but its surface gravity is quite low and the radius is inflated. These properties were confirmed independently from the atmospheric and light curve solutions (see the previous sections).

Table 8.5: Parallaxes and fundamental stellar parameters for the primary of EVR-CB-004 derived from the spectrophotometric approach. Gaia: Based on measured *Gaia* parallax. BJ: Based on distance derived from Bayesian methods [255]. †: 1σ statistical uncertainties only. *: Listed uncertainties result from statistical and systematic errors (see Sects. 8.3 and 8.6.1 for details).

Parameter	Unit	Result
$\varpi_{\rm Gaia}$	[mas]	$0.4529 \pm 0.0474^{\dagger}$
$d_{\rm Gaia}$	[pc]	$2207.993 \pm 231.086^{\dagger}$
$\varpi_{\rm BJ}$	[mas]	$0.4847^{+0.0538\dagger}_{-0.0443}$
$d_{\rm BJ}$	[pc]	$2063.199^{+228.882\dagger}_{-188.519}$
θ	[10^{-11} rad]	$1.239 \pm 0.007^{\dagger}$
$E(B-V)$	[mag]	$0.141 \pm 0.004^{\dagger}$
$R_{\rm Gaia}$	[$R_{\odot}$]	$0.61 \pm 0.07^{*}$
$M_{\rm Gaia}$	[$M_{\odot}$]	$0.50 \pm 0.15^{*}$
$\log{(L_{\rm Gaia}/L_{\odot})}$		$2.98 \pm 0.11^{*}$
$R_{\rm BJ}$	[$R_{\odot}$]	$0.57^{+0.07*}_{-0.06}$
$M_{\rm BJ}$	[$M_{\odot}$]	$0.44 \pm 0.13^{*}$
$\log{(L_{\rm BJ}/L_{\odot})}$		$2.92^{+0.12*}_{-0.10}$

Also surprising, the sdO is close to filling its Roche Lobe or perhaps even fills its Roche Lobe. We would instead expect a post-CE compact binary with a canonical like hot subdwarf to stabilize at a close separation, but beyond any mass transfer point. It is unclear if the system is actively accreting, a possibility given the sdO is so close to filling its Roche Lobe.

The helium content of the primary of EVR-CB-004 ($\log n(\mathrm{He}) = -0.87$, see Table 8.4) is close to solar ($\log n(\mathrm{He}) = -1.07$, see [256]). This is rather unusual for hot subdwarf O stars, which generally tend to be helium-rich, including those in the more luminous subclass (a few examples being HD 49798, KS 292, LSE 153, see [257]).

These surprising properties must be taken into account when considering the sdO and evolutionary history of the EVR-CB-004 system.

8.6.3 Comparison to Stellar Evolution Models

To investigate the nature of the primary, we compare evolutionary tracks of hot subdwarf models of compact pre-helium white dwarfs (pre-He WDs), helium-burning stars and post-asymptotic-branch (post-AGB) stars with our observed properties [258, 259]. We note here that for all stellar evolution models, we adopt a solar metallicity, justified by the helium content of the sdO (see the previous section) and population type (from kinematic analysis we find that EVR-CB-004 is likely a member of the young Galactic thin disc population, see the Appendix for additional details). Following, we discuss four different interpretations as to the nature of the primary in EVR-CB-004.

In the first interpretation, the primary is a helium core-fusing sdO but with a lower than average surface gravity and larger than average radius. This situation might have arisen if the progenitor filled its Roche Lobe as it began core He-burning and expanded. Most of the mass of the outer envelope would be removed during this phase of mass transfer, leaving only a few hundredths of a $M_{\odot}$ of H/He envelope material outside the He-dominated core. The star then evolved to become a He-burning hot subdwarf with a thinner than normal shell and inflated radius, consistent with the observed radius of the EVR-CB-004 primary. However, the measured luminosity $\log{(L/L_{\odot})} \approx 3$ (see Table 8.5) is inconsistent with the typical luminosity for He-core burning star with masses $\approx 0.5\,M_{\odot}$ ($\log{(L/L_{\odot})} \approx 1-2$; [260]).

If instead the progenitor filled its Roche Lobe before reaching the tip of the red giant branch, the star would evolve into a pre-He WD and contract to become a helium WD. The mass of the helium WD depends on the mass of the helium core when the progenitor filled its Roche Lobe. We use the stellar evolution code `MESA` [200–203, 261] to calculate tracks for different pre-He WD models and find that a pre-He WD with a mass of $0.393\,M_{\odot}$ is consistent with the observed $\mathrm{T_{eff}}$ and $\log{(g)}$ (see Fig. 8.9. This mass is inconsistent with the derived mass from the light curve modelling and because the sdO is close to Roche Lobe filling the pre-He WD would just have been born - therefore we consider this solution to be unrealistic.

Next, we consider a more evolved hot subdwarf. Canonical-mass hot subdwarfs with core masses $M \approx 0.47\,\mathrm{M_{\odot}}$ are expected to burn core helium for 100 to 150 Myr. Depending on their hydrogen envelope they are considered to be extreme horizontal branch (EHB) stars (for hydrogen envelopes $\lesssim 0.01\,\mathrm{M_{\odot}}$) or blue horizontal branch (BHB) stars (for hydrogen envelopes of a few hundreds $M_\odot$). Once burning exhausts He in the core, the star evolves toward hotter temperatures. As the core contracts, He burning is predicted to burn in a shell, pushing the surface to a larger radius [219]. This is seen as the peaks in the solid tracks shown for different masses in Figure 8.9. This stage of the evolution is expected to last for only $\approx 10-20$ million years and is commonly referred to as post-EHB or post-BHB evolution. A helpful discussion of EHB/BHB stars and their evolution can be found in [262], [219] and [178]. Figure 8.9 shows the position of the primary of EVR-CB-004 in the T_{eff}-log (g) diagram. It lies nearer to the post-BHB sequence with a mass on the higher end of the canonical range, meaning the object could be a more evolved remnant post-BHB than a core burning sdO hot subdwarf. If the post-BHB interpretation is correct, the primary of EVR-CB-004 is even rarer as we would have to have caught the object during this transitioning state. The only other reasonably similar system (compact binary with a WD companion, ellipsoidal deformation, Doppler boosting, gravitational limb darkening, similar mass, and an old evolved primary) we found in the literature is HZ 22 [263]. However this interesting object is quite different in other ways, with a lower temperature and surface gravity as well as a larger radius.

In addition to the EHB/BHB and post-EHB/BHB evolutionary tracks, we also compared the primary of EVR-CB-004 to post-AGB (post-asymptotic giant branch) tracks for three different masses ($0.524\,M_\odot$, $0.546\,M_\odot$, and $0.565\,M_\odot$; [259]). Post-AGBs are also final stage objects transitioning to a WD; an excellent review of post-AGB stars can be found in [272]. For a recent survey (of hot UV-bright stars in globular clusters) yielding several post-AGB discoveries along with their atmospheric properties, see [273]. In Figure 8.9, the post-AGB evolutionary tracks for a slightly more massive object fit our observed values, but there are two difficulties with this interpretation. First finding a short lived post-AGB star in a very rare compact binary seems highly unlikely. The post-AGB phase is expected to be fast, on the order of 10^5 years [272]. Second, post-AGB stars that are found in binaries have much larger separations and longer periods than EVR-CB-004 (again see [272]). A very tight, compact binary with a post-AGB star is difficult to explain given the AGB cycle. Nonetheless, it is

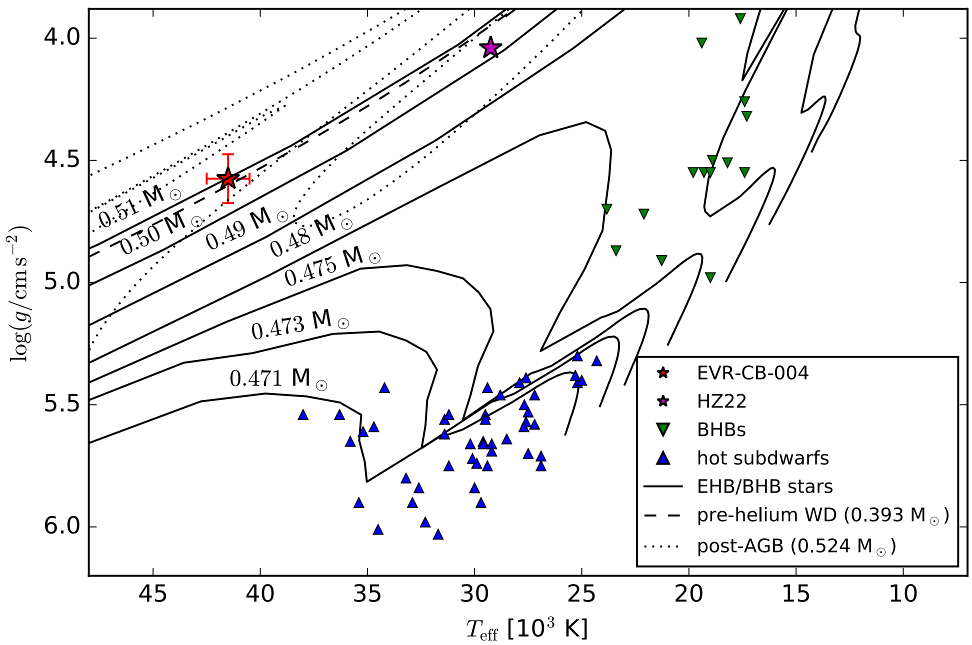

Figure 8.9: $T_{\rm eff}$-log (g) diagram of the primary star in EVR-CB-004 (red star). EHB/BHB evolutionary tracks for different stellar masses (bottom to top: $0.471\,M_{\odot}$, $0.473\,M_{\odot}$, $0.475\,M_{\odot}$, $0.480\,M_{\odot}$, $0.490\,M_{\odot}$, $0.500\,M_{\odot}$, and $0.510\,M_{\odot}$), that is, increasing hydrogen envelope mass (0.000, 0.002, 0.004, 0.009, 0.019, 0.029, and $0.039\,M_{\odot}$, respectively), and solar metallicity according to [258] are shown with solid lines. In addition, the post-AGB tracks according for $0.524\,M_{\odot}$, are displayed with dotted lines [259] as well as the pre-helium WD track calculated with MESA [200–203, 261] shown with dashed lines. The hot subdwarfs are confirmed binaries with WD companions taken from [264]. BHB stars are taken from [55, 265–271]. Plotted error bars include 1σ statistical and systematic uncertainties as presented in the text (see Sect. 8.3 for details).

possible EVR-CB-004 has a post-AGB primary, and would make it a most unusual compact binary system. If the post-AGB interpretation is correct, EVR-CB-004 is even rarer still - and the first object of this type discovered (post-AGB primary in a compact binary with the multi-component light curve variation).

None of the interpretations fit all aspects of the observed data. The post-BHB and post-AGB explanations fit the lower observed surface gravity, but are short-lived phases that are challenging to explain in the already rare compact system. The post-AGB scenario has the additional obstacle of forming a compact binary given the AGB phase. Given the difficulties with a very non-canonical sdO with an inconsistent luminosity and the formation challenges of a post-AGB compact binary, we tend to prefer the post-BHB interpretation of the primary in EVR-CB-004.

Extensive spectroscopic analysis (very high resolution and comprehensive wavelength coverage beyond the scope of this work) could constrain the atmospheric parameters that may favor one interpretation. Two examples revealing post-AGB stars can be found in [274] and [275]. We suggest this as future EVR-CB-004 follow-up work.

8.6.4 Formation and Evolution

According to binary evolution models of [50] WD + hot subdwarf close binaries form via the CE formation channel described in [178], resulting in a compact binary with each component very near the canonical mass. EVR-CB-004 likely formed from a wide main-sequence binary with two phases of mass transfer. As the more massive companion moved off the main sequence, it entered the red-giant branch and began stable mass transfer (RLOF) onto its lower mass main-sequence companion. The initial masses of the components are assumed to be relatively close in this scenario, with the initial mass ratio $q < 1.2 - 1.5$, in order for the mass transfer to be stable [276]. The RGB core eventually enters the WD cooling sequence and the system becomes a WD + main sequence wide binary.

Once the second main-sequence star enters the RGB phase, the mass transfer is unable to accrete onto the WD at a sufficient rate to be stable. A CE is formed and friction causes the orbital period to shrink and the envelope to be ejected. The remnant core of the second RGB star becomes the primary in EVR-CB-004, now in a close orbit with its near canonical mass WD companion.

In § 8.6.3 we identified the hot subdwarf in EVR-CB-004 as most likely being a more evolved object. If the primary is a post-BHB star, the hot subdwarf would start its evolution as a hot subdwarf star with core helium burning lasting for $\approx$150 Myr. Once this process finished it would burn helium in the shell for $\approx$20 Myr [219]. With the start of helium shell burning the hot subdwarf would increase in temperature, and expand to appear as an sdO with a large radius compared to a canonical hot subdwarf. It is possible that we see the EVR-CB-004 system in this short window.

Because the sdO in EVR-CB-004 is so close to Roche Lobe filling, we discuss briefly the likely accretion during the post-BHB stage. The expansion driven by the post-BHB shell burning will push the radius outward to overflow its Roche lobe and start accretion onto the WD companion. As the sdO star accretes onto the WD companion, the sdO will increase in temperature but maintain a constant radius (still consistent with the observed properties of the primary in EVR-CB-004). We would like to emphasize that the current data does not allow us to exclude an accretion disc and ongoing accretion. The sdO in EVR-CB-004 is consistent with a Roche Lobe filling post-BHB star, and with a luminosity of $\log{(L/L_\odot)} \approx 3$ the sdO would outshine an accretion disc in the optical. Additionally, the inclination angle is too small to show any eclipse from an accretion disc. If the sdO in EVR-CB-004 is actively accreting, it is more extreme (longer period/larger sdO star) than the recently discovered ZTF J2130, which was found to be an accreting sdO star at 39 min orbital period where the sdO gets eclipsed by the accretion disc [277]. It is also possible that we see the EVR-CB-004 system as an active accretor in the short post-BHB window. X-ray analysis could confirm the system as an active accretor, and we leave that followup observation and analysis to future work.

If the primary is a post-AGB object (this possibility was also raised in § 8.6.3) the close binary becomes a mystery. Binaries among post-AGB are expected to be long period (to avoid the overflow and spiral-in scenario), with observations supporting this theory [272]. Additionally, the primary in EVR-CB-004 is close to Roche Lobe filling and therefore, must have left the CE very recently as a post-AGB star would start contracting towards the WD sequence immediately after formation. By itself, the primary of EVR-CB-004 is consistent with a post-AGB object, but we cannot explain a tight binary post-AGB + WD.

The EVR-CB-004 system is expected to evolve into a double-degenerate WD + WD binary (regardless of the sdO, post-BHB, or post-AGB interpretation). The orbit will then shrink due to gravitational wave radiation, until the period reaches a few minutes in $\approx 4\,$Gyrs. As the orbit shrinks to this small separation, the less massive (but larger radius) WD will fill its Roche lobe and transfer mass to the more massive companion WD. What happens next depends on several factors, most importantly the mass ratio and the total mass; a helpful discussion of WD merger evolution can be found in [211]. WD merger simulations performed by [278] reveal a narrow range for mass fractions ($2/3 < q < 1$, where q is the mass of the donor / the mass of the accretor) where the WDs are expected to merge via unstable direct impact mass transfer. The mass fraction of EVR-CB-004 ($q = .72$) suggests the system will merge to form a $1.1M_{\odot}$ high mass single WD. Some extraordinary WD merger systems from the ELM survey are presented in [184] (see Figure 6), with EVR-CB-004 falling in the high-mass-outlier regime and well placed in the merger region. However, such a large combined mass can also lead to a thermonuclear supernova in $\approx 4\,$Gyr as discussed in detail in [279–281].

Double WD systems as producers of higher mass single WDs is an active area of research. A recent investigation of merger rates for high mass WD merger rates can be found in [282] showing a less than 10% rate for WD mergers near the total mass of EVR-CB-004. WDs with masses greater than $\approx 1M_{\odot}$, regardless of origin, are predicted and observed to be quite rare. [283] shows rates of a few percent or less, in a sample biased toward the higher mass. EVR-CB-004 is a viable candidate double WD merger forming a single high mass WD or a thermonuclear SN Ia, making it a quite rare system from this aspect alone.

8.6.5 Low Amplitude Light Curve Variation

In addition to the photometric variations from ellipsoidal deformation, Doppler boosting, and gravitational limb darkening, the high precision SOAR, TESS and PROMPT light curves also show a 2.028 hour low amplitude (0.4% in TESS) sinusoidal signal. Shown in Figure 8.10 are the SOAR, TESS, and PROMPT light curves (phase folded on the 6.084 orbital period), with the residuals after removing the astrophysical signal from the solution in § 8.4. Clearly visible in the residuals is a low amplitude signal that is a resonance of the dominant signal. We checked the best period of the residual signals from SOAR and TESS by analysing them with LS and find the results are consistent with the observed period of 2.028 hours. The most challenging aspect of the signal is that the period is a 3/2 resonant of the dominant light curve feature (the ellipsoidal deformation of the primary seen at 3.042 hour cycles) with a phase offset between the low amplitude and dominant light curve signals. This combination of features cannot be due to a poor fit to the data. Following we discuss possible sources of this signal.

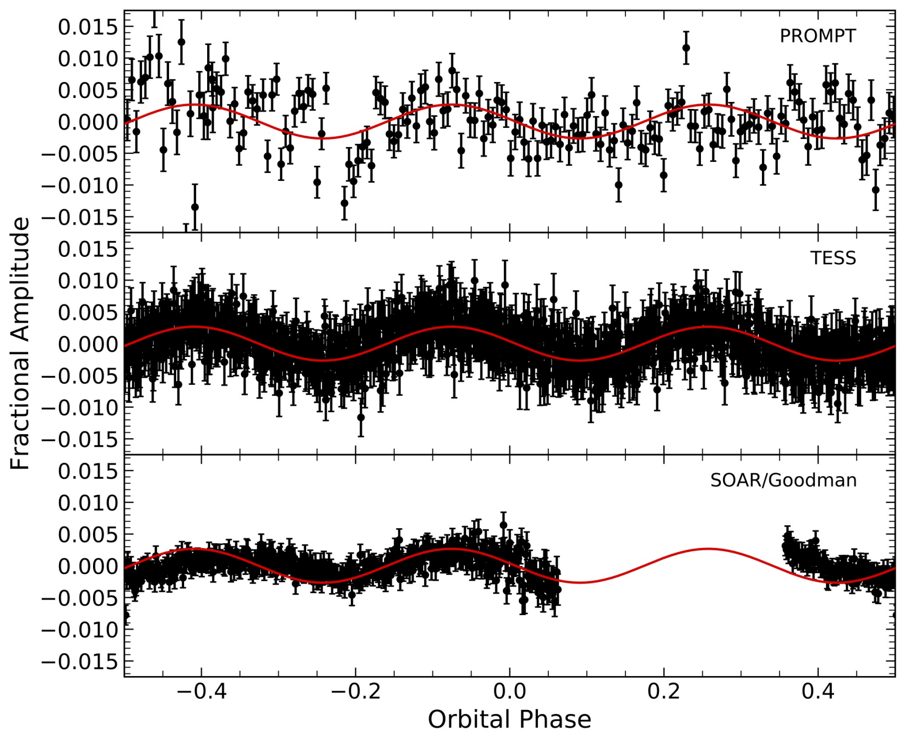

Figure 8.10: Phase-aligned residuals after removing our best–fitting model from the PROMPT (top; R filter), TESS (middle; ∼I filter), and SOAR/Goodman (bottom; V filter) light curves. While strongest in the TESS data, all three residuals show hints of an additional variation at one–third the orbital period. The red line shows a simple sinusoidal fit to the TESS residuals, with the period fixed to one–third the orbital period.

8.6.5.1 Third Body

A third body with a 1/3 period of the binary could produce the low amplitude variability from a reflection effect. However this third orbit would be so close that it would be unstable or nonphysical. There would also be variations in the radial velocity curve that we do not see in the observed data. If instead this was a mass transfer point, we would expect the same period as the binary and would see evidence in the spectra and light curve (again which are not visible in the observed data). For these reasons, we conclude a third body is not the source of the low amplitude sinusoidal signal.

8.6.5.2 Asynchronous Rotation

LCURVE assumes that the deformed sdO star is synchronized to the orbit. If the sdO star is rotating faster than synchronization, this could explain an additional light curve signal. However, the low amplitude variability in the SOAR and TESS light curves (and especially the phase offset with the dominant ellipsoidal signal) does not match any potential super-synchronous signal. Additionally, from the spectroscopic fits and our modeling solution, we *do not* see evidence that the sdO is spun-up. The expected rotational velocity from the light curve solution (115 km s^{-1}) is very close to the value measured from the spectra (116.5 km s^{-1}), and we conclude the sdO is synchronized in rotation with the orbit. We conclude asynchronous rotation does not explain the variability and amplitude, let alone the 2.028 hour resonant period.

8.6.5.3 Eccentricity

LCURVE assumes that the system is in a cicular orbit. Therefore, as with asynchronous sdO rotation, an eccentric binary orbit could explain the additional variability. However, the eccentricity would have to be specific to generate a resonant period and symmetric residual pattern. We cannot identify a mechanism to cause this, and it is challenging to explain why it would occur by random chance.

8.6.5.4 Pulsations

Some hot subdwarfs were discovered to pulsate [284], now known as sdBV or V361 Hya stars. Hot subdwarf pulsators were later shown to belong to two distinct groups with different driving mechanisms. P-mode (acoustic wave) pulsations are rapid (a few minutes) and probe the outer regions of the star, while g-mode (gravity wave) pulsators have longer periods ($\approx$ 1-2 hours) and probe deep within the stellar interior [178]. Amplitudes are typically at the milli-mag level, with some up to a few percent; for examples and an analysis of the driving mechanisms of pulsators see [285]. The discovery of the first g-mode pulsator PG 1716+426 and discussion can be found in [286], while a thorough analysis of the p-mode puslator NY Vir can be found in [287].

Hotter, helium rich hot subdwarfs are also known to pulsate. LS IV-14116 [288] was the first, along with the recent discovery of Feige 46 [289]. These He-rich pulsators are now recognized as a separate class, called V366 Aqr or He-sdOBV pulsators. The pulsation mechanism was originally suspected as g-mode given the longer periods, but is still under debate.

Not all pulsators fit well into the p or g-mode classifications. Two examples are CS 1246 [290] and Balloon 090100001 [291], demonstrated to be larger amplitude ($\approx 6\%$) radial mode pulsators. A new class of pulsators is suggested in the very recent work by [292], presenting additional discoveries of radially driven pulsations, with the light curve variations synchronised to the changes in radial velocity amplitudes. Binarity is ruled out from the short periods (few minutes) and low amplitude RV ($\approx$ 40km s^{-1}). Additionally, some hot subdwarfs show stochastic pulsations, KIC 2991276 [293] being the most compelling example. The stochastic behavior is not well understood, [178] suggests that influence from an unseen close companion could be one cause. These recent developments suggest that not all of the hot subdwarf pulsation types have been observed, nor are all the mechanisms understood.

The sdO in EVR-CB-004 could be a pulsator, with the period (2.028 hour) and low amplitude (0.3% sinusoidal signal) in agreement with observed known g-mode pulsators. The amplitude variation in different filters (SOAR V and TESS) is also expected given a pulsator explanation. A pulsator in a tight binary is rare but not without precedent (see NY Vir referenced above). If so, EVR-CB-004 would be the first compact binary (containing a more massive companion WD) with the hot subdwarf showing pulsations. The tight orbit and massive compact companion perhaps not causing stochastic behavior, but instead driving the 1:3 pulsation/orbit synchronization.

Pulsation / orbit synchronization (tidally induced pulsations with resonant locking) is not without precedent and has been found in heartbeat star and main-sequence binaries. A recent example is KIC 8164262 [294], with the pulsations believed to be caused by the difference in tidal forces throughout the orbit. A very different tidally resonant pulsator is the A-star binary KOI-54 [295]. An extensive discussion of potential mechanisms for tidally induced pulsations on solar type stars can be found in [296]. Although different types of systems than EVR-CB-004, these examples demonstrate tidally induced pulsators are not limited to a specific binary type. The light curves for EVR-CB-004 demonstrate a resonant locked signal from the sdO, with the amplitude level and amplitude difference among filters that is suggestive of a tidally induced pulsation.

8.6.5.5 Source Field

The EVR-CB-004 field has several dim stars near the target, easily separated in the SOAR high resolution images. To check for possible blending in the TESS field and to look for signs of nebula around the target, we stack the 515 SOAR 20 second images to form the deep image of the field (shown in Figure 8.11). EVR-CB-004 is the brightest star in the field, near the bottom center. The star to the upper right of EVR-CB-004 and the two dimmer stars to the right are not blended in the TESS pixels, and the other very dim sources nearby are inconsequential (they look exaggerated since this is a 3-hour image from a 4.3m telescope). However the three nearby stars could still contaminate the TESS aperture photometry, which we check in several ways described below.

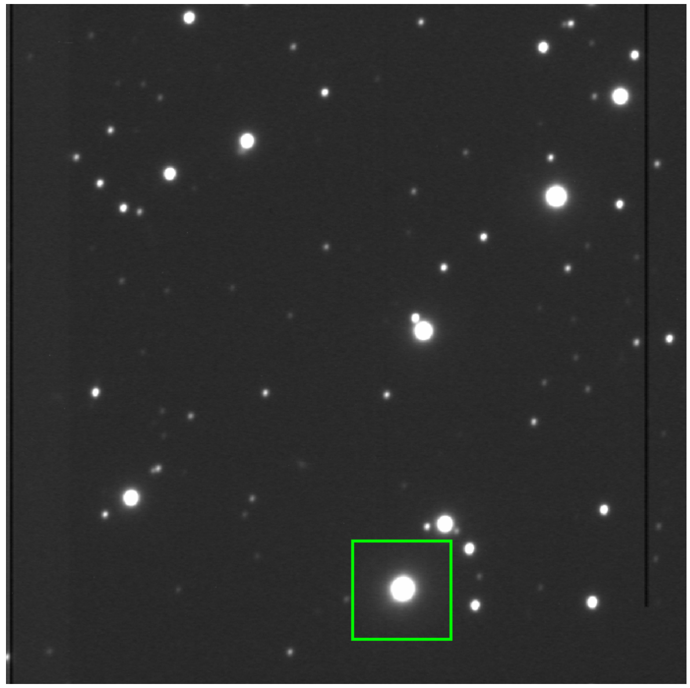

Figure 8.11: The EVR-CB-004 field as seen from stacking the 515 SOAR 20 second images (in V band) to form this final deep image. EVR-CB-004 is the brightest star in the image, located near the bottom center. There are no definitive signs of nebula near the source. The green box is one TESS pixel, with the nearby sources to the right and upper right being potentially blended in the TESS aperture photometry. From the SOAR data, we verified these sources are non-variable and minor in flux (2.5%) compared to the target. The consistent light curve solutions from the SOAR, TESS, and PROMPT data also shows these sources are inconsequential in the TESS data. The image is 3' x 3'.

The crowded field leads to two concerns - influencing the best fit from the light curve solution, and potentially adding an additional variability source. To address the first concern, we fit both the SOAR and TESS light curves independently and the solutions converged on the same results within the reported error ranges. We also adjusted the TESS light curve, based on measurements of the nearby stars using the SOAR data, and found the effect to be minimal and to have no measurable change in our solution.

To address the concern of added variability, we extracted light curves for each of the potential contaminant stars with the same photometric pipeline used to make the SOAR light curve for EVR-CB-004. We measured the combined contribution of the three potential TESS contaminant sources to be 2.5%, and we also confirmed they are non-variable. The appendix shows the light curve of these nearby sources folded on the orbital and on the 1:3 alias periods.

The PROMPT data also provides an opportunity to test the potential contaminant stars. Here we extracted light curves for each of the nearby stars with the same photometric pipeline used to make the PROMPT light curve for EVR-CB-004. The appendix shows the light curve of these nearby sources folded on the orbital and on the 1:3 alias periods, and confirms the non-variability of the SOAR analysis. In the R passband of the PROMPT data, the combined contribution from the nearby stars increases to 35% of the total flux of the target. With this large of a contamination, the amplitude of the main variability would be diluted in the TESS light curve and would influence the system solution. Since our system solution is consistent through all light curves, we conclude the nearby stars do not contribute to the TESS photometry in any significant way.

With the deep image, we check for any signs of nebula surrounding the source as this could lead to an additional light curve variation. The PROMPT data is also stacked to form a deep image in R band, and is shown in Figure 8.12. There is no evidence of nebula and we conclude this is not a contributing factor to the low amplitude light curve variation.

8.6.5.6 Calcium Lines

H and K lines of calcium are visible in the SOAR medium resolution RV spectra, which could be indicative of debris or accretion. They are not visible in the ID spectra as the resolution is too low to detect the features, and they are not visible in the CHIRON data because the wavelength coverage is beyond the 3933Å and 3968Å CaK and CaH absorption lines. The calcium lines are stable in radial velocity and in amplitude within our measurement uncertainty, and we conclude they do not emanate from the EVR-CB-004 system (most likely interstellar).

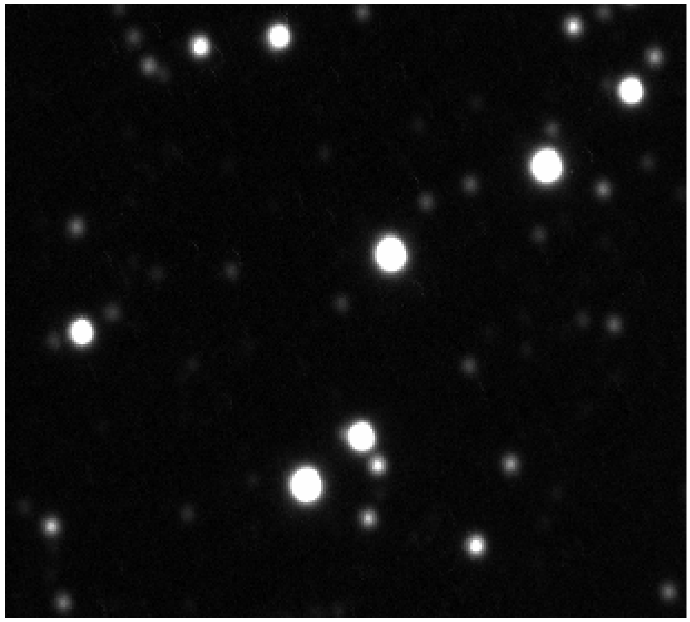

Figure 8.12: The EVR-CB-004 field as seen from stacking the 180 PROMPT 2 minute images (in R band) to form this final deep image. EVR-CB-004 is the brightest star in the image, located near the bottom center. Consistent with the SOAR deep field image, there are no signs of nebulosity near the source. The image is 3' x 3'.

8.6.5.7 Unexplained Source

We have considered all of the obvious (to us) potential sources of the 1/3rd period variability, even including some quite speculative in nature. We acknowledge there could be an astrophysical source we have not thought of that drives this low-amplitude signal. To understand a potential unexplained source, we briefly discuss the approach used in modeling ellipsoidal variable stars.

It is convenient and effective to use a cosine series to analyze ellipsoidal variable star light curves, with the argument being a function of the frequency of the binary orbit. The second harmonic dominates, however the third harmonic is still significant. Higher order terms are inconsequential and are neglected. The amplitudes depend primarily on the radii, mass ratio, orbital inclination, and darkening coefficients. A very good explanation of this approach can be found in [240], with the same methodology used in the LCURVE algorithm we employed in § 8.4 to solve the EVR-CB-004 system.

The models fix the phases of the harmonic terms in order to fit the standard ellipsoidal distortion. The low-amplitude signal in the EVR-CB-004 is not in phase with the main like curve variability, and likely the third harmonic term in LCURVE does not capture the full variability as well as it is intended due to this phase offset. It could be possible some source of asynchronism is responsible. This partially drove us to consider the many different explanations explored in this section.

8.6.5.8 Preferred Solution

Each of the potential solutions to the low amplitude oscillations has challenges, and we have eliminated to our satisfaction all but the asynchronous, unexplained source, or pulsation options. We note that the asynchronous rotation is the simplest explanation, however the measured rotational velocity does not support this conclusion. An unexplained source is certainly possible, but this is limited to speculation. This leads us to favor the pulsator explanation, with the acknowledgement that additional followup is needed to definitively confirm. Although beyond the scope of this work, extremely high precision multi-band photometric analysis and time series spectroscopy (as performed in the followup works [287, 290, 292]) could reveal phase dependent variations in velocity, $T_{\rm eff}$, and $\log{(g)}$ matching the 2.028 hour light curve low amplitude oscillations.

8.7 SUMMARY

We present EVR-CB-004 - the discovery of a close binary (6.08 hour period) with a remnant core primary and an unseen white dwarf companion. The primary is similar in mass and temperature (0.47 $M_\odot$ and 41,250 K) to an sdO, however the inflated radius and lower surface gravity (.62 $R_\odot$ and 4.57 $\log g$) suggest a more evolved object. Independent analysis and comparison to stellar evolution models reveals the primary is likely a post-BHB or post-AGB star, an unexpected find in such a system. We discuss the evidence in support of and against each interpretation, formation scenarios, and further followup that might be done to confirm the nature of the primary. EVR-CB-004 also shows a low-amplitude sinusoidal signal in the light curve, with a 1/3 rd resonant period of the binary period. This signal is visible in multiple filters (R, I, V), with evidence of filter dependent amplitudes. We tentatively identify EVR-CB-004 as a tidally resonant pulsator, and again suggest followup (extremely high-precision multi-band photometry and time series spectroscopy) to confirm. The post CE stage of evolution and favorable mass fraction (0.72) make EVR-CB-004 a viable merger candidate to form a high mass (1.1 $M_{\odot}$) *single* WD. This object was discovered using Evryscope photometric data in a southern-all-sky hot subdwarf (HSD) variability survey. The multi-component light curve features (bright 13.1 m_g source, large amplitude ellipsoidal modulations, Doppler boosting, and gravitational limb darkening), the remnant primary, large WD companion, additional resonant period variation, and merger candidate are unexpected and make EVR-CB-004 an exciting discovery and a unique system.

Acknowledgements

This research was supported by the NSF CAREER grant AST-1555175 and the Research Corporation Scialog grants 23782 and 23822. HC is supported by the NSFGRF grant DGE-1144081. BB is supported by the NSF grant AST-1812874. D. S. is supported by the Deutsche Forschungsgemeinschaft (DFG) under grant HE 1356/70-1. This work was supported by the National Science Foundation through grant PHY 17-148958. We acknowledge the use of the Center for Scientific Computing supported by the California NanoSystems Institute and the Materials Research Science and Engineering Center (MRSEC) at UC Santa Barbara through NSF DMR 1720256 and NSF CNS 1725797. The Evryscope was constructed under NSF/ATI grant AST-1407589. We made use of ISIS functions provided by ECAP/Remeis observatory and MIT (`http://www.sternwarte.uni-erlangen.de/isis/`). We thank J. E. Davis for the development of the `slxfig` module, which has been used to prepare figures in this work. `matplotlib` [297] and `NumPy` [298] were used in order to prepare figures in this work. This work has made use of data from the European Space

Agency (ESA) mission *Gaia* (`https://www.cosmos.esa.int/gaia`), processed by the *Gaia* Data Processing and Analysis Consortium (DPAC, `https://www.cosmos.esa.int/web/gaia/dpac/consortium`). Funding for the DPAC has been provided by national institutions, in particular the institutions participating in the *Gaia* Multilateral Agreement. We made extensive use of NASAs Astrophysics Data System Bibliographic Service (ADS) and the SIMBAD and VizieR database, operated at CDS, Strasbourg, France.

CHAPTER 9: TWO BRIGHT NEW HW VIR DISCOVERIES FROM THE EVRYSCOPE

This section presents results to be published in *The Astrophysical Journal*.[1,2]

9.1 INTRODUCTION

We report the discovery and detailed solutions of two HW Vir eclipsing binary systems - both bright ($m_G = 13.6$ & 13.5) and in the southern sky. Both systems have a hot subdwarf (sdB) primary and a faint M-dwarf secondary, with short orbital periods (6.59 & 3.16 hr) and fast eclipses (≈ 30 min). The discoveries were made with the all-southern-sky Evryscope fast cadence photometric light curves. The rare and difficult to detect HW Vir systems are important for determining fundamental stellar properties and in testing hot subdwarf formation history, but more systems are needed. We add two to the 20 known, solved systems with EVR-CB-002 having one of the most massive secondaries and EVR-CB-003 having a large non-canonical sdB with a comparatively small companion. These attributes do not break hot subdwarf formation models, but they do challenge theory to explain a wider range of values. Spectroscopic followup was performed with the SOAR telescope and photometric followup with the PROMPT network and SOAR telescope. We used the SPAS and LCURVE modeling codes to fit the spectrum and photometric light curves to determine the properties of each system. The best solution for EVR-CB-002 is $M_p = 0.469 \pm 0.054\ M_\odot$ and $M_s =$

[1]Ratzloff JK, Barlow BN, Schaffenroth V, Corcoran K, Corbett, HT, Glaizer A, Howard W, Law NM. Two Bright New HW Vir Discoveries from the Evryscope. *The Astrophysical Journal* 2020; To be submitted in March 2020, currently in final editing stage.

[2]I wrote about 80% of this paper, with the balance from Barlow and Schaffenroth. I discovered the systems, took and processed all of the followup data necessary for the light curve, ID spectra, and RV analysis, and provided this to Schaffenroth who did the detailed atmospheric and light curve fits. I worked with Barlow to compare the discoveries to known systems and in the overall approach to the manuscript.

$0.197 \pm 0.023\ M_\odot$, with $T_{\rm eff}$ = 28,400 ±195 K. For EVR-CB-003 we find: $M_p = 0.633 \pm 0.036\ M_\odot$ and $M_s = 0.142 \pm 0.008\ M_\odot$ with $T_{\rm eff}$ = 31,200 ± 102 K.

Hot subdwarfs are small, dense stars, under-luminous for their high temperature. They are helium core fusing stars with a thin hydrogen layer, understood to form via a significant loss of material during the red giant branch (RGB) phase. The peculiar high temperature (typically 25K to 40K) with a small radius and mass ($R \approx 0.2R_\odot$ and $M \approx 0.5M_\odot$) is attributed to the interruption in stellar evolution at this critical juncture. Hot subdwarfs are classified in two primary categories based on spectral features – B-types (sdBs) in the lower temperature range and hotter O-types (sdOs) that tend to be helium rich. Most sdBs and sdOs are found in binaries, with companions from white dwarfs up to F stars, and periods from a hours to months. A comprehensive review of hot subdwarfs can be found in [52].

A special subclass of hot subdwarf binaries are those with an sdB or sdO primary and an eclipsing M-dwarf or brown dwarf companion. Known as HW Virs after the namesake system [139], these close binaries are formed from a significant hydrogen stripping by a small companion during the red-giant phase of the sdB/sdO progenitor. The small companion is unable to accrete matter (from the hydrogen shell of the red-giant sdB/sdO progenitor) at a fast enough rate and a common envelope (CE) is formed. A common envelope provides an ejection channel which results in angular momentum loss, a tightening of the system, and a shortening in the binary period. A description of hot subdwarf formation including the CE phase can be found in [62]. Extensive simulations of sdB/sdO origins including the compact binary CE channel are performed in [50, 51], with predictions generally matching observed systems.

HW Vir systems typically have periods of less than 6 hours, and eclipse durations of 30 minutes or less; please see [61] for a list of the 20 confirmed and solved HW Vir systems. Despite the rather narrow system parameter window, HW Virs do show variation. This can be seen in a few recent HW Vir discoveries - one showing a very large secondary reflection effect [142], one with a deep eclipse [304], and a fast-period system with a brown dwarf companion [305].

The rare eclipsing HW Vir systems are needed to measure the sdB/sdO masses and radii, understand the variation in properties, and to help verify formation theory. The EREBOS project was specifically designed to find and categorize new HW Vir systems, a project update can be found in [306]. The mass distribution for hot subdwarfs is generally accepted to be the canonical mass ($M = 0.47 M_{\odot}$) [258, 307], but with some outlier systems. Even though HW Vir spectra are dominated by the hot subdwarf due to the temperature difference, the combined spectroscopic and photometric binary light curve analysis provides valuable solutions.

The discovery of HW Vir systems is challenging, despite the unique light curve features. HW Vir light curves have deep eclipses, a strong reflection effect, and a prominent secondary eclipse that is still higher than the nominal flux even at the deepest point in the secondary. However, the eclipse durations are only $\approx$ 30 minutes or less. Additionally, hot subdwarfs themselves are rare objects with a few thousand candidate sdBs/sdOs brighter than $m_G = 14$. This combined with the modest fraction of hot subdwarfs that are HW Virs lessens the potential number of candidates. The detection of HW Vir systems favors high cadence light curves with wide sky coverage to detect the fast eclipse and maximize the target potential.

We present the detailed followup and solutions of two bright, new HV Vir systems (EVR-CB-002 and EVR-CB-003), discovered in our hot subdwarf survey for low mass companions [120] and first reported therein. The systems were discovered searching for variations in the photometric light curves from the Evryscope. The Evryscope [17, 126] is an all-southern-sky system that monitors the sky with continuous 2-minute images intended to find rare, fast event objects. EVR-CB-002 was found with a 6.59015 hour period and EVR-CB-003 (also identified in Jayasinghe et al. in prep as a general variable) a 3.15672 hour period, both with sdB primaries and late M-dwarf secondaries.

This paper is organized as follows: in § 9.2 we describe the discoveries and followup observations. In § 9.3 we describe our spectroscopic analysis of the systems. In § 9.4 we describe our photometric analysis of the systems. The full solutions are given in § 9.5. We discuss our findings in § 9.6 and conclude in § 9.7.

9.2 OBSERVATIONS AND DISCOVERY

9.2.1 Evryscope hot subdwarf Search List

The hot subdwarf survey that discovered EVR-CB-002 and EVR-CB-003 relied on a target search list that is a combination of multiple sources, including a GAIADR2 [102] based candidate list [127] and a machine-learning based stellar classifier developed for the Evryscope magnitude range and field-of-view (FoV). For our field (Dec $< +10$) and survey magnitude range ($m_G < 15$) we identified 11,220 hot subdwarf *candidates* (selected from more than 9M total Evryscope sources), with ≈ 1500 being very high confidence hot subdwarfs. Following we briefly describe the Evryscope GAIA based classifier, combined with the [127] list, which were responsible for identifying EVR-CB-002 and EVR-CB-003 as likely sdBs. For further details on the target selection method, we refer the reader to our hot subdwarf survey paper [120].

The Evryscope Classifier uses a combination of a support vector machine (SVM) and a Gaussian mixture model (GMM) along with multiple color differences to segregate targets in color/magnitude space. The contour boundaries are calculated using training data of known stars in each category. The Evryscope GAIA Classifier constructs contour boundaries in GAIA B-R/G magnitude space according to:

$$G_{abs} = G + 5\log(Parallax/1000) + 10 \quad (9.1)$$

The classifier results are shown in Figure 9.1 with the hot subdwarf candidates in gold and EVR-CB-002 and EVR-CB-003 identified with silver stars.

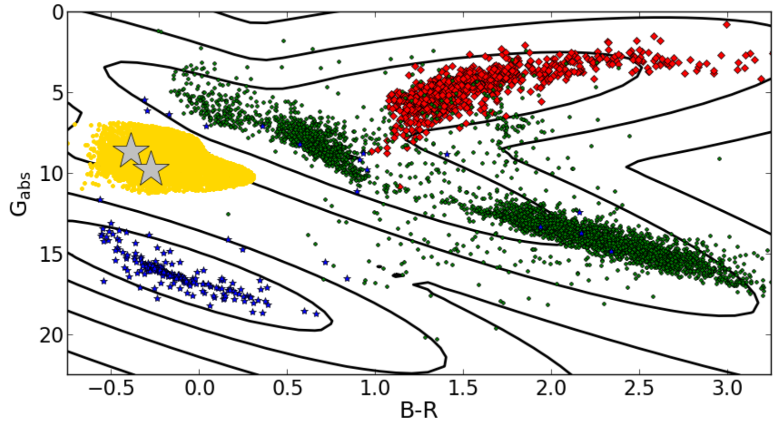

Figure 9.1: The Evryscope GAIA based classifier (see § 9.2.1), a two step Machine Learning based classifier. The black contours are the results of the GMM using training data from known giants (red diamonds), main sequence stars (green circles), white dwarfs (blue squares). The potential hot subdwarf candidates are identified with a SVM step and are shown as the yellow grouping above the white dwarfs and to the left of the main sequence stars. EVR-CB-002 and EVR-CB-003 are shown as the silver stars within the hot subdwarf region, with the hotter EVR-CB-003 to the left. We combine these results with external lists (§ 9.2.1) to identify both objects as highly likely sdBs and check for photometric variability in the Evryscope light curves.

9.2.2 Evryscope Photometry

The Evryscope photometric observations that led to the discoveries of EVR-CB-002 and EVR-CB-003 were taken from January, 2016 to June, 2018. The exposure time was 120s through a Sloan-g filter providing 19,758 and 53,698 filtered data points respectively. The calibration and reduction of images and the construction of light curves is performed with a custom pipeline written in Python. Raw images are filtered with a quality check, calibrated with masterflats and masterdarks, and have large-scale backgrounds removed using the custom Evryscope pipeline. Forced photometry is performed using APASS-DR9 [79] as our master reference catalog. Aperture photometry is performed on all sources using multiple aperture sizes; the final aperture for each source is chosen to minimize light curve scatter. Systematics removal is performed with a custom implementation of the SysRem [77] algorithm. For further details on the Evryscope instrument and the light curve pipeline, we refer the reader to [126].

9.2.3 Evryscope Discovery

We use a panel-detection plot that includes several matched filters to visually inspect the candidates for variability. EVR-CB-002 was discovered using Box Least Squares (BLS) [28, 29] with the settings, pre-filtering, and daily-alias masking described in [120], and with a custom detection algorithm called the Outlier Detector (described in detail in the same work) designed to find fast, deep transits in the Evryscope data. The discovery was found at the best BLS power and lowest Outlier Detector deviation with a 6.59015 hour period. Figure 9.2 shows the phase folded light curve and BLS periodogram.

EVR-CB-003 was discovered with Lomb-Scargle (LS) [31] with a period of 3.15672 hours. The reflection effect dominated the signal in the Evryscope light curve, favoring the LS filter. The phase folded light curve is shown in Figure 9.3.

Both targets were challenging discoveries – EVR-CB-002 is a blended source within 10" of the hot subdwarf target, and EVR-CB-003 is a dense, high air-mass field. Both situations dilute the Evryscope light curve, and in the case of EVR-CB-002, the primary eclipse is reduced to $\approx 8\%$. The unblended source is shown later in the manuscript in § 9.2.4 to be $\approx 50\%$.

9.2.4 PROMPT Photometry

In order to obtain higher signal-to-nose (SNR) light curves in multiple band-passes for modeling, both targets were observed using the PROMPT [36] 0.4 m MO-1 telescope at Meckering Observatory in Australia. The observations were taken during nights in December 2018 to March 2019. We also took one bias image, one 40s or 80s dark depending on the filter, and one 25s flat. The observing details are shown in Table 9.1.

The PROMPT images were processed with a custom aperture photometry pipeline written in Python. The images were dark and bias-subtracted and flat-field-corrected using the master calibration frames. Five reference stars of similar magnitude are selected and aperture photometry is performed using a range of aperture sizes. The background is estimated using

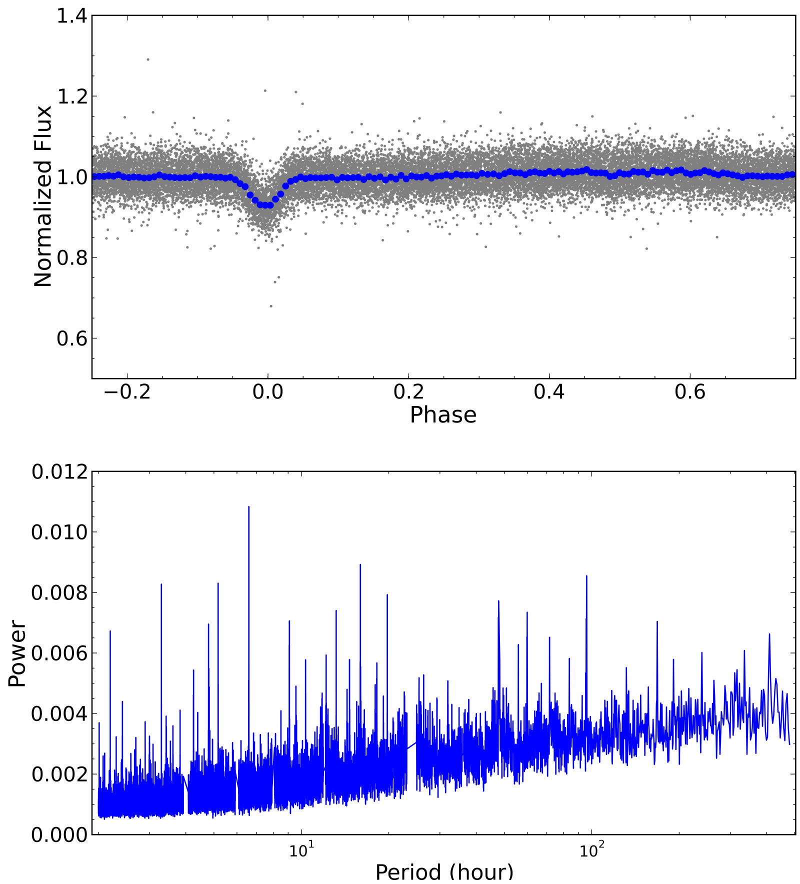

Figure 9.2: *Top:* The Evryscope discovery light curve of EVR-CB-002 folded on its 6.59015 hour period. The discovery was challenging as the target has a nearby star that dilutes the Evryscope light curve, reducing the primary eclipse to $\approx 8\%$. The unblended source is shown in § 9.2.4 to be $\approx 50\%$. The object was originally identified as potentially sub-stellar or grazing, the short 20 minute eclipse duration greatly supported the eclipsing object orbiting a hot subdwarf star. Grey points = 2 minute cadence, Blue points = binned in phase. *Bottom:* The BLS power spectrum peaking at the 6.59015 hour discovery period.

an annulus around the target and each reference star. A centroid step ensures each aperture center is consistent. Light curves are produced for apertures ranging from 5-20 pixels and the rms is computed for each aperture size. The astrophysical signal is removed, and lowest residual rms aperture size is chosen for the final light curve. The final aperture was a radius between 8 and 10 pixels depending on the target and filter. The unblended EVR-CB-002 and EVR-CB-003 PROMPT images are shown in Figures 9.4 and 9.2.4, while the R and B filter light curves for both targets are shown in Figure 9.6.

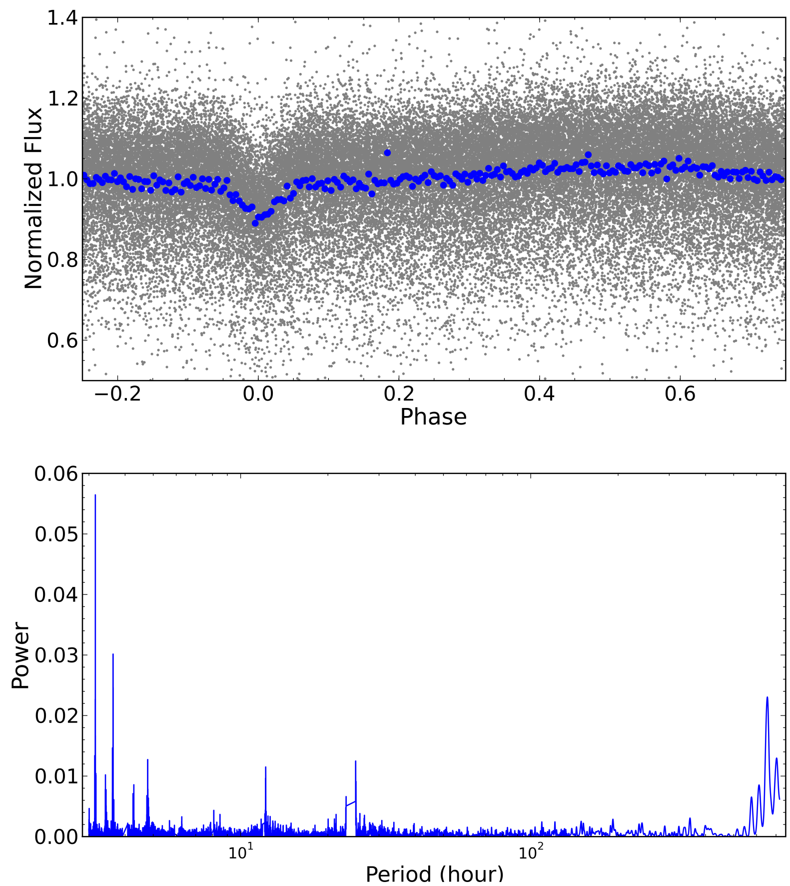

Figure 9.3: *Top:* The Evryscope discovery light curve of EVR-CB-003 folded on its 3.15672 hour period. The discovery was challenging as the target is in a dense, high air-mass field that dilutes the Evryscope light curve. Grey points = 2 minute cadence, Blue points = binned in phase. *Bottom:* The LS periodogram with the peak at the 3.15672 hour discovery period.

9.2.5 SOAR/Goodman Low-Res ID Spectra

In order to obtain the spectra necessary for the atmospheric modeling of the sdBs, we observed the candidates on December 2, 2018 with the SOAR 4.1 m telescope at Cerro Pachon, Chile with the Goodman spectrograph [33]. All observations used the 600 1/mm grating Blue preset mode with 2x2 binning and the 1" slit. This configuration resulted in a wavelength coverage of 3500-6000 Å with spectral resolution of 4.3 Å (R$\sim$1150, at 5000 Å). We took four 360s spectra for the target and for the standard BPM 16274. For calibrations, we took 3 x 60s FeAr lamps, 10 internal quartz flats using 50% quartz power and 30s integrations, and 10 bias frames.

Table 9.1: PROMPT photometric observations of EVR-CB-002 and EVR-CB-003

Target	Date	Filter	Images	Exp.
EVR-CB-002	December 1, 2018	Johnson B	262	90s
EVR-CB-002	February 19, 2019	Johnson R	300	60s
EVR-CB-003	December 5-6, 2018	Johnson B	183	100s
EVR-CB-003	March 1, 2019	Johnson R	150	100s

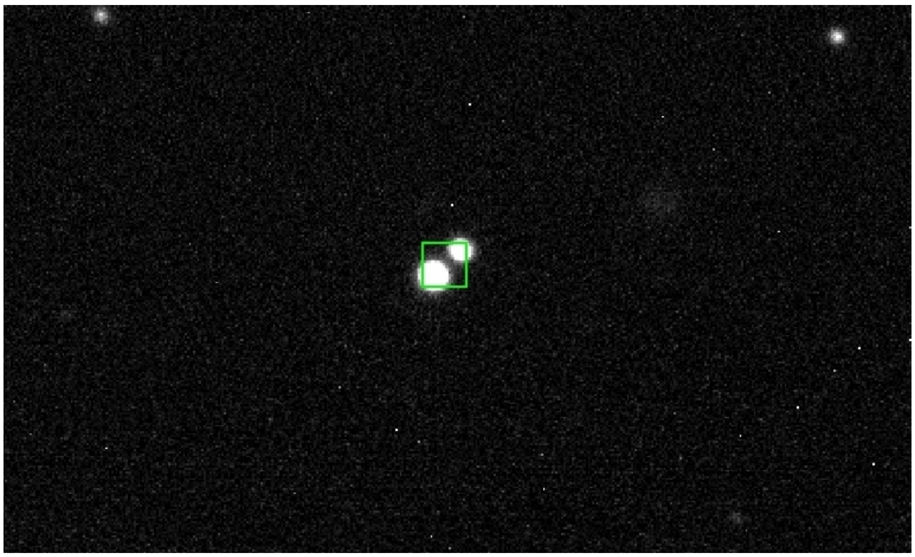

Figure 9.4: The PROMPT followup image for EVR-CB-002, showing the difficult field resulting in a blended source Evryscope LC. The detection was originally flagged as a possible sub-stellar object and is revealed in the PROMPT LC to be an HW Vir system. The sdB is the dimmer central star to the upper right. The Evryscope pixel size (13") is shown by the green box, the image size is 7' by 3.5'.

We processed the spectra with a custom pipeline written in Python. The spectra are individually bias-subtracted and flat-corrected. A 3rd-order polynomial is fit to the brightest pixels in each row; the spectra are then extracted in a 10-pixel range and background subtracted. We identify 16 prominent lamp emission lines and compare with the known lines of the Iron-Argon arc lamp using a Gaussian fit of each feature. We use a 4th-order polynomial to fit the Gaussian peaks and wavelength-calibrate each spectrum. We used the standard star BPM 16274 to flux-calibrate by first removing prominent absorption features then fitting a 7th-order polynomial to the continuum. Each spectrum was then rest-wavelength calibrated using a Gaussian fit to the Hβ through H11 absorption features, as well as several prominent

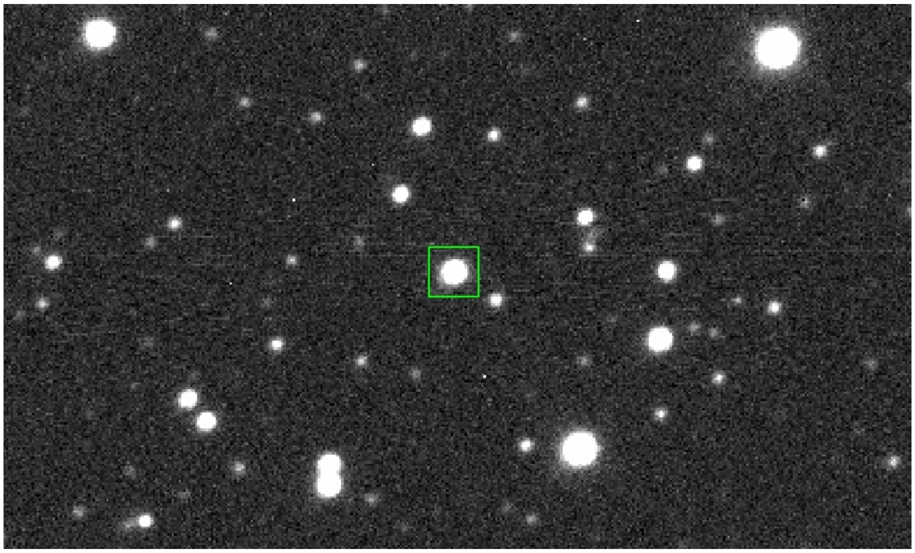

Figure 9.5: The PROMPT image of EVR-CB-003 showing the crowded field. The Evryscope pixel size (13”) is shown by the green box, the image size is 7’ by 3.5’.

He absorption features. The rest-wavelength spectra were median-combined to form the final spectrum (Figure 9.7) with a wavelength coverage of 3500-6000 Angstroms.

9.2.6 SOAR/Goodman Medium-Res RV Spectra

To measure the radial velocities (RV) of the systems, we also took medium resolution spectra. EVR-CB-002 was observed on February 9, 2019 with the SOAR 4.1 m telescope at Cerro Pachon, Chile with the Goodman spectrograph. EVR-CB-003 was observed on January 5, 2019. For both targets, we used the blue camera with the 2100 1/mm grating in custom mode with 1x2 binning and the .46” slit. This configuration resulted in a wavelength coverage of 3700-4400 Å with spectral resolution of 0.34 Å (R ≈11930 at 4000 Å). We observed 8 RV points for EVR-CB-002, and 6 RV points for EVR-CB-003. For each RV point, we median combined four 360s spectra (totaling 32 and 24 individual spectra observed, respectively). For all targets, we took 3 x 60s FeAr lamps after each group of four science images. Calibration images consist of 10 internal quartz flats with 80% quartz lamp power and 60s integration, and 10 bias frames.

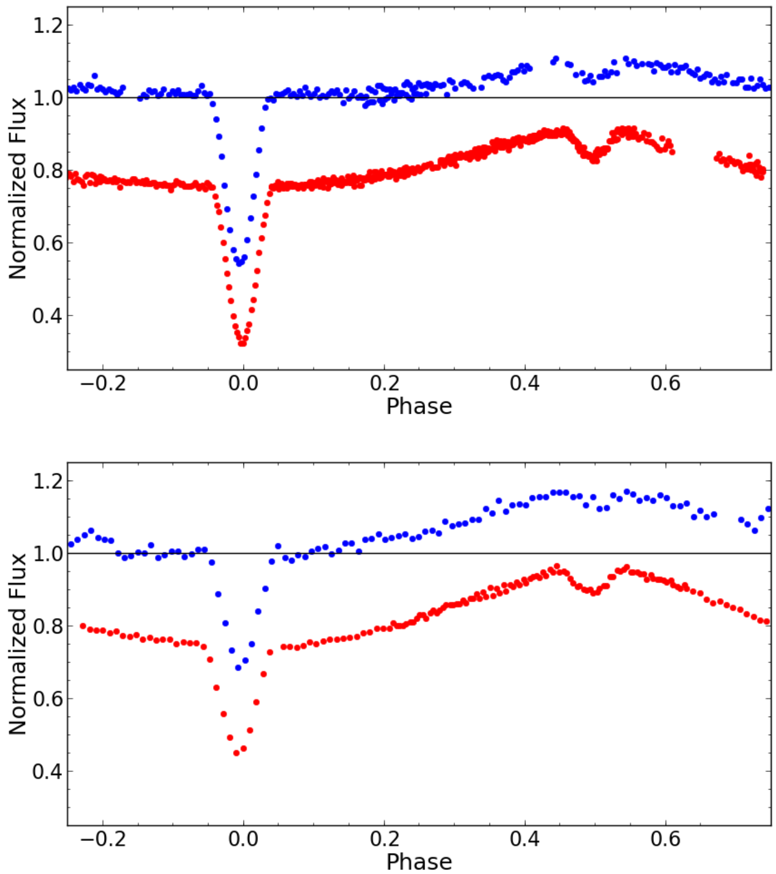

Figure 9.6: *Top:* The PROMPT light curves for EVR-CB-002 for both the B and R filters, with a 0.2 flux offset applied to the red filter for visualization. *Bottom:* The PROMPT light curves for EVR-CB-003. The targets are folded on the binary periods of 6.59015 and 3.15672 hours.

9.2.7 SOAR Photometry

EVR-CB-003 has a very short period with a challenging field, and we were concerned the PROMPT light curve was not well enough sampled and possibly introduced non-trivial phase smearing (which could negatively affect the model fit especially on the primary eclipse). We observed EVR-CB-003 with the 4.1-m SOAR telescope at Cerro Pachon, Chile to obtain a higher SNR light curve, at fast cadence, and in a bluer filter (Bessel V).

Observations were taken on August 2, 2019 with the Goodman spectrograph [33] in imaging mode. We used the blue camera with Bessel-V blocking filter, and took 474 images with 20 second exposure times. The image ROI was reduced to 1300 x 725 pixels with 1x1

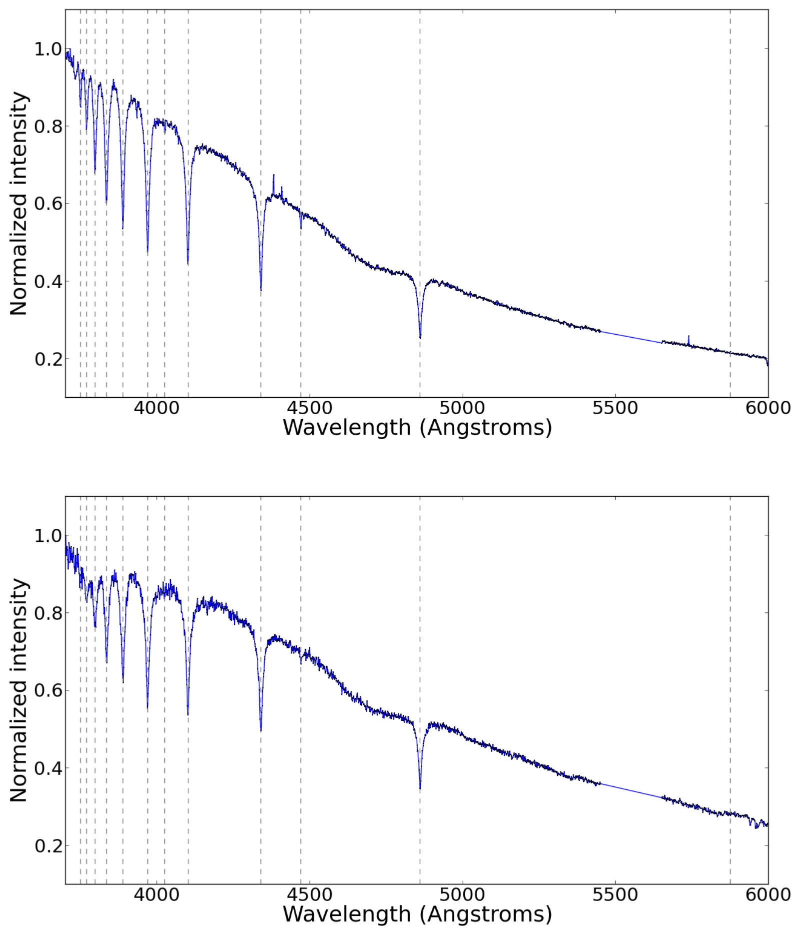

Figure 9.7: The SOAR Low-Res ID spectra used to measure the atmospheric parameters of the sdBs. Absorption lines Hβ to H-11 are shown for reference. *Top:* EVR-CB-002. *Bottom:* EVR-CB-003.

binning. For calibrations, we took 10 dome flats using 25% lamp power and 10s integrations, 10 darks also with 10s integrations, and 10 bias images.

The SOAR images were processed with a custom aperture photometry pipeline written in Python. The images were dark and bias-subtracted and flat-field-corrected using the master calibration frames. Five reference stars of similar magnitude are selected and aperture photometry is performed using a range of aperture sizes. The background is estimated using the same size aperture for dark regions near each reference star. For full details of our SOAR photometry code, we refer the reader to [20]. The resulting SOAR light curve is used as the primary model for EVR-CB-003 and is shown later in the manuscript, in Figure 9.12.

9.3 SPECTROSCOPIC ANALYSIS

9.3.1 Radial Velocity Curve

Spectra were wavelength calibrated using a modified version of the process described in § 9.2.5. We processed the wavelength calibrated spectra using a custom Python code to measure radial velocity. We visually inspected the spectral orders and chose the prominent Hβ to H11 absorption features. Within each of the selected orders, for each observation, we clip a small section (typically 20 Angstroms) encompassing the best absorption features. We fit a Lorentzian to the absorption features and measure the wavelength shift of each observation in each order. For each observation, we sigma clip any outlier orders and use the average shift to calculate the velocity. Using the standard deviation of the measured shifts between the orders, we place error limits. The best fit radial velocity K values are 83.9 ±3.2 km/s and 69.1 ±2.6 km/s (Figure 9.8).

9.3.2 Atmospheric Parameters

We use the rest wavelength SOAR low-res spectra to determine the atmospheric parameters of the sdBs by a simultaneous fitting of H and He line profiles to synthetic spectra as described in [191]. The synthetic spectra are a grid of metal-line-blanketed, hot high gravity stars with the condition of local thermodynamic equilibrium (LTE). The surface gravity (log g), effective temperature ($T_{\rm eff}$), and helium abundance (log y) of the sdBs are determined by fitting the H11 to Hβ Balmer profiles. In the case of EVR-CB-002, the He i lines 4472 Å, 4026 Å, 4713 Å, and 4922 Å were also included in the fitting. The EVR-CB-003 spectrum, with its lower SNR, did not display strong enough He features for this purpose. We use SPAS [237] to fit the spectra and a bootstrapping technique to calculate the errors.

The results from the best fits to the EVR-CB-002 SOAR low-res spectrum are as follows: $T_{\rm eff}$ = 27,963 ±224 K, log g = 5.39 ±0.03, log y = -2.92 ±0.11. The results from the best

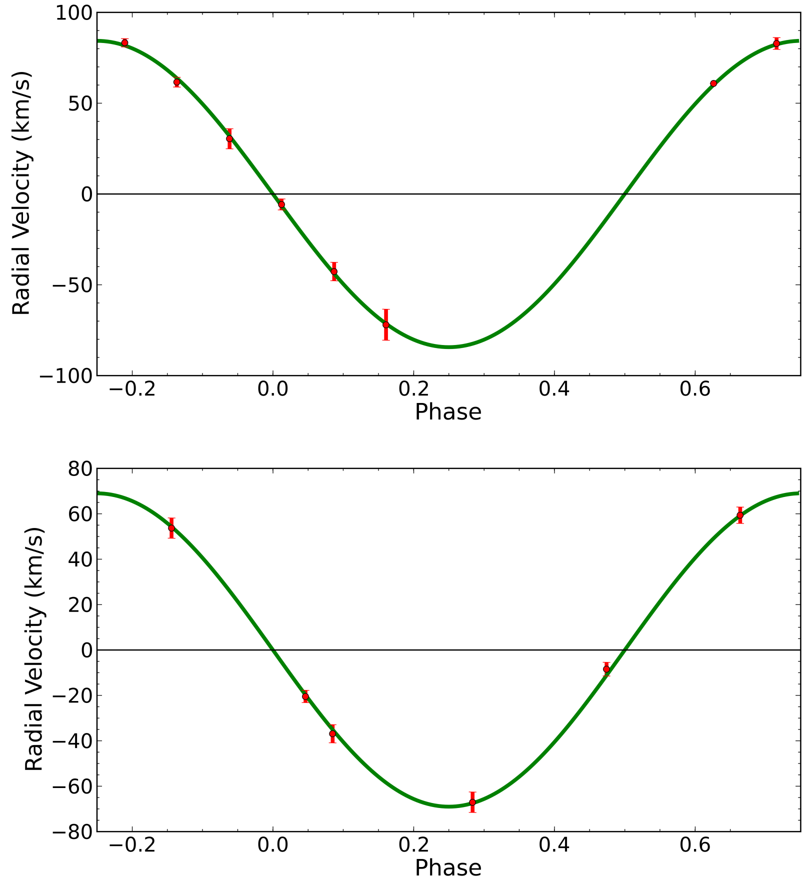

Figure 9.8: *Top:* The SOAR Radial Velocity curve for EVR-CB-002 with a best fit of K=83.9 ±3.2 km/s. *Bottom:* The SOAR Radial Velocity curve for EVR-CB-003 with a best fit of K=69.1 ±2.6 km/s.

fits for EVR-CB-003 are as follows: T_{eff} = 32,552 ±154, log g = 5.78 ±0.03, log y = -3.05 ±0.12. Figures 9.9 and 9.10 displays our best–fitting models on top of the observed spectra.

As a consistency check on the measured atmospheric values, we rest wavelength adjusted the SOAR medium-resolution spectra taken for the RV measurements and median combined them to form a master for each target. We remeasured the surface gravity (log g), effective temperature (T_{eff}), and helium abundance (log y) and found them to be consistent with the results from the low-res spectra. The SOAR medium-res spectrum fits for EVR-CB-002 are: T_{eff} = 28,400 ±195 K, log g = 5.41 ±0.03, log y = -2.65 ±0.04. The results from the best fits for EVR-CB-003 are: T_{eff} = 31,200 ±102, log g = 5.75 ±0.02, log y = -2.97 ±0.13.

The atmospheric parameters we derive for both systems are consistent with those of other known HW Vir binaries (see Figure 3 of [305]). For the light curve modeling discussed in Section 9.4, we used the atmospheric values from the medium-resolution spectra cited above as fixed parameters.

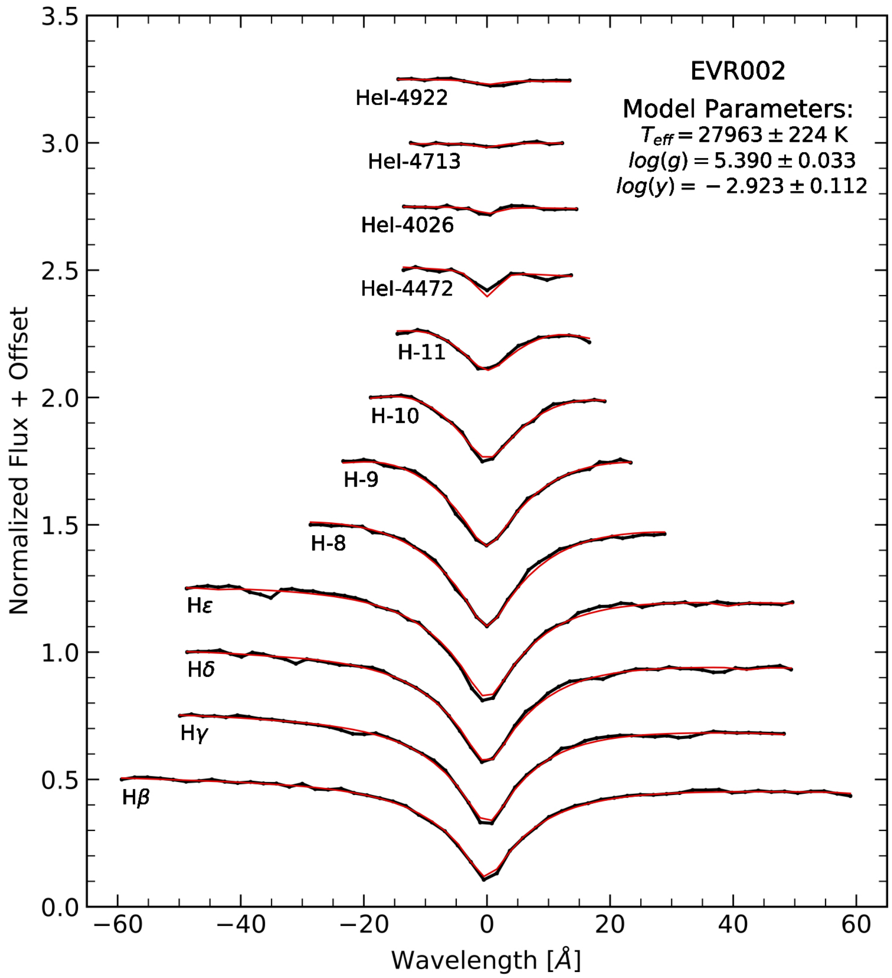

Figure 9.9: The best fits from the atmospheric modeling using the SOAR low-res spectra of EVR-CB-002.

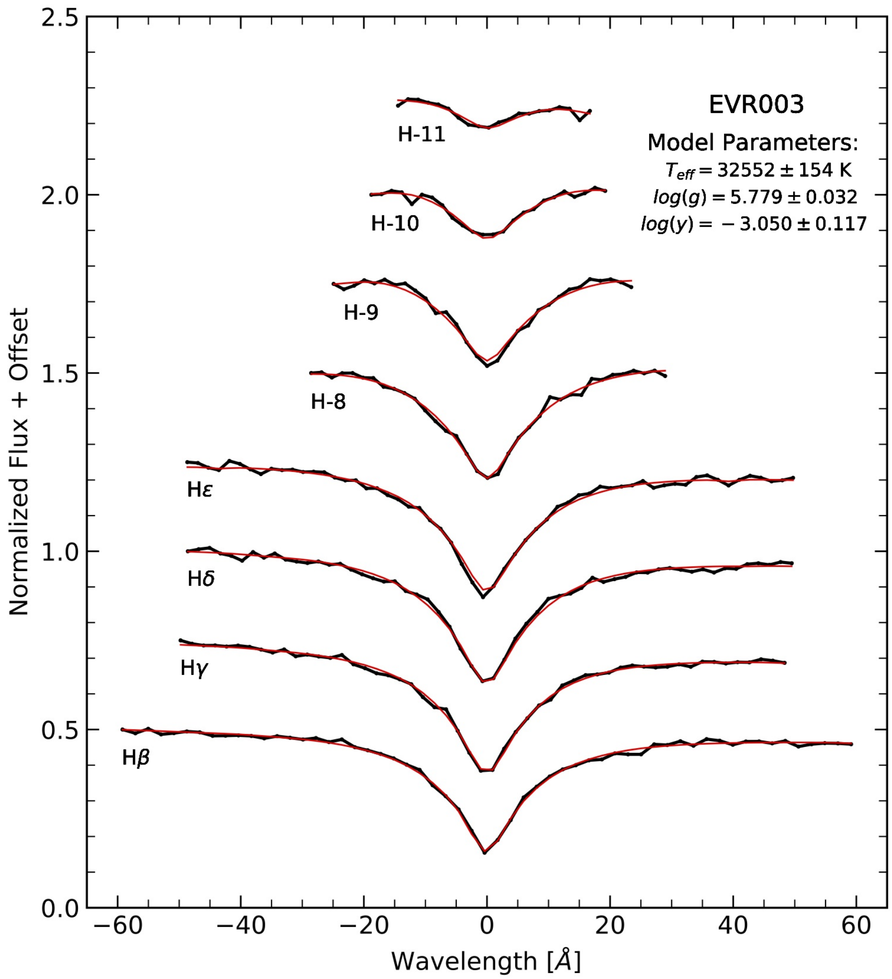

Figure 9.10: The best fits from the atmospheric modeling using the SOAR low-res spectra of EVR-CB-003.

9.4 PHOTOMETRIC ANALYSIS

9.4.1 Binary Light Curve Modeling

A typical sdB has a temperature of $\approx 30,000$ K, while an M-dwarf temperature is $\approx 3,000$ K, both with comparable radii. Thus in HW Vir systems, the factor of ten difference in temperature drives the luminosity ratio of the sdB primary to the M-dwarf companion. The factor of $\approx$ 10,000 difference in luminosity means the sdB will completely dominate the spectra, so directly measuring the spectral shift of both the primary and secondary is not feasible.

We rely on light curve analysis to determine the mass ratio (q), primary and secondary radii ratio, and inclination angle (i). We use the modeling code LCURVE [37] described in [308], which is based on the method discussed by [309] to model the light curves. This approach considers tidal forces to model the structure of close binary systems. The LCURVE code adds radiation pressure effects to the classical gravitational and centrifugal components of the close binary model. This treatment more accurately fits the light curves of HW Vir systems by accounting for changes in stellar shapes and the corresponding Roche lobe extents compared to the classical model. The downside of the LCURVE code is that it has a high number of parameters and the solutions are highly degenerate. To address these challenges, we make certain assumptions, set limits on the initial conditions, fix certain inputs, and use light curves from two different filters (Johnson B and R).

Here we discuss the primary constraints imposed on the model to limit the search space. First, we set the sdB temperature and surface gravity to the $T_{\rm eff}$ and $\log g$ determined in § 9.3.2. The limb darkening and gravitational darkening constants are set by the estimated primary and secondary stellar types. The primary albedo is set to 1.0 and the secondary radiation pressure is set to 0.0, again by assumed properties of the stellar types. We also assume the orbits are circular and the primary and secondary are tidally locked. All assumptions here are consistent with current HW Vir solved systems (e.g., [142, 304, 305]).

The LCURVE model returns solutions for a still large number of free parameters. The mass ratio (q), primary and secondary radii ratios (R_{HSD}/a and R_{comp}/a), inclination angle (i), and other inputs are used to compute light curves which are compared to the observed PROMPT light curves (and the SOAR light curve in the case of EVR-CB-003) and a χ-squared goodness of fit is computed. A *Monte Carlo* algorithm is used to explore the parameter space and find the minimized χ-squared best solution. The light curves and best fits for EVR-CB-002 and EVR-CB-003 are shown in Figures 9.11 and 9.12.

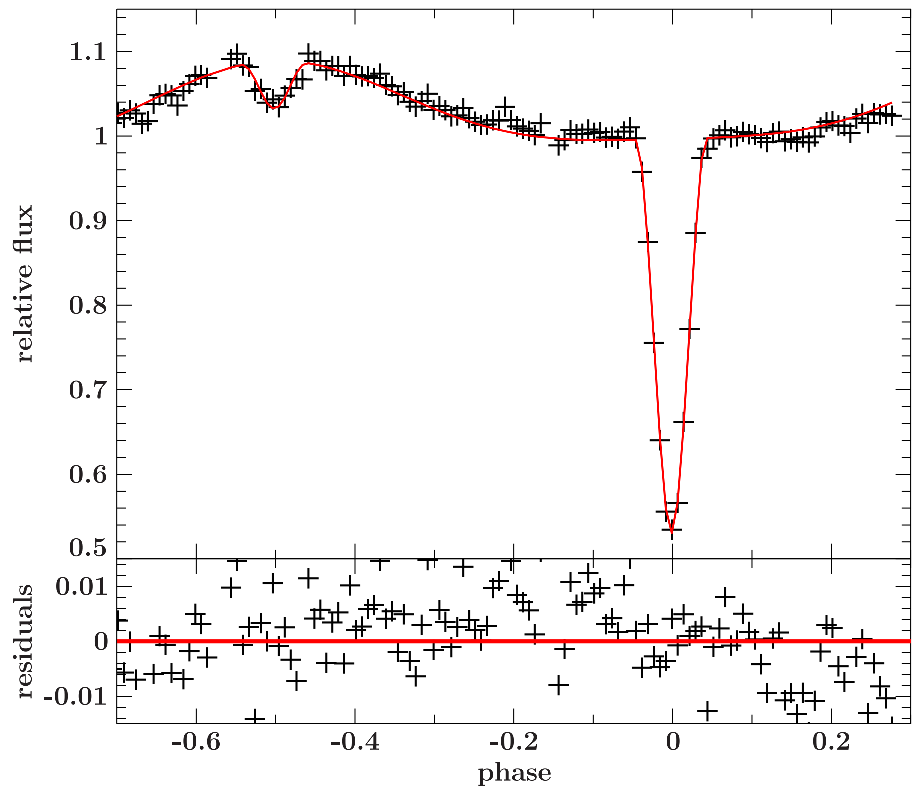

Figure 9.11: The best model fit to the light curve of EVR-CB-002.

9.5 FULL SOLUTION

9.5.1 System Parameters

The full system solution can now be computed using the radial velocity from § 9.3.1, the orbital period, the mass and radius ratios and inclination angle from § 9.4.1. We first use the mass function to determine the hot subdwarf and M-dwarf masses. The orbital separation follows from Kepler's Third Law. And finally, each of the radii can be computed. The final results are shown in Table 9.2, and the corner plots from the *Monte Carlo* are shown in the Appendix.

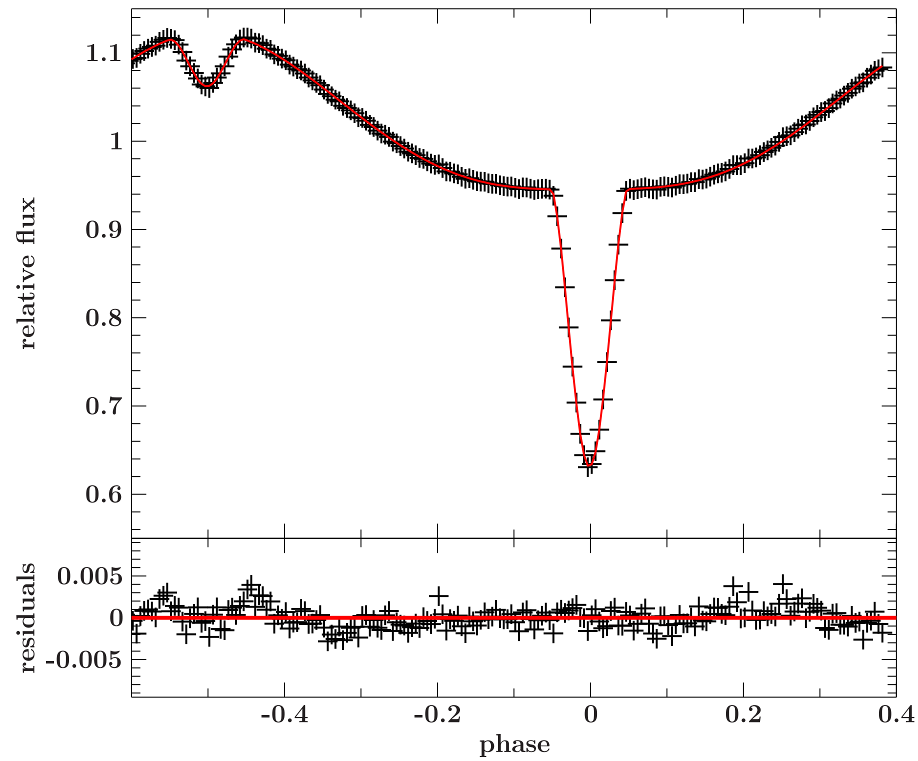

Figure 9.12: The best model fit to the light curve of EVR-CB-003.

9.5.2 Limitations of the Full Solution

The spectroscopic and photometric analysis presented in § 9.3 and § 9.4 successfully capture the astrophysics of the systems as demonstrated in Figure 9.11. However, there are limitations to the full solution that are present in all HW Vir systems.

The solution is heavily dependent on light curve analysis for all parameters except primary temperature and surface gravity. The high number of free parameters leads to degeneracy in the solutions and is especially dependent on mass and radius ratios. Unfortunately, alternate combinations of the free parameters can lead to model fits to the data with similarly good χ-squared values.

We mitigate the modeling challenges by using multiple light curves and in different passbands, high SNR spectra and in different configurations, and a well constrained RV curve. As a reasonableness test we also compare the sdB properties of EVR-CB-002 and EVR-CB-003 to those of other systems (see the following section). The canonical mass of

Table 9.2: System properties of EVR-CB-002 and EVR-CB-003

System Properties			
	EVR-CB-002	EVR-CB-003	
GAIADR2+	969438206889996160	5790285036556643072	
m_G	13.608 ± .003	13.534 ± .009	mag [G]
RA	79.94864	210.480542	
Dec	-19.28164	-75.225875	
P	6.590132(8)	3.1567 ± .0001	hours
q	0.42	0.225	
a	1.552 ± 0.059	0.999 ± 0.038	$R_\odot$
K	83.9 ± 3.2	69.1 ± 2.6	km s^{-1}
i	82.6 ± .0	78.06 ± .04	deg
Primary Properties			
M_p	0.469 ± 0.054	0.632 ± 0.036	$M_\odot$
R_p	0.224 ± 0.009	0.175 ± 0.007	$R_\odot$
T_{eff}	28,400 ± 195	31,200 ± 102	K
log g	5.41 ± 0.032	5.75 ± 0.023	
log y	-2.65 ± 0.035	-2.97 ± 0.126	
SpT	sdB	sdB	
Secondary Properties			
M_s	0.197 ± 0.023	0.142 ± 0.008	$M_\odot$
R_s	0.231 ± 0.009	0.201 ± 0.008	$R_\odot$
T_{eff}	Pending	2757 ± 296	K
SpT	≈M4	M5	

.47 $M_\odot$ is an especially important parameter to consider given its importance in formation theory and that it is somewhat consistent among observed hot subdwarfs.

In the case of EVR-CB-003, we obtained a very high SNR light curve from SOAR in a third passband, as an extra check on our system solution. The solutions to each light curve are shown in the Appendix, and prefer the larger than average sdB mass reported in Table 9.2. We prefer this solution and feel it is justified given the model fits to the data and analysis, however we show in the Appendix the effect of the variance in surface gravity on the sdB mass in EVR-CB-003 for readers interested in considering the canonical mass solution.

9.5.3 Orbital / Rotational Synchronization

Close binaries, including HW Virs, are understood to have short synchronization times and observed systems are expected to show rotational synchronization with the binary period. The SOAR medium resolution spectra (see § 9.3.2) also provided rotational velocity measurements for the sdBs. We find $v_{\mathrm{rot}} \sin i = 31 \pm 13$ [$\mathrm{km\,s^{-1}}$] and $v_{\mathrm{rot}} \sin i = 83 \pm 21$ [$\mathrm{km\,s^{-1}}$] for EVR-CB-002 and EVR-CB-003 respectively, which translates into an 8.71 hour and 3.21 hour period for each system. The EVR-CB-003 sdB rotational period is well matched to the orbital period of 3.1567 hours, and we conclude it is synchronized. The EVR-CB-002 sdB rotational period is slower than the measured orbital period of 6.59 hours, and it is possible the sdB is slightly sub-synchronous. However, we note here that the rotational velocity necessary for synchronization given the orbital period is $v_{\mathrm{rot}} \sin i = 41$ [$\mathrm{km\,s^{-1}}$], which is within our measurement error range.

9.6 DISCUSSION

EVR-CB-002 and EVR-CB-003 are bright southern sky HW Vir discoveries, that facilitated precise solutions to the properties of the systems. Following in Figures 9.13 to 9.16 we compare EVR-CB-002 and EVR-CB-003 to known HW Virs (a recent compilation of the known HW Vir systems is provided in [61]) in various parameter spaces. The effective temperature and surface gravity compared to known systems are shown in Figure 9.13. The most convincing atmospheric properties in confirming the primaries are sdBs, both discoveries in this work are well placed compared to known HW Virs, with expected sdB surface gravity and temperatures.

EVR-CB-002 and EVR-CB-003 have several features that are skewed from known systems, not so far as to be extreme outliers, but unexpected nonetheless. The sdB primary in EVR-CB-003 is non-canonical high mass, as seen in Figure 9.14. The yellow shaded region corresponds to higher-mass sdBs predicted from binary formation simulations in [51], but at a low rate ($\approx 10\%$) of occurrence. Although there are degeneracies in the system solutions (see § 9.5),

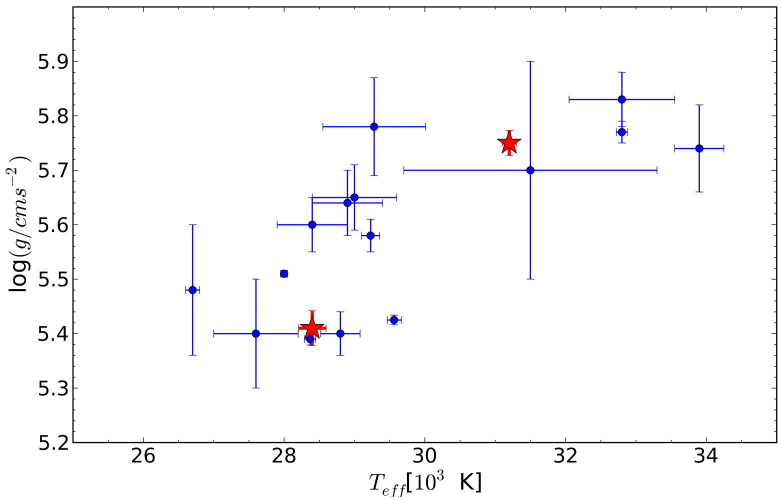

Figure 9.13: The effective temperature vs surface gravity of known HW Virs with sdB primaries shown with the blue circles. EVR-CB-002 and EVR-CB-003 are displayed with the red stars (lower left and upper middle, respectively) and well placed in this parameter space compared to known systems. We find that for the effective temperature $[10^3 K]$ of the population, $\mu = 29.67$ and $\sigma = 1.97$. For the surface gravity ($\log(g/cms^{-2})$), $\mu = 5.59$ and $\sigma = 0.15$. Data is from [61] and for HW Vir from [310], HS2231+2441 [311], 2M1533+3759 [312], SDSSJ162256.66+473051.1 [313], ASAS10232 [150], EC10246-2707 [142], HS0705+6700 [314], NY Vir [287], 2M1938+1603 [315], PTF1J072456+125301 [304], and V2008-1753 [305].

our best solution to EVR-CB-003 compared to the best solutions of other known HW Virs places it in this rare, high mass region. Seemingly a nice example of predicted formation theory.

The M-dwarf companion of EVR-CB-002 is shown to be high mass in comparison to other HW Virs, but with a very canonical mass sdB. Again see Figure 9.14.

The mass radius comparisons for the sdBs and M-dwarfs are shown in Figures 9.15 and 9.16. While there is little discernible correlation for the sdBs, the M-dwarf data follows mass radius expectations well (here we use data from [101]). The massive and large companion of EVR-CB-002 is also evident.

We note that in both systems, the M-dwarf primaries have larger radii than their sdB primaries, not unusual for HW Virs. EVR-CB-003 has a large reflection effect of $\approx 20\%$ in R band (see Figure F.2), possibly with a secondary albedo greater than one. A very high

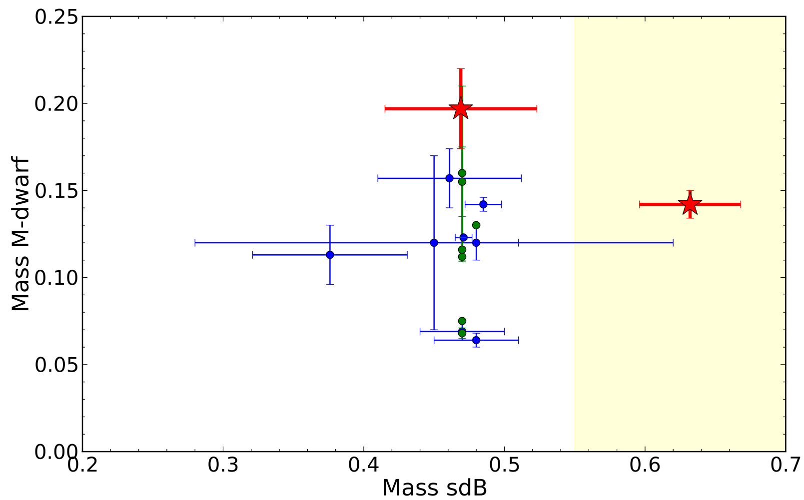

Figure 9.14: The masses of the primary vs the secondary for known HW Virs with sdB primaries are shown in blue and green (the green points are those systems that assume a $.47M_{\odot}$ canonical hot subdwarf). EVR-CB-002 and EVR-CB-003 are shown as the red stars (upper middle and far right, respectively), with the former showing a comparatively high mass companion, and the later with a high mass sdB. We find that for the sdB mass $[M_{\odot}]$ of the population, $\mu = 0.477$ and $\sigma = 0.046$ (the green points were not included for this calculation). This compares well to the results in [307], an asteroseismic study of pulsating sdB stars that found $\mu = 0.469$ and $\sigma = 0.024$. The distribution fits well to the binary evolution models of [51], with the outlier EVR-CB-003 falling in the high-mass wing (denoted with the yellow shading) of the simulation results (see Figure 22 in [51]). For the M-dwarf mass $[M_{\odot}]$ of the population, $\mu = 0.125$ and $\sigma = 0.037$.

reflection from a companion in an HW Vir system is not without precedent, see EC10246-2707 [142] for example.

9.7 SUMMARY

We present the discovery of two bright southern sky HW Vir discoveries, EVR-CB-002 and EVR-CB-003. The discoveries were made with photometric light curves from the Evryscope. Followup spectroscopic observations were made with the SOAR telescope, and photometric followup was made using the PROMPT telescope network and the SOAR telescope. We fit the rest wavelength calibrated spectrum to determine the atmospheric properties of the sdBs, and computed radial velocities from SOAR spectra. Using the LCURVE code, we found the

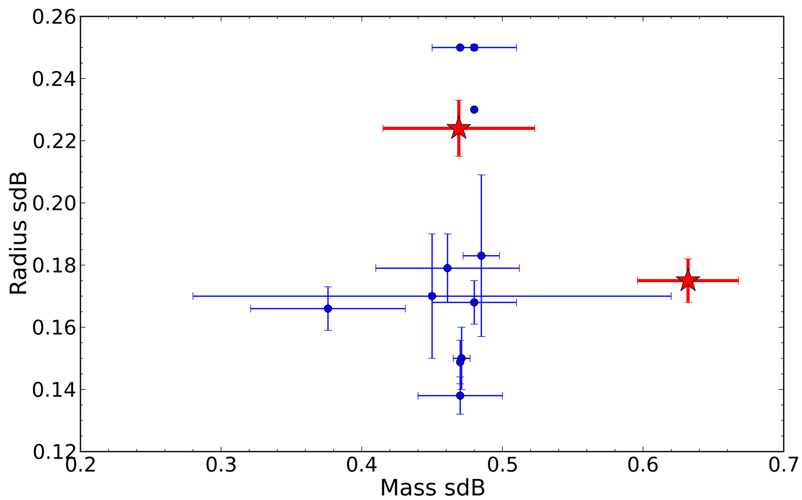

Figure 9.15: The mass vs radius of the sdBs for known HW Virs with sdB primaries are shown in blue. EVR-CB-002 and EVR-CB-003 are shown as the red stars (upper middle and far right, respectively), with the former showing a comparatively high radius sdB, and the later with a high mass sdB. We find that for the sdB radius $[R_{\odot}]$ of the population, $\mu = 0.187$ and $\sigma = 0.037$.

best fits to the PROMPT and SOAR light curves and computed the parameters for each system. For EVR-CB-002 and EVR-CB-003, we find: $M_p = 0.469 \pm 0.054$ and 0.632 ± 0.036 $M_{\odot}$, $M_s = 0.197 \pm 0.023$ and 0.142 ± 0.008 $M_{\odot}$, with periods of 6.59 and 3.16 hours. The secondary mass of EVR-CB-002 is large compared to known HW Vir systems, as is the sdB of EVR-CB-003.

This research was supported by the NSF CAREER grant AST-1555175 and the Research Corporation Scialog grants 23782 and 23822. HC is supported by the NSFGRF grant DGE-1144081. BB is supported by the NSF grant AST-1812874. The Evryscope was constructed under NSF/ATI grant AST-1407589.

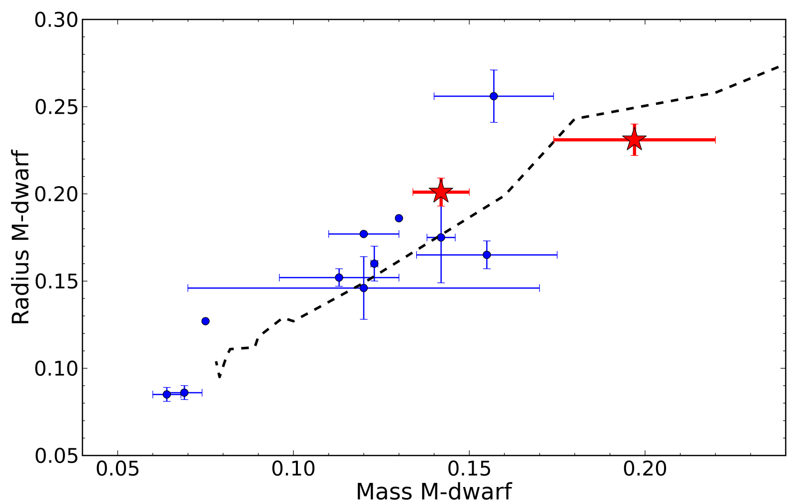

Figure 9.16: The mass vs radius of the M-dwarfs for known HW Virs with sdB primaries are shown in blue. EVR-CB-002 and EVR-CB-003 are shown as the red stars (upper right and middle, respectively), with the massive and large companion of EVR-CB-002 visible. We find that for the M-dwarf radius $[R_\odot]$ of the population, $\mu = 0.165$ and $\sigma = 0.047$. For the M-dwarf mass $[M_\odot]$ of the population, $\mu = 0.125$ and $\sigma = 0.037$. The mass-radius relation for M-dwarfs is shown with the dashed line (data taken from [101]), with a nice fit to the HW Vir companions. The three known brown dwarf companions fall to the lower left of the diagram, as expected.

CHAPTER 10: SUMMARY AND FUTURE WORK

Work in this dissertation is a combination of instrumentation and fast-transit surveys. It began with the design of a new type of telescope, the Evryscope, aimed at achieving continuous all-sky coverage at high cadence. The initial task included creating multiple 3-D designs, testing different options, simulating failure and flexure, and working within the project constraints to select the best model. Once the components were fabricated, the Evryscope was assembled and tested at UNC Chapel, and then shipped and deployed to CTIO, Chile. A camera alignment system (the Robotilters) was developed and integrated to the telescope shortly thereafter. Several years of data have been collected with the Evryscope, used to conduct the three different astronomical surveys described in this work. These surveys resulted in multiple discoveries, including rare compact binaries, and eclipsing binaries with low-mass companions.

Chapter 2 presents the Evryscope, including the motivation for the instrument, the operational concept, and telescope specifications. The design is described in detail, with the unique features highlighted, and the challenges that were solved. The Evryscope uses commercially available optics and cameras; this choice is explained and the benefits described. The modular telescope approach complements the optics and camera choice, and our custom mount design is demonstrated to reach the performance requirements within the system restraints. We describe the robotic control, and fail safe software design. On sky performance from the first three years of operation is presented including PSF quality, limiting magnitudes, and photometric precision. We present example discoveries from initial testing and describe planed variability searches.

The Evryscope camera units required a precision alignment system to achieve our target image quality. The Robotilters are described in chapter 3, our automated lens / CCD alignment solution. We describe in detail the image quality challenges, the need for such a system on the Evryscope, and the lack of a Robotilter like design in current wide field surveys. We highlight mechanical design features, and innovative approaches we took to solve problems. We describe our software solution, which uses a custom quality metric, on sky images, and a grid to analyze the images. We demonstrate the ability to map the focal plane and remove tilt to the level necessary to support our science goals. Example cameras are shown with before and after results in PSF quality, image tilt, and limiting magnitude. Potential application to other instruments is briefly described.

In chapter 4 we describe the Polar survey using Evryscope data from 2016 (the first available season) to search for eclipsing binaries with low-mass secondaries and dwarf stars with gas giant planets. The survey field was confined to the region near the South Celestial Pole to minimize systematics and maximize the number of epochs. We present the methods used to detect the variability, and the filters to select the most likely candidates. We developed a machine-learning based stellar classifier to identify the likely star types of the discoveries. Followup observations and analysis on the most promising candidates is shown, including low-resolution SOAR spectra used to confirm the spectral type, PROMPT photometry, and radial velocity analysis. We flagged several planet candidates, later shown to be eclipsing binaries. We also found several eclipsing binaries with low-mass secondaries. Variability type and parameters are provided for all the discoveries.

Chapter 5 shows the WD survey. Although the search did not reveal any candidates, we considered different assumptions and simulation parameters and analyzed their ramifications on the sensitivity of our survey. We are continuing to develop our simulations, but all indications point to WD transiting objects being much more difficult to recover than was previously understood. We identify limiting factors and suggest potential improvements in future WD transit survey design that may improve the likelihood of detection. We also described the upcoming WD 2 survey using lessons learned here and additional seasons of Evryscope data and including dimmer targets.

Our all-southern-sky (Dec < +10), bright ($M_g < 15$) HSD survey is presented in chapter 6. We used Evryscope data from the first three years of operation to search for CE phase binaries and variability as well as exoplanets. Extensive preparation went into producing the target search list, including enhancing the machine-learning classifier (now including GAIA data), using two independently generated HSD target lists, comparison of the sources, and testing source performance. We consider the light curve database results (compared to the input coordinates), crowded fields, and blended sources to flag possible problematic targets. We also obtained identification spectra from SOAR to test our classifier and search list performance. The results from the multiple input methods helps estimate the total likely targets in our survey at 1400, and prioritizes the discoveries for followup work. We describe the search algorithms used, including a custom code we developed called the Outlier Detector specializing in the recovery of fast, deep transits. The ID spectra are analyzed with *Astroserver* and the stellar type is reported along with the atmospheric parameters. We discovered 2 HSD + WD compact binaries and 2 HW Vir systems, shown here with the Evryscope discovery light curves and with brief descriptions. Subsequent discovery papers solve the systems in detail. We also discovered several HSD reflection effect binaries and highlight the systems we feel could benefit from further followup. We also present other discoveries and identify those with potentially rare features or components. Recovery rate simulations are used to estimate the survey sensitivity, and provide occurrence rate estimations for select systems (HW Virs for instance). We briefly discuss planned future work - a very short period HSD binary search and a second HSD survey with increased FoV and magnitude coverage.

Chapter 7 presents the discovery of EVR-CB-001, a compact binary with low mass WD plus an evolving remnant helium-rich stellar core (pre-He WD), found in our HSD survey. The pre-He WD is in an unlikely state as it is contracting into an extremely low-mass white dwarf. The system is expected to become a fully double degenerate binary, with two rare extremely low mass He WD components. The system should then spin down and merge in to a single hot subdwarf star, very near the canonical mass. EVR-CB-001 shows high amplitude and multiple component variability in the light curve, large radial velocity, a robust spectra with many well resolved features, and is bright - all characteristics that facilitate a precise and full solution to the system. Several stellar evolution theories and models can be tested with the EVR-CB-001 system, including low-mass ELM WD binary formation, He WD intermediate stage study, a double degenerate formation example, and a progenitor single hot subdwarf. The last case is of special interest as the observation of single HSDs is problematic to explain. Formation theory suggests that a merger of two WDs could form a single HSD, and given the non-trivial fraction of seemingly single HSDs, progenitor single HSD systems should be reasonably frequent. But none have been found. EVR-CB-001 is the first viable candidate as a single HSD progenitor, an offers a chance to study this potential formation mechanism and perhaps confirm theoretical predictions. In chapter 6, we describe the discovery and verification process, followup observations, our analysis, and the full solution to the system. We also demonstrate the Evryscope potential by comparing the binned-in-phase Evryscope light curve (using three years of Evryscope data) with the single period SOAR light curve. We discuss the benefits of each instrument, and highlight the specific contribution the Evryscope can make to fast transit science as shown with the EVR-CB-001 discovery and binned-in-phase performance.

In chapter 8 we describe EVR-CB-004, a remnant stellar core + unseen WD compact binary, discovered with the Evryscope in our HSD survey. Our analysis shows the remnant stellar core is likely a more evolved hot subdwarf, found during the final stage (known as a post-BHB) of its evolution before forming a WD. The post-BHB cycle of HSD evolution is not well understood, with a limited number of examples to test and verify theoretical models. Finding a post-BHB in a compact binary with a WD is very suggestive that this evolutionary theory is correct, however none have been found. Although additional followup is needed to definitively confirm the primary in EVR-CB-004 as a post-BHB, the evidence from our discovery and followup is quite strong. The EVR-CB-004 system is the first viable candidate for a post-BHB + WD compact binary, and has the same advantageous characteristics as EVR-CB-001 (high amplitude and multiple component variability in the light curve, large radial velocity, a robust spectra with many well resolved features, and is bright) that allow for a complete and precise solution. It offers an excellent opportunity to study late-stage HSD evolution theory and compact binary models. Besides the post-BHB and rare compact binary, EVR-CB-004 revealed other surprising features. With the inflated radius and high temperature (post-BHBs are larger and hotter than HSDs) as well as the close separation (a 6.08 hour period), the primary is very close to filling its Roche Lobe and is potentially an active accretor. We suggest X-ray followup could confirm and measure the likely accretion. The final state of the system is also intriguing. EVR-CB-004 is expected to first form a WD + WD binary once the post-BHB and final WD contraction phases complete; it will then likely merge into a very-high mass single WD or a double-detonation under-luminous supernova. Not surprisingly, progenitors to these final stages are sought after and needed to advance our understanding. Finally, a completely unexpected low-amplitude additional variation is visible in the light curves of EVR-CB-004. This sinusoidal signal is a 1/3 resonance of the binary period, making it even more odd. We tentatively identify this a tidally-induced resonant pulsation, and suggest additional followup observations that could confirm this hypothesis. We discuss our extensive analysis, observations, modeling, and discussion of the system.

Chapter 9 shows two bright new HW Vir discoveries from the Evryscope, found in our HSD survey and reported here with detailed solutions. The HSD + late M-dwarf eclipsing binary HW Vir systems are critical to verify and understand the CE formation mechanism, late stellar evolution, and HSD binary interaction. Our discoveries add 2 to modest 20 known and confirmed systems. EVR-CB-002 is a long period and large secondary mass system compared to known HW Virs. EVR-CB-003 contains a non-canonical HSD (more massive) and an inflated secondary with a very high reflection effect. These traits are somewhat surprising and do push the distribution of HW Virs. We describe the discovery process, challenges faced, followup observations, analysis, and final solutions, which required significant and very precise SOAR spectroscopy work.

The research presented in this dissertation will lead to future work, through additional surveys modeled after the searches here and from followup of discoveries. The first priority is to run the simulations necessary to complete the WD survey manuscript (as described in chapter 5). The HSD work could benefit from a very short period search, and from a second survey with increased depth and FoV (see chapter 1 and chapter 6 for details). EVR-CB-001 (see chapter 7) and especially EVR-CB-004 (see chapter 8) are likely to have additional manuscripts, exploring the peculiar primaries, the final evolution of each system compared to theoretical models, and in the case of EVR-CB-004 the possible accretion and pulsations. Several additional discoveries (from the HSD survey presented in chapter 6) are strong candidates for followup work and potentially additional papers. The low-amplitude WD accretor / debris disc, the O/B binary, the HB transit, and the HSD reflection effect binaries are the priorities. Likely, we will again work with our HSD collaborators as well as additional experts (depending on the system) to reveal what these interesting objects might be. The Evryscope provides light curves for more than 10M targets, facilitating a wide range of research and with many collaborators. Although not a focus of my work, the Evryscope data has led to stellar activity discoveries and surveys, captured luminous events, and will be the base for a transient detection pipeline, eclipse timing variation searches, and other fast signal detection. We estimate the current Evryscope data will be used for several decades and will support multiple waves of graduate researchers. Finally, the next generation Evryscope is in the conceptual stage, and we are now beginning to test a prototype single camera. We will refine the science goals of this new system and expect to begin creating 3D models soon to evaluate potential options. The fast transit work here certainly would be continued and expanded with a second generation Evryscope.

APPENDIX A: EVRYSCOPE INSTRUMENT PAPER DISCOVERY LISTS, LIGHT CURVES, AND SUPPLEMENTARY MATERIAL

A.1 Polar alignment procedure for an extremely-wide-field telescope

The Evryscope's extremely-wide field of view precludes the use of a pointing/tracking model, because a conventional model optimizes the performance at the sky position at which the telescope is pointing, at the expense of the sky areas away from that direction. The Evryscope effectively points every direction simultaneously, and so the system's polar alignment accuracy is critical for the tracking performance. Conventional polar alignment strategies are made difficult because of the large pixel scale and lack of ability to point individual cameras in a wide variety of positions.

We instead developed a polar-alignment procedure that takes advantage of the Evryscope's extremely wide field of view to produce rapid sub-arcminute-precision alignment. The procedure uses the polar-facing camera to measure both the axis of rotation of the Earth and the axis of rotation of the telescope mount. Iteratively moving the telescope axis then brings the two into alignment; both axes can be measured to within a few-pixel precision. We perform the alignment as follows:

1. Measure the Earth's axis of rotation on the pole-facing camera by taking a long-exposure image with tracking turned off (10-15 minutes). The Earth's rotation axis position is measured in image coordinates using the center of the star trails. The longer the exposure, the greater the achieved positioning accuracy.

2. Measure the mount's axis of rotation by taking a short-exposure image with the mount moving rapidly ($\sim$ greater than 20X tracking rate). The motion of the stars is then dominated by the mount rotation, and the center of the star trails is approximately the center of rotation of the mount (with a small offset from the Earth's rotation during the exposure).

3. Iterate on the mount's polar alignment settings to bring the mount rotation axis closer to the Earth's rotation axis. It is sufficient to follow the improvements simply in pixel coordinates on the polar-facing camera. As the axes align, the offset induced by the residual Earth rotation during the mount axis alignment tends to zero, and so the mount's alignment tends to the correct position.

We found that this procedure could be completed in less than two hours with sub-arcminute-level alignment. This alignment procedure aligns the mount's polar axis but does not precisely locate the celestial pole in the center of the polar camera's FoV; this can be performed later by simply adjusting the mushroom pointing direction.

A.2 List of all variable discoveries from the Evryscope Instrument Paper

Tables A.3 - A.2 show the discovery list of variables and eclipsing binaries from the initial survey discussed in the Evryscope instrument paper; Figures A.1 - A.3 display the light curves.

Table A.1: Transient discovery

ESID (EVRJ+)	RA	Dec	M_v	size	spec	duration	amplitude
194754.19+073408.0	296.9758	7.5689	14.040	ms	M1V	100	1.5

Table A.2: Eclipsing Binary discoveries

ESID (EVRJ+)	RA	Dec	M_v	size	spec	period	depth
054324.82+070043.6	85.8534	7.0121	14.42	ms	K	12.3630	0.415
062259.52+050915.8	95.7480	5.1544	14.14	ms	M0.5V	159.7402	0.286
111947.62+085811.6	169.9484	8.9699	14.02	ms	K3V	56.7865	0.385
171609.43+070050.0	259.0393	7.0139	12.75	ms	K3V	16.0351	0.236
180755.37+063452.0	271.9807	6.5811	14.12	giant	K	51.7911	0.111
181019.32+083846.3	272.5805	8.6462	14.23	giant	A1	32.6179	0.166
181348.53+071553.6	273.4522	7.2649	13.87	ms	G	16.4074	0.145
182614.59+053454.1	276.5608	5.5817	13.21	ms	K	19.6076	0.160
191419.87+083226.5	288.5828	8.5407	14.23	ms	K	61.4905	0.189
192207.27+084849.7	290.5303	8.8138	14.15	ms	K4V	25.9350	0.196
194419.61+072333.4	296.0817	7.3926	–	–	–	18.5312	0.279
201131.20+061020.6	302.8800	6.1724	14.01	ms	K4V	15.1673	0.224
201329.93+050717.0	303.3747	5.1214	11.81	ms	G7V	213.0682	0.093
202807.01+053621.2	307.0292	5.6059	14.29	ms	K5V	28.2712	0.094

Columns 1-4 are identification numbers, right ascension and declination, and magnitude. Columns 5-6 are the estimated the star size and spectral type (see Section 4.2.1). Columns 7 and 8 are the period found in hours, and the fractional eclipse depth from normalized flux.

Table A.3: Variable Star discoveries

ESID (EVRJ+)	RA	Dec	M_v	size	spec	period	amplitude
013131.44+061855.1	22.8810	6.3153	12.99	ms	K3V	56.0725	0.047
024227.96+062556.3	40.6165	6.4323	13.01	ms	K7V	3.3478	0.047
031204.99+073711.3	48.0208	7.6198	13.40	ms	K7V	34.9678	0.076
031736.19+080644.3	49.4008	8.1123	12.65	ms	K5V	10.5253	0.048
033741.28+064752.1	54.4220	6.7978	11.28	ms	G9V	4.5936	0.018
040342.82+051630.0	60.9284	5.2750	12.50	ms	K4V	30.5414	0.028
055815.07+082912.5	89.5628	8.4868	13.65	giant	K5	22.9847	0.047
062900.94+075330.8	97.2539	7.8919	11.86	ms	K2V	136.1824	0.053
063213.30+063835.2	98.0554	6.6431	14.31	ms	G	161.5992	0.165
064304.61+080711.6	100.7692	8.1199	11.90	giant	K	3.2894	0.050
074608.52+064450.3	116.5355	6.7473	13.81	ms	K3V	4.1063	0.068
090345.07+063356.5	135.9378	6.5657	13.27	ms	K2V	1001.4160	0.041
133939.43+080936.4	204.9143	8.1601	13.00	ms	K2V	3.5490	0.050
135123.76+074111.4	207.8490	7.6865	12.47	ms	K3V	103.5052	0.048
150518.17+062323.6	226.3257	6.3899	13.36	ms	K3V	4.0030	0.053
153240.92+054336.1	233.1705	5.7267	11.60	ms	K4V	29.5485	0.021
153936.96+061720.8	234.9040	6.2891	12.61	ms	K3V	1408.9650	0.057
155120.62+061448.8	237.8359	6.2469	13.56	ms	K6V	106.1767	0.047
155543.75+062518.8	238.9323	6.4219	11.24	ms	K4V	29.7894	0.031
164449.03+082109.7	251.2043	8.3527	13.36	ms	K5V	33.4419	0.052
173918.65+081931.4	264.8277	8.3254	13.32	giant	K	6.0188	0.013
175437.66+061028.2	268.6569	6.1745	14.08	ms	G	13.2881	0.079
180850.26+073350.4	272.2094	7.5640	13.48	ms	K2V	3.8693	0.069
182013.44+083523.6	275.0560	8.5899	12.23	giant	K	197.7393	0.040
182020.76+065445.0	275.0865	6.9125	13.25	ms	K5V	183.1411	0.063
183036.48+073707.7	277.6520	7.6188	13.19	ms	K1V	3.8968	0.077
184426.98+073442.2	281.1124	7.5784	13.44	ms	G0V	4.9937	0.133
190325.54+071516.9	285.8564	7.2547	11.47	ms	K3V	243.1183	0.017
190353.14+051812.6	285.9714	5.3035	13.33	ms	K3V	4.0273	0.052
190517.30+073520.0	286.3221	7.5889	13.62	ms	K7V	15.7103	0.041
190632.06+051345.5	286.6336	5.2293	12.64	giant	K7	13.0606	0.080
191341.81+070205.6	288.4242	7.0349	13.32	ms	K3V	12.3459	0.014
191731.06+070124.6	289.3794	7.0235	12.46	ms	K4V	219.8386	0.037
191757.24+090428.2	289.4885	9.0745	14.30	ms	G	22.4846	0.070
191908.38+083523.6	289.7849	8.5899	14.37	ms	K	136.0364	0.059
193728.03+054802.2	294.3668	5.8006	13.09	ms	G9V	16.6612	0.034
194947.38+060847.8	297.4474	6.1466	12.92	ms	K2V	5.8423	0.123
195419.58+084303.0	298.5816	8.7175	13.75	giant	K	236.7087	0.022
195728.85+074311.6	299.3702	7.7199	14.01	ms	K6V	4.5788	0.033
201533.41+082530.4	303.8892	8.4251	12.64	ms	K4V	28.9305	0.052
203320.59+090539.8	308.3358	9.0944	14.00	ms	K2V	3.1976	0.105
204952.97+054416.1	312.4707	5.7378	12.97	ms	K3V	161.5235	0.088
210125.78+082428.8	315.3574	8.4080	–	none	none	20.9755	0.018

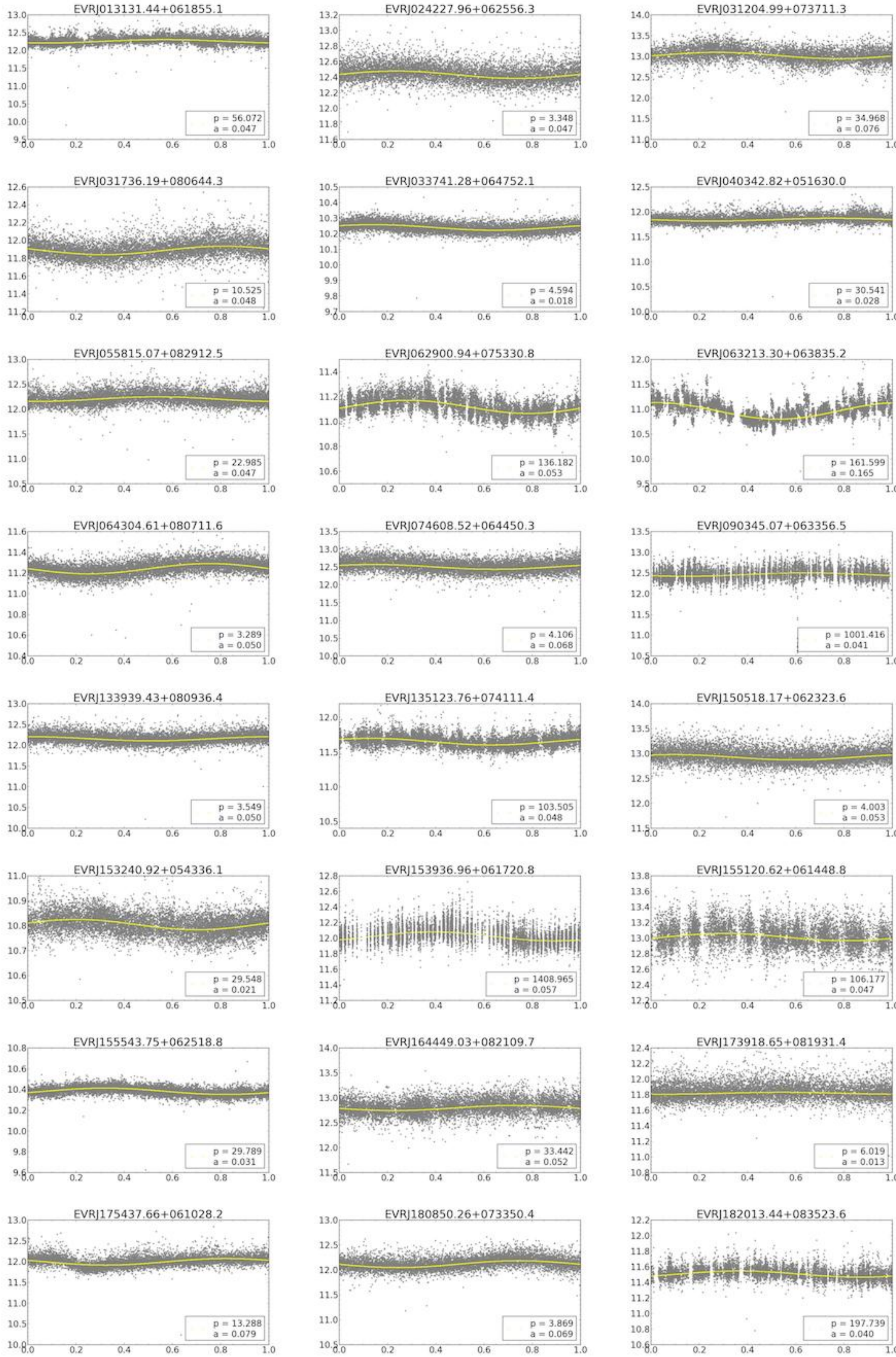

Figure A.1: Variable star discoveries. Y-axis is instrument magnitude, x-axis is the phase.

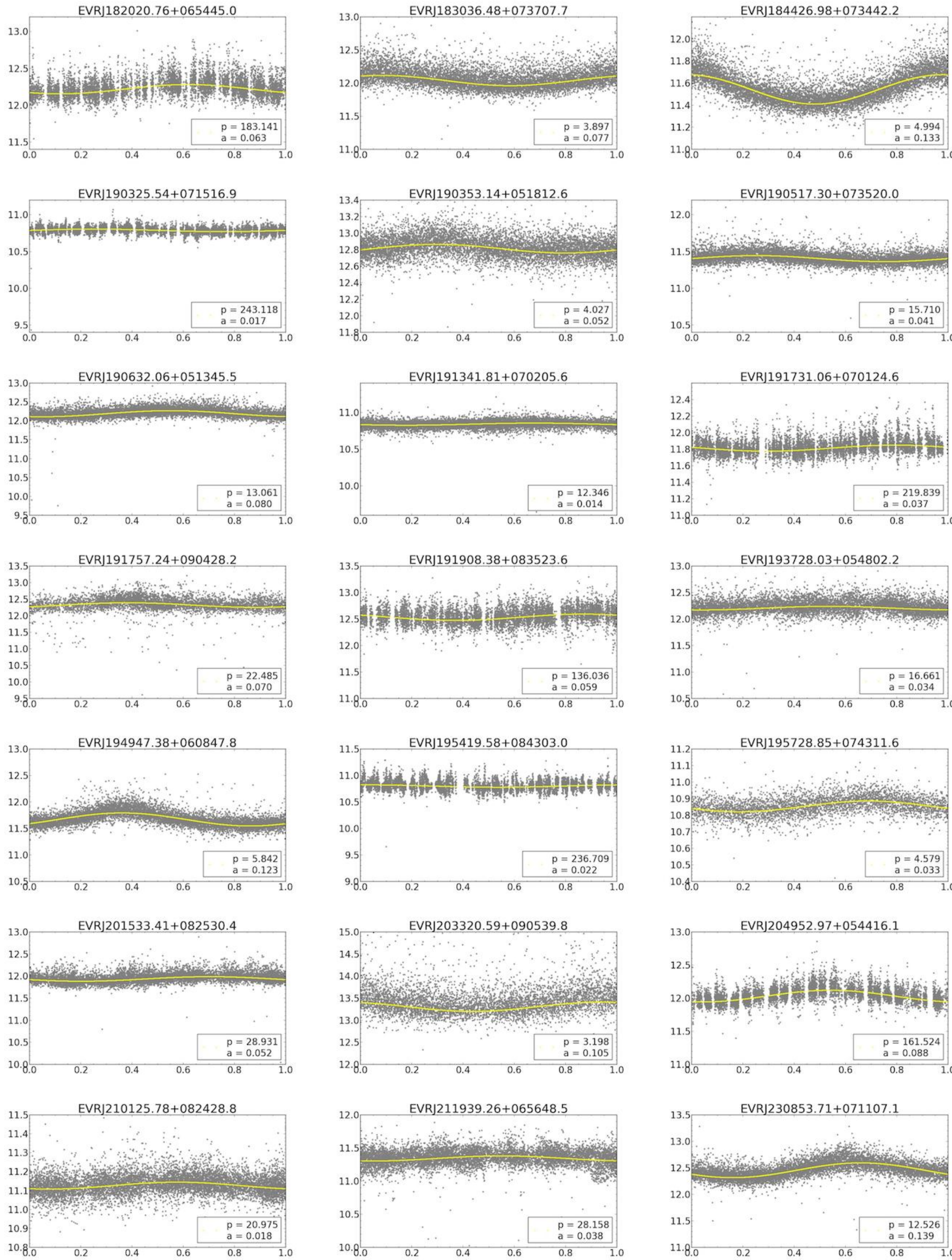

Figure A.2: Variable star discoveries (continued). Y-axis is instrument magnitude, x-axis is the phase, p = period found in hours, a = amplitude change in magnitude. Gray points are two minute cadence, yellow is the best LS fit.

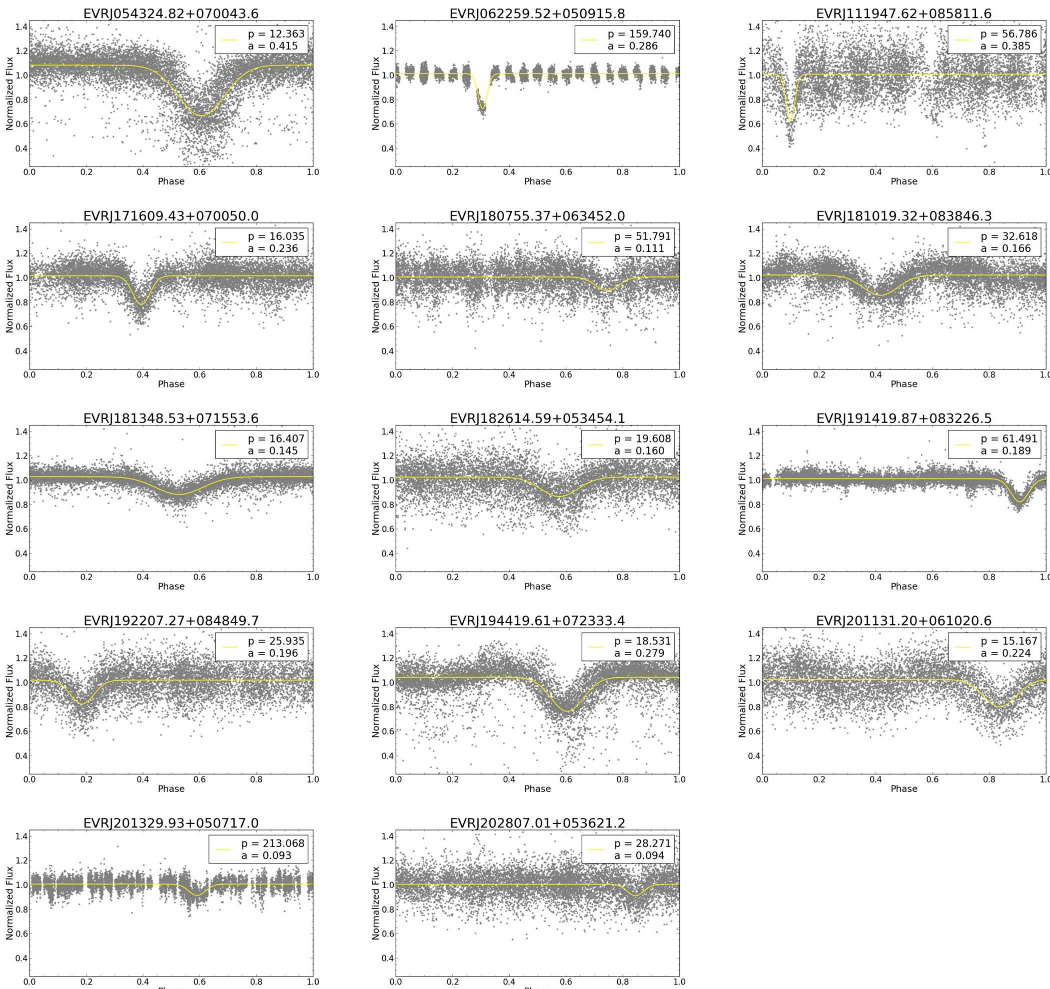

Figure A.3: Eclipsing Binary discoveries. Y-axis is normalized flux, x-axis is the phase, p = period found in hours, a = eclipse depth. Gray points are two minute cadence, yellow is the best fit.

APPENDIX B: POLAR SURVEY DISCOVERY LISTS AND LIGHT CURVES

This section presents all discoveries and light curves from the Polar Survey.

B.1 List of Eclipsing Binary discoveries from the Polar Survey with low-mass secondaries

Shown in Tables B.1 and B.2 are eclipsing binary discoveries with low-mass secondaries and peculiar discoveries. Columns 1-4 are identification numbers, right ascension and declination, and magnitude. Columns 5-6 are the spectral type from the classifier and from the SOAR ID spectra. Column is 7 the period found in hours, columns 8-15 are the mass of the primary and secondary derived from SOAR radial velocity, along with the one sigma error.

Table B.1: Eclipsing Binary discoveries with low-mass secondaries

ESID	RA (J2000)	Dec (J2000)	Mv	sptp	SOAR	period (hours)	mp $M_\odot$	+/-	rp $R_\odot$	+/-	ms $M_\odot$	+/-	rs $R_\odot$	+/-
EVRJ06456.10-823501.0	101.2754	-82.5836	11.80	G9V	G8V	63.53	0.90	.04	.876	.059	.37	.02	.26	.01
EVRJ103938.18-872853.8	159.9091	-87.4816	13.78	K6V	K7V	20.85	0.63	.04	.655	.037	.24	.02	.20	.01
EVRJ110815.96-870153.8	167.0665	-87.0316	12.68	K3V	K4V	12.28	0.72	.04	.725	.028	.20	.03	.35	.02
EVRJ165050.23-843634.6	252.7093	-84.6096	13.84	K4V	K5V	25.86	0.68	.05	.699	.037	.06	.01	.40	.02
EVRJ180826.26-842418.0	272.1094	-84.405	13.51	G6V	G5V	17.31	0.98	.01	.983	.043	.19	.01	.56	.01
EVRJ184114.02-843436.8	280.3084	-84.5769	13.34	K3V	K2V	137.16	0.78	.07	.764	.052	.28	.03	.24	.02

Table B.2: Peculiar Eclipsing Binary discoveries

ESID	RA(J2000)	Dec(J2000)	Mv	sptp	SOAR	period	note
EVRJ053513.22-774248.2	83.8051	-77.7134	12.05	K1V	G7V	50.96	Nearly identical primary and secondary
EVRJ114225.51-793121.0	175.6063	-79.5225	12.81	K3V	–	91.82	Visual Double in SOAR image
EVRJ211905.47-865829.3	319.7728	-86.9748	13.97	K6V	K5V	18.61	Nearly identical primary and secondary

B.2 List of all variable discoveries from the Polar Survey

Shown in Table B.3 are the variable discoveries in this work. Columns 1-4 are identification numbers, right ascension and declination, and magnitude. Columns 5-7 are the reduced proper motion (RPM) and color difference (B-V) which we use to estimate the star size and spectral type (see Section 4.2.1). Columns 8 and 9 are the period found in hours, and the amplitude of the variability in magnitudes.

Shown beginning in Figure B.2 are the Evryscope light curves for the discoveries in this work. For the variable star discoveries: the Y-axis is instrument magnitude, x-axis is the phase, p = period found in hours, a = amplitude change in magnitude. Gray points are two minute cadence, yellow is the best LS fit. For Eclipsing Binary discoveries: the Y-axis is normalized flux, x-axis is the phase, p = period found in hours, a = eclipse depth. Gray points are two minute cadence, yellow is the best fit to the primary eclipse.

Table B.3: Variable Star discoveries

ESID (EVRJ+)	RA (J2000)	Dec (J2000)	Mv	RPM	B-V	spec	period (hours)	amp (Δ M)
000411.09-862200.5	1.0462	-86.3668	12.91	10.3	1.00	K3V	3.7893	0.048
004033.86-852556.3	10.1411	-85.4323	13.88	8.56	0.57	G0V	11.9673	0.108
010354.79-845024.4	15.9783	-84.8401	13.07	9.70	1.06	K6V	66.0947	0.067
010428.68-752821.7	16.1195	-75.4727	12.74	8.80	0.44	F1V	4.4661	0.056
010628.13-821135.5	16.6172	-82.1932	10.79	6.12	0.29	A1V	11.5043	0.021
011610.92-853620.5	19.0455	-85.6057	13.56	9.95	0.82	G8V	4.0396	0.061
013112.26-754727.2	22.8011	-75.7909	12.69	7.03	1.18	K6III	565.236	0.057
014744.62-750722.8	26.9359	-75.1230	13.43	9.75	0.34	F2V	7.9793	0.022
015507.25-842951.4	28.7802	-84.4976	12.03	1.82	1.13	K4III	207.486	0.048
020014.59-824041.2	30.0608	-82.6781	13.68	11.1	0.66	F3V	3.8633	0.048
020627.84-854259.4	31.6160	-85.7165	13.10	5.95	0.58	F1V	4.2580	0.049
021301.18-850613.7	33.2549	-85.1038	14.18	8.74	0.74	F9V	14.5239	0.044
022525.78-871212.6	36.3574	-87.2035	13.72	5.85	0.58	F9V	5.4833	0.128
023633.12-841813.7	39.1380	-84.3038	12.99	8.31	1.55	M	3.0339	0.026
024105.09-852056.8	40.2712	-85.3491	10.84	6.65	1.16	M0III	383.356	0.031
031048.98-774610.2	47.7041	-77.7695	13.43	9.01	0.44	F1V	5.5437	0.107
031437.25-812625.4	48.6552	-81.4404	11.83	10.2	0.65	G6V	22.5360	0.038
032340.58-833811.4	50.9191	-83.6365	11.73	5.37	0.74	G8III	3.6540	0.115
032442.50-780853.9	51.1771	-78.1483	11.38	6.51	0.45	F5V	4.6764	0.022
034027.74-771628.9	55.1156	-77.2747	11.26	8.02	0.95	K4V	527.569	0.041
035648.91-810628.4	59.2038	-81.1079	12.66	8.40	0.28	A9V	10.7653	0.035
040145.72-794920.3	60.4405	-79.8223	13.50	7.80	0.45	F1V	4.3002	0.063
041253.57-812919.7	63.2232	-81.4888	13.91	12.7	0.81	G	5.5612	0.061
041719.75-803105.5	64.3323	-80.5182	11.38	6.23	1.61	M	583.939	0.066
042003.70-803034.9	65.0154	-80.5097	12.35	5.20	1.21	M0III	423.776	0.158
042008.90-790539.1	65.0371	-79.0942	13.38	8.98	0.58	G2V	5.0229	0.085
044109.58-774556.5	70.2899	-77.7657	10.19	5.99	1.55	M	426.295	0.046
044130.53-761227.0	70.3772	-76.2075	13.13	8.14	0.96	K3V	3.3209	0.065
044735.35-775219.9	71.8973	-77.8722	11.30	8.69	0.50	G1V	3.3276	0.026
050012.05-811743.4	75.0502	-81.2954	12.48	8.09	0.86	G9V	3.4901	0.076
051213.46-761626.0	78.0561	-76.2739	12.99	9.39	0.60	G1V	6.3173	0.074
051707.51-851934.3	79.2813	-85.3262	14.56	11.5	-0.09	F0	17.4600	0.138
053531.56-792945.6	83.8815	-79.4960	13.45	10.6	0.75	K0V	4.8621	0.061
053802.81-775651.0	84.5117	-77.9475	12.60	9.47	0.50	G0V	6.8030	0.048
053857.96-840027.0	84.7415	-84.0075	13.18	8.45	0.69	K2V	3.7923	0.120
053921.36-823350.0	84.8390	-82.5639	11.37	7.67	1.15	K5III	294.188	0.042
055148.46-761552.6	87.9519	-76.2646	11.87	4.41	0.89	K4III	98.4013	0.048
055157.14-810831.9	87.9881	-81.1422	12.74	9.85	0.69	F5V	4.9623	0.208
055856.16-785946.3	89.7340	-78.9962	13.06	9.65	0.98	K4V	3.1286	0.078
060627.19-841156.4	91.6133	-84.1990	14.67	9.83	0.01	F0	6.8412	0.142
061823.95-780812.1	94.5998	-78.1367	10.11	1.02	1.65	M	544.372	0.064
062714.64-794039.0	96.8110	-79.6775	13.19	8.31	0.66	G2V	5.1073	0.080

Table B.4: Variable Star discoveries

ESID (EVRJ+)	RA (J2000)	Dec (J2000)	Mv	RPM	B-V	spec	period (hours)	amp (Δ M)
064843.42-793349.3	102.1809	-79.5637	13.01	9.15	1.24	M1III	534.153	0.095
070444.11-752812.7	106.1838	-75.4702	13.39	8.69	0.69	G6V	4.9315	0.098
070553.98-813347.5	106.4749	-81.5632	13.28	12.3	0.78	G	208.114	0.080
070751.77-861600.8	106.9657	-86.2669	13.88	10.3	0.70	G6V	4.4384	0.137
071040.15-854213.0	107.6673	-85.7036	13.28	10.5	0.68	G7V	14.0116	0.042
071054.50-775214.5	107.7271	-77.8707	12.75	8.38	0.98	K6V	119.774	0.061
072150.93-814705.3	110.4622	-81.7848	12.48	3.69	1.02	K4III	569.996	0.073
072411.33-865020.0	111.0472	-86.8389	12.06	7.72	0.80	G8V	3.8106	0.036
074325.18-780127.5	115.8549	-78.0243	11.58	7.86	0.50	F7V	3.3874	0.029
080401.49-824005.9	121.0062	-82.6683	11.55	7.70	0.97	K6III	4.2669	0.028
083403.17-811922.4	128.5132	-81.3229	13.54	-1.5	0.93	K4III	5.1269	0.047
084757.72-781627.1	131.9905	-78.2742	13.17	12.1	1.00	K4V	266.613	0.064
085910.42-813844.9	134.7934	-81.6458	13.69	9.23	0.41	A4V	6.5406	0.073
090816.25-840058.0	137.0677	-84.0161	13.73	9.56	0.60	G1V	4.1451	0.159
092130.62-780552.1	140.3776	-78.0978	12.06	7.58	1.17	K8III	14.2823	0.036
092934.58-883002.5	142.3941	-88.5007	12.70	11.8	1.04	K4V	14.9276	0.072
094546.82-845901.7	146.4451	-84.9838	11.40	4.88	0.34	F4V	10.5364	0.023
094914.47-765810.9	147.3103	-76.9697	11.94	7.38	0.67	G1V	4.7866	0.047
095103.38-775148.6	147.7641	-77.8635	12.64	8.52	0.39	A9V	3.3413	0.052
103805.95-823919.8	159.5248	-82.6555	12.25	9.15	1.12	K5V	188.785	0.037
103843.68-841342.6	159.6820	-84.2285	14.34	9.32	0.82	K1V	3.4514	0.095
104338.88-812945.6	160.9120	-81.4960	13.10	12.8	1.05	K	9.2306	0.071
104928.30-840709.1	162.3679	-84.1192	14.41	10.3	0.66	G5V	4.3652	0.071
110736.10-801214.8	166.9004	-80.2041	13.20	8.60	0.65	G6V	5.2520	0.103
112926.09-790251.7	172.3587	-79.0477	12.82	10.0	0.74	K3V	3.2616	0.032
113221.60-773934.2	173.0900	-77.6595	12.62	7.52	0.64	F6V	2.2946	0.089
113648.94-770820.8	174.2039	-77.1391	13.07	10.7	0.87	K2V	40.9161	0.049
113950.33-823313.7	174.9597	-82.5538	12.70	8.23	0.69	G9V	12.2413	0.045
121247.35-782517.8	183.1973	-78.4216	12.77	8.67	0.75	G8V	7.1346	0.071
124042.22-852021.1	190.1759	-85.3392	12.33	7.11	0.73	K1V	51.6660	0.093
124521.96-772053.5	191.3415	-77.3482	13.16	8.11	0.84	G8V	5.0777	0.089
124614.88-851715.4	191.5620	-85.2876	13.75	12.4	0.71	G8V	3.6741	0.109
124711.98-784313.8	191.7999	-78.7205	–	–	–	–	4.0535	0.100
125757.58-773925.9	194.4899	-77.6572	12.88	9.03	0.97	K2V	13.6397	0.065
130148.17-831417.9	195.4507	-83.2383	12.92	8.20	1.49	M3III	121.844	0.068
130916.78-775637.7	197.3199	-77.9438	13.61	9.88	0.99	K4V	7.8242	0.153
131216.99-803701.6	198.0708	-80.6171	11.08	5.79	0.72	G9V	7.9778	0.008
131228.85-782429.2	198.1202	-78.4081	–	–	–	–	136.768	0.047
131248.91-794104.9	198.2038	-79.6847	10.48	7.50	1.04	K4III	5.5061	0.015
134036.82-810805.3	205.1534	-81.1348	13.08	10.7	0.90	K0V	3.4605	0.038
134909.43-795116.2	207.2893	-79.8545	12.69	9.02	0.96	K1V	4.4504	0.032

Table B.5: Variable Star discoveries

ESID (EVRJ+)	RA (J2000)	Dec (J2000)	Mv	RPM	B-V	spec	period (hours)	amp (Δ M)
135636.96-852904.9	209.1540	-85.4847	13.04	9.29	0.67	G8V	5.5375	0.039
135847.35-753616.9	209.6973	-75.6047	12.64	4.90	0.55	F8V	13.0043	0.081
135948.38-773732.9	209.9516	-77.6258	12.25	7.12	0.59	G0V	6.4798	0.063
142647.47-774451.4	216.6978	-77.7476	13.36	11.3	0.39	F0	3.0402	0.110
143601.82-832825.3	219.0076	-83.4737	13.62	9.82	0.52	F2V	6.8145	0.117
150519.75-753054.0	226.3323	-75.5150	10.53	4.96	1.03	K3III	6.7618	0.036
151320.26-833642.1	228.3344	-83.6117	11.52	7.98	0.94	K3V	202.201	0.027
152213.03-850853.2	230.5543	-85.1481	12.59	7.32	0.80	K0V	44.3809	0.081
152422.85-765355.7	231.0952	-76.8988	10.58	5.74	0.37	A7V	3.3395	0.042
154618.22-824405.3	236.5759	-82.7348	13.77	11.1	0.70	F6V	4.5592	0.091
155137.18-824810.8	237.9049	-82.8030	12.70	8.58	0.44	F5V	8.0204	0.052
155320.98-824654.8	238.3374	-82.7819	12.98	5.06	0.49	F8V	10.0283	0.044
155645.07-802819.2	239.1878	-80.4720	11.75	6.08	0.03	B9V	116.986	0.032
155942.19-824514.8	239.9258	-82.7541	12.12	5.33	0.58	G0V	14.6855	0.038
162259.47-805820.3	245.7478	-80.9723	11.73	8.04	0.55	F1V	4.8019	0.048
162554.07-854342.2	246.4753	-85.7284	13.37	11.4	0.53	F5V	5.0865	0.083
163031.56-834849.7	247.6315	-83.8138	13.35	8.31	0.63	G0V	12.2352	0.089
163252.27-832748.2	248.2178	-83.4634	12.51	6.51	0.94	K6III	150.450	0.092
163852.99-843744.0	249.7208	-84.6289	13.21	10.5	0.80	K2V	32.2767	0.048
165216.22-825416.6	253.0676	-82.9046	13.94	9.91	0.45	F8V	15.1777	0.367
165457.58-775615.7	253.7399	-77.9377	12.87	5.49	0.30	F1V	7.4973	0.069
171344.76-825649.9	258.4365	-82.9472	13.44	7.62	0.51	F3V	5.2027	0.075
171929.86-800819.0	259.8744	-80.1386	12.85	8.54	0.66	F3V	4.5325	0.071
171939.84-852016.4	259.9160	-85.3379	14.67	13.0	1.39	K6V	3.2852	0.072
172044.45-811413.2	260.1852	-81.2370	10.80	7.87	0.71	G1V	12.2459	0.019
173256.64-833249.9	263.2360	-83.5472	14.11	10.7	0.42	F8V	7.1155	0.135
173854.53-825617.2	264.7272	-82.9381	13.40	11.0	0.34	F3	6.2448	0.087
174904.92-853647.9	267.2705	-85.6133	13.89	7.33	0.69	G1V	4.3006	0.093
175053.26-794941.5	267.7219	-79.8282	11.96	8.79	0.84	K0V	134.465	0.051
175230.22-785048.8	268.1259	-78.8469	12.01	7.88	0.32	F1V	8.3917	0.041
175340.68-753831.9	268.4195	-75.6422	12.35	7.83	0.72	G8V	5.0187	0.089
175347.33-854135.5	268.4472	-85.6932	12.81	8.92	0.54	F9V	4.4685	0.051
180742.10-824651.6	271.9254	-82.7810	14.02	10.1	0.39	F0V	7.0683	0.224
181807.06-800525.4	274.5294	-80.0904	11.04	4.80	1.59	M	370.816	0.025
182044.62-754759.6	275.1859	-75.7999	11.50	5.52	0.50	F7V	3.4102	0.026
182608.74-864925.3	276.5364	-86.8237	14.41	10.1	0.90	K2V	4.2908	0.130
183802.93-811827.4	279.5122	-81.3076	10.90	10.2	0.83	K1V	48.6808	0.051
192029.45-860534.4	290.1227	-86.0929	13.27	9.80	0.35	A7V	6.0642	0.025
195449.01-840216.4	298.7042	-84.0379	12.73	10.2	0.73	G9V	5.5082	0.063
200551.67-820620.5	301.4653	-82.1057	13.63	8.88	0.71	G9V	5.5203	0.087
203404.49-871549.0	308.5187	-87.2636	13.87	9.50	0.36	F1V	4.8050	0.095
204931.97-845034.4	312.3832	-84.8429	14.21	15.1	0.72	G	4.4090	0.078

Table B.6: Variable Star discoveries

ESID (EVRJ+)	RA (J2000)	Dec (J2000)	Mv	RPM	B-V	spec	period (hours)	amp (Δ M)
205037.49-774637.2	312.6562	-77.7770	11.00	6.99	0.46	F8V	3.3040	0.023
205225.92-855742.5	313.1080	-85.9618	14.07	12.4	0.97	K3V	133.559	0.062
205802.14-793349.7	314.5089	-79.5638	12.97	8.41	0.61	F7V	6.2271	0.048
210729.26-763906.5	316.8719	-76.6518	13.58	10.4	0.23	F3	4.7894	0.024
210937.03-785828.2	317.4043	-78.9745	12.99	6.25	1.07	K4III	180.803	0.051
213403.58-865953.5	323.5149	-86.9982	12.69	8.97	0.60	F9V	4.7182	0.082
215744.06-790828.7	329.4336	-79.1413	13.51	7.75	1.11	K5III	10.6690	0.148
220737.90-813510.0	331.9079	-81.5861	11.93	14.4	0.90	G	14.9246	0.016
223616.97-773616.2	339.0707	-77.6045	13.55	8.89	1.15	K6III	2074.797	0.299
235019.03-840248.8	357.5793	-84.0469	11.40	7.79	0.39	F5V	5.8564	0.020

Table B.7: Eclipsing Binary discoveries

ESID	RA (J2000)	Dec (J2000)	Mv	RPM	B-V	spec	period (hours)	depth (frac)
002445.62-784031.1	6.1901	-78.6753	11.78	6.21	0.56	G9V	109.365	0.118
004748.46-754942.6	11.9519	-75.8285	11.79	5.20	0.52	F9V	157.422	0.229
005637.85-782127.0	14.1577	-78.3575	12.39	8.65	0.63	G5V	74.0640	0.273
010726.33-774753.2	16.8597	-77.7981	12.96	8.26	0.30	A5V	15.7654	0.148
012740.66-841645.1	21.9194	-84.2792	13.25	7.92	0.65	G1V	20.0793	0.109
013849.70-842426.6	24.7071	-84.4074	13.24	14.2	0.90	K	198.583	0.172
014115.60-800737.9	25.3150	-80.1272	14.97	9.44	0.23	G2V	22.1010	0.187
023605.38-852430.6	39.0224	-85.4085	12.75	7.47	0.54	F1V	118.771	0.225
024203.26-750224.0	40.5136	-75.0400	11.98	6.76	0.31	F4V	30.9563	0.243
024438.52-835122.7	41.1605	-83.8563	12.50	8.28	0.72	G8V	25.9882	0.303
030147.71-761211.5	45.4488	-76.2032	10.14	2.93	0.92	K3III	68.3947	0.065
032000.70-760821.5	50.0029	-76.1393	13.15	10.0	0.59	F9V	79.5734	0.202
032206.70-752842.6	50.5279	-75.4785	12.91	9.86	1.00	K4V	7.3698	0.147
032355.42-783922.7	50.9809	-78.6563	11.40	8.26	0.62	F8V	22.0561	0.215
033317.16-792812.7	53.3215	-79.4702	13.30	9.82	0.38	A8V	21.1649	0.095
043634.42-863132.9	69.1434	-86.5258	14.30	11.4	0.76	F1V	8.1408	0.221
043913.51-855448.6	69.8063	-85.9135	10.23	8.34	0.82	G3V	36.8604	0.054
043932.02-794339.0	69.8834	-79.7275	11.53	6.84	0.59	F9V	61.6244	0.117
044501.22-771324.6	71.2551	-77.2235	11.33	10.8	0.59	F9V	85.9685	0.217
044545.98-770625.6	71.4416	-77.1071	13.16	4.63	0.30	F1V	17.5505	0.387
045203.19-853702.6	73.0133	-85.6174	12.49	10.4	0.09	F9	30.2652	0.092
045807.78-772037.7	74.5324	-77.3438	12.58	8.92	0.69	G6V	38.1567	0.379
050731.01-760919.8	76.8792	-76.1555	13.38	10.1	0.64	G2V	10.7099	0.065
052042.43-753131.8	80.1768	-75.5255	11.06	3.14	0.05	A1V	64.8150	0.322
053006.26-811232.4	82.5261	-81.2090	11.95	7.32	0.49	F8V	45.1688	0.217
053504.90-834045.5	83.7704	-83.6793	12.40	9.23	0.41	F9V	35.7837	0.130
053541.69-753728.6	83.9237	-75.6246	12.75	8.21	0.81	K2V	31.2876	0.113
054814.83-772912.5	87.0618	-77.4868	13.85	9.49	0.47	G3V	17.3382	0.611
055000.48-780018.7	87.5020	-78.0052	13.60	8.79	0.44	G0V	22.1010	0.243
055918.00-861604.1	89.8250	-86.2678	12.51	8.16	0.54	G6V	16.0350	0.101
060300.82-763227.2	90.7534	-76.5409	13.01	9.37	0.63	G6V	35.3178	0.368
060956.86-842635.9	92.4869	-84.4433	12.32	8.02	0.03	F1	64.7228	0.106
061730.58-853507.8	94.3774	-85.5855	13.76	9.17	-0.23	A0	19.5420	0.064
061942.89-872037.7	94.9287	-87.3438	12.77	8.30	0.53	G0V	11.7925	0.176
062614.11-812323.6	96.5588	-81.3899	12.84	9.76	0.45	F8V	22.1397	0.057
065136.84-775609.6	102.9035	-77.9360	11.32	4.24	0.66	G5III	154.225	0.158
065350.93-840014.0	103.4622	-84.0039	12.91	9.75	0.60	K0V	45.7400	0.212
065609.43-810853.5	104.0393	-81.1482	13.49	12.3	0.71	K0V	13.4842	0.116
070327.70-813323.4	105.8654	-81.5565	13.29	9.59	0.45	A9V	22.2891	0.357
071503.55-792949.6	108.7648	-79.4971	13.08	7.32	0.41	G1V	35.9922	0.599
071744.33-854505.4	109.4347	-85.7515	13.09	6.75	0.77	K3V	101.685	0.314
071748.29-844104.6	109.4512	-84.6846	14.52	10.4	0.39	G3V	7.6682	0.184

Table B.8: Eclipsing Binary discoveries

ESID	RA (J2000)	Dec (J2000)	Mv	RPM	B-V	spec	period (hours)	depth (frac)
072710.08-815757.2	111.7920	-81.9659	13.73	5.29	0.54	G9V	41.0657	1.000
073157.14-815943.4	112.9881	-81.9954	9.93	6.74	0.19	F1V	60.0174	0.074
074851.14-844938.3	117.2131	-84.8273	13.18	8.90	0.56	F	23.3998	0.115
075512.70-831036.1	118.8029	-83.1767	12.40	8.05	0.54	F8V	68.9536	0.237
080959.06-765721.2	122.4961	-76.9559	12.33	8.08	0.52	F8V	109.365	0.257
082431.85-771708.5	126.1327	-77.2857	10.99	6.53	0.55	G1V	46.0730	0.162
083235.69-814208.3	128.1487	-81.7023	13.27	10.9	0.48	G7V	22.5004	0.273
083610.66-822751.1	129.0444	-82.4642	12.08	7.46	1.30	K	15.4668	0.066
084853.45-755536.1	132.2227	-75.9267	10.01	5.34	0.28	F8V	59.1296	0.081
085629.66-833101.6	134.1236	-83.5171	12.47	4.96	0.51	F1V	59.1383	0.250
090851.91-835702.5	137.2163	-83.9507	13.29	8.89	0.42	F1V	10.8306	0.337
091345.72-822820.3	138.4405	-82.4723	11.75	6.95	0.60	G5V	43.7381	0.182
092241.74-833802.0	140.6739	-83.6339	13.77	8.53	0.54	G0V	4.4717	0.145
093342.00-865534.0	143.4250	-86.9261	13.03	8.34	0.75	G9V	106.173	0.347
093554.48-763543.8	143.9770	-76.5955	13.59	4.56	0.67	F6III	35.6159	0.248
093619.37-811153.2	144.0807	-81.1981	13.13	10.3	0.82	K1V	129.285	0.239
094641.04-781309.8	146.6710	-78.2194	13.00	7.60	0.56	G2V	33.1735	0.231
095515.41-830705.9	148.8142	-83.1183	12.88	9.48	0.59	G5V	151.760	0.345
100205.04-814503.2	150.5210	-81.7509	12.79	6.15	0.30	F5V	67.4233	0.196
100426.40-803846.0	151.1100	-80.6461	13.09	7.01	0.59	F6V	28.3768	0.095
100649.61-801046.9	151.7067	-80.1797	12.65	12.9	0.51	F4	44.7694	0.205
101423.47-774932.5	153.5978	-77.8257	13.29	13.2	1.05	K	35.1543	0.083
103443.51-775813.1	158.6813	-77.9703	10.88	10.8	0.64	G4V	20.9396	0.029
105421.24-782234.7	163.5885	-78.3763	12.41	10.8	1.00	K6V	20.3265	0.081
105445.86-785351.4	163.6911	-78.8976	12.69	10.6	0.61	G9V	62.0270	0.169
110105.30-864038.6	165.2721	-86.6774	13.73	9.45	0.58	G7V	42.5378	0.096
110815.96-870153.8	167.0665	-87.0316	12.68	9.77	0.84	K3V	12.2767	0.230
111244.66-830219.7	168.1861	-83.0388	13.18	7.43	0.49	G7V	17.3342	0.277
111447.02-811836.7	168.6959	-81.3102	12.41	10.9	0.62	G6V	35.0246	0.171
112755.49-842109.7	171.9812	-84.3527	13.81	9.72	0.34	F8V	8.4533	0.252
114502.30-771447.0	176.2596	-77.2464	12.29	7.73	0.78	G4V	39.2816	0.209
114706.02-835834.7	176.7751	-83.9763	12.90	9.39	0.87	K3V	54.3094	0.091
120501.68-852738.9	181.2570	-85.4608	12.73	9.41	0.48	F6V	103.691	0.144
120856.86-770450.9	182.2369	-77.0808	13.21	6.55	0.92	K2III	40.7350	0.275
122230.55-772324.4	185.6273	-77.3901	11.60	8.26	0.77	K0V	100.801	0.248
125134.08-790133.2	192.8920	-79.0259	10.32	9.09	0.57	G8V	114.771	0.157
125505.76-851321.7	193.7740	-85.2227	11.73	6.37	0.38	F3V	30.5570	0.083
131324.31-792126.3	198.3513	-79.3573	12.28	6.37	0.31	F7V	33.7030	0.228
131504.46-763140.1	198.7686	-76.5278	12.08	7.84	0.69	G9V	21.5120	0.055
131906.34-840040.3	199.7764	-84.0112	11.58	5.87	1.07	K3III	23.8310	0.086
131909.89-834711.0	199.7912	-83.7864	12.74	8.79	0.40	F0V	15.7910	0.368
132210.78-790543.1	200.5449	-79.0953	13.29	9.33	0.48	F8V	37.6460	0.108

Table B.9: Eclipsing Binary discoveries

ESID	RA (J2000)	Dec (J2000)	Mv	RPM	B-V	spec	period (hours)	depth (frac)
132915.46-763040.0	202.3144	-76.5111	12.65	8.42	0.53	F	19.3470	0.205
133026.14-852532.2	202.6089	-85.4256	12.55	8.51	1.08	K5III	12.6020	0.038
133347.26-833757.7	203.4469	-83.6327	13.39	8.35	0.56	G3V	17.8470	0.057
133848.86-834425.4	204.7036	-83.7404	13.58	10.2	0.58	G7V	71.4170	0.455
134321.74-845650.6	205.8406	-84.9474	12.78	8.18	0.55	G5V	9.7290	0.365
135211.09-844337.9	208.0462	-84.7272	13.73	9.53	0.60	G8V	27.8460	0.382
135212.36-785333.7	208.0515	-78.8927	12.07	6.17	0.59	F9V	61.0300	0.443
135431.18-815457.2	208.6299	-81.9159	11.19	6.69	0.26	A4V	79.1580	0.050
135907.01-842606.7	209.7792	-84.4352	13.05	7.80	0.42	F7V	14.1710	0.324
140102.93-823656.9	210.2622	-82.6158	10.79	9.06	0.75	K0V	43.2894	0.188
140546.42-835919.0	211.4434	-83.9886	11.29	8.38	0.76	G9V	33.0580	0.044
141018.94-830332.8	212.5789	-83.0591	11.89	4.11	0.21	F1V	18.8112	0.123
141043.54-834026.4	212.6814	-83.6740	12.19	10.8	0.86	G3V	13.7081	0.045
142633.19-825021.5	216.6383	-82.8393	12.92	11.7	0.75	G9V	13.7050	0.176
143328.56-833750.5	218.3690	-83.6307	12.77	8.89	0.68	G5V	129.948	0.420
143842.46-813049.0	219.6769	-81.5136	13.07	8.39	0.67	G1V	16.4483	0.153
143916.73-844909.5	219.8197	-84.8193	12.18	6.11	0.55	F	26.6630	0.082
144001.37-842946.7	220.0057	-84.4963	12.67	7.87	0.42	F6V	18.0120	0.126
144437.08-775109.4	221.1545	-77.8526	12.23	4.31	0.30	F1V	40.6480	0.151
144607.85-835647.8	221.5327	-83.9466	12.20	8.33	0.73	G6V	16.1201	0.081
145302.21-823117.0	223.2592	-82.5214	12.80	8.93	0.87	K0V	52.0750	0.236
145519.22-761940.8	223.8301	-76.3280	13.50	5.89	0.71	G7V	20.7599	0.242
150051.41-823800.6	225.2142	-82.6335	11.69	7.50	1.42	M2III	50.1160	0.071
150534.08-873605.8	226.3920	-87.6016	12.70	8.88	0.55	F7V	178.933	0.127
151657.05-782900.6	229.2377	-78.4835	11.51	8.78	0.60	G7V	155.488	0.187
152229.16-855039.1	230.6215	-85.8442	12.70	11.5	0.76	K0V	55.5406	0.319
152858.46-781119.0	232.2436	-78.1886	12.08	7.47	0.53	F2V	37.9090	0.124
152933.41-755721.2	232.3892	-75.9559	9.95	5.49	0.27	A6V	27.9790	0.099
153920.90-820531.2	234.8371	-82.0920	13.86	8.80	0.64	G2V	21.6105	0.093
154507.37-793351.1	236.2807	-79.5642	12.75	7.16	0.66	G5V	12.6404	0.244
160954.46-851858.3	242.4769	-85.3162	12.76	7.60	0.33	F4V	44.7430	0.189
161508.66-835940.6	243.7861	-83.9946	13.18	11.2	0.73	K0V	144.540	0.403
162303.89-810023.4	245.7662	-81.0065	12.34	3.25	0.56	G7V	62.7963	0.313
163423.28-841700.6	248.5970	-84.2835	13.63	9.48	0.99	K2V	4.7610	0.397
163736.60-853222.2	249.4025	-85.5395	12.70	6.11	0.67	G2V	25.4995	0.076
164003.19-835758.7	250.0133	-83.9663	12.91	9.45	0.57	G6V	41.2660	0.247
164326.83-861143.8	250.8618	-86.1955	14.13	7.55	0.86	G	9.7203	0.336
164433.50-860655.4	251.1396	-86.1154	12.22	5.87	0.59	F1V	63.6382	0.219
165236.34-775955.0	253.1514	-77.9986	12.57	6.78	0.53	F9V	45.8782	0.215
170835.06-804042.2	257.1461	-80.6784	13.36	10.8	0.64	G6V	11.7251	0.185
171020.11-794022.8	257.5838	-79.6730	13.38	9.62	0.60	G0V	34.9601	0.224
173306.41-841023.5	263.2767	-84.1732	11.94	7.48	0.01	B8V	62.0777	0.107

Table B.10: Eclipsing Binary discoveries

ESID	RA (J2000)	Dec (J2000)	Mv	RPM	B-V	spec	period (hours)	depth (frac)
071938.74-794442.4	109.9114	-79.7451	12.18	5.14	0.39	F2V	20.8352	0.107
175021.89-833451.2	267.5912	-83.5809	12.90	10.6	0.45	G1V	97.8154	0.670
175151.98-770054.7	267.9666	-77.0152	12.99	7.95	0.60	F1V	14.0583	0.312
175821.86-823023.4	269.5911	-82.5065	13.32	8.36	0.68	G6V	32.6439	0.272
181441.14-755531.1	273.6714	-75.9253	11.71	9.14	0.66	G3V	70.3589	0.235
181713.66-870538.4	274.3069	-87.0940	11.79	12.4	0.66	K0V	8.4675	0.138
181714.18-773047.2	274.3091	-77.5131	13.02	7.02	0.51	G1V	36.9321	0.603
181841.30-822733.5	274.6721	-82.4593	12.83	3.05	0.62	G2III	76.6038	0.070
184428.49-823046.8	281.1187	-82.5130	13.66	9.22	0.54	G8V	71.0168	0.238
184600.48-775012.5	281.5020	-77.8368	12.93	8.55	0.56	G1V	37.1489	0.192
185649.78-802355.0	284.2074	-80.3986	12.77	8.40	0.71	K1V	11.4201	0.128
190936.96-825733.8	287.4040	-82.9594	12.21	9.17	0.81	K1V	20.9770	0.097
191030.65-852500.5	287.6277	-85.4168	13.72	7.03	0.40	F8V	69.7130	0.580
191957.17-815827.8	289.9882	-81.9744	11.82	8.40	0.76	G9V	49.7553	0.190
195938.52-800854.6	299.9105	-80.1485	13.38	8.73	0.66	G6V	11.8792	0.362
200844.69-841100.6	302.1862	-84.1835	12.36	6.21	0.74	G8V	25.0280	0.183
204029.23-792542.2	310.1218	-79.4284	12.04	7.83	0.74	G8V	27.8260	0.149
211629.93-755719.1	319.1247	-75.9553	11.50	8.69	0.41	F4V	15.3512	0.213
213512.74-762221.4	323.8031	-76.3726	13.06	9.38	0.70	G4V	21.3854	0.100
214611.09-783816.4	326.5462	-78.6379	13.01	7.87	0.74	K1V	58.0007	0.138
215221.58-830052.9	328.0899	-83.0147	12.85	3.57	1.43	M2III	14.9228	0.069
215337.54-775041.6	328.4064	-77.8449	12.46	10.2	0.66	G4V	4.7476	0.086
215538.66-830823.6	328.9111	-83.1399	12.97	9.49	0.77	G9V	14.9228	0.095
223125.73-803027.7	337.8572	-80.5077	11.82	5.48	0.58	F9V	41.7888	0.068
223812.41-780109.1	339.5517	-78.0192	13.50	10.3	0.38	A8V	15.0893	0.256
225743.22-782429.2	344.4301	-78.4081	11.86	8.36	0.49	G6V	19.8070	0.071
225936.22-830757.0	344.9009	-83.1325	11.22	9.34	0.69	K0V	12.8218	0.064
230355.18-773000.7	345.9799	-77.5002	12.58	8.47	0.59	G2V	34.7999	0.138
231712.07-790607.6	349.3003	-79.1021	11.51	8.15	0.66	G6V	195.014	0.154
232322.32-771336.5	350.8430	-77.2268	12.43	5.89	0.71	G6V	66.0742	0.196
233038.69-760536.6	352.6612	-76.0935	12.56	9.29	0.60	G0V	84.7218	0.390
234021.77-780703.4	355.0907	-78.1176	13.66	8.99	0.47	F8V	11.6461	0.136
234130.91-790731.8	355.3788	-79.1255	13.36	7.75	0.53	F5V	90.6906	0.291

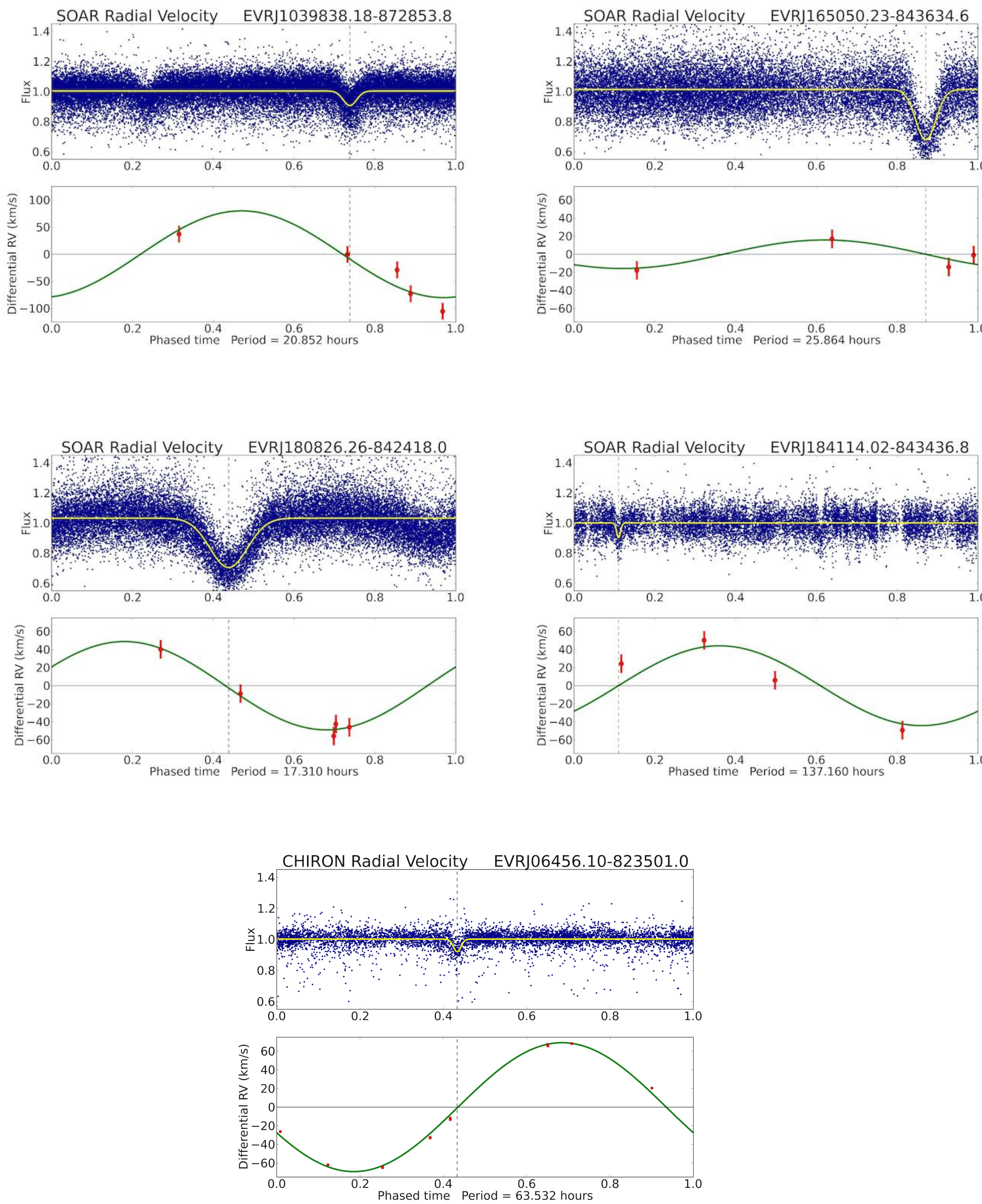

Figure B.1: Low mass secondary discoveries. Top panels are the Evryscope light curves with the best transit fit. Bottom panels are the SOAR RV points (red) with the best sinusoidal fit. Primary and secondary mass and radius values are shown in Table 2.

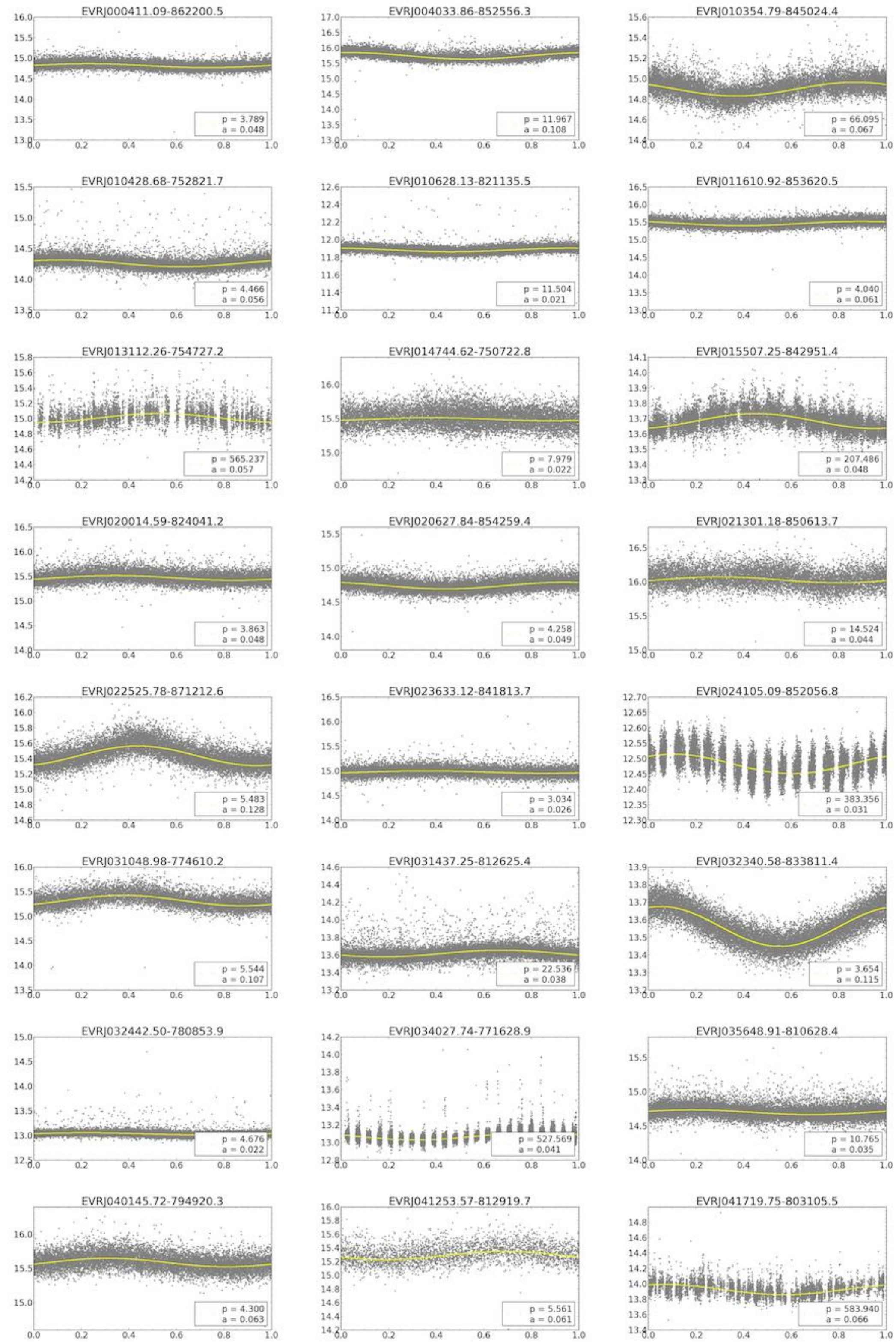

Figure B.2: Variable star discoveries. Y-axis is instrument magnitude, x-axis is the phase.

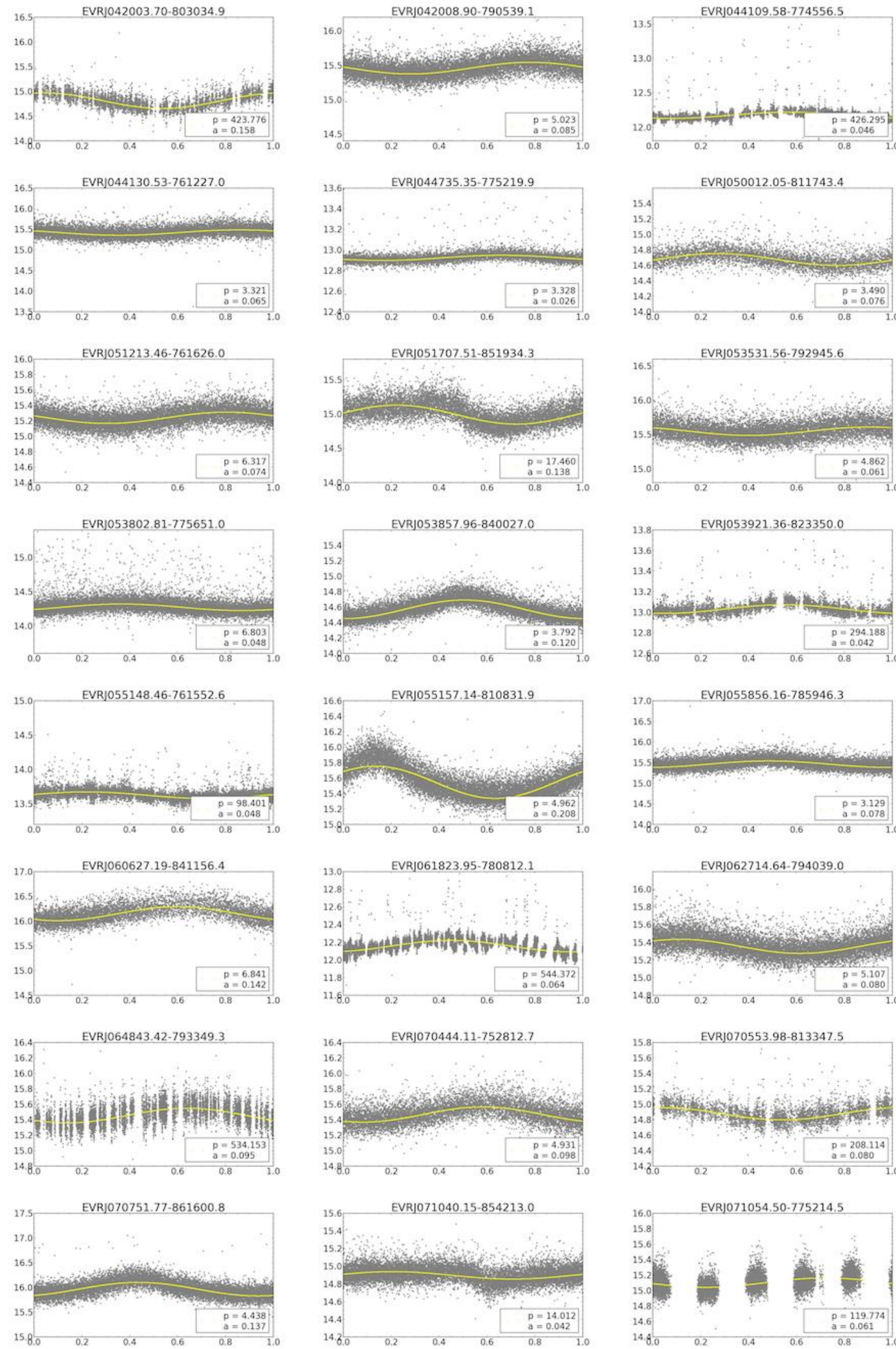

Figure B.3: Variable star discoveries. Y-axis is instrument magnitude, x-axis is the phase.

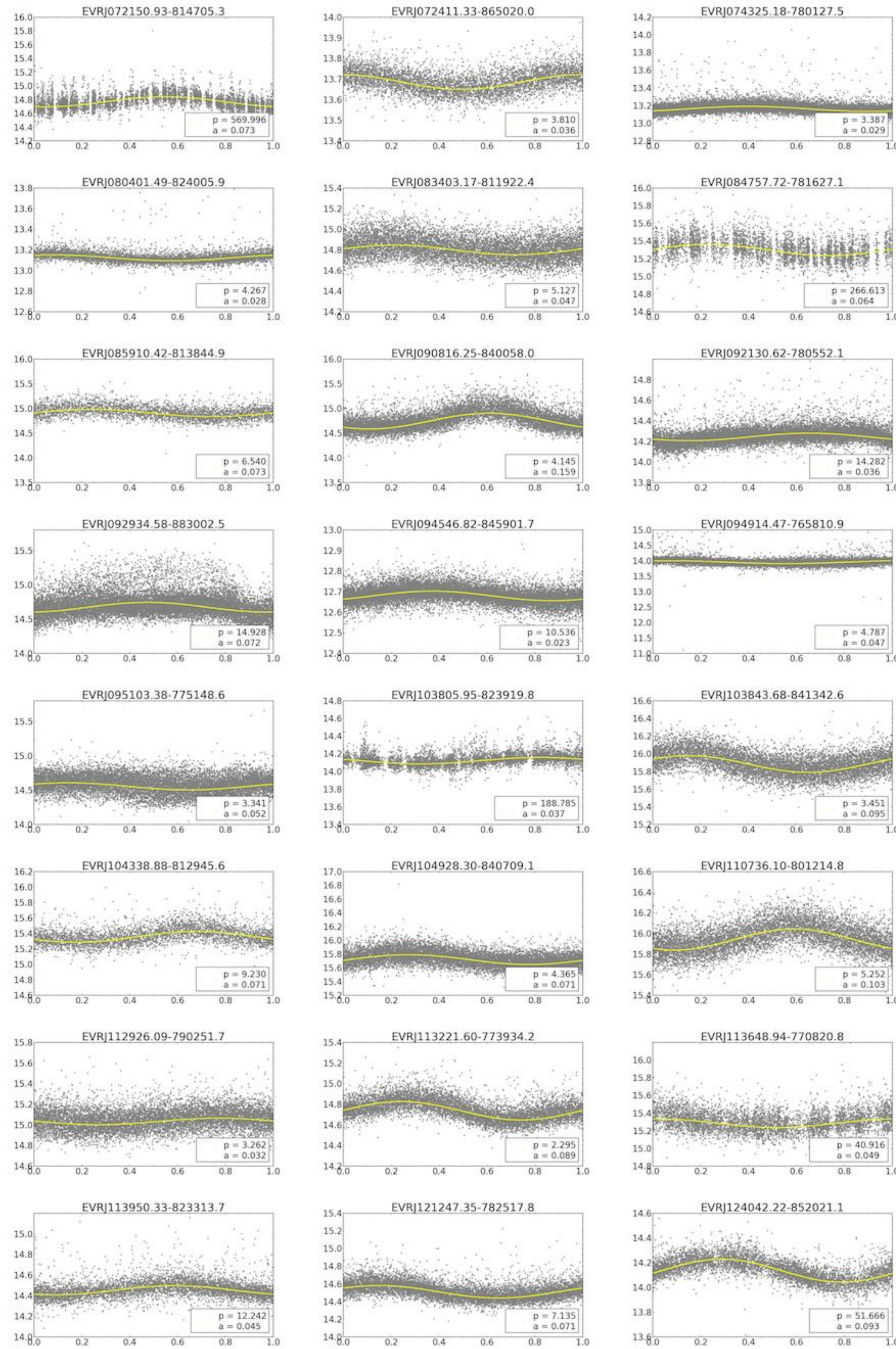

Figure B.4: Variable star discoveries. Y-axis is instrument magnitude, x-axis is the phase.

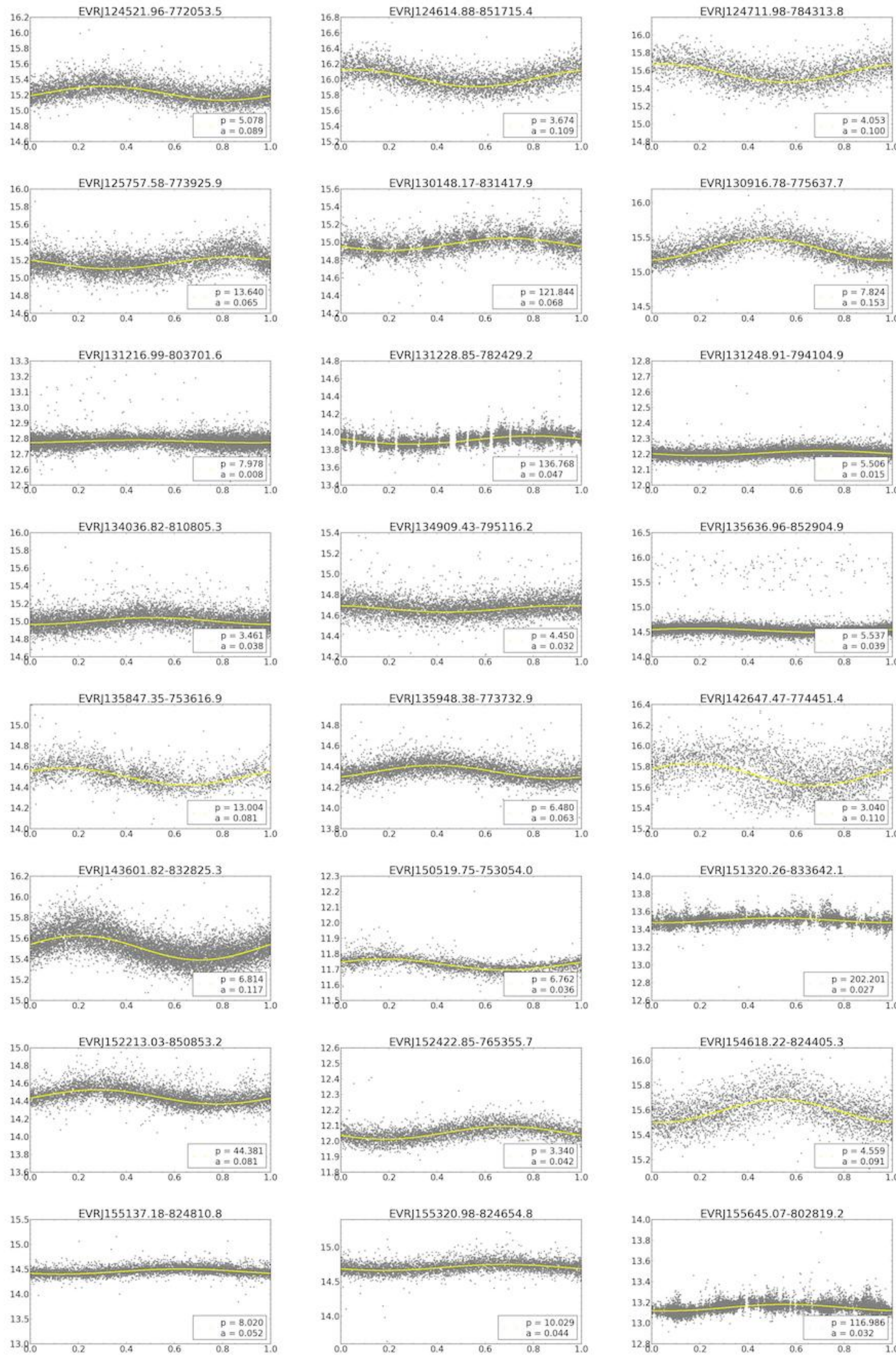

Figure B.5: Variable star discoveries. Y-axis is instrument magnitude, x-axis is the phase.

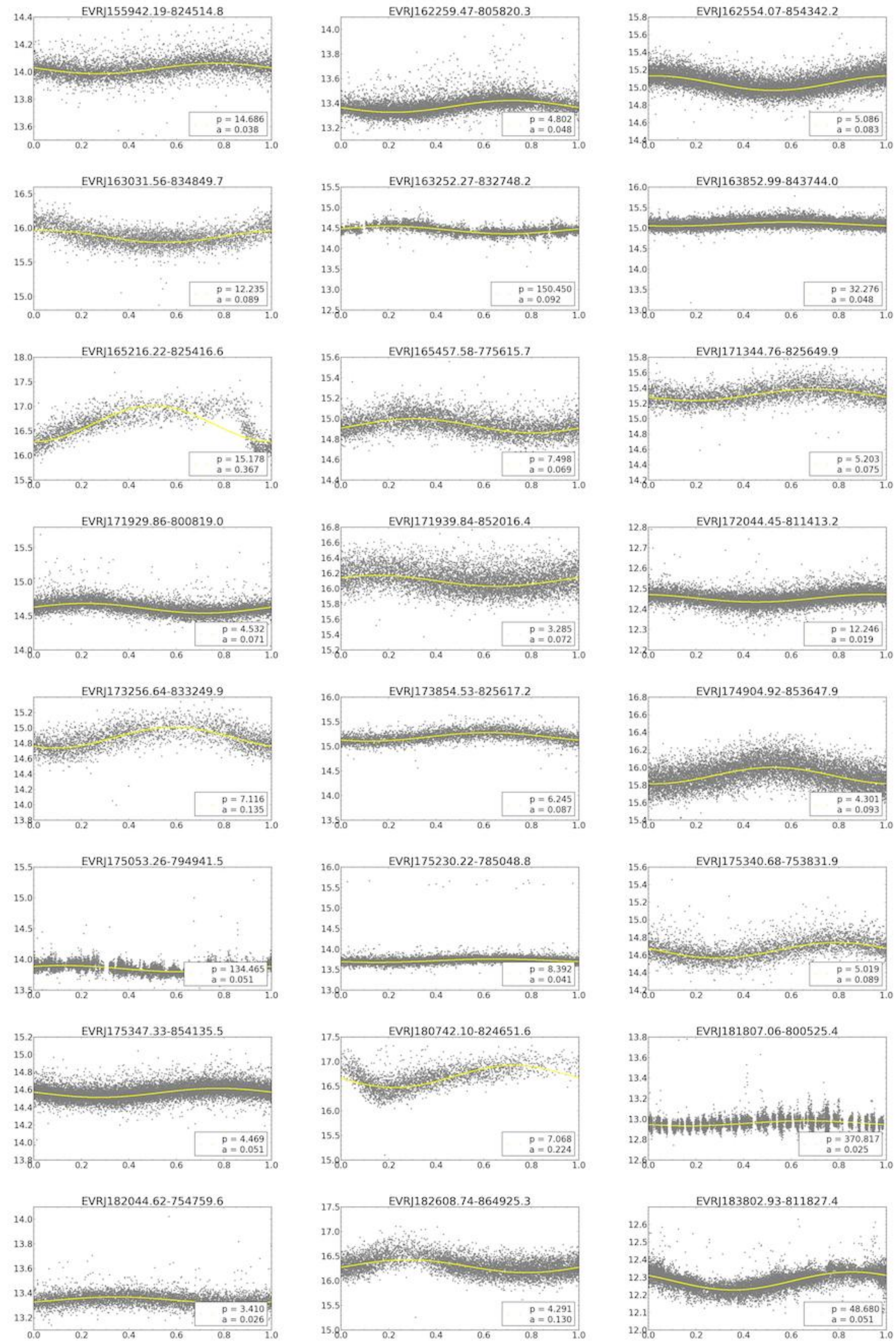

Figure B.6: Variable star discoveries. Y-axis is instrument magnitude, x-axis is the phase.

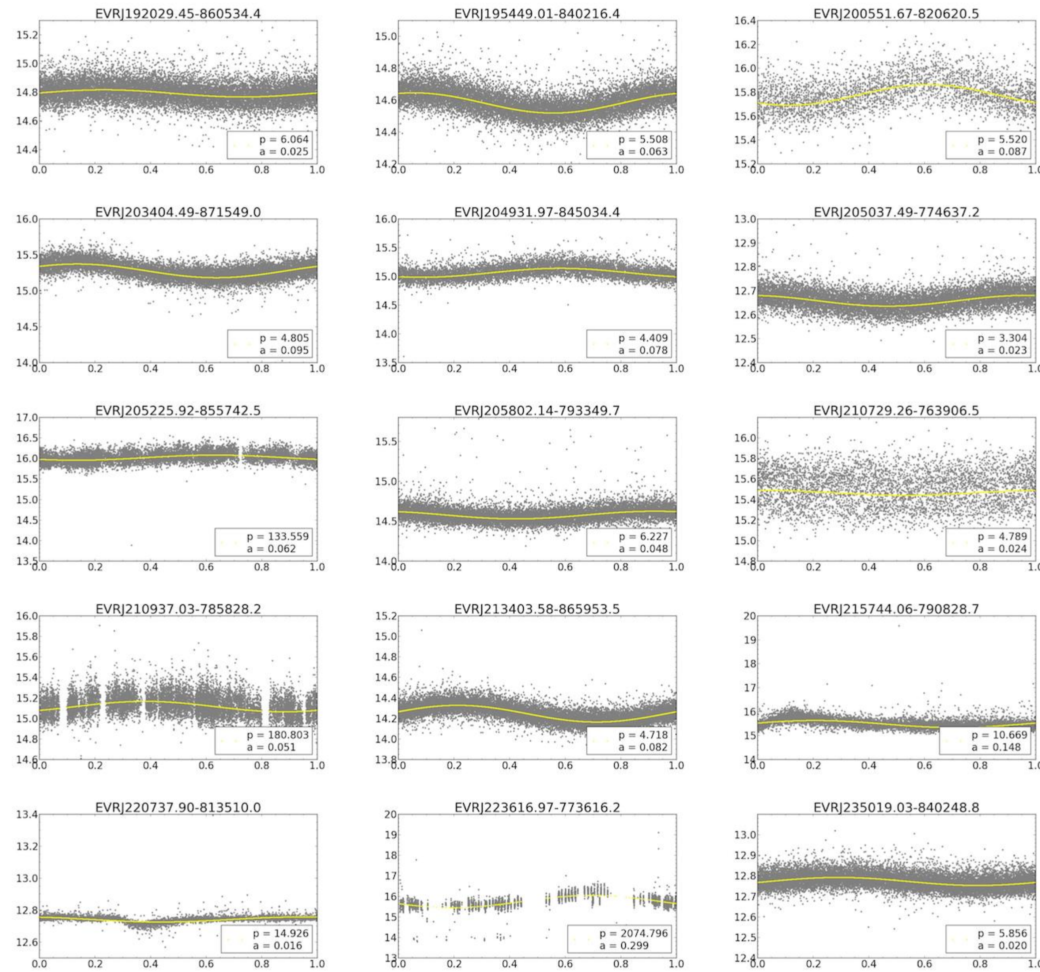

Figure B.7: Variable star discoveries. Y-axis is instrument magnitude, x-axis is the phase.

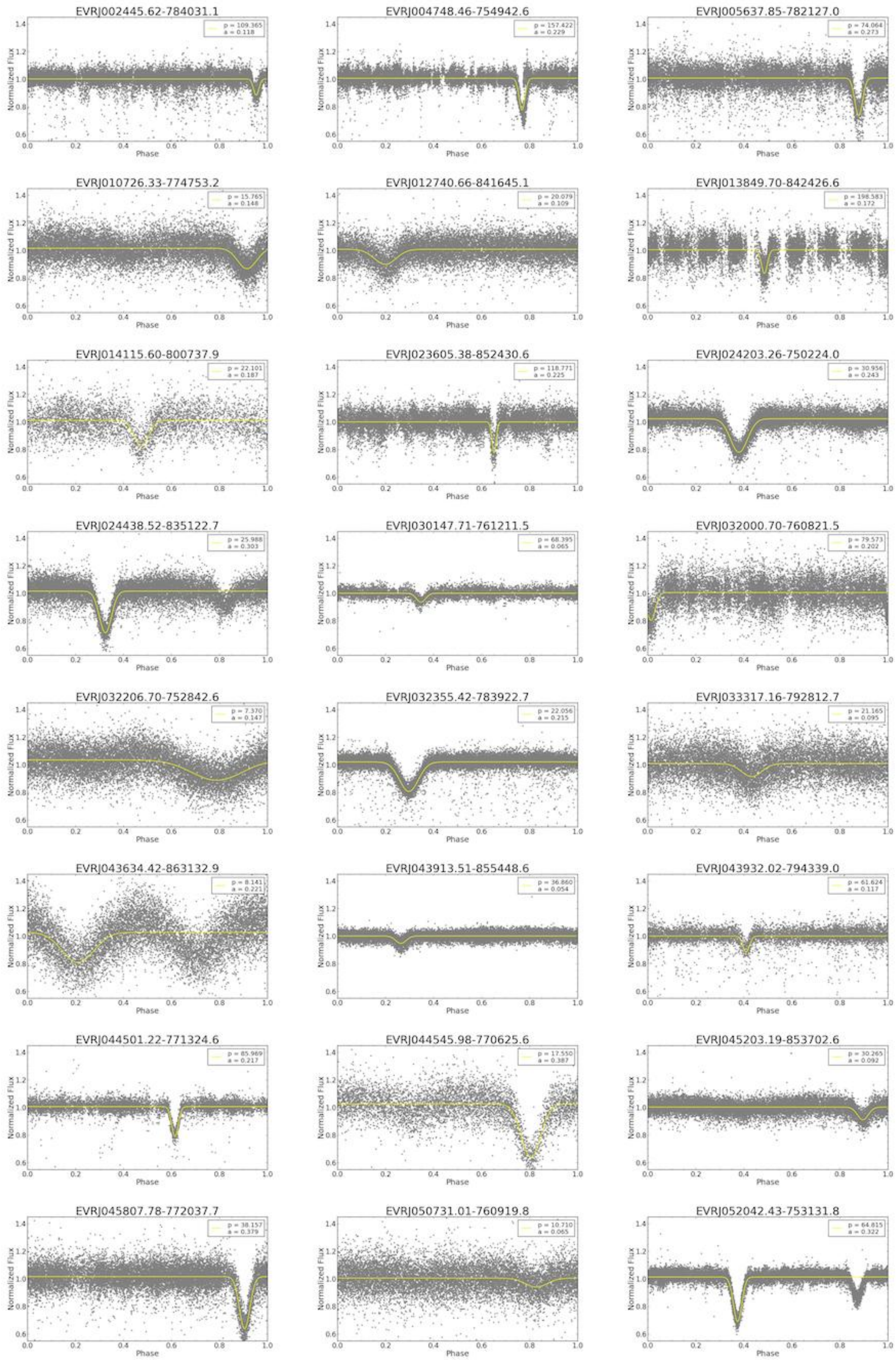

Figure B.8: Eclipsing Binary discoveries. Y-axis is normalized flux, x-axis is the phase.

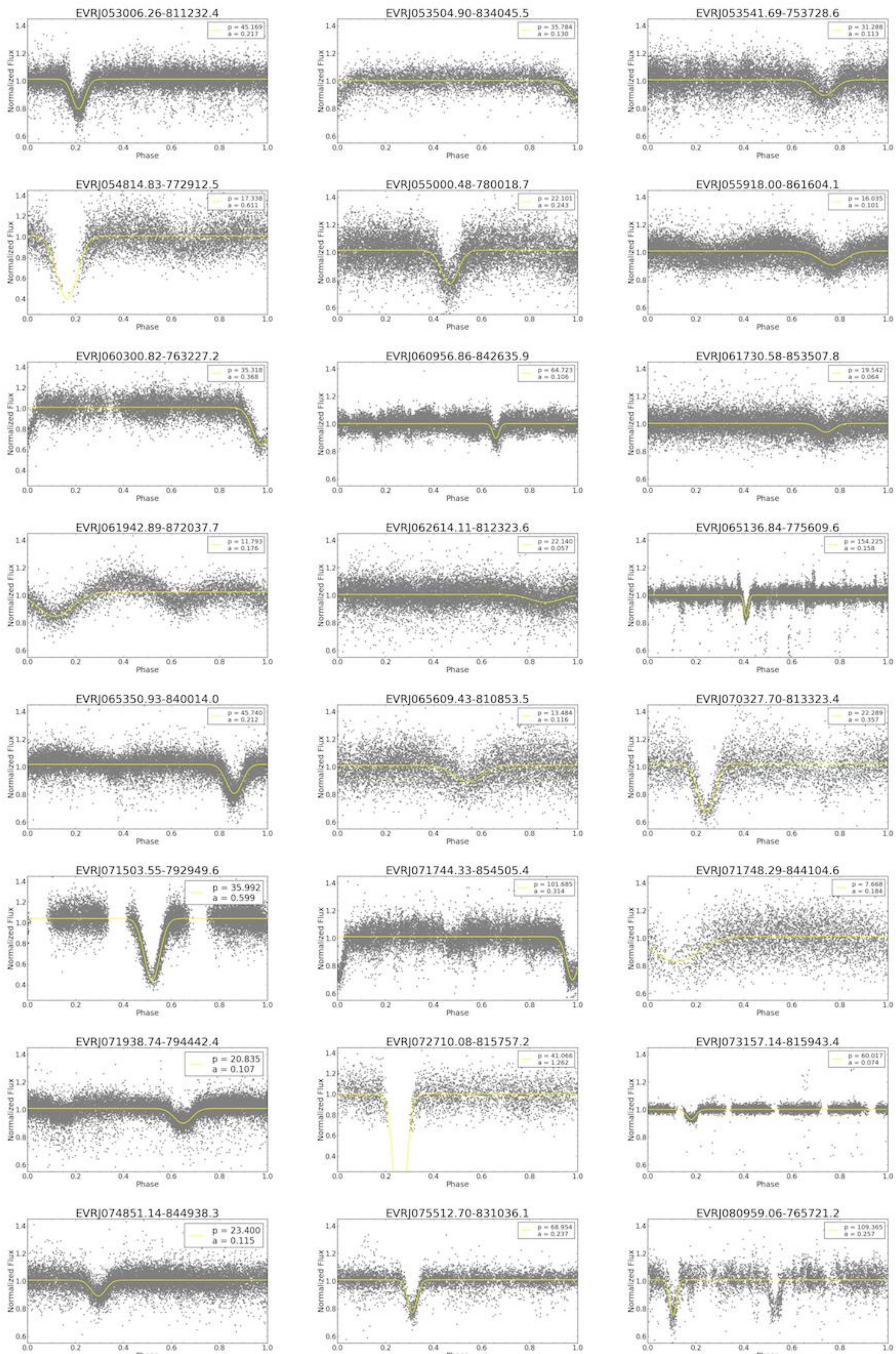

Figure B.9: Eclipsing Binary discoveries. Y-axis is normalized flux, x-axis is the phase.

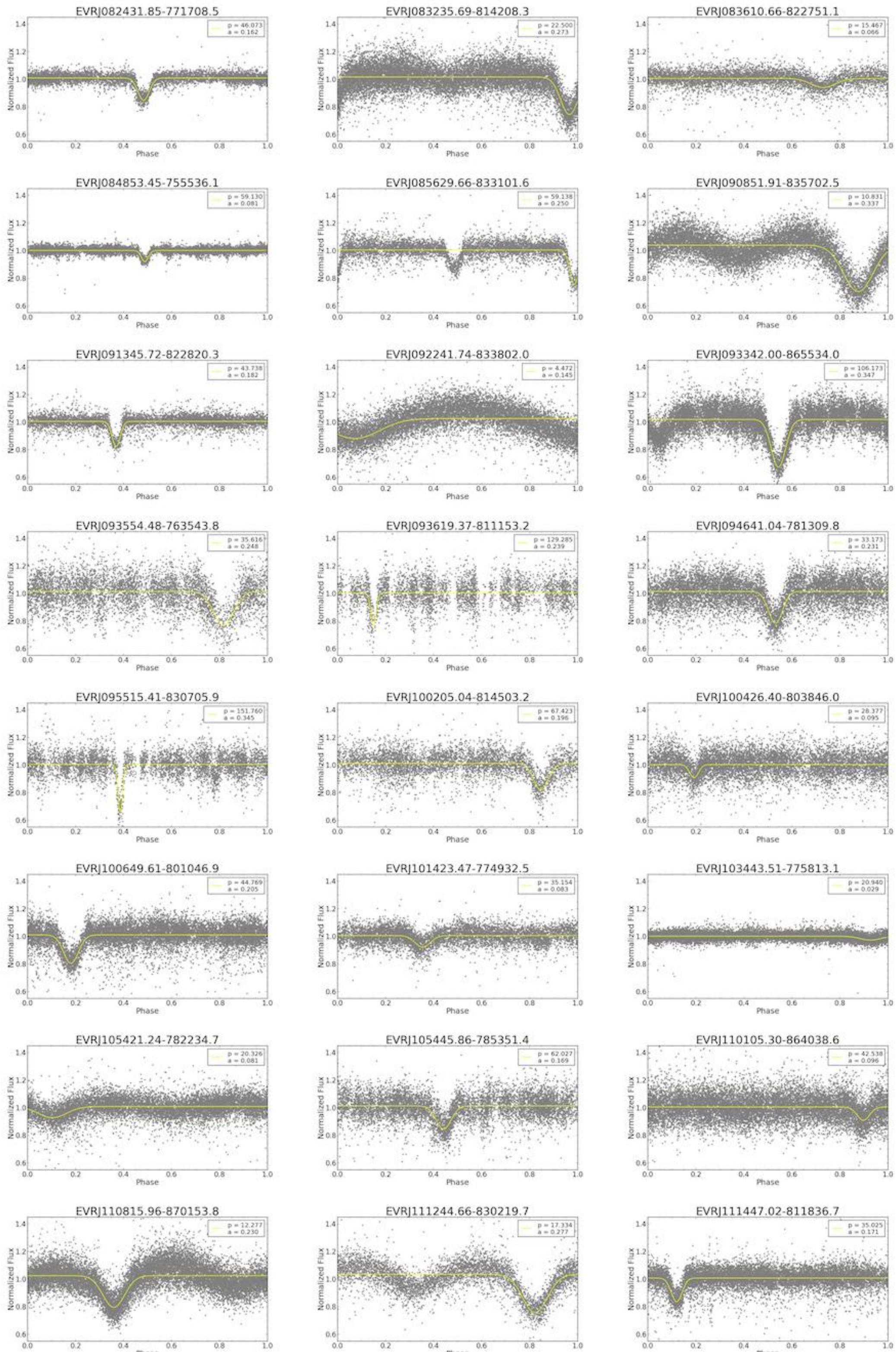

Figure B.10: Eclipsing Binary discoveries. Y-axis is normalized flux, x-axis is the phase.

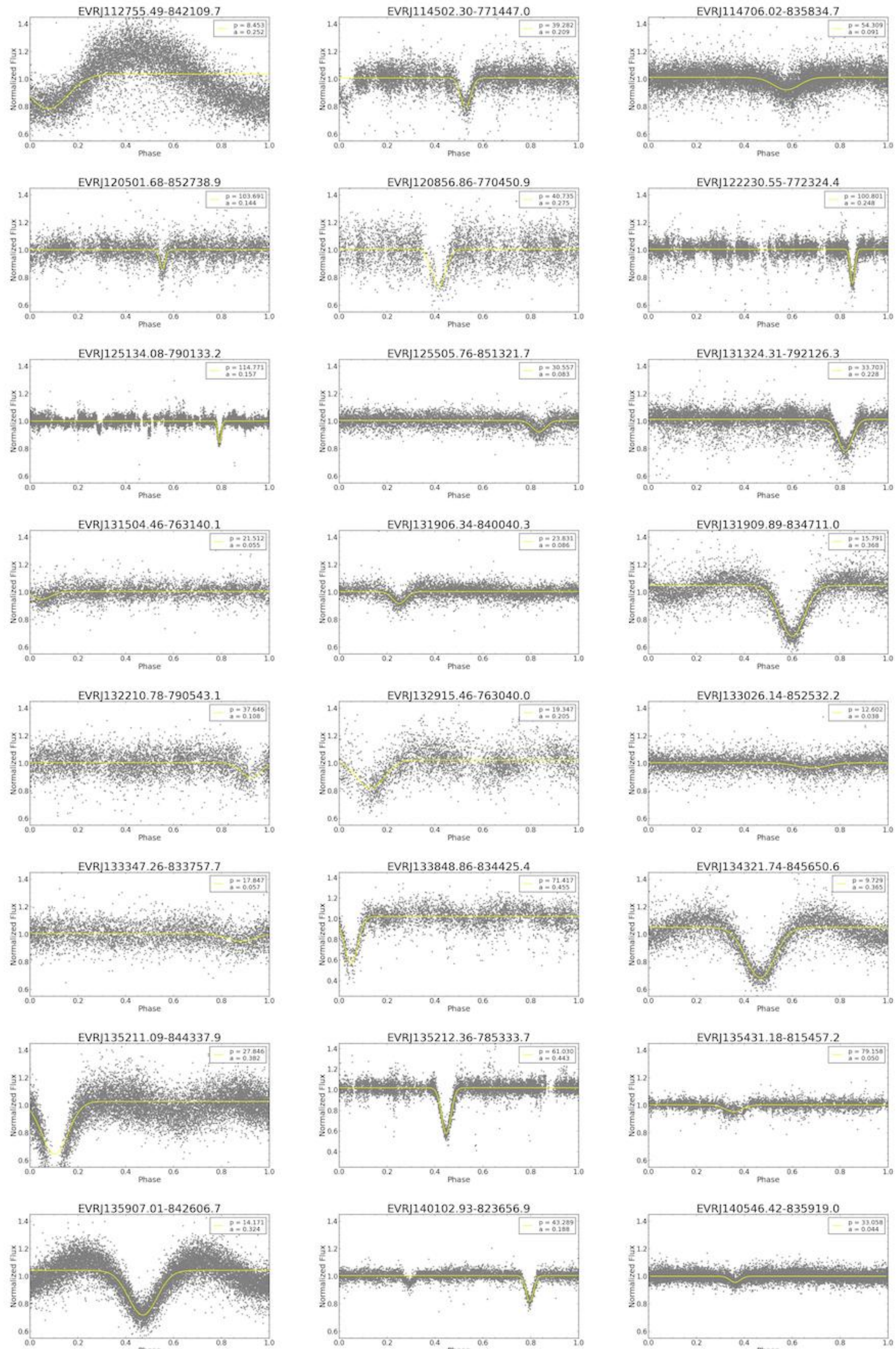

Figure B.11: Eclipsing Binary discoveries. Y-axis is normalized flux, x-axis is the phase.

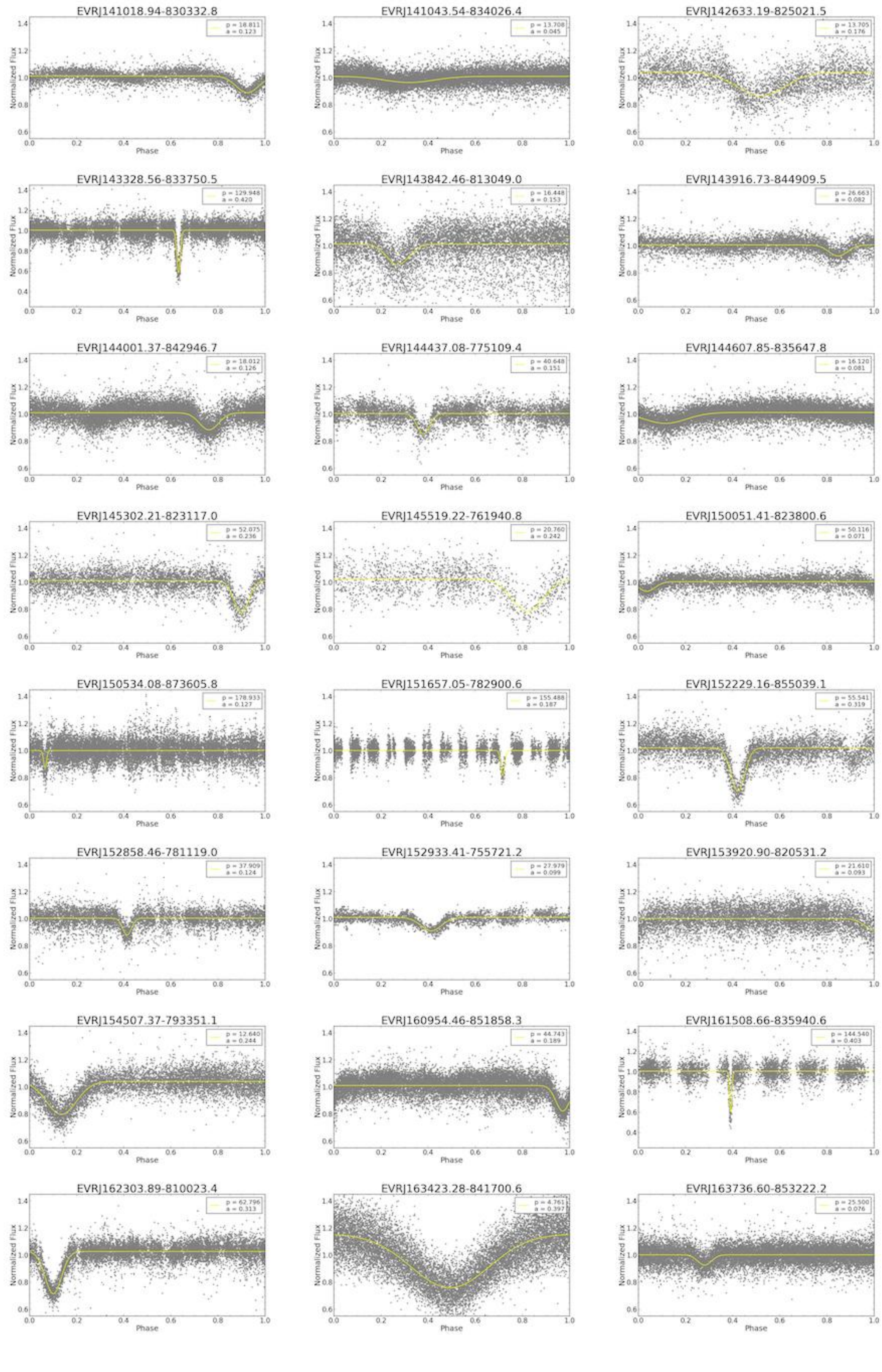

Figure B.12: Eclipsing Binary discoveries. Y-axis is normalized flux, x-axis is the phase.

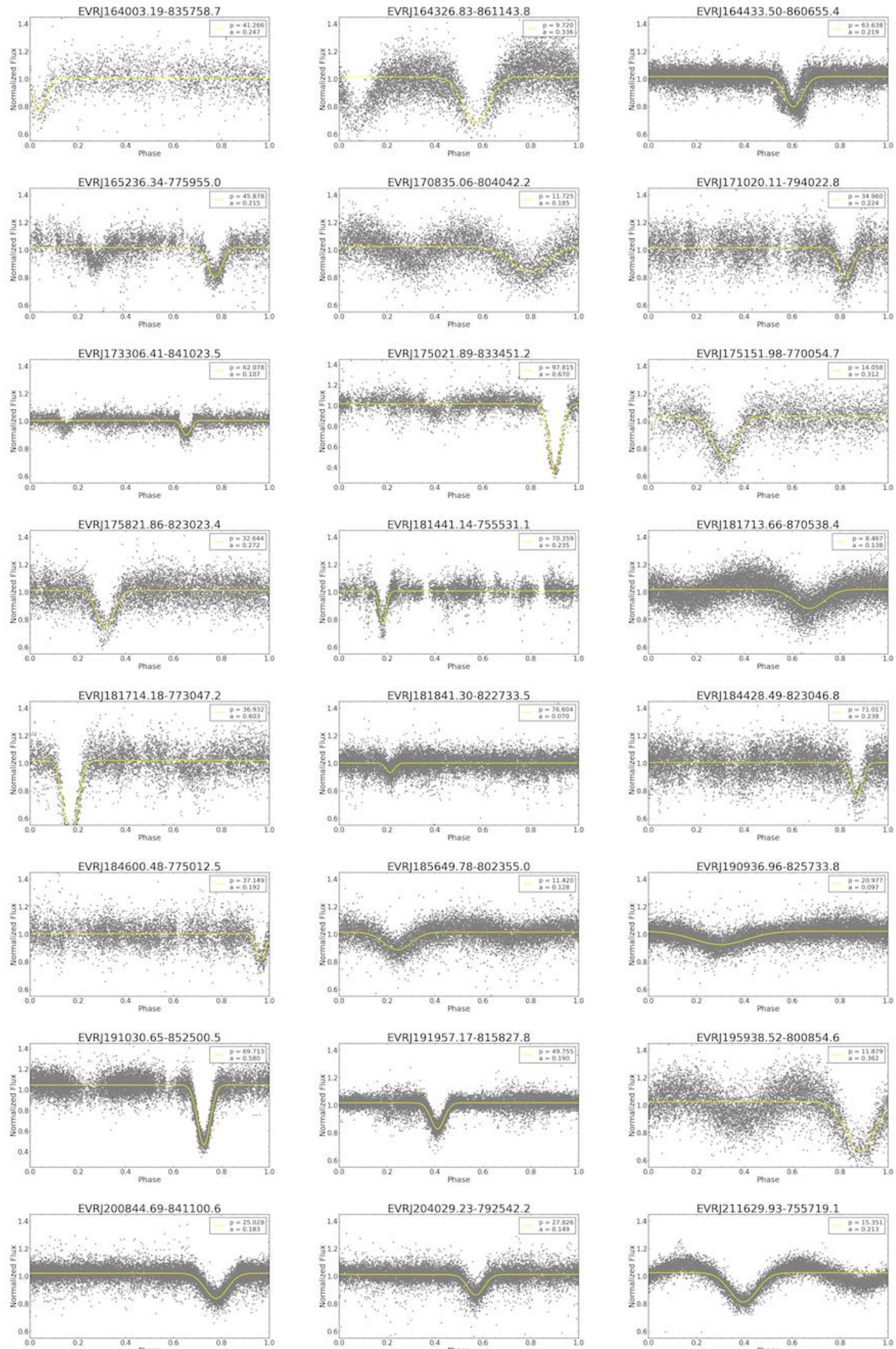

Figure B.13: Eclipsing Binary discoveries. Y-axis is normalized flux, x-axis is the phase.

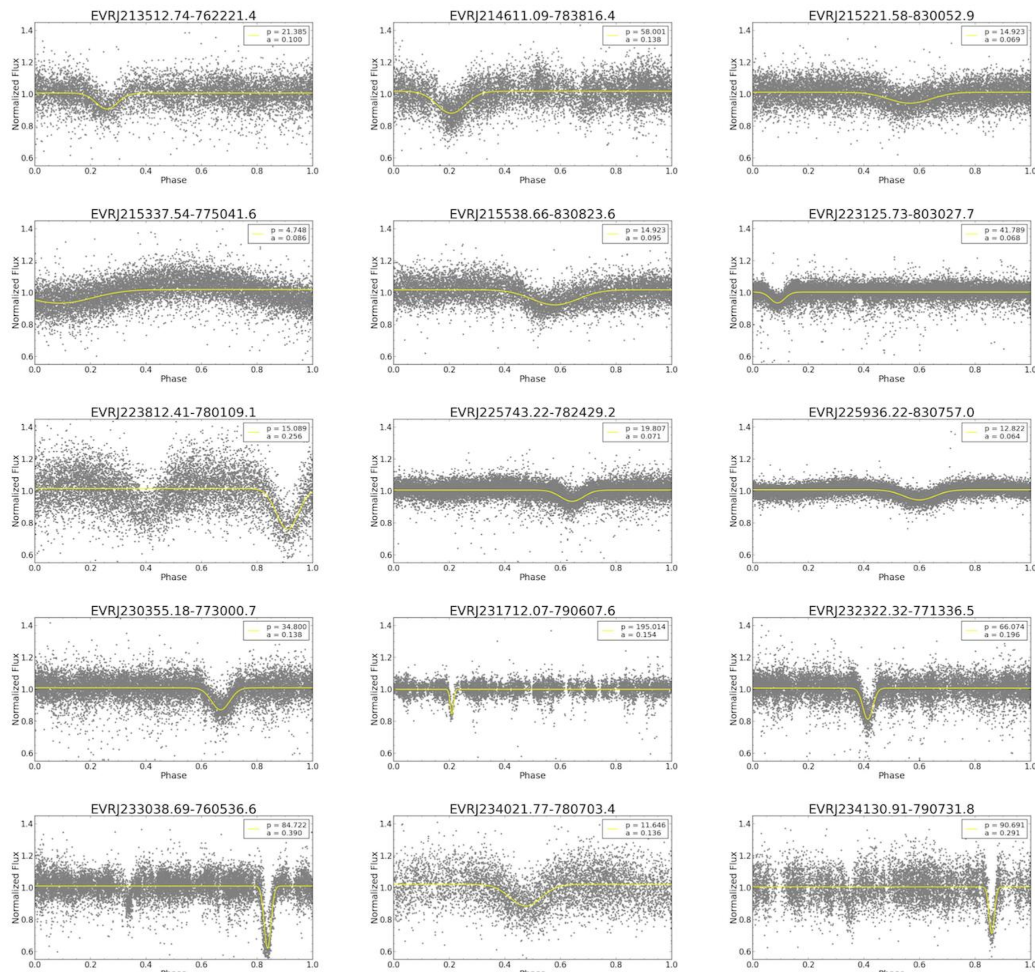

Figure B.14: Eclipsing Binary discoveries. Y-axis is normalized flux, x-axis is the phase.

APPENDIX C: HSD SURVEY OTHER DISCOVERIES AND LIGHT CURVES

C.1 HSD Survey Other Discoveries

C.1.1 Discovery Comments

C.1.1.1 EVRJ150433.67-170155.2, EVRJ155252.37-645012.5

Periodic transit like features are visible in these variables with no ellipsoidal effects or secondary eclipses evident. The transit durations are too long (2-3 hours) for the primary to be a HSD, but too short to be an O or B star. The 10.9041 and 21.1933 hour period variables could be CVs or Novae; they require further followup to reveal the characteristics of the systems.

C.1.1.2 EVRJ072950.66-133935.3

A 166.1992 hour long period, very eccentric EB with $\approx$ 9 hour eclipse durations. Both primary and secondary are reasonably deep (0.26 primary). We suspect the system is likely comprised of O and B stars, making this a potentially rare eclipsing binary with very hot and massive components. Again the bright magnitude will aid in followup.

Table C.1: Variables (Likely A or B-stars misclassified as HSDs)

ID	ID	RA	Dec	mag [G]	Period [h]
New Discoveries					
EVRJ044348.48-854516.6	GaiaDR24614260804078737792	70.9520	-85.7546	10.587 ±.001	35.9327 ±.0004
EVRJ052817.76-690418.5[a]	GaiaDR24658105788836255360	82.0740	-69.0718	11.272 ±.002	474.7 ±.6
EVRJ053824.72-663523.6[b]	GaiaDR24659534879024982528	84.6030	-66.5899	13.941 ±.002	36.287 ±.003
EVRJ065540.80-234417.5	GaiaDR22922396976293672576	103.9200	-23.7382	10.396 ±.001	21.6214 ±.0001
EVRJ071431.63-60949.0	GaiaDR23058298056594337920	108.6318	-6.1636	12.753 ±.001	55.335 ±.001
EVRJ072950.66-133935.3[c]	GaiaDR23033287603040592896	112.4611	-13.6598	12.691 ±.001	166.199 ±.009
EVRJ074738.21+053614.4	GaiaDR23137857549744826752	116.9092	5.6040	14.167 ±.001	3.60397 ±.00001
EVRJ075018.70-252635.5	GaiaDR25602331396479925120	117.5779	-25.4432	13.829 ±.001	509.3 ±.8
EVRJ075521.12-163622.3	GaiaDR25718296303734937856	118.8380	-16.6062	13.618 ±.001	57.997 ±.001
EVRJ080955.39-461701.3	GaiaDR25519602045642615808	122.4808	-46.2837	11.029 ±.001	19.9735 ±.0001
EVRJ081242.38-180840.6	GaiaDR25719913582258286592	123.1766	-18.1446	13.243 ±.001	196.78 ±.01
EVRJ090801.42-461506.1	GaiaDR25327604500572716928	137.0059	-46.2517	10.476 ±.001	112.444 ±.004
EVRJ150433.67-170155.2	GaiaDR26305932286056884480	226.1403	-17.0320	13.584 ±.001	10.90413 ±.00003
EVRJ155252.37-645012.5[d]	GaiaDR25825969999996438656	238.2182	-64.8368	12.814 ±.006	21.1933 ±.0001

[a](noted as a potential super giant in [164], and as an unidentifiable variable in [149]),
[b](noted as a potential OB star in [165]),
[c](noted as a potential OB star in [166]),
[d](noted as a unidentifiable variable ASASSN-V J155246.87-644843.7 in [167])

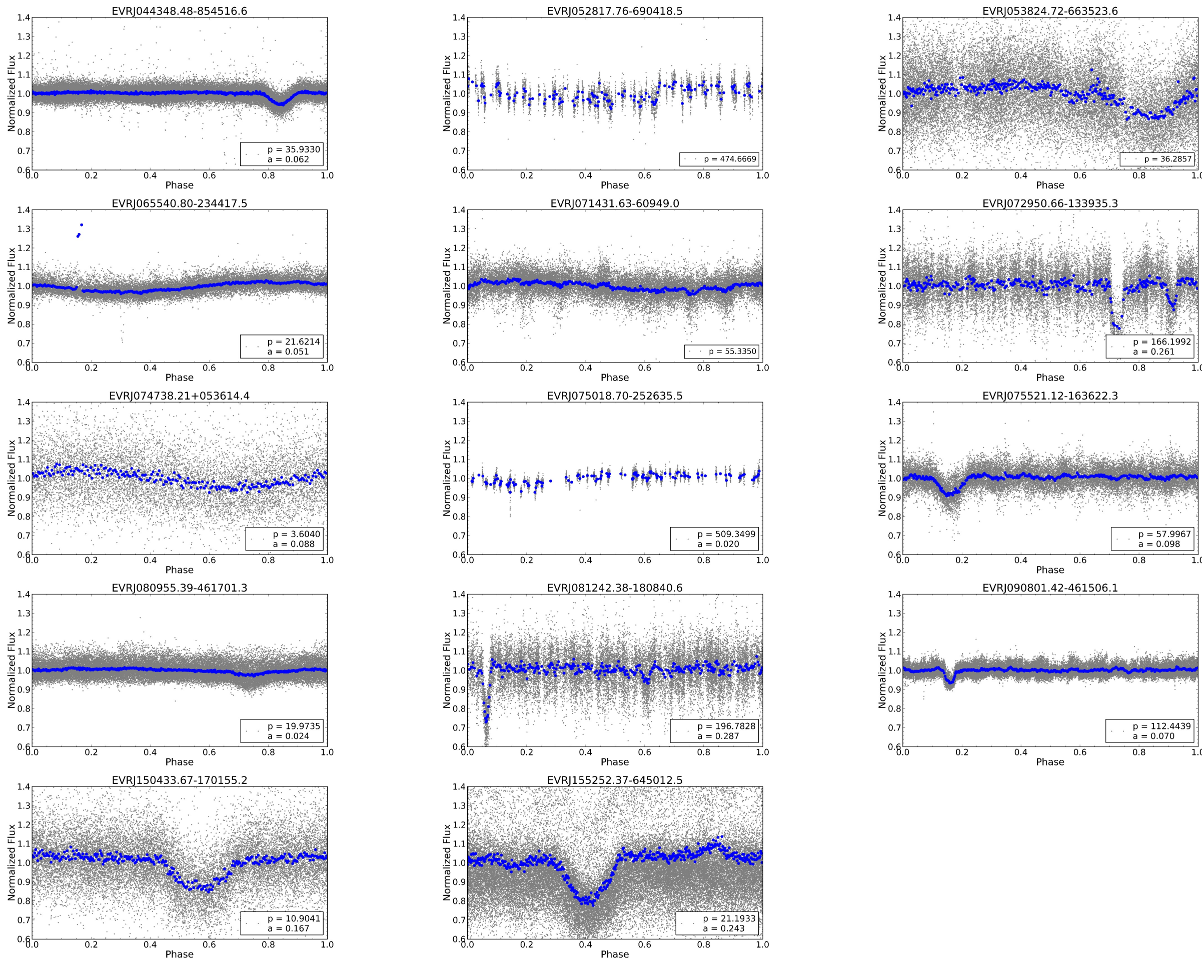

Figure C.1: The Evryscope light curves of variable discoveries (likely A stars or other stellar types) showing variable signals with periods ranging from a few hours to several months. The period and amplitudes shown are from the best LS fit for the sinusoidal variables, and for the eclipsing binaries a Gaussian is fit to the primary eclipse to measure the depth. Grey points = 2 minute cadence, blue points = binned in phase.

APPENDIX D: EVR-CB-001 OTHER INFORMATION

Table D.1: Radial Velocity Measurements for EVR-CB-001

Date (HJD - 2400000)	HRV (km s^{-1})	Error (km s^{-1})
58471.803878	-174.6	5.6
58472.774916	-159.5	6.3
58480.807545	-37.3	8.7
58480.814542	59.6	7.8
58480.821538	136.8	6.3
58481.780158	-68.2	6.5
58481.787154	21.2	6.6
58481.794151	96.3	7.1
58483.747175	121.3	10.5
58483.754171	174.0	6.5
58483.761167	209.6	6.3
58484.759870	72.3	7.5
58484.766867	-13.3	6.9
58484.773863	-100.0	6.1
58494.797850	197.6	6.8
58494.804847	172.4	8.0
58494.811844	95.1	8.4
58495.678095	214.6	10.4
58495.685092	167.9	11.1
58495.692088	67.5	18.6
58498.616498	116.1	7.7
58498.623495	21.7	9.7
58498.630492	-78.2	7.7
58508.806792	-150.3	7.5
58508.813790	-96.6	6.9
58508.820784	-22.3	9.8
58511.718685	-151.1	6.4
58511.725684	-179.1	5.5
58511.732681	-171.9	5.8

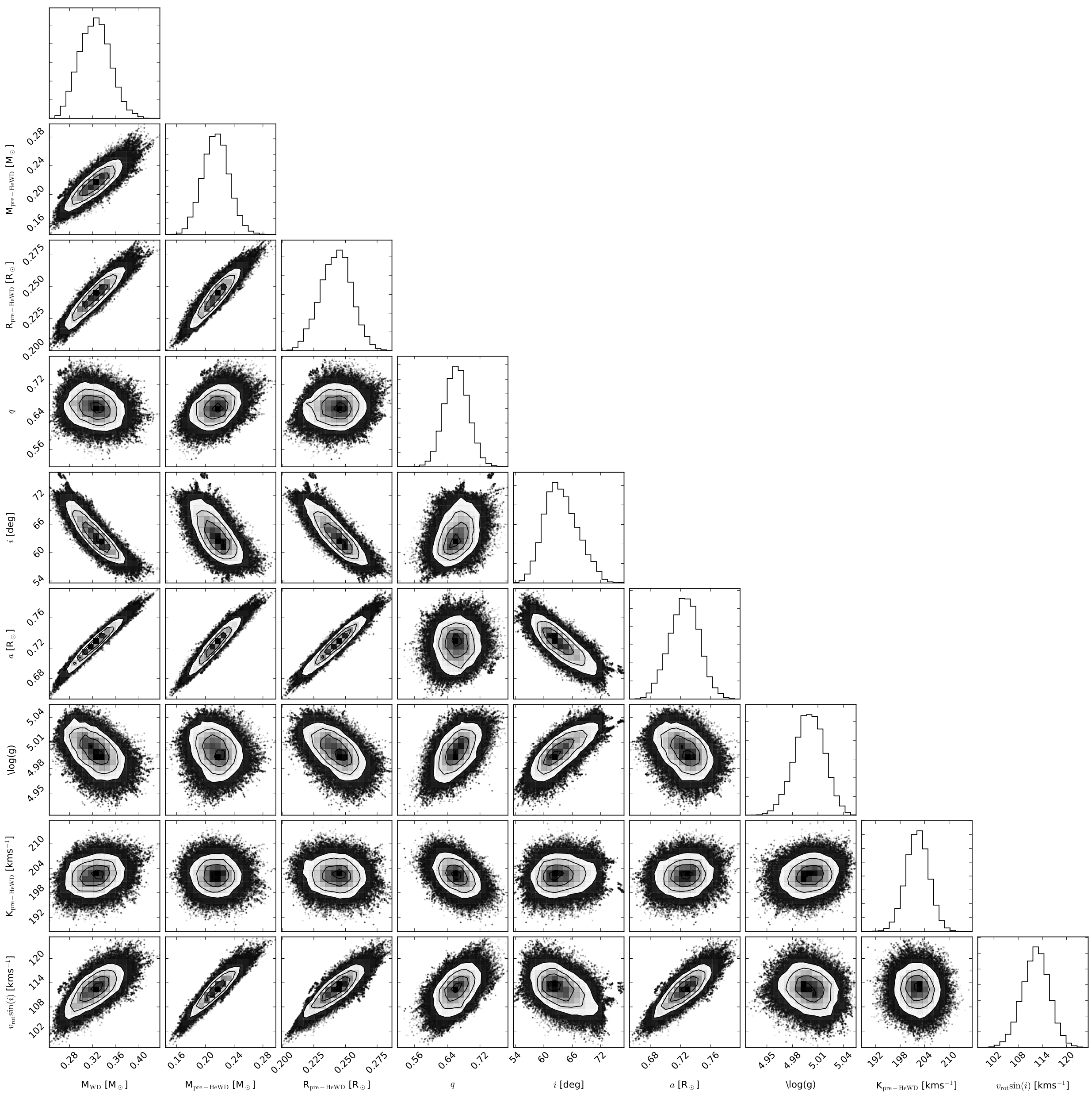

Figure D.1: Corner plots of the lightcurve fit of EVR-CB-001. The solution converged at low masses ($0.32M_{\odot}$ for the He WD and $0.21M_{\odot}$ for the pre-He WD), an inflated pre-He WD radius ($0.24R_{\odot}$). Shown on the x-axis from left to right are: M_2, M_1, R_1, i, a as well as the photometrically constrained $\log(g)$, velocity semi-amplitude K_1 and projected rotational velocity $v_{\rm rot}\sin(i)$.

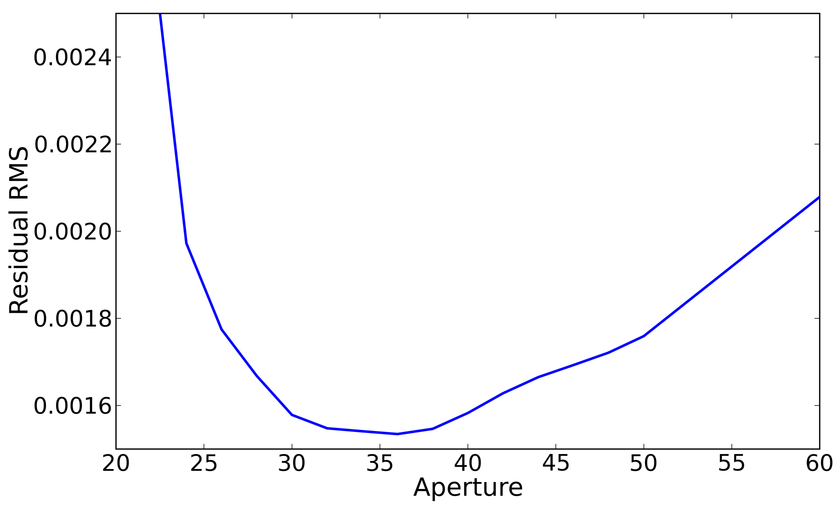

Figure D.2: The best aperture for the EVR-CB-001 SOAR light curve is a radius of 36 pixels giving a residual rms of .00153.

APPENDIX E: EVR-CB-004 OTHER INFORMATION

Shown following in Figure E.1 are the corner plots demonstrating the light curve goodness of fit and convergence. Listed in Table E.1 is the data used for the SED fitting. Figure E.2 shows the SOAR light curve of the nearby stars, potentially blended in the TESS pixels. They are shown here to be non variable. Finally, we domonstrate that EVR-CB-004 is likely a member of the Galactic thin disc population by performing a kinematic analysis.

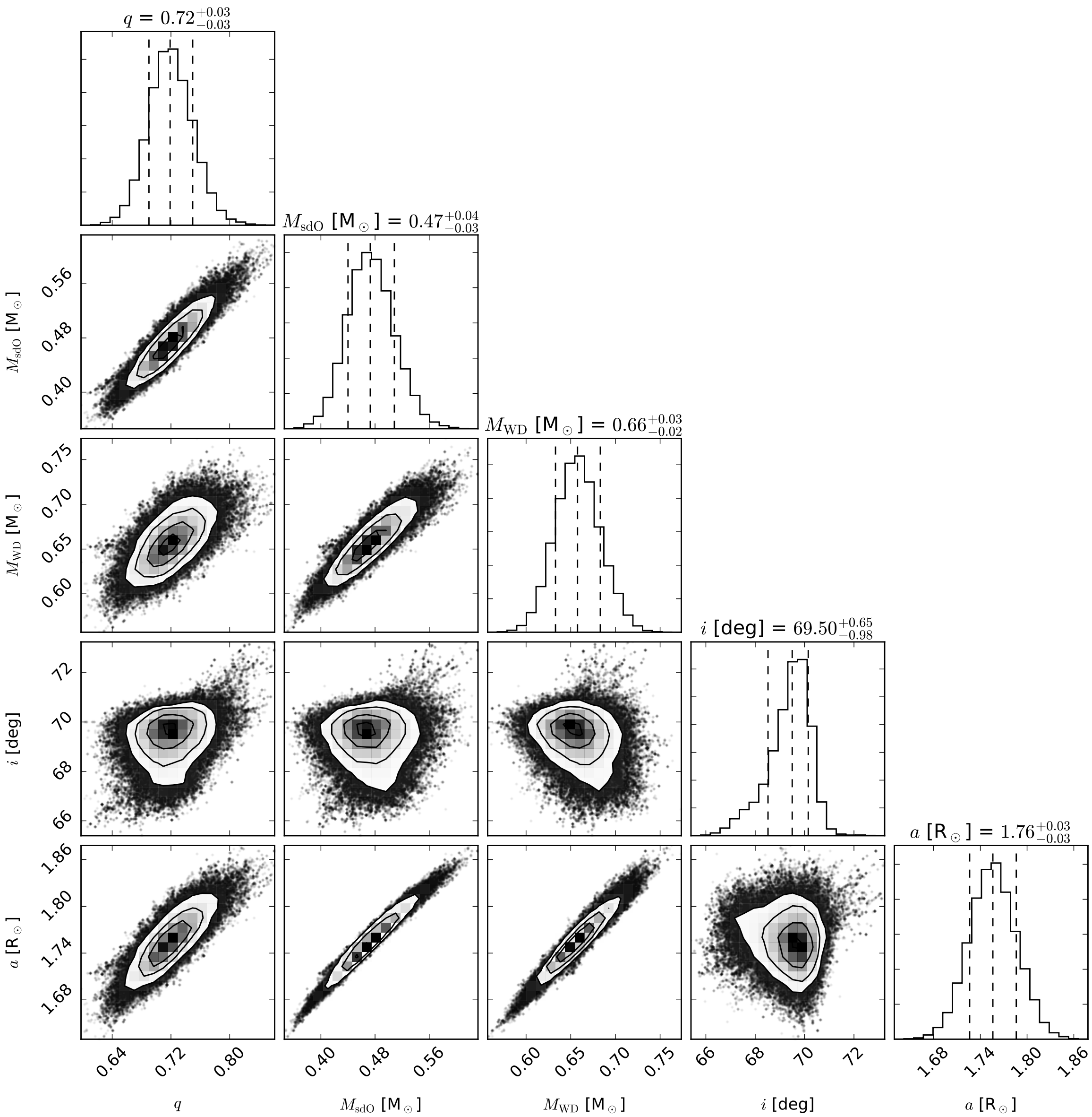

Figure E.1: Corner plots of the lightcurve fit of EVR-CB-004. The solution converged at masses ($0.66M_{\odot}$ for the WD and $0.47M_{\odot}$ for the sdO), an inflated sdO radius ($0.62R_{\odot}$). Shown on the x-axis from left to right are: M_2, M_1, R_1, i and a

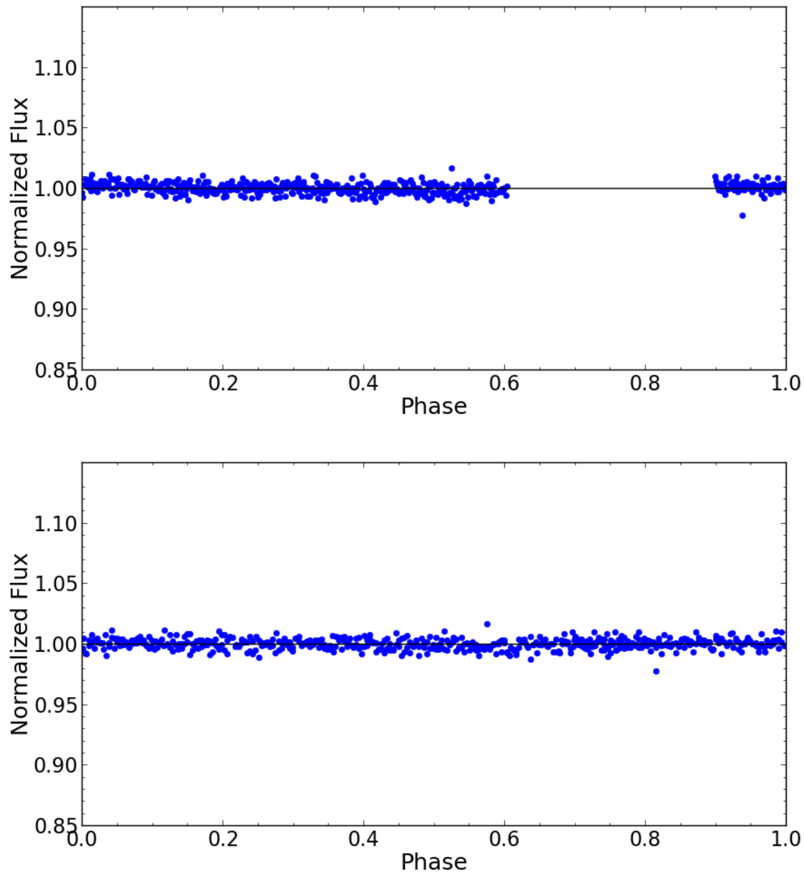

Figure E.2: *Top:* The combined light curve from the SOAR data of the three nearby stars, processed with the same photometric pipeline used to generate the EVR-CB-004 SOAR light curve. The data is folded on the 6.084 hour orbital period, and shows no signs of variability. The total flux of these three stars is 2.5% of the total flux from EVR-CB-004, shown normalized here. *Bottom:* The same data folded on the 2.028 hour alias period, again showing no signs of variability. This analysis demonstrates the potential contaminants in the TESS photometric aperture do not introduce additional variability into the light curve. Most notably the low amplitude resonant signal cannot be attributed to a TESS blended pixel systematic.

Table E.1: Photometric data of EVR-CB-004 used for the SED fitting. $\star$: 1σ statistical uncertainties only; $\dagger$: Extracted from: http://skymapper.anu.edu.au/cone-search/requests/9AVUPMK7/edit/

System	Passband	Magnitude	Uncertainty	Reference
Gaia	G	13.1266	0.0023*	(Gaia Collaboration et al. 2018, Gaia DR2: I/345/gaia2)
Gaia	GBP	12.9693	0.0093*	(Gaia Collaboration et al. 2018, Gaia DR2: I/345/gaia2)
Gaia	GRP	13.2841	0.0072*	(Gaia Collaboration et al. 2018, Gaia DR2: I/345/gaia2)
SDSS	g	13.0270	0.0060*	(Ahn et al. 2012, SDSS DR9)
SkyMapper	u	12.7480	0.0030*	(Wolf et al. 2018, SkyMapper DR1†)
SkyMapper	v	12.8860	0.0030*	(Wolf et al. 2018, SkyMapper DR1†)
SkyMapper	g	13.0620	0.0030*	(Wolf et al. 2018, SkyMapper DR1†)
SkyMapper	r	13.3200	0.0030*	(Wolf et al. 2018, SkyMapper DR1†)
SkyMapper	i	13.6760	0.0030*	(Wolf et al. 2018, SkyMapper DR1†)
SkyMapper	z	13.9660	0.0040*	(Wolf et al. 2018, SkyMapper DR1†)
PanSTARRS	i	13.6400	0.0516*	(Chambers et al. 2016, PanSTARRS DR1: II/349/ps1)
PanSTARRS	z	13.8743	0.0160*	(Chambers et al. 2016, PanSTARRS DR1: II/349/ps1)
PanSTARRS	y	14.0211	0.0060*	(Chambers et al. 2016, PanSTARRS DR1: II/349/ps1)
2MASS	H	13.7170	0.0270*	(Skrutskie et al. 2006, 2MASS: II/246/out)
2MASS	J	13.5910	0.0270*	(Skrutskie et al. 2006, 2MASS: II/246/out)
2MASS	K	13.8150	0.0520*	(Skrutskie et al. 2006, 2MASS: II/246/out)
WISE	W1	13.8210	0.0260*	(Wright et al. 2010; Cutri et al. 2013, AllWISE: II/328/allwise)
WISE	W2	13.8750	0.0360*	(Wright et al. 2010; Cutri et al. 2013, AllWISE: II/328/allwise)

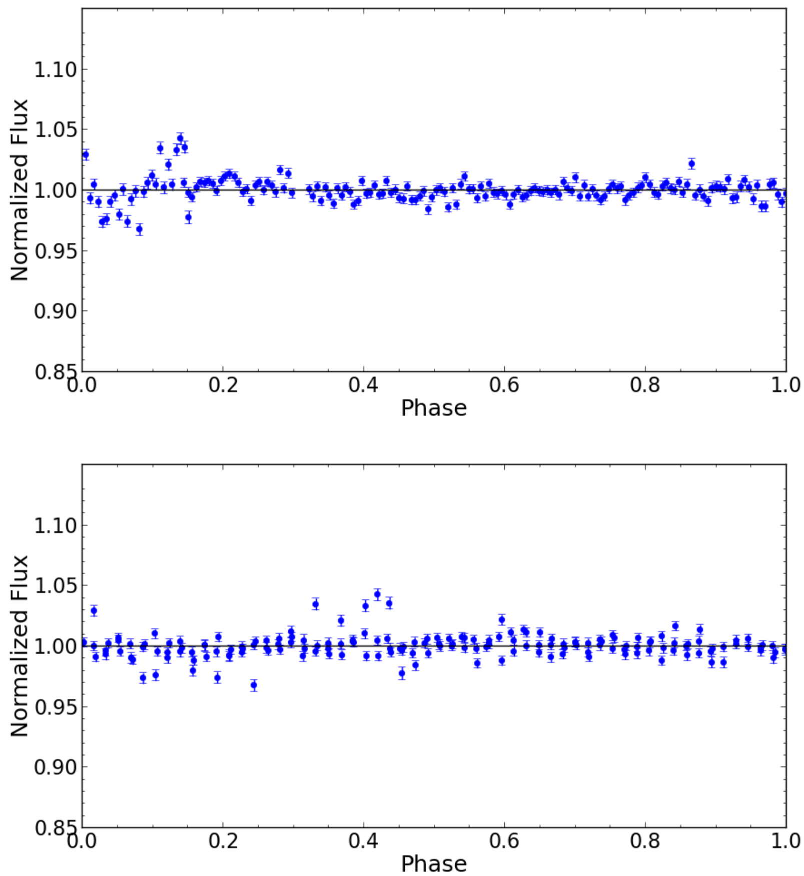

Figure E.3: *Top:* The combined light curve from the PROMPT data of the three nearby stars, processed with the same photometric pipeline used to generate the EVR-CB-004 PROMPT light curve. The data is folded on the 6.084 hour orbital period, and shows no signs of variability. *Bottom:* The same data folded on the 2.028 hour alias period, again showing no signs of variability. In the PROMPT R passband, the total flux of these three stars increases to 35% of the total flux from EVR-CB-004. This concern is mitigated by the constant signal that again demonstrates the potential contaminants in the TESS photometric aperture do not introduce additional variability into the light curve. Most notably the low amplitude resonant signal cannot be attributed to a TESS blended pixel systematic. The constant signal in this filter could dilute the EVR-CB-004 light curve amplitude, and consequently affect the fit. The main light curve variation shows no signs of this, the amplitudes are consistent from the different observations, and independent system solutions are the same (within the measurement precision) using SOAR, PROMPT, and TESS data. We therefore conclude the nearby stars did not contribute in any significant way to the TESS photometry.

We studied the kinematics of EVR-CB-004 by integrating the equation of motion in a Galactic motions using the code developed by [299] and the Galactic mass model of [300]. In order to study the characteristics of the Galactic orbits we calculated the Galactic velocity components U, V, and W as described by [299], the z component of the orbital angular momentum, and the eccentricity of the Galactic orbit as described in [301] and constructed diagnostic diagrams, that is the U-V and J_z-e diagram to compare with the kinematical properties of Galactic stellar populations . In addition, we inspected the morphology of the Galactic orbit and categorized its population membership [for details see 302], by also making the Toomre diagram (see Fig. E.4). All indicators point to EVR-CB-004 being a member of the Galactic thin disk.

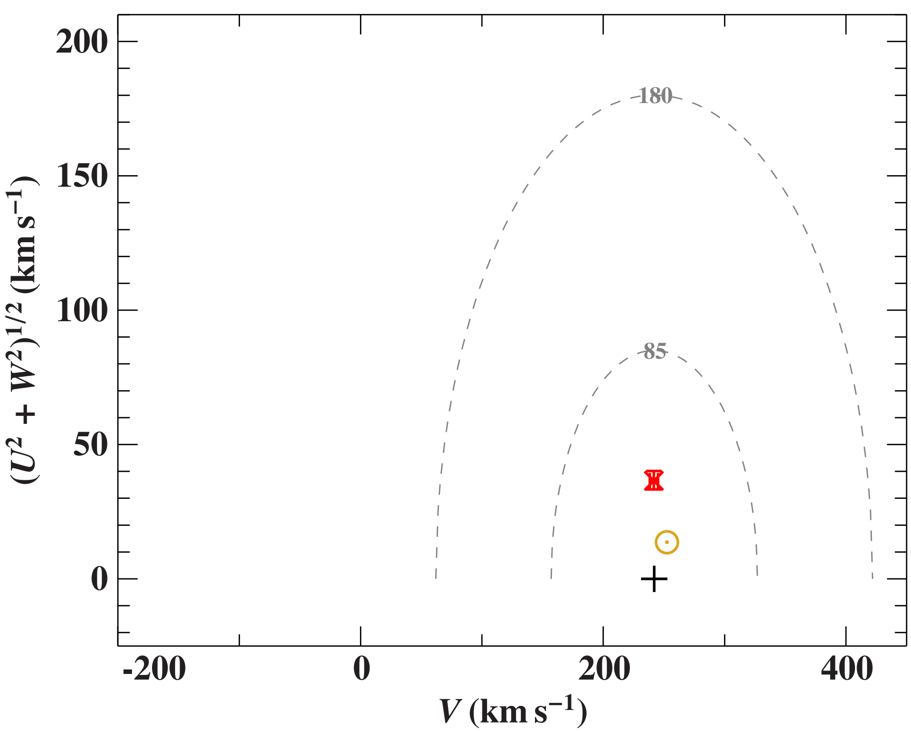

Figure E.4: The Toomre diagram for EVR-CB-004 (the red cross), showing the combined vertical and radial velocity on the y-axis and the rotational velocity on the x-axis (and representative of the kinetic energy components). Stars with lower total velocities (constrained by $v_{\mathrm{tot}} = \sqrt{U^2 + W^2 + V^2} < 85$ km s^{-1} in this parameter space, as indicated by the inner dashed line) are rotationally dominated and likely to be part of the thin disc population, whereas stars with $v_{\mathrm{tot}} > 180$ km s^{-1} likely belong to the halo. In between, the thick disc population is likely to be found. See [303] for further details.

APPENDIX F: HWVIR DISCOVERIES OTHER INFORMATION

Shown in the Appendix are the corner plots for the systems, multi-filter light curve solutions, the canonical sdB mass for EVR-CB-003, and the light curve modeling parameters.

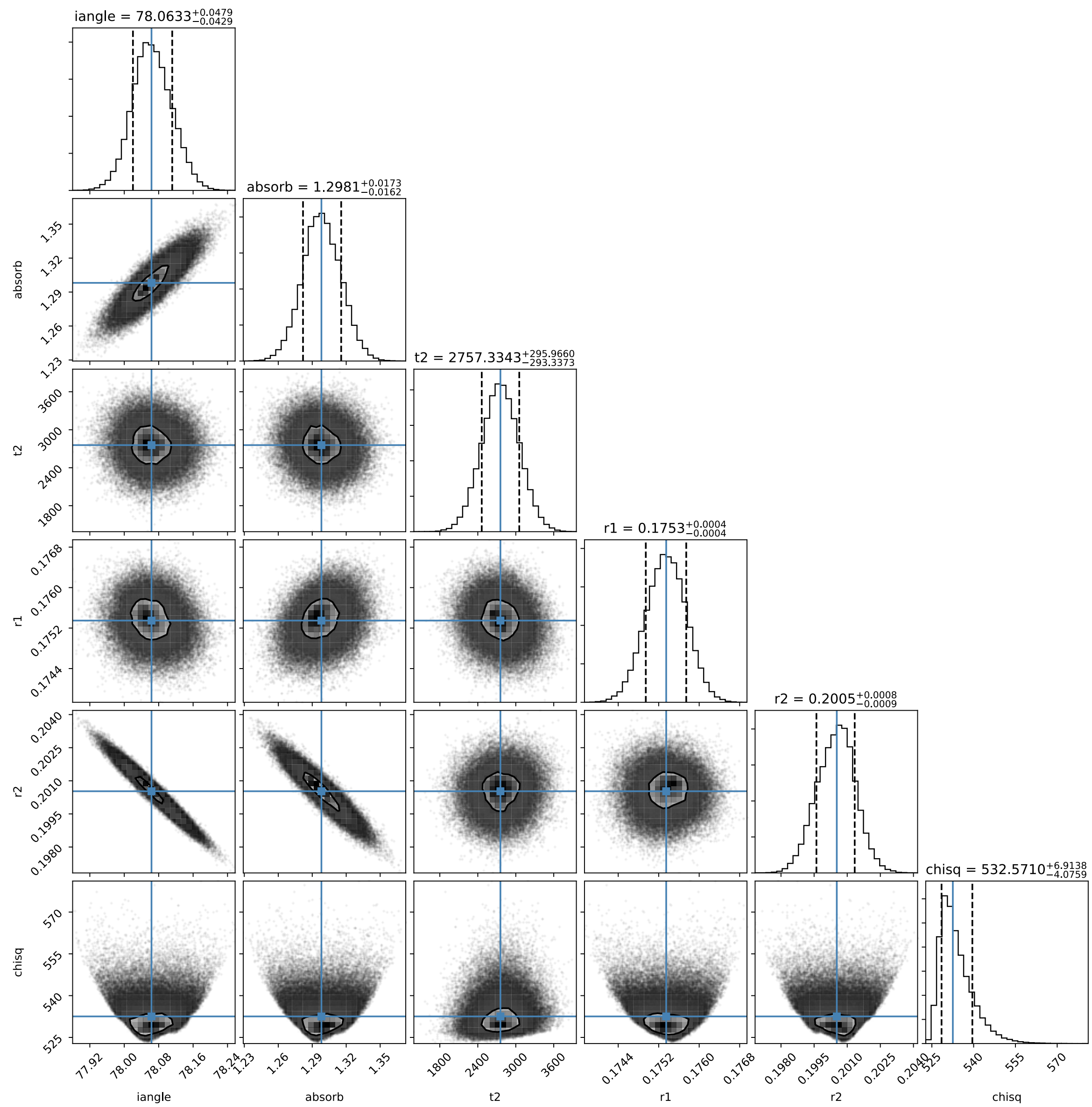

Figure F.1: Corner plot of EVR-CB-003.

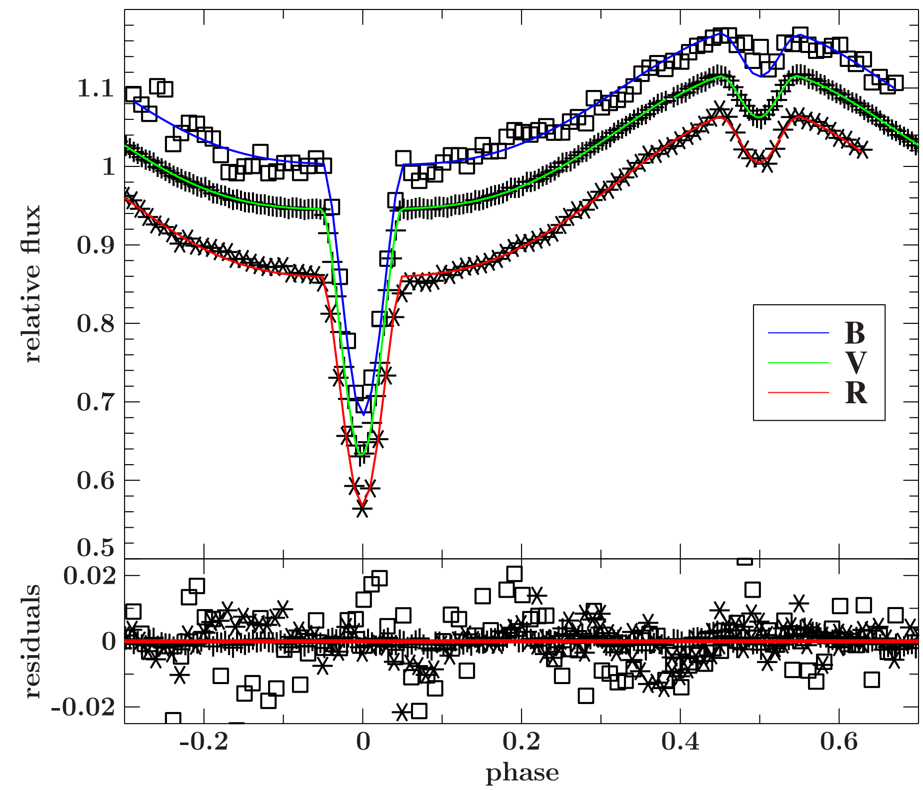

Figure F.2: The light curve modeling solutions to EVR-CB-003 using multiple passbands and with a very high SNR SOAR light curve fit shown in green.

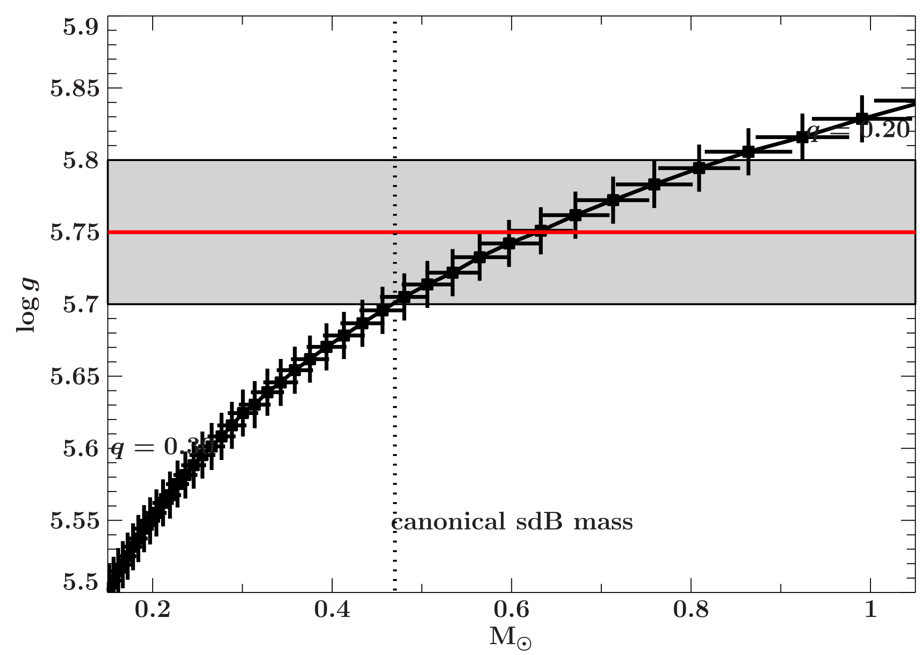

Figure F.3: The sdB mass vs surface gravity for EVR-CB-003. The canonical mass would require a 3-σ difference in surface gravity from our measured value. The slightly higher than average surface gravity and smaller radius are also consistent with the preferred higher mass solution.

REFERENCES

[1] Law NM, Kulkarni SR, Dekany RG, Ofek EO, Quimby RM, Nugent PE, Surace J, Grillmair CC, Bloom JS, Kasliwal MM, Bildsten L, Brown T, Cenko SB, Ciardi D, Croner E, Djorgovski SG, van Eyken J, Filippenko AV, Fox DB, Gal-Yam A, Hale D, Hamam N, Helou G, Henning J, Howell DA, Jacobsen J, Laher R, Mattingly S, McKenna D, Pickles A, Poznanski D, Rahmer G, Rau A, Rosing W, Shara M, Smith R, Starr D, Sullivan M, Velur V, Walters R, Zolkower J. The Palomar Transient Factory: System Overview, Performance, and First Results. *PASP* 2009; 121:1395–1408.

[2] Bellm EC. Life Beyond PTF. *ArXiv e-prints* 2018; .

[3] Kaiser N, Burgett W, Chambers K, Denneau L, Heasley J. Pan-STARRS. In: *Society of Photo-Optical Instrumentation Engineers*, In: *Society of Photo-Optical Instrumentation Engineers*, January 2010

[4] Keller SC, Schmidt BP, Bessell MS, Conroy PG, Francis P, Granlund A, Kowald E, Oates AP, Martin-Jones T, Preston T, Tisserand P, Vaccarella A, Waterson MF. The SkyMapper Telescope and The Southern Sky Survey. *PASP* 2007; 24:1–12.

[5] Ivezić Ž, Kahn SM, Tyson JA, Abel B, Acosta E, Allsman R, Alonso D, AlSayyad Y, Anderson SF, Andrew J, et al. LSST: From Science Drivers to Reference Design and Anticipated Data Products. *ApJ* 2019; 873:111.

[6] Bakos G, Noyes RW, Kovács G, Stanek KZ, Sasselov DD, Domsa I. Wide-Field Millimagnitude Photometry with the HAT: A Tool for Extrasolar Planet Detection. *PASP* 2004; 116:266–277.

[7] Bakos GÁ. “The HATNet and HATSouth Exoplanet Surveys”, p. 111. 2018.

[8] Pollacco DL, Skillen I, Collier Cameron A, Christian DJ, Hellier C, Irwin J, Lister TA, Street RA, West RG, Anderson DR, Clarkson WI, Deeg H, Enoch B, Evans A, Fitzsimmons A, Haswell CA, Hodgkin S, Horne K, Kane SR, Keenan FP, Maxted PFL, Norton AJ, Osborne J, Parley NR, Ryans RSI, Smalley B, Wheatley PJ, Wilson DM. The WASP Project and the SuperWASP Cameras. *PASP* 2006; 118:1407–1418.

[9] Pepper J, Pogge RW, DePoy DL, Marshall JL, Stanek KZ, Stutz AM, Poindexter S, Siverd R, O’Brien TP, Trueblood M, Trueblood P. The Kilodegree Extremely Little Telescope (KELT): A Small Robotic Telescope for Large-Area Synoptic Surveys. *PASP* 2007; 119:923–935.

[10] McCullough PR, Stys JE, Valenti JA, Fleming SW, Janes KA, Heasley JN. The XO Project: Searching for Transiting Extrasolar Planet Candidates. *PASP* 2005; 117:783–795.

[11] Talens GJJ, Spronck JFP, Lesage AL, Otten GPPL, Stuik R, Pollacco D, Snellen IAG. The Multi-site All-Sky CAmeRA (MASCARA). Finding transiting exoplanets around bright stars. *AAP* 2017; 601:A11.

[12] Nutzman P, Charbonneau D. Design Considerations for a Ground-Based Transit Search for Habitable Planets Orbiting M Dwarfs. *PASP* 2008; 120:317.

[13] Csépány G, Pál A, Vida K, Regály Z, Mészáros L, Oláh K, Kiss C, Döbrentei L, Jaskó A, Mezõ G, Farkas E. The Fly's Eye Camera System: An Instrument Design for Large Étendue Time Domain Surveys. In: "*Astronomical Data Analysis Software and Systems XXII* (Friedel DN, Ed.), In: "*Astronomical Data Analysis Software and Systems XXII* (Friedel DN, Ed.), October 2013 p. 369.

[14] Piotrowski LW, Batsch T, Czyrkowski H, Cwiok M, Dabrowski R, Kasprowicz G, Majcher A, Majczyna A, Malek K, Mankiewicz L, Nawrocki K, Opiela R, Siudek M, Sokolowski M, Wawrzaszek R, Wrochna G, Zaremba M, Żarnecki AF. PSF modelling for very wide-field CCD astronomy. *AAP* 2013; 551:A119.

[15] Shappee B, Prieto J, Stanek KZ, Kochanek CS, Holoien T, Jencson J, Basu U, Beacom JF, Szczygiel D, Pojmanski G, Brimacombe J, Dubberley M, Elphick M, Foale S, Hawkins E, Mullins D, Rosing W, Ross R, Walker Z. All Sky Automated Survey for SuperNovae (ASAS-SN or "Assassin"). In: *American Astronomical Society Meeting Abstracts #223*, In: *American Astronomical Society Meeting Abstracts #223*, January 2014 p. 236.03.

[16] Ricker GR, Winn JN, Vanderspek R, Latham DW, Bakos GÁ, Bean JL, Berta-Thompson ZK, Brown TM, Buchhave L, Butler NR, Butler RP, Chaplin WJ, Charbonneau D, Christensen-Dalsgaard J, Clampin M, Deming D, Doty J, De Lee N, Dressing C, Dunham EW, Endl M, Fressin F, Ge J, Henning T, Holman MJ, Howard AW, Ida S, Jenkins J, Jernigan G, Johnson JA, Kaltenegger L, Kawai N, Kjeldsen H, Laughlin G, Levine AM, Lin D, Lissauer JJ, MacQueen P, Marcy G, McCullough PR, Morton TD, Narita N, Paegert M, Palle E, Pepe F, Pepper J, Quirrenbach A, Rinehart SA, Sasselov D, Sato B, Seager S, Sozzetti A, Stassun KG, Sullivan P, Szentgyorgyi A, Torres G, Udry S, Villasenor J. Transiting Exoplanet Survey Satellite (TESS). In: *Space Telescopes and Instrumentation 2014: Optical, Infrared, and Millimeter Wave*, In: *Space Telescopes and Instrumentation 2014: Optical, Infrared, and Millimeter Wave*, August 2014 p. 914320.

[17] Law NM, Fors O, Ratzloff J, Wulfken P, Kavanaugh D, Sitar DJ, Pruett Z, Birchard MN, Barlow BN, Cannon K, Cenko SB, Dunlap B, Kraus A, Maccarone TJ. Evryscope science: Exploring the potential of all-sky gigapixel-scale telescopes. *PASP* 2015; 127.

[18] Tonry JL, Stubbs CW, Lykke KR, Doherty P, Shivvers IS, Burgett WS, Chambers KC, Hodapp KW, Kaiser N, Kudritzki RP, Magnier EA, Morgan JS, Price PA, Wainscoat RJ. The Pan-STARRS1 Photometric System. *ApJ* 2012; 750:99.

[19] Ratzloff JK, Law NM, Fors O, Corbett HT, Howard WS, del Ser D, Haislip J. Building the Evryscope: Hardware Design and Performance. *arXiv e-prints* 2019; p. arXiv:1904.11991.

[20] Ratzloff JK, Barlow BN, Kupfer T, Corcoran KA, Geier S, Bauer E, Corbett HT, Howard WS, Glazier A, Law NM. EVR-CB-001: An Evolving, Progenitor, White Dwarf Compact Binary Discovered with the Evryscope. *ApJ* 2019; 883:51.

[21] Tokovinin A, Corbett H, Fors O, Howard W, Law NM, Moe M, Ratzloff J, Walter FM. Young and Eccentric: The Quadruple System HD 86588. *AJ* 2018; 156:120.

[22] Kosiarek MR, Crossfield IJM, Hardegree-Ullman KK, Livingston JH, Benneke B, Henry GW, Howard WS, Berardo D, Blunt S, Fulton BJ, Hirsch LA, Howard AW, Isaacson H, Petigura EA, Sinukoff E, Weiss L, Bonfils X, Dressing CD, Knutson HA, Schlieder JE, Werner M, Gorjian V, Krick J, Morales FY, Astudillo-Defru N, Almenara JM, Delfosse X, Forveille T, Lovis C, Mayor M, Murgas F, Pepe F, Santos NC, Udry S, Corbett HT, Fors O, Law NM, Ratzloff JK, del Ser D. Bright Opportunities for Atmospheric Characterization of Small Planets: Masses and Radii of K2-3 b, c, and d and GJ3470 b from Radial Velocity Measurements and Spitzer Transits. *AJ* 2019; 157:97.

[23] Howard WS, Tilley MA, Corbett H, Youngblood A, Loyd ROP, Ratzloff JK, Law NM, Fors O, del Ser D, Shkolnik EL, Ziegler C, Goeke EE, Pietraallo AD, Haislip J. The first naked-eye superflare detected from proxima centauri. *The Astrophysical Journal Letters* 2018; 860:L30.

[24] Corbett H, Law N, Goeke E, Ratzloff J, Howard W, Fors O, del Ser D, Quimby RM. Pre-Discovery Detection of ASASSN-18fv by Evryscope. *The Astronomer's Telegram* 2018; 11467.

[25] Torres G. On the Use of Empirical Bolometric Corrections for Stars. *AJ* 2010; 140:1158–1162.

[26] Mann AW, Feiden GA, Gaidos E, Boyajian T, von Braun K. How to Constrain Your M Dwarf: Measuring Effective Temperature, Bolometric Luminosity, Mass, and Radius. *ApJ* 2015; 804:64.

[27] Kraus AL, Douglas ST, Mann AW, Agüeros MA, Law NM, Covey KR, Feiden GA, Rizzuto AC, Howard AW, Isaacson H, Gaidos E, Torres G, Bakos G. The Factory and the Beehive. III. PTFEB132.707+19.810, A Low-mass Eclipsing Binary in Praesepe Observed by PTF and K2. *ApJ* 2017; 845:72.

[28] Kovacs G, Zucker S, Mazeh T. A box-fitting algorithm in the search for periodic transits. *Astron. Astrophys.* 2002; 391:369–377.

[29] Ofir A. Optimizing the search for transiting planets in long time series. *AAP* 2014; 561:A138.

[30] Lomb NR. Least-Squares Frequency Analysis of Unequally spaced data. *Astrophysics and Space Science* 1975; 39:447–462.

[31] Scargle JD. Studies in Astronomical Time Series Analysis II. Statistical Aspects of Spectral Analysis of Unevenly spaced data. *Astrophysics and Space Science* 1982; 263:835–853.

[32] Jayasinghe T, Stanek KZ, Kochanek CS, Shappee BJ, Holoien TWS, Thompson TA, Prieto JL, Dong S, Pawlak M, Pejcha O, Shields JV, Pojmanski G, Otero S, Hurst N, Britt CA, Will D. The ASAS-SN catalogue of variable stars III: variables in the southern TESS continuous viewing zone. *MNRAS* 2019; 485:961–971.

[33] Clemens JC, Crain JA, Anderson R. The Goodman spectrograph. In: "*Ground-based Instrumentation for Astronomy* (Moorwood AFM, Iye M, Eds.), In: "*Ground-based Instrumentation for Astronomy* (Moorwood AFM, Iye M, Eds.), September 2004 pp. 331–340.

[34] Kesseli A, West AA, Harrison B, Veyette M, Feldman D. PyHammer: An Automatic and Visual Suite for Spectral Typing Stars. In: *American Astronomical Society Meeting Abstracts #229*, In: *American Astronomical Society Meeting Abstracts #229*, Jan 2017 p. 240.35.

[35] Németh P. Astroserver - Research Services in the Stellar Webshop. *Open Astronomy* 2017; 26:179–186.

[36] Reichart D, Nysewander M, Moran J, Bartelme J, Bayliss M, Foster A, Clemens JC, Price P, Evans C, Salmonson J, Trammell S, Carney B, Keohane J, Gotwals R. PROMPT: Panchromatic Robotic Optical Monitoring and Polarimetry Telescopes. *Nuovo Cimento C Geophysics Space Physics C* 2005; 28:767.

[37] Copperwheat CM, Marsh TR, Dhillon VS, Littlefair SP, Hickman R, Gänsicke BT, Southworth J. Physical properties of IP Pegasi: an eclipsing dwarf nova with an unusually cool white dwarf. *MNRAS* 2010; 402:1824–1840.

[38] Tokovinin A, Fischer DA, Bonati M, Giguere MJ, Moore P, Schwab C, Spronck JFP, Szymkowiak A. CHIRON A Fiber Fed Spectrometer for Precise Radial Velocities. *PASP* 2013; 125:1336.

[39] Farihi J, Koester D, Zuckerman B, Vican L, Gänsicke BT, Smith N, Walth G, Breedt E. Solar abundances of rock-forming elements, extreme oxygen and hydrogen in a young polluted white dwarf. *Monthly Notices of the Royal Astronomical Society* 2016; 463:3186–3192.

[40] Zuckerman B, Melis C, Klein B, Koester D, Jura M. Ancient Planetary Systems are Orbiting a Large Fraction of White Dwarf Stars. *The Astrophysical Journal* 2010; 722:725–736.

[41] van Lieshout R, Kral Q, Charnoz S, Wyatt MC, Shannon A. Exoplanet recycling in massive white-dwarf debris discs. *Monthly Notices of the Royal Astronomical Society* 2018; 480:2784–2812.

[42] Agol E. Transit Surveys for Earths in the Habitable Zones of White Dwarfs. *ApJL* 2011; 731:L31.

[43] Faedi F, West RG, Burleigh MR, Goad MR, Hebb L. Detection Limits for Close Eclipsing and transiting Sub-Stellar and Planetary Companions to White Dwarfs in the WASP Survey. In: "*American Institute of Physics Conference Series* (Schuh S, Drechsel H, Heber U, Eds.), In: "*American Institute of Physics Conference Series* (Schuh S, Drechsel H, Heber U, Eds.), Mar 2011 pp. 254–261.

[44] Fulton BJ, Tonry JL, Flewelling H, Burgett WS, Chambers KC, Hodapp KW, Huber ME, Kaiser N, Wainscoat RJ, Waters C. A Search for Planetary Eclipses of White Dwarfs in the Pan-STARRS1 Medium-deep Fields. *ApJ* 2014; 796:114.

[45] Rowan DM, Tucker MA, Shappee BJ, Hermes JJ. Detections and constraints on white dwarf variability from time-series GALEX observations. *MNRAS* 2019; 486:4574–4589.

[46] van Sluijs L, Van Eylen V. The occurrence of planets and other substellar bodies around white dwarfs using K2. *MNRAS* 2018; 474:4603–4611.

[47] Vanderburg A, Johnson JA, Rappaport S, Bieryla A, Irwin J, Lewis JA, Kipping D, Brown WR, Dufour P, Ciardi DR. A disintegrating minor planet transiting a white dwarf. *Nature* 2015; 526:546–549.

[48] Hallakoun N, Maoz D, Kilic M, Mazeh T, Gianninas A, Agol E, Bell KJ, Bloemen S, Brown WR, Debes J, Faigler S, Kull I, Kupfer T, Loeb A, Morris BM, Mullally F. SDSS J1152+0248: an eclipsing double white dwarf from the Kepler K2 campaign. *MNRAS* 2016; 458:845–854.

[49] Gentile Fusillo NP, Tremblay PE, Gänsicke BT, Manser CJ, Cunningham T, Cukanovaite E, Hollands M, Marsh T, Raddi R, Jordan S. A Gaia Data Release 2 catalogue of white dwarfs and a comparison with SDSS. *MNRAS* 2019; 482:4570–4591.

[50] Han Z, Podsiadlowski P, Maxted PFL, Marsh TR, Ivanova N. The origin of subdwarf B stars - I. The formation channels. *MNRAS* 2002; 336:449–466.

[51] Han Z, Podsiadlowski P, Maxted PFL, Marsh TR. The origin of subdwarf B stars - II. *MNRAS* 2003; 341:669–691.

[52] Heber U. Hot subluminous stars. *Publications of the Astronomical Society of the Pacific* 2016; 128:082001.

[53] Maxted PFL, Heber U, Marsh TR, North RC. The binary fraction of extreme horizontal branch stars. *MNRAS* 2001; 326:1391–1402.

[54] Napiwotzki R, Karl CA, Lisker T, Heber U, Christlieb N, Reimers D, Nelemans G, Homeier D. Close binary EHB stars from SPY. *APSS* 2004; 291:321–328.

[55] Copperwheat CM, Morales-Rueda L, Marsh TR, Maxted PFL, Heber U. Radial-velocity measurements of subdwarf B stars. *MNRAS* 2011; 415:1381–1395.

[56] Maxted PFL, Marsh TR, North RC. KPD 1930+2752: a candidate Type Ia supernova progenitor. *MNRAS* 2000; 317:L41–L44.

[57] Geier S, Nesslinger S, Heber U, Przybilla N, Napiwotzki R, Kudritzki RP. The Subdwarf B+ White Dwarf Binary KPD 1930+2752, a Supernova Type Ia Progenitor Candidate. In: "*15th European Workshop on White Dwarfs* (Napiwotzki R, Burleigh MR, Eds.), In: "*15th European Workshop on White Dwarfs* (Napiwotzki R, Burleigh MR, Eds.), Sep 2007 p. 393.

[58] Vennes S, Kawka A, O'Toole SJ, Németh P, Burton D. The Shortest Period sdB Plus White Dwarf Binary CD-30 11223 (GALEX J1411-3053). *ApJL* 2012; 759:L25.

[59] Geier S, Marsh TR, Wang B, Dunlap B, Barlow BN, Schaffenroth V, Chen X, Irrgang A, Maxted PFL, Ziegerer E, Kupfer T, Miszalski B, Heber U, Han Z, Shporer A, Telting JH, Gänsicke BT, Østensen RH, O'Toole SJ, Napiwotzki R. A progenitor binary and an ejected mass donor remnant of faint type Ia supernovae. *AAP* 2013; 554:A54.

[60] Kupfer T, van Roestel J, Brooks J, Geier S, Marsh TR, Groot PJ, Bloemen S, Prince TA, Bellm E, Heber U, Bildsten L, Miller AA, Dyer MJ, Dhillon VS, Green M, Irawati P, Laher R, Littlefair SP, Shupe DL, Steidel CC, Rattansoon S, Pettini M. PTF1 J082340.04+081936.5: A Hot Subdwarf B Star with a Low-mass White Dwarf Companion in an 87-minute Orbit. *ApJ* 2017; 835:131.

[61] Schaffenroth V, Geier S, Heber U, Gerber R, Schneider D, Ziegerer E, Cordes O. The MUCHFUSS photometric campaign. *AAP* 2018; 614:A77.

[62] Heber U. Extreme horizontal branch stars. *MEMSAI* 2008; 79:375.

[63] Chen X, Han Z, Deca J, Podsiadlowski P. The orbital periods of subdwarf B binaries produced by the first stable Roche Lobe overflow channel. *MNRAS* 2013; 434:186–193.

[64] Tonry JL. An Early Warning System for Asteroid Impact. *PASP* 2011; 123:58–73.

[65] Djorgovski SG, Drake AJ, Mahabal AA, Graham MJ, Donalek C, Williams R, Beshore EC, Larson SM, Prieto J, Catelan M, Christensen E, McNaught RH. The Catalina Real-Time Transient Survey (CRTS). *ArXiv e-prints* 2011; .

[66] Ratzloff JK, Corbett HT, Law NM, Barlow BN, Glazier A, Howard WS, Fors O, del Ser D, Trifonov T. Variables in the Southern Polar Region Evryscope 2016 Dataset. *arXiv e-prints* 2019; .

[67] Law NM, Sivanandam S, Murowinski R, Carlberg R, Ngan W, Salbi P, Ahmadi A, Steinbring E, Halman M, Graham J. New Exoplanet Surveys in the Canadian High Arctic at 80 Degrees North. In: *Ground-based and Airborne Telescopes IV*, In: *Ground-based and Airborne Telescopes IV*, September 2012 p. 84445C.

[68] Law NM, Carlberg R, Salbi P, Ngan WHW, Ahmadi A, Steinbring E, Murowinski R, Sivanandam S, Kerzendorf W. Exoplanets from the Arctic: The First Wide-field Survey at 80deg $N. 2013; 145 : 58$.

[69] Law NM, Fors O, Ratzloff J, Corbett H, del Ser D, Wulfken P. The Evryscope: design and performance of the first full-sky gigapixel-scale telescope. In: *Ground-based and Airborne Telescopes VI*, In: *Ground-based and Airborne Telescopes VI*, August 2016 p. 99061M.

[70] Ratzloff JK, Law NM, Corbett HT, Fors O, del Ser D. Robotilter: an automated lens/CCD alignment system for the Evryscope. *Journal of Astronomical Telescopes, Instruments, and Systems* 2020; 6:1 – 30.

[71] Pai C, Grossman S, Huang, J. Effects of Moisture on Thermal and Mechanical Properties of Nylon-6,6. *Advances in Polymer Technology* 1989; 2:157–163.

[72] PeterM.Lewis, HowardRogers RHS. A radiometric all-sky infrared camera (rasicam) for des/ctio. A radiometric all-sky infrared camera (rasicam) for des/ctio, 2010. pp. 7735 – 7735 – 12.

[73] Bertin E, Arnouts S. SExtractor: Software for source extraction. *AAPS* 1996; 117:393–404.

[74] Lang D, Hogg DW, Mierle K, Blanton M, Roweis S. Astrometry.net: Blind Astrometric Calibration of Arbitrary Astronomical Images. *AJ* 2010; 139:1782–1800.

[75] Gorski KM, Hivon E, Banday AJ, Wandelt BD, Hansen FK, Reinecke M, Bartelmann M. HEALPix: A framework for high-resolution discretization and fast analysis of data distributed on the sphere. *The Astrophysical Journal* 2005; 622:759–771.

[76] Corcoran KA, Barlow B, Corbett H, Fors O, Howard WS, Law N, Ratzloff J. Updated O-C Diagrams for Several Bright HW Vir Binaries Observed with the Evryscope. In: *American Astronomical Society Meeting Abstracts #231*, In: *American Astronomical Society Meeting Abstracts #231*, Jan 2018 p. 150.23.

[77] Tamuz O, Mazeh T, Zucker S. Correcting systematic effects in a large set of photometric light curves. *MNRAS* 2005; 356:1466–1470.

[78] Roeser S, Demleitner M, Schilbach E. The PPMXL Catalog of Positions and Proper Motions on the ICRS. Combining USNO-B1.0 and the Two Micron All Sky Survey (2MASS). *AJ* 2010; 139:2440–2447.

[79] Henden AA, Levine S, Terrell D, Welch DL. APASS - The Latest Data Release. In: *American Astronomical Society Meeting Abstracts*, In: *American Astronomical Society Meeting Abstracts*, January 2015 p. 336.16.

[80] Loeb A, Maoz D. Detecting biomarkers in habitable-zone earths transiting white dwarfs. *MNRAS* 2013; 432:L11–L15.

[81] Veras D, Xu S, Rebassa-Mansergas A. The critical binary star separation for a planetary system origin of white dwarf pollution. *MNRAS* 2018; 473:2871–2880.

[82] Geier S, Østensen RH, Nemeth P, Heber U, Gentile Fusillo NP, Gänsicke BT, Telting JH, Green EM, Schaffenroth J. Meet the family - the catalog of known hot subdwarf stars. *Open Astronomy* 2017; 26:164–168.

[83] Stanek KZ, Holoien TWS, Kochanek CS, Shields JV, Thompson TA, Chomiuk L, Strader J, Shappee BJ, Prieto JL, Dong S, Stritzinger M. ASAS-SN Discovery of a Possible, Very Bright Galactic Nova ASASSN-18fv. *The Astronomer's Telegram* 2018; 11454.

[84] Kuschnig R, Pigulski A, Moffat AFJ, Matthews JM, Zwintz K, Baade D, Handler G, Weiss WW, Wade GA, Rucinski SM, Pablo H, Koudelka O, Smolec R, Popowicz A, Neiner C, Daszynska-Daszkiewicz J, Lovekin C, St-Louis N, Pamyatnykh AA, Rowe J, Orleanski P, Mochnacki S, Schwarzenberg-Czerny A. BRITE nanosatellite serendipitously captures oscillatory rise and fall of ASASSN-18fv. *The Astronomer's Telegram* 2018; 11508.

[85] Li KL, Metzger BD, Chomiuk L, Vurm I, Strader J, Finzell T, Beloborodov AM, Nelson T, Shappee BJ, Kochanek CS, Prieto JL, Kafka S, Holoien TWS, Thompson TA, Luckas PJ, Itoh H. A nova outburst powered by shocks. *Nature Astronomy* 2017; 1:697–702.

[86] Kaiser N, Burgett W, Chambers K, Denneau L, Heasley J, Jedicke R, Magnier E, Morgan J, Onaka P, Tonry J. The Pan-STARRS wide-field optical/NIR imaging survey. In: *Ground-based and Airborne Telescopes III*, In: *Ground-based and Airborne Telescopes III*, Jul 2010 p. 77330E.

[87] Sebag J, Gressler W, Schmid T, Rolland JP, Thompson KP. LSST Telescope Alignment Plan Based on Nodal Aberration Theory. *PASP* 2012; 124:380.

[88] Duggan GE, Dekany R, Milburn J. Aligning the ZTF science focal plane using stellar images. In: *Ground-based and Airborne Instrumentation for Astronomy VII*, In: *Ground-based and Airborne Instrumentation for Astronomy VII*, Jul 2018 p. 107024K.

[89] Ratzloff JK, Law NM, Fors O, Ser Dd, Corbett HT. Evryscope Robotilter automated camera / ccd alignment system. In: *Ground-based and Airborne Instrumentation for Astronomy VI*, In: *Ground-based and Airborne Instrumentation for Astronomy VI*, Aug 2016 p. 99080W.

[90] Bakos GÁ. The HATNet and HATSouth Exoplanet Surveys. *ArXiv e-prints* 2018; .

[91] Wang S, Zhang H, Zhou X, Zhou JL, Fu JN, Yang M, Liu H, Xie J, Wang L, Wang L, Wittenmyer RA, Ashley MCB, Feng LL, Gong X, Lawrence JS, Liu Q, Luong-Van DM, Ma J, Peng X, Storey JWV, Wu Z, Yan J, Yang H, Yang J, Yuan X, Zhang T, Zhang X, Zhu Z, Zou H. Photometric Variability in the CSTAR Field: Results from the 2008 Data Set. *ApJS* 2015; 218:20.

[92] Law NM, Carlberg R, Salbi P, Ngan WHW, Ahmadi A, Steinbring E, Murowinski R, Sivanandam S, Kerzendorf W. Exoplanets from the arctic: The first wide-field survey at 80n. *The Astronomical Journal* 2013; 145:58.

[93] Kraus AL, Ireland MJ, Martinache F, Hillenbrand LA. Mapping the Shores of the Brown Dwarf Desert. II. Multiple Star Formation in Taurus-Auriga. *ApJ* 2011; 731:8.

[94] Law NM, Kraus AL, Street R, Fulton BJ, Hillenbrand LA, Shporer A, Lister T, Baranec C, Bloom JS, Bui K, Burse MP, Cenko SB, Das HK, Davis JTC, Dekany RG, Filippenko AV, Kasliwal MM, Kulkarni SR, Nugent P, Ofek EO, Poznanski D, Quimby RM, Ramaprakash AN, Riddle R, Silverman JM, Sivanandam S, Tendulkar SP. Three New Eclipsing White-dwarf-M-dwarf Binaries Discovered in a Search for Transiting Planets around M-dwarfs. *ApJ* 2012; 757:133.

[95] Chaturvedi P, Sharma R, Chakraborty A, Anandarao BG, Prasad NJSSV. Masses and Radii of Four Very Low-mass Stars in F+M Eclipsing Binary Systems. *AJ* 2018; 156:27.

[96] Christ CN, Montet BT, Fabrycky DC. Observations of the Kepler Field with TESS: Predictions for Planet Yield and Observable Features. *ArXiv e-prints* 2018; .

[97] Stassun KG, Oelkers RJ, Pepper J, Paegert M, De Lee N, Torres G, Latham DW, Charpinet S, Dressing CD, Huber D, Kane SR, Lépine S, Mann A, Muirhead PS, Rojas-Ayala B, Silvotti R, Fleming SW, Levine A, Plavchan P. The TESS Input Catalog and Candidate Target List. *AJ* 2018; 156:102.

[98] Jones E. Reduced-Proper-Motion Diagrams. *ApJ* 1972; 173:671–676.

[99] Pedregosa F, Varoquaux G, Gramfort A, Michel V, Thirion B, Grisel O, Blondel M, Prettenhofer P, Weiss R, Dubourg V, Vanderplas J, Passos A, Cournapeau D, Brucher M, Perrot M, Duchesnay E. Scikit-learn: Machine learning in Python. *Journal of Machine Learning Research* 2011; 12:2825–2830.

[100] Wenger M, Ochsenbein F, Egret D, Dubois P, Bonnarel F, Borde S, Genova F, Jasniewicz G, Laloë S, Lesteven S, Monier R. The SIMBAD astronomical database. The CDS reference database for astronomical objects. *AAPS* 2000; 143:9–22.

[101] Pecaut MJ, Mamajek EE. Intrinsic Colors, Temperatures, and Bolometric Corrections of Pre-main-sequence Stars. *ApJS* 2013; 208:9.

[102] Gaia Collaboration, Brown AGA, Vallenari A, Prusti T, de Bruijne JHJ, Babusiaux C, Bailer-Jones CAL, Biermann M, Evans DW, Eyer L, et al. Gaia Data Release 2. Summary of the contents and survey properties. *AAP* 2018; 616:A1.

[103] Raddi R, Gentile Fusillo NP, Pala AF, Hermes JJ, Gänsicke BT, Chote P, Hollands MA, Henden A, Catalán S, Geier S, Koester D, Munari U, Napiwotzki R, Tremblay PE. Multiband photometry and spectroscopy of an all-sky sample of bright white dwarfs. *MNRAS* 2017; 472:4173–4192.

[104] Pietro Gentile Fusillo N, Raddi R, Gänsicke BT, Hermes JJ, Pala AF, Fuchs JT, Chehade B, Metcalfe N, Shanks T. A catalogue of white dwarf candidates in VST ATLAS. *ArXiv e-prints* 2017; .

[105] Pietro Gentile Fusillo N, Gaensicke BT, Greiss S. A photometric selection of White Dwarf candidates in SDSS DR10. *ArXiv e-prints* 2015; .

[106] Lépine S, Gaidos E. An All-sky Catalog of Bright M Dwarfs. *AJ* 2011; 142:138.

[107] Kharchenko NV. All-sky compiled catalogue of 2.5 million stars. *Kinematika i Fizika Nebesnykh Tel* 2001; 17:409–423.

[108] Fuchs JT, Dunlap BH, Clemens JC, Meza JA, Dennihy E, Koester D. Understanding Systematics in ZZ Ceti Model Fitting to Enable Differential Seismology. In: "*20th European White Dwarf Workshop* (Tremblay PE, Gaensicke B, Marsh T, Eds.), In: "*20th European White Dwarf Workshop* (Tremblay PE, Gaensicke B, Marsh T, Eds.), Mar 2017 p. 263.

[109] Merline WJ, Howell SB. A Realistic Model for Point-sources Imaged on Array Detectors: The Model and Initial Results. *Experimental Astronomy* 1995; 6:163–210.

[110] Young AT. Errors in extinction determination. *AJ* 1967; 72:328.

[111] Collins KA, Kielkopf JF, Stassun KG, Hessman FV. AstroImageJ: Image Processing and Photometric Extraction for Ultra-precise Astronomical Light Curves. *AJ* 2017; 153:77.

[112] Mayor M, Pepe F, Queloz D, Bouchy F, Rupprecht G, Lo Curto G, Avila G, Benz W, Bertaux JL, Bonfils X, Dall T, Dekker H, Delabre B, Eckert W, Fleury M, Gilliotte A, Gojak D, Guzman JC, Kohler D, Lizon JL, Longinotti A, Lovis C, Megevand D, Pasquini L, Reyes J, Sivan JP, Sosnowska D, Soto R, Udry S, van Kesteren A, Weber L, Weilenmann U. Setting New Standards with HARPS. *The Messenger* 2003; 114:20–24.

[113] Covey KR, Ivezić Ž, Schlegel D, Finkbeiner D, Padmanabhan N, Lupton RH, Agüeros MA, Bochanski JJ, Hawley SL, West AA, Seth A, Kimball A, Gogarten SM, Claire M, Haggard D, Kaib N, Schneider DP, Sesar B. Stellar SEDs from 0.3 to 2.5 μm: Tracing the Stellar Locus and Searching for Color Outliers in the SDSS and 2MASS. *AJ* 2007; 134:2398–2417.

[114] Press WH, Teukolsky SA, Vetterling WT, Flannery BP, "Numerical Recipes 3rd Edition: The Art of Scientific Computing". Cambridge University Press, New York, NY, USA, 3 ed., 2007.

[115] Rowell N, Hambly N. White Dwarfs in the SuperCOSMOS Sky Survey: the Thin Disk, Thick Disk and Spheroid Luminosity Functions. *ArXiv e-prints* 2011; .

[116] Kepler SO, Koester D, Romero AD, Ourique G, Pelisoli I. White Dwarf Mass Distribution. In: "*20th European White Dwarf Workshop* (Tremblay PE, Gaensicke B, Marsh T, Eds.), In: "*20th European White Dwarf Workshop* (Tremblay PE, Gaensicke B, Marsh T, Eds.), March 2017 p. 421.

[117] Brown WR, Gianninas A, Kilic M, Kenyon SJ, Allende Prieto C. The ELM Survey. VII. Orbital Properties of Low-Mass White Dwarf Binaries. *APJ* 2016; 818:155.

[118] Koester D, Napiwotzki R, Christlieb N, Drechsel H, Hagen HJ, Heber U, Homeier D, Karl C, Leibundgut B, Moehler S, Nelemans G, Pauli EM, Reimers D, Renzini A, Yungelson L. High-resolution UVES/VLT spectra of white dwarfs observed for the ESO SN Ia progenitor survey (SPY). I. *Astronomy and Astrophysics* 2001; 378:556–568.

[119] Bédard A, Bergeron P, Fontaine G. Measurements of Physical Parameters of White Dwarfs: A Test of the Mass-Radius Relation. *The Astrophysical Journal* 2017; 848:11.

[120] Ratzloff JK, Barlow BN, Németh P, Corbett HT, Walser S, Galliher NW, Glazier A, Howard WS, Law NM. Hot subdwarf all southern sky fast transit survey with the evryscope. *The Astrophysical Journal* 2020; 890:126.

[121] Schaffenroth V, Classen L, Nagel K, Geier S, Koen C, Heber U, Edelmann H. Two candidate brown dwarf companions around core helium-burning stars. *AAP* 2014; 570:A70.

[122] Stark MA, Wade RA. Single and Composite Hot Subdwarf Stars in the Light of 2MASS Photometry. *AJ* 2003; 126:1455–1471.

[123] Reed MD, Stiening R. A Search for Main-Sequence Companions to Subdwarf B Stars Using the Two Micron All Sky Survey. *PASP* 2004; 116:506–515.

[124] Vos J, Németh P, Vučković M, Østensen R, Parsons S. Composite hot subdwarf binaries - I. The spectroscopically confirmed sdB sample. *MNRAS* 2018; 473:693–709.

[125] Vos J, Vučković M, Chen X, Han Z, Boudreaux T, Barlow BN, Østensen R, Németh P. The orbital period-mass ratio relation of wide sdB+MS binaries and its application to the stability of RLOF. *MNRAS* 2019; 482:4592–4605.

[126] Ratzloff JK, Law NM, Fors O, Corbett HT, Howard WS, del Ser D, Haislip J. Building the Evryscope: Hardware Design and Performance. *PASP* 2019; 131:075001.

[127] Geier S, Raddi R, Gentile Fusillo NP, Marsh TR. The population of hot subdwarf stars studied with Gaia. II. The Gaia DR2 catalogue of hot subluminous stars. *AAP* 2019; 621:A38.

[128] Kilkenny D. The eclipsing binary LB 3459. *The Observatory* 1978; 98:207.

[129] Lisker T, Heber U, Napiwotzki R, Christlieb N, Han Z, Homeier D, Reimers D. Hot subdwarfs from the ESO Supernova Ia Progenitor Survey. I. Atmospheric parameters and cool companions of sdB stars. *AAP* 2005; 430:223–243.

[130] Stroeer A, Heber U, Lisker T, Napiwotzki R, Dreizler S, Christlieb N, Reimers D. Hot subdwarfs from the ESO supernova Ia progenitor survey. II. Atmospheric parameters of subdwarf O stars. *AAP* 2007; 462:269–280.

[131] Németh P, Kawka A, Vennes S. A selection of hot subluminous stars in the GALEX survey - II. Subdwarf atmospheric parameters. *MNRAS* 2012; 427:2180–2211.

[132] Derekas A, Németh P, Southworth J, Borkovits T, Sárneczky K, Pál A, Csák B, Garcia-Alvarez D, Maxted PFL, Kiss LL, Vida K, Szabó GM, Kriskovics L. A New sdO+dM Binary with Extreme Eclipses and Reflection Effect. *ApJ* 2015; 808:179.

[133] Mandel K, Agol E. Analytic Light Curves for Planetary Transit Searches. *ApJL* 2002; 580:L171–L175.

[134] Hubeny I, Lanz T. A brief introductory guide to TLUSTY and SYNSPEC. *arXiv e-prints* 2017; p. arXiv:1706.01859.

[135] Hubeny I, Lanz T. TLUSTY User's Guide II: Reference Manual. *arXiv e-prints* 2017; p. arXiv:1706.01935.

[136] Hubeny I, Lanz T. TLUSTY User's Guide III: Operational Manual. *arXiv e-prints* 2017; p. arXiv:1706.01937.

[137] Feinstein AD, Montet BT, Foreman-Mackey D, Bedell ME, Saunders N, Bean JL, Christiansen JL, Hedges C, Luger R, Scolnic D, Cardoso JVdM. eleanor: An Open-source Tool for Extracting Light Curves from the TESS Full-frame Images. *PASP* 2019; 131:094502.

[138] Vennes S, Kawka A, O'Toole SJ, Nmeth P, Burton D. The shortest period sdb plus white dwarf binary cd30 11223 (galex j14113053). *The Astrophysical Journal Letters* 2012; 759:L25.

[139] Menzies JW, Marang F. A New B-Subdwarf Eclipsing Binary with an Extremely Short Period. In: "*Instrumentation and Research Programmes for Small Telescopes* (Hearnshaw JB, Cottrell PL, Eds.), In: "*Instrumentation and Research Programmes for Small Telescopes* (Hearnshaw JB, Cottrell PL, Eds.), Jan 1986 p. 305.

[140] Wils P, di Scala G, Otero SA. NSVS 14256825: A New HW Vir Type System. *Information Bulletin on Variable Stars* 2007; 5800:1.

[141] Kilkenny D, O'Donoghue D, Koen C, Lynas-Gray AE, van Wyk F. The EC 14026 stars - VIII. PG 1336-018: a pulsating sdB star in an HWVir-type eclipsing binary. *MNRAS* 1998; 296:329–338.

[142] Barlow BN, Kilkenny D, Drechsel H, Dunlap BH, O'Donoghue D, Geier S, O'Steen RG, Clemens JC, LaCluyze AP, Reichart DE, Haislip JB, Nysewander MC, Ivarsen KM. EC 10246-2707: an eclipsing subdwarf B + M dwarf binary. *MNRAS* 2013; 430:22–31.

[143] Walser S, Corcoran KA, Barlow B, Mycroft S, Aube J, Ratzloff J, Law N, Corbett HT, Fors O, Howard WS. Evryscope Photometry of the New Hot Subdwarf Reflection Effect Binary EC 01578-1743. In: *American Astronomical Society Meeting Abstracts #233*, In: *American Astronomical Society Meeting Abstracts #233*, Jan 2019 p. 464.03.

[144] Kupfer T, Geier S, Heber U, Østensen RH, Barlow BN, Maxted PFL, Heuser C, Schaffenroth V, Gänsicke BT. Hot subdwarf binaries from the MUCHFUSS project. Analysis of 12 new systems and a study of the short-period binary population. *AAP* 2015; 576:A44.

[145] Henry GW, Murray S, Hall DS. HD 185510: a New Variable Star. *Information Bulletin on Variable Stars* 1982; 2215:1.

[146] Drake AJ, Djorgovski SG, Mahabal A, Beshore E, Larson S, Graham MJ, Williams R, Christensen E, Catelan M, Boattini A, Gibbs A, Hill R, Kowalski R. First Results from the Catalina Real-Time Transient Survey. *ApJ* 2009; 696:870–884.

[147] Kilkenny D, Worters HL, O'Donoghue D, Koen C, Koen T, Hambly N, MacGillivray H, Stobie RS. The Edinburgh-Cape Blue Object Survey V. The end: Partial Zones 46; Galactic latitudes 50
gt;b
gt;90. *Monthly Notices of the Royal Astronomical Society* 2016; 459:4343–4352.

[148] Kawka A, Vennes S, O'Toole S, Nmeth P, Burton D, Kotze E, Buckley DAH. New binaries among UV-selected, hot subdwarf stars and population properties. *Monthly Notices of the Royal Astronomical Society* 2015; 450:3514–3548.

[149] Pojmanski G. The All Sky Automated Survey. Catalog of Variable Stars. I. 0 h - 6 hQuarter of the Southern Hemisphere. *ACTAA* 2002; 52:397–427.

[150] Schaffenroth V, Geier S, Drechsel H, Heber U, Wils P, Østensen RH, Maxted PFL, di Scala G. A new bright eclipsing hot subdwarf binary from the ASAS and SuperWASP surveys. *AAP* 2013; 553:A18.

[151] Chen A, O'Donoghue D, Stobie RS, Kilkenny D, Roberts G, van Wyk F. EC11575-1845: a new close binary with a large reflection effect discovered by the Edinburgh-Cape Survey. *MNRAS* 1995; 275:100–114.

[152] Landolt AU, Drilling JS. Multicolor photometry of the binary central star LSS 2018. *AJ* 1986; 91:1372–1375.

[153] Edelmann H, Heber U, Altmann M, Karl C, Lisker T. High resolution spectroscopy of bright subdwarf B stars. I. Radial velocity variables. *AAP* 2005; 442:1023–1030.

[154] Kamath D, Wood PR, Van Winckel H. Optically visible post-AGB stars, post-RGB stars and young stellar objects in the Large Magellanic Cloud. *MNRAS* 2015; 454:1468–1502.

[155] Drilling JS, Bergeron LE. An Extension of the Case-Hamburg OB Star Surveys. *PASP* 1995; 107:846.

[156] Griffiths RE, Lamb DQ, Ward MJ, Wilson AS, Charles PA, Thorstensen J, McHardy IM, Lawrence A. The optical identification of H 2252-035 with a cataclysmic variable. *MNRAS* 1980; 193:25P–33.

[157] Downes RA, Webbink RF, Shara MM, Ritter H, Kolb U, Duerbeck HW. A Catalog and Atlas of Cataclysmic Variables: The Living Edition. *PASP* 2001; 113:764–768.

[158] Tuohy IR, Buckley DAH, Remillard RA, Bradt HV, Schwartz DA. Identification of two southern X-ray emitting cataclysmic variables. *ApJ* 1986; 311:275–298.

[159] McLaughlin DB. The Light Curves of Novae (concluded). *Popular Astronomy* 1939; 47:538.

[160] Pala AF, Gänsicke BT, Breedt E, Knigge C, Hermes JJ, Gentile Fusillo NP, Holland s MA, Naylor T, Pelisoli I, Toonen S, Aungwerojwit A, Cukanovaite E, Dennihy E, Manser CJ, Pretorius ML, Scaringi S, Schreiber MR, Toloza O. The Space Density of Cataclysmic Variables from *Gaia* DR2. *arXiv e-prints* 2019; p. arXiv:1907.13152.

[161] Schmidt GD, Szkody P, Silvestri NM, Cushing MC, Liebert J, Smith PS. Discovery of a Magnetic White Dwarf/Probable Brown Dwarf Short-Period Binary. *ApJL* 2005; 630:L173–L176.

[162] Longstaff ES, Casewell SL, Wynn GA, Page KL, Williams PKG, Braker I, Maxted PFL. Signs of accretion in the white dwarf + brown dwarf binary NLTT5306. *MNRAS* 2019; 484:2566–2574.

[163] Steele PR, Burleigh MR, Dobbie PD, Jameson RF, Barstow MA, Satterthwaite RP. White dwarfs in the UKIRT Infrared Deep Sky Survey Large Area Survey: the substellar companion fraction. *MNRAS* 2011; 416:2768–2791.

[164] Neugent KF, Massey P, Skiff B, Meynet G. Yellow and Red Supergiants in the Large Magellanic Cloud. *ApJ* 2012; 749:177.

[165] Sanduleak N. A deep objective-prism survey for Large Magellanic Cloud members. *Contributions from the Cerro Tololo Inter-American Observatory* 1970; 89.

[166] Stephenson CB, Sanduleak N. Luminous stars in the Southern Milky Way. *Publications of the Warner & Swasey Observatory* 1971; 1:1.

[167] Jayasinghe T, Kochanek CS, Stanek KZ, Shappee BJ, Holoien TWS, Thompson TA, Prieto JL, Dong S, Pawlak M, Shields JV, Pojmanski G, Otero S, Britt CA, Will D. The ASAS-SN catalogue of variable stars I: The Serendipitous Survey. *MNRAS* 2018; 477:3145–3163.

[168] Postnov KA, Yungelson LR. The Evolution of Compact Binary Star Systems. *Living Reviews in Relativity* 2014; 17:3.

[169] Marsh TR, Dhillon VS, Duck SR. Low-Mass White Dwarfs Need Friends - Five New Double-Degenerate Close Binary Stars. *MNRAS* 1995; 275:828.

[170] Bloemen S, Marsh TR, Østensen RH, Charpinet S, Fontaine G, Degroote P, Heber U, Kawaler SD, Aerts C, Green EM. Kepler observations of the beaming binary KPD 1946+4340. *MNRAS* 2011; 410:1787–1796.

[171] Rebassa-Mansergas A, Nebot Gómez-Morán A, Schreiber MR, Girven J, Gänsicke BT. Post-common envelope binaries from SDSS-X: the origin of low-mass white dwarfs. *MNRAS* 2011; 413:1121–1131.

[172] Debes JH, Kilic M, Tremblay PE, López-Morales M, Anglada-Escude G, Napiwotzki R, Osip D, Weinberger A. A New Merging Double Degenerate Binary in the Solar Neighborhood. *AJ* 2015; 149:176.

[173] Nelemans G, Napiwotzki R, Karl C, Marsh TR, Voss B, Roelofs G, Izzard RG, Montgomery M, Reerink T, Christlieb N, Reimers D. Binaries discovered by the SPYproject. IV. Five single-lined DA double white dwarfs. *AAP* 2005; 440:1087–1095.

[174] Han Z, Podsiadlowski P, Maxted PFL, Marsh TR, Ivanova N. The origin of subdwarf B stars - I. The formation channels. *MNRAS* 2002; 336:449–466.

[175] Han Z, Podsiadlowski P, Maxted PFL, Marsh TR. The origin of subdwarf B stars - II. *MNRAS* 2003; 341:669–691.

[176] Heber U. The atmosphere of subluminous B stars. II - Analysis of 10 helium poor subdwarfs and the birthrate of sdB stars. *AAP* 1986; 155:33–45.

[177] Heber U. Hot Subdwarf Stars. *ARAA* 2009; 47:211–251.

[178] Heber U. Hot Subluminous Stars. *Publications of the Astronomical Society of the Pacific* 2016; 128:082001.

[179] Istrate AG, Marchant P, Tauris TM, Langer N, Stancliffe RJ, Grassitelli L. Models of low-mass helium white dwarfs including gravitational settling, thermal and chemical diffusion, and rotational mixing. *AAP* 2016; 595:A35.

[180] Brown WR, Kilic M, Allende Prieto C, Kenyon SJ. The ELM Survey. I. A Complete Sample of Extremely Low-mass White Dwarfs. *APJ* 2010; 723:1072–1081.

[181] Wang B, Han Z. Progenitors of type Ia supernovae. *New Astronomy Reviews* 2012; 56:122–141.

[182] Geier S, Nesslinger S, Heber U, Przybilla N, Napiwotzki R, Kudritzki RP. The hot subdwarf B + white dwarf binary KPD 1930+2752. A supernova type Ia progenitor candidate. *AAP* 2007; 464:299–307.

[183] Gianninas A, Dufour P, Kilic M, Brown WR, Bergeron P, Hermes JJ. Precise Atmospheric Parameters for the Shortest-period Binary White Dwarfs: Gravitational Waves, Metals, and Pulsations. *ApJ* 2014; 794:35.

[184] Kilic M, Brown WR, Allende Prieto C, Kenyon SJ, Heinke CO, Agüeros MA, Kleinman SJ. The ELM Survey. IV. 24 White Dwarf Merger Systems. *ApJ* 2012; 751:141.

[185] Koen C, Orosz JA, Wade RA. KPD 0422+5421: a new short-period subdwarf B/white dwarf binary. *MNRAS* 1998; 300:695–704.

[186] Kupfer T, van Roestel J, Geier S, Marsh T. PTF1 j082340.04081936.5: A hot subdwarf b star with a low-mass white dwarf companion in an 87-minute orbit. *The Astrophysical Journal* 2017; 835:131.

[187] Kupfer T, Ramsay G, van Roestel J, Brooks J, MacFarlane SA, Toma R, Groot PJ, Woudt PA, Bildsten L, Marsh TR, Green MJ, Breedt E, Kilkenny D, Freudenthal J, Geier S, Heber U, Bagnulo S, Blagorodnova N, Buckley DAH, Dhillon VS, Kulkarni SR, Lunnan R, Prince TA. The OmegaWhite Survey for Short-period Variable Stars. V. Discovery of an Ultracompact Hot Subdwarf Binary with a Compact Companion in a 44-minute Orbit. *ApJ* 2017; 851:28.

[188] Jones E, Oliphant T, Peterson P et al. SciPy: Open source scientific tools for Python, 2001, [Online].

[189] Eastman J, Siverd R, Gaudi BS. Achieving Better Than 1 Minute Accuracy in the Heliocentric and Barycentric Julian Dates. *PASP* 2010; 122:935.

[190] Baldry I. "Time series spectroscopy of pulsating stars". PhD thesis, University of Sydney, 1999.

[191] Heber U, Reid IN, Werner K. Spectral analysis of multi mode pulsating sdB stars. II. Feige 48, KPD 2109+4401 and PG 1219+534. *AAP* 2000; 363:198–207.

[192] Verbunt F, Rappaport S. Mass transfer instabilities due to angular momentum flows in close binaries. *ApJ* 1988; 332:193–198.

[193] Claret A. A new non-linear limb-darkening law for LTE stellar atmosphere models III. Sloan filters: Calculations for -5.0 $\leq$ $log[M/H]\leq +1, 2000K\leq T_{eff} \leq 50000Katseveralsurfacegravities. A\&A2004; 428: 1001--1005.$

[194] Bloemen S, Marsh TR, Østensen RH, Charpinet S, Fontaine G, Degroote P, Heber U, Kawaler SD, Aerts C, Green EM, Telting J, Brassard P, Gänsicke BT, Handler G, Kurtz DW et al. Kepler observations of the beaming binary KPD 1946+4340. *MNRAS* 2011; 410:1787–1796.

[195] Claret A, Bloemen S. Gravity and limb-darkening coefficients for the Kepler, CoRoT, Spitzer, uvby, UBVRIJHK, and Sloan photometric systems. *AAP* 2011; 529:A75.

[196] Foreman-Mackey D, Hogg DW, Lang D, Goodman J. emcee: The MCMC Hammer. *Publications of the Astronomical Society of the Pacific* 2013; 125:306.

[197] Gaia Collaboration, et al. Gaia Data Release 2. Summary of the contents and survey properties. *AAP* 2018; 616:A1.

[198] Bessell MS, Castelli F, Plez B. Model atmospheres broad-band colors, bolometric corrections and temperature calibrations for O - M stars. *AAP* 1998; 333:231–250.

[199] Lallement R, Vergely JL, Valette B, Puspitarini L, Eyer L, Casagrande L. 3D maps of the local ISM from inversion of individual color excess measurements. *AAP* 2014; 561:A91.

[200] Paxton B, Bildsten L, Dotter A, Herwig F, Lesaffre P, Timmes F. Modules for Experiments in Stellar Astrophysics (MESA). *ApJs* 2011; 192:3.

[201] Paxton B, Cantiello M, Arras P, Bildsten L, Brown EF, Dotter A, Mankovich C, Montgomery MH, Stello D, Timmes FX, Townsend R. Modules for Experiments in Stellar Astrophysics (MESA): Planets, Oscillations, Rotation, and Massive Stars. *ApJs* 2013; 208:4.

[202] Paxton B, Marchant P, Schwab J, Bauer EB, Bildsten L, Cantiello M, Dessart L, Farmer R, Hu H, Langer N, Townsend RHD, Townsley DM, Timmes FX. Modules for Experiments in Stellar Astrophysics (MESA): Binaries, Pulsations, and Explosions. *ApJs* 2015; 220:15.

[203] Paxton B, Schwab J, Bauer EB, Bildsten L, Blinnikov S, Duffell P, Farmer R, Goldberg JA, Marchant P, Sorokina E, Thoul A, Townsend RHD, Timmes FX. Modules for Experiments in Stellar Astrophysics (MESA): Convective Boundaries, Element Diffusion, and Massive Star Explosions. *ApJS* 2018; 234:34.

[204] Bours MCP, Marsh TR, Parsons SG, Copperwheat CM, Dhillon VS, Littlefair SP, Gaensicke BT, Gianninas A, Tremblay PE. A Detailed Study of CSS 41177: an Eclipsing Double White Dwarf. In: "*19th European Workshop on White Dwarfs* (Dufour P, Bergeron P, Fontaine G, Eds.), In: "*19th European Workshop on White Dwarfs* (Dufour P, Bergeron P, Fontaine G, Eds.), Jun 2015 p. 313.

[205] Hermes JJ, Kilic M, Brown WR, Montgomery MH, Winget DE. Two New Tidally Distorted White Dwarfs. *ApJ* 2012; 749:42.

[206] Hermes JJ, Brown WR, Kilic M, Gianninas A, Chote P, Sullivan DJ, Winget DE, Bell KJ, Falcon RE, Winget KI, Mason PA, Harrold ST, Montgomery MH. Radius Constraints from High-speed Photometry of 20 Low-mass White Dwarf Binaries. *ApJ* 2014; 792:39.

[207] Hermes JJ, Kilic M, Brown WR, Winget DE, Allende Prieto C, Gianninas A, Mukadam AS, Cabrera-Lavers A, Kenyon SJ. Rapid Orbital Decay in the 12.75-minute Binary White Dwarf J0651+2844. *ApJL* 2012; 757:L21.

[208] Kilic M, Brown WR, Allende Prieto C, Agüeros MA, Heinke C, Kenyon SJ. The ELM Survey. II. Twelve Binary White Dwarf Merger Systems. *ApJ* 2011; 727:3.

[209] Heber U, Edelmann H, Lisker T, Napiwotzki R. Discovery of a helium-core white dwarf progenitor. *AAP* 2003; 411:L477–L480.

[210] Schwab J. Hot subdwarfs formed from the merger of two He white dwarfs. *MNRAS* 2018; 476:5303–5311.

[211] Schwab J, Shen KJ, Quataert E, Dan M, Rosswog S. The viscous evolution of white dwarf merger remnants. *MNRAS* 2012; 427:190–203.

[212] Zhang X, Jeffery CS. Evolutionary models for double helium white dwarf mergers and the formation of helium-rich hot subdwarfs. *MNRAS* 2012; 419:452–464.

[213] Marsh TR, Nelemans G, Steeghs D. Mass transfer between double white dwarfs. *MNRAS* 2004; 350:113–128.

[214] Gokhale V, Peng XM, Frank J. Evolution of Close White Dwarf Binaries. *ApJ* 2007; 655:1010–1024.

[215] Shen KJ. Every Interacting Double White Dwarf Binary May Merge. *ApJ* 2015; 805:L6.

[216] Brown WR, Kilic M, Kenyon SJ, Gianninas A. Most Double Degenerate Low-mass White Dwarf Binaries Merge. *APJ* 2016; 824:46.

[217] Heber U. Hot Subdwarf Stars. *ARAA* 2009; 47:211–251.

[218] Jeffery CS, Baran AS, Behara NT, Kvammen A, Martin P, Naslim N, Østensen RH, Preece HP, Reed MD, Telting JH, Woolf VM. Discovery of a variable lead-rich hot subdwarf: UVO 0825+15. *MNRAS* 2017; 465:3101–3124.

[219] Østensen RH. Asteroseismology and Evolution of EHB stars. *Communications in Asteroseismology* 2009; 159:75–87.

[220] Downes RA. The KPD Survey for Galactic Plane Ultraviolet-Excess Objects: Space Densities of White Dwarfs and Subdwarfs. *ApJS* 1986; 61:569.

[221] Billéres M, Fontaine G, Brassard P, Charpinet S, Liebert J, Saffer RA. Detection of p-Mode Pulsations and Possible Ellipsoidal Luminosity Variations in the Hot Subdwarf B Star KPD 1930+2752. *APJ* 2000; 530:441–453.

[222] Orosz JA, Wade RA. Confirmation of eclipses in KPD 0422+5421, a binary containing a white dwarf and a subdwarf B star. *MNRAS* 1999; 310:773–783.

[223] Ratzloff JK, Barlow BN, Nemeth P, Corbett HT, Walser S, Galliher NW, Glazier A, Howard WS, Law NM. Hot Subdwarf All Southern Sky Fast Transit Survey with the Evryscope. *arXiv e-prints* 2019; p. arXiv:1912.10993.

[224] Smith JC, Stumpe MC, Van Cleve JE, Jenkins JM, Barclay TS, Fanelli MN, Girouard FR, Kolodziejczak JJ, McCauliff SD, Morris RL, Twicken JD. Kepler Presearch Data Conditioning II - A Bayesian Approach to Systematic Error Correction. *PASP* 2012; 124:1000.

[225] Stumpe MC, Smith JC, Catanzarite JH, Van Cleve JE, Jenkins JM, Twicken JD, Girouard FR. Multiscale Systematic Error Correction via Wavelet-Based Bandsplitting in Kepler Data. *PASP* 2014; 126:100.

[226] Jenkins JM, Twicken JD, McCauliff S, Campbell J, Sanderfer D, Lung D, Mansouri-Samani M, Girouard F, Tenenbaum P, Klaus T, Smith JC, Caldwell DA, Chacon AD, Henze C, Heiges C, Latham DW, Morgan E, Swade D, Rinehart S, Vanderspek R. The TESS science processing operations center. In: *ProcSPIE*, In: *ProcSPIE*, Aug 2016 p. 99133E.

[227] Hubeny I. A computer program for calculating non-LTE model stellar atmospheres. *Computer Physics Communications* 1988; 52:103–132.

[228] Hubeny I, Lanz T. Non-LTE line-blanketed model atmospheres of hot stars. 1: Hybrid complete linearization/accelerated lambda iteration method. *ApJ* 1995; 439:875–904.

[229] Hubeny I, Lanz T. Model Photospheres with Accelerated Lambda Iteration. In: "*Stellar Atmosphere Modeling* (Hubeny I, Mihalas D, Werner K, Eds.), In: "*Stellar Atmosphere Modeling* (Hubeny I, Mihalas D, Werner K, Eds.), January 2003 p. 51.

[230] Schindewolf M, Németh P, Heber U, Battich T, Miller Bertolami MM, Irrgang A, Latour M. A quantitative NLTE analysis of visual and ultraviolet spectra of four helium-rich subdwarf O stars. *AAP* 2018; 620:A36.

[231] Naslim N, Jeffery CS, Hibbert A, Behara NT. Discovery of extremely lead-rich subdwarfs: does heavy metal signal the formation of subdwarf B stars? *MNRAS* 2013; 434:1920–1929.

[232] Tremblay PE, Bergeron P. Spectroscopic Analysis of DA White Dwarfs: Stark Broadening of Hydrogen Lines Including Nonideal Effects. *ApJ* 2009; 696:1755–1770.

[233] Shamey LJ. “Stark Broadening of Important Helium i Lines and Their Forbidden Components.”. PhD thesis, UNIVERSITY OF COLORADO AT BOULDER., Jan 1969.

[234] Barnard AJ, Cooper J, Smith EW. The broadening of He I lines including ion dynamic corrections, with application to lambda 4471 Å. *JQSRT* 1974; 14:1025–1077.

[235] Schoening T, Butler K. Stark broadening of He II lines. *AAPS* 1989; 78:51–87.

[236] Napiwotzki R, Yungelson L, Nelemans G, Marsh TR, Leibundgut B, Renzini R, Homeier D, Koester D, Moehler S, Christlieb N. Double degenerates and progenitors of supernovae type Ia. In: "*Spectroscopically and Spatially Resolving the Components of the Close Binary Stars* (Hilditch RW, Hensberge H, Pavlovski K, Eds.), In: "*Spectroscopically and Spatially Resolving the Components of the Close Binary Stars* (Hilditch RW, Hensberge H, Pavlovski K, Eds.), Dec 2004 pp. 402–410.

[237] Hirsch HA. “Hot subluminous stars: On the Search for Chemical Signatures of their Genesis”. PhD thesis, Friedrich-Alexander University Erlangen-Nürnberg, Oct 2009.

[238] Napiwotzki R. Spectroscopic investigation of old planetaries. IV. Model atmosphere analysis. *AAP* 1999; 350:101–119.

[239] Nelder JA, Mead R. A Simplex Method for Function Minimization. *The Computer Journal* 1965; 7:308–313.

[240] Morris SL. The ellipsoidal variable stars. *ApJ* 1985; 295:143–152.

[241] Lindegren L, Hernández J, Bombrun A, Klioner S, Bastian U, Ramos-Lerate M, de Torres A, Steidelmüller H, Stephenson C, Hobbs D, Lammers U, Biermann M, Geyer R, Hilger T, Michalik D, Stampa U, McMillan PJ, Castañeda J, Clotet M, Comoretto G, Davidson M, Fabricius C, Gracia G, Hambly NC, Hutton A, Mora A, Portell J, van

Leeuwen F, Abbas U, Abreu A, Altmann M, Andrei A, Anglada E, Balaguer-Núñez L, Barache C, Becciani U, Bertone S, Bianchi L, Bouquillon S, Bourda G, Brüsemeister T, Bucciarelli B, Busonero D, Buzzi R, Cancelliere R, Carlucci T, Charlot P, Cheek N, Crosta M, Crowley C, de Bruijne J, de Felice F, Drimmel R, Esquej P, Fienga A, Fraile E, Gai M, Garralda N, González-Vidal JJ, Guerra R, Hauser M, Hofmann W, Holl B, Jordan S, Lattanzi MG, Lenhardt H, Liao S, Licata E, Lister T, Löffler W, Marchant J, Martin-Fleitas JM, Messineo R, Mignard F, Morbidelli R, Poggio E, Riva A, Rowell N, Salguero E, Sarasso M, Sciacca E, Siddiqui H, Smart RL, Spagna A, Steele I, Taris F, Torra J, van Elteren A, van Reeven W, Vecchiato A. Gaia Data Release 2. The astrometric solution. *AAP* 2018; 616:A2.

[242] Arenou F, Luri X, Babusiaux C, Fabricius C, Helmi A, Muraveva T, Robin AC, Spoto F, Vallenari A, Antoja T, Cantat-Gaudin T, Jordi C, Leclerc N, Reylé C, Romero-Gómez M, Shih IC, Soria S, Barache C, Bossini D, Bragaglia A, Breddels MA, Fabrizio M, Lambert S, Marrese PM, Massari D, Moitinho A, Robichon N, Ruiz-Dern L, Sordo R, Veljanoski J, Eyer L, Jasniewicz G, Pancino E, Soubiran C, Spagna A, Tanga P, Turon C, Zurbach C. Gaia Data Release 2. Catalogue validation. *AAP* 2018; 616:A17.

[243] Riess AG, Casertano S, Yuan W, Macri L, Bucciarelli B, Lattanzi MG, MacKenty JW, Bowers JB, Zheng W, Filippenko AV, Huang C, Anderson RI. Milky Way Cepheid Standards for Measuring Cosmic Distances and Application to Gaia DR2: Implications for the Hubble Constant. *ApJ* 2018; 861:126.

[244] Zinn JC, Pinsonneault MH, Huber D, Stello D. Confirmation of the Gaia DR2 Parallax Zero-point Offset Using Asteroseismology and Spectroscopy in the Kepler Field. *ApJ* 2019; 878:136.

[245] Schönrich R, McMillan P, Eyer L. Distances and parallax bias in Gaia DR2. *MNRAS* 2019; 487:3568–3580.

[246] Heber U, Irrgang A, Schaffenroth J. Spectral energy distributions and colours of hot subluminous stars. *Open Astronomy* 2018; 27:35–43.

[247] Wolf C, Onken CA, Luvaul LC, Schmidt BP, Bessell MS, Chang SW, Da Costa GS, Mackey D, Martin-Jones T, Murphy SJ, Preston T, Scalzo RA, Shao L, Smillie J, Tisserand P, White MC, Yuan F. SkyMapper Southern Survey: First Data Release (DR1). *PASA* 2018; 35:e010.

[248] Ahn CP, Alexandroff R, Allende Prieto C, Anderson SF, Anderton T, Andrews BH, Aubourg É, Bailey S, Balbinot E, Barnes R, Bautista J, Beers TC, Beifiori A, Berlind AA, Bhardwaj V, Bizyaev D, Blake CH, Blanton MR, Blomqvist M, Bochanski JJ, Bolton AS, Borde A, Bovy J, Brandt WN, Brinkmann J, Brown PJ, Brownstein JR, Bundy K, Busca NG, Carithers W, Carnero AR, Carr MA, Casetti-Dinescu DI, Chen Y, Chiappini C, Comparat J, Connolly N, Crepp JR, Cristiani S, Croft RAC, Cuesta AJ, da Costa LN, Davenport JRA, Dawson KS, de Putter R, De Lee N, Delubac T, Dhital S, Ealet A, Ebelke GL, Edmondson EM, Eisenstein DJ, Escoffier S, Esposito M, Evans ML, Fan X, Femenía Castellá B, Fernández Alvar E, Ferreira LD, Filiz Ak N, Finley H,

Fleming SW, Font-Ribera A, Frinchaboy PM, García-Hernández DA, García Pérez AE, Ge J, Génova-Santos R, Gillespie BA, Girardi L, González Hernández JI, Grebel EK, Gunn JE, Guo H, Haggard D, Hamilton JC, Harris DW, Hawley SL, Hearty FR, Ho S, Hogg DW, Holtzman JA, Honscheid K, Huehnerhoff J, Ivans II, Ivezić Ž, Jacobson HR, Jiang L, Johansson J, Johnson JA, Kauffmann G, Kirkby D, Kirkpatrick JA, Klaene MA, Knapp GR, Kneib JP, Le Goff JM, Leauthaud A, Lee KG, Lee YS, Long DC, Loomis CP, Lucatello S, Lundgren B, Lupton RH, Ma B, Ma Z, MacDonald N, Mack CE, Mahadevan S, Maia MAG, Majewski SR, Makler M, Malanushenko E, Malanushenko V, Manchado A, Mandelbaum R, Manera M, Maraston C, Margala D, Martell SL, McBride CK, McGreer ID, McMahon RG, Ménard B, Meszaros S, Miralda-Escudé J, Montero-Dorta AD, Montesano F, Morrison HL, Muna D, Munn JA, Murayama H, Myers AD, Neto AF, Nguyen DC, Nichol RC, Nidever DL, Noterdaeme P, Nuza SE, Ogand o RLC, Olmstead MD, Oravetz DJ, Owen R, Padmanabhan N, Palanque-Delabrouille N, Pan K, Parejko JK, Parihar P, Pâris I, Pattarakijwanich P, Pepper J, Percival WJ, Pérez-Fournon I, Pérez-Ràfols I, Petitjean P, Pforr J, Pieri MM, Pinsonneault MH, Porto de Mello GF, Prada F, Price-Whelan AM, Raddick MJ, Rebolo R, Rich J, Richards GT, Robin AC, Rocha-Pinto HJ, Rockosi CM, Roe NA, Ross AJ, Ross NP, Rossi G, Rubiño-Martin JA, Samushia L, Sanchez Almeida J, Sánchez AG, Santiago B, Sayres C, Schlegel DJ, Schlesinger KJ, Schmidt SJ, Schneider DP, Schultheis M, Schwope AD, Scóccola CG, Seljak U, Sheldon E, Shen Y, Shu Y, Simmerer J, Simmons AE, Skibba RA, Skrutskie MF, Slosar A, Sobreira F, Sobeck JS, Stassun KG, Steele O, Steinmetz M, Strauss MA, Streblyanska A, Suzuki N, Swanson MEC, Tal T, Thakar AR, Thomas D, Thompson BA, Tinker JL, Tojeiro R, Tremonti CA, Vargas Magaña M, Verde L, Viel M, Vikas SK, Vogt NP, Wake DA, Wang J, Weaver BA, Weinberg DH, Weiner BJ, West AA, White M, Wilson JC, Wisniewski JP, Wood-Vasey WM, Yanny B, Yèche C, York DG, Zamora O, Zasowski G, Zehavi I, Zhao GB, Zheng Z, Zhu G, Zinn JC. The Ninth Data Release of the Sloan Digital Sky Survey: First Spectroscopic Data from the SDSS-III Baryon Oscillation Spectroscopic Survey. *ApJS* 2012; 203:21.

[249] Chambers KC, Magnier EA, Metcalfe N, Flewelling HA, Huber ME, Waters CZ, Denneau L, Draper PW, Farrow D, Finkbeiner DP, Holmberg C, Koppenhoefer J, Price PA, Rest A, Saglia RP, Schlafly EF, Smartt SJ, Sweeney W, Wainscoat RJ, Burgett WS, Chastel S, Grav T, Heasley JN, Hodapp KW, Jedicke R, Kaiser N, Kudritzki RP, Luppino GA, Lupton RH, Monet DG, Morgan JS, Onaka PM, Shiao B, Stubbs CW, Tonry JL, White R, Bañados E, Bell EF, Bender R, Bernard EJ, Boegner M, Boffi F, Botticella MT, Calamida A, Casertano S, Chen WP, Chen X, Cole S, Deacon N, Frenk C, Fitzsimmons A, Gezari S, Gibbs V, Goessl C, Goggia T, Gourgue R, Goldman B, Grant P, Grebel EK, Hambly NC, Hasinger G, Heavens AF, Heckman TM, Henderson R, Henning T, Holman M, Hopp U, Ip WH, Isani S, Jackson M, Keyes CD, Koekemoer AM, Kotak R, Le D, Liska D, Long KS, Lucey JR, Liu M, Martin NF, Masci G, McLean B, Mindel E, Misra P, Morganson E, Murphy DNA, Obaika A, Narayan G, Nieto-Santisteban MA, Norberg P, Peacock JA, Pier EA, Postman M, Primak N, Rae C, Rai A, Riess A, Riffeser A, Rix HW, Röser S, Russel R, Rutz L, Schilbach E, Schultz ASB, Scolnic D, Strolger L, Szalay A, Seitz S, Small E, Smith KW,

Soderblom DR, Taylor P, Thomson R, Taylor AN, Thakar AR, Thiel J, Thilker D, Unger D, Urata Y, Valenti J, Wagner J, Walder T, Walter F, Watters SP, Werner S, Wood-Vasey WM, Wyse R. The Pan-STARRS1 Surveys. *arXiv e-prints* 2016; .

[250] Skrutskie MF, Cutri RM, Stiening R, Weinberg MD, Schneider S, Carpenter JM, Beichman C, Capps R, Chester T, Elias J, Huchra J, Liebert J, Lonsdale C, Monet DG, Price S, Seitzer P, Jarrett T, Kirkpatrick JD, Gizis JE, Howard E, Evans T, Fowler J, Fullmer L, Hurt R, Light R, Kopan EL, Marsh KA, McCallon HL, Tam R, Van Dyk S, Wheelock S. The Two Micron All Sky Survey (2MASS). *AJ* 2006; 131:1163–1183.

[251] Wright EL, Eisenhardt PRM, Mainzer AK, Ressler ME, Cutri RM, Jarrett T, Kirkpatrick JD, Padgett D, McMillan RS, Skrutskie M, Stanford SA, Cohen M, Walker RG, Mather JC, Leisawitz D, Gautier, III TN, McLean I, Benford D, Lonsdale CJ, Blain A, Mendez B, Irace WR, Duval V, Liu F, Royer D, Heinrichsen I, Howard J, Shannon M, Kendall M, Walsh AL, Larsen M, Cardon JG, Schick S, Schwalm M, Abid M, Fabinsky B, Naes L, Tsai CW. The Wide-field Infrared Survey Explorer (WISE): Mission Description and Initial On-orbit Performance. *AJ* 2010; 140:1868–1881.

[252] Cutri RM et al. VizieR Online Data Catalog: AllWISE Data Release (Cutri+ 2013). *VizieR Online Data Catalog* 2013; 2328.

[253] Houck JC, Denicola LA. ISIS: An Interactive Spectral Interpretation System for High Resolution X-Ray Spectroscopy. In: "*Astronomical Data Analysis Software and Systems IX* (Manset N, Veillet C, Crabtree D, Eds.), In: "*Astronomical Data Analysis Software and Systems IX* (Manset N, Veillet C, Crabtree D, Eds.), Jan 2000 p. 591.

[254] Fitzpatrick EL. Correcting for the Effects of Interstellar Extinction. *PASP* 1999; 111:63–75.

[255] Bailer-Jones CAL, Rybizki J, Fouesneau M, Mantelet G, Andrae R. Estimating Distance from Parallaxes. IV. Distances to 1.33 Billion Stars in Gaia Data Release 2. *AJ* 2018; 156:58.

[256] Asplund M, Grevesse N, Sauval AJ, Scott P. The Chemical Composition of the Sun. *ARAA* 2009; 47:481–522.

[257] Heber U, Hunger K. CASPEC observations of sdO stars - Are some sdOs lazy remnants from the AGB? *The Messenger* 1987; 47:36–38.

[258] Dorman B, Rood RT, O'Connell RW. Ultraviolet Radiation from Evolved Stellar Populations. I. Models. *ApJ* 1993; 419:596.

[259] Bloecker T. Stellar evolution of low- and intermediate-mass stars. II. Post-AGB evolution. *AAP* 1995; 299:755.

[260] Götberg Y, de Mink SE, Groh JH, Kupfer T, Crowther PA, Zapartas E, Renzo M. Spectral models for binary products: Unifying subdwarfs and Wolf-Rayet stars as a sequence of stripped-envelope stars. *AAP* 2018; 615:A78.

[261] Paxton B, Smolec R, Schwab J, Gautschy A, Bildsten L, Cantiello M, Dotter A, Farmer R, Goldberg JA, Jermyn AS, Kanbur SM, Marchant P, Thoul A, Townsend RHD, Wolf WM, Zhang M, Timmes FX. Modules for Experiments in Stellar Astrophysics (MESA): Pulsating Variable Stars, Rotation, Convective Boundaries, and Energy Conservation. *ApJS* 2019; 243:10.

[262] Moehler S. Hot Stars in Globular Clusters: A Spectroscopist's View. *PASP* 2001; 113:1162–1177.

[263] Young A, Nelson B, Mielbrecht R. An Old Evolved Binary in the Galactic Halo. *ApJ* 1972; 174:27.

[264] Kupfer T, Geier S, Heber U, Østensen RH, Barlow BN, Maxted PFL, Heuser C, Schaffenroth V, Gänsicke BT. Hot subdwarf binaries from the MUCHFUSS project. Analysis of 12 new systems and a study of the short-period binary population. *A&A* 2015; 576:A44.

[265] Saffer RA, Keenan FP, Hambly NC, Dufton PL, Liebert J. A Large-Scale Spectroscopic Survey of Early-Type Stars at High Galactic Latitudes. *ApJ* 1997; 491:172–180.

[266] Ramspeck M, Heber U, Edelmann H. Early type stars at high galactic latitudes. II. Four evolved B-type stars of unusual chemical composition. *AAP* 2001; 379:235–244.

[267] Vennes S, Kawka A, Smith JA. CPD -20 1123 (Albus 1) Is a Bright He-B Subdwarf. *ApJL* 2007; 668:L59–L61.

[268] Naslim N, Jeffery CS, Ahmad A, Behara NT, Şahìn T. Abundance analyses of helium-rich subluminous B stars. *MNRAS* 2010; 409:582–590.

[269] Østensen RH, Degroote P, Telting JH, Vos J, Aerts C, Jeffery CS, Green EM, Reed MD, Heber U. KIC 1718290: A Helium-rich V1093-Her-like Pulsator on the Blue Horizontal Branch. *ApJL* 2012; 753:L17.

[270] Geier S, Østensen RH, Heber U, Kupfer T, Maxted PFL, Barlow BN, Vučković M, Tillich A, Müller S, Edelmann H, Classen L, McLeod AF. Orbital solutions of eight close sdB binaries and constraints on the nature of the unseen companions. *AAP* 2014; 562:A95.

[271] Schneider D, Irrgang A, Heber U, Nieva MF, Przybilla N. NLTE spectroscopic analysis of the ^{3}He anomaly in subluminous B-type stars. *AAP* 2018; 618:A86.

[272] van Winckel H. Post-AGB Stars. *ARAA* 2003; 41:391–427.

[273] Moehler S, Landsman WB, Lanz T, Miller Bertolami MM. Hot UV-bright stars of galactic globular clusters. *AAP* 2019; 627:A34.

[274] Heber U, Kudritzki RP. NLTE-analysis of the sdO star ROB 162 in the globular cluster NGC 6397. *AAP* 1986; 169:244–250.

[275] Chayer P, Dixon WV, Fullerton AW, Ooghe-Tabanou B, Reid IN. FUSE, STIS and Keck spectroscopic analysis of the UV-bright star vZ 1128 in M3 (NGC 5272). *MNRAS* 2015; 452:2292–2305.

[276] Podsiadlowski P. "The Evolution of Close Binaries", Vol. 401 of *Astronomical Society of the Pacific Conference Series*, p. 63. 2008.

[277] Kupfer T, Bauer EB, Marsh TR, van Roestel J, Bellm EC, Burdge KB, Coughlin MW, Fuller J, Hermes J, Bildsten L, Kulkarni SR, Prince TA, Szkody P, Dhillon VS, Murawski G, Burruss R, Dekany R, Delacroix A, Drake AJ, Duev DA, Feeney M, Graham MJ, Kaplan DL, Laher RR, Littlefair SP, Masci FJ, Riddle R, Rusholme B, Serabyn E, Smith RM, Shupe DL, Soumagnac MT. The first ultracompact Roche lobe-filling hot subdwarf binary. *arXiv e-prints* 2020; p. arXiv:2002.01485.

[278] Marsh TR, Nelemans G, Steeghs D. Mass transfer between double white dwarfs. *MNRAS* 2004; 350:113–128.

[279] Shen KJ, Boubert D, Gänsicke BT, Jha SW, Andrews JE, Chomiuk L, Foley RJ, Fraser M, Gromadzki M, Guillochon J, Kotze MM, Maguire K, Siebert MR, Smith N, Strader J, Badenes C, Kerzendorf WE, Koester D, Kromer M, Miles B, Pakmor R, Schwab J, Toloza O, Toonen S, Townsley DM, Williams BJ. Three Hypervelocity White Dwarfs in Gaia DR2: Evidence for Dynamically Driven Double-degenerate Double-detonation Type Ia Supernovae. *ApJ* 2018; 865:15.

[280] Perets HB, Zenati Y, Toonen S, Bobrick A. Normal type Ia supernovae from disruptions of hybrid He-CO white-dwarfs by CO white-dwarfs. *arXiv e-prints* 2019; p. arXiv:1910.07532.

[281] Zenati Y, Toonen S, Perets HB. Formation and evolution of hybrid He-CO white dwarfs and their properties. *MNRAS* 2019; 482:1135–1142.

[282] Cheng S, Cummings JD, Ménard B, Toonen S. Double-White-Dwarf Merger Products among High-Mass White Dwarfs. *arXiv e-prints* 2019; p. arXiv:1910.09558.

[283] Tremblay PE, Cummings J, Kalirai JS, Gänsicke BT, Gentile-Fusillo N, Raddi R. The field white dwarf mass distribution. *MNRAS* 2016; 461:2100–2114.

[284] Kilkenny D, Koen C, O'Donoghue D, Stobie RS. A new class of rapidly pulsating star - I. EC 14026-2647, the class prototype. *MNRAS* 1997; 285:640–644.

[285] Fontaine G, Brassard P, Charpinet S, Green EM, Chayer P, Billères M, Rand all SK. A Driving Mechanism for the Newly Discovered Long-Period Pulsating Subdwarf B Stars. *ApJ* 2003; 597:518–534.

[286] Green EM, Fontaine G, Reed MD, Callerame K, Seitenzahl IR, White BA, Hyde EA, Østensen R, Cordes O, Brassard P, Falter S, Jeffery EJ, Dreizler S, Schuh SL, Giovanni M, Edelmann H, Rigby J, Bronowska A. Discovery of A New Class of Pulsating Stars: Gravity-Mode Pulsators among Subdwarf B Stars. *ApJL* 2003; 583:L31–L34.

[287] Vučković M, Aerts C, Östensen R, Nelemans G, Hu H, Jeffery CS, Dhillon VS, Marsh TR. The binary properties of the pulsating subdwarf B eclipsing binary ¡ASTROBJ¿PG 1336-018¡/ASTROBJ¿ (NY Virginis). *AAP* 2007; 471:605–615.

[288] Green EM, Guvenen B, O'Malley CJ, O'Connell CJ, Baringer BP, Villareal AS, Carleton TM, Fontaine G, Brassard P, Charpinet S. The Unusual Variable Hot B Subdwarf LS IV-14°116. *ApJ* 2011; 734:59.

[289] Latour M, Green EM, Fontaine G. Discovery of a second pulsating intermediate helium-enriched sdOB star. *AAP* 2019; 623:L12.

[290] Barlow BN, Dunlap BH, Clemens JC, Lynas-Gray AE, Ivarsen KM, Lacluyze AP, Reichart DE, Haislip JB, Nysewander MC. Photometry and spectroscopy of the new sdBV CS 1246. *MNRAS* 2010; 403:324–334.

[291] Oreiro R, Ulla A, Pérez Hernández F, Østensen R, Rodríguez López C, MacDonald J. ¡ASTROBJ¿Balloon 090100001¡/ASTROBJ¿: A bright, high amplitude sdB pulsator. *AAP* 2004; 418:243–247.

[292] Kupfer T, Bauer EB, Burdge KB, Bellm EC, Bildsten L, Fuller J, Hermes J, Kulkarni SR, Prince TA, van Roestel J, Dekany R, Duev DA, Feeney M, Giomi M, Graham MJ, Kaye S, Laher RR, Masci FJ, Porter M, Riddle R, Shupe DL, Smith RM, Soumagnac MT, Szkody P, Ward C. A New Class of Large-amplitude Radial-mode Hot Subdwarf Pulsators. *ApJL* 2019; 878:L35.

[293] Østensen RH, Reed MD, Baran AS, Telting JH. Stochastic pulsations in the subdwarf-B star KIC 2991276. *AAP* 2014; 564:L14.

[294] Hambleton K, Fuller J, Thompson S, Prša A, Kurtz DW, Shporer A, Isaacson H, Howard AW, Endl M, Cochran W, Murphy SJ. KIC 8164262: a heartbeat star showing tidally induced pulsations with resonant locking. *MNRAS* 2018; 473:5165–5176.

[295] Burkart J, Quataert E, Arras P, Weinberg NN. Tidal asteroseismology: Kepler's KOI-54. *MNRAS* 2012; 421:983–1006.

[296] Witte MG, Savonije GJ. Orbital evolution by dynamical tides in solar type stars. Application to binary stars and planetary orbits. *AAP* 2002; 386:222–236.

[297] Hunter JD. Matplotlib: A 2D Graphics Environment. *Computing in Science and Engineering* 2007; 9:90–95.

[298] van der Walt S, Colbert SC, Varoquaux G. The NumPy Array: A Structure for Efficient Numerical Computation. *Computing in Science and Engineering* 2011; 13:22–30.

[299] Irrgang A, Wilcox B, Tucker E, Schiefelbein L. Milky Way mass models for orbit calculations. *AAP* 2013; 549:A137.

[300] Allen C, Santillan A. An improved model of the galactic mass distribution for orbit computations. *RMxAA* 1991; 22:255.

[301] Pauli EM, Napiwotzki R, Altmann M, Heber U, Odenkirchen M, Kerber F. 3D kinematics of white dwarfs from the SPY project. *AAP* 2003; 400:877–890.

[302] Pauli EM, Napiwotzki R, Heber U, Altmann M, Odenkirchen M. 3D kinematics of white dwarfs from the SPY project. II. *AAP* 2006; 447:173–184.

[303] Fuhrmann K. Nearby stars of the Galactic disk and halo. III. *Astronomische Nachrichten* 2004; 325:3–80.

[304] Schindewolf M, Levitan D, Heber U, Drechsel H, Schaffenroth V, Kupfer T, Prince T. A new HW Vir binary from the Palomar Transient Factory. PTF1 J072455.75+125300.3: An eclipsing subdwarf B binary with a M-star companion. *AAP* 2015; 580:A117.

[305] Schaffenroth V, Barlow BN, Drechsel H, Dunlap BH. An eclipsing post common-envelope system consisting of a pulsating hot subdwarf B star and a brown dwarf companion. *AAP* 2015; 576:A123.

[306] Schaffenroth V, Barlow B, Geier S, Vučković M, Kilkenny D, Schaffenroth J. News From The Erebos Project. *Open Astronomy* 2017; 26:208–213.

[307] Fontaine G, Brassard P, Charpinet S, Green EM, Randall SK, Van Grootel V. A preliminary look at the empirical mass distribution of hot B subdwarf stars. *AAP* 2012; 539:A12.

[308] Drechsel H, Haas S, Lorenz R, Gayler S. Radiation pressure effects in early-type close binaries and implications for the solution of eclipse light curves. *AAP* 1995; 294:723–743.

[309] Wilson RE, Devinney EJ. Realization of Accurate Close-Binary Light Curves: Application to MR Cygni. *ApJ* 1971; 166:605.

[310] Lee JW, Kim SL, Kim CH, Koch RH, Lee CU, Kim HI, Park JH. The sdB+M Eclipsing System HW Virginis and its Circumbinary Planets. *AJ* 2009; 137:3181–3190.

[311] Østensen R, Oreiro R, Drechsel H, Heber U, Baran A, Pigulski A. "HS 2231+2441: A New Eclipsing sdB Binary of the HW Vir Type", Vol. 372 of *Astronomical Society of the Pacific Conference Series*, p. 483. 2007.

[312] For BQ, Green EM, Fontaine G, Shaw S. A rare reflection effect eclipsing sdB+dM binary: 2M 1533+3759. *ApSS* 2010; 329:87–90.

[313] Schaffenroth V, Geier S, Heber U, Kupfer T, Ziegerer E, Heuser C, Classen L, Cordes O. Binaries discovered by the MUCHFUSS project. SDSS J162256.66+473051.1: An eclipsing subdwarf B binary with a brown dwarf companion. *AAP* 2014; 564:A98.

[314] Drechsel H, Heber U, Napiwotzki R, Østensen R, Solheim JE, Johannessen F, Schuh SL, Deetjen J, Zola S. HS 0705+6700: A new eclipsing sdB binary. *AAP* 2001; 379:893–904.

[315] Østensen RH, Green EM, Bloemen S, Marsh TR, Laird JB, Morris M, Moriyama E, Oreiro R, Reed MD, Kawaler SD, Aerts C, Vučković M, Degroote P, Telting JH, Kjeldsen H, Gilliland RL, Christensen-Dalsgaard J, Borucki WJ, Koch D. 2M1938+4603: a rich, multimode pulsating sdB star with an eclipsing dM companion observed with Kepler. *MNRAS* 2010; 408:L51–L55.